
Annual Reports on
NMR SPECTROSCOPY

VOLUME **67**

Edited by

GRAHAM A. WEBB

Royal Society of Chemistry

Burlington House

Piccadilly, London, UK



Amsterdam • Boston • Heidelberg • London • New York • Oxford
Paris • San Diego • San Francisco • Singapore • Sydney • Tokyo
Academic Press is an imprint of Elsevier



Academic Press is an imprint of Elsevier
Linacre House, Jordan Hill, Oxford OX2 8DP, UK
32, Jamestown Road, London NW1 7BY, UK
Radarweg 29, PO Box 211, 1000 AE Amsterdam, The Netherlands
30 Corporate Drive, Suite 400, Burlington, MA 01803, USA
525 B Street, Suite 1900, San Diego, CA 92101-4495, USA

First edition 2009

Copyright © 2009 Elsevier Ltd. All rights reserved

No part of this publication may be reproduced, stored in a retrieval system or transmitted in any form or by any means electronic, mechanical, photocopying, recording or otherwise without the prior written permission of the publisher

Permissions may be sought directly from Elsevier's Science & Technology Rights Department in Oxford, UK: phone (+44) (0) 1865 843830; fax (+44) (0) 1865 853333; email: permissions@elsevier.com. Alternatively you can submit your request online by visiting the Elsevier web site at <http://www.elsevier.com/locate/permissions>, and selecting *Obtaining permission to use Elsevier material*

Notice

No responsibility is assumed by the publisher for any injury and/or damage to persons or property as a matter of products liability, negligence or otherwise, or from any use or operation of any methods, products, instructions or ideas contained in the material herein. Because of rapid advances in the medical sciences, in particular, independent verification of diagnoses and drug dosages should be made

ISBN: 978-0-12-375058-7

ISSN: 0066-4103

For information on all Academic Press publications
visit our web site at elsevierdirect.com

Printed and bound in Great Britain

09 10 11 12 13 10 9 8 7 6 5 4 3 2 1

Working together to grow
libraries in developing countries

www.elsevier.com | www.bookaid.org | www.sabre.org

ELSEVIER

BOOK AID
International

Sabre Foundation

CONTRIBUTORS

J. Autschbach

Department of Chemistry, University at Buffalo, State University of New York,
Buffalo, NY, USA

Bikash Baishya

NMR Research Centre, Indian Institute of Science, Bangalore, India

Vratislav Blechta

Institute of Chemical Process Fundamentals, Academy of Sciences of Czech
Republic, Czech Republic

N. Chandrakumar

Department of Chemistry, Indian Institute of Technology-Madras, Chennai,
Tamil Nadu, India

Uday R. Prabhu

NMR Research Centre, Indian Institute of Science, Bangalore, India; Solid State
and Structural Chemistry Unit, Indian Institute of Science, Bangalore, India

N. Suryaprakash

NMR Research Centre, Indian Institute of Science, Bangalore, India

S. Zheng

Department of Chemistry, University at Buffalo, State University of New York,
Buffalo, NY, USA

PREFACE

It is my pleasure to introduce Volume 67 of *Annual Reports on NMR*. As is usual with this series of reports, contributions from a diverse selection of fields of research activity are included.

The first area to be covered is 'Relativistic Computations of NMR Parameters from First Principles: Theory and Applications' by J. Autschbach and S. Zheng; V. Blechta provides an account of 'Applications of Silicon–Carbon Coupling Constants'; following this is a review of '1D Double Quantum Filter NMR Studies' by N. Chandrakumar; finally B. Baishya, U.R. Prabhu and N. Suryaprakash cover the 'Analysis of Proton NMR Spectra of Strongly and Weakly Dipolar Coupled Spins: Special Emphasis on Spectral Simplification, Chiral Discrimination, and Discerning of Degenerate Transitions'.

My thanks go to all of these reporters for their thorough and interesting contributions. I am also indebted to the Elsevier production staff for their efforts in the timely appearance of the volumes of *Annual Reports on NMR*.

G.A. Webb
Royal Society of Chemistry
Burlington House
Piccadilly
London, UK

Relativistic Computations of NMR Parameters from First Principles: Theory and Applications

J. Autschbach and **S. Zheng**

Contents		
1. Introduction		2
2. Relativistic Methods for NMR Computations		4
2.1 The importance of special relativity in chemistry		5
2.2 Defining nuclear shielding and spin–spin coupling parameters as second-order energy derivatives		6
2.3 Energy and wavefunctions: relativistic vs. nonrelativistic		8
2.4 Computing energy derivatives to second order		16
2.5 Perturbation operators for NMR: relativistic vs. nonrelativistic approaches		20
2.6 Contributions from the various operators to shielding and spin–spin coupling		26
2.7 The gauge-origin problem for the nuclear magnetic shielding		28
2.8 Vibrational and thermal averaging; isotope effects		29
2.9 Analyzing NMR parameters from first-principles computations		30
3. Benchmark Data and Case Studies		32
3.1 Acronyms used		32
3.2 Illustrative examples for the influence of relativity: the FC term in PbH ₄ and the spin–orbit shielding in HI		33
3.3 When are relativistic methods needed for NMR computations?		38
3.4 Chemical shifts in heavy-element systems		40
3.5 Spin–spin coupling in heavy-element systems		68
3.6 Electric field gradients		83
4. Concluding Remarks		87
Acknowledgments		87
References		87

Abstract

An overview of relativistic theoretical methods to calculate NMR parameters (nuclear magnetic shielding and indirect spin–spin coupling) of molecules with heavy nuclei is presented. Computational benchmark data and a number of case studies are discussed, with emphasis on first-principles methods (wavefunction-based *ab initio* methods or density functional theory). The chapter also contains a brief section about relativistic computations of electric field gradient (EFG) tensors.

Keywords: quantum theory; density functional theory; chemical shift; indirect nuclear spin–spin coupling; electric field gradients; relativistic effects

1. INTRODUCTION

The past 10 years have seen a surge in computations of NMR parameters based on first-principles theory and *relativistic* methods. Having once been a niche for specialists, relativistic quantum chemistry is now a mature field of research and its products have started to enter the mainstream of computational chemistry. Efficient relativistic computational methods continue to make their way into popular program packages. It has long been realized that heavy-element chemistry is significantly influenced by the extremely large electron velocities caused by high nuclear charges in atoms and molecules. To describe the electronic structure in such a system calls for a consideration of Einstein's special relativity.^a

Relativistic effects are the differences between the results of a relativistic and a nonrelativistic calculation. The word *nonrelativistic* refers here to Galilei's principle of relativity where velocities simply add up, as opposed to Einstein's relativity principle. Since the laws of nature are relativistic, relativistic effects as defined here are not observable experimentally. However, when considering the behavior of elements down the groups and along the rows of the periodic table, there are numerous trends, reversal of trends, and peculiar behavior of heavy elements that are clearly attributable to relativistic effects. They contribute to the observable chemical and physical properties of many atoms and molecules. Examples where relativistic effects, along with the lanthanoid contraction, influence chemical properties are the rather small atomic radii of heavy elements (e.g., $\text{Cu} < \text{Ag} \approx \text{Au}$) or the stabilization of low oxidation numbers for heavy main group elements (Tl(I) vs. Tl(III), Pb(II) vs. Pb(IV), etc.). Famous examples are the special stability of the 6s shells of Au and Hg which are partially responsible for the color of solid gold and the liquid state of mercury under ambient conditions. These and numerous other examples have been collected by Pyykkö in a seminal review paper.¹ It has been somewhat controversial for some time why relativistic effects are large for *valence* shells; we will briefly comment on this in Section 2.

Molecular properties are in quantum theory represented by their corresponding operators. If these operators are large, in the vicinity of the nuclei a property

^aAn influence from *gravitational forces* between pairs of electrons or electrons and nucleons that would require general relativity can be safely neglected for chemical phenomena.

can be particularly susceptible to relativistic effects. This is certainly the case for NMR-relevant molecular parameters, for instance, for nuclear magnetic shielding and chemical shifts, indirect or reduced indirect nuclear spin–spin coupling (J -coupling), or nuclear quadrupole coupling which is particularly important in solid-state NMR (SSNMR) of quadrupolar nuclei. For NMR parameters of heavy NMR nuclei such as W, Pt, Hg, Tl, and Pb, relativistic effects can be spectacularly large, in their relative magnitude sometimes far surpassing relativistic effects on other molecular properties. For somewhat lighter elements (Xe, Te, I, Sn, Cd, etc.), relativistic effects can still play an important role; particularly noteworthy are spin–orbit (SO) coupling effects on the chemical shifts of nearby nuclei induced by heavy p-block elements.

Methodology for relativistic computations of NMR parameters based on first-principles theory is not quite as widespread as methods to compute structure and energy. Nonetheless, researchers have now a range of computational methods at their disposal to perform such computations efficiently and often with impressive accuracy. Theoretical and computational methods for NMR chemical shifts and J -coupling were specifically reviewed in 2002.² Ref. 3 is a convenient source of information regarding magnetic resonance parameter computations which also contains several chapters specifically dedicated to relativistic effects, covering literature up to 2003.^{4–6} We further note a 2002 review by Vaara et al. which contains many references to relativistic J -coupling computations,⁷ a review by Kaupp on relativistic effects on nuclear shielding,⁸ several reviews on NMR computations of transition metal NMR parameters where relativistic effects were mentioned,^{9–11} and a number of more general articles on molecular property computations in which NMR parameters and relativistic effects were considered.^{12,13} Bühl has recently reviewed density functional theory (DFT) computations of transition metal chemical shifts¹⁴; this article is a rich source of information including the most recent computational work on heavy metal chemical shifts. See also a recent review on *ab initio* calculations of NMR chemical shifts¹⁵ featuring a section on relativistic methods, as well as the review series on nuclear magnetic shielding by C. Jameson, and by C. Jameson and A. de Dios, in the *Nuclear Magnetic Resonance, Specialist Periodical Reports* series of publications. Recent years have seen a sizeable number of new applications of relativistic NMR programs as well as new theoretical developments, thus providing motivation for writing this chapter, with the aim of collecting some old and new benchmark data in a single chapter and highlighting results from various applications that were performed over the past decade. We also take the opportunity to present some of the underlying formalism in a self-contained manner. Apart from shielding and spin–spin coupling, a “nuclear” property that is also strongly affected by relativistic effects and that plays an important role in the interpretation of SSNMR spectra is the nuclear quadrupole coupling tensor which is proportional to the electric field gradient (EFG) at the nuclear position. A short section on relativistic effects of EFGs has therefore been included at the end of our survey.

This chapter is organized as follows: we will begin Section 2 by describing some of the theoretical basics of relativistic NMR computations. The first part will

be devoted to the origin of relativistic effects of valence orbitals in heavy atoms, followed by an outline of some general aspects of relativistic quantum chemistry that the reader should be aware of. Next, differences between the well-known nonrelativistic formalism of Ramsey and various relativistic formulations for NMR parameters will be discussed. Section 2.6 partially summarizes these sections by highlighting the origin of SO and scalar-relativistic effects as related to the perturbation operators. After a discussion of the so-called gauge-origin problem, and a discussion of how to include dynamic effects, a brief subsection follows which is devoted to various aspects of *analyzing* NMR parameters in a molecular-orbital framework. Section 3 is devoted to case studies and benchmark data, with emphasis on NMR parameters in heavy transition metal complexes and molecules with heavy main group elements. Some well-known benchmark systems such as the H-X series ($X = \text{F, Cl, Br, I}$) will also be discussed because these and other small molecules keep being used as the main test cases for new theoretical developments. After a short section on EFGs and their relativistic effects, some concluding remarks can be found in Section 4.

2. RELATIVISTIC METHODS FOR NMR COMPUTATIONS

Full quantum mechanical studies of molecules involving all degrees of freedom are rarely undertaken and, for large molecules, hardly feasible at present. NMR parameters are *electronic* properties. Thus, in this section we will focus on the electronic degrees of freedom. The Born–Oppenheimer approximation is assumed throughout. Correction terms to NMR parameters due to nuclear vibrations and internal rotations may be computed separately; Section 2.8 will be devoted to this topic. Electromagnetic fields will be treated semiclassically, not as quantized fields. The program implementations to compute NMR parameters quantum mechanically as discussed in this chapter are based on these approximations. We will also focus on closed-shell molecules and forgo a discussion of paramagnetic NMR.¹⁶

In the methodology section, Hartree atomic units (a.u.) are used throughout. Here, the electron mass $m_e = 1$, unit of charge $e = 1$, the proportionality constant in Coulomb’s law $1/(4\pi\epsilon_0) = 1$, Planck’s constant $\hbar = 2\pi$, and speed of light $c \approx 137.036$ a.u. Factors of 1 (e , m_e , $1/(4\pi\epsilon_0)$, and $\hbar/2\pi$) will usually be dropped. Results are generally computed in these dimensionless a.u. and converted to the desired units afterwards, for example, masses are in electron masses, lengths in bohr radii ($a_0 = 52.918$ pm), and energies in Hartree ($1 \text{ H} = 2,625.5 \text{ kJ/mol}$). In a universe with an infinite speed of light, there would be no difference between Einstein’s special relativity and Galilei relativity and the Schrödinger equation would provide the correct description of chemical phenomena. Therefore, the nonrelativistic limit of a particular equation can be obtained from letting the speed of light $c \rightarrow \infty$. For magnetic properties, we follow the choice of McWeeny’s textbook¹⁷ here, based on equations in SI units that are converted to a.u. using the conversion factors above. Factors of $\mu_0/(4\pi)$ translate to $1/c^2$ factors in a.u. which do not indicate relativistic corrections and cannot be set to zero when taking

nonrelativistic limits. Nuclear magnetic shielding constants are dimensionless and therefore no unit conversions are needed. Reduced spin–spin couplings K are converted from a.u. as follows: the SI unit is T^2/J , or alternatively $\text{kg}/(\text{m}^2\text{C}^2)$; thus, the a.u. is $m_e/(a_0^2e^2)$ which is approximately equal to $1.267 \times 10^{27} \text{ kg}/(\text{m}^2\text{C}^2)$. In SI units, the nuclear magnetic moment vector potential carries a factor of $\mu_0/(4\pi)$, the square of which enters the final result for the coupling constant. Due to its smallness, this $1/c^4$ factor is usually omitted during the computation — to avoid small numbers — and instead absorbed in the final conversion from a.u. to SI. The numerical conversion factor from “a.u.” (excluding the c^{-4} factor) to SI units is in this case $1.267 \times 10^{27}/(137.0)^4$ or 3.593×10^{19} . Indeed, K -couplings are often on the order of a few to a few thousand 10^{19} SI units.

2.1 The importance of special relativity in chemistry

Relativistic effects are critically dependent on the nuclear charges involved. To understand why, it is illustrative to consider the Bohr model: the energy of the electron in the Bohr model with a nuclear charge Z is $E = -Z^2/2$ a.u. which also happens to be the correct quantum mechanical result (for a point nucleus). According to the virial theorem, the kinetic energy is $T = -E = +Z^2/2$. Since in classical physics $T = (1/2)mv^2$, one can infer a “velocity” for the electron of $+Z$ a.u. ($m_e = 1$ a.u., thus $v = \sqrt{2T}$). In these units, $c \approx 137$ and therefore a substantial fraction of the speed of light is reached in atoms with heavy nuclei, at least in the 1s shell. Relativistic effects in classical physics are on the order $(Z/c)^2$; for a Hg nucleus, this amounts to about 34%.

At first sight, it is perhaps not obvious why relativistic effects should play a big role in chemistry: the chemical behavior as well as trends in NMR parameters such as nuclear magnetic shielding and indirect spin–spin coupling is predominantly determined by what happens in the *valence* shell of the atoms. The inner shells shield the nucleus and the electrons should only be exposed to an effective charge $Z_{\text{eff}} \ll Z$, where Z_{eff} is typically within the same range of small values no matter what the atom is. Thus, one may expect relativistic effects in the valence shells of all atoms to be small and not increasing substantially as Z increases. However, this is not found when performing relativistic computations: instead, the relativistic effects on valence-orbital energies are of the same leading order $(Z/c)^2$, not $(Z_{\text{eff}}/c)^2$, and can even be of similar magnitude, percentage-wise, as those for core orbitals.¹⁸

Valence orbitals in heavy atoms are orthogonal to inner orbitals. As a consequence, valence orbitals have *tails* in the outer and inner core regions. A possible origin of the relativistic effects on valence orbitals could therefore be that they are simply reacting via orthogonalization on the relativistic effects of the innermost orbitals which see the bare or nearly the bare nuclear charge Z . However, it has been found that this is not the important mechanism¹⁸: instead, through relativistic modification of the kinetic and potential energy operators, the valence orbitals afford *direct* relativistic effects, in particular s and $p_{1/2}$ orbitals. These effects can be large for valence orbitals in heavy atoms because the inner tails are exposed to a much less shielded nuclear charge than what would be

expected for the orbital's outermost density maximum. These effects have profound implications for the chemical and physical properties of heavy-element compounds. Typically, in neutral many-electron atoms, s- and p-orbitals relativistically stabilize and contract,^b whereas d- and f-orbitals expand and become less stabilized mainly as a consequence of s and p contraction within the same atomic shell and in the shell with next higher quantum number.¹⁹ In molecules, bonds often shorten relativistically (although counter examples are known) and in many cases the bonds are stabilized. The origin of these effects has been thoroughly investigated.^{1,18}

2.2 Defining nuclear shielding and spin–spin coupling parameters as second-order energy derivatives

This section contains little new for a scientist who is familiar with NMR but it will help to introduce some notations needed later. Consider the presence of nuclear spin magnetic moments $\mathbf{m}_A, \mathbf{m}_B, \dots$ of nuclei A, B, \dots in a molecule, and a static homogeneous external magnetic field \mathbf{B} . The magnetic moment is related to the nuclear spin I_A via $\mathbf{m}_A = \gamma_A I_A$, where γ_A is the nuclear magneto-gyric ratio. The nuclear shielding σ_A and the indirect nuclear spin–spin coupling \mathbb{K}_{AB} are rank-2 tensors^c that can be defined via the phenomenological Hamiltonians

$$H = -\mathbf{m}_A(1 - \sigma_A)\mathbf{B} \quad (1a)$$

for the shielding tensor and

$$H = \mathbf{m}_A \mathbb{K}_{AB} \mathbf{m}_B \quad (1b)$$

for the spin–spin coupling. σ_A is dimensionless and usually reported in parts per million (ppm). \mathbb{K}_{AB} is in SI units given in T²/J (or kg/(m²C²)) and, as mentioned earlier, it tends to be on the order of one to several thousand times 10¹⁹ SI units. The isotropic shielding σ_A and spin–spin coupling constants K_{AB} are obtained from (1/3) of the sum of the principal values of the tensors. Just like in the experiment, the chemical shift δ is defined via a reference (ref) nucleus. In terms of shielding constants, the chemical shift is given as

$$\delta = \frac{\sigma^{\text{ref}} - \sigma}{1 - \sigma^{\text{ref}}} \quad (2)$$

which is to a very good approximation equal to $\sigma^{\text{ref}} - \sigma$ for chemical shifts of light nuclei where σ and σ^{ref} are small. The approximation is often also used for heavy-element shifts where shielding constants can be on the order of 10⁴ ppm; however, this may lead to deviations on the order of a percent compared to (2). The reference can also be a hypothetical shielding related to a well-defined spectrometer frequency, as it is customary, for example, for ¹⁰³Rh NMR.²⁰

^bHere and in the following, a statement like this refers to a comparison of a relativistic with a nonrelativistic calculation.

^cWe use fonts like in $\mathbb{A}, \mathbb{B}, \mathbb{C}, \dots$ to indicate matrices and tensors in this chapter.

In first-principles theory, the problem is approached as follows: the electronic energy of the molecule is considered in the presence of the external magnetic field and the nuclear spins. In a next step, the energy expression is expanded in a power series (perturbation series) in the magnetic moments and the external field around $\mathbf{B} = 0$; $\mathbf{m}_A = 0$, $\mathbf{m}_B = 0$ which yields

$$E(\mathbf{m}_A, \mathbf{m}_B, \mathbf{B}) = E^{(0)} + E^{(m_A)} \mathbf{m}_A + E^{(m_B)} \mathbf{m}_B + E^{(B)} \mathbf{B} \\ + \mathbf{m}_A E^{(m_A, m_B)} \mathbf{m}_B + \mathbf{m}_A E^{(m_A, B)} \mathbf{B} + \text{higher orders} \quad (3)$$

Here, a symbol $E^{(A)}$ indicates the partial derivative of E with respect to a variable A , taken at the expansion point, $E^{(A, B)}$ a second derivative, and so on, and $E^{(0)}$ the energy in the absence of the field and the magnetic moments. The shielding and spin-spin coupling tensors are then, according to Equation (1), given by the energy terms bilinear in the magnetic moments (\mathbb{K}_{AB}) and bilinear in one of the magnetic moments and the external field (σ_A).^d Thus, by comparison with the phenomenological Hamiltonians (1a) and (1b), one identifies the two bilinear energy-derivative terms at the end of expression (3) with the NMR K -coupling and the nuclear magnetic shielding. NMR parameters are “double perturbation properties” (with respect to the molecular energy as the perturbed quantity). Explicit expressions will be given later. We will also see later that the first-order response^e of the electrons due to the presence of the field and the nuclear magnetic moment is required to compute the shielding and K -coupling tensor; therefore, nuclear shielding and K -coupling may also be called *linear response* properties of the molecule.

The nuclear Zeeman term $-\mathbf{m}_A \cdot \mathbf{B}$ is not part of the electronic energy. It accounts for the “1” in $(1 - \sigma_A)$ of Equation (1a). Thus, with E being the electronic energy, one defines

$$\sigma_A = E^{(m_A, B)} = \left. \frac{\partial^2 E}{\partial \mathbf{m}_A \partial \mathbf{B}} \right|_{\substack{\mathbf{m}_A=0 \\ \mathbf{B}=0}} \quad (4)$$

and

$$\mathbb{K}_{AB} = E^{(m_A, m_B)} = \left. \frac{\partial^2 E}{\partial \mathbf{m}_A \partial \mathbf{m}_B} \right|_{\substack{\mathbf{m}_A=0 \\ \mathbf{B}=0}} \quad (5)$$

Both expressions are in formal agreement with the phenomenological Hamiltonians (1a) and (1b). Measured J -coupling constants are related to the rotational average of the K -coupling tensor as

$$J_{AB} = \frac{\hbar}{2\pi} \gamma_A \gamma_B K_{AB} \quad (6)$$

with magnitudes typically on the order of a few to a few thousand Hertz.

^dNote that the differentiations are with respect to vectors, that is, the result is a quantity with two indices, one for a component of each of the perturbing vectors.

^e“Response” means the following here: how, to first order, does the electronic structure change due to (respond to) the presence of the field/magnetic moments?

It should be emphasized that chemical shifts σ and indirect nuclear spin–spin coupling constants K are response properties of the *electronic* system. Their measurement by NMR obviously relies on the presence of nuclear spins but the computational result is dependent neither on the nuclear spins, nor on the magneto-gyric ratios. Therefore, in the “clamped nucleus” approximation, chemical shifts calculated for different isotopes of the same element are identical. Isotope effects on chemical shifts, spin–spin coupling, and other response properties can be obtained from considering vibrational corrections or by treating the system dynamically. If calculated J -coupling constants are reported, then obviously the value depends on the isotopes via the magneto-gyric ratios (Equation (6)), whereas the indirect couplings K are not isotope-dependent unless vibrational corrections are included.

The take-home message from this subsection is: nuclear shielding and spin–spin coupling can be computed from second derivatives of the energy as defined in Equations (4) and (5). The energy E in these expressions is the electronic energy of the atom or molecule. In quantum theory, this energy can be computed using approximate methods, among those Hartree–Fock (HF) and DFT, or explicitly correlated wavefunction-based methods. *If the energy E is a relativistic energy, then the NMR parameters afford relativistic effects and the formalism is applicable to heavy-element compounds. If the energy expression is from a nonrelativistic theory, the NMR parameters do not include relativistic effects unless added a posteriori.*

2.3 Energy and wavefunctions: relativistic vs. nonrelativistic

A brief overview of some popular relativistic quantum chemical methods will be given here to facilitate the discussion of the NMR operators in various relativistic schemes and in the nonrelativistic limit in Section 2.5. Much of the discussion in this section can also be found in ref. 2. Nonrelativistic quantum chemistry deals with the solution of the nonrelativistic time-independent many-electron Schrödinger equation

$$\hat{\mathcal{H}}_{\text{nrel}}\Psi = \Psi E \quad (7)$$

or approximations thereof. Here, Ψ is the many-electron wavefunction of an atom or molecule (as mentioned earlier, the nuclei are considered to be fixed in space) and E is called the total energy. The nonrelativistic Hamiltonian is

$$\hat{\mathcal{H}}_{\text{nrel}} = \sum_i \frac{\hat{p}_i^2}{2} + V_{\text{Ne}} + V_{\text{ee}} + V_{\text{NN}} \quad (8)$$

It contains the nonrelativistic kinetic energy operator $\hat{p}_i^2/2$ for each electron i , the electron–nucleus attraction potential $V_{\text{Ne}} = -\sum_{A,i} Z_A/r_{Ai}$ added up for each electron–nucleus pair, the nonrelativistic electron–electron Coulomb repulsion $V_{\text{ee}} = \sum_{j>i} 1/r_{ij}$, and the internuclear repulsion potential^f

^f V_{NN} is not an electronic term but usually added to the electronic energy such that E represents a potential energy surface that can be used to study chemical reactions, nuclear motion, and so on.

$V_{\text{NN}} = \sum_{B>A} Z_A Z_B / R_{AB}$. We use i and j for electron labels, \mathbf{r} for electron coordinates, labels A and B for nuclei, and \mathbf{R} for nuclear coordinate vectors. Further, r_{Ai} is an electron–nucleus distance, r_{ij} an electron–electron distance, and R_{AB} a nucleus–nucleus distance. Z_A is a nuclear charge, and $\hat{\mathbf{p}} = -i\nabla$ the momentum operator in space representation. Since analytic solutions of Equation (7) for many-electron systems are not feasible, approximations have to be made.

In relativistic quantum chemistry, $\hat{\mathcal{H}}_{\text{nrrel}}$ in Equation (7) is replaced by its relativistic counterpart and Ψ by a relativistic wavefunction. The challenges of nonrelativistic many-electron theory are present in the relativistic formulation as well, most importantly the electron correlation problem. Hence, similar techniques are common in order to find approximate solutions, in particular the use of orbital models, use of DFT, treating the electron correlation problem by perturbation theory or the coupled cluster (CC) ansatz, or other common methods. Moreover, it is customary to use basis functions in order to discretize the equations. Further, there are additional challenges specific to relativistic quantum chemistry. One of these has for some time been the lack of a relativistic many-particle Hamiltonian for general molecules derived from quantum electrodynamics (QED). Relativistic many-electron atomic and molecular computations often rely on the use of the four-component no-pair Dirac–Coulomb–Breit Hamiltonian (DCB) or some approximation obtained from it:

$$\hat{\mathcal{H}}_{\text{DCB}} = \sum_{i=1}^N (c\vec{\alpha}_i \hat{\mathbf{p}}_i + \beta_i c^2) + V_{\text{Ne}} + V_{\text{ee}} + \sum_{j>i=1}^N \hat{\mathcal{H}}_{ij}^{\text{B}} + V_{\text{NN}} \quad (9)$$

Here, $\vec{\alpha}$ and β are a set of 4×4 matrices introduced by Dirac in order to obtain a relativistic wave equation for spin-1/2 particles from the “classical” relativistic Hamilton function. In its standard representation, $\vec{\alpha}$ is written in terms of the well-known 2×2 Pauli spin-matrices $\vec{\sigma}_s$ (not to be confused with the symbol for the nuclear shielding tensor) as

$$\vec{\alpha} = \begin{pmatrix} 0 & \vec{\sigma}_s \\ \vec{\sigma}_s & 0 \end{pmatrix} \text{ and } \beta = \begin{pmatrix} 1 & 0 \\ 0 & -1 \end{pmatrix},$$

where each sub-matrix is of dimension 2×2 . See ref. 21 for further details. The $\hat{\mathcal{H}}_{ij}^{\text{B}}$ (Breit interaction; see, e.g., ref. 22) represents relativistic corrections to V_{ee} from magnetic interactions and further accounts for the fact that the electron–electron interaction is not instantaneous but is transmitted with a finite speed. It is possible to cure some problematic features of the Dirac–Coulomb (–Breit) operator by restricting its solutions to the positive energy spectrum, the eigenfunctions of which are identified with the desired electronic states (no-pair approximation^{23,24}). Although $\hat{\mathcal{H}}_{\text{DCB}}$ is in general not truly Lorentz invariant, it “provides an excellent approximation to the full theory.”²⁵ QED corrections may be added, for example, based on perturbation-theory calculations.

Apart from the $\hat{\mathcal{H}}_{ij}^B$ terms, the difference between the four-component relativistic and the nonrelativistic Hamiltonian is seen to be the replacement of the kinetic energy operator for an electron, $\hat{p}^2/2$ in $\hat{\mathcal{H}}_{\text{nrrel}}$, by the term $c\vec{\alpha}\hat{p} + \beta c^2$ in the relativistic Equation (9). This term takes into account, for instance, the relativistic increase of the electron mass due to high velocities, includes the electron's rest mass energy ($m_e c^2$), incorporates the electron spin-dependent terms in the Hamiltonian, and also causes the spin-orbit (SO) coupling. Although the electron spin needs to be considered also in the nonrelativistic theory in an *ad hoc* manner in order to account for experimental facts, a coupling between spin and orbital degrees of freedom occurs only in the relativistic theory. We will not explicitly consider the Breit interaction. Its relative importance to, for example, total atomic energies was found to decrease with increasing nuclear charge from $\sim 50\%$ in He to $\sim 2\%$ in Hg relative to the one-electron relativistic corrections.²⁶

As a starting point for practical computations, the N -electron equation is usually separated into N effective one-electron equations for one-particle wavefunctions ψ_i (atomic orbitals (AOs) or molecular orbitals (MOs)). An explicit treatment of correlation may follow in wavefunction-based methods. In DFT, the correlation effects are dealt with in the effective potential. For simplicity, we will refer to one-electron equations with an effective one-electron potential (or true one-electron systems) in the following, and use the symbol ψ for a one-electron wavefunction or orbital. Particular details of common approximations to treat the correlation problem will not be discussed here.

One way of performing a relativistic molecular computation in order to obtain a starting point for calculating energy-derivative properties is to use directly the Dirac equation

$$\hat{\mathcal{H}}_D \psi_D = \psi_D E \quad (10)$$

with

$$\hat{\mathcal{H}}_D = c\vec{\alpha}\hat{p} + \beta c^2 + V \quad (11)$$

Note that we use here the aforementioned notation for (effective) one-electron equations. Because $\vec{\alpha}$ and β are 4×4 matrices, the orbital ψ_D has to be a four-component object (a spinor)

$$\psi_D = \begin{bmatrix} \psi_1(\mathbf{r}) \\ \psi_2(\mathbf{r}) \\ \psi_3(\mathbf{r}) \\ \psi_4(\mathbf{r}) \end{bmatrix} \quad (12)$$

for which each component is in general a complex function of space. Due to the four components and complex algebra, such molecular computations tend to be quite demanding compared to nonrelativistic ones, and the explicit inclusion of electron correlation is a formidable task.

Many attempts have been made to transform the four-component Equation (10) into two-component form, in order to keep interpretations more

simple^g and to reduce the computational effort. Here we will give an account of some of these methods to illustrate the general idea. When writing $\vec{\alpha}$ explicitly in terms of the 2×2 Pauli spin-matrices $\vec{\sigma}_s$, the four-component Dirac Equation (10) reads

$$(\hat{\mathcal{H}}_D - E)\psi_D = \begin{pmatrix} V - E & c\vec{\sigma}_s\hat{\mathbf{p}} \\ c\vec{\sigma}_s\hat{\mathbf{p}} & V - E - 2c^2 \end{pmatrix} \begin{pmatrix} \varphi \\ \chi \end{pmatrix} = 0 \quad (13)$$

The zero of the energy scale has been shifted in the above-mentioned equation to $+mc^2$, $m = 1$, the rest mass energy of the electron, such that bound states have negative energy as usual in nonrelativistic quantum chemistry. Here, $\varphi = \begin{pmatrix} \psi_1 \\ \psi_2 \end{pmatrix}$ and $\chi = \begin{pmatrix} \psi_3 \\ \psi_4 \end{pmatrix}$ are the “upper” and “lower” components of the four-component orbital ψ_D . In turn, each of these two components is itself made up of two components. The functions φ and χ are also frequently referred as the “large” and “small” components because of the $1/2c$ prefactor in Equation (14).^h Because of the $c\vec{\sigma}_s\hat{\mathbf{p}}$ terms, the nonrelativistic limit of the Dirac equation is not immediately obvious from Equation (13) but it leads indeed to the nonrelativistic limit for $c \rightarrow \infty$ as will be seen shortly.

By multiplying out the terms from the second row of the 2×2 matrix, one obtains the following equation:

$$\chi = X\varphi = \frac{1}{2c}k\vec{\sigma}_s\hat{\mathbf{p}}\varphi \quad (14)$$

where

$$k = \left(1 - \frac{V - E}{2c^2}\right)^{-1}, \quad X = \frac{1}{2c}k\vec{\sigma}_s\hat{\mathbf{p}} \quad (15)$$

Equation (14) provides the relation between the upper and the lower components for an exact solution of the Dirac equation. It means that, in principle, the knowledge of φ should be sufficient since χ can be determined from it, or vice versa. Hence, it ought to be possible to obtain a relativistic equation for φ or χ alone, the solutions of which contain the same information (no further approximations) as ψ_D . We may call this the fully relativistic two-component approach as compared to the fully relativistic four-component approach based on the Dirac equation.

In the elimination of the small component (ESC) scheme, Equation (14) is directly substituted in the equation obtained by multiplying the terms of the first row of the matrix in (13). This yields the two-component ESC Hamiltonian:

$$\hat{\mathcal{H}}^{\text{ESC}} = V + \frac{1}{2}(\vec{\sigma}_s\hat{\mathbf{p}})k(\vec{\sigma}_s\hat{\mathbf{p}}) \quad (16)$$

^gHowever, so-called picture-change effects occur which may complicate certain operators. See, for example, refs. 18,22,27.

^hDepending on the potential and the location, the “small component” can be much larger than the “large” one, for example, for atomic $p_{1/2}$ orbitals close to the nucleus, and therefore the terms “upper” and “lower” component will be used here.

with k being defined in Equation (15). In the nonrelativistic limit, for $c \rightarrow \infty$ one finds that $k \rightarrow 1$. We also note that $(\vec{\sigma}_s \hat{p})^2 = \hat{p}^2 1$, that is, a nonrelativistic Schrödinger Hamiltonian is recovered from the ESC operator (16)

$$\hat{\mathcal{H}}_{\text{nrel}} = V + \frac{1}{2}(\vec{\sigma}_s \hat{p})^2 \quad (17)$$

It is convenient to leave the spin-dependent terms in (17) for the derivation of certain nonrelativistic magnetic property operators where electron–spin interactions are needed. Another way in which to obtain the nonrelativistic limit is to multiply (10) with $\hat{\mathcal{H}}_{\text{D}}$ before taking the limit $c \rightarrow \infty$. Although the ESC equation is a fully relativistic two-component equation, its Hamiltonian depends (through k) on the unknown energy E . It is therefore not usable in actual linear variational calculations.

In order to arrive at an energy-independent two-component equation, a transformation (Foldy–Wouthuysen transformation) of $\hat{\mathcal{H}}_{\text{D}}$ to block-diagonal form can be devised as

$$\hat{\mathcal{H}}^{\text{FW}} = U \hat{\mathcal{H}}_{\text{D}} U^{-1} \quad (18)$$

In case the transformation makes $\hat{\mathcal{H}}^{\text{FW}}$ block-diagonal and does not introduce an energy dependence of the operator, this would completely uncouple the equations for the upper and the lower components and yield the desired two-component relativistic equation, along with $\chi = X\varphi$, an energy-independent relation between upper and lower components (see Equations (14) and (15)). We will omit details here on how to obtain U ; for the purpose of this section, it shall be sufficient to know that approximate forms of this transformation can be devised. Often, the transformation U is constructed from an approximation for X . Different approximations for X yield different approximate two-component Hamiltonians in which the decoupling of the two components is not complete (but the lower component is neglected anyway, which then constitutes the approximation). These approximate two-component Hamiltonians are sometimes collectively denoted as “quasi-relativistic.” For approaches to construct an exact two-component operator, see refs. 28–30. In recent years, some methodology to compute NMR parameters from such Hamiltonians has been reported, as will be discussed later in Section 3.4.1. These methods are not yet in widespread use. Approximate two-component Hamiltonians have been used for most computational applications in the NMR field. Some of these will be discussed next.

A rather simple approach is to expand k in (14) to zeroth order in c^{-2} . The speed of light is large compared to velocities normally encountered in everyday life and therefore an expansion in inverse powers of c or c^2 may appear straightforward. Letting $k \rightarrow 1$ yields $X \approx c \vec{\sigma}_s \hat{p} / (2c^2)$, which results in the famous Pauli Hamiltonian³¹ after carrying out the transformation (18) with $U(X)$:

$$\hat{\mathcal{H}}_{\text{Pauli}} = \hat{\mathcal{H}}_{\text{nrel}} - \frac{\hat{p}^4}{8c^2} - \frac{\hat{p}^2 V}{8c^2} + \frac{i}{4c^2} \vec{\sigma}_s [(\hat{p}V) \times \hat{p}] \quad (19)$$

(here and elsewhere $i^2 = -1$). The second, third, and fourth terms on the RHS of (19) are the mass velocity (MV), Darwin (DAR), and SO terms, respectively.

They represent corrections of order c^{-2} to the nonrelativistic Hamiltonian. They modify the kinetic energy of the electron and the electron–nucleus potential, and introduce the coupling between spin and angular momentum of an electron. Close to a nucleus, the magnitude of the electron–nuclear attraction potential in V is very large (it goes to $-\infty$ for point-like nuclei). In this case, the term $(V-E)/2c^2$ in k of Equation (15) is not small and expanding k in Equation (14) in powers of c^{-2} is not justified. As a result, the Pauli operator affords undesirable singularities. Moreover, it is not variationally stable and permits only a perturbational treatment to first order.^{32,33} Higher-order contributions yield diverging terms. Variational computations based on the Pauli operator have been carried out, by using frozen cores and minimal basis sets in the core regions for valence orbitals, under which circumstances the variational instability can be kept somewhat under control. Such pseudovariational procedures are now depreciated. A *scalar-relativistic* or *spin-free relativistic* approach is obtained by omitting the SO term in (19) and other two-component methods. This yields a one-component formalism analogous to the nonrelativistic scheme with pure α - and β -spin orbitals.ⁱ

A better justified expansion of k is used to construct the zeroth-order regular approximation (ZORA)³⁴ or Chang–Pélissier–Durand³⁵ Hamiltonian. The ZORA operator can be obtained from the zeroth-order term of an expansion of k in Equation (15) in powers of $E/(2c^2-V)$, or by letting $X \approx (c\vec{\sigma}_s\hat{p})/(2c^2-V)$ as the main approximation when performing the transformation of Equation (18). If we write k from Equation (15) as

$$k = \left(1 - \frac{V-E}{2c^2}\right)^{-1} = \frac{2c^2}{2c^2-V} \left(1 + \frac{E}{2c^2-V}\right)^{-1} \quad (20)$$

the inverse $(\dots)^{-1}$ may be expanded in a power series in $E/(2c^2-V)$. The two-component ZORA Hamiltonian represents the zeroth-order term of this expansion, that is, one uses $(1+\text{small})^{-1} \approx 1$, leading to the Hamiltonian

$$\hat{\mathcal{H}}_{\text{ZORA}} = V + \frac{1}{2}(\vec{\sigma}_s\hat{p})\mathcal{K}(\vec{\sigma}_s\hat{p}) \quad (21a)$$

$$= V + \frac{1}{2}\hat{p}\mathcal{K}\hat{p} + \frac{1}{2}\vec{\sigma}_s[(\hat{p}\mathcal{K}) \times \hat{p}] \quad (21b)$$

where

$$\mathcal{K} = \frac{2c^2}{2c^2-V} = \frac{1}{1-V/(2c^2)} \quad (22)$$

The third term in (21b) is the ZORA SO operator. The ZORA operator has the desirable feature of being variationally stable. The expansion of k in terms of $E/(2c^2-V)$ is justified in regions where V is small or very large in magnitude and negative, as long as E remains small. Therefore, the ZORA provides a good

ⁱIt is also possible to separate off a spin–orbit part in the Dirac equation and in four-component perturbation theories which leaves two components to deal with.

relativistic approximation for valence orbitals and outer core orbitals with comparatively small energy, even in the near-nucleus region of a heavy atom. For core orbitals of heavy atoms with very large E , the ZORA affords substantial errors. Note the formal similarity to the ESC Hamiltonian in (16), with k replaced by \mathcal{K} . The nonrelativistic limit corresponds to letting $\mathcal{K} \rightarrow 1$ in which case we also have $(\hat{p}\mathcal{K}) = 0$ and the SO operator vanishes. The ZORA operator affords contributions beyond c^{-2} in the relativistic perturbation order, yet some other contributions of order c^{-2} and higher are missing due to the approximate nature of the operator. Conceptually, the ZORA operator has the disadvantage of not being invariant with respect to a change of the origin of the energy scale (gauge invariance), as can be seen from the fact that only V but not $(V-E)$ occurs in the operator. The standard choice for the potential is $V(r) \rightarrow 0$ for $r \rightarrow \infty$. Some of the resulting problems can be circumvented by a “scaling” procedure or by the use of frozen-core potentials or model potentials for the construction of \mathcal{K} . For example, the “sum-of-atomic-potentials approximation” (SAPA)³⁶ was shown to be a good approximation. In the SAPA, one uses $V = \sum_A V^A$ in the denominator of \mathcal{K} , where local atomic potentials V^A are taken, for instance, from density functional computations of the neutral atoms.

Improved regular approximations have been developed to cure certain deficiencies of ZORA. Dyall and van Lenthe³⁷ introduced an “infinite-order regular approximation” (IORA) which, however, is not the same as an infinite-order expansion of Equation (20). The IORA Hamiltonian includes all relativistic terms of order c^{-2} correctly. Unfortunately, the development effort in particular for magnetic properties is quite a bit more involved than when using the ZORA operator.³⁸

A different way of transforming the Dirac Hamiltonian to two-component form is used in the Douglas–Kroll–Hess (DKH) method. Here, U in Equation (18) is obtained via subsequent transformations that uncouple the upper and lower components to some order n in c^{-2} which can be written as

$$U_n = \sqrt{1 + W_n^2} + W_n \quad \text{or} \quad U_n = e^{W_n} \quad (23)$$

or by using other possible parameterizations³⁹ for U , with W_n being anti-Hermitian. For U_0 , the FW transformation for the free electron is used. To higher orders, equations for W_n have to be solved in order to achieve further uncoupling. Already with U_1 (the DKH1 level), a substantial fraction of the relativistic effects is recovered but for magnetic property computations the better choice is to go to second order (DKH2) or higher. We refer the reader to, for example, ref. 25 for details and original references. In particular due to the work of Hess and coworkers,³⁹ the DKH method has been established as a reliable tool in quantum chemistry for the computation of heavy-element compounds. To some extent, the ZORA and the DKH method to lowest order yield quite comparable results for many molecular properties. As an advantage, the DKH method does not suffer from a gauge invariance problem and it is significantly more accurate for core orbitals. The improved accuracy comes at the expense of a somewhat more complicated formalism in particular

when incorporating terms from external or internal magnetic fields or SO coupling. Fortunately, a number of developments for magnetic properties within the DKH framework have been reported in the literature in recent years^{40–45} but these methods have not been applied as widely as, for example, ZORA.

In order to arrive at a relativistic perturbation theory that avoids the infinities of the Pauli Hamiltonian to higher orders, so-called “direct” or “Dirac” four-component perturbation theory (DPT) can be employed. By a change of metric between upper and lower components in the Dirac equation (13), an expansion of the resulting four-component equation in powers of c^{-2} is straightforward and leads to nonsingular first- and higher-order expressions for E and ψ .^{46,47} A treatment of magnetic properties has been described in detail in the literature.⁴⁸ For an implementation of magnetic properties, see, for example, ref. 49. Perturbation expansions tend to become computationally rather expensive to evaluate in high order. At the same time, first-order relativistic perturbation theory may not be sufficient to describe relativistic effects on properties of molecules with such “strongly relativistic” elements as Au, Pt, Hg, Pb, etc. A variational procedure (Dirac, regular approximations, DKH, etc.) might be easier to implement and computationally less expensive than a higher-order perturbational method for relativistic effects.

As an alternative to the aforementioned methods which incorporate relativity directly into the calculations, the use of relativistic effective core potentials (ECPs) allows for consideration of relativistic effects in molecular computations. Inclusion of SO coupling is also possible in these methods. Extensive benchmark calculations⁵⁰ have shown that ECPs can yield very reliable properties of heavy-element compounds. For genuine valence properties (see Section 2.6) where the core tails of the valence orbitals are not of concern, pseudopotentials are straightforward to apply in property computations. For magnetic properties such as NMR shifts or spin–spin coupling, the all-electron electronic structure near the nuclei needs to be reconstructed. Some authors have taken such an approach in projector-augmented plane-wave computations.^{51,52} In this chapter, we will not discuss the use of ECP or projector methods in detail but focus on computational approaches where relativity is directly taken into consideration in the Hamiltonian.

As already mentioned, the potential V in the equations in this section might not simply refer to the external potential (e.g., V_{Ne}) for one-electron systems but to an effective many-electron potential. In this case, V appearing in the relativistic operators accounts in a mean-field sense for some relativistic effects on the electron–electron Coulomb repulsion $1/r_{ij}$. The explicit transformation of $1/r_{ij}$ to two-component form yields in order c^{-2} a two-electron Breit–Pauli SO and a two-electron Darwin operator. The transformation of the $\hat{\mathcal{H}}_{ij}^{\text{B}}$ terms of Equation (9) to two-component form yields further two-electron terms. Use of an effective (mean-field) electron–repulsion potential in V in the one-electron SO and Darwin operators accounts, to some extent, for some of the two-electron terms. Indeed, on formal substitution of the potential V_N in the Pauli SO operator (19) by the electrostatic potential $V_{ij} = 1/r_{ij}$ between two electrons, one obtains the

electron–electron SO operator

$$\hat{\mathcal{H}}^{\text{eeSO}} = \frac{l}{4c^2} \sum_{i \neq j} \vec{\sigma}_s(i) [(\hat{\mathbf{p}}_i V_{ij}) \times \hat{\mathbf{p}}_i] \quad (24)$$

and analogously the two-electron Darwin operator. The correct derivation would involve an order- c^{-2} transformation of the DCB Hamiltonian to two-component form.²² Using an effective potential in the one-electron kinetic energy and SO operators of other two-component Hamiltonians (e.g., ZORA) also yields mean-field approximations of their corresponding two-electron operators. Other two-electron terms have to be added explicitly, that is, their contributions are not covered in a mean-field sense when an effective potential is used in the one-electron part of a two-component relativistic operator. For example, the interaction of the spin of one electron with the orbital angular momentum of another electron (the spin–other orbit (SOO) interaction) is often considered in its Breit–Pauli form:

$$\hat{\mathcal{H}}^{\text{SOO}} = -\frac{i}{2c^2} \sum_{i \neq j} \vec{\sigma}_s(i) [(\hat{\mathbf{p}}_i V_{ij}) \times \hat{\mathbf{p}}_j] \quad (25)$$

Mean-field approximations to compute matrix elements of this operator efficiently have been used successfully in molecular property computations as well.⁵³

2.4 Computing energy derivatives to second order

In Section 2.2, it was shown that nuclear magnetic shielding and spin–spin coupling tensors can be obtained from computing second derivatives of the energy. In Section 2.3, a selection of methods has been outlined by which a good approximation of the relativistic energy, or the nonrelativistic limit, can be computed. The next step toward a relativistic NMR method is to take the energy expectation value expression (Ψ normalized)

$$E = \langle \Psi | \hat{\mathcal{H}} | \Psi \rangle \quad (26)$$

evaluated using the computational method of choice, and to differentiate twice, with respect to \mathbf{m}_A and \mathbf{B} (shielding) or with respect to \mathbf{m}_A and \mathbf{m}_B (spin–spin coupling). We will formulate the approach assuming exact wavefunctions but it should be kept in mind that the derivation has to be carried out specifically for the approximate energy expression. Expressions valid for DFT will be given at the end of this subsection. The derivations are somewhat simplified if the energy is variationally optimized (example: HF, DFT, and configuration interaction methods). For nonvariational energies (e.g., for correlated Moller–Plesset energies or in CC methods), additional equations need to be solved to obtain the derivatives.

Let λ_1 and λ_2 be two general perturbations, such as \mathbf{m}_A , \mathbf{m}_B , or \mathbf{B} or an electric field, for instance. The first-order derivative of (26) with respect to λ_1 is

$$E^{(\lambda_1)} = \langle \Psi^{(0)} | \hat{\mathcal{H}}^{(\lambda_1)} | \Psi^{(0)} \rangle \quad (27)$$

(note that the derivative is evaluated where $\lambda_1, \lambda_2, \dots = 0$). To arrive at the last equation, use has been made of the fact that the other two terms involving $\Psi^{(\lambda_1)}$ obtained from differentiating (26) vanish (Hellmann–Feynman theorem). Expanding each term in (27) in a power series in λ_2 and keeping terms to first order in λ_1, λ_2 then yields^j

$$E^{(\lambda_1, \lambda_2)} = \langle \Psi^{(0)} | \hat{\mathcal{H}}^{(\lambda_1, \lambda_2)} | \Psi^{(0)} \rangle + 2\text{Re} \langle \Psi^{(0)} | \hat{\mathcal{H}}^{(\lambda_1)} | \Psi^{(\lambda_2)} \rangle \quad (28)$$

As one should expect for the energy as a “well-behaved” function, the order of differentiation does not matter (interchange theorem). Thus, one can choose the perturbation to compute $\Psi^{(\lambda_2)}$ such that the computational effort or the program development effort or both are minimized. Now the term “linear response” when designating the second-order energy property becomes obvious: it is necessary to know how the wavefunction of the molecule changes in response to at least one of the perturbations. This is the linear response of the electronic structure to the perturbation.

Computing $\Psi^{(\lambda_2)}$ is usually the computational bottleneck. Through an expansion of $\hat{\mathcal{H}}\Psi = \Psi \cdot E$ in λ_2 , on collecting terms linear in λ_2 , the equation to determine $\Psi^{(\lambda_2)}$ is

$$\hat{\mathcal{H}}^{(\lambda_2)}\Psi^{(0)} + \hat{\mathcal{H}}^{(0)}\Psi^{(\lambda_2)} = \Psi^{(\lambda_2)} \cdot E^{(0)} + \Psi^{(0)} \cdot E^{(\lambda_2)} \quad (29)$$

(linear response equation). Thus, $\hat{\mathcal{H}}^{(\lambda_1)}$, $\hat{\mathcal{H}}^{(\lambda_2)}$, and $\hat{\mathcal{H}}^{(\lambda_1, \lambda_2)}$ are needed to compute the second-order energy.

The linear response equation is usually solved in a basis set expansion, based on the approximations made to treat correlation. If we knew *all* the ground- and excited-state wavefunctions of the unperturbed system, these functions may be used as a basis set to represent $\Psi^{(\lambda_2)}$. Substituting $\Psi^{(\lambda_2)} = \sum_{j \neq 0} \Psi_j^{(0)} C_j$ in (29) and equating the unknown coefficients C_j yields

$$\Psi^{(\lambda_2)} = \sum_{j \neq 0} \Psi_j \frac{\langle \Psi_j | \hat{\mathcal{H}}^{(\lambda_2)} | \Psi_0 \rangle}{E_0 - E_j} \quad (30)$$

where the superscript (0) has been dropped everywhere on the right-hand side. The perturbation is calculated for the ground state. From now on, wavefunctions and energies without a perturbation-order superscript are assumed to be those of the unperturbed system. Substituting this last equation into the expression for $E^{(\lambda_1, \lambda_2)}$, equation (28), yields the “sum-over-states” (SOS) form for a second energy-derivative/linear response property:

$$E^{(\lambda_1, \lambda_2)} = \langle \Psi_0 | \hat{\mathcal{H}}^{(\lambda_1, \lambda_2)} | \Psi_0 \rangle + 2 \sum_{j \neq 0} \text{Re} \frac{\langle \Psi_0 | \hat{\mathcal{H}}^{(\lambda_1)} | \Psi_j \rangle \langle \Psi_j | \hat{\mathcal{H}}^{(\lambda_2)} | \Psi_0 \rangle}{E_0 - E_j} \quad (31)$$

The perturbation parameters appear symmetrically which shows again that the result is not dependent on the order in which the derivatives are taken. The SOS equation is impractical to use because it requires the knowledge of all

^jNote that with $\hat{\mathcal{H}}^{(\lambda_1)}$ being a Hermitian operator, $\langle \Psi^{(0)} | \hat{\mathcal{H}}^{(\lambda_1)} | \Psi^{(\lambda_2)} \rangle + \langle \Psi^{(\lambda_2)} | \hat{\mathcal{H}}^{(\lambda_1)} | \Psi^{(0)} \rangle = 2\text{Re} \langle \Psi^{(0)} | \hat{\mathcal{H}}^{(\lambda_1)} | \Psi^{(\lambda_2)} \rangle$.

excited-state wavefunctions. With a finite basis set, there are a finite number of excited states but these are typically still too many for the SOS equation to be of practical use. Instead, it is faster to solve (29) for a perturbed set of wavefunction parameters (e.g., MO coefficients) without taking the detour via the excited states. However, the SOS equation is useful for qualitative interpretations. For example, because of the energy gap $E_0 - E_j$ in the denominator, one may expect a relatively large contribution from low-lying excited states for which the perturbation matrix elements $\langle \Psi_0 | \hat{\mathcal{H}}^{(\lambda_1)} | \Psi_j \rangle$ and $\langle \Psi_0 | \hat{\mathcal{H}}^{(\lambda_2)} | \Psi_j \rangle$ are large.

In calculations of magnetic properties, the $\langle \Psi_0 | \hat{\mathcal{H}}^{(\lambda_1, \lambda_2)} | \Psi_0 \rangle$ term in (28) is called the *diamagnetic* term while the SOS part is called the *paramagnetic* term. Likewise, there are diamagnetic (bilinear) and paramagnetic (linear) perturbation operators.

We can now write down the expressions for the shielding tensor and the K-coupling tensor in wavefunction notation:

$$\sigma_A = \text{Eq. (28)} \quad \text{with } \lambda_1, \lambda_2 \rightarrow \mathbf{m}_A, \mathbf{B} \quad (32a)$$

$$K_{AB} = \text{Eq. (28)} \quad \text{with } \lambda_1, \lambda_2 \rightarrow \mathbf{m}_A, \mathbf{m}_B \quad (32b)$$

The corresponding SOS equations are

$$\sigma_A = \text{Eq. (31)} \quad \text{with } \lambda_1, \lambda_2 \rightarrow \mathbf{m}_A, \mathbf{B} \quad (33a)$$

$$K_{AB} = \text{Eq. (31)} \quad \text{with } \lambda_1, \lambda_2 \rightarrow \mathbf{m}_A, \mathbf{m}_B \quad (33b)$$

Finally, it is useful to take a look at the corresponding expressions in DFT because DFT has been used for many of the computational studies of NMR parameters employing relativistic methods, in particular on larger systems. The energy is now written as a functional of the electron density ρ which in turn is obtained from a set of Kohn–Sham (KS) molecular spin-orbital^k φ_i (MOs), that is

$$E = E[\rho]; \quad \rho = \sum_i^{\text{occ}} \varphi_i^* \varphi_i \quad (34)$$

where the MOs are obtained from the KS equations

$$[\hat{h} + V_{\text{HXC}}] \varphi_i = \varphi_i \varepsilon_i \quad (35)$$

with ε_i being the orbital energy. The one-electron part of the KS operator, \hat{h} , contains the electron–nuclear potential V and the nonrelativistic kinetic energy term $\hat{p}^2/2$ or one of the relativistic operators of Section 2.3 (two- or four-component, or a scalar-relativistic version). The orbitals have one, two, or four components, accordingly. Further, V_{HXC} represents the sum of the Coulomb (“Hartree potential”) and the DFT-specific exchange–correlation (XC) potential. V_{HXC} is an example for the aforementioned effective potential in MO-based methods. In computations using a basis set expansion of the MOs, one also obtains a large number of unoccupied MOs. Similar in spirit to using the unperturbed excited-state wavefunctions in Equation (30), one can also write the

^kThe notation is based on a set of N singly occupied spin-orbitals for the N -electron system.

perturbation of each MO on the basis of the unoccupied orbitals,¹ that is, $\varphi_i^{(\lambda_2)} = \sum_a^{\text{unocc}} \varphi_a C_{ai}$ is solved for the unknown coefficients C_{ai} . These coefficients can be used to compute the linear response of the molecule's density, spin density, and current density to first order which is then used, similar in spirit as the perturbed wavefunction in Equation (28), to compute a second-order energy derivative.^m Using lowercase symbols for the perturbed operators in the KS DFT scheme, the expressions for the shielding and the K-coupling are in DFT given as

$$\sigma_A = \sum_i^{\text{occ}} \langle \varphi_i | \hat{h}^{(m_A, B)} | \varphi_i \rangle + 2 \sum_i^{\text{occ}} \sum_a^{\text{unocc}} \text{Re} \frac{\langle \varphi_i | \hat{h}^{(B)} + V_{\text{HXC}}^{(B)} | \varphi_a \rangle \langle \varphi_a | \hat{h}^{(m_B)} | \varphi_i \rangle}{\varepsilon_i - \varepsilon_a} \quad (36a)$$

$$K_{AB} = \sum_i^{\text{occ}} \langle \varphi_i | \hat{h}^{(m_A, m_B)} | \varphi_i \rangle + 2 \sum_i^{\text{occ}} \sum_a^{\text{unocc}} \text{Re} \frac{\langle \varphi_i | \hat{h}^{(m_A)} + V_{\text{HXC}}^{(m_A)} | \varphi_a \rangle \langle \varphi_a | \hat{h}^{(m_B)} | \varphi_i \rangle}{\varepsilon_i - \varepsilon_a} \quad (36b)$$

where a complete basis set was assumed. In a DFT computation, one needs to evaluate the first-order perturbation of the V_{HXC} potential which is usually done in a self-consistent field (SCF) procedure, by solving the “coupled-perturbed KS equations.” These are the DFT response equations obtained from perturbation expansions of (35). With functionals that do not depend on the current density (which includes all nonhybrid density functionals) and perturbation operators that are imaginary (e.g., the one for B), the contribution $V_{\text{HXC}}^{(B)}$ is zero. Such a situation is usually referred as an “uncoupled” DFT perturbation method. The result can then be simply computed from the perturbation operator matrix elements and the SCF step of the response calculation can be skipped. Qualitative interpretations of the above equations may focus on small orbital gaps in the denominators, for instance, or the magnitudes of the matrix elements in the numerators.

The perturbation of V_{HXC} does not appear symmetrically in the DFT expressions for the shielding and the K -coupling. This is a consequence of the derivation: the perturbed orbitals are only calculated for *one* of the perturbations, just like for the derivation of Equation (28) or (31) in exact wavefunction theory the perturbed wavefunction is only needed for one of the perturbations. However, the reader is reminded that this result was based on a simplification of the first-order derivative (Equation (27)) where terms containing $\Psi^{(\lambda_1)}$ were eliminated. This is done for computational efficiency. If these terms are kept, $\Psi^{(\lambda_1)}$, $\Psi^{(\lambda_2)}$, and $\Psi^{(\lambda_1, \lambda_2)}$ enter the expression for $E^{(\lambda_1, \lambda_2)}$ with a lot of canceling terms in the final expression. Likewise, if in DFT the Hellmann–Feynman theorem is not exploited for the first derivative step, $E^{(\lambda_1, \lambda_2)}$ will contain terms from $V_{\text{HXC}}^{(\lambda_1)}$, $V_{\text{HXC}}^{(\lambda_2)}$ and $V_{\text{HXC}}^{(\lambda_1, \lambda_2)}$ with a symmetric appearance of each perturbed term. It should be pointed out that the results of Equations (36a) and (36b) are

¹This approach does *not* approximate the excited states by orbital to orbital transitions or the excitation energies by orbital energy differences, despite the fact that the resulting equations may suggest so.

^mFor magnetic perturbations, one should rather use a current-density functional theory in which magnetic field-dependent terms are built in right from the start. Numerous benchmarks have shown, however, that applying the approach in DFT (nonhybrid or hybrid) is rather successful. Further, some studies have reported that the contributions from the current density-dependent part of the functional are small at least as far as NMR nuclear magnetic shielding in light atomic molecules is concerned.⁵⁴

nonetheless independent of the order of differentiation, that is, the perturbation superscripts may be interchanged.

To compute the shielding tensor, it is generally more efficient to solve the response equations for the external field. In turn, the shielding tensor can be computed for a large range of nuclei at little additional cost. If the opposite order of differentiation is chosen, the program would need to solve the coupled-perturbed KS equations for each of the nuclei of interest, which is usually the computational bottleneck, in particular when hybrid functionals are used.

2.5 Perturbation operators for NMR: relativistic vs. nonrelativistic approaches

To obtain the complete expressions for the NMR parameters, it remains to derive the perturbation operators from the nonrelativistic or relativistic Hamiltonians. We will consider the perturbation operators for the nonrelativistic case, for the approximate two-component ZORA and DKH1 formalisms, and for the four-component case. Among the available approximate two-component approaches, ZORA was selected as a representative example for a number of reasons, two of which are: (i) there have been numerous applications in the NMR field indicating that for NMR chemical shifts and spin–spin coupling it is a very good approximation to the fully relativistic treatment, and (ii) the magnetic perturbation operators can be easily derived in closed form allowing for an easy side-by-side comparison with the nonrelativistic and the four-component case. The DKH 1 case provides an interesting comparison with ZORA.

We will focus on the most important one-electron operators here and only briefly comment on perturbation terms arising from two-electron operators, that is, the Hamiltonian for an N -electron system is written as $\hat{\mathcal{H}} = \sum_{i=1}^N \hat{h}(i) + \text{two-electron terms}$, and we focus on the various perturbation operators obtained from expanding \hat{h} in terms of \mathbf{m}_A , \mathbf{m}_B , \mathbf{B} , etc. From Section 2.4, it can be seen that for nuclear shielding and spin–spin coupling the operators linear and bilinear in \mathbf{m}_A , \mathbf{m}_B , and \mathbf{B} are needed. For magnetic properties, the approach is as follows: one makes the “minimal substitution” $\hat{\mathbf{p}} \rightarrow \hat{\mathbf{p}} + \mathbf{A}$ for the momentum operator in \hat{h} , where \mathbf{A} is the magnetic vector potential. Its relation to the magnetic field is

$$\mathbf{B} = \nabla \times \mathbf{A} \quad (37)$$

There are two sources of magnetic fields: the homogeneous static external field \mathbf{B} for which the following expression is generally used for the vector potential:

$$\mathbf{A}^{\text{ext}} = -\frac{1}{2} \mathbf{r} \times \mathbf{B} \quad (38)$$

The last equation satisfies (37). Then there are the magnetic fields arising from the nuclear spins. If these fields are caused by a set of nuclear *point dipoles* \mathbf{m}_A , \mathbf{m}_B , ..., the corresponding vector potential is

$$\mathbf{A}^{\text{nuc}} = \sum_A^{\text{Nuclei}} \mathbf{A}_A^{\text{nuc}}(\mathbf{r}) = \frac{1}{c^2} \sum_A^{\text{Nuclei}} \frac{\mathbf{m}_A \times \mathbf{r}_A}{r_A^3} \quad (39)$$

Modifications to treat extended nuclei can be made in (39).

We will discuss the nonrelativistic case first. Substitution of $\hat{\mathbf{p}} \rightarrow \hat{\mathbf{p}} + \mathbf{A}$ in the nonrelativistic one-electron Hamiltonian yields

$$\hat{h}_{\text{nel}}(\mathbf{m}_A, \mathbf{m}_B, \dots, \mathbf{B}) = \hat{h}_{\text{nel}}^{(0)} + \hat{h}_{\text{nel}}^{\text{pert}}(\mathbf{m}_A, \mathbf{m}_B, \dots, \mathbf{B}) \quad (40)$$

with $h_{\text{nel}}^{(0)} = \hat{\mathbf{p}}^2/2 + V$ andⁿ

$$\hat{h}_{\text{nel}}^{\text{pert}} = \frac{1}{2}(\mathbf{A}\hat{\mathbf{p}} + \hat{\mathbf{p}}\mathbf{A} + i\vec{\sigma}_s[\hat{\mathbf{p}} \times \mathbf{A} + \mathbf{A} \times \hat{\mathbf{p}}] + \mathbf{A}^2) \quad (41)$$

Substituting $\mathbf{A} = \mathbf{A}^{\text{ext}} + \mathbf{A}^{\text{nuc}}$ into the above equation, with \mathbf{A}^{ext} from Equation (38) and \mathbf{A}^{nuc} from Equation (39), yields the one-electron magnetic perturbation operators

$$\hat{h}_{\text{nel}}^{\text{pert}} = \hat{h}^{\text{DM}} + \hat{h}^{\text{OZ}} + \hat{h}^{\text{SZ}} + \hat{h}^{\text{OP}} + \hat{h}^{\text{DS}} + \hat{h}^{\text{FC}} + \hat{h}^{\text{SD}} + \hat{h}^{\text{OD}} \quad (42)$$

with

$$\hat{h}^{\text{DM}} = \frac{1}{4}(\mathbf{r} \times \mathbf{B}) \cdot (\mathbf{r} \times \mathbf{B}) \quad (43a)$$

$$\hat{h}^{\text{OZ}} = -\hat{\boldsymbol{\mu}}_e \cdot \mathbf{B} = -\frac{1}{2}(\mathbf{r} \times \hat{\mathbf{p}}) \cdot \mathbf{B} = -\frac{1}{2}\hat{\mathbf{L}} \cdot \mathbf{B} \quad (43b)$$

$$\hat{h}^{\text{SZ}} = -\hat{\boldsymbol{\mu}}_s \cdot \mathbf{B} = \frac{1}{2}\vec{\sigma}_s \cdot \mathbf{B} \quad (43c)$$

$$\hat{h}^{\text{OP}} = \frac{1}{c^2} \sum_A \mathbf{m}_A \left(\frac{\mathbf{r}_A}{r_A^3} \times \hat{\mathbf{p}} \right) \quad (43d)$$

$$\hat{h}^{\text{DS}} = \frac{1}{2c^2} \sum_A \left[(\mathbf{m}_A \cdot \mathbf{B}) \left(\frac{\mathbf{r}_A}{r_A^3} \cdot \mathbf{r} \right) - (\mathbf{m}_A \cdot \mathbf{r}) \left(\mathbf{B} \cdot \frac{\mathbf{r}_A}{r_A^3} \right) \right] \quad (43e)$$

$$\hat{h}^{\text{FC}} + \hat{h}^{\text{SD}} = \frac{1}{2c^2} \sum_A \vec{\sigma}_s \left[\mathbf{m}_A \left(\nabla \cdot \frac{\mathbf{r}_A}{r_A^3} \right) - (\mathbf{m}_A \cdot \nabla) \frac{\mathbf{r}_A}{r_A^3} \right] \quad (43f)$$

$$\hat{h}^{\text{OD}} = \frac{1}{2c^4} \sum_{B \neq A} \frac{(\mathbf{m}_A \cdot \mathbf{m}_B)(\mathbf{r}_A \cdot \mathbf{r}_B) - (\mathbf{m}_A \cdot \mathbf{r}_B)(\mathbf{m}_B \cdot \mathbf{r}_A)}{r_A^3 r_B^3} \quad (43g)$$

Here, (43a) is the operator for the diamagnetic magnetizability, (43b) the orbital Zeeman term, (43c) the spin Zeeman, (43d) the paramagnetic orbital, (43e) the diamagnetic shielding, (43f) the Fermi-contact+spin dipole, and (43g) the diamagnetic orbital term, respectively. The terms (43d)–(43g) are the nuclear hyperfine terms. The individual FC and SD operators, in particular the well-known δ function for the FC term, are obtained by explicitly carrying out the differentiation of \mathbf{r}_A/r_A^3 in (43f).^o The first term on the right-hand side of (43f)

ⁿThe spin-dependent terms are only obtained if the substitution is made in the kinetic energy operator written as in Equation (17) using $(\vec{\sigma}_s \hat{\mathbf{p}})^2$ instead of $\hat{\mathbf{p}}^2$ (see the text following Equation (16)). The derivation makes use of $(\vec{\sigma}_s \hat{\mathbf{A}})(\vec{\sigma}_s \hat{\mathbf{B}}) = \hat{\mathbf{A}}\hat{\mathbf{B}} + i\vec{\sigma}_s \cdot (\hat{\mathbf{A}} \times \hat{\mathbf{B}})$ for general vector operators $\hat{\mathbf{A}}$ and $\hat{\mathbf{B}}$.

^oUsing $\nabla_i(r_j/r^3) = (4\pi/3)\delta_{ij} \cdot \delta(\mathbf{r}) + (\delta_{ij}/r^3) - (3r_i r_j/r^5)$.

yields 3/2 of the FC operator, while the second term yields $-1/2$ FC plus the SD operator. One obtains the more familiar expressions

$$\hat{h}^{\text{FC}} = \frac{4\pi}{3c^2} \delta(\mathbf{r}_A) \mathbf{m}_A \cdot \vec{\sigma}_s \quad (44a)$$

$$\hat{h}^{\text{SD}} = \frac{1}{2c^2} \cdot \frac{3(\vec{\sigma}_s \cdot \mathbf{r}_A)(\mathbf{m}_A \cdot \mathbf{r}_A) - r_A^2 \mathbf{m}_A \cdot \vec{\sigma}_s}{r_A^5} \quad (44b)$$

In (43b), $\hat{\mu}_e = -(1/2)(\mathbf{r} \times \hat{\mathbf{p}}) = -(1/2)\hat{\mathbf{L}}$ is the magnetic moment operator for an electron's orbital motion which is proportional to the angular momentum operator $\hat{\mathbf{L}}$. By comparison of (43b) with (43c), the magnetic moment operator with respect to an electron spin degree of freedom is $\hat{\mu}_s = -\vec{\sigma}_s/2$. Since the spin terms in nonrelativistic limit have been obtained from the Dirac equation, the electronic g -factor is exactly 2 and not written explicitly. Experimental evidence and more sophisticated theoretical treatments show that the correct value is rather $g_e \approx 2.0023 \dots$. The electronic g -factor can be included via factors of $(g_e/2)$ in the spin-dependent operators where applicable. In the operator list, the nuclear Zeeman terms, $-\mathbf{m}_A \cdot \mathbf{B}$ for each nucleus, were omitted because they do not contribute to the electronic energy of the molecule.

The perturbation operators are now obtained from differentiating $\hat{h}_{\text{rel}}^{\text{pert}}$ with respect to \mathbf{m}_A , \mathbf{m}_B , and \mathbf{B} as prescribed in Section 2.4. $\hat{h}^{(m_A)}$ and $\hat{h}^{(m_B)}$ are obtained from differentiating the OP, FC, and SD operators with respect to one of the nuclear spin magnetic moments.^P It is customary to use the same names for the perturbation operators, too, that is, the OP, FC, and SD perturbation operators are obtained. An alternative name for OP is “paramagnetic spin-orbital” (PSO). $\hat{h}^{(B)}$ is obtained from differentiating the OZ and SZ terms. $\hat{h}^{(m_A, m_B)}$ is obtained from differentiating the OD operator twice with respect to two different nuclear magnetic moments. An alternative name for this operator is “diamagnetic spin-orbital” (DSO). Finally, $\hat{h}^{(m_A, B)}$ is obtained from differentiating the DS with respect to the field and one of the nuclear spin magnetic moments (hence the name of the operator). Substituting these operators for the perturbation operators in the SOS equation (31) in Section 2.4 yields the famous *Ramsey* equations for nonrelativistic nuclear magnetic shielding and spin-spin coupling.^{55,56} The DM operator is not relevant for NMR but would be needed, for instance, to calculate the magnetizability of a molecule.

Now compare the nonrelativistic limit with a two-component relativistic formalism. We use the ZORA as an illustrative example. Substitution of $\hat{\mathbf{p}} \rightarrow \hat{\mathbf{p}} + \mathbf{A}$ in the ZORA operator (Equation (21a)) yields

$$\hat{h}_{\text{ZORA}}(\mathbf{m}_A, \mathbf{m}_B, \dots, \mathbf{B}) = \hat{h}_{\text{ZORA}}^{(0)} + \hat{h}_{\text{ZORA}}^{\text{pert}}(\mathbf{m}_A, \mathbf{m}_B, \dots, \mathbf{B}) \quad (45)$$

^PThe bilinear operators OD and DS do not contribute to $\hat{h}^{(m_A)}$ and $\hat{h}^{(m_B)}$ because the derivatives are taken at $\mathbf{m}_A = 0$, $\mathbf{m}_B = 0$, $\mathbf{B} = 0$, that is, after the differentiation one sets all remaining perturbation parameters to zero in which case the first derivatives of the bilinear operators vanish.

with $\hat{h}_{\text{ZORA}}^{(0)}$ as in Equation (21a) and

$$\hat{h}_{\text{ZORA}}^{\text{pert}} = \frac{1}{2}(\hat{\mathbf{p}}\mathcal{K}\mathbf{A} + \mathbf{A}\mathcal{K}\hat{\mathbf{p}} + i\vec{\sigma}[\hat{\mathbf{p}} \times (\mathcal{K}\mathbf{A}) + \mathbf{A} \times (\mathcal{K}\hat{\mathbf{p}})] + \mathcal{K}\mathbf{A}^2) \quad (46)$$

Letting $\mathcal{K} = 1$ yields perturbation terms that are identical to the nonrelativistic ones (Equation (41)). Indeed, the limit $c \rightarrow \infty$ in \mathcal{K} leads to $\mathcal{K} \rightarrow 1$ as already mentioned in Section 2.3, which represents the nonrelativistic limit in the ZORA formalism. The nonrelativistic limit is therefore obtained term-by-term and thus, when substituting $\mathbf{A} = \mathbf{A}^{\text{ext}} + \mathbf{A}^{\text{nuc}}$ into (46), with \mathbf{A}^{ext} from Equation (38) and \mathbf{A}^{nuc} from Equation (39), a two-component ZORA analog for each of the operators DM, OZ, SZ, OP, DS, FC, SD, and OD is obtained. They differ from the expressions (43a)–(43g) by the presence of \mathcal{K} which regularizes the operators at the nuclei. One could think of this as “kinematic factors” that take care of the high velocities of the electron near the nuclei. Instead of giving a list of all operators, we shall focus on a few examples. The DM, DS, and OD operators simply contain an additional factor of \mathcal{K} in all terms. The ZORA analog of the sum of FC and SD operators obtained from (46) is

$$\hat{h}_{\text{ZORA}}^{\text{FC+SD}} = \frac{1}{2c^2} \sum_A \vec{\sigma}_s \left[\mathbf{m}_A \left(\nabla \cdot \left[\mathcal{K} \frac{\mathbf{r}_A}{r_A^3} \right] \right) - (\mathbf{m}_A \cdot \nabla) \left[\mathcal{K} \frac{\mathbf{r}_A}{r_A^3} \right] \right] \quad (47)$$

The ZORA analog of the Fermi-contact term itself is given by (2/3) of the first term in the above equation, that is

$$\hat{h}_{\text{ZORA}}^{\text{FC}} = \frac{1}{3c^2} \sum_A \vec{\sigma}_s \left[\mathbf{m}_A \left(\nabla \cdot \left[\mathcal{K} \frac{\mathbf{r}_A}{r_A^3} \right] \right) \right] \quad (48)$$

and the ZORA SD term by the remainder of the operator. For nuclear point-charge potentials with Z approximately 118 or less, the factor of \mathcal{K} in the ZORA hyperfine terms regularizes the operator and as a result there is no actual “contact” (delta-function like) term for point nuclei.^q Thus, there is a profound difference between the relativistic and the nonrelativistic operators for finite speeds of light. The overall mechanism is still similar, though: the relativistic version of the FC operator mainly samples the values and slopes of s-orbitals very close to the nuclei. If $\mathcal{K} = 1$, one can differentiate the \mathbf{r}_A/r_A^3 terms to obtain the familiar δ -function expression for the FC operator. The OP operator is also obtained in a form resembling (43d), but again the operator’s singular $1/r_A^2$ behavior is regularized by the presence of \mathcal{K} and its behavior very close to a nucleus is quite different from the nonrelativistic OP operator:

$$\hat{h}_{\text{ZORA}}^{\text{OP}} = \frac{1}{2c^2} \sum_A \left(\mathbf{m}_A \cdot \mathcal{K} \left[\frac{\mathbf{r}_A}{r_A^3} \times \hat{\mathbf{p}} \right] + \mathbf{m}_A \cdot \left[\frac{\mathbf{r}_A}{r_A^3} \times \hat{\mathbf{p}} \right] \mathcal{K} \right) \quad (49)$$

^qIf nuclei were point charges, the four-component Dirac equation would not be applicable for nuclei with charges $Z > c \approx 137$. The breakdown of the ZORA for magnetic perturbations before $Z = 137$ is reached is a consequence of its approximate character and the strongly singular behavior of \mathbf{A}^{nuc} ; too strong singularities such as from a point magnetic dipole for $Z > 118$ cannot be regularized. There would be no such problems with extended nuclei.

Nonetheless, the overall mechanism for OP and interpretations based thereupon are similar to the nonrelativistic limit, for example, the operator acts somewhat like an angular momentum operator centered on nucleus A . We will see in Section 2.6 that in two-component methods, new cross terms between FC and OP, for instance, arise that do not contribute at the nonrelativistic limit or in spin-free relativistic theories. For the ZORA analogs of other magnetic perturbation operators, we refer the reader to the original literature on ZORA NMR.^{57–60} As in the nonrelativistic case, differentiation of these magnetic operators with respect to \mathbf{m}_A , \mathbf{m}_B , and \mathbf{B} yields the ZORA analogs of the various perturbation operators to be used in the second derivative expression for the energy (Equation (28)) to compute NMR parameters.

Regarding other two-component methods mentioned in Section 2.3, the Breit–Pauli operator affords severe singularities for Coulomb potentials (point nuclei) and the magnetic perturbation operators associated with it are not so well behaved either. Within a first-order perturbation scheme to treat relativity, that is, keeping relativistic terms to order c^{-2} only, response functions for molecular properties can still be calculated in many cases. The perturbation operators can be derived analogous to the ZORA case, that is, after minimal substitution in the Dirac Hamiltonian the resulting operator is transformed to the approximate two-component form. Some of the operators that arise from this transformation are obtained when substituting $\hat{\mathbf{p}} \rightarrow \hat{\mathbf{p}} + \mathbf{A}$ in the one-electron Pauli Hamiltonian (Equation (19)). An extensive list of operators relevant for magnetic resonance has been given by Manninen et al.⁶¹ See also the books by Moss²² and Harriman.⁶²

For comparison with ZORA where the relativistic corrections in the operator show up as relativistic “kinematic factors” \mathcal{K} in the operators (which approach unity in the nonrelativistic limit), it is also illustrative to take a look at the magnetic perturbation operators in the DKH formalism. We follow the derivation of Melo et al.⁴³ Let ($m_e = 1$)

$$E_p = c\sqrt{p^2 + c^2}; \quad K = \sqrt{\frac{E_p + c^2}{2E_p}}; \quad R = \frac{c}{E_p + c^2} \quad (50)$$

The perturbation operator in the DKH1 scheme (first-order DKH) is then⁴³

$$\hat{h}_{\text{DKH1}}^{\text{pert}} = c(K[R\hat{\mathbf{p}}\mathbf{A} + \hat{\mathbf{p}}\mathbf{A}R]K + i\sigma K[R\hat{\mathbf{p}} \times \mathbf{A} + \hat{\mathbf{p}} \times \mathbf{A}R]K) \quad (51)$$

Here, K and R can also be thought of kinematic factors modifying the operators compared to the nonrelativistic limit. Because of the frequent occurrence of p^2 , the DKH operators are usually computed in a basis where the operator p^2 is diagonal and subsequently transformed back to the original basis representation. A diamagnetic term of order A^2 is not obtained at the DKH1 level. In the nonrelativistic limit, $E_p \rightarrow c^2$, $K \rightarrow 1$, $R \rightarrow 1/(2c)$, and the paramagnetic part of $\hat{h}_{\text{nr}}^{\text{pert}}$ is obtained (Coulomb gauge). The expressions for DKH2 are lengthier but also contain similar kinematic terms. At the DKH2 level, a diamagnetic operator is obtained which has the nonrelativistic DS operator as its $c \rightarrow \infty$ limit. See refs. 43,41 for explicit expressions and further details.

In the four-component picture, the derivation of the perturbation operators is quite straightforward: substitution of $\hat{\mathbf{p}} \rightarrow \hat{\mathbf{p}} + \mathbf{A}$ in the part of the Dirac Hamiltonian that contains $\hat{\mathbf{p}}$, that is, in $c\vec{\alpha}\hat{\mathbf{p}}$ yields

$$\hat{h}_D(\mathbf{m}_A, \mathbf{m}_B, \dots, \mathbf{B}) = \hat{h}_D^{(0)} + \hat{h}_D^{\text{pert}}(\mathbf{m}_A, \mathbf{m}_B, \dots, \mathbf{B}) \quad (52)$$

with $\hat{h}_D^{(0)}$ as in Equation (11) and

$$\hat{h}_D^{\text{pert}} = c\vec{\alpha}\mathbf{A}(\mathbf{r}) \quad (53)$$

Thus, with \mathbf{A}^{ext} from Equation (38) and \mathbf{A}^{nuc} from Equation (39), the one-electron operators accounting for magnetic fields are

$$\hat{h}_D^{\text{mag}} = -\frac{c}{2}\vec{\alpha} \cdot (\mathbf{r} \times \mathbf{B}) + \frac{1}{2c} \cdot \sum_A^{\text{Nuclei}} \frac{\mathbf{m}_A \times \mathbf{r}_A}{r_A^3} \quad (54)$$

These operators look very different from the nonrelativistic and the two-component operators. Perhaps most notably is the *absence* of operators that are bilinear in the perturbations which is a direct consequence of the fact that $\hat{\mathbf{p}}$ appears only linear in the Dirac equation. Therefore, there are no terms $\hat{h}_D^{(m_A, m_B)}$ and $\hat{h}_D^{(m_A, B)}$ contributing to the second energy derivative (28). However, it has been shown that a diamagnetic contribution to a second-order derivative property is indeed contained in the four-component scheme. It has been numerically traced back to the contributions from negative energy eigenfunctions of $\hat{\mathcal{H}}_D$ if the complete spectrum of this operator is used as a basis set to represent $\Psi^{(\lambda_2)}$ in Equation (28),⁶³ even though there is only a paramagnetic perturbation operator (53). The role of the negative energy states for diamagnetic shielding has also been pointed out by Pyykkö in early theoretical work on NMR chemical shifts.⁶⁴ For a recent in-depth discussion, see ref. 65. Recent work by Liu and coworkers has been aimed at ways to simplify the four-component treatment of nuclear magnetic shielding^{66,67}; the issue of diamagnetic terms has also been addressed in these works. See also ref. 68.

The absence of derivative operators ($\hat{\mathbf{p}}$ or ∇) in (54) is in stark contrast to the derivative-containing operators in the two-component methods or in nonrelativistic theory. Derivative operators implicitly enter the formalism via $\vec{\alpha}$ which couples the upper with the lower components of the orbitals/wavefunction. Recall that the upper and lower components are linked by a derivative-containing operator as in Equation (14) and it becomes clear that the lack of derivative operators in (54) is somewhat deceptive. It was shown explicitly in refs. 69–71 how the matrix elements of (54) approach the nonrelativistic limit and how the derivative operators enter the expressions along the way.

We note in passing that additional magnetic perturbation operators are obtained from making the minimal substitution in relativistic two-electron operators such as the two-electron SO and Darwin terms, or in the SOO term (25). The use of these operators in NMR calculations has been discussed, for example, in refs. 53,72–74. It was already mentioned that some of the two-electron contributions (but not the SOO-related terms) are obtained in a mean-field sense when using an effective potential in place of V in the one-electron perturbation

operators. Previous experience with two-electron SO contributions indicates that their *relative* importance decreases in comparison to their one-electron counterparts when the nuclear charges become larger.^{26,53,72,73}

2.6 Contributions from the various operators to shielding and spin–spin coupling

Consider the various perturbation operators that may be obtained from differentiating magnetic operators such as those derived in the previous section. In the nonrelativistic and two-component relativistic methods, the various one-electron mechanisms contributing to the nuclear magnetic shielding and the spin–spin coupling may be written as given in the following sub-sections, using for convenience a SOS formulation.

2.6.1 Nuclear magnetic shielding

$$\sigma_A = \langle \Psi_0 | DS^{(m_A, B)} | \Psi_0 \rangle + 2 \sum_{j \neq 0} \text{Re} \frac{\langle \Psi_0 | (OP + FC + SD)^{(m_A)} | \Psi_j \rangle \langle \Psi_j | (OZ + SZ)^{(B)} | \Psi_0 \rangle}{E_0 - E_j} \quad (55)$$

where, for example, $OP^{(m_A)}$ indicates the first derivative of the nonrelativistic one-electron OP operator or of a two-component analog thereof (e.g., (43e) and (49)) for each electron with respect to m_A , and similar for the other operators. The first term in (55) is the *diamagnetic shielding*. In the paramagnetic (the SOS) part, the leading contribution which is present in both nonrelativistic and relativistic calculations is the OP–OZ term.^r For a closed-shell molecule, if SO coupling is absent (i.e., in the nonrelativistic or a scalar-relativistic method), this is the only paramagnetic contribution. As can be seen from Equation (55), there are also (FC+SD)–OZ, (FC+SD)–SZ, and OP–SZ mechanisms. However, for a spin-free closed-shell system, their contributions vanish.

It is helpful to recall the analog of (55) in a MO-based formalism (Equation (36a)) to see why these mechanisms vanish: FC and SD are spin-dependent operators (triplet operators). They perturb α - and β -orbitals in equal but opposite ways, causing a spin-density perturbation in the atom or molecule. The OP term is spin-independent (a singlet operator) causing a paramagnetic current-density perturbation in the system. It acts equally on α - and β -orbitals. Thus, in a closed-shell system where α - and β -orbitals come in pairs with identical spatial parts, all (FC+SD)–OP contributions summed over the α -orbitals identically cancel those summed over the β -orbitals. All terms involving the nonrelativistic SZ term cancel for the following reason: this operator has no spatial component, thus its matrix elements involve the spatial overlap between occupied and unoccupied orbitals (or in the SOS formula the overlap between the ground- and excited-state wavefunctions) which is zero.

^rOP–OZ meaning the sum in (55) containing only $\langle \Psi_0 | OP^{(m_A)} | \Psi_j \rangle \langle \Psi_j | OZ^{(B)} | \Psi_0 \rangle$ matrix elements in the numerator.

If SO coupling is nonnegligible, the orbitals are not pure α - and β -orbitals anymore, and complete cancelation between spin-dependent and spin-independent mechanisms does not occur. Thus, for nuclear magnetic shielding in two-component theories, there are SO shielding terms involving a (FC+SD)–OZ mechanism, as well as contributions from the two-component form of SZ. These are the celebrated SO contributions to the shielding which enter the paramagnetic (SOS) part of the shielding expression. Numerical studies have indicated that the FC–OZ term tends to be the dominant one. Its interpretation is often given as follows: the OZ operator resulting from the external field acts differently on the α and β components of a two-component orbital $\varphi_i(\mathbf{r}) = \begin{pmatrix} \varphi_i^\alpha(\mathbf{r}) \\ \varphi_i^\beta(\mathbf{r}) \end{pmatrix}$, thus in effect causing a spin-density perturbation in the molecule which is “picked up” by the FC (and SD) mechanisms at the nucleus of interest. One may also interpret the formula with FC+SD as the initial perturbation, inducing a current density in the SO coupled system which is then “detected” by the OZ mechanism.

2.6.2 Indirect nuclear spin–spin coupling

$$\begin{aligned} \mathbb{K}_{AB} = & \langle \Psi_0 | \text{OD}^{(m_A, m_B)} | \Psi_0 \rangle \\ & + 2 \sum_{j \neq 0} \text{Re} \frac{\langle \Psi_0 | (\text{OP} + \text{FC} + \text{SD})^{(m_A)} | \Psi_j \rangle \langle \Psi_j | (\text{OP} + \text{FC} + \text{SD})^{(m_B)} | \Psi_0 \rangle}{E_0 - E_j} \end{aligned} \quad (56)$$

The diamagnetic contribution to the K -coupling tensor is obtained from the derivatives of the OD operator. The diamagnetic part of the spin–spin coupling is often small, although counter examples are known.⁷⁵ The various paramagnetic mechanisms are usually separated into the spin-dependent mechanisms FC–FC (“FC mechanism,” often dominant), FC–SD+SD–FC (“FC–SD cross term”, anisotropic), SD–SD (SD mechanism, sometimes important), the spin-independent mechanism OP–OP (“paramagnetic mechanism,” often large for couplings involving p-block elements), as well as SO cross terms between spin-dependent and spin-independent operators, such as FC–OP, etc. The latter vanish in a nonrelativistic or scalar-relativistic treatment for the same reasons as outlined above for the SO terms in the shielding tensor, that is, there is complete cancelation of the contributions from the α - and β -orbitals. If SO coupling is large, the FC–OP and other SO cross terms can become quite large (e.g., for heavy p-block diatomics).

Relativistic effects on NMR parameters may show up in several ways:

- (i) Via spin-free (scalar) relativistic effects on $\Psi^{(0)}$ and $\Psi^{(m_A)}, \Psi^{(B)}$, along with scalar-relativistic modifications in the operators. That is, based on the previous two equations, one of the main differences between nonrelativistic and relativistic calculations is the behavior of the operators and of the wavefunction/orbitals in the vicinity of the nuclei.
- (ii) Via SO coupling terms. For instance, as we have seen that for a closed-shell system, all cross terms between spin-free operators and spin-dependent operators cancel in the absence of SO coupling. However, these cross

terms can become quite large if SO coupling is substantial, such as for elements in the 5d block, actinides, or heavy p-block elements.

- (iii) Relativistic effects may substantially alter the *geometry* of the molecule. This may be considered an indirect effect that shall not be analyzed further in this chapter. That is, we assume that a comparison between relativistic and nonrelativistic results is made for the same (experimental or relativistically optimized) geometry.

In four-component methods, all scalar-relativistic and SO contributions are contained in a single, formally paramagnetic, term. As already mentioned, the diamagnetic contributions are implicitly contained in the four-component relativistic results. In a matrix formulation in a basis set, diamagnetic terms may appear explicitly^{66,67} if the formalism is suitably chosen.

2.7 The gauge-origin problem for the nuclear magnetic shielding

The DFT expressions (36a) and (36b) assume in their derivation a complete basis set. The SOS equations assume exact wavefunctions. In practice, the basis sets are finite, of course, and wavefunctions and the electron density are approximate. For the shielding constant and other molecular properties that depend on an external magnetic field, using equations that were derived for the complete basis set limit leads to origin-dependent results, a problem that is intimately related to the following situation: adding the gradient ∇f of any scalar function $f(\mathbf{r})$ to the vector potential \mathbf{A} does not affect $\mathbf{B} = \nabla \times \mathbf{A}$, because $\nabla \times \nabla f(\mathbf{r}) = 0$. Therefore, \mathbf{A} is undetermined up to adding ∇f ("gauge freedom"). Note that the balance between paramagnetic and diamagnetic terms depends on the gauge chosen for \mathbf{A} . Often, f is chosen such that $\nabla \mathbf{A} = 0$ (Coulomb gauge).

A different gauge of \mathbf{A} can, for example, be chosen implicitly by adopting a different origin for the coordinate representation of \mathbf{A} which can be seen from Equations (37) and (38): shifting the coordinate origin by a constant vector \mathbf{a} , that is, changing \mathbf{r} to $\mathbf{r} - \mathbf{a}$ in Equation (38) has no effect on the field calculated as $\mathbf{B} = \nabla \times \mathbf{A}$ because $\nabla \times \mathbf{a} = 0$. For the strongly inhomogeneous magnetic field from a nuclear spin, there is a natural gauge origin, which is the position of the nucleus. For the homogeneous external field, however, the gauge origin is arbitrary. Although for a large class of variationally determined wavefunctions in a complete basis the calculated properties would not depend on the chosen gauge, this is not generally true for incomplete basis sets¹⁷ and care needs to be taken that origin-independent results are computed. Presently, the standard remedy is to adopt a "gauge including atomic orbital" (GIAO) basis set (also frequently referred as "London AOs").^{76,77} This eliminates the origin dependence in variational methods such as HF, KS DFT, multiconfigurational SCF (MCSCF), or variational CI theories, and often also leads to improved basis set convergence of the response property. Other methods to cure the origin problem are also in use, including the "individual gauge of localized orbitals" (IGLO),⁷⁸ a "localized orbital/local origin" (LORG),⁷⁹ or applying a "continuous set of gauge transformations" (CSGT).⁸⁰ Magnetic properties computed with nonvariational

methods such as CC theory do not in general become origin invariant in a GIAO basis.⁸¹

The use of GIAOs leads to additional terms in the DFT expressions for the NMR shielding given in Section 2.4 and other magnetic properties which arise from basis function derivatives with respect to the external field amplitude. In a complete basis, these terms cancel.^{82,83} For qualitative interpretations of DFT results, it is often appropriate to use Equation (36a) but for quantitative analyses the additional terms need to be explicitly considered.

2.8 Vibrational and thermal averaging; isotope effects

Computations of NMR parameters are usually carried out at a single optimized geometry, or for a few low-energy conformations if a molecule has multiple local minimum structures. As already mentioned, nuclear magnetic shielding and reduced indirect nuclear spin–spin coupling are electronic properties independent of the nature of the nuclei.

Since nuclei vibrate in molecules, a possible dependence on the nuclear masses may arise through vibrational corrections. These corrections, in turn, may be temperature dependent if the excited vibrational modes afford different vibrational averages for the property under consideration. Vibrational averages of a molecular property P , such as NMR tensor elements but also other properties, can be calculated to lowest order in an expansion around the value P_e obtained for the equilibrium structure as

$$\langle P \rangle_T = P_e - \frac{1}{4} \sum_i \frac{1}{\hbar \omega_i} \left(\frac{\partial P}{\partial q_i} \right) \sum_j \coth \left(\frac{\hbar \omega_j}{2kT} \right) k_{ijj} + \frac{1}{4} \sum_i \coth \left(\frac{\hbar \omega_i}{2kT} \right) \left(\frac{\partial^2 P}{\partial q_i^2} \right) \quad (57)$$

where T is the temperature, ω_i the fundamental vibrational frequency of normal mode number i with dimensionless normal coordinate q_i , and k_{ijj} one of the cubic force constants.^{84–86} The expression also yields a vibrationally averaged structure by considering P as the set of nuclear coordinates in the system. Other authors have chosen to expand the PES around the effective geometry which yields a simpler expression for the vibrational average⁸⁷ (but for T -trends these expressions would require to repeat the averaging at a different expansion point for each temperature). For application of vibrational averaging in nonrelativistic NMR computations, see ref. 88. Since the vibrational models depend on the nuclear masses, Equation (57) or alternative formulations can be used to compute isotope effects as well. There have not yet been many applications of vibrational averaging techniques in computational NMR studies employing relativistic methods (other than with scalar ECPs); as an example, we cite an investigation of the ⁹⁹Tc shielding and Tc–O spin–spin coupling constants in the TcO₄[−] ion in water.⁸⁹ The authors used a ZORA DFT computational method including SO coupling. The computations reproduced the increase of the Tc shift by about 2 ppm between 280 and 320 ppm, temperature effects on $K(\text{Tc–O})$, as well as isotope effects on $K(\text{Tc–O})$ and $\delta(\text{Tc})$ very well. Bühl et al. have applied vibrational averaging in computations of the NMR of metal complexes quite

extensively; we refer to ref. 14 for further details and references as well as applications using nonrelativistic NMR programs.

If the molecule under scrutiny has several local minimum structures, temperature effects on NMR parameters might occur due to a change in the mole fractions (Boltzmann populations) for each conformer. Another possibility to obtain thermally averaged molecular properties is to use molecular dynamics (MD) or Monte-Carlo-type (MC) simulations at finite temperature. Effects due to vibrational distortions of the molecule are also included in such simulations. However, often in such simulations, the nuclei are treated as classical (nonquantum) particles which means the approach is in many aspects complementary to the vibrational averaging procedure outlined above which is based on treating the vibrations as quantum harmonic oscillators with perturbational anharmonicity terms. In MD/MC, a thermal average of a NMR parameter can be obtained from averaging a large number of configurations. See ref. 90 for an early application of this technique to average NMR parameters for metal complexes (vanadium, nonrelativistic NMR computations). For an application to a relativistic system, see, for example, Spiegel et al.'s computational study of the binding of cisplatin ($cis\text{-}[\text{Pt}(\text{NH}_3)_2\text{Cl}_2]^{2+}$) to DNA oligomers.⁹¹ The authors reported that the MD average yielded only qualitative agreement with experiment, with large error bars of the MD averages due to a noted strong sensitivity of the Pt shift to structural parameters. Scalar ZORA DFT computations were employed for the Pt chemical shift averages. Our group has recently employed MD as part of a study designed to find out why Pt chemical shifts are difficult to compute.⁹² We will provide further details in Section 3.4.3.

2.9 Analyzing NMR parameters from first-principles computations

It is sometimes helpful to know which regions in a molecule or which orbitals contribute most to a molecular property in order to understand, for example, why it affords or does not afford large relativistic corrections. The electron density of a molecule may be analyzed in detail, for example, by using topological analyses.⁹³ Contributions to the energy *per orbital* can be calculated straightforwardly although for the energy itself this approach is not as common as for energy-derivative properties when using canonical delocalized MOs. Localized orbital methods such as natural bond orbitals (NBOs) have been used extensively for bond energy analyses.⁹⁴ Energy decomposition methods to separate steric, electrostatic, etc., terms^{95,96} also remain to be very popular.⁹⁷ One can devise analysis methods for energy-derivative properties as well. For instance, suppose there is a one-electron property P with an associated operator $\hat{P}(\tau)$. The expectation value is

$$P = \langle \Psi | \hat{P} | \Psi \rangle = \int d\tau ds \cdot \Psi^*(\tau, s) \hat{P} \Psi(\tau, s) = \int d^3r \cdot P(\mathbf{r}) \quad (58)$$

where, after integration over spin (s) and all but one spatial coordinates in τ , the integrand of the remaining 3D integral may be called the “property density” function $P(\mathbf{r})$. From (58), one can identify regions of *space* that contribute the most to the property. For a first-order energy-derivative property, the approach

is straightforward; one may use Equation (27) and thus $\hat{P} = \hat{\mathcal{H}}^{(\lambda_1)}$. For the second-order derivative (to analyze NMR parameters), the operator is more complicated. It can be written in SOS form as $\hat{P} = \hat{\mathcal{H}}^{(\lambda_1, \lambda_2)} + \sum_{j \neq 0} (|\hat{\mathcal{H}}^{(\lambda_1)}|\Psi_j\rangle\langle\Psi_j|\hat{\mathcal{H}}^{(\lambda_2)})/(E_0 - E_j) + \text{c.c.}$ (and similar for its MO counterpart). Nonetheless, spatial analyses are possible in this way.

Another intuitive way for partitioning expectation value integrals is obtained in molecular-orbital methods. Typically, in this case a property can be written as a sum over integrals involving the occupied orbitals, or sums of terms involving occupied–unoccupied terms such as the expressions (36a) and (36b). Instead of partitioning the sum per spatial contributions from the integral, one carries out the integration for each MO pair separately. As a result, the property is partitioned per MO or MO pair instead. Such analyses have been performed extensively for NMR parameters using the canonical MOs directly as in Equations (36a) and (36b). For the MO basis, a localized or a delocalized description may be chosen which often yields complementary information about the origin of the property. In (KS) DFT, an orbital partitioning of energy and properties is essentially built into the formalism since the electron density is constructed from a set of KS MOs. In correlated wavefunction-based methods, one can, for instance, express the density matrix in terms of natural orbitals which would also lead to a convenient orbital-based partitioning of one-electron properties.

NMR parameters have been analyzed extensively using various decomposition methods. Occupied–unoccupied contributions straight from Equations (36a) and (36b) are available in many codes. As examples, we mention the relativistic ZORA NMR DFT programs developed by Ziegler and coworkers.^{58,98} Other analysis methods can be devised, based on transformations of the orbital basis and/or the integrands. Cremer et al. have studied a large range of “nonrelativistic” molecules with various decomposition schemes for spin–spin coupling.^{99–103} NBOs and natural localized MOs (NLMOs) as devised by Weinhold⁹⁴ have been applied to analyze nonrelativistic *J*-coupling^{104–106} and nuclear shielding.¹⁰⁷ Malkina and coworkers^{108,109} and Soncini and Lazzeretti^{110,111} have employed density-based methods to study nonrelativistic spin–spin coupling pathways. See also ref. 112. Autschbach et al. have studied light and heavy atomic systems by scalar-relativistic and nonrelativistic methods and decomposed spin–spin coupling into contributions from AOs, canonical MOs, and Boys-localized MOs.^{113–115} Recently, we have extended the formalism for NBO/NLMO analyses for two-component relativistic DFT, for both spin–spin coupling¹¹⁶ and nuclear magnetic shielding (using a GIAO basis).^{117,118} Some of the results obtained with these relativistic localized orbital analyses will be discussed in Section 3.

An orbital partitioning can be complementary to a space partitioning. For example, suppose the integrand in Equation (58) indicates that a property has large contributions from the core regions in the molecule (the regions very close to the nuclei). An orbital analysis might indicate that the core orbitals are the main contributors. In this case, it would be reasonable to identify the property as a core property. The NMR nuclear magnetic shielding is a good example for such a property. On the other hand, an orbital partitioning might determine instead

that valence orbitals are the biggest contributors to a property for which a spatial analysis finds that core regions play a big role. This appears contradictory. We note, however, that valence orbitals have core tails. The two analyses can be reconciled if it turns out that the core tails of the valence orbitals near the nuclei determine the major contributions to the property. In this case, the interpretation would be that the property is determined by the valence orbitals, but that it strongly weighs the atomic core regions because the property operators are large there. A prime example for such a valence property determined by the core tails of the valence orbitals is the indirect NMR nuclear spin–spin coupling (J -coupling). Another example is the NMR chemical shift for which most of the core region–core-orbital contributions cancel and only the core region–valence-orbital contributions are of importance (along with semicore (outer core) contributions). EFGs also fall into this category. A third, rather clear-cut, scenario is one where the spatial analysis indicates that the origin of the property is the valence region, and the orbital analysis finds that the valence orbitals are responsible for the property. In this case, the property would reasonably be identified as a valence-shell property. The electric polarizability is an example for such a property.

Core and valence orbitals are directly impacted by relativistic effects. For valence-shell properties, particularly large relativistic effects are obtained if the property operators are large in the core regions of the heavy atoms. According to Section 2.5, large relativistic effects should therefore be expected for heavy-nucleus chemical shifts or J -couplings of heavy nuclei because the nonrelativistic hyperfine operators sample the near-nucleus regions via their r_A/r_A^3 terms or derivatives thereof, and as we have seen this is similar for their relativistic analogs. For such properties, relativistic effects can be very large indeed — to the point where the notion of a relativistic *correction* becomes fuzzy. What is the meaning of a 100% or even larger relativistic “correction term”? It would probably be more appropriate to speak of (approximately) correct vs. incorrect instead. Genuine core properties may also afford very large relativistic effects. For other valence properties that do not specifically sample the near-nuclear regions, relativistic effects are often of similar relative magnitude as those on the binding energies. Examples are dipole moments, polarizabilities, vibrational frequencies, or excited-state properties.

In Section 3.2, spatial and orbital contributions to the nuclear spin–spin coupling in the PbH_4 molecule will be used as an example for the types of analyses discussed in this section. A corresponding analysis of ^{195}Pt chemical shifts will also be presented in Section 3.4.3 and additional spin–spin coupling examples will be discussed in Section 3.5.3.

3. BENCHMARK DATA AND CASE STUDIES

3.1 Acronyms used

In this section, we will frequently use some acronyms for various computational methods. Some of these have been introduced earlier: DFT for density functional theory, HF for Hartree–Fock, and SO for electronic SO coupling.

We will use SC occasionally to designate a scalar-relativistic or spin-free method, that is, excluding SO coupling. “Pauli” or “Breit–Pauli” will be short for computations using the Pauli operator excluding or including two-electron SO terms, either variationally with frozen cores or as a perturbation. DKH2 will be used for the second-order DKH-transformed relativistic Hamiltonian, and DKH for generic references to this method. ZORA refers to the zeroth-order regular approximate Hamiltonian, and “Dirac” will occasionally be used to refer to four-component relativistic methods. ESC refers to elimination of the “small component schemes.” DKH, ZORA and higher-order regular approximations, Dirac, etc., are variational relativistic methods. Some of the relativistic benchmark data cited later were obtained with variational Pauli-operator computations. Although for some time it has found widespread application, this method is now depreciated because of its variational instability. The Breit–Pauli operator is still used extensively in computations where relativistic effects are treated as another perturbation. Acronyms for correlated *ab initio* methods are: MCSCF, MP2 (second-order Moller–Plesset), and CC.

The acronyms HALA and HABA¹¹⁹ are sometimes used in the context of relativistic NMR computations: HALA refers to a heavy-atom effect on light-atom NMR parameters, and HABA are heavy-atom (relativistic) effects on the heavy-atom’s own NMR parameters.

3.2 Illustrative examples for the influence of relativity: the FC term in PbH₄ and the spin–orbit shielding in HI

It is illustrative to first discuss small molecules to demonstrate the influence of relativity on NMR parameters. The plumbane molecule, PbH₄, has often served as a benchmark molecule for computations because it contains one of the heaviest NMR nuclei but does not have other electron-rich ligands that would lead to overly CPU-intensive computations. Consider the Pb–H spin–spin coupling constant. Some benchmark data for the Pb–H coupling in PbH₄ and other plumbanes are listed in Table 1. In particular, the more recent DFT computations based on hybrid DFT and including spin-free and SO effects reproduce the experimental data quite well. Regarding the overall significance of the relativistic effects: nonrelativistic computations typically yield results of only half the magnitude, that is, with the nonrelativistic results as the reference, the relativistic “corrections” are on the order of 100%. SO effects on $K(\text{Pb–H})$ are quite noticeable but much smaller than the scalar-relativistic effects. The MCSCF computation by Kirpekar and Sauer did not include scalar-relativistic effects but it reproduced the magnitude of the SO effect on $K(\text{Pb–H})$ very well.

As we have seen in Section 2.5, the “contact” operator (FC) is the one that samples the electronic structure right *at* the nuclei. Its relativistic analogs sample the very near-nuclear regions. This operator — because of its large prefactor^s — tends

^s $4\pi/3 \approx 4.2$ for FC compared to OP, which means the FC–FC mechanism has an order of magnitude larger factor than OP–OP.

Table 1 Reduced Pb–H spin–spin coupling constant in plumbanes, in $10^{20} \text{ T}^2 \text{ J}^{-1}$

	PbH_4	$\text{Pb}(\text{CH}_3)_2\text{H}_2$	$\text{Pb}(\text{CH}_3)_3\text{H}$
<i>Spin-free ZORA</i>			
PBE ^a	118	95.9	86.1
PBE0 ^a	134	112	103
BP86/ $X\alpha$ ^b	132	107	97.8
<i>Spin-orbit ZORA</i>			
PBE ^a	110	88.0	78.6
PBE0 ^a	126	104	95.0
BP86/ $X\alpha$ ^b	123	98.3	89.1
<i>Selected other literature data^c</i>			
IORA BLYP ^d	127		109
IORA B3LYP ^d	137		121
Dirac HF ^e	182		167
MCSCF+Pauli SO ^f	48		
Nonrel. MCSCF ^f	56		
Expt. ^g	(112)	98.7	92.3

^aDFT with nonhybrid PBE and hybrid PBE0 functional (ref. 120).

^bDFT with nonhybrid BP86 potential and $X\alpha$ response kernel (ref. 60).

^cFor semiempirical data for PbH_4 , see refs. 125,126. For a DFT study with frozen cores using the scalar Pauli operator variationally, see ref. 127.

^dSpin-free DFT calculations using an infinite-order regular approximation (IORA) (Filatov and Cremer³⁸).

^eFour-component basis Hartree–Fock computations (Enevoldsen et al.¹²¹). A scaled value for PBH_4 based on a correlated nonrelativistic calculation to account for electron correlation was given as 138.3.

^fNonrelativistic MCSCF computations with first-order corrections from the Pauli SO operator, Kirpekar and Sauer.¹²²

^gExperimental value for PbH_4 extrapolated from the experimental data for the methyl derivatives $\text{Pb}(\text{CH}_3)_3\text{H}$ and $\text{Pb}(\text{CH}_3)_2\text{H}_2$. Experimental data from ref. 123. An alternative experimental value for $\text{Pb}(\text{CH}_3)_3\text{H}$ is 94.6, from ref. 124.

to dominate most coupling constants, including $K(\text{Pb–H})$ in PbH_4 , and should also be the one that samples relativistic effects most effectively. Figure 1 demonstrates the strong influence of relativity and the importance of the core regions on the Pb–H spin–spin coupling: in Figure 1, the FC-like contribution to the Pb–H coupling is partitioned spatially, as in Equation (58), and shown as a radial integral around the Pb nucleus. We observe a number of details that are typical for spin–spin coupling involving heavy elements: overall, there is a huge relativistic increase in $K(\text{Pb–H})$ which, percentage-wise, far exceeds relativistic effects usually found for structural parameters and bond energies of sixth-row element compounds. Obviously, a bond will not contract 100% due to relativity, and a molecule that is only very weakly bound nonrelativistically, but moderately strongly bound in the relativistic case, might afford a very large percentage bond energy correction. But

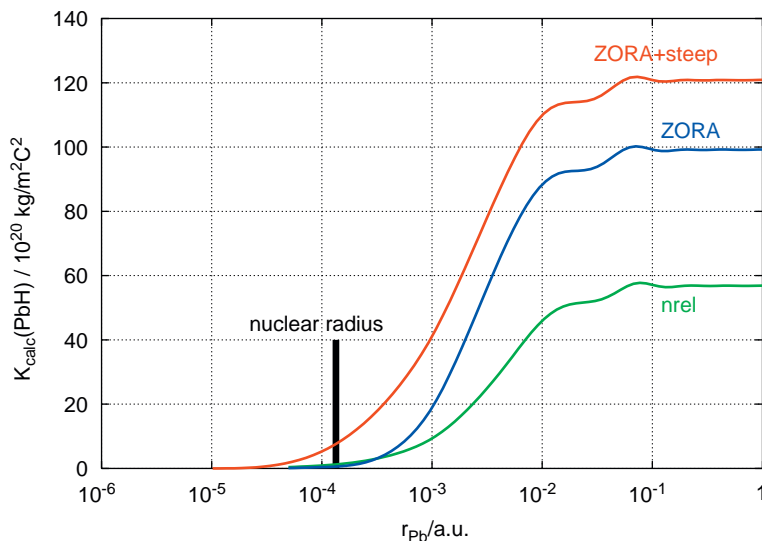


Figure 1 $K(\text{Pb-H})$ spin-spin coupling constant of PbH_4 obtained from a radial integral of a “coupling constant density” (cf. Equation (58)) around the Pb nucleus, from spin-free ZORA and nonrelativistic (nrel) DFT computations with the VWN local density functional.⁵⁹ The total computed coupling constant is obtained as $r_{\text{Pb}} \rightarrow \infty$. FC-type mechanism only. ZORA+steep means that a range of high-exponent (“steep” and “tight”) functions was added to the basis set in order to describe the relativistic effects near the Pb nucleus better. A point nucleus was used for the computations. The size of the Pb nucleus is indicated in the figure.

the large relativistic increase of the already large Pb-H coupling constant indeed nicely illustrates the very strong effect that relativity has on this NMR parameter.

We further note that most of the difference between ZORA and “nrel” results from regions less than about 1/100 bohr radii around the Pb nucleus. The nonrelativistic result is strongly determined by this region to begin with, and most of the relativistic effects also contribute in this region. This finding highlights the fact that the operators that are involved are large near the nuclei. Another important finding is the large increase observed for $K(\text{Pb-H})$ when high-exponent basis functions are added to the basis set in order to describe the nuclear tails of the orbitals better. In general, computing relativistic NMR parameters requires basis sets that are very flexible in the near-nuclear region. For a point nucleus, the analytic solutions of the one-electron Dirac equation exhibit weak singularities for $s_{1/2}$ and $p_{1/2}$ orbitals. In a regular basis set, this behavior can be approximated by adding high-exponent (“tight”) basis functions, which is necessary in particular if properties with “contact”-type operators are of interest. In Figure 1, it is seen that the additional increase in $K(\text{Pb-H})$ indeed results from regions very close to the nuclear radius. Although with finite nuclei no singular terms arise, the importance of the near-nuclear regions — and therefore basis sets to describe the electronic structure there — would be quite similar. The case is further illustrated in Figure 2 which shows the electron density of the Hg atom obtained from numerical DFT computations.

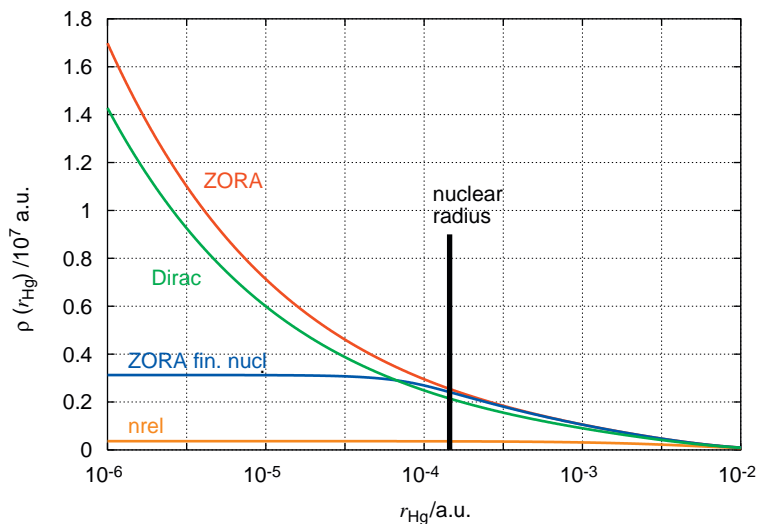


Figure 2 Electron density of the Hg atom in the near-nucleus region, from numerical DFT computations.⁵⁹ The difference between ZORA and Dirac is in part due to the picture change, and in part due to the ZORA approximations.

In a previous paper,⁵⁹ we argued that adding too many tight functions to a basis set to describe the strong increase of the density for radii less than the nuclear radius is not particularly desirable. Treating the point nucleus correctly in this respect would likely lead to an overestimation of the “contact” term magnitudes. The problem is somewhat alleviated if the basis set is restricted to provide good coverage for regions outside the nuclear radius. Numerical evidence has been provided in ref. 71. Ultimately, though, when considering the data shown in Figure 1, it is clear that for computations of nuclear spin–spin coupling it would be best to adopt a finite-nucleus model.

We have recently revisited the PbH_4 case (along with other molecules) and studied the coupling constant with an analysis method based on using spin-free relativistic localized orbitals.¹¹⁶ An analysis per canonical MO was also carried out. The results are illustrated in Figure 3. Both spin-free and SO results are provided. The important conclusion from the orbital decomposition is that the coupling constant is determined by the Pb–H bonding orbitals (i.e., by the valence shell) along with sizeable contributions from the Pb 5s orbital. The result for this and other molecules studied in ref. 116, results from other relativistic analyses of spin–spin coupling,^{113,114} as well as, for example, results from analyses of nonrelativistic spin–spin couplings performed by Ziegler and coworkers^{128,129} therefore suggest that spin–spin coupling is predominantly a valence-shell property (*cf.* Section 2.9). Since the spatial analysis (Figure 1) yields most of the contributions from the core region, the origin of the property can be traced back to the core tails of the valence orbitals. Indeed, very similar results are obtained for the spin–spin coupling in PbH_4 if a *frozen* core (1s–4d) is used (this was explicitly demonstrated in ref. 59 for Hg–C coupling constants,

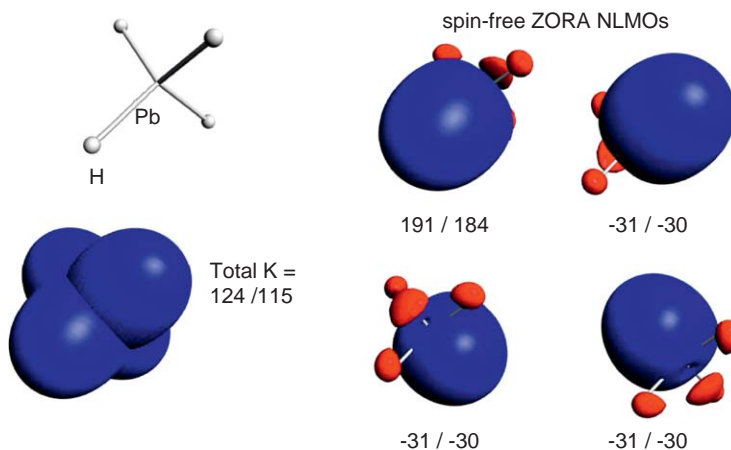


Figure 3 Pb–H spin–spin coupling in PbH_4 analyzed in terms of spin-free localized orbitals (here: natural localized MOs⁹⁴). ZORA DFT computations from ref. 116 with the PBE functional. Spin-free/spin-orbit results reported in units of $10^{20} \text{ T}^2 \text{ J}^{-1}$. Contributions from the Pb 5s orbital are: spin-free 24 and spin-orbit 24. The combined PBE results shown here differ slightly from those of Table 1 because of a different basis set used for H and small differences in the geometries used.

the corresponding Pb data are unpublished). The main contribution is — as one might expect — from the Pb–H bonding orbital for the pair of nuclei under consideration. The analysis also finds three equivalent negative contributions from the other Pb–H bonds which are somewhat less intuitive and which do not show up in the light atomic analog methane. The computations indicated that the electronic structure in PbH_4 is quite a bit more delocalized than methane. In other words, each Pb–H bond is delocalized over the other three bonds. The loss of localized charge density in the bond shows up as negative contributions to $K(\text{Pb–H})$ from other orbitals as well as in a positive contribution from the Pb–H bonding orbitals that is significantly higher than the total K .

SO effects on nuclear magnetic shielding constants have been studied theoretically for quite some time before scalar-relativistic effects for shielding or spin–spin coupling were considered. It has been known for a long time that the shielding of nuclei in the vicinity of a halogen strongly increases as the halogen nuclear charge increases. This leads to a decreasing shift of atoms neighboring $\text{X} = \text{F}, \text{Cl}, \text{Br}, \text{I}$, with increasing nuclear charge of X which is called “normal halogen dependence” (NHD). An example is the proton shift in the hydrogen halides H–X . It had been argued already in the late 1960s¹³¹ that SO coupling must be responsible for the increasing shielding of the proton along the series. Computational studies of the proton shielding in the HX series date back to the 1970s, when perturbation approaches employing the SO part of the Pauli operator together with semiempirical LCAO wavefunctions have been used.^{132–134} Since then, numerous computations have confirmed that the NHD is induced by SO coupling. As an example, Figure 4 shows data from MCSCF computations by Manninen et al. who included relativistic effects

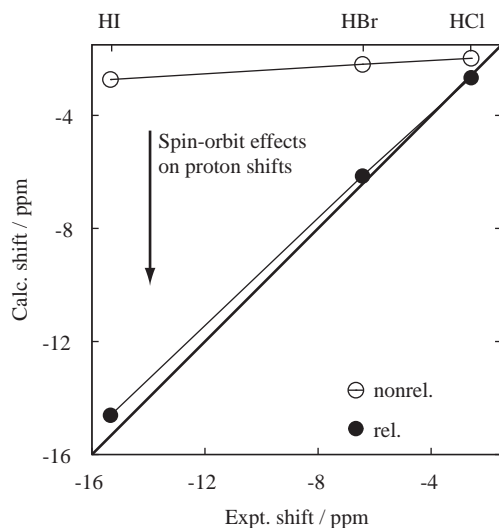


Figure 4 Proton chemical shift of HX, X = Cl, Br, I, with respect to HF. MCSCF computations including (rel) or excluding (nrel) first-order (Breit–Pauli) relativistic corrections to the shielding constant. Computational results were taken from Manninen et al.⁶¹ Experimental data as quoted in ref. 130. The straight thick line indicates where calculated = experiment.

perturbationally to first order in c^{-2} at the Breit–Pauli level.⁶¹ The relativistic results are in good agreement with experiment and demonstrate the large SO effect, in particular for HI. A compilation of literature data for the HX series can be found in Section 3.4.1. The physical mechanism of NHD is related to that of spin–spin coupling in some sense since in both cases a contact-type mechanism (FC), and also SD, is involved.^{135,136} The situation has been outlined in Section 2.6: around a heavy atom where SO coupling is strong, the external magnetic field not only induces a paramagnetic current density but also a spin-density perturbation. This perturbation transfers through the chemical bonds and causes nonvanishing spin-dependent terms in the shielding tensor at light neighboring nuclei via the (FC+SD)–OP mechanism.

There is of course also a possibility that the FC+SD–OP mechanism picks up this spin density at the heavy atom’s *own* nucleus. This would be an example for a HAHA effect on a heavy-atom nuclear magnetic shielding. As we have seen in the PbH_4 example, the “contact” FC-like terms can become very large for heavy nuclei and therefore large SO effects on their shielding tensors must be expected, along with other relativistic effects affecting, for instance, the paramagnetic mechanism. Further examples of HAHA and HALA effects on NMR chemical shifts will be given in Section 3.4.

3.3 When are relativistic methods needed for NMR computations?

It should be clear from the discussion in Section 3.2 that use of a relativistic computational method is mandatory if a spin–spin coupling constant

involving a heavy nucleus is of interest, that is, for heavy-atom–light-atom or heavy-atom–heavy-atom couplings. Because of the importance of the core tails of valence and outer core orbitals, an all-electron method (or a reconstruction of the all-electron orbitals) is required which means that for such coupling constants the straightforward use of an ECP on the heavy atom is not applicable. Numerous benchmarks, some of which will be discussed below, have shown that for elements from the sixth row of the periodic table relativistic effects on one-bond couplings involving *one* heavy nucleus may exceed 100% of the nonrelativistic value. Relativistic effects on coupling between two nuclei can be even larger. Available data on coupling through multiple bonds are still rather scarce but if there is a heavy nucleus on one end a relativistic method should certainly be used. Since spin–spin coupling is also quite sensitive to electron correlation, the computation should be done with a post-HF wavefunction method or at the DFT level. Relativistic effects of roughly an order of magnitude smaller should be expected for atoms from the fifth row of the periodic table (with comparatively large corrections from both scalar and SO effects in the p-block, thus calling for a relativistic treatment of coupling constants with Te, I, and Xe), and correspondingly smaller for lighter atoms. Relativistic effects on coupling constants involving elements such as Se can still be on the order of 20% which exceeds the accuracy limit of popular DFT methods. For lighter elements, relativistic corrections are needed for high accuracy computations.

The same considerations about ECPs apply to heavy-nucleus shielding constants/tensors. Spin-free ECP computations for heavy-atom shielding have occasionally been undertaken^{137–139} but even though some of the available data indicate that chemical shift trends of the correct direction might be obtained (but with grossly erroneous magnitudes) using this approach should be strongly discouraged. Because the shielding itself is not observed directly but rather the chemical shift (Equation (2)), a large portion of the relativistic effects on the shielding may cancel in the chemical shift. The available data indicate that chemical shifts of 4d transition metals and lighter atoms are often well reproduced with nonrelativistic computations,¹⁴ and for qualitative estimates the nonrelativistic approach may be extended even to somewhat heavier atoms. Once relativistic effects significantly change the bonding features in the valence shell, nonrelativistic computations of heavy-atom chemical shifts should not be considered reliable. This certainly applies to the 5d metals and heavier elements.

A situation where a spin-free ECP can be applied straightforwardly is when coupling between light atoms or a light-atomic chemical shift, for instance, in a heavy metal complex, is of interest. This applies to situations where the heavy element is quite well treated by a spin-free relativistic method (i.e., SO HALA effects are negligible) and/or if the light atoms are far away from the heavy atom and HALA effects are small altogether. Since such computations are nonrelativistic in essence, we will not consider applications of scalar-relativistic ECPs in this chapter. The range of applicability of scalar-relativistic ECPs might be limited in NMR computations: as we have seen, chemical shifts in the neighborhood of heavy atoms are often strongly influenced by SO relativistic effects; see Section 3.4.1 for further examples. Regarding spin–spin coupling, the authors of ref. 140

concluded from a study of $K(\text{H-H})$ in H_2Y ($\text{Y} = \text{O}, \text{S}, \text{Se}, \text{Te}$) that the SO effects may yield the dominant contribution for HALA effects as is the case for many nuclear shieldings. A large relativistic change of $K(\text{H-H})$ in PbH_4 has been predicted using four-component HF computations.¹²¹ On the other hand, ref. 122 reports rather small SO corrections to $K(\text{H-H})$ in PbH_4 , based on a nonrelativistic HF wavefunction with SO coupling included as a perturbation. Likewise, HALA effects on chemical shifts might be quenched. For example, in a recent study of fluorine chemical shifts in fluorine–tantalum clusters, we did not find large SO effects although their inclusion improved agreement with experiment.¹⁴¹ In an another study, it was shown that H–D coupling constants in dihydrogen and dihydride heavy metal complexes were not strongly affected by SO coupling¹⁴² and therefore computational studies of such complexes may proceed at the scalar-relativistic level or by using a spin-free ECP. See refs. 85,143,144 for examples of computational studies on these fascinating systems.

If the molecule under scrutiny contains heavy p-block elements or a 5d metal and one is interested in NMR parameters in the vicinity of these heavy atoms, it is advisable to test for sizeable SO HALA effects, at least for some representative systems or a model system, before proceeding with scalar-relativistic computations. If benchmarks show that SO effects can be neglected for the desired accuracy level of the computations, the use of a scalar ECP or a scalar-relativistic all-electron Hamiltonian such as DKH and ZORA offers the most efficient way for NMR computations of such systems.

When discussing various applications in the following sections, we will put emphasis on computations that were based on a variational relativistic method (i.e., using a relativistic zeroth-order Hamiltonian along with the accompanying perturbation operators). A number of computational studies where relativistic effects (usually SO coupling) were treated by perturbation theory will also be discussed.

3.4 Chemical shifts in heavy-element systems

3.4.1 Benchmark data, spin–orbit effects, halogen dependence

The intriguing case of the proton shift in the HX series, where $\text{X} = \text{F}, \text{Cl}, \text{Br}, \text{I}$, has been discussed in Section 3.2. Numerical benchmark data are provided in Table 2 which were obtained with a variety of computational approaches (uncorrelated, correlated *ab initio*, DFT, various levels of relativistic treatment, and various levels of basis set convergence).

This series is arguably the most frequently used benchmark set of molecules for relativistic NMR implementations, due to the strong SO shifts (HALA) for the heavier X , significant HALA effects on the shielding of X , and the availability of theoretical as well as experimental data. Another advantage of this series as a benchmark set is that electron correlation effects are quite noticeable. From the dates in the table, the reader will notice a steady stream of new developments for computations of relativistic NMR shielding tensors. We have excluded some of the available computational studies where data for the systems with lighter X were not reported or where the study focused on analyses of a subset of the relativistic contributions.^{66,162–164} The currently most accurate point-nucleus

Table 2 A selection of computed proton chemical shifts in HX where X = Cl, Br, I

$-\delta_{\text{H}}^{\text{a}}$ (method/year)	Cl		Br		I	
	nrel ^b	rel	nrel	rel	nrel	rel
Semiemp. PSO ^c /1973 ¹³²	8.02	8.24	11.24	13.85	13.08	20.92
Semiemp. PSO/1978 ^{c,133}	2.1	2.7	5.75	10.0	3.22	16.8
REX/1987 ^{d,135}		0.45		3.35		11.01
HF PSO/1995 ^{e,145}	2.43	3.17	2.57	7.72	3.07	18.93
HF DKH2 PSO/1996 ^{f,146}	1.92	2.69	2.36	7.87	0.04	19.93
DFT PSO/1996 ^{g,147}	1.68	2.31	1.23	5.34	1.61	13.24
DFT PSC/1997 ^{h,148}	1.4	1.5	1.7	1.8	2.1	2.3
MCSCF PSO/1998 ^{i,73}	1.98	2.57	2.19	6.04	2.74	14.68
DFT Pauli/1998 ^{j,130}		1.43		5.34		11.79
HF scalar DKH2/1999 ^{k,149}	2.08	2.17	2.39	3.06	2.62	4.95
HF Dirac/1999 ^{l,150}	2.39	3.13	2.82	8.21	3.32	20.11
HF Dirac/1999 ^{l,151}		2.68		4.91		10.71
DFT SO-ECP/2001 ^{m,152}	1.68	2.39	1.21	6.42	1.61	14.87
DFT ZORA/2002 ^{n,2}	1.57	2.45	1.84	5.31	2.19	13.60
HF ZORA/2002 ^{o,153}	2.28	2.57	2.64	4.86	2.83	13.49
HF DKH2/2002 ^{p,153,154}	2.28	3.20	2.64	8.23	2.83	20.26
HF DKH2/2003 ^{p,42}	2.45	3.22	2.65	8.81	3.06	21.38
HF Pauli/2003 ^{q,61}	2.25	3.18	2.42	8.33	3.06	21.85
MCSCF Pauli/2003 ^{r,61}	1.98	2.66	2.19	6.14	2.73	14.61
HF BS/FPT-1/2004 ^{s,155}	2.29	3.19	2.65	8.39	2.84	21.05
HF BS/FPT-2/2004 ^{t,155}	2.29	3.2	2.65	8.13	2.84	
HF BS/CHF/2004 ^{u,155}	2.29	2.82	2.65	7.89	2.84	20.14
HF BS/CHF/2005 ^{v,45}	3.16	3.36	3.32	8.89	10.42	19.07
HF DKH2/2005 ^{p,45}	3.16	3.36	3.32	8.88	10.42	19.04
CCSD/2005 ^{w,156}		2.61		5.67		15.39
SDCI/2005 ^{x,156}		2.65		5.72		15.56
HF Pauli/2005 ^{y,74}	2.25	3.18	2.42	8.33	3.06	22.05
HF Dirac/2005 ^{z,74}		3.15		7.83		19.02
HF SORA+J _{LL} /2006 ^{aa,157}	3.33	3.14	2.98	7.63	3.04	18.84
HF NESC/SORA/2006 ^{ab,158}		3.2		7.93		19.91
HF NESC/ZORA/2006 ^{ac,158}		3.2		7.93		19.94
HF SORA-Met/2007 ^{ad,159}		3.2		7.92		19.91
HF ZORA-Met/2007 ^{ae,159}		3.2		7.92		19.94
HF MIOTC/2007 ^{af,160}	3.33	3.34	2.98	8.48	3.04	20.78
DFT mDKS-RMB/2008 ^{ag,68}	1.94	2.68	1.70	5.89	2.09	14.58
Exp (± 0.02) ^{ah}		2.58		6.43		15.34

^aIn parts per million, with respect to HF, all values $\times (-1)$.^bNonrelativistic values listed if reported in reference.^cSemiempirical calculation including Pauli SO operator.^dRelativistic extended Hückel calculation.^eHartree-Fock, Pauli SO operator included variationally.

Table 2 (Continued)

^f Hartree–Fock, DKH2 relativistic Hamiltonian with Pauli SO operator included variationally.
^g DFT, Pauli SO operator included as perturbation. Preliminary results published in 1995 (ref. 161).
^h DFT, scalar part of Pauli operator used variationally with frozen cores.
ⁱ Multiconfigurational SCF, Pauli SO operator included as perturbation.
^j DFT, Pauli scalar, and spin–orbit operator used variationally with frozen cores.
^k Hartree–Fock, relativistic approach using the scalar DKH2 operator.
^l Four-component Hartree–Fock.
^m DFT with a spin–orbit effective core potential (ECP).
ⁿ DFT with the two-component ZORA operator.
^o Hartree–Fock with the two-component ZORA operator.
^p Hartree–Fock, DKH2 relativistic operator.
^q Hartree–Fock, Breit–Pauli operator as perturbation, some $\mathcal{O}(c^{-2})$ terms not included.
^r Multiconfigurational SCF, Breit–Pauli operator as perturbation.
^s Hartree–Fock, BS/FTP-1 = Barysz and Sadlej (BS) two-component transformation, ²⁹ finite perturbation method for B .
^t Hartree–Fock, BS/FTP-2 = BS, finite perturbation for B and m_A .
^u Hartree–Fock, BS/CHF = BS, approximate analytical differentiation.
^v Hartree–Fock, modified BS/CHF analytical scheme.
^w Four-component, correlated <i>ab initio</i> (coupled-cluster singles and doubles).
^x Four-component, correlated <i>ab initio</i> (configuration interaction with singles and doubles).
^y Hartree–Fock, Breit–Pauli operator including all $\mathcal{O}(c^{-2})$ terms as perturbation.
^z Dirac Hartree–Fock, no approximation for diamagnetic terms.
^{aa} Hartree–Fock, NESC SORA with two-electron spin–orbit terms.
^{ab} Hartree–Fock, NESC/SORA: normalized elimination of the small component with second-order regular approximation.
^{ac} Hartree–Fock, NESC/ZORA: normalized elimination of the small component with zero-order regular approximation.
^{ad} Hartree–Fock, SORA-Met: NESC-SORA including additional magnetic interaction terms in the metric operator.
^{ae} Hartree–Fock, ZORA-Met: NESC-ZORA including additional magnetic interaction terms in the metric operator.
^{af} Hartree–Fock, MIOTC: modified infinite-order two-component method, related to BS/CHF.
^{ag} Four-component DFT, mDKS-RMB: matrix Dirac–Kohn–Sham method with restricted magnetically balanced basis sets.
^{ah} Experimental values as quoted in ref. 130. Uncertainty due to the experimental value for HF (measured w.r.t. CH ₄).

relativistic HF data are the four-component results from 2005 (Manninen et al.⁷⁴). The effect of truncation of the relativistic treatment to order c^{-2} can be seen by comparison with the 2005 HF Pauli results. The various correlated treatments, either wavefunction based or most of the DFT results, agree better with experiment which demonstrates the influence of correlation effects that do not completely cancel when the proton shielding constants are subtracted to obtain the chemical shift. Nonhybrid DFT methods have a tendency of underestimating the proton shift in HI.

As already mentioned earlier, instead of differentiating a relativistic energy expression twice to obtain the NMR parameters, one may also use third-order perturbation theory and treat leading-order relativistic effects by perturbation theory. In this approach, NMR parameters are first computed with a

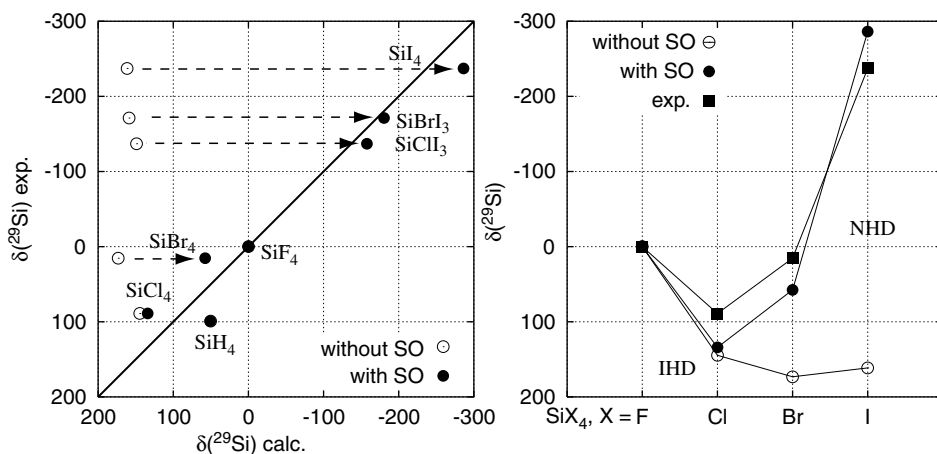


Figure 5 ^{19}Si chemical shifts with respect to SiF_4 in silane and some silicon halides, from Hartree–Fock data (Nakatsuji et al.¹⁷⁴). Scalar rel. and SO effects considered here via ECPs on the halide ligands. (Left) Experimental vs. computed Si shifts. (Right) NHD and IHD along the SiX_4 series.

nonrelativistic method and relativistic corrections are added subsequently which are computed from an expression of the form

$$\Delta^{\text{rel}}_{\sigma_A} = c^{-2} \cdot \left. \frac{\partial^3 E}{\partial \mathbf{B} \partial \mathbf{m}_A \partial c^{-2}} \right|_{c \rightarrow \infty, m_A=0, B=0} + \mathcal{O}(c^{-4}) \quad (59)$$

and similar for spin–spin coupling. Here, c^{-2} is used as the perturbation parameter for “relativity.” One of the advantages is the straightforward interpretation of relativistic effects in various orders. The perturbation operators in the third-order derivatives are relativistic magnetic operators, including those that would be obtained from making the substitution $\hat{\mathbf{p}} \rightarrow \hat{\mathbf{p}} + \mathbf{A}$ in the Pauli Hamiltonian (19) and the associated two-electron operators (see the end of Section 2.3). Unfortunately, the Pauli operator including its scalar-relativistic terms has not been found suitable for spin–spin coupling calculations, because of the combination of highly singular perturbation operators.^{61,t} For nuclear magnetic shielding, the $\mathcal{O}(c^{-2})$ perturbation-theory approach for relativistic NMR based on the Breit–Pauli operator has been applied extensively; see, for example, refs. 57,61,74,164,166–172. Further references to perturbation methods can be found in Table 2.

Numerous theoretical studies have been devoted to NHD-type SO effects. Figure 5 shows HF data obtained in 1995 by Nakatsuji et al. for a set of silicon halides. Very similar results for these and related compounds were obtained in the same year by using a semiempirical approach with SO coupling.¹⁷³ A decreasing HOMO–LUMO gap due to decreasing electronegativity of the

^tApplications of a nonsingular four-component relativistic perturbation theory^{46,47,165} to the calculation of spin–spin coupling in molecules would be an alternative. A route for the calculation of the respective matrix elements of the magnetic perturbations that show up in the formalism⁴⁸ has been discussed.⁴⁹

halogen in the series $X = \text{F, Cl, Br, I}$ should result in a larger magnitude of the paramagnetic shielding, as long as the matrix elements in the sum over excited states can be assumed approximately constant, because of the energy denominators in Equation (36a). Since the nonrelativistic paramagnetic shielding contribution is typically negative, such a behavior would result in an increasingly positive chemical shifts (inverse halogen dependence (IHD)). The NHD, as shown earlier, is due to the more pronounced influence of SO coupling, which often increases the shielding and therefore causes increasingly negative chemical shifts. The diamagnetic shielding, as a core property, is usually found to be of small influence concerning the chemical shifts. From the relativistic nature of the NHD, it becomes clear why explanations of the NHD that only take the (nonrelativistic) paramagnetic shielding into account cannot be convincing.

The SO effects on $\delta(^{13}\text{C})$ in methyl halides are not as spectacular as for the hydrogen halides. Still, qualitative agreement with experimental data can only be achieved on inclusion of SO coupling in the shielding calculation. Scalar-relativistic effects are of minor importance. Benchmark data for these and other small molecules have been published, for example, in refs. 45,61,73,74,130,134,135,145,147,152,156. Rare gas atomic shieldings^{41,45,61,66,67,74,175} are also popular for benchmarks and to test the computational limits regarding their absolute shielding scales. Extremely large SO corrections to the phosphorus chemical shift in PX_4^+ have been reported in ref. 176 and were attributed to the pronounced s-character of the L–X bonds due to the high oxidation state of phosphorus.

The importance of the influence of two-electron (2e-) SO operators has been investigated. Early studies can be found, for example, in refs. 53,73,72. For $\sigma(^1\text{H})$ in HX and $\sigma(^{13}\text{C})$ in MeX, the 2e-SO contributions were found to be small and of opposite sign to the 1e-SO shielding terms. The relative importance of the two-electron terms appears to be generally decreasing for these systems as the heavy atom becomes heavier, contributing about 30% to the (small) SO shift for F substituents and about 7% to the (large) SO shift for iodine substituents. Similar conclusions for the relative importance of the 2e-SO terms were obtained for the shielding of the heavy atom,⁷³ for which the scalar-relativistic effects should not be neglected. The available data indicate that for increasingly heavy X, the scalar-relativistic corrections may be of higher importance than the two-electron SO terms. On the other hand, scalar-relativistic (Pauli operator) DFT values 148 did not indicate particularly large scalar-relativistic corrections. More recently, Ootani et al. studied the HX series with a normalized elimination of the small component (NESC) treatment followed by ZORA and second-order regular approximation (SORA)¹⁵⁷ (see also Table 2). In these calculations, inclusion of some two-electron SO terms was found to improve the results compared to four-component HF results. As already mentioned, some two-electron contributions are also obtained in a mean-field sense if an effective potential is used in the place of V in the relativistic operators and in the transformations from four- to two-component form. In the work of Ootani et al., two-electron integrals between the upper components of the orbitals were included in the potential when constructing the transformation U to two-component form.

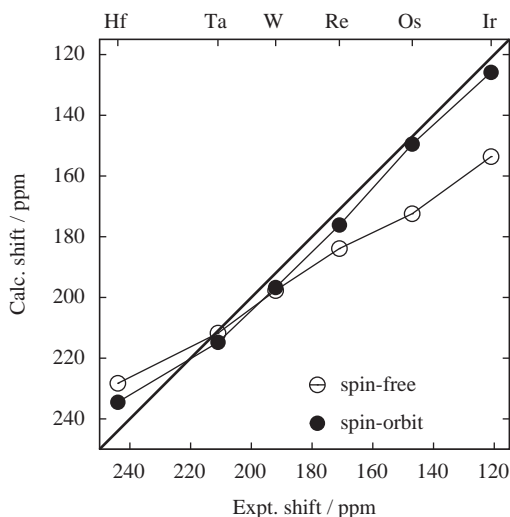


Figure 6 Carbon chemical shifts (reference: TMS) of transition metal carbonyls $[M(CO)_6]^n$ where n ranges from +3 (Ir) to -2 (Hf). Spin-free relativistic data from Ehlers et al.,¹⁷⁷ SO and experimental data were taken from Wolff and Ziegler.¹³⁰ The straight thick line indicates where calculated = experiment.

In transition metal chemistry, NHD-type effects may also occur. Several groups have investigated the carbon shifts in heavy transition metal carbonyls. Figure 6 shows a comparison of scalar and SO results obtained with the Pauli operator (using frozen cores to avoid variational collapse).^{130,177} The inclusion of SO coupling noticeably improves the agreement with experiment, in particular for the metals with higher group numbers/complexes with smaller shifts. Vaara et al. have also studied this series using a SO ECP for the metal and obtained similarly good agreement with experiment.¹⁵² The SO effect for the shielding follows a somewhat unintuitive trend: the HOMO–LUMO gaps $\Delta\epsilon$ and energy differences between other pairs of occupied and unoccupied orbitals enter the denominator in the DFT shielding tensor expression (36a). The magnitude of $\Delta\epsilon$ increases from Hf to Ir, but so does the magnitude of SO term in the shielding. As analyzed by Wolff and Ziegler,¹³⁰ as the metal's oxidation state increases from Hf to Ir, ligand–metal σ -bonding increases and π -back donation decreases.⁴ The increase in σ character of the metal–ligand bond is able to transfer the spin density more effectively from the metal to the carbon nucleus. This effect outweighs the increase in the orbital energy gap in the shielding expression. Such a balance of effects appears to be very typical in the NMR of transition metal complexes.¹¹ A balance between orbital gap trends and bonding characteristics was also noted, for example, for Pt chemical shifts.¹⁷⁸

⁴In a computational analysis, such changes in bonding tend to show up in significantly increased or reduced matrix elements in the numerator of the shielding tensor expression (Equation (36a)).

The authors of ref. 179 investigated a number of Ti tetrahalides and Nb hexahalides. Rather typical for early transition metal halides, almost vanishing net SO effects on the metal shielding were observed even for the tetra- and hexa-iodides, caused by a cancelation of positive SO contributions from the FC mechanism and negative changes of the paramagnetic shielding in the presence of SO coupling. In this case, IHD for the series $X = \text{F, Cl, Br, I}$ is observed for the chemical shifts, in agreement with experiment. This has been interpreted in terms of the different nature of the metal d-orbitals binding to the ligands as compared to (s- and) p-orbitals in the case of main group elements exhibiting NHD.

3.4.2 Heavy-atom shielding

For the shielding constant of a heavy metal nucleus, both scalar and SO relativistic effects can be expected to be important.^{2,4} Relativistic effects on shielding constants are quite large already for 4d metals and the main group elements up to around Xe. An increase of the scalar-relativistic effects of the shielding of the heavy-nucleus X with $\sim Z^{3.5}$ has been found for the HX series.¹⁸⁰ Other authors found a scaling of $Z^{2.3}$ for the metal shielding in the M-F series, where $M = \text{Cu, Ag, Au}$.¹⁸¹ Benchmark data for absolute shieldings of atoms,¹⁸² in particular for the closed-shell gas atoms,^{41,45,61,74,66,67,175} are available. However, as already pointed out, a large portion of the relativistic effects for shielding constants of most elements cancel when the chemical shift is evaluated. For 5d metals and the heaviest main group elements, this is usually not the case anymore. Sizeable spin-free and SO relativistic HAHA effects on the chemical shifts of NMR nuclei such as W, Pt, Hg, Tl, or Pb are obtained in computations. The relative magnitudes of scalar vs. SO effects depend on the element and the bonding environment.

Relativistic effects on heavy-atom shieldings in the series HX with $X = \text{F, Cl, Br, I}$, H_2Y with $\text{Y} = \text{O, S, Se, Te}$, and YH_3 with $\text{Y} = \text{N, P, As, Sb, Bi}$ have been extensively benchmarked, for instance, in ref. 183 (H_2Y , $\text{Y} = \text{O, S, Se, Te}$) or 184 (H_2Y , $\text{Y} = \text{O, S, Se, Te, Po}$, and YH_3 , $\text{Y} = \text{N, P, As, Sb, Bi}$). A collection of data for the shielding constant of X in the HX series, with references, can be found in Table 3.

The H_2Y series was studied by a perturbational approach based on the Pauli SO operator in ref. 185 where a comparison with experimental data has been made. The experimental estimate of 4,954 ppm for σ_{Te} in $\text{H}_2^{125}\text{Te}$ was underestimated by more than 1,000 ppm in the computations (HF and MCSCF), likely due to the missing scalar-relativistic effects. The SO contributions were -233 ppm. In comparison, in ref. 184, the total relativistic change for σ_{TCe} was reported as +1,963 ppm (Dirac HF) showing the importance of spin-free relativistic HAHA effects. Electron correlation effects on the heavy-nucleus shielding were found to be only modest.¹⁸⁵ The H_2X series was reinvestigated in ref. 74 at the HF level with both perturbational methods and four-component theory for relativistic effects. The Te shielding in HeH_2 was computed as 4,617 ppm with relativistic effects of order c^{-2} and 4,807 ppm at the fully relativistic HF level.

Table 3 A selection of computed halide shielding constants in HX where X = Cl, Br, I

σ_x (method/year)	F		Cl		Br		I	
	nrel	rel	nrel	rel	nrel	rel	nrel	rel
HF PSO/1996 ^{166,167}	413.6	412.0	952.0	941.7	2652.6	2562.3	4562.8	4272.4
HF PSO/1998 ⁷³	413.6	414.0	946.8	949.5	2633.9	2666.7	4551.7	4686.8
MCSCF PSO/1998 ^{a,73}	422.5	422.8	968.6	970.5	2682.0	2704.5	4654.5	4743.0
MCSCF PSO/1999 ^{b,185}		422.5	421.3	968.6	960.0	2682.0	2624.6	4654.5
HF Dirac/1998 ⁷²		418.1	409.5	961.2	1027.7			4469.6
HF Dirac/1999 ¹⁵⁰		414.3	423.3	957.0	1020.1	2634.2	3224.6	4541.4
HF scalar DKH2/1999 ¹⁴⁹		413.5	415.8	950.1	969.1	2643.2	2863.8	4538.2
HF DKH2/2002 ^{c,153,154}		413.5	422.3	949.9	1014.7	2641.3	3401.2	4539.8
HF ZORA/2002 ¹⁵³		413.5	416.4	949.9	970.1	2641.3	2851.0	5487.3
DFT ZORA/2003 ⁴		412.8	414.9	940.3	957.3	2574.2	2801.5	5478.6
HF DKH2/2003 ⁴²		416.8	423.4	957.5	1018.9	2634.9	3164.9	6508.5
HF Pauli/2003 ⁶¹		413.6	422.7	946.8	1009.5	2633.9	3222.8	6652.5
MCSCF Pauli/2003 ⁶¹		422.5	431.5	968.6	1030.9	2682.1	3265.5	6732.8
HFBS/FPT-1/2004 ¹⁵⁵		413.5	418.1	949.9	982.1	2641.3	2978.6	6077.0
HF BS/FPT-2/2004 ¹⁵⁵		413.5	417.9	949.9	970.9	2641.3		4539.8
HF BS/CHF/2004 ¹⁵⁵		413.5	422.1	949.9	996.0	2641.3	3032.9	6370.4
HF BS/CHF/2005 ⁴⁵		407.5	412.6	947.2	982.8	2612.0	2968.7	6242.7
HF DKH2/2005 ⁴⁵		407.5	412.6	947.2	983.3	2612.0	2978.6	6301.1
HF Pauli/2005 ⁷⁴		413.6	418.6	946.8	980.4	2633.9	2952.9	5700.0
HF Dirac/2005 ⁷⁴			418.4		984.5		2959.4	5913.7
HF SORA+J _{LL} /2006 ¹⁵⁷		412.0	420.6	953.1	992.8	2615.9	3013.6	6161.4
HF NESC/SORA/2006 ¹⁵⁸			421.0		994.3		3023.3	6192.4
HF NESC/ZORA/2006 ¹⁵⁸			421.0		994.4		3011.5	5924.5
HF SORA-Met/2007 ¹⁵⁹			419.7		985.7		2946.4	5892.0
HF ZORA-Met/2007 ¹⁵⁹			419.8		985.9		2939.3	5680.6
HF MIOTC/2007 ¹⁶⁰		412.0	419.6	953.1	986.2	2615.9	2966.7	5927.3
DFT mDKS-RMB/2008 ⁶⁸		405.6	411.4	908.6	936.3	2547.8	2887.9	5705.1
Expt. ^d			410±6		952		2617	4510

See footnotes of Table 2 for acronym definitions.

^aNeglecting contributions due to the minimal substitution in the Pauli-SO operator.

^bIncluding contributions due to the minimal substitution in the Pauli-SO operator.

^cEmploying nonrelativistic operators regarding the m_A and B perturbations.

^dExperimental data as compiled in ref. 73. Estimates based on a combination of computed diamagnetic shielding constants and experimentally determined spin-rotation constants, employing the nonrelativistic relation between spin-rotation constants and the paramagnetic shielding tensor.¹⁸⁶

Lantto et al. used the relativistic Breit–Pauli perturbation approach to investigate HAAA effects.¹⁷⁰ The heavy-atom shielding tensors in group 14 hydrides, X^{4+} , X^{2+} , XH_2 , and XH_3^- where $X = \text{Si–Pb}$, and hydrides and fluorides of group 15 elements, X^{3+} , XH_3 , and XF_3 where $X = \text{P–Bi}$, were computed (HF theory). Perturbation-theory results were compared to four-component computations to assess the magnitude of missing relativistic effects not covered in the $\mathcal{O}(c^{-2})$ relativistic perturbation theory. Perturbation calculations were also

performed at a correlated *ab initio* level (CASSCF). Correlation effects on the shielding were found to be modest and mainly affecting the nonrelativistic level. A localized orbital analysis was carried out to rationalize trends for the relativistic corrections. The dominating FC mechanism of the HAHA effect was found to increase roughly as Z^3 with nuclear charge Z of the heavy atom.

Comparisons between HF and DFT can be made for ^{125}Te shielding constants to estimate the influence of electron correlation. In ref. 187, an uncorrelated (HF) DKH2 approach has been applied by Hada et al. to a subset of Te compounds that were previously studied by Ziegler et al.^{188,189} with the a variational scalar Pauli DFT method.¹⁴⁸ In ref. 188, because of the rather good agreement with experimental data, Ruiz-Morales et al. concluded that SO corrections are not vital for the evaluation of Te chemical shifts, and thus reasonable predictions can be made by a scalar approach alone. Indeed, the HF DKH2 results of ref. 187 also showed that for the data set considered, the SO contributions to the chemical shifts were only modest, although not completely negligible. However, this seems to be due to a cancelation between different compounds when evaluating the chemical shift, since large SO contributions of $\sim 2 \times 10^3$ ppm to the shielding were reported. Roughly the same quality of agreement with experimental chemical shifts was obtained in both studies. An absolute Te shielding scale correction of -945 ppm proposed by Ziegler et al. has been questioned by Hada et al. because their calculated absolute shieldings agreed better with the original shielding scale of ref. 190. Tellurium shifts have been revisited by Fukuda and Nakatsuji in 2005¹⁹¹ using a correlated *ab initio* level of theory. Electron correlation was considered at the MP2 perturbation level while relativistic effects were included via the DKH2 Hamiltonian. Some of the results are displayed in Figure 7 in comparison with experiment. Compared to otherwise similar HF calculations, the correlation treatment significantly improved the results, with the mean absolute deviation (MAD) dropping from 147 ppm (HF) to 83 ppm (MP2). SO effects were found to be important when comparing Te shift of different oxidation states: Te(IV) systems afforded a roughly 200 ppm smaller shielding constant and generally improved agreement with experiment. For some of the systems, computation and experiment deviated by more than 100 ppm. The authors identified as possible reasons for the deviations, along with basis set incompleteness and the selection of an active space for the MP2 treatment, experimental uncertainties (for TeH_2), lack of treating solvent effects (for TeMe_3Cl), and in one case a particularly large correlation effect that might not be sufficiently well described at the MP2 level (for $\text{Te}(\text{CF}_3)_2$). The chemical shift trends were analyzed. The paramagnetic term correlated well with the population of the Te 5p shell. For the hypervalent Te(IV) compounds, the contributions from Te 5d AOs were also found to be important. Chemical shifts for Te and Se have also been studied by a scalar-relativistic ZORA projector-augmented plane-wave DFT code.^{52,192} In contrast to other methodology cited in this chapter, the nonrelativistic approach adopted in ref. 52 is able to treat extended periodic systems. It explicitly deals with the presence of the pseudopotential by a method devised by Van de Walle and Blöchl⁵¹ where the all-electron structure of the orbitals is reconstructed for the purpose of NMR

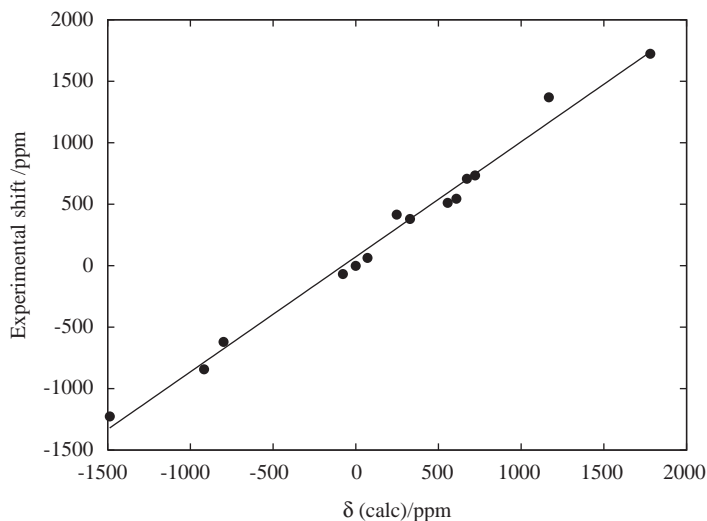


Figure 7 Te chemical shifts for Te_2Me_2 , MeSeTeMe , TeH_2 , TeEt_2 , $\text{Te}(\text{CF}_3)_2$, $\text{Te}(\text{SiMe}_3)_2$, $\text{Te}(\text{SnMe}_3)_2$, TeMe_4 , TeMe_3Cl , TeMe_2Cl_2 , TeCl_4 , TeF_6 , and $\text{Te}(\text{OH})_6$, computed from a MP2 *ab initio* approach with relativistic effects treated at the DKH2 level, compared with experiment. Reference: TeMe_2 . Data compiled from Fukuda and Nakatsuji.¹⁹¹

computations. In ref. 192, the authors have adapted the procedure to the scalar ZORA operator. The DFT results for ^{125}Te absolute shieldings were in fair agreement with the variational scalar Pauli frozen-core DFT results of Ruiz-Morales et al.¹⁸⁸ taking into account that different density functionals have been employed (PBE in ref. 192 vs. BP in ref. 188) and that the basis sets and many technical aspects of the codes are very different.

Xenon NMR has found widespread use due to favorable NMR properties of the ^{129}Xe nucleus and the large chemical shift range, making this atom a very sensitive NMR probe. Benchmark computations are abundant. Scalar ZORA DFT computations for Xe shieldings and spin–spin couplings in XeF_2 , FXeOSO_2F , $\text{FXeN}(\text{SO}_2\text{F})_2$, XeF_4 , XeO_2F_2 , XeOF_4 , XeF_6 , XeF^+ , XeF_2F_3^+ , and XeCl^+ are provided in ref. 193. Some results are shown in Figure 8. The agreement with experiment is quite good for the most part but several outliers, the systems XeF^+ , XeCl^+ , (and XeF_6 , for J -coupling) tarnish the record. The authors computed large SO effects on $\delta(\text{Xe})$ for the ionic systems (e.g., over $-1,400$ ppm in magnitude for XeF^+); however, this correction while having the desired sign does not completely reconcile computations and experiment. The experimental data for the ionic systems were obtained in superacids; thus, there are reasons to assume that the species present in solution have a shift that might be significantly different from those of the isolated XeF^+ and XeCl^+ ions that were computed. Similarly, the authors of ref. 193 mentioned structural uncertainties regarding XeF_6 . Overall, relativistic corrections improved the agreement with experiment although most of the relativistic effects on $\sigma(\text{Xe})$ cancel when evaluating the chemical shift. In 2003, two publications dealt with the chemical shift of Xe encapsulated in the C_{60}

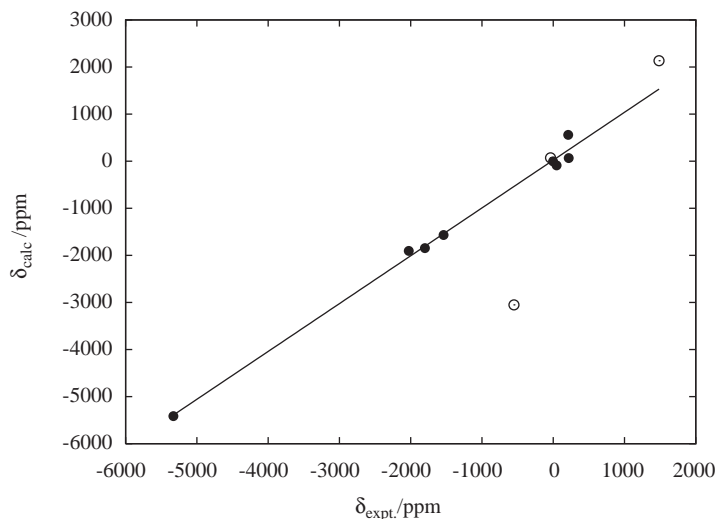


Figure 8 ^{129}Xe chemical shifts. Scalar ZORA DFT computations vs. experiment. Data compiled from Bagno and Saielli.¹⁹³ The straight line is a linear fit to the data set excluding some data points indicated by open markers. Slope = 1.02, intercept = 23 ppm.

fullerene. Sears and Jameson obtained excellent agreement with the (for Xe rather small) experimental shift of 174 ppm with respect to Xe gas by using the B3LYP hybrid functional in nonrelativistic computations. (The authors subsequently applied similar DFT computations to investigate Xe in cryptophane cages¹⁹⁴.) Autschbach and Zurek employed the ZORA relativistic method with nonhybrid DFT.¹⁹⁵ In this case, the computations consistently overestimated the shift by up to about 120 ppm. The higher shift was in part caused by relativistic effects (about 22 ppm scalar and 6 ppm SO effects on the shift); adding these corrections to the Sears and Jameson result would have led to a too high computed result. Electron correlation is also very important for this system; HF calculations yield a strong underestimation of the shift, about 100 ppm or less depending on the basis set.^{195,196} Straka et al. have reinvestigated Xe@C₆₀ recently and arrived at the so far best computed DFT Xe shift of 153 ppm which included relativistic effects and dynamic effects (together about 20% of the total shift), solvent effects (negligible), and was based on a hybrid functional.¹⁹⁷ The remaining difference with experiment was tentatively attributed to approximations in the functional. The computations highlight the difficulty to obtain quantitative agreement with experiment in NMR computations, in particular for a sensitive atom like Xe with a chemical shift range of many thousand parts per million. A relativistic perturbation approach was recently applied to investigate NMR parameters (shielding tensors and nuclear quadrupole coupling) in the weakly bound Xe dimer using HF, correlated wavefunctions, and DFT.¹⁶⁹ The molecule HXeCCH serving as a model for organo-xenon compounds was studied with a perturbational relativistic approach including correlated *ab initio* and DFT methods.¹⁷² DFT was found not to perform well for this system; however, the

relativistic correction terms from DFT appeared to be reliable which may allow to add them to nonrelativistic high-level correlated data.

In ref. 198, the ZORA DFT approach was used to benchmark computations of Pb chemical shifts. The computations were found to reproduce experimental data for a number of ^{207}Pb shifts quite well, with a mean error of 4% of the shift range. In comparison, DFT computations employing the Pauli operator variationally with frozen-core basis sets resulted in a mean error of 16%. A very large SO-induced chemical shift change of $-8,000$ ppm was predicted for the PbI_4 molecule, which represents an extreme combination of “heavy atom–other heavy atom” (we suggest the acronym HAOHA) and HAAHA effects. Dmitrenko et al. have recently investigated the relationship between Pb chemical shifts and the solid-state structure in Pb(II) compounds.¹⁹⁹ Some of the computational results, which were obtained with a ZORA SO DFT approach, are displayed in Figure 9. The local geometries in the PbX_2 salts were modeled by PbX_n^{2-n} clusters based on the crystal structures, leading to the spread of computed data in Figure 9. The authors performed a larger set of computations on a PbI_6^{4-} cluster and reported that the isotropic shifts depended strongly, and linearly, on the interatomic distances and that the tensor span had a nonlinear dependence on the atomic distances and a roughly linear dependence on local angular distortions. The authors attributed trends such as the ones computed for PbI_6^{4-} to local distortions which are responsible for NMR trends found experimentally for solids as function of temperature and pressure. Briand et al.²⁰⁰ have also recently investigated Pb chemical shifts as well as the shift tensor anisotropy in a concerted SSNMR and computational study on coordination compounds of Pb(II) with 4-substituted pyridine and thiolate ligands. Analyses of ZORA DFT

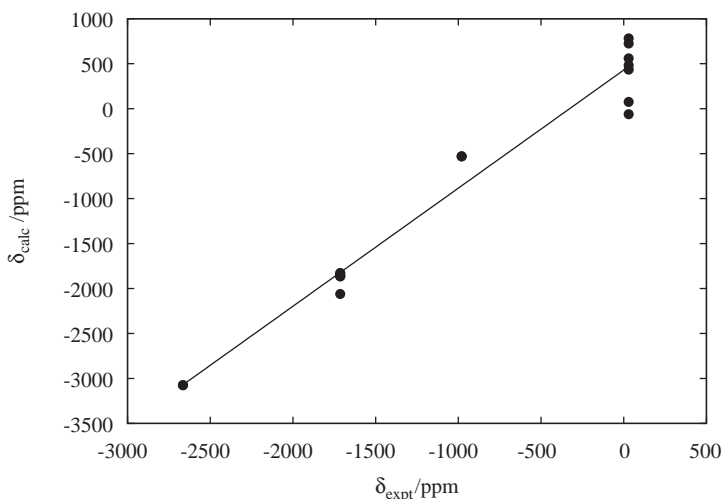


Figure 9 Computed vs. experimental ^{207}Pb chemical shifts in PbX_2 , $\text{X} = \text{F}, \text{Cl}, \text{Br}, \text{I}$ (left to right). Reference: PbMe_4 . Data compiled from Dmitrenko et al.¹⁹⁹ Multiple computational values refer to different clusters models for the solid. ZORA DFT computations including SO effects. The straight line is a linear fit to the data set. Slope = 1.31, intercept = 430 ppm.

computations in terms of paramagnetic shielding tensor contributions in terms of occupied and unoccupied canonical MOs indicated dominant contributions from occupied sulfur-centered MOs and unoccupied Pb 6p orbitals.

3.4.3 Heavy metal chemical shifts

Computational data obtained with different theoretical methods are available for ^{183}W chemical shifts. With respect to the reference WO_4^{2-} , the tungsten shifts in $\text{W}(\text{CO})_6$, WF_6 , and WCl_6 were calculated with the variational Pauli (frozen cores) and ZORA DFT approaches as $-3,306$, -107 , and $1,773$ ppm and $-3,876$, -630 , $1,932$ ppm, respectively.¹⁹⁸ The experimental shifts are $-3,446$, $-1,121$, and $2,181$ ppm for the series, as compiled in ref. 198. A scalar variational Pauli DFT approach had previously predicted a chemical shift of $-3,703$ ppm for $\text{W}(\text{CO})_6$, with modest relativistic corrections of $+372$ ppm. Tungsten chemical shifts have also been computed by a variational HF scalar DKH2 with Pauli SO terms approach in ref. 201 for WO_4^{2-} , WF_6 , and WCl_6 , using a number of different basis sets. The “basis set C” data yielded tungsten chemical shifts of $-1,135$ and $2,686$ ppm for WF_6 and WCl_6 , respectively (nonrelativistic: $-1,795$ and $2,266$ ppm). Overall, in ref. 198, the DFT-ZORA method was found to yield a mean error of approximately 3% of the chemical shift range of 7,000 ppm for a larger number of tungsten complexes. The variational Pauli DFT calculations resulted in a mean error of about 6% for these systems. Tungsten chemical shifts were also benchmarked in ref. 202 using ZORA DFT computations. Figure 10 displays some of the data for small W complexes which demonstrates good

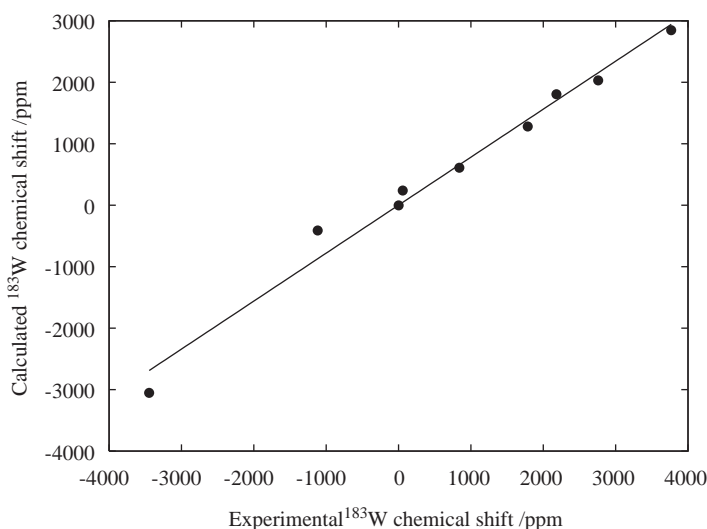


Figure 10 ^{183}W chemical shifts for WO_3S^{2-} , $\text{WO}_2\text{S}_2^{2-}$, WOS_3^{2-} , WS_4^{2-} , WF_6 , $\text{W}(\text{CO})_6$, WCl_6 , and $\text{W}_6\text{O}_{19}^{2-}$, from spin-free ZORA DFT computations with frozen cores. Data compiled from Bagno et al.²⁰² Reference: WO_4^{2-} . The straight line is a linear fit to the data set excluding some outliers indicated by open markers. Slope = 0.78, intercept = 1 ppm. Ref. 202 reported that the slope can be improved substantially by adopting an all-electron basis.

correlation between computations and experiments. However, the slope of only 0.78 of the fit line indicates that the shift trend is quite severely underestimated by the computations which employed frozen cores. Additional benchmark computations with all-electron basis sets and including SO corrections showed that the agreement with experiment can be improved substantially, yielding a slope of the linear fit of 0.95 and a MAD of 290 ppm or 4% of the shift range in scalar relativistic and a slope = 0.97 and MAD = 360 ppm for SO computations. The benchmarks were part of a broader study on polyoxotungstenate NMR spectra; we will discuss such compounds in a separate section.

Ref. 203, *inter alia*, contains a collection of computed (ZORA DFT) vs. experimental ^{181}Ta NMR chemical shifts for TaS_4^{3-} , TaSe_4^{3-} , TaTe_4^{3-} , TaCl_6^- , TaF_6^- , $\text{Ta}(\text{CO})_6^-$, and TaF_7^{2-} with a chemical shift range of roughly 7,000 ppm. Although the correlation between computations and experiment was acceptable (linear fit with $r^2 = 0.97$), the trend was quite strongly overestimated (slope of 1.3). The overestimation may hint at problems with the nonhybrid density functional employed for the computations but the authors also pointed out that the experimental accuracy is limited and that the calculation–experiment correlation has an adequate predictive value.²⁰³

A comparison of the ZORA DFT and the variational Pauli-DFT methods for metal shieldings in group 6–8 tetraoxo-metallates has been made by Bouten et al.⁵⁷ It has been concluded that the ZORA method yields superior results over the variational Pauli approach, which corroborates the previous findings in ref. 198 for tungsten and lead complexes. The tetraoxo-metallates have previously been used as a benchmark set for the DFT computation of ^{17}O shielding constants in transition metal systems.^{148,204} Unfortunately, Bouten et al. did not report the oxygen shieldings for comparison.

^{99}Ru chemical shifts have been the subject of a number of investigations, including some studies on the relativistic effects and the influence of solvent. Because of the large chemical shift range of approximately 18,000 ppm reported so far for Ru,²⁰⁵ even comparatively small differences in structure and bonding can result in sizeable chemical shift changes. Therefore, Ru NMR represents a stringent test for computational models. Computations of Ru chemical shifts have been performed by Bühl et al.,²⁰⁶ Bagno and Bonchio,^{138,207} Ooms and Wasylishen,²⁰⁵ and Autschbach and Zheng.²⁰⁸ The latter study in part focused on solvent effects on the Ru chemical shift of for *fac*- $[\text{Ru}(\text{CO})_3\text{I}_3]^-$. It was shown that the recipe of using static computations with a few explicit solvent molecules and an additional continuum model was able to reproduce the solvent trends for this complex quite well. This paper also reinvestigated the performance of various computational models used in the other studies, and in particular the importance of relativistic effects for a benchmark set of different Ru complexes. It was confirmed that: (i) relativistic effects are of relatively minor importance for Ru chemical shifts (and likely for chemical shifts of other 4d metals which will therefore not be discussed further in this chapter) although their inclusion improves agreement with experiment, (ii) the choice of the density functional is important (hybrid functionals perform somewhat better for Ru chemical shifts),

and (iii) neither just a continuum model nor just a few solvent molecules were sufficient for reproducing solvent trends; both were required.

On the far end of the heavy-atom range are the actinides. Schreckenbach et al. have computed the shielding of ^{235}U as well as ligand shieldings in uranium compounds^{58,209,210} using variational Pauli and ZORA DFT computations. Scalar-relativistic ECPs were also applied in refs. 209,210 for the ligand shifts. A chemical shift range of at least 21,000 ppm for ^{235}U has been predicted; however, so far no experimental chemical shifts are available. Regarding the U shieldings, it could be demonstrated that the trends for the ^{235}U shielding constants among the set of 23 complexes that were studied are determined by the average energy gap between the HOMO U-5f_{xyz} and the seven lowest lying virtual MOs (U-5f with antibonding ligand contributions), whereas the HOMO–LUMO gap itself does not explain the trends.²¹⁰ This finding underlines that it is important to pick the right orbitals for an analysis in terms of orbital energy gaps: it need to be those with large matrix elements for the perturbations, in the numerator of Equation (36a). An orbital-based analysis that quantifies per-orbital contributions, such as discussed in Sections 2.6 and 3.2, can be helpful. Regarding the chemical shifts of light ligands in uranium compounds, it was found that while the nonhybrid density functionals could not reproduce the trends for the ^{19}F -shift in the $\text{UF}_{6-n}\text{Cl}_n$ series,²⁰⁹ they were successful to reproduce those for $\text{UF}_{5-n}(\text{OCH}_3)_n$, $n = 1\text{--}4$.²¹⁰ Also, the trends for the ^{17}O -shifts in uranyl complexes could be reproduced though still underestimating the oxygen shifts by about 10%. For the $\text{UF}_{6-n}\text{Cl}_n$ series, an ECP approach with the B3LYP hybrid functional could reproduce the trends for the ^{19}F shifts; however, the magnitudes of the shifts were systematically overestimated. Some of these inconsistencies were later traced back to the inadequacy of large-core ECPs; Schreckenbach²¹¹ and Straka et al.²¹² concluded independently that reliable computations of the ligand shifts can be performed with small-core ECPs. It appears that despite the proximity of the heavy uranium atom, SO HALA effects on the ligand shifts are not particularly large.

Lanthanum chemical shift tensors have been measured and computed by Ooms et al.²¹³ and Willans et al.²¹⁴ Relativistic ZORA DFT calculations of ^{139}La chemical shift tensors on cluster models including La and its nearest neighbor atoms qualitatively reproduced the trends in isotropic shifts and tensor spans observed experimentally by SSNMR. Quadrupole coupling tensors were also computed and measured. The authors reported improved agreement with experiment when SO effects were included in the computations. The computations confirmed the trends of the isotropic shift, the tensor spans, and the quadrupole couplings, as a function of the La coordination number. To obtain better agreement with experiment would require modeling the solid-state electronic structure more closely, for instance, via band structure methods, or using large clusters with Madelung potentials or alternative methods to treat long-range electrostatic interactions. In ref. 213, computations on the complexes LaX_3 with $\text{X} = \text{F}, \text{Cl}, \text{Br}, \text{I}$ were performed to rationalize the observed trends for the shielding tensors in the LaX_3 solids. The nuclear shielding constants computed at the ZORA SO level are collected in Table 4. Interestingly, the La shielding

Table 4 Computed isotropic nuclear shielding constants for LaX_3 , data from Ooms et al.²¹³

Complex	σ_{iso}
LaF_3	4933
LaCl_3	3549
LaBr_3	2891
LaI_3	1628

ZORA DFT computations with SO coupling. The series exhibits IHD.

decreases from F to I which means that for the chemical shift IHD would be observed, a trend which is in agreement with the SSNMR results for the LaX_3 solids.²¹³ The computations revealed that SO coupling is a secondary effect in the La shielding tensor, that is, the IHD is predominantly caused by the increasing magnitude of the negative paramagnetic shielding along the series. The SO shielding also becomes less positive from $X = \text{F}$ to I (also an IHD trend); this is likely related to the significant changes in the La–X bonding reported in ref. 213.

^{195}Pt is one of the heaviest NMR nuclei. Techniques for detecting the nuclear magnetic resonance of ^{195}Pt have been developed quite early.^{215,216} Pt NMR has since become a powerful tool to study the chemistry of platinum complexes.^{217,218} A large number of experimental data are available which is extremely helpful for the benchmarking of relativistic theoretical NMR methods. The abundance of experimental data along with the immense interest in cisplatin and related compounds for cancer therapy has prompted a sizeable number of computational studies of Pt chemical shifts. We note that many of the available computational studies reported varying degrees of difficulties with reproducing experimental chemical shifts.

The first DFT investigation of Pt chemical shifts was performed by Gilbert and Ziegler¹⁷⁸ on *cis*- and *trans*- PtX_2Y_2 systems with $X = \{\text{Cl}, \text{Br}, \text{I}\}^-$ and $Y = \{\text{Cl}, \text{Br}, \text{I}\}^-$ or $\{\text{SMe}_2, \text{NH}_3, \text{PMe}_3, \text{AsMe}_3\}^+$ and yielded a RMS deviation of about 300 ppm between theory and experiment for a set of 24 complexes. The overall agreement with experiment is quite good considering that the chemical shift range of these compounds spans about 3,400 ppm. However, one of the compounds, $\text{PtCl}_2(\text{SMe}_2)_2$, had to be chosen as the NMR reference in order to obtain such good agreement. In the experiments, the Pt reference is often a solution of Na_2PtCl_6 in water which is not easy to model computationally. Indeed, Gilbert and Ziegler already hinted in their paper at the difficulties of modeling the NMR parameters of charged complex ions in coordinating polar solvents.

The main results of Gilbert and Ziegler's computational study are typical for metal chemical shifts¹¹: often, explanations of trends for chemical shifts among similar compounds are sought in terms of trends regarding the HOMO–LUMO gap, which in turn center Equation (36a) in the paramagnetic shielding tensor elements. The argument is that a large energy separation between occupied and unoccupied orbitals causes the paramagnetic component of the nuclear shielding to be small (large denominators). However, in metal complexes, the trends are

often opposite to what would be expected based on the magnitude of the HOMO–LUMO gap because the matrix elements in the numerator of (36a) may yield opposite trends. This is also what Gilbert and Ziegler found for their set of Pt chemical shifts. The balance between the trends was termed “delicate,” which means it is not easy to estimate qualitatively which term is dominating without performing a computation. Overall, Gilbert and Ziegler found that qualitative rules for Pt shifts based on hard–soft acid–base concepts, namely that softer ligands yield more negative Pt shifts, were reproduced in the computations.

Autschbach and Le Guennic studied the metal chemical shifts of the Pt–Tl bonded complexes 1–7 shown in Figure 11. During the course of a computational study of the Pt and Tl chemical shifts of 1–5,²¹⁹ pronounced difficulties were noted in obtaining agreement with experimental data for the Pt shifts in these complexes when using the standard experimental reference $[\text{PtCl}_6]^{2-}$ in the computations. Better agreement with experiment was obtained when using the complex $[\text{Pt}(\text{CN})_6]^{2-}$ as a reference which was attributed to the higher similarity of the ligands. The authors suspected that approximations in the density functional contributed to this issue. Overall, the best agreement with experiment was obtained when using complex 4 as an internal computational reference. Even with complex 4 as the reference, computed solvent effects on the Pt and Tl chemical shifts were found to be very large, which emphasizes the necessity of modeling solvent effects (here: water) in transition metal NMR computations. The data shown in Figure 12 support the main conclusion of the computational study: as a minimal requirement the computations need to include explicit solvent molecules to fill the first coordination sphere of the metals as well as a model for outer solvation shells at least in form of a continuum model the (the

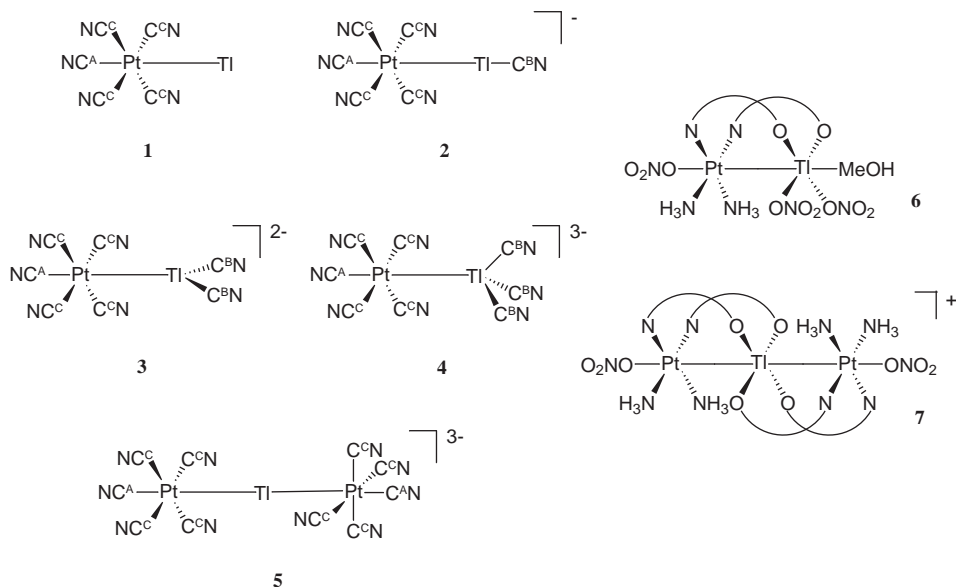


Figure 11 Structures of various Pt–Tl bonded complexes (1–7).

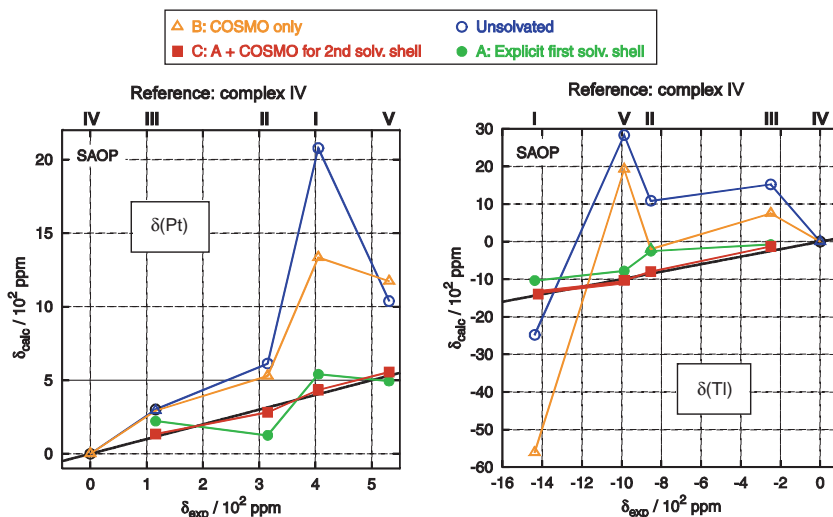


Figure 12 ^{195}Pt and ^{205}Tl chemical shifts of the complexes 1–5 shown in Figure 11, from ref. 219. Calculated vs. experimental shifts. The straight line indicates where $\delta_{\text{calc}} = \delta_{\text{exp}}$. Solvent is water. COSMO is a continuum solvent model.

conductor-like screening model (COSMO) was used for the computational study reported in ref. 219).

In 2005, Fowe et al. reported excellent agreement between computations and experiment of the Pt chemical shifts for the series $[\text{PtCl}_{6-n}\text{Br}_n]^{2-}$, $n = 0-6$. The authors applied a very similar nonhybrid ZORA DFT approach as used by Gilbert and Ziegler,¹⁷⁸ and by Autschbach and Le Guennic.^{114,219} Fowe et al. also noted a strong sensitivity of the Pt chemical shift with respect to Pt–ligand bond lengths. It was verified by calculations on $[\text{PtCl}_6]^{2-}$ and $[\text{PtBr}_6]^{2-}$ using a continuum solvent model that solvent-induced structural changes have a strong impact on the calculated Pt shielding constants. Since the first coordination sphere of the metal in the $[\text{PtCl}_{6-n}\text{Br}_n]^{2-}$ series is already occupied by regular ligands, one might expect a similar performance of the computational model as found by Autschbach and Le Guennic for 1–5 (the computations used similar functionals, basis sets, and relativistic operators), which was indeed the case. Recently, Koch et al. investigated the Pt NMR chemical shifts of a variety of Pt(IV) species including the $[\text{PtCl}_{6-n}\text{Br}_n]^{2-}$ ($n = 0-6$) and $[\text{PtCl}_{5-n}\text{Br}_n(\text{H}_2\text{O})]^-$ ($n = 0-5$) series as well as species with hydroxy ligands experimentally and computationally.^{220,221} The computational approach was similar to those used in the other DFT studies of Pt NMR discussed so far. Excellent agreement with experiment and the correct trends for ligand substitution were obtained in this work. Very systematic trends on ligand substitution found experimentally and verified by computations allowed to identify a number of previously unidentified species as well as the identification of various geometric isomers.

Kogut et al. have investigated the system $\text{Pt}[\text{S}_2\text{C}_2(\text{CF}_3)_2]_2$ (Pt bis-dithiolene) with SSNMR and ZORA DFT computations.²²² MAS spectra yielded principal

values of the shift tensor of $-1,378$, $-3,289$, and $-7,291$ ppm, and an isotropic shift of $-3,986$ ppm. The computations yielded -506 , $-2,391$, and $-7,366$ ppm for the tensor components and $-3,421$ ppm for the chemical shift. The agreement with experiment is reasonable. It can be seen that some of the errors in the principal components cancel, leading to a less than 600 ppm deviation between the measured and the calculated isotropic shifts. Deviations of this magnitude are not untypical for Pt shifts calculated at this level of theory and may be attributed in part to the lack of modeling the crystal packing. The computations were used to determine the shielding tensor orientation. Oziminski et al. considered three platinum complexes with histamine (his), two Pt(II) and one Pt(IV) complex.¹³⁹ With a ZORA DFT approach, the Pt chemical shift for Pt(hist)Cl₂ was computed as $-1,766$ ppm (reference: [PtCl₆]²⁻) compared to an experimental value of $-2,240$ ppm. Note that a basis set with a rather limited flexibility was used and SO effects were neglected; it is unclear if these approximations provided some cancelation of errors. In ref. 223, NMR parameters were computed with the ZORA DFT method for the systems M[N(ⁱPr₂PSe)₂]₂ where M = Pd, Pt or Se, Te. For the Pt system, the calculated chemical shift of $-6,347$ ppm (SO) did not agree well with the SSNMR experiment ($-4,580$ ppm). SO effects helped to bring the span of the tensor closer to experiment. It is conceivable that due to the sensitivity of Pt chemical shifts, the applied cluster model did not represent the solid's local electronic structure well enough, but as was noted earlier Pt chemical shifts can afford substantial errors if the computational reference is not similar to the probe. As a note aside, the Te shift reported in ref. 223 afforded quite substantial SO effects, increasing the isotropic shift from 295 to 508 ppm (experiment: 645 ppm).

We have so far discussed several studies where some difficulties were reported with reproducing Pt chemical shifts (including the MD study of cisplatin–DNA oligomer complexes⁹¹ cited in Section 2.8) unless the reference was chosen to be very similar to the complexes of interest. Possible implications regarding the principle performance of the density functionals prompted Sterzel and Autschbach to investigate Pt chemical shifts in solution for a set of complexes with different oxidation states, and different coordination and solvation spheres.⁹² The purpose of this work was to eliminate some of the potential fortuitous error compensation that arises when comparing chemical shifts among a series of similar compounds, and to test in particular the modeling of solvation effects. The complexes [PtCl₄]²⁻, [PtCl₆]²⁻, and the dinuclear amidate-bridged Pt(III) complex **M3** of Figure 13 were chosen. In addition to static computations, Born–Oppenheimer molecular dynamics simulations (BOMD) were also performed on [PtCl₄]²⁻ and [PtCl₆]²⁻. It turned out to be rather challenging to compute the chemical shift of [PtCl₄]²⁻ with respect to the standard Pt reference [PtCl₆]²⁻. As a main result of the study, it was concluded that previous computations on Pt complexes did not employ a flexible enough basis set, neither for the metal nor for the ligands, and that error compensation masked this important factor. Another issue was the modeling of unspecific solvent effects for which, in principle, explicit solvation in conjunction with MD simulations appeared to be necessary. By comparison of static with BOMD computations,

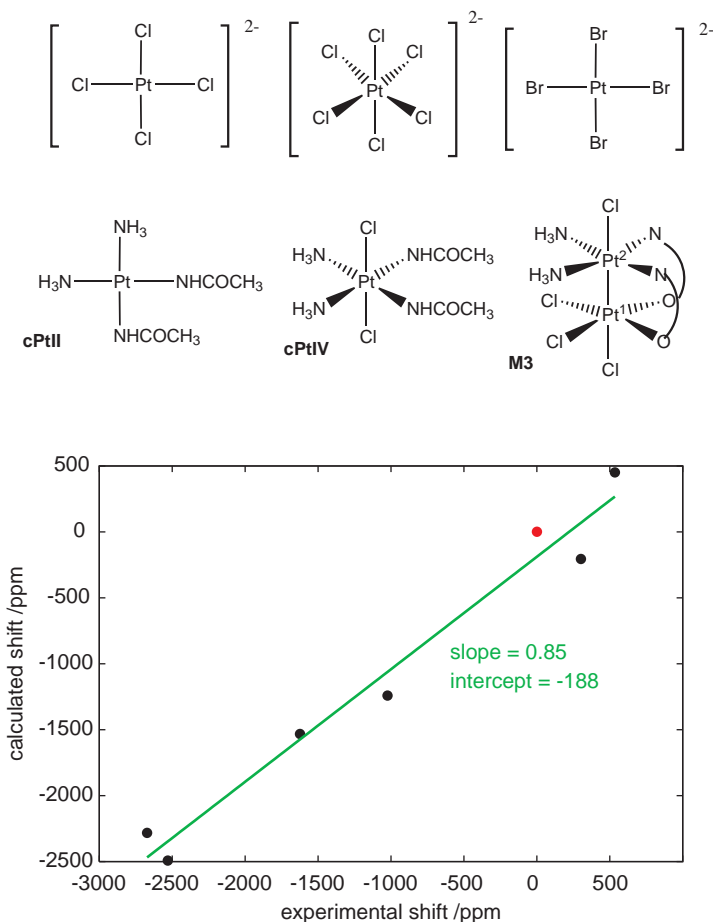


Figure 13 Pt systems analyzed in refs. 117,118, and overall agreement of computed (ZORA DFT) with experimental ^{195}Pt chemical shifts. Reference: $[\text{PtCl}_6]^{2-}$. The bridging ligand is the amidate $\text{HN}^{\ominus}-\text{C}(\text{CR}_3)=\text{O}$.

it was found that the best performing static computational model, yielding $-1,528$ ppm for the Pt chemical shift of $[\text{PtCl}_4]^{2-}$ compared to the experimental value of $-1,630$ ppm, still benefited from error compensation. This model used a more flexible Pt basis than previous studies (a quadruple-zeta quadruply polarized basis) and a polarized triple-zeta basis for the ligands. A trade-off between truncating the basis set and treating the solvent-solute interactions approximately was found to be one of the major factors. Using this static model, the Pt two shifts of **M3** were reasonably well reproduced in the computations. Sterzel et al. reported a pronounced sensitivity of the Pt chemical shifts with respect to geometric parameters in particular for negatively charged species. These findings are in line with results obtained by Bühl et al. from molecular-dynamics studies on 3d transition metal complexes, for example, of $\text{Fe}^{24,225}$ and

Co.²²⁶ It appears that in Pt chemical shift calculations, issues with density functional are perhaps less pronounced than previously thought^{219,114} but that modeling of the complex structure and solvation is even more critical than indicated by some of the earlier work on Pt chemical shifts.

Computed Pt chemical shifts have been analyzed recently using a localized orbital technique^{117,118} (based on so-called NBOs and NLMOs), as outlined in Section 2.9. The technique is related to the spin–spin coupling analysis discussed in Section 3.2 for the PbH_4 molecule; both are capable of analyzing spin-free and SO terms in the NMR tensors. The shielding analysis was carried out for the Pt complexes shown in Figure 13. In this figure is also shown the overall agreement with experimental data for this set of complexes which turned out to be quite reasonable. The analysis has focused on the role of nonbonding Pt 5d orbitals. For instance, when considering the chemical shift of $[\text{PtCl}_4]^{2-}$ with respect to the standard reference $[\text{PtCl}_6]^{2-}$, computed as $-1,532$ ppm, experiment $-1,630$ ppm, the analysis showed combined contributions of $-1,567$ ppm from Pt 5d nonbonding orbitals, the 5d lone pairs, and the Pt–Cl bonds. The contributions from the 5d orbitals alone added up to $-1,943$ ppm which therefore represented the main difference between these two complexes. As usual, diamagnetic and core-orbital contributions did not change significantly among the set of complexes. The reason for the negative chemical shift is a larger deshielding of the Pt nucleus originating from paramagnetic terms located in the 5d shell which was rationalized with an orbital rotation model for 5d orbitals. See Figure 14 for an illustration. For instance, according to the SOS equation for the shielding, or its MO analog (36a), an occupied orbital yields a large paramagnetic term if the action of the OZ and OP operators results in a function that overlaps well with a

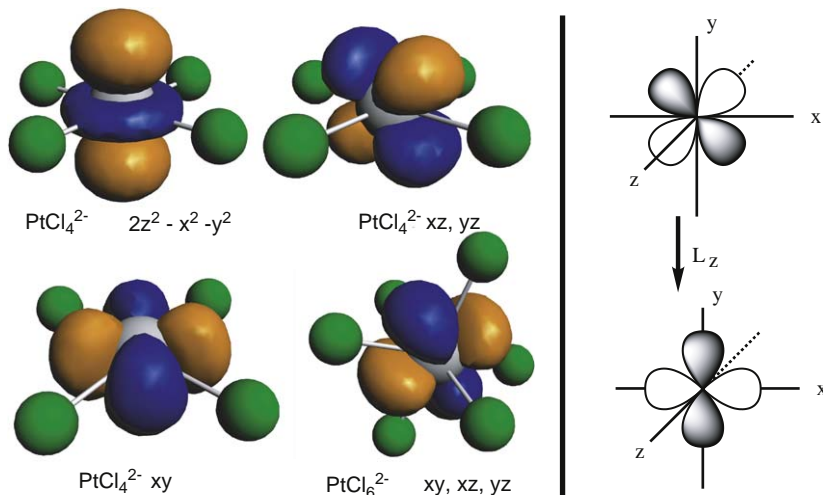


Figure 14 (Left) Localized nonbonding Pt-centered orbitals (NLMOs) in $[\text{PtCl}_4]^{2-}$ and $[\text{PtCl}_6]^{2-}$, from spin-free ZORA DFT computations with subsequent NBO/NLMO analysis (ref. 118). Iso-surface values: 0.03 a.u. (Right) Qualitative result of the action of the angular momentum operator on a d-orbital.

low-lying unoccupied orbital. Both operators contain angular momentum-type terms (see the OP and OZ perturbation operators in Section 2.5). The action of an angular momentum operator on a d-orbital yields a rotated d-orbital as shown qualitatively in Figure 14. In $[\text{PtCl}_4]^{2-}$ for the $5d_{xz}$ and $5d_{yz}$ lone pairs, upon rotation (action of one of the angular momentum operators), only two lobes overlap with antibonding metal–ligand σ^* orbitals. The rotated–bonding–antibonding overlap is much less effective than for the $5d_{xy}$ where after rotation in plane all four lobes overlap with antibonding M–L orbitals. Thus, there are two smaller and one large deshielding contributions from the 5d shell in $[\text{PtCl}_4]^{2-}$. For $[\text{PtCl}_6]^{2-}$, rotation of each of the three lone pair orbitals yields a function where all four lobes overlap with antibonding M–L orbitals. Therefore, in $[\text{PtCl}_6]^{2-}$, there are three large paramagnetic deshielding contributions from the 5d shell. Overall, the paramagnetic deshielding is much stronger in $[\text{PtCl}_6]^{2-}$ leading to the negative chemical shift for $[\text{PtCl}_4]^{2-}$. The analysis confirmed that this trend also holds for other pairs of related Pt(IV)/Pt(II) systems, and it was shown that less pronounced trends among Pt(II) and Pt(IV) systems, respectively, could be explained in intuitive terms with the helps of the localized orbital analysis.¹¹⁸

Mercury shielding constants have been studied by a number of authors. A comparison between ZORA DFT and DKH2-HF is made for δ_{Hg} in the series HgX_2 and MeHgX ($\text{X} = \text{Cl}, \text{Br}, \text{I}, \text{Me} = \text{CH}_3$) in Table 5. Additional computational data for Hg shifts are collected in Table 6. Due to a possible strong influence of electron correlation on the shielding tensor in general, it is difficult to rate the quality of the results separately in terms of relativistic and correlation contributions. The basis sets that were applied for the different computations

Table 5 ^{199}Hg chemical shifts for HgX_2 and MeHgX , $\text{X} = \text{Cl}, \text{Br}, \text{I}, \text{Me} = \text{CH}_3$, without and including the spin–orbit-induced terms in the shielding tensor

Molecule	DFT ZORA ^{a,58}		nrel	HF DKH2 ^{a,42}		Expt. ^b
	No SO	Including SO		No SO	Including SO	
HgMeCl	922.1	942.6	561.8	1002.1	485.2	861
HgMeBr	840.3	1068.2	538.9	863.8	953.3	915
HgMeI	500.8	1024.9	354.4	555.1	1411.1	1097
HgCl ₂	1368.7	1555.9	859.0	1408.2	1168.7	1519
HgBr ₂	1484.3	2684.4	1063.3	1561.0	3462.1	2213
HgI ₂	1029.2	3506.0	567.0	863.3	4779.4	3447

Note: Chemical shifts with respect to HgMe_2 . All shifts multiplied by -1 .

^aCalculated from the reported data in the respective publication. “No SO” refers to relativistic shielding constants calculated from a two-component spin–orbit coupled wavefunction/Kohn–Sham orbitals from which the FC and SD spin–orbit contributions to σ_{Hg} have been subtracted. These values are similar, but not identical, to those that would be obtained from scalar relativistic computations (see ref. 227 for some scalar ZORA data for HgMeX).

^bExperimental data as compiled in ref. 58. Solvent for HgX_2 was THF.

Table 6 Additional ^{199}Hg chemical shift computations

Compound ^a	δ exp. ^b	DFT ZORA ⁵⁸	HF DKH2 ²²⁸
$\text{Hg}(\text{SiH}_3)_2$	+196		+232
$\text{Hg}(\text{GeH}_3)_2$	−147		−289
$\text{HgMe}(\text{CN})$	−766	−861	
$\text{Hg}(\text{CN})_2$	−1386	−1724	
$\text{HgCl}_2(\text{NH}_3)_2^c$	−1280	−1086	
$\text{HgBr}_2(\text{NH}_3)_2^c$	−1622	−1858	
$\text{HgI}_2(\text{NH}_3)_2^c$	−2355	−2836	

^aMe = CH₃.^bWith respect to HgMe_2 , as compiled in refs. 58,228. Experimental values for HgX_2 in pyridine.^cNH₃ to simulate the solvent pyridine in the computations.

are not directly comparable, which also makes an assessment somewhat difficult. It has been previously noted that “cross terms” between scalar and SO contributions to σ_{Hg} are very important.²²⁹ This statement means that the SO-induced change of σ_{Hg} strongly depends on the (mainly) scalar-relativistic effects on the Hg–ligand bonds¹ (i.e., relativity-induced changes in the metal’s s/d hybridization affect the magnitude of the SO HAA effect on the Hg shielding). The results in Table 5 indicate that for accurate computations of mercury chemical shifts, both scalar and SO relativistic effects are of high importance, since the experimental trends for σ_{Hg} are only reproduced when the SO contributions are included.

The series $\text{Hg}(\text{LH}_3)_2$, L = C, Si, Ge, has been computed with a spin-free DKH-transformed Hamiltonian including the Pauli SO operator. See Table 6 for results. The rather small magnitudes of Hg chemical shifts were attributed to cancelation of large relativistic and nonrelativistic shielding contributions.²²⁸ Even the often negligible SD contribution to the chemical shift was here comparable in magnitude to the shift itself. The authors considered missing solvent effects as a possible source of error. The influence of solvent effects on mercury chemical shifts has been computed by Wolff et al.⁵⁸ Experimentally, solvent effects on, for example, the Hg shift in HgI_2 can amount to more than 1,000 ppm (pyridine vs. THF). Wolff et al. showed that direct coordination of the metal by a nucleophilic solvent (pyridine, simulated by NH₃ in the ZORA DFT computations) is the main reason for the large solvent effects. The computations yielded a large positive contribution to $\delta(^{199}\text{Hg})$ from coordination of the solvent to Hg. Compare the HgX_2 data in Tables 5 and 6. The resulting geometry change (bending of X–Hg–X by approximately 30°) on complexation was found to increase the magnitude of the chemical shift by ~600 ppm for HgCl_2 , while the electronic interaction of the solvent with the heavy atom caused a large decrease of δ by ~−1,100 ppm. THF was supposed to coordinate much less strongly to Hg and not to cause a significant change of the linear structure of HgX_2 . A possible influence on the chemical shift due to THF that might account for the differences between theory and experiment in Table 6 has therefore not been investigated.

3.4.4 Gold cages and poly-oxo-metallates

Pyykkö and coworkers predicted, among a variety of other optical and spectroscopic parameters, the ^{183}W chemical shift and Au–Au spin–spin couplings in WAu_{12} .²³⁰ This species was theoretically predicted by Pyykkö and Runeberg to be stable for reasons of strong relativistic effects, a perfect 18-electron bonding, and aurophilic attraction.²³¹ Subsequently, WAu_{12} was detected in mass-spectrometry experiments.²³² In a follow-up computational study,²³⁰ the W nucleus in the center of the icosahedral Au_{12} cage was predicted to be exceptionally strongly shielded, resulting in a chemical shift of about $-13,000$ ppm with respect to the reference WO_4^{2-} . Relativistic effects represent only a secondary contribution to this extraordinarily large shielding (most notably a HAHA and HAOHA contribution of 3,850 ppm from SO coupling which exceeds the largest SO shielding found in an earlier DFT benchmark study of ^{183}W shifts by a factor of 2¹⁹⁸). The most important influence was found to be a strong paramagnetic shielding of the external field by the Au cage. The reduced W–Au and Au–Au spin–spin coupling constants were also computed. For $K(\text{W–Au})$, the spin-free relativistic result was $7,350 \times 10^{10} \text{ T}^2 \text{ J}^{-1}$ compared to a nonrelativistic value of $3,322 \times 10^{19} \text{ T}^2 \text{ J}^{-1}$. The average of one- to three-bond Au–Au couplings in WAu_{12} was calculated as $12,365 \times 10^7 \text{ T}^2 \text{ J}^{-1}$ elastivistically, but only 2,459 nonrelativistically.

The carbon atom inside an Au_6 cage can be used as a probe for the electronic structure of the gold gage in the interesting complex $[(\text{Ph}_3\text{PAu})_6\text{C}]^{2+}$ shown in Figure 15. The complex was synthesized by Schmidbaur and coworkers in 1988 and extensively investigated by single crystal X-ray diffraction and NMR spectroscopy.^{234,235} For a related system, the complex $[\text{C}\{\text{Au}[\text{P}(\text{C}_6\text{H}_5)_2(p\text{-C}_6\text{H}_4\text{NMe}_2)]\}_6]^{2+}$, Schmidbaur et al. unambiguously assigned a signal at

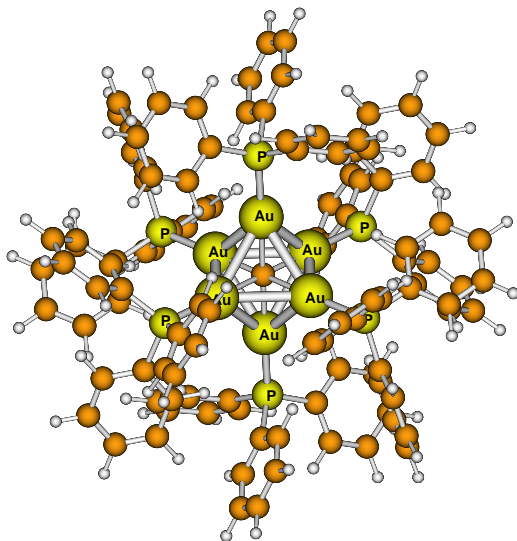


Figure 15 Optimized structure of $[(\text{Ph}_3\text{PAu})_6\text{C}]^{2+}$, from ref. 233.

$\delta = 137.27$ ppm to the interstitial carbon atom.²³⁶ Using this information, a weak ^{13}C signal at $\delta = 135.2$ ppm in the parent complex $[(\text{Ph}_3\text{PAu})_6\text{C}]^{2+}$ was identified as originating from the interstitial carbon. The ^{13}C resonance of this carbon atom appeared in a completely unexpected region. A computational study of these systems by Le Guennic et al.²³³ concluded that the quenching of strongly shielding HALA SO contributions from the Au cage due to electronic effects from the phosphine ligands is responsible for the chemical shift of the central carbon. Without the phosphine ligands, a “naked” Au_6^{2+} cage would cause the carbon nucleus inside to be very strongly shielded, similar to the “NHD” of carbon and proton shifts. The mechanism that suppresses the SO terms is probably the same that causes metal–metal and metal–ligand J -couplings to decrease if a strongly σ -bonding ligand is added *trans* to the bond that transfers the J -coupling, as will be discussed in Section 3.5. The HALA SO contribution to nuclear shielding is similar to the dominant Fermi-contact spin-mechanism of J -coupling^{2,136}, therefore, similar effects from *trans* ligands may be expected.

A number of computational studies have appeared in recent years focusing on NMR chemical shifts of metal and hetero-atoms in poly-oxo-metallates (POM). Poblet, Kazansky, and coworkers considered ^{17}O and ^{183}W chemical shifts for a set of poly-oxo-tungstanates,²³⁷ among them $[\text{W}_6\text{O}_{19}]^{2-}$, $[\text{CH}_3\text{OTiW}_5\text{O}_{18}]^{3-}$, $[\text{W}_5\text{O}_{18}\text{WNO}_3]^-$, $[\text{W}_{10}\text{O}_{32}]^{4-}$, α - δ - γ - $[\text{XW}_{12}\text{O}_{40}]^{n-}$ with $\text{X} = \text{As}, \text{Ga}, \text{Ge}, \text{P}, \text{Si}, \text{Al}, \text{B}$, β - $[\text{PW}_9\text{O}_{28}\text{Br}_6]^{3-}$, $[\text{P}_2\text{W}_{18}\text{O}_{62}]^{6-}$, $[\text{PW}_2\text{O}_{14}]^{3-}$, and $[\text{W}_7\text{O}_{24}]^{6-}$. The number of heavy atoms in some of these systems is seen to be very large by *ab initio* computational chemistry standards, making the computation of their NMR parameters a daunting task. For small W complexes, Ziegler and coworkers had previously found a very good correlation between theory and experiment, with the slope of a linear fit of calculated vs. experimental ^{183}W shifts near unity.¹⁹⁸ In their POM study, Poblet, Kazansky, and coworkers also found a good linear correlation between experimental and calculated ^{183}W shifts. However, the slope of the fit line was only 0.785 which was tentatively attributed to the basis sets that had to be employed in order to keep the computational effort manageable²³⁷ (see also Figure 10) and — a related issue — to the quality of the optimized structures. For the ^{17}O shifts, a much better slope of 1.06 was obtained. Overall, the structure–NMR trends for these POMs were satisfactorily reproduced. A reliable assignment of the POMs’ structure by a comparison of computed and experimental shifts was deemed reliable only in the case of widely separated NMR shifts. The authors also hinted at the need for including solvent effects for POMs with large q/m (charge-to-mass) ratio.

In a follow-up study,²³⁸ Poblet, Kazansky, and coworkers focused on the *reduced* poly-oxo-tungstanates $[\text{W}_5\text{O}_{18}\text{WNO}]^{3-}$, γ - $[\text{SiW}_{12}\text{O}_{40}]^{6-}$, $[\text{P}_2\text{W}_{18}\text{O}_{62}]^{8-}$, and $[\text{W}_{10}\text{O}_{32}]^{6-}$, using similar computational methods as applied in ref. 237. In comparison with the oxidized forms, it was found that overall the computations described the chemical shift changes on reduction well, although some large discrepancies between some of the calculated shifts and experiments were noted, in particular for $[\text{W}_5\text{O}_{18}\text{WNO}]^{3-}$. These discrepancies were attributed to problems with the density functional describing the interaction between W and the NO ligand. We note in passing an earlier study by Kazansky and Yamase²³⁹

where atomic charges in POMs computed at the extended-Hückel level were correlated with experimental chemical shifts for V, Mo, and W, with increasing electronic population per metal leading to increased metal shielding (lower chemical shift) for POMs, and an opposite trend for reduced POMs.

Bagno et al. have recently performed a study of ^{183}W shifts in tungsten POMs²⁴⁰ including solvent effects, using relativistic all-electron DFT methods.^{58,195} Previous work by Bagno and Bonchio employed ECPs.¹³⁷ See also ref. 241. Bagno et al. reported in ref. 240 a computational study of several POM's belonging to various structural groups: Lindqvist ($[\text{W}_6\text{O}_{19}]^{2-}$, $[\text{VW}_5\text{O}_{19}]^{3-}$, and $[\text{V}_2\text{W}_4\text{O}_{19}]^{4-}$), Anderson ($[\text{W}_7\text{O}_{24}]^{6-}$ and $[\text{TeW}_6\text{O}_{24}]^{6-}$), α -Keggin ($[\text{BW}_{12}\text{O}_{40}]^{5-}$, $[\text{PW}_{12}\text{O}_{40}]^{3-}$, $[\text{SiW}_{12}\text{O}_{40}]^{4-}$, and $[\text{GeW}_{12}\text{O}_{40}]^{4-}$), and decatungstates ($[\text{W}_{10}\text{O}_{32}]^{4-}$ and $[\text{W}_{10}\text{O}_{32}]^{6-}$); see Figure 16 for an example of the structures that were computed. As for other NMR computations on POMs,^{237,238} the large number of heavy atoms made the computational study very challenging. A focus here has been the consideration of solvent effects by means of the COSMO model. The best agreement was obtained at the highest computational level which included solvent effects and SO coupling. Despite the rather narrow chemical shift range of the sample set (about 500 ppm) as compared to the 8,000 ppm shift range found overall for ^{183}W , the computations performed very satisfactorily; see Figure 16 for an overview. The average deviation was 35 ppm or only about 7% of the shift range considered. The largest deviations seen in Figure 16 were found for species with large q/m or q/A (charge-to-surface area ratio) where inclusion of solvent effects also had the strongest impact, highlighting once more the importance of modeling the chemical environment of metal systems for the purpose of NMR computations. The small intercept of the linear fit in Figure 16 was possible because one of the POMs, $\text{W}_6\text{O}_{19}^{2-}$, was selected as the NMR

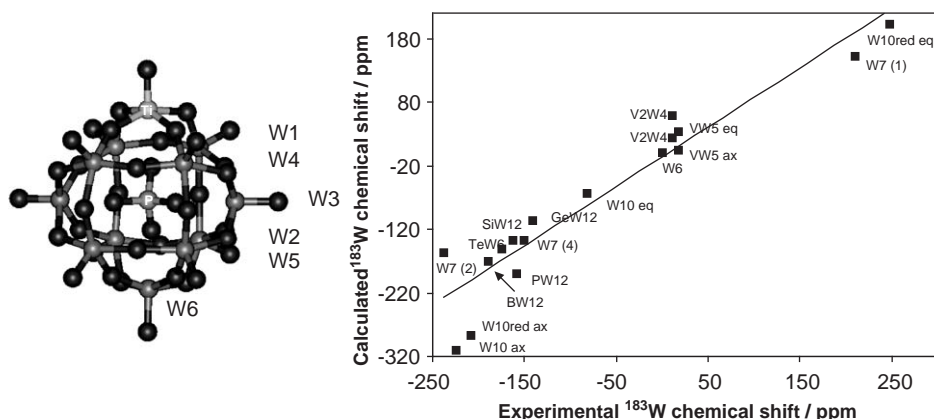


Figure 16 (Left) Structure of $[\text{PW}_{11}\text{TiO}_{40}]^{5-}$ as an example of the poly-oxo-metallates (POM) studied by Bagno et al.²⁴⁰ (Right) Correlation between calculated and experimental ^{183}W chemical shifts relative to $[\text{W}_6\text{O}_{19}]^{2-}$ in various POM. All-electron spin-orbit DFT computations; COSMO solvation model for water. The correlation line has a slope of 0.93, intercept -7 ppm.

reference. The absolute errors with respect to the standard reference WO_4^{2-} would have been larger but this is inconsequential for the all-important trends and rather highlight difficulties with the modeling of WO_4^{2-} in solution (large q/A). Inclusion of solvent effects systematically improved the results, both directly in the NMR computations as well as through application of the solvent model in the geometry optimizations, which tended to cause some shrinkage of the POM structures.

3.4.5 Shielding tensor anisotropies

Besides the isotropic shielding σ_A , the anisotropy $\Delta\sigma_A$ also carries important information about the geometric and electronic structure around nucleus A. In many of the already cited publications, theoretical values for $\Delta\sigma_A$ have been reported, and frequently very large relativistic effects have been found. Measurements of anisotropies can be carried out for completely or partially oriented systems, for instance, with SSNMR or liquid-crystal NMR (LCNMR). An example for small “benchmark” systems with strong relativistic effects for which experimental data are available is presented in Table 7 for $\Delta\sigma$ of ^{199}Hg in methylmercury halides and HgMe_2 . As in the case of the isotropic shieldings discussed earlier, the experimentally observed trends along the series $\text{X} = \text{Cl}, \text{Br}, \text{I}$ are only reproduced in the computations if SO coupling is considered. Interestingly, as in the case of the chemical shifts, the shielding anisotropies for the two different computational approaches DFT-ZORA vs. HF-DKH2 *without* the SO contributions are rather similar, but drastically change when SO contributions are included due to their different signs. With both methods, the experimental trends are correctly reproduced; however, the DFT-ZORA results significantly overestimate $\Delta\sigma$, whereas it is strongly underestimated in the HF-DKH2 calculations. Whether the reason lies in the relativistic approach, or is due to electron correlation, is yet unclear. Environmental effects due to the liquid-crystal solvents should also be explicitly considered in the computations. This is strongly

Table 7 ^{199}Hg chemical shift anisotropies $\Delta\sigma$ for MeHgX , $\text{X} = \text{Cl}, \text{Br}, \text{I}$, $\text{Me} = \text{CH}_3$, without and including the spin-orbit-induced terms in the shielding tensor

Molecule	DFT ZORA ^{a,227}		nrel	HF DKH ^{b,242}		Expt. ²⁴²	Expt. ²²⁷
	No SO	Including SO		No SO	Including SO		
HgMe_2	6462	7857	4473.3	5877.0	4843.6	7325 ± 55	7355 ± 55
HgMeCl	5179	6319	3677.5	4913.1	4258.0	5535 ± 80	5430 ± 40
HgMeBr	5322	6168	3718.6	5121.3	3570.0	5455 ± 100	5140 ± 90
HgMeI	5763	6071	4000.0	5574.4	2731.1	5480 ± 300	4840 ± 70

^aMethod “C” of ref. 227 referring to DFT-ZORA computations with the same basis set employed as in ref. 58 (Table 5) for comparison. Shielding anisotropies with an extended basis (method “B” in ref. 227) were consistently larger by 600–1,000 ppm.

^bSee footnote a of Table 5. For this reason, the values here somewhat differ from the scalar relativistic results reported in ref. 227.

indicated by the previously mentioned computational study of Hg chemical shifts by Wolff et al.⁵⁸

Other examples for which relativistic corrections to shielding anisotropies, often also for a heavy nucleus, have been frequently reported are the following series of small molecules which remain very popular with theoreticians for benchmarks of relativistic and electron correlation methods: HX (X = F, Cl, Br, I),^{73,149,150,153,154,166,180,185} H₂Y (Y = O, S, Se, Te [Po]),^{185,184} YH₃ (Y = N, P, As, Sb, Bi),¹⁸⁴ and CH₃X (X = F, Cl, Br, I).^{73,185}

An increasing number of chemical shift anisotropies are becoming available from SSNMR measurements. Several of the combined SSNMR experimental–theoretical studies cited so far have in fact focused on the tensor properties of the shielding. Often, the computations provide important information about the local orientation of the shielding tensor. We shall discuss one last example. The XeF₂ molecule has been investigated experimentally and by computations. Experimental SSNMR data for the Xe and F shielding anisotropies for xenon fluorides were reported by Forgeron et al.,²⁴³ along with ZORA DFT computations. Kudo et al. also performed computations on this system using an infinite-order two-component relativistic approach with a HF wavefunction.²⁴⁴ Some of the data are collected in Table 8. Both relativistic methods perform quite well in reproducing the experimental $\Delta\sigma$. The tensor anisotropy affords large relativistic effects. The nonrelativistic calculations strongly overestimate $\Delta\sigma$. Part of the chemical shift tensor anisotropy relative to the Xe atom results from a paramagnetic+SO shielding tensor component parallel to the Xe–F bond, $\sigma_{||}$ of about $-1,000$ ppm. The corresponding chemical shift tensor component of $\delta_{||} = +1,000$ ppm was determined experimentally prompting Forgeron et al. to state that this was “the first experimental demonstration that relativistic effects play an important role in the nuclear magnetic shielding for xenon.”²⁴³ In nonrelativistic theory, this component (from the SOS part of the shielding tensor) is zero by symmetry which can be seen from Equation (55): the only mechanism that contributes nonrelativistically in the SOS part of the equation is OP–OZ, where the OZ operator is given by the *B*-derivative of (43c). The resulting operator is proportional to \hat{L} , the angular momentum operator. For a linear molecule, the wavefunctions are eigenfunctions of the angular momentum along the molecule’s axis, that is, $\hat{L}_{||}\Psi_k = \Psi_k \cdot L_{||}$ with eigenvalue $L_{||}$. As a

Table 8 ¹²⁹Xe nuclear shielding tensor in XeF₂

	σ_{iso}	$\Delta\sigma$
Relativistic DFT ^a	3006.7	4469
Relativistic HF ^b	3570	4276
Nonrelativistic DFT ^a	2275.4	5066.7
Nonrelativistic HF ^b	2020	5163
Expt. ^a		4245(20)

^aReference 243, Forgeron et al.

^bRef. 244, Kudo et al.

consequence, $\langle \Psi_j | \text{OZ}^{(B_{\parallel})} | \Psi_0 \rangle = \text{constant} \cdot \langle \Psi_j | \Psi_0 \rangle = 0$ in Equation (55). In a relativistic formalism, the other mechanisms may lead to nonvanishing SOS contributions. Since the diamagnetic shielding rarely contributes to chemical shift trends (which was confirmed by the computations), the δ_{\parallel} component of 10^3 ppm measured experimentally indeed probes the relativistic effects on the shielding tensor.

3.5 Spin–spin coupling in heavy-element systems

3.5.1 General considerations, small-molecule benchmark data

Relativistic benchmark data for spin–spin coupling constants and tensors were previously compiled in refs. 2,5,7. In Section 3.2, we have shown how strongly relativistic effects can affect spin–spin coupling, in particular the contact-type terms (the FC–FC mechanism of Equation (56)). One aspect of these strong relativistic effects is simply the relativistic increase in the AO matrix elements of the FC-type operators. A second aspect is the relativistic change in the bonding environment of the heavy element, and a third influence is the SO contributions such as from FC–OP cross terms in Equation (56). The first part has for some time been dealt with semiempirically through *relativistic scaling factors* for hyperfine integrals.^{245,246} Such RSFs, or hyperfine integrals obtained from relativistic atomic computations, have also found use in semiempirical codes for spin–spin coupling.^{247–250,126} Occasionally, researchers have scaled nonrelativistic spin–spin coupling data involving a heavy element to allow for comparison with experiment.^{121,251} A somewhat related procedure has been proposed in ref. 127 where ratios of nonrelativistic and scalar-relativistic (Pauli operator, frozen cores) values for the orbitals at the nuclei have been used to scale the matrix elements of the FC operator in nonrelativistic molecular computations. Since such scaling methods, if used in otherwise nonrelativistic computations, do not include the relativistic changes in the electronic structure, their predictive power is limited. However, they yield useful order-of-magnitude estimates for relativistic effects on spin–spin coupling. As an example, for the Hg 6s orbital, the relativistic correction factor for the hyperfine integral is about 2.44.²⁴⁵ If the bond between Hg and a ligand atom L is mostly involving the Hg 6s orbital, a relativistic change of $K(\text{Hg}–\text{L})$ by up to a factor of 3 can be expected. For molecules where strong relativistic effects on bonding are present, where the FC term is not the only important contribution to the coupling constant, or where electronic SO coupling is large, or if HALA effects are of interest, it is obviously desirable to determine spin–spin coupling from relativistic first-principles calculations. We will forgo a discussion of semiempirical methods but point out that relativistic trends in many heavy-atomic systems have been rationalized in early application of relativistic extended Hückel theory (REX).^{125,252}

Small molecules, such as H_2Y where $\text{Y} = \text{O}, \text{S}, \text{Se}, \text{Te} (\text{Po})$ and YH_4 where $\text{Y} = \text{C}, \text{Si}, \text{Ge}, \text{Sn}, \text{Pb}$, have been popular systems for benchmark studies and new theoretical developments. Early work has employed four-component HF theory.^{253,150,121,63,184} The data indicated that along the series $K(\text{H}–\text{X})$ decreases, predicting a negative coupling constant for TeH_2 . A correlated study (MCSCF)

including the Pauli SO operator yielded a positive coupling constant for this system, likely because of the missing spin-free relativistic corrections.¹⁴⁰ Spin-spin coupling tensors are sensitive to electron correlation effects. This is also the case in relativistic theories. While HF benchmark studies are still very common for relativistic nuclear magnetic shielding computations, as evidenced by Table 2, the relativistic HF approach is usually not accurate enough for computations of spin-spin coupling. Another problem that tends to plague HF and semiempirical computations of spin-spin coupling is a triplet instability of the unperturbed HF wavefunction.²⁵⁴ Such triplet instabilities have not been noted as major issues in KS DFT computations of spin-spin coupling, while at the same time DFT incorporates the desired effects from electron correlation (within the approximations of the functional, of course). Consequently, the majority of first-principles relativistic spin-spin coupling computations have been performed with relativistic DFT methods. Among the available implementations, we note the ZORA approach by Autschbach and Ziegler^{59,60} and its recent extensions^{120,116} (hybrid DFT, SO), the IORamm approach by Filatov and Cremer³⁸ (hybrid DFT, spin-free), and a DKH2 code by Melo et al.⁴³ (hybrid DFT, SO, numerical differentiation). Some of the data obtained by Filatov and Cremer for plumbanes are already listed in Table 1. Other systems that were studied in ref. 38 include the remainder of the YH_4 series, CdMe_2 , HgMe_2 , $\text{Hg}(\text{CN})_2$, and the series HgMeX with $\text{X} = \text{Cl}, \text{Br}, \text{I}$. In general, good agreement with available nonhybrid ZORA DFT reference data⁵⁹ was noted, although the influence from a hybrid functional was shown to be quite pronounced in some cases. We already emphasized this in Section 3.2 when discussing the Pb-H coupling in plumbanes. Trends from including some HF exchange in the functional and trends from SO coupling appear to cancel at least partially for these systems. For comparison with experiment, for the Hg complexes it is necessary to consider solvent effects as will be discussed below. Melo et al.⁴³ performed test calculations on the YH_4 series where $\text{Y} = \text{C}, \text{Si}, \text{Ge}, \text{Sn}$, with HF and DFT. The authors reported good agreement with four-component HF benchmark data but also noted that their DFT results agreed better with experiment. Unfortunately no results were reported for PbH_4 or larger systems.

Main group diatomics, often with p-block elements, have also been benchmarked extensively. Because of the importance of SO coupling for the spin-spin coupling in such systems and the interest in their coupling anisotropies, we will discuss them in a separate section (Section 3.5.5).

3.5.2 Heavy-atom–light-atom couplings

Large relativistic effects on one-bond heavy-atom–ligand spin-spin coupling constants have consistently been calculated for systems with sixth-row elements. Figure 17 shows a comparison of a number of tungsten–ligand coupling constants in comparison to their nonrelativistic counterparts and to experiment. It is clear that relativistic effects on these one-bond couplings are extremely large; in some cases they are comparable to the total nonrelativistic result. Coupling constants involving other elements from the sixth row of the periodic table, such as Hg and Pt, are similarly strongly affected, mainly by spin-free relativistic

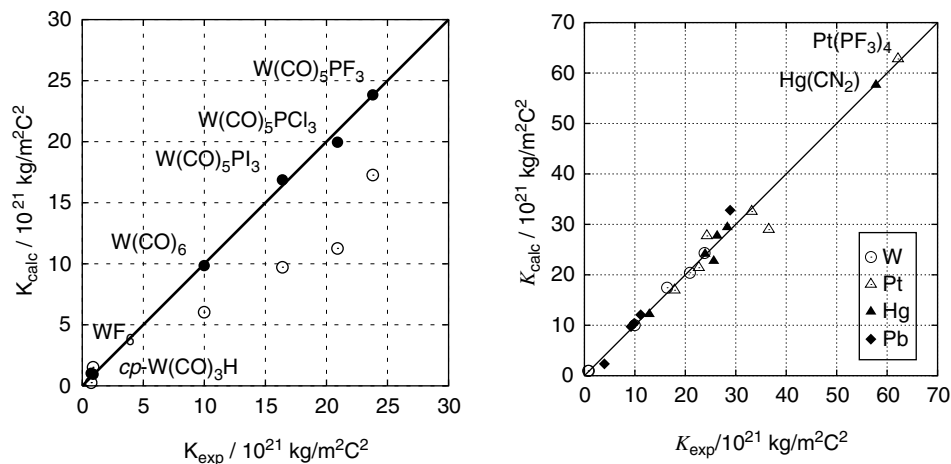


Figure 17 (Left) One-bond tungsten–ligand spin–spin coupling constants, computation vs. experiment, from ref. 59. (●): Scalar-relativistic ZORA; (○): nonrelativistic DFT results. (Right) A range of one-bond metal–ligand reduced nuclear spin–spin coupling constants (absolute values) for 5d metal complexes. Scalar-relativistic ZORA DFT results (VWN functional) vs. experimental values. A few data points for Pb are also included. Data taken from refs. 59,258. For not octahedrally or tetrahedrally coordinated metal centers, the first coordination shell has been completed with solvent molecules, as described in ref. 255. The straight thick lines indicate where calculated = experiment.

effects.¹¹ Figure 17 includes a larger collection of one-bond coupling constants which shows that the relativistic DFT computations are quite capable of reproducing the experimental data. A similar test set of complexes has also been investigated by Khandogin and Ziegler¹²⁷ using variational frozen-core computations with the Pauli operator and a relativistic correction term for the FC mechanism of spin–spin coupling as discussed above. Based on the discussion in Section 3.2, it should be clear that a flexible basis for the core region is required to obtain reliable heavy-nucleus FC matrix elements which makes the use of a variationally stable method mandatory. As a consequence, the computations have met with rather limited success regarding the agreement with experiment. Qualitatively, however, the relativistic trends were reproduced, which allowed a study of the origin of *trans* effect in square planar Pt complexes and its relation to the one-bond Pt–P coupling constants.

For complexes with open coordination sites (linear and square planar, as opposed to tetrahedral or octahedral) that may be accessed by solvent molecules, it has been found necessary to complete the first solvation shell with solvent molecules in the computations in order to achieve reasonable agreement with experiment.²⁵⁵ In some cases, noticeable solvent effects were predicted even for supposedly inert solvent such as chloroform. For more strongly coordinating solvents, the effects can be considerable. Consider the case of $\text{Hg}(\text{CN})_2$: the nonrelativistic Hg–C coupling is only about 40% of the experimental value. However, a gas-phase relativistic computation yielded “only” $443 \times 10^{20} \text{ T}^2 \text{ J}^{-1}$

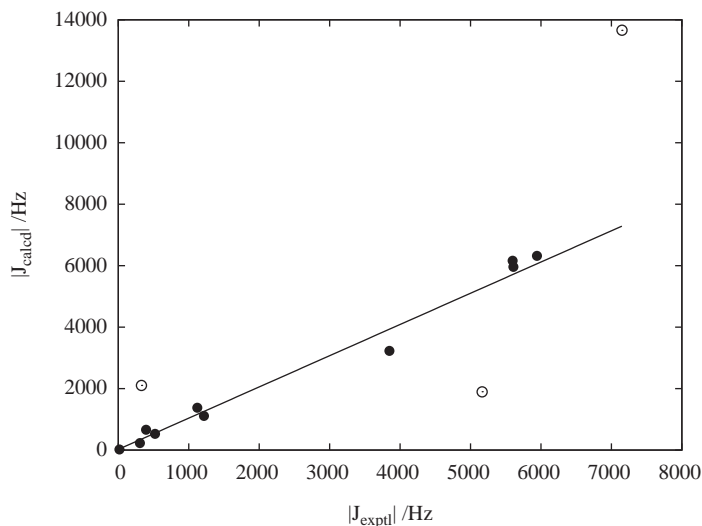


Figure 18 Spin–spin coupling constants involving ^{129}Xe . Scalar ZORA DFT computations vs. experiment. Data from Bagno and Saielli.¹⁹³ The straight line is a linear fit to the data set excluding some outliers indicated by open markers. Slope = 1.05, intercept = -18 Hz.

which is still significantly short of the experimental value of 577.8. Coordination of four methanol molecules to the Hg center increased the coupling constant by another $135 \times 10^{20} \text{ T}^2 \text{ J}^{-1}$, yielding almost exactly the experimental value. It was shown that the solvent effect does not predominantly result from a geometry distortion but is of electronic origin.

Scalar ZORA DFT computations for J -couplings involving ^{129}Xe in XeF_2 , FXeOSO_2F , $\text{FXeN}(\text{SO}_2\text{F})_2$, XeF_4 , XeO_2F_2 , XeOF_4 , XeF_6 , XeF^+ , XeF_2F_3^+ , and XeCl^+ were provided in ref. 193. Some results are shown in Figure 18. The agreement with experiment is seen to be quite good. For XeF^+ , large SO corrections for the Xe–F spin–spin coupling were obtained, changing J from $-13,655$ to $-10,302$ Hz, which is still about double the magnitude of the quoted experimental value. The outliers were discussed earlier in Section 3.4.2; the deviations are likely due to uncertainties about which solvated species are involved in the NMR spectrum of “ XeF^+ ” in superacid. Spin–spin couplings involving Xe were also investigated by Bryce and Wasylishen²⁵⁶ for a number of polyatomic Xe fluorides, along with group-17 fluorides. The test set comprised $\text{K}(\text{Cl–F})$ in ClF_2^+ , ClF_3 , ClF_4^+ , ClF_5 , ClF_6^- , and ClF_6^+ , $\text{K}(\text{Br–F})$ in BrF_3 , BrF_6^- , and BrF_6^+ , and $\text{K}(\text{I–F})$ in IF_4^+ and IF_6^+ , as well as $\text{K}(\text{Xe–F})$ in XeF^+ , XeF_2 , XeF_3^+ , XeF_4 , XeF_5^- , and XeF_5^+ with a large variety of bonding environments. The authors obtained excellent agreement between ZORA DFT computations and experiment which allowed to assign unknown signs of the coupling constants in some cases. The success of the computations was attributed to the inclusion of both spin-free and SO relativistic effects. Analysis of the data showed that in the set of molecules, the OP mechanism strongly depended on the number of valence-shell lone pairs of the heavy atom while the SO contributions were sensitive to the bond distances.

By considering these two factors, the trends in the experimental data for the test set could be rationalized. For some apparently closely related systems such as BrF_6^+ and BrF_6^- , the Xe–F coupling constants were found to be of opposite sign. This indicates a serious potential trap when interpreting trends in experimental results for which the sign is unknown. We have recently computed Xe–F coupling constants which were used, along with computed fluorine and xenon chemical shifts, to determine terminal and bridging coordination modes of XeF_2 in the solids $[\text{Mg}(\text{XeF}_2)_2][\text{AsF}_6]_2$, $[\text{Mg}(\text{XeF}_2)_4][\text{AsF}_6]_2$, $[\text{Ca}(\text{XeF}_2)_{2.5}][\text{AsF}_6]_2$, $[\text{Ba}(\text{XeF}_2)_3][\text{AsF}_6]_2$, and $[\text{Ba}(\text{XeF}_2)_5][\text{AsF}_6]_2$.²⁵⁷ Although the cluster model was not capable of delivering quantitative agreement with experiment, for example, leading to a $\sim 10\%$ underestimation of the Xe–F coupling magnitudes, the trends for bridging and terminal fluorines were well reproduced in the computations.

A concerted experimental SSNMR/computational study has been directed at the X–Cl one-bond spin–spin coupling tensor in $\text{Ph}_3\text{X–Cl}$ where $\text{X} = \text{C, Si, Ge, Sn, Pb}$.²¹⁴ Both the isotropic coupling and the anisotropy ΔK of the coupling tensor obtained from ZORA DFT computations agreed well with experimental data, with increasing magnitudes as the atom X becomes heavier. As one might expect, relativistic effects were found to be important for the $\text{X} = \text{Sn, Pb}$ systems. SO effects were found to be of particular importance for the Pb compound where they led to an almost complete vanishing of ΔK because of cancelation with equally large but opposite anisotropies from the OP mechanism.

Some of the Pt and Pb systems for which data are shown in Figure 17 have recently been reinvestigated using a newly developed hybrid DFT version of the ZORA spin–spin coupling program and using an extended basis set that included high-exponent basis functions at the light nuclei also.¹²⁰ Some of the data for plumbanes have already been listed in Table 1; the influence of the hybrid functional is evident by comparing the PBE data (nonhybrid) with PBE0 (a hybrid functional with 25% HF exchange). For the Pt complexes, some sensitivity to the computational model was noted. The earlier benchmark data of ref. 59 for Pt were shown to have benefited somewhat from error cancelations. As an example, for the complex $\text{Pt}(\text{PF}_3)_4$, the best value for $K(\text{Pt–P})$ obtained with the hybrid functional and the extended basis was $663 \times 10^{20} \text{ T}^2 \text{ J}^{-1}$ compared to an experimental value of $622 \text{ T}^2 \text{ J}^{-1}$. The nonhybrid DFT results from ref. 59 using basis set for P without additional high-exponent functions and an approximate form of the $V_{\text{HXC}}^{(m_A)}$ term of Equation (36b) were 610 and $627 \times 10^{20} \text{ T}^2 \text{ J}^{-1}$ using the BP and the VWN functional, respectively. Thus, the combined effects from extending the basis set and improving the functional led to a slightly larger difference with experiment. Similar trends were obtained for two other Pt complexes. Most likely, the lack of treating solvent effects along with remaining approximations in the functional and basis set makes up for most of the difference between computation and experiment.

Coupling constants involving Pt and a light ligand atom were studied experimentally and by ZORA DFT computations by Klein et al.²⁵⁹ and Gudat et al.²⁶⁰ Klein et al.²⁵⁹ considered $[\text{DMSO}_2\text{Pr}(\text{aryl})_2]$ complexes and used a comparison of computed with experimental data to assign the configurations as

cis or *trans*. For example, for the aryl=phenyl complex, computed $^1J(^{195}\text{Pt}-^{13}\text{C})$ of 1,018 Hz (*cis*) vs. 539 Hz (*trans*) vs. 995 Hz (experiment) clearly indicated a *cis* complex. For the aryl=mesityl complex, computed $^1J(^{195}\text{Pt}-^{13}\text{C})$ of 1,130 Hz (*cis*) vs. 546 Hz (*trans*) vs. 605 Hz (experiment) clearly indicated *trans* complex. Gudat et al.²⁶⁰ used a similar protocol, based on computed Pt–C and Pt–P one-bond couplings, to determine the *cis/trans* isomerism in the related systems $[\text{Pt}(\text{aryl})_2(\text{PEt}_3)_2]$. The Pt–C coupling constants were in particularly good agreement with experiment. The Pt–P couplings also agreed well with experiments for the *trans* complexes, and the experimental trend of much higher Pt–P couplings for the *trans* complexes was reproduced. For the *cis* systems, the computed *cis* and *trans* Pt–P couplings bracketed the experimental data; however, the authors noted that the simplification of the phosphine ligand in the computations (methyl instead of ethyl) might have been responsible for systematic errors.

3.5.3 Heavy-atom–heavy-atom coupling constants

Extremely large relativistic effects might be obtained for spin–spin coupling between two heavy nuclei. We have studied metal–metal spin–spin coupling constants quite extensively over the past few years, for instance, for Pt–Pt,¹¹³ Pt–Ti,^{261,262,263,114,116} or Hg–Hg couplings.^{264,265} Generally, good agreement with experiment was obtained from relativistic DFT computations, whereas non-relativistic computations cannot be meaningful for such couplings. For instance, Hg–Hg couplings can be as large as several hundred kilohertz, with the large magnitude caused by the s– σ character of the Hg–Hg bonds and the fact that the hyperfine integrals for the 6s Hg orbital may increase relativistically by about a factor of 3.^{71,69} For a pair of Hg nuclei, this increase would lead to an order-of-magnitude increase of the 6s–6s orbital contributions in the coupling tensor. These studies have also shown that relativistic effects on the coupling constants tend to act as a *magnifying glass* for subtle effects in the metal–metal and metal–ligand bonds. This means that NMR is a particularly sensitive tool to study details of bonding in these heavy-atomic systems.

Experimental data for Pt–Pt spin–spin coupling constants are abundant. Interestingly, in some chemically closely related dinuclear complexes, $J(^{195}\text{Pt}-^{195}\text{Pt})$ may differ by an order of magnitude,^{217,266,267,268} and these variations do not correlate with distances between the Pt centers. Examples are $[\{\text{Pt}(\text{CO})_3\}_2]^{2+}$, $[\{\text{PtCl}(\text{CO})(\text{PPh}_3)\}_2]$, and $[\{\text{Pt}(\text{CNCH}_3)_3\}_2]^{2+}$, with small Pt–Pt coupling constants of 551, 760, and 507 Hz, respectively, and on the other hand $[\{\text{PtCl}_2(\text{CO})\}_2]^{2-}$ and $[\{\text{PtBr}_2(\text{CO})\}_2]^{2-}$, with large Pt–Pt coupling constants of 5,250 and 4,770 Hz, respectively. Other examples can be found, for example, in ref. 266. The Pt oxidation state is +I in all of the aforementioned cases. ZORA DFT computations of the Pt–Pt coupling constants in $[\text{Pt}_2(\text{CO})_6]^{2+}$ and $[\text{Pt}_2(\text{CO})_2\text{Cl}_4]^{2-}$ were performed as representatives for the groups of complexes with small and large $J(\text{Pt}-\text{Pt})$, respectively. The computations helped to uncover the origin of these order-of-magnitude differences¹¹³: a strongly σ -interacting ligand has negative contributions to the metal–metal coupling (CO vs. Cl^-) in particular in *trans* position to the metal–metal bond. Relativistic effects increase the metal–ligand σ -bonding character in the complexes. In the case of $[\text{Pt}_2(\text{CO})_6]^{2+}$, the strong relativistic

increase of the FC contributions in $J(\text{Pt-Pt})$ is then largely suppressed by increasingly negative influences from the Pt-ligand bonds. In $[\text{Pt}_2(\text{CO})_2\text{Cl}_4]^{2-}$, the chloride ligands have a much weaker effect and the relativistic increase of $J(\text{Pt-Pt})$ is not so strongly suppressed. The result is an order-of-magnitude difference of the metal-metal coupling in these two systems. This example shows that metal-metal and metal-ligand bonding characteristics affecting the NMR can be strongly amplified by relativistic effects.

Le Guennic et al. have studied the metal NMR parameters of a set of nonbuttressed Pt-Tl bonded systems $[(\text{NC})_5\text{Pt-Tl}(\text{CN})_n]^{n-}$, $n = 0, 1, 2, 3$ (1–4) and the related system $[(\text{NC})_5\text{Pt-Tl-Pt}(\text{CN})_5]^{3-}$ (5) synthesized by Glaser and coworkers^{269,270} and two bridged amidate complexes 6 and 7 synthesized by Matsumoto and coworkers^{263,114} and model systems based thereupon. See Figure 11. The chemical shifts of some of these systems were discussed in Section 3.4. We focus here on the metal-metal J -coupling constants. Data reported here refer to the isotopes ^{195}Pt and ^{205}Tl .

An earlier computational investigation by Autschbach and Ziegler had suggested that at least half of the huge magnitude of the Pt-Tl coupling constant of the $n = 1$ system (experiment: 57 kHz) is due to coordination of Tl by solvent molecules (water).²⁶¹ Computations on the whole series 1–4 as well as complex 5 showed that solvent coordination effects on $^1J(\text{Pt-Tl})$ of the $n = 0$ system are even larger,^{262,114} changing the gas-phase result of about -10 kHz into a solution result of about $+55$ kHz in computations that differed only by the absence or presence of solvent. It was also found that both explicit solvent molecules and bulk solvent effects need to be included in the computations on 1–4 in order to obtain the same trend for $^1J(\text{Pt-Tl})$ as found experimentally, and that the simultaneous application of both a continuum solvent model (COSMO^{271,272}) and an asymptotically correct DFT XC potential (SAOP^{273,274}) is beneficial. A summary of the computational results obtained by Autschbach and Le Guennic²⁶² is displayed in graphical form in Figure 19. For model “C,” very good agreement with experiment was obtained. Results for the metal-ligand coupling constants for these systems have also been reported in ref. 262, with similar success of the solvation model. The Tl-C coupling constants are very strongly influenced by the solvent coordination, whereas the Pt-C coupling constants are less affected, although some improvement is obtained from considering solvent effects. Solvent coordination had previously also been found to be responsible for the unintuitive relative magnitudes of $^1J(^{205}\text{Tl-}^{13}\text{C})$ and $^2J(^{205}\text{Tl-}^{13}\text{C})$ for complex 2,²⁶¹ with the latter being more than three times larger than the former. The findings from the theoretical investigation of metal-metal and metal-ligand coupling constants in 1–5 can be briefly summarized as follows: (i) The trend for $^1J(^{195}\text{Pt-}^{205}\text{Tl})$ along the series is caused by solvent coordination, mainly by direct coordination of the Tl atom. In gas phase or a weakly coordinating solvent, $^1J(^{195}\text{Pt-}^{205}\text{Tl})$ for 1–4 would exhibit the opposite trend. (ii) In computational modeling of heavy metal NMR parameters, a reasonable description of the experimental trends requires to include at least one explicit solvation shell in case the metal has open coordination sites, and at least a continuum solvation model to estimate the effects of a second, third, etc., solvation shell. Reproducing trends for different

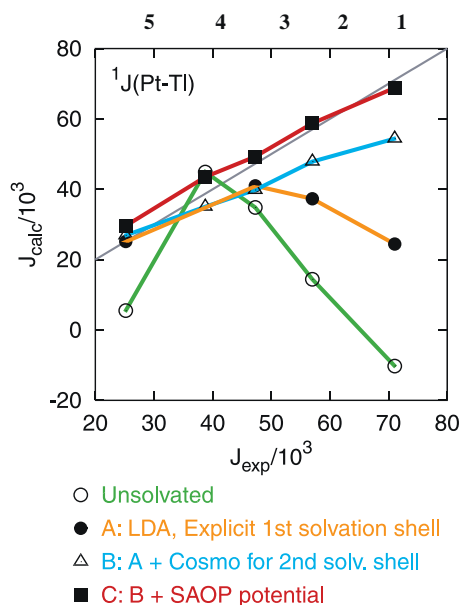


Figure 19 $^1J(^{195}\text{Pt}-^{205}\text{Tl})$ for complexes 1–5, calculated vs. experimental data. The straight line indicates where $\delta_{\text{calc}} = \delta_{\text{exp}}$. Solvent is water. COSMO is a continuum solvent model. Nonhybrid DFT computations.

solvents might require further refinement of the model. The importance to fill the metal's first coordination sphere with solvent molecules has also been highlighted in computations on other heavy-atomic systems.^{255,264}

Unfortunately, the computational protocol that led to nearly quantitative agreement with experiment for $^1J(^{195}\text{Pt}-^{205}\text{Tl})$ of 1–5 turned out to significantly overestimate the Pt–Tl coupling constants in the amidate-bridged complexes 6 and 7 shown in Figure. 11.²⁷⁵ As an example, the record-large $^1J(\text{Pt}-\text{Tl})$ of 146.8 kHz of 6 was calculated as 159.6 kHz when using the COSMO solvation model (gas-phase calculation: 114.2 kHz) but this good agreement with experiment was only achieved *without* using the asymptotically corrected SAOP potential. With SAOP and COSMO applied simultaneously, the computations yielded 221.7 kHz for $^1J(\text{Pt}-\text{Tl})$ in spin-free relativistic calculations. Calculations including SO coupling yielded 172.9 kHz (COSMO) and 236.8 kHz (COSMO+SAOP), respectively. For 7, the experimental $^1J(\text{Pt}-\text{Tl})$ is 88.8 kHz. The computations yielded 80.6 kHz (COSMO) and 105.5 kHz (COSMO+SAOP) with spin-free relativistic DFT, respectively. The SO results were 87.9 and 113.3 kHz. The trends regarding the computational model and the sign of the SO corrections are the same for both complexes. Whereas the inclusion of the asymptotic correction in the functional yielded a welcome but relatively minor increase of $^1J(^{195}\text{Pt}-^{205}\text{Tl})$ for 1–5, complexes 6 and 7 turned out to be very sensitive. Le Guennic et al. have analyzed the situation in detail¹¹⁴ and traced this sensitivity back to small metal 6s-contributions in low-lying unoccupied σ -orbitals that change considerably, percentage-wise, depending on the computational model.

It is likely that quantitative agreement between theory and experiment for complexes such as **6** and **7** will only be achieved at a very high level of theory since their sensitivity leaves little room for error suppression/compensation.

It is interesting to note the drastic differences in the Pt–Tl coupling constants between **6** and **7** and among the series **1**–**5**. Le Guennic et al. employed existing, and developed a range of new, analysis tools for spin–spin coupling constants for the study **6** and **7**¹¹⁴ (see also some educational applications to organic molecules as described in ref. 115). Figure 20 (left) shows the contributions of the metal–metal σ -bonding localized orbitals to $^1J(^{195}\text{Pt}^{205}\text{Tl})$ of **6** and **7**. In both cases, the orbitals are significantly delocalized along the complexes' long axis which rationalizes the strong influence in particular of the ligands *trans* to the metal–metal bond. The large differences between $^1J(^{195}\text{Pt}^{205}\text{Tl})$ for **6**, **7**, **1**, and **2**, for instance, can to a large extent be traced back to the σ -coordinating ability of this axial ligand. The stronger this coordination, the smaller the metal–metal coupling — a typical *trans*-effect. The same mechanism also causes Pt–Pt coupling constants to vary by an order of magnitude,¹¹³ and Hg–Hg coupling constants to stay well below an upper theoretical estimate of almost 1 MHz calculated for $[\text{Hg}^{2+}\text{Hg}]^{2+}$.²⁶⁴ Complex **6** was also recently reinvestigated by the NLMO/NBO analysis discussed earlier in Section 3.2 when the Pb–H coupling in PbH_4 was analyzed. The results (Figure 20, right) supported the earlier conclusions regarding the *trans*-ligand influence.

In ref. 264, the extremely large coupling constants between Hg and Hg in complexes containing Hg_2^{2+} and Hg_3^{2+} have been investigated. It was found that *coordination* and *polarization* of a metal–metal fragment explain the magnitude of the metal–metal coupling constants. The coordination can thereby be due to ligands or solvent molecules. Unlike other systems with one metal center wherein a number of computational studies reported an increase of the coupling magnitude on solvent coordination,^{255,261} solvent or ligand coordination of both metals of a metal–metal fragment reduces its coupling constant in the systems investigated so far. This can be rationalized by a simple MO argument based on Hückel theory.²⁶⁴ For the complex of Hg_2^{2+} with the crown ethers 18-crown-6 and 15-crown-5, very good agreement with the experimental $^1J(\text{Hg}^{199}\text{Hg})$ of 284 kHz (^{199}Hg)²⁷⁶ could be achieved. To our knowledge, this value is still the largest experimentally determined J -coupling constant. The calculated scalar DFT-ZORA result is 278 kHz; missing SO corrections were estimated to be of the order of –10% or smaller. See Figure 21 for an illustration. The coupling constants of the (hypothetical) free Hg_2^{2+} were estimated to be around 0.9 MHz, indicating that the upper limit for Hg–Hg coupling constants has not yet been reached in experiments. However, a system such as the $\text{Hg}_2(18\text{-crown-6})_2$ complex in Figure 21 for which the coupling constant was predicted to be about 0.6 MHz does not allow an easy NMR detection of $J(\text{Hg}^{199}\text{Hg})$ due to its symmetry. A polarization of the Hg_2^{2+} fragment due to an unsymmetric environment would reduce the likely coupling, though.

In the same work, ref. 264, the one- and two-bond Hg–Hg coupling constants in Hg_3^{2+} have been considered. The first ^{199}Hg – ^{199}Hg coupling ever detected experimentally,²⁷⁷ and for a long time the largest known nuclear spin–spin

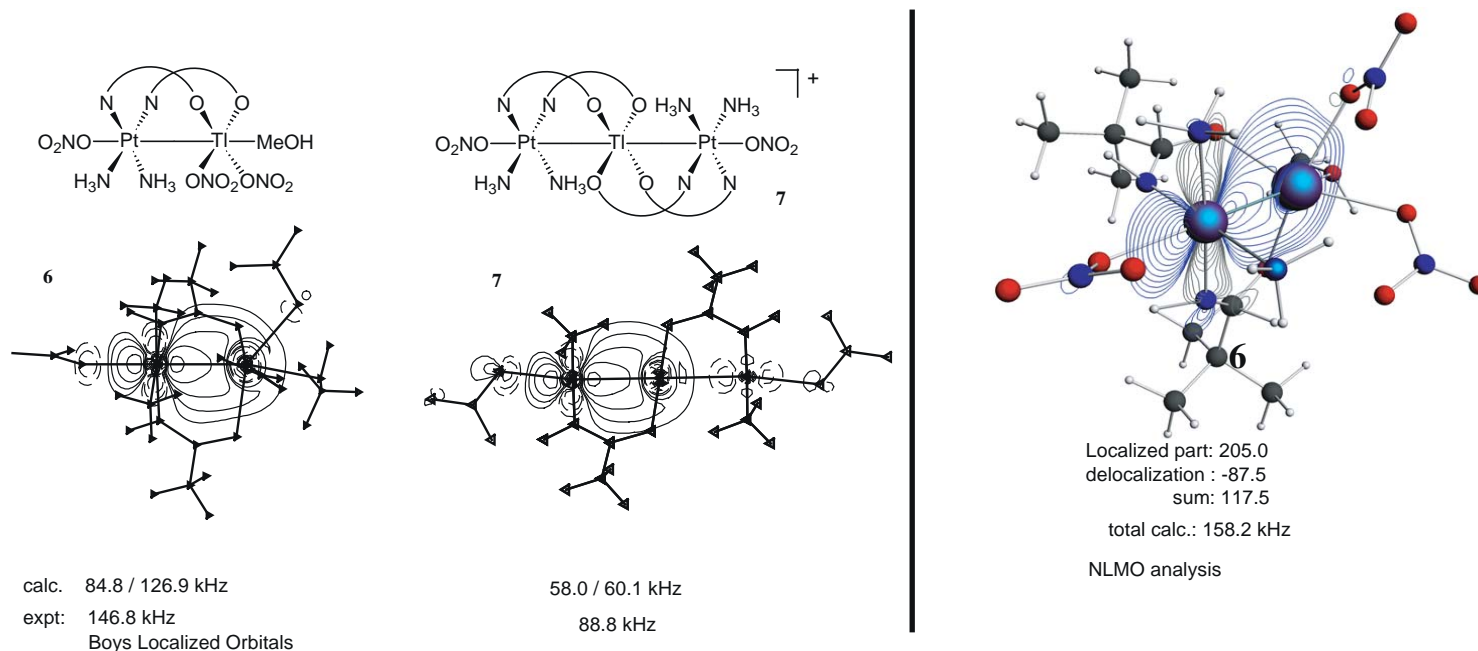


Figure 20 (Left) Contribution from Pt-Tl σ -bond Boys-localized orbitals to $^1J(^{195}\text{Pt}-^{205}\text{Tl})$ vs. total computed coupling constant vs. experiment for complexes **6** and **7** (Fermi-contact term only, spin-free, no solvent effects included).^{114,263} The σ -bonding orbital is considerably delocalized along the molecular axis. The axial ligands have therefore a strong influence on $^1J(^{195}\text{Pt}-^{205}\text{Tl})$. (Right) NLMO analysis of the Pt-Tl coupling, from ref. 116 (spin-orbit, solvent effects included). Shown is the contribution from the Pt-Tl bonding NLMO, broken down into its localized part (the corresponding “parent NBO” contribution), and from its delocalization tail. The large negative contribution to $J(\text{Pt-Tl})$ from this delocalization tail supports the conclusions drawn from the analysis in terms of Boys-localized orbitals. The main difference between the Pt-Tl bond contributions and the total $J(\text{Pt-Tl})$ can be attributed to the Pt 5s orbital.

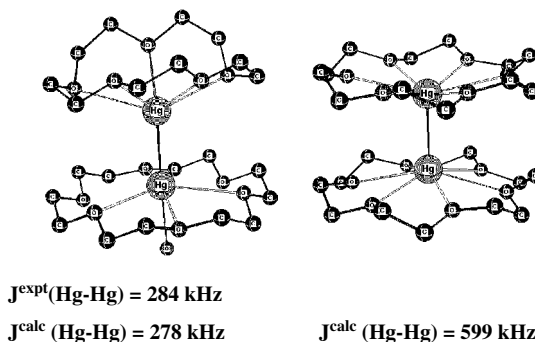


Figure 21 Reduced Hg–Hg coupling constants (^{199}Hg) for crown ether complexes of Hg_2^{2+} , from ref. 264. Computations based on the scalar DFT-ZORA approach. The left complex (mixed 18-crown-6 and 15-crown-5) has been computed based on the crystal structure of ref. 276, the right one (both 18-crown-6) based on an optimized geometry.

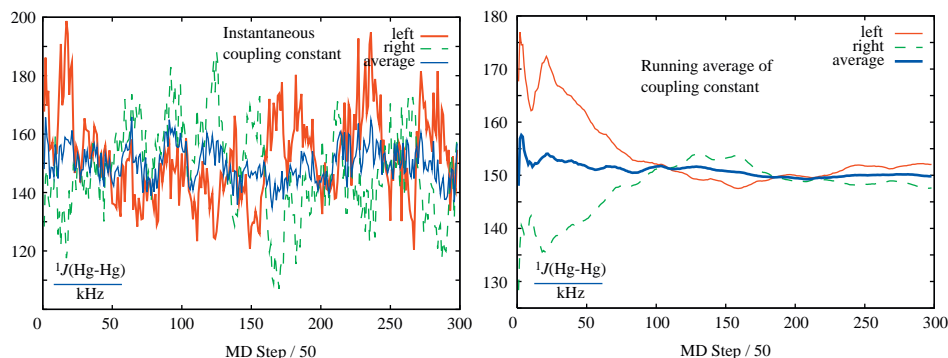


Figure 22 $^1J(\text{Hg-Hg})$ in Hg_3^{2+} , from a MD simulation with subsequent averaging of ZORA DFT spin–spin coupling computations. Data from ref. 265. The experimental value is 140 kHz.

coupling constant is the 139.7(3) kHz one-bond coupling in the $[\text{Hg-Hg-Hg}]^{2+}$ ion; the coupling was measured in 1984 by Gillespie et al.²⁷⁸ at -70°C in liquid SO_2 . The relativistic DFT computations of ref. 264 indicated that $^2J(\text{Hg-Hg})$ should be much larger than the one-bond coupling, in agreement with an estimate based on Hückel theory as well as REX calculations.^{279,280} Again, environmental effects, here from the solvent SO_2 , were estimated to be very pronounced, but due to the weak solute–solvent bonding interactions the static computations based on optimized geometries were not deemed reliable. The Hg_3^{2+} system has recently been revisited with a MD approach.²⁶⁵ Using a small number of explicit SO_2 solvent molecules and an *ab initio* Born–Oppenheimer MD simulation from which 300 configurations were used to average $^1J(\text{Hg-Hg})$, the coupling constant was computed as 149 kHz which agrees quite well with the experimental value of 140 kHz. Figure 22 shows the instantaneous and averaged coupling constant over the 300 MD configurations. Statistics collected along the MD run showed that the terminal Hg atoms afford close contacts with the

solvent's oxygen atoms but the central Hg atom does not, which is crucial for the enormous drop of the coupling constant from its computed gas-phase value of 260 kHz to the final MD average of 149 kHz. For comparison, a computation with a continuum solvent model (COSMO) yielded 236 kHz, the difference with the gas-phase result mainly being due to a Hg–Hg bond shortening. The solvent coordination effect and the preferred close solvent–solute contacts with the terminal Hg atoms are evidently not described by the continuum model. The study highlights once more the importance of considering a molecule's environment in NMR computations, in particular for sensitive and relativistically amplified heavy-atom spin–spin couplings.

Bagno and Saielli have considered the spin–spin coupling in the Hg_4^{2+} ion.²⁰³ The trend predicted for Hg_3^{2+} appears to continue here, that is, the two-bond coupling was found to be larger, 150 kHz, than the central (100 kHz) or the terminal (33 kHz) one-bond couplings. The three-bond coupling was computed as 178 kHz. The instability of this species in solution was noted; thus, an experimental verification would most likely come from SSNMR. Pronounced effects from the ion's surrounding should be expected. Another system studied by Bagno and Saielli was a model for a Lehn “grid compound” where metal centers such as Hg(II) and others are arranged on a self-assembled grid. At 7 Å grid spacing between the Hg atoms and no direct bonds, the J -couplings were predicted to be negative and up to about –40 Hz in magnitude. Ref. 203 reviews a number of other relativistic DFT studies performed by Bagno et al., some of which have been mentioned elsewhere in this chapter.

3.5.4 Two- or multi-bond couplings

Two- or higher-bond coupling constants have not yet been extensively investigated by relativistic computations. $^2J(\text{Hg}–\text{Hg})$ in Hg_n ions have been briefly discussed in the preceding subsection. Kaupp has reported significant relativistic effects on the $^{31}\text{P}–^{31}\text{P}$ two-bond coupling constants in *cis*- and *trans*- $\text{M}(\text{CO})_4(\text{PH}_3)_2$, $\text{M} = \text{Cr}, \text{Mo}, \text{W}$, leading to a reversal of the trend of increasing P–P coupling for the W complex as the metal becomes heavier.²⁸¹ Noticeable SO effects on a three-bond C–C coupling constant were reported by Autschbach and Ziegler for the complex $[(\text{NC})_5\text{Pt}–\text{Ti}(\text{CN})]^-$.²⁶¹ It is likely that significant relativistic corrections on multi-bond coupling constants between light atoms are obtained when the coupling path involves a heavy metal, as is the case for the two examples mentioned. Bagno and Saielli have computed nuclear spin–spin coupling constants between DNA base pairs mediated by a heavy metal (Hg).²⁸² A structure with two thymines (T–H) was set up shown as follows for the Hg system:

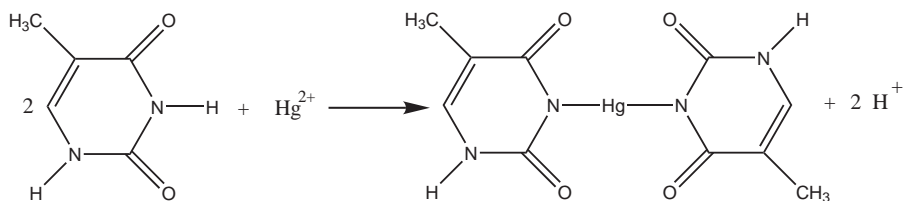


Table 9 Computed metal-mediated spin–spin couplings between DNA base pairs, from Bagno and Saielli²⁸²

	TZnT	TCdT	THgT
$^1J(\text{N-metal})$	–28.2	227	–670
$^2J(\text{N-N})$	0.8	0.4	1.7
$\delta(\text{Metal})$	N/A	–648	–1727

T: deprotonated thymine. A Zn chemical shift was not provided because the reference $\text{Zn}^{2+}(\text{aq})$ would be difficult to model. Isotopes: ^{15}N , ^{113}Cd , ^{67}Zn , and ^{199}Hg .

The computed J -couplings are listed in Table 9. Spin-free ZORA DFT computations predicted a large increase in the N–metal one-bond couplings, as one might expect from the strong increase in the FC-type matrix elements for heavy nuclei. For Hg, the computation for the metal-mediated two-bond N–N coupling yielded 1.7 Hz which compared reasonably well to an experimental value of 2.4 Hz quoted in ref. 282. The authors confirmed that the metal's orbitals are directly involved in the J -coupling; comparisons with nonrelativistic computations were not made to quantify the role of relativity in the two-bond coupling. Bagno and Bonchio investigated W–W couplings across W–O–W in polyoxo-tungstanates²⁸³ using a ZORA DFT approach. These coupling constants are useful to assign POM structures; depending on the W–O–W angle, one may identify edge- or corner-sharing units. The authors demonstrated that the coupling depends on both the W–O distances and the W–O–W angle, as one might expect, and therefore cautioned about structural assignments considering only an angular dependence. Computations on two POMs with known structure yielded good agreement with experimental data.

3.5.5 Spin–orbit effects and coupling anisotropies

SO effects on one-bond couplings were often found to be relatively small in comparison to the spin-free effects. A notable exception is the series of TI-X where $X = \text{F}, \text{Cl}, \text{Br}, \text{I}$. Figure 23 shows the isotropic $K(\text{Pb-X})$ as well as the coupling tensor anisotropy ΔK for the series as computed with hybrid DFT and the ZORA relativistic approach. Nonrelativistic data are not shown but were previously found to be only about half the magnitude of the experiment and had the correct trend for the wrong reasons.⁶⁰ For the isotropic coupling, the spin-free relativistic computations barely predict any change along the series while a very strong trend is present in the SO results as well as the experiment. For TI-I , the SO OP–FC cross term is the largest individual term in the coupling tensor.⁶⁰ Like for TI-X with heavier halogens X , SO effects on spin–spin coupling tend to be important when coupling between two p-block elements is involved. There is also a strong dependence of the result on the density functional: nonhybrid functionals perform reasonably well for the isotropic coupling constants, albeit with significant underestimation of K for TIBr and TI . However, these functionals, especially the simple local density functional VWN, very strongly

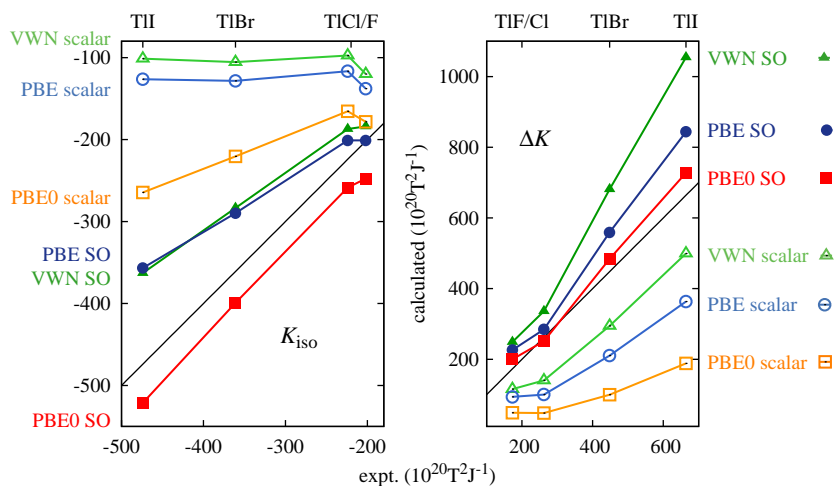


Figure 23 Spin–orbit effects on the nuclear spin–spin coupling in the series TI–X, X = F, Cl, Br, I. ZORA DFT computations with various functionals vs. experiment. Isotropic coupling K and coupling tensor anisotropy ΔK . Computational data from ref. 120. Experimental data from refs. 284–287; see also refs. 288,289. The straight thick lines indicate where calculated = experiment.

overestimate the coupling anisotropy. It has for quite some time been suspected that approximations in the density functionals are responsible for the under- and overestimation of the trend for K and ΔK , respectively.^{59,289} In particular, numerical data have indicated that paramagnetic terms in isotropic NMR parameters tend to be underestimated in magnitude when a nonhybrid functional is applied to shielding or spin–spin coupling involving p-block atoms with many lone pairs. The development of a hybrid DFT version of the ZORA DFT code¹²⁰ has recently allowed us to verify the functional’s influence in the TI–X coupling: the improved PBE0 hybrid functional results shown in Figure 23 agree well with experiment for *both* the isotropic coupling and the coupling tensor anisotropy. In the same paper, a number of additional interhalogen diatomics XY (X, Y = F, Cl, Br, I and X \neq Y) that were previously studied by Bryce et al.²⁸⁹ were computed at the hybrid SO DFT level.¹²⁰ Overall the difference between nonhybrid and hybrid DFT results of refs. 289,120 were not very large. In both studies, a good correlation of the magnitude of K and ΔK with the product of the nuclear charges of X and Y was obtained, as shown in Figure 24. These trends and magnitudes are partially attributable to SO effects, for example, for ClI the spin-free relativistic results corresponding to the data shown in Figure 24 are $K = 346$, $\Delta K = -369$, and for BrI $K = 781$, $\Delta K = -804$ (in $10^{20} \text{T}^2 \text{J}^{-1}$), leading to higher magnitudes of the coupling tensor elements. A slight reversal of the trend is seen for the coupling anisotropies of IF ($Z_1 Z_2 = 477$) vs. ClBr ($Z_1 Z_2 = 595$).

Available studies have shown that even in those cases where the SO effect on the isotropic coupling constant is rather small, the anisotropy ΔK can be quite strongly influenced by SO coupling. The range of available ΔK studies molecules

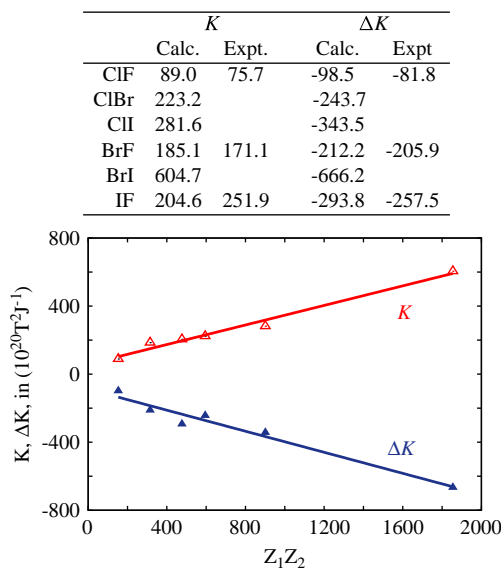


Figure 24 Isotropic coupling constant and coupling anisotropy for interhalogen diatomics, in $10^{20} \text{ T}^2 \text{ J}^{-1}$, from ZORA hybrid DFT computations including SO coupling (ref. 120). Computed results plotted vs. the product of nuclear charges. Exp. data from Refs. 301, 302.

with heavy atoms is still rather limited. However, it is clear that future investigations of ΔK and interpretations of experimental data will need to include relativistic effects if heavy-atom systems are studied, and both scalar and SO effects will be of importance.

Kantola and coworkers have recently reported measurements and ZORA DFT computations of the ^{199}Hg – ^{13}C spin–spin coupling tensor in the MeHgX ($X = \text{Cl}, \text{Br}, \text{I}$) systems²⁹⁰ along with data for the reference compound HgMe_2 . The experimental data were obtained from measurements in liquid crystals. Within the rather large experimental error bars, the computations agreed with experiment as long as some explicit solvent effects were considered in the computations. The measured ΔJ for ^{199}Hg – ^{13}C were between 1.0 and 1.3 kHz and calculated as 1.2 kHz for the MeHgX systems. For dimethylmercury, theory and experiment agreed somewhat better, yielding ΔJ of 0.85 kHz (experiment) vs. 0.82 kHz (calculated). Relative anisotropies, $\Delta J/J$, were consistently computed somewhat too high compared to experiment. The study confirmed early theoretical estimates by Pyykkö⁶⁹ that SO coupling increases the relative anisotropy of the Hg–C coupling tensor.

Many of the available small-molecule benchmark studies have also reported ΔK data. Examples for such computations other than those already discussed are Me_3XY systems ($X = \text{C}, \text{Si}, \text{Sn}, \text{Pb}$; $Y = \text{F}, \text{Cl}$; semiempirical study, ref. 249), XF ($X = \text{F}, \text{Cl}, \text{Br}, \text{I}$; DFT-ZORA, ref. 60), XY (DFT-ZORA, ref. 289), HX (HF-Dirac, ref. 150; MCSCF-pPSO, ref. 140), H_2Y (HF-Dirac, ref. 184; MCSCF-pPSO, ref. 140), Xe and halogen fluorides (DFT-ZORA, ref. 256), and refs. 63,125. We also refer to the

spin–spin coupling tensor overview by Vaara et al.⁷ cited earlier, and to ref. 291 for further examples and additional details.

3.6 Electric field gradients

The electronic and nuclear charges in a molecule create an electric field. We may refer to it as the “intrinsic” electric field of the molecule, as opposed to an external electric field and field gradient perturbing the molecule. The internal field’s inhomogeneity is to first order given by its first derivative, the EFG. EFGs interact with electric quadrupole moments. To derive the expressions of the internal field gradient, imagine a (hypothetical or actual) point quadrupole with Cartesian quadrupole tensor elements G_{uv} which is placed somewhere in the molecule as a probe. The quadrupole–EFG interaction term has then to be added to the Hamiltonian analogous to dipole and higher-order multipole terms for an electric field. Consider next the first-order energy change $E^{(G_{uv})}G_{uv}$ due to the quadrupole–EFG interaction. The derivative $E^{(G_{uv})}$ is then — according to first-order perturbation theory — given by Equation (27) with the unperturbed wavefunction, with $\hat{\mathcal{H}}^{(G_{uv})}$ being the EFG operator at the position of the quadrupole. The electric field is given by the (negative) derivative of the scalar potential V of the nuclei and the electrons. The EFG operator for the quadrupole perturbation is defined accordingly as the (negative) *second* derivative of the scalar potential operator for the internal field^v, that is

$$\hat{V}_{uv} = \frac{\partial^2 \hat{\phi}}{\partial r_u \partial r_v}, \quad u, v \in \{x, y, z\} \quad (60)$$

The internal EFG is then computed from an expectation value of the operator (60) where the second derivative can be considered at any point in space.^w The EFG is a rank-2 tensor which may be characterized by three principal components, V_{ii} and its principal axes. Important applications arise when considering the EFG at the position of a quadrupolar nucleus, and evaluating the interaction energy of the internal EFG with the nuclear quadrupolar charge distribution. Nuclear quadrupole coupling constants C_Q are related to the EFG tensor via

$$C_Q = \frac{eQV_{33}}{h} \quad (61)$$

where V_{33} is the largest magnitude component of the EFG tensor and Q the nuclear quadrupole moment. The nuclear quadrupole–field gradient interaction

^vThe EFG proper is $-\hat{V}_{uv}$. We use the term EFG but omit the negative sign here which is consistent with the definition of the quadrupole coupling in Equation (61).

^wThis is conceptually similar to the magnetic shielding tensor which may also be defined at any point in space by considering a point magnetic dipole $\boldsymbol{\mu}$ at a position \mathbf{r}_X and using its vector potential $A^X = (1/c^2)(\boldsymbol{\mu} \times \mathbf{r}_X/r_X^3)$ instead of the nuclear vector potential (39) in the derivation of the NMR shielding. In NMR, the measurement relies on the presence of a nuclear spin and therefore the shielding tensor is measured at the position of the nucleus.

is very important in SSNMR²⁹¹ and, with modern ultrahigh-field instruments, measurements of NMR parameters and C_Q of formerly inaccessible quadrupolar nuclei are now possible. With reliable EFG tensor computations at hand, a fit to experimental data might then in turn be used to obtain nuclear quadrupole moments. A large set of quadrupole moments based on literature data up to 2001 has been compiled by Pyykkö²⁹² (a new updated 2008 data set is upcoming). In this chapter, the reader can find references to relativistic computational work for many heavy nuclei including various actinides. We also point to an extensive review by Schwerdtfeger et al.²⁹³ covering the literature up to 2003.

Taking the expectation value of (60) yields

$$V_{uv}^{\text{el}}(\mathbf{R}_A) = - \int d\mathbf{r} \cdot \rho(\mathbf{r}) \frac{3(\mathbf{r} - \mathbf{R}_A)_u(\mathbf{r} - \mathbf{R}_A)_v - \delta_{u,v}|\mathbf{r} - \mathbf{R}_A|^2}{|\mathbf{r} - \mathbf{R}_A|^5} \quad (62)$$

for the electronic term. There is also a nuclear term

$$V_{uv}^{\text{nuc}}(\mathbf{R}_A) = \sum_{B \neq A} Z_B \frac{3(\mathbf{R}_B - \mathbf{R}_A)_u(\mathbf{R}_B - \mathbf{R}_A)_v - \delta_{u,v}|\mathbf{R}_B - \mathbf{R}_A|^2}{|\mathbf{R}_B - \mathbf{R}_A|^5} \quad (63)$$

In (62) and (63), the EFG is considered at the position of nucleus A . The equation for the electronic part is valid in the four-component and the non-relativistic regime. In two-component formalisms, the perturbation operator has additional *picture-change corrections* which are of order c^{-2} . These result from new terms in the Hamiltonian on transformation of the EFG operator from four- to two-component form.^{22,27,18,40,294} The picture-change terms vanish again in the nonrelativistic limit.

Given the large magnitude of the electronic EFG operator in the near-nucleus region from its overall $1/r_A^3$ behavior, one should expect large relativistic effects on the EFG percentage-wise. However, any filled and perfectly spherical atomic shell around the nucleus of interest will not contribute to the EFG.^{*} Therefore, small deformations of the core orbitals in a molecular environment and the overall arrangement of the chemical bonds determine the magnitude of V which makes it overall a very useful “chemical” property.

The magnitude of relativistic effects on EFGs in heavy-element systems is clearly demonstrated in Figure 25 for the iodine EFG in group-13 iodides.²⁹⁵ Similar to the nuclear spin-spin coupling constants in TIX that were discussed earlier, both spin-free as well as SO relativistic effects can be important for heavy p-block diatomics, in particular for TII. If the bonding partner is not a sixth-row or heavier element, however, the scalar effects appear to be significantly more important which implies that for semiquantitative results SO effects might be neglected for such systems. As an example, a range of additional ^{127}I C_Q results for iodine-halides reported in ref. 295 agreed well with experiment at both the spin-free and the SO level. Marked improvements of iodine quadrupole coupling

^{*}The EFG also vanishes in highly symmetric environments such as tetrahedral or octahedral.

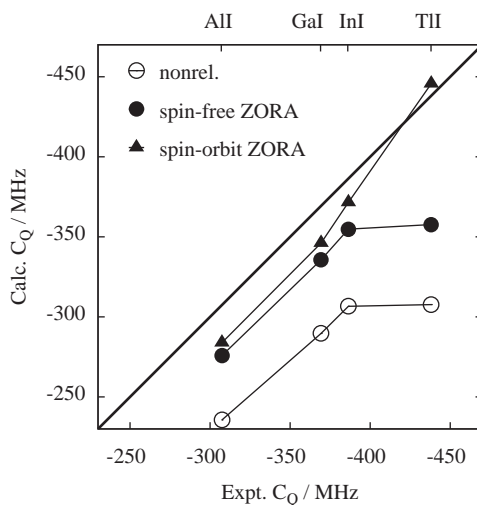


Figure 25 ^{127}I nuclear quadrupole coupling constants in group-13 iodide diatomics. ZORA DFT computations vs. experiment; data were taken from van Lenthe and Baerends.²⁹⁵ The straight thick line indicates where calculated = experiment.

constants over nonrelativistic results were also obtained by Malkin et al. from second-order DKH scalar-relativistic computations for the diatomics ICl, IBr, ICN, HI, and IK.⁴⁰

The general (potential) importance of SO coupling for EFGs of heavy-element molecules was pointed out by Visscher et al.²⁹⁶ who performed four-component HF and correlated *ab initio* computations of the H-X (X = F, Cl, Br, I) series of diatomics. For HI, the iodine EFG increased from 9.65 to 11.59 a.u. at the Dirac HF level. An orbital contribution analysis was carried out for HI which showed that most of the electronic contributions were due to valence-shell orbitals. The interpretation of the EFG mechanism was based on a model where a bond is formed between H^+ and a spherically symmetric (zero EFG) I^- . The bond formation amounts to forming a nonspherical hole in the iodine valence shell causing most of the EFG. Some semicore and core-polarization contributions were also found in the EFG analysis for HI. Inclusion of SO coupling slightly lowered the magnitude of the EFG. This effect was attributed to the σ - π mixing in the bond: the electron hole on the iodine side acquires partial π character which is somewhat less asymmetric than the hole caused by a pure σ bond. Overall, the SO effect was small (-0.05 a.u.) compared to the total 1.82 a.u. relativistic increase. The H-X series of molecules has been very popular for theoretical benchmarks and was considered by many other authors. We cite ref. 27 as an early numerical study of picture-change effects which were demonstrated by computations of EFGs.

Picture-change effects on EFGs were studied by a number of authors. As already mentioned, in a recent paper, Mastalerz et al. revisited the series H-X where X = F, Cl, Br, I, At, and demonstrated that picture-change effects can

represent a considerable fraction of the relativistic correction to the EFG.²⁹⁴ It should be noted that the bulk of the picture-change effects were already obtained with the lowest order transformation of the operator. A comparison was made with data obtained recently by other research groups, such as a study by Neese et al.²⁹⁷ (four-component and DKH HF), Malkin et al.⁴⁰ (DFT and HF with DKH), and Visscher et al.²⁹⁶ (four-component HF, MP2, CCSD, and CCSD(T)). All these studies have highlighted the importance of relativistic effects and of picture-change effects for this electric property.

The DKH method has recently been applied to calculate a large range of ^{119}Sn EFGs.²⁹⁸ Scalar-relativistic DFT calculations with the B3LYP functional were performed for 34 Sn complexes for which experimental Mössbauer quadrupole splitting parameters ΔE were available. The EFGs were in the range of -4 to $+5$ a.u. It was noted that picture-change effects entered the results as a systematic error of constant magnitude. Both picture-change corrected and picture-change uncorrected results showed an excellent linear correlation with the experimental ΔE . Based on the linear fit, a quadrupole moment of $13.2 \pm 0.1 \text{ fm}^2$ was obtained for the ^{119}Sn nucleus, in good agreement with the 2001 reference value of $12.8 \pm 0.7 \text{ fm}^2$.²⁹²

For metal atom EFGs, Schwerdtfeger et al. pointed out problems with DFT to correctly describe the electron distribution in 3d transition metals.²⁹³ As an example, for the CuCl molecule, the Cu EFG varies between $+0.67$ and $+0.15$ for various functionals including hybrids while a CCSD(T) result of -0.34 a.u., likely to be very accurate, agrees well with experiment. It is known that 3d metals pose challenges for many of the popular functionals which is reflected in a rather poor performance in EFG computations. DFT results for heavier transition metal nuclei were not compared in ref. 293. van Lenthe and Baerends also considered Cu–X (X = halide) diatomics in their ZORA study of EFGs cited earlier,²⁹⁵ along with Ag–X. The main focus has been on the halide C_Q ; however, they did not agree as well with experiment as those for the main group diatomics which also points toward deficient charge distributions for these systems obtained at the DFT level. Bast and Schwerdtfeger performed a DFT benchmark study of EFGs in 2003²⁹⁹ with a test set comprising various Sc, Cu, and Ga diatomics and concluded that “it is difficult (if not impossible in some cases) to obtain accurate [EFGs] for transition elements,” while good performance of DFT was found for the main group element gallium. Willans et al. made a comparison between theory (ZORA DFT) and experiment for the ^{139}La C_Q .²¹⁴ Experimental data were derived from SSNMR. The agreement was poor irrespective of whether SO coupling was included in the computations or not. However, the authors noted that the crystal environment was not modeled in the computations but might have a profound impact on the EFGs. Lanthanum chemical shifts computed at the same level of theory agreed reasonably well with experiment. Somewhat poor agreement with experiment for a Ru EFG with both hybrid and nonhybrid DFT was noted by Ooms and Wasylishen,²⁰⁵ albeit for a single carbonyl complex. Recently, Thierfelder et al. proposed to apply Coulomb-attenuated hybrid functionals for the computation of late transition metal EFGs.³⁰⁰ The authors concluded that computations on the molecules CuH, AuH, and CuX, AuX, OC–CuX, and

OC-AuX, where X = H, F, Cl, Br, I, yielded reliable results with a CAM-B3LYP functional. Linear fits of the EFGs computed at this level of theory vs. experimental C_Q yielded nuclear quadrupole moments that were in good agreement with experimental data.

4. CONCLUDING REMARKS

NMR parameters such as nuclear magnetic shielding and indirect spin–spin coupling tensors, or nuclear quadrupole coupling tensors, can be computed from first-principles quantum theory as energy derivatives. Although continuing developments aim at further improvements regarding the speed and accuracy of such computational methods, in particular during the past 15 years a large number of publications have demonstrated the maturity and reliability of available relativistic methods for NMR computations. Relativistic effects on these “nuclear” properties can be very large. Examples are $\sim 100\%$ or more relativistic increases of heavy-atom–light-atom nuclear spin–spin couplings. NMR chemical shifts and nuclear quadrupole coupling constants can also be very strongly affected by relativistic modifications of the molecule’s electronic structure. There are now a number of program implementations available that researchers can use to compute such properties efficiently at some level of approximation for the treatment of relativistic kinematics, even for quite large molecules.

ACKNOWLEDGMENTS

The authors would like to acknowledge support of our research by the National Science Foundation. We are indebted to the present and past members of our research group as well as many collaborators for their contributions to the projects that we have been working on — some of which have been presented in this chapter. Special thanks to Profs. Alessandro Bagno, Michael Bühl, and Markus Reiher for providing re/preprints of some of their work.

REFERENCES

1. P. Pyykkö, *Chem. Rev.*, 1988, **88**, 563–594.
2. J. Autschbach and T. Ziegler, Relativistic computation of NMR shieldings and spin–spin coupling constants, in: *Encyclopedia of Nuclear Magnetic Resonance*, D. M. Grant and R. K. Harris, eds., Vol. 9, Wiley, Chichester, 2002, pp. 306–323.
3. M. Kaupp, M. Bühl and V. G. Malkin, eds., *Calculation of NMR and EPR Parameters. Theory and Applications*, Wiley-VCH, Weinheim, 2004.
4. J. Autschbach, Calculation of heavy-nucleus chemical shifts: relativistic all-electron methods, in: *Calculation of NMR and EPR Parameters. Theory and Applications*, M. Kaupp, M. Bühl and V. G. Malkin, eds., Wiley-VCH, Weinheim, 2004.
5. J. Autschbach and T. Ziegler, Relativistic calculation of spin–spin coupling constants, in: *Calculation of NMR and EPR Parameters. Theory and Applications*, M. Kaupp, M. Bühl and V. G. Malkin, eds., Wiley-VCH, Weinheim, 2004.
6. J. Vaara, P. Manninen and P. Lantto, Perturbational and ECD calculation of relativistic effects in NMR shielding and spin–spin coupling, in: *Calculation of NMR and EPR Parameters*.

- Theory and Applications*, M. Kaupp, M. Bühl and V. G. Malkin, eds., Wiley-VCH, Weinheim, 2004, pp. 209–226.
7. J. Vaara, J. Jokisaari, R. E. Wasylishen and D. L. Bryce, *Prog. Nucl. Magn. Res. Spectrosc.*, 2002, **41**, 233–304.
 8. M. Kaupp, Relativistic effects on NMR chemical shifts, in: *Relativistic Electronic Structure Theory*, P. Schwerdtfeger, ed., Vol. 2, Elsevier, Amsterdam, 2004.
 9. M. Kaupp, V. G. Malkin and O. L. Malkina, NMR of transition metal compounds, in: *Encyclopedia of Computational Chemistry*, P. von Ragué Schleyer, ed., Wiley, Chichester, 1998, pp. 1857–1866.
 10. M. Bühl, NMR of transition metal compounds, in: *Calculation of NMR and EPR Parameters. Theory and Applications*, M. Kaupp, M. Bühl and V. G. Malkin, eds., Wiley-VCH, Weinheim, 2004, pp. 421–431.
 11. J. Autschbach, The calculation of NMR parameters in transition metal complexes, in: *Principles and Applications of Density Functional Theory in Inorganic Chemistry I*, Vol. 112 of *Structure and Bonding*, N. Kaltsoyannis and J. E. McGrady, eds., Springer, Heidelberg, 2004, pp. 1–48.
 12. T. Ziegler and J. Autschbach, *Chem. Rev.*, 2005, **105**, 2695–2722.
 13. J. Autschbach, *Coord. Chem. Rev.*, 2007, **251**, 1796–1821.
 14. M. Bühl, *Annu. Rep. NMR Spectrosc.*, 2008, **64**, 77–126.
 15. L. B. Casabianca and A. C. de Dios, *J. Chem. Phys.*, 2008, **128**, 052201.
 16. S. Moon and S. Patchkovskii, First-principles calculations of paramagnetic NMR shifts, in: *Calculation of NMR and EPR Parameters. Theory and Applications*, M. Kaupp, M. Bühl and V. G. Malkin, eds., Wiley-VCH, Weinheim, 2004, pp. 325–338.
 17. R. McWeeny, *Methods of molecular quantum mechanics*, 2nd edn., Academic Press, London, 1992.
 18. W. H. E. Schwarz, Fundamentals of relativistic effects in chemistry, in: *The Concept of the Chemical Bond*, Z. B. Masic, ed., Vol. 2, Springer, Berlin, 1990, pp. 559–643.
 19. J. Autschbach, S. Sikierski, P. Schwerdtfeger, M. Seth and W. H. E. Schwarz, *J. Comput. Chem.*, 2002, **23**, 804–813.
 20. B. E. Mann, Rhodium-103, in: *Transition Metal Nuclear Magnetic Resonance*, P. S. Pregosin, ed., Elsevier, Amsterdam, 1991, pp. 177–215.
 21. K. G. Dyall and K. Faegri Jr, *Relativistic Quantum Chemistry*, Oxford University Press, New York, NY, 2007.
 22. R. E. Moss, *Advanced Molecular Quantum Mechanics*, Chapman and Hall, London, 1973.
 23. A. J. Sadlej, Methods of relativistic quantum chemistry, in: *Lecture Notes in Chemistry II*, Vol. 64 of *Lecture Notes in Chemistry*, B. O. Roos, ed., Springer, Berlin, 1994, pp. 203–230.
 24. J. Almlöf and O. Gropen, Relativistic effects in chemistry, in: *Reviews in Computational Chemistry*, K. B. Lipkowitz and D. B. Boyd, eds., Vol. 8, VCH Publishers Inc., New York, 1996, Ch. 4, pp. 203–244.
 25. B. A. Hess, Relativistic theory and applications, in: *Encyclopedia of Computational Chemistry*, P. von Ragué Schleyer, ed., Wiley, Chichester, NY, 1998, pp. 2499–2508.
 26. S. Okada, M. Shinada and O. Matsuoka, *J. Chem. Phys.*, 1990, **93**, 5013–5019.
 27. V. Kellö and A. J. Sadlej, *Int. J. Quantum Chem.*, 1998, **68**, 159–174.
 28. M. Barysz and A. J. Sadlej, *J. Mol. Struct. (THEOCHEM)*, 2001, **573**, 181–200.
 29. M. Barysz and A. J. Sadlej, *J. Chem. Phys.*, 2002, **116**, 2696–2704.
 30. M. Ilias and T. Saue, *J. Chem. Phys.*, 2007, **126**, 064102.
 31. W. Pauli, Die allgemeinen Prinzipien der Wellenmechanik, in: *Handbuch der Physik*, Vol. 5, Springer, Berlin, 1958.
 32. J. D. Morrison and R. E. Moss, *Mol. Phys.*, 1980, **41**, 491–507.
 33. R. E. Moss and H. P. Trivedi, *Mol. Phys.*, 1979, **38**, 1611–1619.
 34. E. van Lenthe, E. J. Baerends and J. G. Snijders, *J. Chem. Phys.*, 1993, **99**, 4597–4610.
 35. C. Chang, M. Pelissier and M. Durand, *Phys. Scr.*, 1986, **34**, 394–404.
 36. P. H. T. Philipsen, E. van Lenthe, J. G. Snijders and E. J. Baerends, *Phys. Rev. B*, 1997, **56**, 13556–13562.
 37. K. Dyall and E. van Lenthe, *J. Chem. Phys.*, 1999, **111**, 1366–1372.
 38. M. Filatov and D. Cremer, *J. Chem. Phys.*, 2004, **120**, 11407–11422.

39. A. Wolf, M. Reiher and B. A. Hess, *J. Chem. Phys.*, 2002, **117**, 9215–9226.
40. I. Malkin, O. L. Malkina and V. G. Malin, *Chem. Phys. Lett.*, 2002, **361**, 231–236.
41. R. Fukuda, M. Hada and H. Nakatsuji, *J. Chem. Phys.*, 2003, **118**, 1015–1026.
42. R. Fukuda, M. Hada and H. Nakatsuji, *J. Chem. Phys.*, 2003, **118**, 1027–1035.
43. J. I. Melo, M. C. Ruiz de Azúa, J. E. Peralta and G. E. Scuseria, *J. Chem. Phys.*, 2005, **123**, 204112.
44. I. Malkin, O. L. Malkina, V. G. Malkin and M. Kaupp, *J. Chem. Phys.*, 2005, **123**, 244103.
45. K. Kudo and H. Fukui, *J. Chem. Phys.*, 2005, **123**, 114102.
46. A. Rutkowski, *J. Phys. B*, 1986, **19**, 149–158.
47. W. Kutzelnigg, *Z. Phys. D*, 1989, **11**, 15–28.
48. W. Kutzelnigg, *J. Comput. Chem.*, 1999, **20**, 1199–1219.
49. A. C. Hennum, W. Klopper and T. Helgaker, *J. Chem. Phys.*, 2001, **115**, 7356–7363.
50. P. Schwerdtfeger, J. R. Brown, J. K. Laerdahl and H. Stoll, *J. Chem. Phys.*, 2000, **113**, 7110–7118.
51. C. G. Van de Walle and P. E. Blöchl, *Phys. Rev. B*, 1993, **47**, 4244–4255.
52. C. J. Pickard and F. Mauri, *Phys. Rev. B*, 2001, **63**, 245101–245113.
53. O. L. Malkina, B. Schimmelpfennig, M. Kaupp, B. A. Hess, P. Chandra, U. Wahlgren and V. G. Malkin, *Chem. Phys. Lett.*, 1998, **296**, 93–104.
54. A. M. Lee, N. C. Handy and S. M. Colwell, *J. Chem. Phys.*, 1995, **103**, 10095–10109.
55. N. F. Ramsey, *Phys. Rev.*, 1950, **78**, 699–703.
56. N. F. Ramsey, *Phys. Rev.*, 1953, **91**, 303–307.
57. R. Bouten, E. J. Baerends, E. van Lenthe, L. Visscher, G. Schreckenbach and T. Ziegler, *J. Chem. Phys.*, 2000, **104**, 5600–5611.
58. S. K. Wolff, T. Ziegler, E. van Lenthe and E. J. Baerends, *J. Chem. Phys.*, 1999, **110**, 7689–7698.
59. J. Autschbach and T. Ziegler, *J. Chem. Phys.*, 2000, **113**, 936–947.
60. J. Autschbach and T. Ziegler, *J. Chem. Phys.*, 2000, **113**, 9410–9418.
61. P. Manninen, P. Lantto and J. Vaara, *J. Chem. Phys.*, 2003, **119**, 2623–2637.
62. J. E. Harriman, *Theoretical Foundations of Electron Spin Resonance*, Academic Press, New York, NY, 1978.
63. G. A. Aucar, T. Saue, L. Visscher and H. J. A. Jensen, *J. Chem. Phys.*, 1999, **110**, 6208–6218.
64. P. Pykkö, *Chem. Phys.*, 1983, **74**, 1–7.
65. W. Kutzelnigg, *Phys. Rev. A*, 2003, **67**, 032109.
66. Y. Xiao, D. Peng and W. Liu, *J. Chem. Phys.*, 2007, **126**, 081101.
67. Y. Xiao, W. Liu, L. Cheng and D. Peng, *J. Chem. Phys.*, 2007, **126**, 214101.
68. S. Komorovsky, M. Repisk, O. L. Malkina, V. G. Malkin and I. M. Ondik and M. Kaupp, *J. Chem. Phys.*, 2008, **128**, 104101.
69. P. Pykkö, *Chem. Phys.*, 1977, **22**, 289–296.
70. P. O. Lipas, P. Pykkö and E. Pajanne, *J. Chem. Phys.*, 1973, **58**, 3248–3254.
71. J. Autschbach, *Theor. Chem. Acc.*, 2004, **112**, 52–57.
72. Y. Ishikawa, T. Nakajima, M. Hada and H. Nakatsuji, *Chem. Phys. Lett.*, 1998, **283**, 119–124.
73. J. Vaara, K. Ruud, O. Vahtras, H. Ågren and J. Jokisaari, *J. Chem. Phys.*, 1998, **109**, 1212–1222.
74. P. Manninen, K. Ruud, P. Lantto and J. Vaara, *J. Chem. Phys.*, 2005, **122**, 114107.
75. J. Kowalewski, *Annu. Rep. NMR Spectrosc.*, 1982, **12**, 81–176.
76. F. London, *J. Phys. Radium*, 1937, **8**, 397–409.
77. R. Ditchfield, *Mol. Phys.*, 1974, **27**, 789–807.
78. W. Kutzelnigg, U. Fleischer and M. Schindler, The IGLO-method: Ab initio calculation and interpretation of NMR chemical shifts and magnetic susceptibilities, in: *NMR Basic Principles and Progress*, P. Diehl, E. Fluck, H. Gunther, R. Kosfeld and J. Seelig, eds., Vol. 23, Springer-Verlag, Heidelberg, Germany, 1990.
79. A. E. Hansen and T. D. Bouman, *J. Chem. Phys.*, 1985, **82**, 5035–5047.
80. T. A. Keith and R. F. W. Bader, *Chem. Phys. Lett.*, 1993, **210**, 223–231.
81. T. B. Pedersen, H. Koch, L. Boman and A. M. J. Sánchez de Merás, *Chem. Phys. Lett.*, 2004, **393**, 319–326.
82. G. Schreckenbach, *Theor. Chem. Acc.*, 2002, **108**, 246–253.
83. M. Krykunov and J. Autschbach, *J. Chem. Phys.*, 2006, **125**, 034102–034110.

84. S. P. A. Sauer and M. J. Packer, The ab initio calculation of molecular properties other than the potential energy surface, in: *Computational Molecular Spectroscopy*, P. R. Bunker and P. Jensen, eds., Wiley, London, 2000, pp. 221–252.
85. B. C. Mort and J. Autschbach, *J. Am. Chem. Soc.*, 2006, **128**, 10060–10072.
86. B. C. Mort and J. Autschbach, *Chem. Phys. Chem.*, 2008, **9**, 159–170.
87. K. Ruud, P. R. Taylor and P.-O. Åstrand, *Chem. Phys. Lett.*, 2001, **337**, 217–223.
88. T. Ruden and K. Ruud, Ro-vibrational corrections to NMR parameters, in: *Calculation of NMR and EPR Parameters*, M. Kaupp, M. Bühl and V. G. Malkin, eds., Wiley-VCH, Weinheim, 2004.
89. H. Cho, W. A. de Jong, B. K. McNamara, B. M. Rapko and I. E. Burgeson, *J. Am. Chem. Soc.*, 2004, **126**, 11583–11588.
90. M. Bühl and M. Parrinello, *Chem. Eur. J.*, 2001, **7**, 4487–4494.
91. K. Spiegel, U. Rothlisberger and P. Carloni, *J. Phys. Chem. B*, 2004, **108**, 2699.
92. M. Sterzel and J. Autschbach, *Inorg. Chem.*, 2006, **45**, 3316–3324.
93. R. F. W. Bader, *Atoms in Molecules. A Quantum Theory*, Oxford University Press, 1990.
94. F. Weinhold, Natural bond orbital methods, in: *Encyclopedia of Computational Chemistry*, P. von Ragué Schleyer, ed., Wiley, Chichester, 1998, pp. 1792–1811.
95. K. Morukuma, *Acc. Chem. Res.*, 1977, **10**, 294–300.
96. T. Ziegler and A. Rauk, *Theor. Chim. Acta*, 1977, **46**, 1–10.
97. G. Frenking and N. Frohlich, *Chem. Rev.*, 2000, **100**, 717–774.
98. J. Autschbach, T. Ziegler, S. J. A. van Gisbergen and E. J. Baerends, *J. Chem. Phys.*, 2002, **116**, 6930–6940.
99. A. Wu, J. Graefenstein and D. Cremer, *J. Phys. Chem. A*, 2003, **107**, 7043–7056.
100. D. Cremer, E. Kraka, A. Wu and W. Lüttke, *Chem. Phys. Chem.*, 2004, **5**, 349–366.
101. J. Gräfenstein, T. Tuttle and D. Cremer, *J. Chem. Phys.*, 2004, **120**, 9952–9968.
102. J. Gräfenstein and D. Cremer, *J. Phys. Chem.*, 2004, **121**, 12217–12232.
103. J. Gräfenstein and D. Cremer, *Magn. Reson. Chem.*, 2004, **42**, S138–S157.
104. S. J. Wilkens, W. M. Westler, J. L. Markley and F. Weinhold, *J. Am. Chem. Soc.*, 2001, **123**, 12026–12036.
105. S. J. Wilkens, W. M. Westler, F. Weinhold and J. L. Markley, *J. Am. Chem. Soc.*, 2002, **124**, 1190–1191.
106. R. H. Contreras, A. L. Esteban, E. Diez, N. J. Head and E. W. Della, *Mol. Phys.*, 2006, **104**, 485–492.
107. J. A. Bohmann, F. Weinhold and T. C. Farrar, *J. Chem. Phys.*, 1997, **104**, 1173–1184.
108. O. L. Malkina and V. G. Malkin, *Angew. Chem. Int. Ed.*, 2003, **42**, 4335–4338.
109. M. Kaupp, A. Patravkov, R. Reviakine and O. L. Malkina, *Chem. Eur. J.*, 2005, **11**, 2773–2782.
110. A. Soncini and P. Lazzeretti, *Chem. Phys. Lett.*, 2005, **409**, 177–186.
111. A. Soncini and P. Lazzeretti, *Chem. Phys. Chem.*, 2006, **7**, 679–684.
112. C. F. Matta, J. Hernandez-Trujillo and R. F. W. Bader, *J. Phys. Chem. A*, 2002, **106**, 7369–7375.
113. J. Autschbach, C. D. Igna and T. Ziegler, *J. Am. Chem. Soc.*, 2003, **125**, 1028–1032.
114. B. Le Guennic, K. Matsumoto and J. Autschbach, *Magn. Res. Chem.*, 2004, **42**, S99–S116.
115. J. Autschbach and B. Le Guennic, *J. Chem. Educ.*, 2007, **84**, 156–171.
116. J. Autschbach, *J. Chem. Phys.*, 2007, **127**, 124106.
117. J. Autschbach, *J. Chem. Phys.*, 2008, **128**, 164111.
118. J. Autschbach and S. Zheng, *Magn. Reson. Chem.*, 2008, s48–s55.
119. U. Edlund, T. Lejon, P. Pykkö, T. K. Venkatachalam and E. Buncel, *J. Am. Chem. Soc.*, 1987, **109**, 5982–5985.
120. J. Autschbach, *J. Chem. Phys.*, 2008, **129**, 094105. Erratum: *J. Chem. Phys.*, 2009, **130**, 209901.
121. T. Enevoldsen, L. Visscher, T. Saue, H. J. A. Jensen and J. Oddershede, *J. Chem. Phys.*, 2000, **112**, 3493–3498.
122. S. Kirpekar and S. P. A. Sauer, *Theor. Chem. Acc.*, 1999, **103**, 146–153.
123. C. Schumann and H. Dreeskamp, *J. Magn. Reson.*, 1970, **3**, 204–217.
124. N. Flitcroft and H. D. Kaesz, *J. Am. Chem. Soc.*, 1963, **85**, 1377–1380.
125. P. Pykkö and L. Wiesenfeld, *Mol. Phys.*, 1981, **43**, 557–580.
126. R. M. Lobayan and G. A. Aucar, *J. Mol. Struct.*, 1998, **452**, 1–11.

127. J. Khandogin and T. Ziegler, *J. Phys. Chem. A*, 2000, **104**, 113–120.
128. R. M. Dickson and T. Ziegler, *J. Phys. Chem.*, 1996, **100**, 5286–5290.
129. J. Khandogin and T. Ziegler, *Spectrochim. Acta A*, 1999, **55**, 607–624.
130. S. K. Wolff and T. Ziegler, *J. Chem. Phys.*, 1998, **109**, 895–905.
131. Y. Nomura, Y. Takeuchi and N. Nakagawa, *Tetrahedron Lett.*, 1969, **8**, 639–642.
132. I. Morishima, K. Endo and T. Yonezawa, *J. Chem. Phys.*, 1973, **59**, 3356–3364.
133. M. I. Volodicheva and T. K. Rebane, *Teoreticheskaya i Eksperimental'naya Khimiya (Engl. ed. Theor. Exp. Chem.)*, 1978, **14**, 348–354.
134. A. A. Cheremisin and P. V. Schastnev, *J. Magn. Reson.*, 1980, **40**, 459–468.
135. P. Pykkö, A. Görling and N. Rösch, *Mol. Phys.*, 1987, **61**, 195–205.
136. M. Kaupp, O. L. Malkina, V. G. Malkin and P. Pykkö, *Chem. Eur. J.*, 1998, **4**, 118–126.
137. A. Bagno and M. Bonchio, *Chem. Phys. Lett.*, 2000, **317**, 123–128.
138. A. Bagno and M. Bonchio, *Eur. J. Inorg. Chem.*, 2002, 1475–1483.
139. W. P. Oziminski, P. Garnuszek, E. Bednarek and J. C. Dobrowolski, *Inorg. Chim. Acta*, 2007, **360**, 1902–1914.
140. J. Vaara, K. Ruud and O. Vahtras, *J. Comput. Chem.*, 1999, **20**, 1314–1327.
141. T. Alam, J. Clawson, F. Bonhomme, S. Thoma, M. Rodriguez, S. Zheng and J. Autschbach, *Chem. Mater.*, 2008, **20**, 2205–2217.
142. B. Le Guennic, S. Patchkovskii and J. Autschbach, *J. Chem. Theor. Comput.*, 2005, **1**, 601–611.
143. N. S. Hush, *J. Am. Chem. Soc.*, 1997, **119**, 1717–1719.
144. D. Gusev, *J. Am. Chem. Soc.*, 2004, **126**, 14249–14257.
145. H. Nakatsuji, H. Takashima and M. Hada, *Chem. Phys. Lett.*, 1995, **233**, 95–101.
146. C. B. Ballard, M. Hada, H. Kaneko and H. Nakatsuji, *Chem. Phys. Lett.*, 1996, **254**, 170–178.
147. V. G. Malkin, O. L. Malkina and D. R. Salahub, *Chem. Phys. Lett.*, 1996, **261**, 335–345.
148. K. Schreckenbach and T. Ziegler, *Int. J. Quantum Chem.*, 1997, **61**, 899–918.
149. T. Baba and H. Fukui, *J. Chem. Phys.*, 1999, **110**, 131–137.
150. L. Visscher, T. Enevoldsen, T. Saue, H. J. A. Jensen and J. Oddershede, *J. Comput. Chem.*, 1999, **20**, 1262–1273.
151. M. Hada, Y. Ishikawa, J. Nakatani and H. Nakatsuji, *Chem. Phys. Lett.*, 1999, **310**, 342–346.
152. J. Vaara, O. L. Malkina, H. Stoll, V. G. Malkin and M. Kaupp, *J. Chem. Phys.*, 2001, **114**, 61–71.
153. H. Fukui and T. Baba, *J. Chem. Phys.*, 2002, **117**, 7836–7844.
154. T. Baba and H. Fukui, *Mol. Phys.*, 2002, **100**, 623–633.
155. H. Fukui, T. Baba, Y. Shiraishi, S. Imanishi, K. Kudo, K. Mori and M. Shimoji, *Mol. Phys.*, 2004, **102**, 641–648.
156. M. Kato, M. Hada, R. Fukuda and H. Nakatsuji, *Chem. Phys. Lett.*, 2005, **408**, 150–156.
157. Y. Ootani, H. Yamaguti, H. Maeda and H. Fukui, *J. Chem. Phys.*, 2006, **125**, 164106.
158. K. Kudo, H. Maeda, T. Kawakubo, Y. Ootani, M. Funaki and H. Fukui, *J. Chem. Phys.*, 2006, **124**, 224106.
159. H. Maeda, Y. Ootani and H. Fukui, *J. Chem. Phys.*, 2007, **126**, 174102.
160. Y. Ootani, H. Maeda and H. Fukui, *J. Chem. Phys.*, 2007, **127**, 084117.
161. V. G. Malkin, O. L. Malkina, L. A. Eriksson and D. R. Salahub, The calculation of NMR and ESR spectroscopy parameters using density functional theory, in: *Modern Density Functional Theory: A Tool for Chemistry*, J. M. Seminario and P. Politzer, eds., Vol. 2, Elsevier, 1995, pp. 273–347.
162. S. S. Gomez, R. H. Romero and G. A. Aucar, *Chem. Phys. Lett.*, 2003, **367**, 265–269.
163. M. C. Ruiz de Azua, J. I. Melo and C. G. Giribet, *Mol. Phys.*, 2003, **101**, 3103–3109.
164. J. I. Melo, M. C. Ruiz de Azua, C. G. Giribet, G. A. Aucar and R. H. Romero, *J. Chem. Phys.*, 2003, **118**, 471–486.
165. J. Autschbach and W. H. E. Schwarz, *Theor. Chem. Acc.*, 2000, **104**, 82–88.
166. H. Fukui, T. Baba and H. Inomata, *J. Chem. Phys.*, 1996, **105**, 3175–3186.
167. H. Fukui, T. Baba and H. Inomata, *J. Chem. Phys.*, 1997, **106**, 2987.
168. P. Manninen, K. Ruud, P. Lantto and J. Vaara, *J. Chem. Phys.*, 2006, **124**, 149901.
169. M. Hanni, P. Lantto, M. Iliáš, H. J. A. Jensen and J. Vaara, *J. Chem. Phys.*, 2007, **127**, 164313.
170. P. Lantto, R. H. Romero, S. S. Gómez and G. A. Aucar, *J. Chem. Phys.*, 2006, **125**, 184113.

171. P. Lantto and J. Vaara, *J. Chem. Phys.*, 2006, **125**, 174315.
172. M. Straka, P. Lantto, M. Räsänen and J. Vaara, *J. Chem. Phys.*, 2007, **127**, 234314.
173. K. Endo, K. Yamamoto and H. Okada, *Bull. Chem. Soc. Jpn.*, 1995, **68**, 3341–3345.
174. H. Nakatsuji, T. Nakajima, M. Hada, H. Takashima and S. Tanaka, *Chem. Phys. Lett.*, 1995, **247**, 418–424.
175. J. Vaara and P. Pyykkö, *J. Chem. Phys.*, 2003, **118**, 2973–2976.
176. M. Kaupp, C. Aubauer, G. Engelhardt, T. M. Klapötke and O. L. Malkina, *J. Chem. Phys.*, 1999, **110**, 3897–3902.
177. A. W. Ehlers, Y. Ruiz-Morales, E. J. Baerends and T. Ziegler, *Inorg. Chem.*, 1997, **36**, 5031–5036.
178. T. M. Gilbert and T. Ziegler, *J. Phys. Chem. A*, 1999, **103**, 7535–7543.
179. H. Nakatsuji, Z.-M. Hu and T. Nakajima, *Chem. Phys. Lett.*, 1997, **275**, 429–436.
180. H. Fukui and T. Baba, *J. Chem. Phys.*, 1998, **108**, 3854–3862.
181. J. David and A. Restrepo, *Phys. Rev. A*, 2007, **76**, 052511.
182. D. Kolb, W. R. Johnson and P. Shorer, *Phys. Rev. A*, 1982, **26**, 19–31.
183. M. Hada, R. Fukuda and H. Nakatsuji, *Chem. Phys. Lett.*, 2000, **321**, 452–458.
184. S. S. Gomez, R. H. Romero and G. A. Aucar, *J. Chem. Phys.*, 2002, **117**, 7942–7946.
185. J. Vaara, K. Ruud and O. Vahtras, *J. Chem. Phys.*, 1999, **111**, 2900–2908.
186. W. H. Flygare, *Chem. Rev.*, 1974, **74**, 653–687.
187. M. Hada, J. Wan, R. Fukuda and H. Nakatsuji, *J. Comput. Chem.*, 2001, **22**, 1502–1508.
188. Y. Ruiz-Morales, G. Schreckenbach and T. Ziegler, *J. Phys. Chem. A*, 1997, **101**, 4121–4127.
189. G. Schreckenbach and T. Ziegler, *Theor. Chem. Acc.*, 1998, **99**, 71–82.
190. C. K. Jameson and A. K. Jameson, *Chem. Phys. Lett.*, 1987, **135**, 254.
191. R. Fukuda and H. Nakatsuji, *J. Chem. Phys.*, 2005, **123**, 044101.
192. J. R. Yates, C. J. Pickard, M. C. Payne and F. Mauri, *J. Chem. Phys.*, 2003, **118**, 5746–5753.
193. A. Bagno and G. Saielli, *Chem. Eur. J.*, 2003, **9**, 1486–1495.
194. D. N. Sears and C. J. Jameson, *J. Chem. Phys.*, 2003, **119**, 12231–12244.
195. J. Autschbach and E. Zurek, *J. Phys. Chem. A*, 2003, **107**, 4967–4972.
196. M. Bühl, *Chem. Phys. Lett.*, 1997, **267**, 251–257.
197. M. Straka, P. Lantto and J. Vaara, *J. Phys. Chem. A*, 2008, **112**, 2658–2668.
198. A. Rodriguez-Fortea, P. Alemany and T. Ziegler, *J. Phys. Chem. A*, 1999, **103**, 8288–8294.
199. O. Dmitrenko, S. Bai, P. A. Beckmann, S. van Bramer, C. Vega and A. J. Dybowski, *J. Phys. Chem. A*, 2008, **112**, 3046–3052.
200. G. G. Briand, A. D. Smith, G. Schatte, A. J. Rossini and R. W. Schurko, *Inorg. Chem.*, 2007, **46**, 8625–8637.
201. M. Hada, H. Kaneko and H. Nakatsuji, *Chem. Phys. Lett.*, 1996, **261**, 7–12.
202. A. Bagno, M. Bonchio, A. Sartorel and G. Scorrano, *ChemPhysChem*, 2003, **4**, 517–519.
203. A. Bagno and G. Saielli, *Theor. Chem. Acc.*, 2007, **117**, 603.
204. M. Kaupp, V. G. Malkin, O. L. Malkina and D. R. Salahub, *J. Am. Chem. Soc.*, 1995, **117**, 1851–1852. Erratum *ibid.*, p. 8492
205. K. J. Ooms and R. E. Wasylishen, *J. Am. Chem. Soc.*, 2004, **126**, 10972–10980.
206. M. Bühl, S. Gaemers and C. J. Elsevier, *Chem. Eur. J.*, 2000, **6**, 3272–3280.
207. A. Bagno and M. Bonchio, *Magn. Reson. Chem.*, 2004, **42**, s79–s87.
208. J. Autschbach and S. Zheng, *Magn. Reson. Chem.*, 2006, **44**, 989–1007.
209. G. Schreckenbach, S. K. Wolff and T. Ziegler, *J. Phys. Chem. A*, 2000, **104**, 8244–8255.
210. G. Schreckenbach, *Inorg. Chem.*, 2002, **41**, 6560–6572.
211. G. Schreckenbach, *Int. J. Quantum Chem.*, 2005, **101**, 372–380.
212. M. Straka, P. Hrobarik and M. Kaupp, *J. Am. Chem. Soc.*, 2005, **127**, 2591–2599.
213. K. J. Ooms, K. W. Feindel, M. J. Willans, R. E. Wasylishen, J. V. Hanna, K. J. Pike and M. E. Smith, *Solid State Nucl. Magn. Reson.*, 2005, **28**, 125–134.
214. M. J. Willans, K. W. Feindel, K. J. Ooms and R. E. Wasylishen, *Chem. Eur. J.*, 2006, **12**, 159–168.
215. G. Proctor and W. F. Yu, *Phys. Rev.*, 1951, **81**, 20–30.
216. A. Zelevsky, *Helv. Chim. Acta*, 1968, **51**, 803.

217. P. S. Pregosin, *Annu. Rep. NMR Spectrosc.*, 1986, **17**, 285–349.
218. B. M. Still, P. G. A. Kumar, J. R. Aldrich-Wright and W. S. Price, *Chem. Soc. Rev.*, 2007, **36**, 665–686.
219. J. Autschbach and B. Le Guennic, *Chem. Eur. J.*, 2004, **10**, 2581–2589.
220. J. Kramer and K. Koch, *Inorg. Chem.*, 2006, **45**, 7843–7855.
221. K. R. Koch, M. R. Burger, J. Kramer and A. N. Westra, *Dalton Trans.*, 2006, 3277–3284.
222. E. Kogut, J. A. Tang, A. J. Lough, C. M. Widdifield, R. W. Schurko and U. Fekl, *Inorg. Chem.*, 2006, **45**, 8850.
223. B. A. Demko and R. E. Wasylishen, *Inorg. Chem.*, 2008, **47**, 2786–2797.
224. M. Bühl and F. T. Mauschick, *Phys. Chem. Chem. Phys.*, 2002, **4**, 5508–5514.
225. M. Bühl, F. T. Mauschick, F. Terstegen and B. Wrackmeyer, *Angew. Chem. Int. Ed.*, 2002, **41**, 2312–2315.
226. M. Bühl, S. Grigoleit, H. Kabrede and F. T. Mauschick, *Chem. Eur. J.*, 2006, **12**, 477–488.
227. J. Jokisaari, S. Järvinen, J. Autschbach and T. Ziegler, *J. Phys. Chem. A*, 2002, **106**, 9313–9318.
228. J. Wan, R. Fukuda, M. Hada and H. Nakatsuji, *J. Phys. Chem. A*, 2001, **105**, 128–133.
229. H. Nakatsuji, M. Hada, H. Kaneko and C. C. Ballard, *Chem. Phys. Lett.*, 1996, **255**, 195–202.
230. J. Autschbach, B. A. Hess, P. A. Johansson, J. Neugebauer, M. Patzschke, P. Pykkö, M. Reiher and D. Sundholm, *Phys. Chem. Chem. Phys.*, 2004, **6**, 11–22.
231. P. Pykkö and N. Runeberg, *Angew. Chem. Int. Ed.*, 2002, **41**, 2174–2176.
232. X. Li, B. Kiran, J. Li, H.-J. Zhai and L.-S. Wang, *Angew. Chem. Int. Ed.*, 2002, **41**, 4786–4789. ‘German version’ Vol. 114, pp. 4980–4983
233. B. Le Guennic, J. Neugebauer, M. Reiher and J. Autschbach, *Chem. Eur. J.*, 2005, **11**, 1677–1686.
234. F. Scherbaum, A. Grohmann, B. Huber, C. Krüger and H. Schmidbaur, *Angew. Chem.*, 1988, **100**, 1602–1604.
235. F. Scherbaum, A. Grohmann, B. Huber, C. Krüger and H. Schmidbaur, *Angew. Chem. Int. Ed.*, 1988, **27**, 1544–1546. (*Angew. Chem.*, 1988, **100**, 1602–1604)
236. H. Schmidbaur, B. Brachthäuser and O. Steigelmann, *Angew. Chem. Int. Ed.*, 1991, **30**, 1488–1490. (*Angew. Chem.*, 1991, **103**, 1552–1553)
237. J. Gracia, J. M. Poblet, J. Autschbach and L. P. Kazansky, *Eur. J. Inorg. Chem.*, 2006, 1139–1148.
238. J. Gracia, J. M. Poblet, J. A. Fernández, J. Autschbach and L. P. Kazansky, *Eur. J. Inorg. Chem.*, 2006, 1149–1154.
239. L. P. Kazansky and T. Yamase, *J. Phys. Chem. A*, 2004, **108**, 6437.
240. A. Bagno, M. Bonchio and J. Autschbach, *Chem. Eur. J.*, 2006, **12**, 8460–8471.
241. A. Bagno and G. Saielli, *Theor. Chem. Acc.*, 2006, 603–619.
242. J. D. Kennedy and W. McFarlane, *J. Chem. Soc. Faraday Trans. 2*, 1976, **72**, 1653.
243. M. A. M. Forgeron, R. E. Wasylishen and G. H. Penner, *J. Phys. Chem. A*, 2004, **108**, 4751–4758.
244. K. Kudo, Y. Ootani, M. Funaki and H. Fukui, *J. Chem. Phys.*, 2006, **124**, 116101.
245. P. Pykkö, E. Pajanne and M. Inokuti, *Int. J. Quantum Chem.*, 1973, **7**, 785–806.
246. D. K. Dalling and H. S. Gutowsky, *J. Chem. Phys.*, 1971, **55**, 4959.
247. G. A. Aucar and R. H. Contreras, *J. Magn. Reson.*, 1991, **93**, 413–418.
248. G. A. Aucar, E. Botek, S. Gómez, E. Sproviero and R. H. Contreras, *J. Organomet. Chem.*, 1996, **524**, 1–7.
249. J. A. González, G. A. Aucar, M. C. Ruiz de Azúa and R. H. Contreras, *Int. J. Quantum Chem.*, 1997, **61**, 823–833.
250. R. M. Lobayan and G. A. Aucar, *J. Mol. Struct.*, 1998, **452**, 13–23.
251. O. L. Malkina, D. R. Salahub and V. G. Malkin, *J. Chem. Phys.*, 1996, **105**, 8793–8800.
252. P. Pykkö, *J. Organomet. Chem.*, 1982, **232**, 21–32.
253. G. A. Aucar and J. Oddershede, *Int. J. Quantum Chem.*, 1993, **47**, 425–435.
254. T. Helgaker, M. Jaszuński and K. Ruud, *Chem. Rev.*, 1999, **99**, 293–352.
255. J. Autschbach and T. Ziegler, *J. Am. Chem. Soc.*, 2001, **123**, 3341–3349.
256. D. L. Bryce and R. E. Wasylishen, *Inorg. Chem.*, 2002, **41**, 3091–3101.

257. M. Gerken, P. Hazendonk, A. Iuga, J. Nieboer, M. Tramsek, E. Goreshnik, B. Zemva, S. Zheng and J. Autschbach, *Inorg. Chem.*, 2007, **46**, 6069–6077.
258. J. Autschbach and T. Ziegler, *J. Chem. Phys.*, 2002, **116**, 891–896.
259. A. A. Klein, T. Schurr, A. Knodler, D. Gudat, K.-W. Klinkhammer, V. K. Jain, S. Zalis and W. Kaim, *Organometallics*, 2005, **24**, 4125.
260. D. Gudat, V. K. Jain, A. Klein, T. Schurr and S. Zalis, *Eur. J. Inorg. Chem.*, 2005, 4056.
261. J. Autschbach and T. Ziegler, *J. Am. Chem. Soc.*, 2001, **123**, 5320–5324.
262. J. Autschbach and B. Le Guennic, *J. Am. Chem. Soc.*, 2003, **125**, 13585–13593.
263. W. Chen, F. Liu, K. Matsumoto, J. Autschbach, B. Le Guennic, T. Ziegler, M. Maliarik and J. Glaser, *Inorg. Chem.*, 2006, **45**, 4526–4536.
264. J. Autschbach, C. D. Igna and T. Ziegler, *J. Am. Chem. Soc.*, 2003, **125**, 4937–4942.
265. J. Autschbach and M. Sterzel, *J. Am. Chem. Soc.*, 2007, **129**, 11093–11099.
266. N. M. Boag, J. Browning, C. Crocker, P. L. Goggin, R. J. Goodfellow, M. Murray and J. L. Spencer, *J. Chem. Res. (M)*, 1978, 2962–2990.
267. N. M. Boag, P. L. Goggin, R. J. Goodfellow and I. R. Herbert, *J. Chem. Soc. Dalton Trans.*, 1983, 1101–1107.
268. Q. Xu, B. T. Heaton, C. Jacob, K. Mogi, Y. Ichihashi, Y. Souma, K. Kanamori and T. Eguchi, *J. Am. Chem. Soc.*, 2000, **122**, 6862–6870.
269. K. E. Berg, J. Glaser, M. C. Read and I. Tóth, *J. Am. Chem. Soc.*, 1995, **117**, 7550–7751.
270. M. Maliarik, K. Berg, J. Glaser, M. Sandström and I. Tóth, *Inorg. Chem.*, 1998, **37**, 2910–2919.
271. A. Klamt and G. Schüürmann, *J. Chem. Soc. Perkin Trans.*, 1993, **2**, 799–805.
272. C. C. Pye and T. Ziegler, *Theor. Chem. Acc.*, 1999, **101**, 396–408.
273. P. R. T. Schipper, O. V. Gritsenko, S. J. A. van Gisbergen and E. J. Baerends, *J. Chem. Phys.*, 2000, **112**, 1344–1352.
274. J. Poater, E. van Lenthe and E. J. Baerends, *J. Chem. Phys.*, 2003, **118**, 8584–8593.
275. B. Le Guennic, W. Hieringer, A. Görling and J. Autschbach, *J. Phys. Chem. A*, 2005, **109**, 4836–4846.
276. R. Malleier, H. Kopacka, W. Schuh, K. Wurst and P. Peringer, *Chem. Commun.*, 2001, 51–52.
277. P. Granger, Groups 11 and 12: copper to mercury, in: *Transition Metal Nuclear Magnetic Resonance*, P. S. Pregosin, ed., Elsevier, Amsterdam, 1991, pp. 264–364.
278. R. J. Gillespie, P. Granger, K. R. Morgan and G. J. Schrobilgen, *Inorg. Chem.*, 1984, **23**, 887–891.
279. R. H. Contreras and J. C. Facelli, *Annu. Rep. NMR Spectrosc.*, 1993, **27**, 255–356.
280. P. Pyykkö, unpublished REX results for Hg_3^{2+} .
281. M. Kaupp, *Untersuchung der Strukturen, Energien und NMR-Eigenschaften von Übergangsmetallverbindungen mit Hilfe quantenchemischer Methoden, habilitationsschrift*, Universität Stuttgart, Germany, 1996.
282. A. Bagno and G. Saielli, *J. Am. Chem. Soc.*, 2007, **129**, 11360–11361.
283. A. Bagno and M. Bonchio, *Angew. Chem. Int. Ed.*, 2005, **44**, 2023–2026.
284. R. Boeckh, G. Graeff and R. Ley, *Z. Phys.*, 1964, **179**, 285–313.
285. J. T. Dickinson, D. A. Stephenson and J. C. Zorn, *J. Chem. Phys.*, 1970, **53**, 1525–1529.
286. R. H. Hammerle, J. T. Dickinson, R. G. VanAusdal, D. A. Stephenson and J. C. Zorn, *J. Chem. Phys.*, 1969, **50**, 2086–2088.
287. D. A. Stephenson, J. T. Dickinson and J. C. Zorn, *J. Chem. Phys.*, 1970, **53**, 1529–1532.
288. D. L. Bryce and R. E. Wasylishen, *J. Am. Chem. Soc.*, 2000, **122**, 3197–3205.
289. D. L. Bryce, R. E. Wasylishen, J. Autschbach and T. Ziegler, *J. Am. Chem. Soc.*, 2002, **124**, 4894–4900.
290. J. Autschbach, A. Kantola and J. Jokisaari, *J. Phys. Chem. A*, 2007, **111**, 5343–5348.
291. R. Wasylishen, Characterization of NMR tensors via experiment and theory, in: *Calculation of NMR and EPR Parameters. Theory and Applications*, M. Kaupp, M. Bühl and V. G. Malkin, eds., Wiley-VCH, Weinheim, 2004, pp. 433–447.
292. P. Pyykkö, *Mol. Phys.*, 2001, **99**, 1617–1629.
293. P. Schwerdtfeger, M. Pernpointner and W. Nazarewicz, Calculation of nuclear quadrupole coupling constants, in: *Calculation of NMR and EPR Parameters: Theory and Applications*, M. Kaupp, M. Bühl and V. G. Malkin, eds., Wiley-VCH, Weinheim, 2004, pp. 279–291.

- 294. R. Mastalerz, G. Barone, R. Lindh and M. Reiher, *J. Chem. Phys.*, 2007, **127**, 074105.
- 295. E. van Lenthe and E. J. Baerends, *J. Chem. Phys.*, 2000, **112**, 8279–8292.
- 296. L. Visscher, T. Enevoldsen, T. Saue and J. Oddershede, *J. Chem. Phys.*, 1998, **109**, 9677–9684.
- 297. F. Neese, A. Wolf, T. Fleig, M. Reiher and B. A. Hess, *J. Chem. Phys.*, 2005, **122**, 204107.
- 298. G. Barone, G. Mastalerz, M. Reiher and R. Lindh, *J. Phys. Chem. A*, 2008, **112**, 1666–1672.
- 299. R. Bast and P. Schwerdtfeger, *J. Chem. Phys.*, 2003, **119**, 5988–5994.
- 300. C. Thierfelder, P. Schwerdtfeger and T. Saue, *Phys. Rev. A*, 2007, **76**, 034502.
- 301. B. Fabricant and J. S. Muentert, *J. Chem. Phys.*, 1977, **66**, 5274.
- 302. H. S. P. Mueller and M. C. L. Gerry, *J. Chem. Phys.*, 1995, **103**, 577.

CHAPTER 2

Applications of Silicon–Carbon Coupling Constants

Vratislav Blechta

Contents		
	1. Experimental Methods	98
	1.1 Sensitivity of ^{13}C and ^{29}Si NMR spectra	98
	1.2 Measurement of magnitudes of ^{29}Si – ^{13}C couplings	100
	1.3 ^{29}Si – ^{13}C couplings with signs	105
	2. Couplings — Results	111
	2.1 General theory	112
	2.2 $^1J(^{29}\text{Si}, ^{13}\text{C})$ couplings	113
	2.3 $J(^{29}\text{Si}, ^{13}\text{C})$ couplings over two and more bonds	131
	Acknowledgments	136
	References	136
	Appendices	141
	Appendix A	142
	Appendix B1	175
	Appendix B2	192
	Appendix B3	203
	Appendix B4	228
	Appendix C	230
	Appendix D	248

Abstract

Experimental methods used for detection of silicon–carbon coupling constants are summarized with an emphasis on multiple-bond couplings. Values of silicon–carbon coupling constants are related to electronic structure parameters such as electronegativity of substituents, *s*-character of silicon–carbon bond, *s*-electron densities and others. Extensive tables of silicon–carbon coupling constants are given in appendices.

Keywords: silicon–carbon coupling constants; silicon–carbon coupling constant sign; ^{29}Si NMR; ^{13}C NMR; s-character of bond; electronegativity of substituent; s-electron densities

1. EXPERIMENTAL METHODS

The measurement of relatively large one-bond silicon–carbon coupling constants usually does not pose problems. Contrary to that, the measurement of small silicon–carbon multiple-bond coupling constants similarly as detection of sign of any coupling constant needs special NMR techniques. This chapter is devoted mainly to a description of these techniques. A design of an experiment for detection of coupling constants is generally highly specific, depending on a coupling network and abundances of isotopes in a play. For this reason, from a huge number of existing experiments, only those dealing with ^{29}Si – ^{13}C spin–spin interactions were considered here. A great number of the experiments described in this section can be found in a review.¹

1.1 Sensitivity of ^{13}C and ^{29}Si NMR spectra

In this section, a brief description of NMR properties of ^{13}C and ^{29}Si nuclei and basic NMR methods for detection of their NMR spectra are quoted. A comprehensive description of NMR properties of both the nuclei can be found in the book,² particularly for ^{13}C NMR in Levy and Nelson³ and for ^{29}Si NMR in Brevard and Granger.⁴

A natural abundance of ^{29}Si isotope is 4.7% contrary to 1.1% of natural abundance of ^{13}C isotope. Due to slightly higher magnetogyric ratio of ^{13}C , the relative receptivity of silicon with respect to carbon is 2.09.² Another factor influencing an NMR signal intensity in a basic one-pulse experiment with proton decoupling is a longitudinal relaxation time T_1 (longer T_1 needs longer relaxation delay and the experiment lasts longer time) and a value of Nuclear Overhauser Effect (NOE). Brevard and Granger⁴ state that typical $T_1(^{29}\text{Si})$ values are in a range 5–150 s; similar span can be seen in ref. 5 with exception of silicates with relaxation even below 1 s. Similarly $T_1(^{13}\text{C})$ values lie in a range 1–100 s according to Harris and Mann² or Levy and Nelson.³ On the other hand, it seems that in most practical cases $T_1(^{29}\text{Si})$ values are usually in a range tenths of seconds and ^{13}C longitudinal relaxation times are frequently one order shorter. It results in a fact that ^{13}C one-pulse experiments are routinely carried with recycle delays of a few seconds while ^{29}Si one-pulse experiments need recycle delays usually one order longer. The NOE contribution to an NMR signal intensity of nucleus X under decoupling of protons H lies in a range from zero to $\gamma_{\text{H}}/(2\gamma_{\text{X}})$; consequently, overall signal intensity falls within an interval from 1 to $(1+\gamma_{\text{H}}/(2\gamma_{\text{X}}))$. Therefore, for $\text{X} = ^{13}\text{C}$ both magnetogyric ratios are positive and NOE contribution enlarges the signal intensity up to a triple while for $\text{X} = ^{29}\text{Si}$ the

magnetogyric ratio γ_{Si} is negative and NOE contribution subtracts from the basic signal intensity. This could result in diminishing or even cancelation of the ^{29}Si NMR signal. One-pulse ^{29}Si experiments are for this reason carried out without NOE effect (gated decoupling–decoupling is off during a recycle delay) and due to a long recycle delays are usually much less sensitive than ^{13}C one-pulse experiments with NOE.

The situation dramatically changes when some polarization transfer experiments (e.g. INEPT^{6–9} and DEPT¹⁰) are considered. For these experiments, the signal intensity is dependent on a number of protons coupled to a nucleus X and certainly on optimization of delays or flip angles in the above-cited sequences. A maximal signal intensity A_{max} transferred from N protons coupled by the same coupling constant to the nucleus X is shown in Table 1.¹¹

Polarization transfer experiments on silicon compounds (one of the first was by Schraml¹²) usually utilize $^2J(^{29}\text{Si}-\text{C}-^1\text{H})$ or $^3J(^{29}\text{Si}-\text{C}-\text{C}-^1\text{H})$ coupling constants with magnitudes in a range 4–13 Hz.⁵ The most frequently appearing and used protons are from methyls bonded to the silicon with fairly uniform values of silicon–hydrogen couplings 7 ± 1 Hz. The number N of such coupled protons is usually higher, typically one, two or three CH_3 groups offering N equal to 3, 6 or 9. Taking into consideration such numbers of attached protons and the value of $\gamma_{\text{H}}/\gamma_{\text{X}}$ equal to roughly 5, the signal enhancement of silicon signal in such an experiment is between 5.8 and 9.4 (see Table 1). The necessary recycle delays are no more governed by the long $T_1(^{29}\text{Si})$ but by much shorter proton longitudinal relaxation times. With this fact and with the relative receptivity of silicon to carbon 2.09 (see above), it can be concluded that INEPT or DEPT experiments on ^{29}Si could give about 12–20 times more intensive signal than that given by a one-pulse experiment without NOE on ^{13}C or 4–20 times more intensive signal than that given by a common ^{13}C one-pulse experiment with NOE (value 20 is for negligible ^{13}C NOE). A disadvantage of longer ^{29}Si T_1 relaxation times changes to a benefit when using these polarization transfer experiments. Compounds with longer T_1 relaxation times usually have longer T_2 relaxation times too and consequently narrower and stronger spectral lines. Really, ^{13}C NMR lines are usually much broader than ^{29}Si lines. If enough long acquisition time is used and a sample is properly shimmed, the ^{29}Si lines could be usually easily narrowed to about 0.1 Hz. If it is supposed that silicon lines are on an average about 5 times narrower than carbon lines, we can expect for ^{29}Si experiment with polarization

Table 1 Values of maximum enhancement A_{max} dependent on number of coupled protons N

	N											
	1	2	3	4	5	6	7	8	9	12	15	
A_{\max}^{a}	1.00	1.00	1.16	1.30	1.43	1.55	1.67	1.77	1.87	2.15	2.39	
$A_{\max(\text{Si})}^{\text{b}}$	5.00	5.00	5.77	6.50	7.16	7.76	8.33	8.86	9.36	10.73	11.15	

^aIn units $(\gamma_{\text{H}}/\gamma_{\text{X}})$.

^bAbsolute enhancement for ^{29}Si ($A_{\text{max}}(\text{Si}) = (\gamma_{\text{H}}/\gamma_{\text{Si}})A_{\text{max}} = 5.00A_{\text{max}}$).

transfer about 60–100 times or 20–100 times higher sensitivity than for one-pulse ^{13}C experiment without or with NOE enhancement, respectively.

1.2 Measurement of magnitudes of ^{29}Si – ^{13}C couplings

Absolute values of almost all published one-bond silicon–carbon coupling constants and even a part of multiple-bond silicon–carbon coupling constants are taken from normal NMR spectra from either ^{29}Si satellites in ^{13}C NMR spectra or ^{13}C satellites in ^{29}Si NMR spectra. Example of ^{13}C satellites in ^{29}Si NMR spectrum is shown in Figure 1.

The ability of basic NMR spectra to offer small values of coupling constants can be increased when using a method called “ultrahigh resolution NMR”.^{13–16}

The method does only one thing — it eliminates instrumental sources of a line broadening to narrow lines as possible. By narrowing the lines, the satellites should be less obscured by a signal of much stronger, partially non-magnetic ($^{28,30}\text{Si}^{13}\text{C}$ or $^{12}\text{C}^{29}\text{Si}$) isotopomers with zero silicon–carbon coupling. The method is based on a recognition that the resolution performance of usual commercial spectrometer is much better than the resolution normally achieved in spectra. A real limiting factor is a temperature gradient in a sample tube in concert with temperature dependence of chemical shifts. By eliminating the temperature gradients,^{13,16} much better line resolution (and signal-to-noise value) can be gained at least for naturally narrow NMR lines. The ^{29}Si NMR lines seem be particularly suitable because of their frequently low natural line width. The method was applied^{17–19} among others for detection of $^{2,3,5}J(^{29}\text{Si}, ^{13}\text{C})$, some of them with magnitudes below 1 Hz.

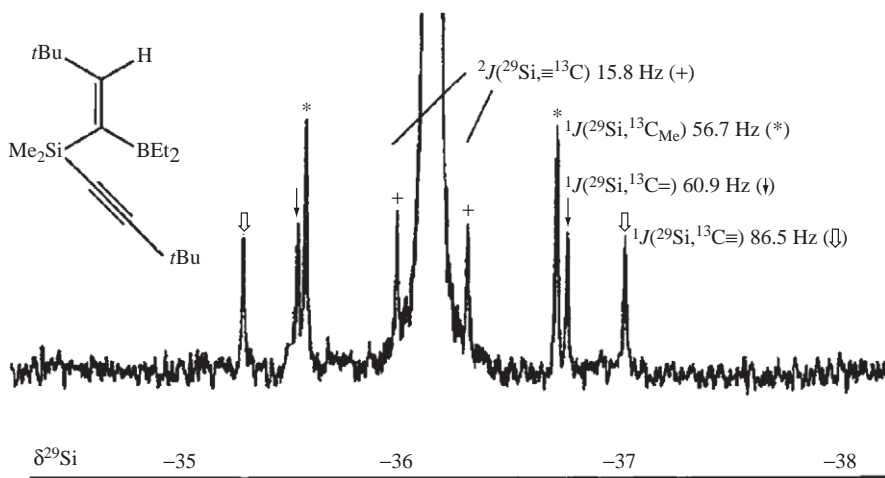


Figure 1 Example of ^{13}C satellites by $^1J(\text{Si}, \text{C})$ and $^2J(\text{Si}, \text{C})$ couplings around a parent silicon line in ^{29}Si NMR spectrum. Reproduced from ref. 105 with permission from Wiley & Sons Limited.

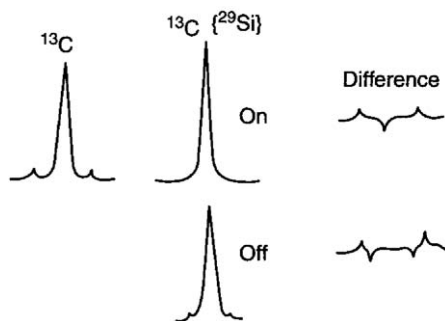


Figure 2 Scheme of resultant ^{13}C spectrum formation from two mutually subtracted spectra with different decoupling frequencies. Reproduced from ref. 20 with permission of the Institute of Organic Chemistry and Biochemistry, Academy of Sciences of the Czech Republic.

Another way to see low-abundant nuclei satellites by small couplings buried below a base of high central lines is to suppress the central line. From a huge number of existing methods for such suppression, only few were applied to multiple-bond silicon–carbon couplings. A very simple one²⁰ uses selective decoupling of silicon while observing carbon signal under a broadband proton decoupling. The method is illustrated in Figure 2. In one experiment, the silicon is irradiated during acquisition in a very nearby position (or on resonance) by a selective decoupling and in the second experiment the silicon decoupler is at a large frequency distance. Two spectra arise with a satellite separations differently scaled. The central peaks not connected to the irradiated isotopomer are not influenced. By subtracting the two spectra, the central peaks are completely canceled while non-equally scaled satellites are retained. The experiment was originally published as a correlation experiment but if in the second decoupling far away from the silicon position the decoupler is simply switched off, the satellites originating from this transient have sought natural distance. A disadvantage is $\sqrt{2}$ times lower signal-to-noise ratio because only half of the transients contribute to the signal of satellites. An experiment designed not only for silicon–carbon correlation but also directly for silicon–carbon satellites filtration is selective heteronuclear INADEQUATE²¹; see Figure 3a. The experiment is a copy of standard carbon–carbon INADEQUATE^{22,23} experiment where all pulses are applied simultaneously to both ^{29}Si and ^{13}C nuclei. The phase cycling is different. As in a standard INADEQUATE experiment, only satellite signals (^{29}Si satellites in detected ^{13}C spectrum for this case) pass through the sequence, the central lines being canceled by phase cycling. The experiment was proposed as one-dimensional with selective silicon pulses acting on one of the silicon lines only, so only satellites by the irradiated silicon line are present in the spectrum. Two compounds, 2,3,4-*O*-tris(trimethylsilyl)-1,6-anhydro- β -D-glukopyranoside and methyl 2,3,4-*O*-tris(trimethylsilyl)-1,6-anhydro- β -D-glukopyranoside, were studied and $^2J(^{29}\text{Si}-^{13}\text{C})$ and $^3J(^{29}\text{Si}-^{13}\text{C})$ couplings were found. It appears that the experiment can be simplified to a more clear ^{29}Si -filtered ^{13}C experiment; see Figure 3b. This is probably the first experiment where the silicon filter was used to reveal small (~ 2 Hz) couplings.

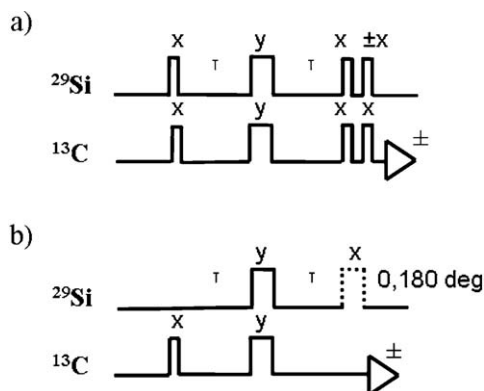


Figure 3 (a) Scheme of pulse sequence heteronuclear INADEQUATE. (b) Simplified functional scheme. Delay τ is set to a value $1/(4 \times J(\text{Si}, \text{C}))$; proton decoupling is on during whole sequence.

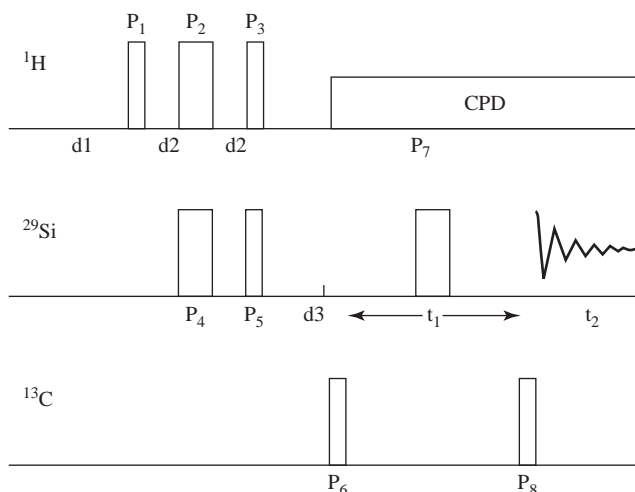


Figure 4 INEPT-HMQC correlation experiment by Berger for ^{13}C - ^{29}Si correlation. Reproduced from ref. 26 with permission from Elsevier Science.

Instead of 1D correlations discussed above for central line suppression, two-dimensional X-Y correlations (HETCOR, HMQC and HSQC pulse sequences, X and Y being general nuclei) as are reviewed^{1,24,25} could be principally used. It appears that no such correlation was tested on silicon-carbon pair of nuclei. More efforts were devoted to much sensitive sequences with polarization transfers from proton, which will be discussed in the next paragraphs.

The INEPT-HMQC correlation²⁶ (see Figure 4) was tested on a polymer silicon oil. As discussed above, the polarization transfer from protons to silicon, which is in the initial part of the sequence (delay $2 \times d_2 = 1/(2 \times J(^{29}\text{Si}, ^1\text{H}))$, polarization part of INEPT), usually substantially increases the signal intensity.

A normal HMQC²⁷ follows after P3–P5 pair of pulses with delay d_3 serving for both ^{29}Si – ^1H INEPT refocusing and ^{29}Si – ^{13}C polarization transfer due to $^1J(^{29}\text{Si}, ^{13}\text{C})$ in an initial part of HMQC. The d_3 delay must be optimized. As a result, the experiment shows ^{29}Si – ^{13}C chemical shift correlation with $^1J(^{29}\text{Si}, ^{13}\text{C})$ coupling constants along F_2 dimension. It should be said that one-bond silicon–carbon couplings could be easily detected from normal 1D spectra. Generally much valuable is detection of small multiple-bond silicon–carbon couplings. For the multiple-bond couplings, the maximum polarization transfer may not be achievable by optimization of the d_3 delay in this sequence, so lower signal-to-noise ratio can result. A high suppression of central lines is necessary for measurement of small couplings because they can be easily obscured by residua of the central lines and it is the question whether it is achievable without a gradient filtration.

Other sequences, INEPT-(Si, C)gCOSY and INEPT-(Si, C, Si)gHMQC, were proposed²⁸ especially for long-range silicon–carbon coupling studies; see Figure 5a and b. Gradient pulses are used for a good suppression of signals of unfavorable isotopomers (making a signal of central lines) but at the expense of a sensitivity being lowered to 1/2 of that in an experiment without gradient selection. INEPT-(Si, C)gCOSY (the label (Si, C) means that there is $^{29}\text{Si} \rightarrow ^{13}\text{C}$ polarization transfer) is a simple concatenation of $^1\text{H} \rightarrow ^{29}\text{Si}$ INEPT polarization

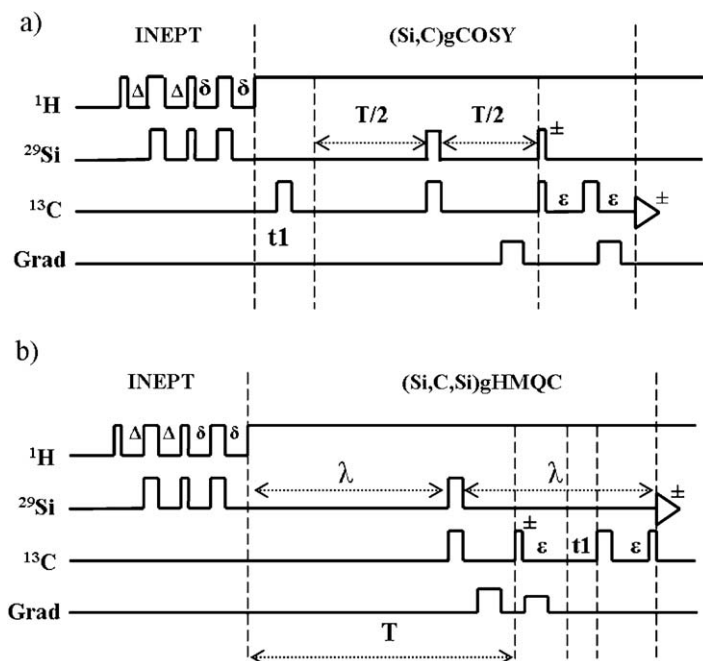


Figure 5 (a) INEPT-(Si, C)gCOSY and (b) INEPT-(Si, C, Si)gHMQC pulse sequences for measurement of ^{13}C – ^{29}Si (mainly multiple-bond) coupling constants and correlations. For a detailed description of sequences, see original paper. Reproduced from ref. 28 with permission from Wiley & Sons Limited.

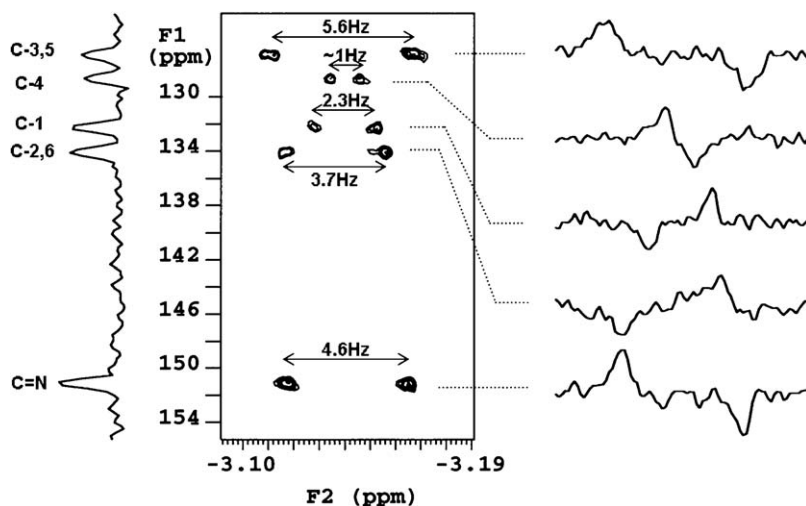


Figure 6 Example of INEPT-(Si, C, Si)gHMQC spectra on a solution of (*Z*)-*tert*-butyldiphenylsilyl *N-tert*-butyldiphenylsiloxybenzoimidate (CC(C)(C)C1=CC=C(C=C1)OSi(C)(C)C2=CC=CC=C2N(C1=CC=CC=C1)OSi(C)(C)C3=CC=CC=C3). Only correlations of siloxy group bonded to carbon of C=N fragment are shown; only aromatic region in F_1 (^{13}C) dimension was measured. Assignment of carbons C2–C6 refers to phenyls on silicon, C1 carbon is the C_{ipso} of benzohydroxamic acid. Reproduced from ref. 28 with permission from Wiley & Sons Limited.

transfer with a phase-sensitive gradient heteronuclear $^{29}\text{Si} \rightarrow ^{13}\text{C}$ COSY without a refocusing period. Only cross-peaks of isotopomers with a pair of ^{29}Si and ^{13}C isotopes coupled by some $^nJ(^{29}\text{Si}, ^{13}\text{C})$ are shown in a 2D plane, ^{29}Si chemical shifts being scattered along F_1 axis and ^{13}C signals split to antiphase doublets by $^nJ(^{29}\text{Si}, ^{13}\text{C})$ are along F_2 axis.

Similarly INEPT-(Si, C, Si)gHMQC²⁸ (the label (Si, C, Si) means that there is $^{29}\text{Si} \rightarrow ^{13}\text{C}$, $^{29}\text{Si} \rightarrow ^{29}\text{Si}$ polarization transfer) is a concatenation of $^1\text{H} \rightarrow ^{29}\text{Si}$ INEPT with gradient (Si, C, Si)gHMQC. The (Si, C, Si)gHMQC part is designed particularly for fully phase-sensitive detection of small $^nJ(^{29}\text{Si}, ^{13}\text{C}) \leq 2\text{--}3\text{ Hz}$. The detailed explanation of the sequence is in the original paper. Example of a spectrum is shown in Figure 6. Contrary to the previous sequence, ^{13}C chemical shifts are along F_1 dimension and ^{29}Si ones along F_2 dimension, $^nJ(^{29}\text{Si}, ^{13}\text{C})$ antiphase doublet splitting being along F_2 dimension.

Both these sequences suffer from a signal intensity loss due to the gradient pulses during proton decoupling. Gradient pulses typically last 1 ms and during these pulses most of the sample is not in the region where the proton decoupling is efficient. The heteronuclear proton–carbon or proton–silicon evolution by one-bond heteronuclear couplings takes place during these millisecond pulses which results in a signal loss. Both these sequences were redesigned to improve them and were successfully tested.²⁹ INEPT-(Si, C)gCOSY was simply substituted by non-gradient INEPT-(Si, C)COSY (Figure 7a) which is a concatenation of known experiments. A perfect gradient suppression of a central carbon peak by $^{28,30}\text{Si}$

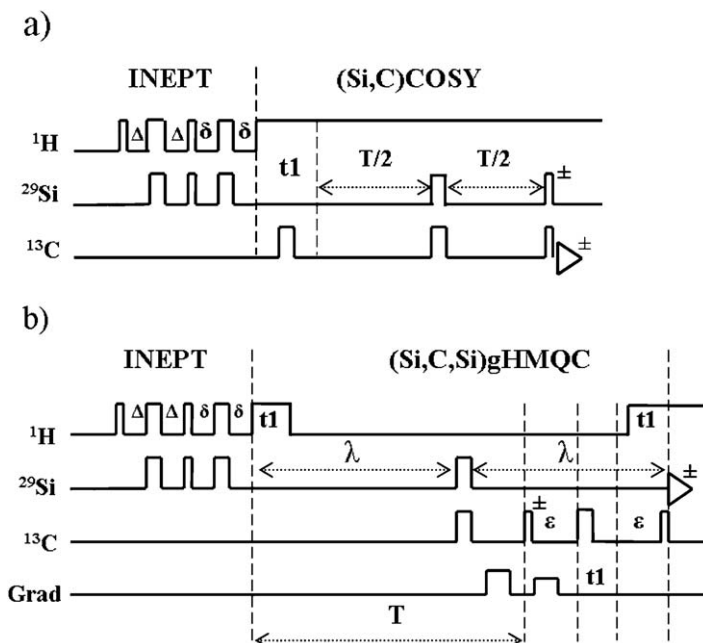


Figure 7 (a) INEPT-(Si, C)COSY and (b) new version of INEPT-(Si, C, Si)gHMQC. Reproduced from ref. 29 with permission from Wiley & Sons Limited.

isotopes is not in this case necessary because the signal by ^{29}Si isotope satellites not only has natural integral intensity 4.7% but also is almost 10 times increased by proton–silicon polarization transfer (for $\text{Si}(\text{CH}_3)_3$ groups, see Table 1). So the integral intensity of such ^{29}Si satellites in a carbon spectrum can achieve about 44% of an integral intensity of the central carbon peak by $^{28,30}\text{Si}$ isotopes and the latter is easily suppressed enough by a phase cycling. A new version of INEPT-(Si, C, Si)gHMQC (Figure 7b) has only moderately modified the proton decoupling during the gHMQC part and t_1 evolution delay is shifted after last refocusing ^{13}C pulse. Due to selected positions and lengths of the decoupling delays during the gHMQC part, the sequence behaves as the original one but the decoupling is off during the gradient pulses, so no attenuation described above takes place. Symbols in the schemes in Figure 7a and b for both sequences have the same meaning as for the original pulse sequences in Figure 5.

1.3 ^{29}Si – ^{13}C couplings with signs

For later purposes, the reduced coupling constant $K(X, Y)$ is defined² by a relation

$$J(X, Y) = \frac{h \times \gamma_X \times \gamma_Y \times K(X, Y)}{4 \times \pi^2} \quad (1)$$

NMR cannot identify absolute signs of coupling constants. Only relative signs of two coupling constants could be measured. For such experiment, at least three different atoms (positions) in the molecule are necessary; let us call them

X, Y and Z. At least two couplings between these atoms must be of non-zero value and a result of the experiment is a finding whether both couplings have equal or different sign and also detection of magnitudes of both couplings. In our case of $J(^{29}\text{Si}, ^{13}\text{C})$ couplings, the third atom in the coupling triad must be one of the natural abundant nucleus such as ^1H , ^{19}F or ^{31}P , else we run into a severe problem with sensitivity when trying to detect isotopomers with three low-abundant nuclei (e.g. for a ^{29}Si – ^{13}C – ^{13}C isotopomer, the natural abundance would be about 5×10^{-6}).

1.3.1 One-dimensional experiments

Older experiments (spin tickling,³⁰ spin decoupling and selective polarization transfer (SPT or SPI)^{31–33}) for relative coupling sign estimation will be briefly described in this chapter. These experiments were originally used for assignment purposes or polarization transfer enhancement and are only scarcely used nowadays but may be of some use for solution of simple problems. The spin tickling and selective decoupling experiment differ only in the intensity of decoupling field applied; the spin tickling field has “intensity” usually few hertz while the selective spin decoupling should be enough intense to collapse an observed multiplet into a single line. These experiments can be frequently found under a term “perturbation” or “double resonance” and some of them are connected with measurement of $J(^{29}\text{Si}, ^{13}\text{C})$ coupling constants.^{34–39} SPT or SPI experiment applied to a pair of mutually coupled nuclei X and Y selectively inverts one line of the first (X) nucleus multiplet causing no equilibrium change in populations of both nuclei. Then hard excitation pulse is applied on Y nucleus and a signal is detected. The overall result is a polarization transfer from X nucleus to Y nucleus. For a detailed description of these experiments, see the papers quoted above.

In the next, an application of these experiments for relative coupling constant sign elucidation is described. Let us consider a hypothetical molecular fragment Si–C–H for illustration purposes with close to reality coupling constant $^1J(^{29}\text{Si}, ^{13}\text{C}) = -50 \text{ Hz}$, $^1J(^{13}\text{C}, ^1\text{H}) = +120 \text{ Hz}$ and $^2J(^{29}\text{Si}, ^1\text{H}) = +7 \text{ Hz}$ (note that the signs of the couplings are supposed). Homonuclear proton–proton couplings are not considered here. A rough drawing of ^{29}Si and ^1H NMR multiplets for ^{29}Si – ^{13}C – ^1H isotopomer is presented in Figure 8a. Let us suppose that we irradiate a lower-frequency ^1H doublet in the ^{29}Si spectrum (e.g. lines 3 and 4) by a selective decoupling (i.e. lines 1 and 2 are not influenced — they are off resonance) and that we simultaneously observe ^1H NMR spectrum (see Figure 8b). The lines 3 and 4 in the silicon spectrum and lines d and e in the proton spectrum belong to the carbon spin state $m_z(\text{C}) = -1/2$. So the proton lines c and d will collapse to a singlet by the silicon-selective decoupling of lines 3 and 4. The lines 1 and 2 in the silicon spectrum and the lines a and b in the proton spectrum belong to the carbon spin state $m_z(\text{C}) = +1/2$. The lines 1 and 2 are not affected by the selective silicon decoupling; consequently, lines a and b in proton spectrum are left intact. Similarly selective decoupling of high-frequency proton doublet in silicon spectrum would cause collapse of high-frequency silicon doublet in proton spectrum. According to Harris and Mann,² it means that reduced couplings

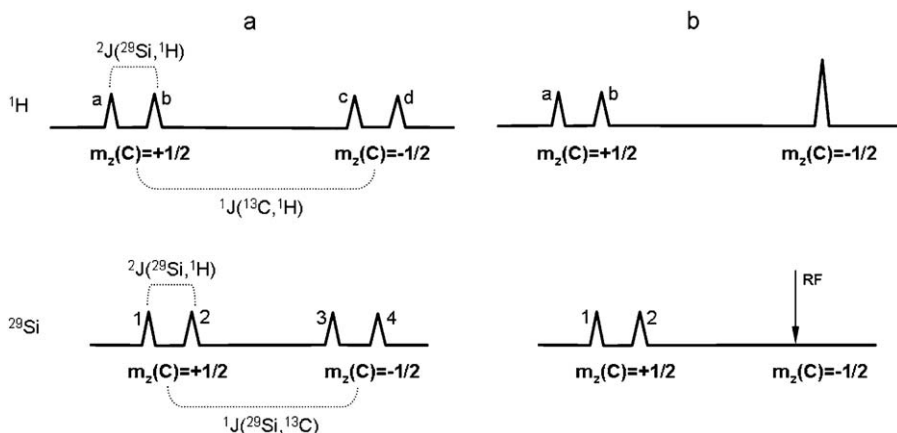


Figure 8 (a and b) Illustration of spin tickling or selective spin decoupling experiments for detection of relative signs of coupling constants $J(\text{Si}, \text{C})$ and $J(\text{C}, \text{H})$.

(for a definition, see Equation (1)) $K({}^{13}\text{C}, {}^1\text{H})$ and $K({}^{29}\text{Si}, {}^{13}\text{C})$ have identical sign. Accounting for different signs of magnetogyric ratios γ_{H} and γ_{Si} , the couplings $J({}^{13}\text{C}, {}^1\text{H})$ and $J({}^{29}\text{Si}, {}^{13}\text{C})$ (see Equation (1)) should have different sign.

Explanation of the rule above published by Harris is not so easy because of generally different signs of magnetogyric ratios of nuclei involved and because only absolute values of resonance frequencies are observed in NMR. The topic can be clarified in, e.g., the case of ${}^{29}\text{Si}$ – ${}^{13}\text{C}$ – ${}^1\text{H}$ isotopomer. The carbon satellite positions $\nu_{\text{H}}(m_z(\text{C}))$ and $\nu_{\text{Si}}(m_z(\text{C}))$ in ${}^1\text{H}$ and ${}^{29}\text{Si}$ spectra can be expressed by Equations (2a) and (2b) (mutual silicon–proton coupling not considered here):

$$\nu_{\text{H}}(m_z(\text{C})) = |\gamma_{\text{H}}[B_0(1 + \sigma_{\text{H}}) + m_z(\text{C})\gamma_{\text{C}}K({}^{13}\text{C}, {}^1\text{H})]| \quad (2a)$$

$$\nu_{\text{Si}}(m_z(\text{C})) = |\gamma_{\text{Si}}[B_0(1 + \sigma_{\text{Si}}) + m_z(\text{C})\gamma_{\text{C}}K({}^{29}\text{Si}, {}^{13}\text{C})]| \quad (2b)$$

here B_0 is a static magnetic field ($B_0 > 0$ by definition) and σ_{H} and σ_{Si} the individual chemical shifts of hydrogen and silicon. The first terms in Equations (2a) and (2b) are resonance frequencies of uncoupled nuclei in the B_0 static field while the second terms represent coupling splitting. It is seen from Equations (2a) and (2b) that when both reduced coupling constants K have the same sign, then the carbon magnetic quantum number $m_z(\text{C})$ shifts the resonance frequency for both silicon and proton in the same direction with respect to the products $B_0(1 + \sigma_{\text{H/Si}})$ (increases or decreases it). When the reduced coupling constants are of different signs, then the satellite by $m_z(\text{C}) = +1/2$ is at higher frequency for one nucleus and at lower frequency for the other nucleus.

If Si–C–H_n fragment is considered in the selective experiments, the solution is similar as for Si–C–H fragment. Instead of doublet by silicon–proton coupling, there will be a multiplet in ${}^{29}\text{Si}$ spectrum with larger number of lines spread over a broader region. Stronger selective decoupling can solve this change. Homonuclear proton–proton couplings add some splittings to the proton spectrum but the experiment should be still efficient.

The above example of selective decoupling can be directly extended to the other selective methods (SPI or SPT) from this chapter.

The basic problem of these experiments when aimed at measuring small couplings is the impossibility to suppress much stronger signals of highly abundant isotopomers ($^{28,30}\text{Si}-^{13}\text{C}-^1\text{H}$, $^{29}\text{Si}-^{12}\text{C}-^1\text{H}$ and $^{28,30}\text{Si}-^{12}\text{C}-^1\text{H}$; not shown in Figure 8) which can completely bury small and closely spaced satellites of $^{29}\text{Si}-^{13}\text{C}-^1\text{H}$ isotopomer. The more abundant isotopomers can be efficiently suppressed in 2D experiment described in a following chapter.

1.3.2 Two-dimensional experiments

By far the most important principle for elucidation of relative signs and values of coupling constants was probably shown first by Bax and Freeman.⁴⁰ They noted that when two-dimensional correlation between two nuclei X and Y is performed, a third nucleus Z coupled to both X and Y nuclei and not influenced by the pulses of the sequence sets up what is now called E-COSY pattern suitable for comparison of signs of $K(X, Z)$ and $K(Y, Z)$ reduced couplings (see Equation (1)) and consequently signs of both coupling constants. The Z nucleus is called “passive nucleus”. An example of E-COSY cross-peak is in Figure 9. The E-COSY pattern has either a positive tilt (cross-peak positions are $(\omega_X + 1/2 \times J(X, Z), \omega_Y + 1/2 \times J(Y, Z))$ and $(\omega_X - 1/2 \times J(X, Z), \omega_Y - 1/2 \times J(Y, Z))$ in 2D plane) or a negative tilt (cross-peak positions are $(\omega_X - 1/2 \times J(X, Z), \omega_Y + 1/2 \times J(Y, Z))$ and $(\omega_X + 1/2 \times J(X, Z), \omega_Y - 1/2 \times J(Y, Z))$ in 2D plane). According to the rule from Harris and Mann² or Equations (2a) and (2b), if the peaks tilt to the right the reduced couplings $K(X, Z)$ and $K(Y, Z)$ have the same sign. If the peaks tilt to the left, the reduced couplings have opposite signs. In general, almost any two-dimensional correlation (e.g. HETCOR, HMQC, HSQC and HMBC; see, e.g. Ernst et al.⁴¹) could be used for X and Y nuclei under assumption that the nucleus Z remains passive during the whole duration (or its important part) of the experiment. In practice, a large number of usually $^{13}\text{C}-^1\text{H}$ HETCOR experiments (^1H excitation and ^{13}C detection) were carried in a group of Wrackmeyer^{42–44} to detect signs and values of silicon–carbon coupling constants and many others.

If the passive nucleus Z has a naturally abundant isotope Z^0 with a zero nuclear spin number (as are NMR inactive isotopes $^{28,30}\text{Si}$ and ^{12}C , natural abundances about 95% and 99%, respectively), the intense cross-peak by the Z^0 isotope (central peak) could either cause problems with a dynamic range of a receiver or even can bury the E-COSY pattern. To solve this effect, the indirect detection experiments with simultaneous suppression of a signal due to isotopomers with magnetically inactive Z^0 isotope were proposed and tested by Kupče et al.^{45–47} In Ψ -BIRD-HMQC and Ψ -BIRD-HSQC^{45,46} (see Figure 10), a central peak corresponding to isotopomer containing Z^0 isotope is selectively inverted by the first two proton pulses spaced by delay τ (initial Ψ -BIRD part of the sequences) while satellites by magnetically active Z isotope remain not inverted. The Z^0 isotope center band is then left to relax during delay T to zero. Then ^1H –Y indirect experiments starts. The result is a usual ^1H –Y heterocorrelation spectrum with passive Z isotope satellites making E-COSY pattern and with the central line due to the Z^0 isotope diminished. In the case of small silicon–carbon coupling constants, there is usually a correlation

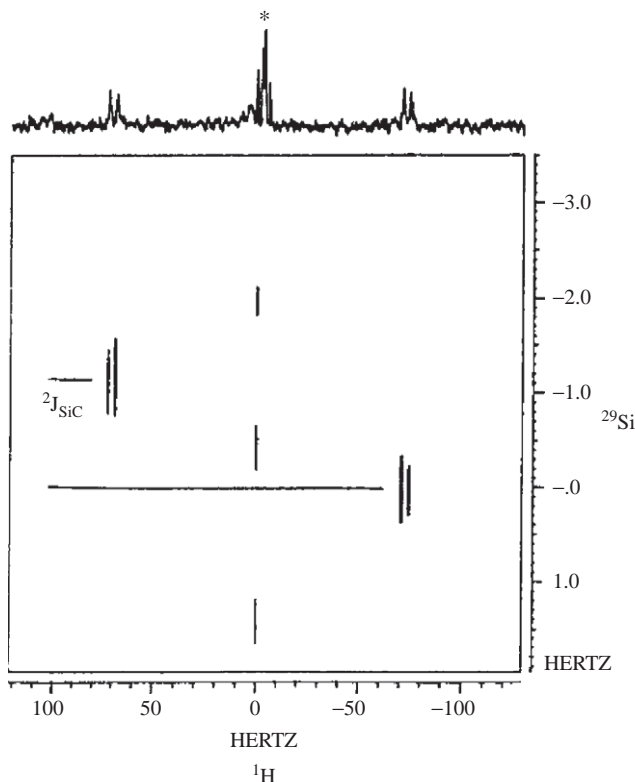


Figure 9 ^1H – ^{29}Si Ψ -BIRD-HSQC experiment applied to $\text{Si}(\text{OMe})_4$ through $^3J(^1\text{H}\text{--}\text{C}\text{--}\text{O}\text{--}^{29}\text{Si})$ coupling. E-COSY pattern has splitting by $^2J(^{29}\text{Si}\text{--}\text{O}\text{--}^{13}\text{C})$ coupling on vertical ^{29}Si scale and standard splitting by $^1J(^{13}\text{C}, ^1\text{H})$ on ^1H scale. Left tilt of E-COSY pattern indicates different signs of $^2K(^{29}\text{Si}, ^{13}\text{C})$ and $^1K(^{13}\text{C}, ^1\text{H})$ which points to positive value of $^2J(^{29}\text{Si}\text{--}\text{O}\text{--}^{13}\text{C}) = +1.2\text{ Hz}$. Star marks not totally suppressed signal of central peak by $^1\text{H}\text{--}^{28,30}\text{Si}\text{--}^{12}\text{C}$ and (or) by $^1\text{H}\text{--}^{29}\text{Si}\text{--}^{12}\text{C}$ isotopomers. Reproduced from ref. 45 with permission from Wiley & Sons Limited.

$^1\text{H}\text{--}^{29}\text{Si}$ done with ^{13}C as passive nucleus (Z^0 isotope being ^{12}C). For an example spectrum, see Figure 9 from the paper in ref. 45, where $^2J(^{29}\text{Si}, ^{13}\text{C})$ was detected. An effect essentially similar to the Ψ -BIRD excitation can be achieved by selective inversion of the central line by some of the suitably shaped pulses⁴⁸ followed by the delay T . A BIS-HMQC experiment⁴⁷ is a standard HMQC experiment where the first excitation proton broadband pulse is substituted by a train of hard binominal pulses. The train selectively excites only the NMR active Z isotope satellites, thus leaving Z^0 isotope central line (almost) not affected and (almost) not contributing to a signal. Meier et al.⁴⁹ used the same trick but applied shaped pulse instead for the same task in $^1\text{H}\text{--}^{13}\text{C}$ HMQC and $^{31}\text{P}\text{--}^{13}\text{C}$ HMQC experiment with ^{57}Fe as a passive nucleus.

The experiments described up to this point in this chapter require non-zero values for all three couplings $J(\text{Si}, \text{H})$, $J(\text{C}, \text{H})$ and $J(\text{Si}, \text{C})$. gHSQC-RELAY (P) and gHSQC-RELAY (D) pulse sequences⁵⁰ (Figure 11) represent a possibility to

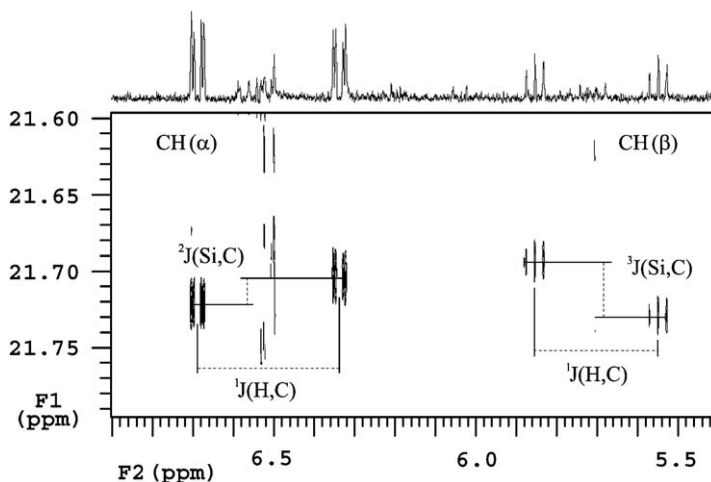


Figure 12 gHSQC-RELAY(D) sequence applied to (*E*)-(buta-1,3-dienyloxy)trimethylsilane $(\text{CH}_3)_3\text{Si}-\text{O}-\text{C}(\alpha)\text{H}=\text{C}(\beta)\text{H}-\text{CH}=\text{CH}_2$. Due to applied ^{13}C filter, all E-COSY patterns have changed tilt (right tilt changed to left tilt and *vice versa*), which must be accounted for. This gives for $^2J(^{29}\text{Si}, ^{13}\text{C})$ negative value and for $^3J(^{29}\text{Si}, ^{13}\text{C})$ positive value. Reproduced from ref. 50 with permission from Wiley & Sons Limited.

$^1\text{H}^\alpha$ – ^{29}Si HSQC experiment followed by the RELAY transfer (by INEPT^{6–9} step) $\text{H}^\alpha \rightarrow \text{H}^\beta$ (non-zero $^3J(\text{H}^\alpha, \text{H}^\beta)$ is needed), so both cross-peaks for C^α and C^β appear in the HSQC spectra. The RELAY step is incorporated in a back polarization transfer $^{29}\text{Si} \rightarrow ^1\text{H}^\alpha$. This is possible due to the fact that (and only if) $^3J(^{29}\text{Si}, ^1\text{H}^\alpha)$ are smaller than $^3J(\text{H}^\alpha, \text{H}^\beta)$. To cope with undesirable coherence loss due to homonuclear proton–proton evolution during the sequences, either band-selective pulses (gHSQC-RELAY (P)) or optimized delays (gHSQC-RELAY (D)) are used. Gradient selection of coherence transfer pathways ensures good suppression of the strongest $^{28,30}\text{Si}$ – ^{12}C – ^1H isotopomers. For suppression of ^{29}Si – ^{12}C – ^1H isotopomers, a simple non-gradient broadband filter based on $^1J(^{13}\text{C}, ^1\text{H})$ can be incorporated. The experiments give E-COSY patterns with $^{2,3}J(^{29}\text{Si}, ^{13}\text{C})$ along F_1 dimension a $^1J(^{13}\text{C}, ^1\text{H})$ along F_2 dimension. For an example, see Figure 12. The single RELAY transfer restricts the method to $^{2,3}J(^{29}\text{Si}, ^{13}\text{C})$ and is used to limit the polarization transfer to H^α and H^β because silicon–carbon couplings over four and more bonds appear to be smaller than about 0.5–0.7 Hz and they do not carry usable information. When it would appear necessary to measure more than three-bond silicon–carbon couplings in some compounds, TOCSY^{51,52} proton–proton polarization transfer would be a better choice than the RELAY. A modification of the sequences would be necessary.

2. COUPLINGS — RESULTS

Fundamentals of the theory of isotropic coupling constants can be found, for example, by Harris and Mann² and in the references cited therein.

Surveys concerning silicon–carbon coupling constants appeared in the past as paragraphs or chapters in more general review articles dealing usually with silicon compounds. A lot of the information appearing in this chapter can be found in the book² and in the review articles by Marsmann,⁵ Coleman,⁵³ Kupče and Lukevics,⁵⁴ Takeuchi and Takayama⁵⁵ and Wrackmeyer.⁵⁶

2.1 General theory

The basic formula for indirect (nuclear) spin–spin interaction was earlier formulated by Ramsey⁵⁷ on the basis of Hamiltonian \hat{H} :

$$\hat{H} = \hat{H}^{\text{SO(a)}} + \hat{H}^{\text{SO(b)}} + \hat{H}^{\text{SS}} + \hat{H}^{\text{FC}} \quad (3)$$

The first two terms in the above equation represent spin–orbital interaction between nuclear spin and orbital moment of electrons, \hat{H}^{SS} is spin–spin interaction between nuclear and electron spins and \hat{H}^{FC} a Fermi contact term

$$\hat{H}^{\text{FC}} = \frac{4\mu_0\mu_B\hbar}{3(\sum \gamma_A \delta(\mathbf{r}_{\text{kA}}) \mathbf{S}_k \cdot \mathbf{I}_A)} \quad (4)$$

where μ_B is Bohr magneton, γ_A and \mathbf{I}_A the magnetogyric ratio and spin operator of the nucleus A, \mathbf{S}_k a spin operator of the electron k, \mathbf{r}_{kA} a distance vector between the nucleus A and the electron k, and δ the Dirac delta function. The total nuclear spin–spin coupling energy E_{AB} between nuclei A and B was expressed by Ramsey⁵⁷ for non-viscous, isotropic and not oriented fluids by second-order perturbation theory as a sum of four independent contributions each originating from one of the four Hamiltonian parts in Equation (3) without cross-terms:

$$E_{\text{AB}} = E_{\text{AB}}^{\text{SO(a)}} + E_{\text{AB}}^{\text{SO(b)}} + E_{\text{AB}}^{\text{SS}} + E_{\text{AB}}^{\text{FC}} \quad (5)$$

Consequently, spin–spin coupling $J(\text{A}, \text{B})$ between nuclei A and B can be similarly expressed as a sum of four different contributions without cross-terms:

$$J(\text{A}, \text{B}) = J(\text{A}, \text{B})^{\text{SO(a)}} + J(\text{A}, \text{B})^{\text{SO(b)}} + J(\text{A}, \text{B})^{\text{SS}} + J(\text{A}, \text{B})^{\text{FC}} \quad (6)$$

On the basis of Ramsey's formulas, Pople and Santry⁵⁸ derived formulas for all four terms in Equation (5) under the assumption of independent electron model and minimum valence shell atomic orbitals. The most important and widely used is the formula for the Fermi contact contribution:

$$J(\text{A}, \text{B})^{\text{FC}} = - \left(\frac{16h\mu_0\mu_B^2}{9} \right) \gamma_A \gamma_B \langle s_A | \delta(\mathbf{r}_A) | s_A \rangle \langle s_B | \delta(\mathbf{r}_B) | s_B \rangle \\ \times \sum \sum (E_k - E_j)^{-1} C_{\text{jsA}} C_{\text{ksA}} C_{\text{ksB}} C_{\text{jsB}} \quad (7)$$

where s_A and s_B refer to s orbitals on the atoms A and B, E_j and E_k the energies of basic and excited molecular orbital state and C coefficients the LCAO coefficients for s_A and s_B for the basic j and the excited k molecular orbital states. The formula

is frequently used in a different form

$$J(A, B)^{\text{FC}} = - \left(\frac{4h\mu_0\mu_B^2}{9} \right) \gamma_A \gamma_B \Psi_{sA}(0)^2 \Psi_{sB}(0)^2 \Pi_{AB} \quad (8)$$

where $\Psi_{sA}(0)$ and $\Psi_{sB}(0)$ are (s) electron densities of bonding molecular orbital on atoms A and B and mutual polarizability Π_{AB} is defined as

$$\Pi_{AB} = 4 \sum_k \sum_j (E_k - E_j)^{-1} C_{jsA} C_{ksA} C_{ksB} C_{jsB} \quad (9)$$

Equations (8) and (9) are frequently simplified to the following equation in a literature (written for ^{29}Si and ^{13}C nuclei):

$$J(^{29}\text{Si}, ^{13}\text{C}) = J(^{29}\text{Si}, ^{13}\text{C})^{\text{FC}} = \left(\frac{16h\mu_B^2}{9\Delta E} \right) \gamma_{\text{Si}} \gamma_{\text{C}} \eta^2 \Psi_{s\text{Si}}(0)^2 \Psi_{s\text{C}}(0)^2 c_{\text{Si}}^2 c_{\text{C}}^2 \quad (10)$$

here ΔE is (average) energy difference between basic and excited bonding molecular orbital functions, c_{Si} and c_{C} the coefficients of the s orbitals in the bonding molecular orbital functions and η^2 a normalization constant. Note that this frequently used average excitation energy approximation could give only negative $^1J(^{29}\text{Si}, ^{13}\text{C})$ due to the fact that all the quantities in Equation (10) are positive with the exception of γ_{Si} .

2.2 $^1J(^{29}\text{Si}, ^{13}\text{C})$ couplings

Results of studies made on silicon–carbon one-bond couplings are sketched in the following text. General conclusion from these works is that substantial contribution to the silicon–carbon couplings is due to the Fermi contact term (Equations (7)–(9)), and that signs of all these couplings are negative. Generally, the higher the s-character of the silicon–carbon bond, the higher is absolute value of the coupling, so the couplings increase from C(sp³) through C(sp²) to maxima for C(sp) hybridized carbons. This is in accord with Equation (10). Similarly, electronegative substituents on silicon or carbon increase the s-character of the silicon–carbon bond too and lead to an increase in the absolute value of the silicon–carbon coupling. The magnitudes of the couplings range from about 15 Hz⁵⁹ (1 Hz coupling was found for coordinative bond⁶⁰) to 177 Hz for Cl₃Si–C≡C–*n*Bu.⁶¹ Most of the values lie in a region from 40 Hz to below 100 Hz. Extremely small values can be found usually in compounds with somewhat weakened silicon–carbon bonds and the highest values are connected with SiCl₃ group.

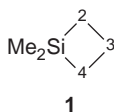
The chapter then proceeds with silicon–carbon couplings in specific kinds of compounds and finally pays attention to the isotope-induced chemical shifts and assignment problems in connection with silicon–carbon couplings.

A particular application of Equation (10) was proposed^{62,63} to establish pivotal role of Fermi contact interaction in a set of compounds. It is based on the observation that $|\Psi_{sX}(0)|$ is directly proportional to the atomic number Z_X . Let us assume that we have a set of compounds where only one position X is substituted by different atoms with similar bonding properties, for example, C, Si, Sn and Pb group. Then $c_X^2 c_Y^2 / \Delta E$ is expected to be constant and the linear

dependence of $|^1K(X, Y)|^{1/2}$ on Z_X could be expected if Fermi contact term plays a dominant role. If such dependence is observed, then it is supposed that the value of $^1K(X, Y)$ is dominated by the Fermi contact term. Dreeskamp and Stegmeier³⁹ and Weigert et al.⁶⁴ applied successfully this correlation to $^1J(X, C)$ in a compound set of XMe_4 ($X = C, Si, Sn, Pb$) (see Figure 13).

Köhler et al.⁶⁵ used this correlation for a set of cyclopentadienyl anions $(Me_3X-cp)_2Fe$ ($X = C, Si, Sn, Pb$) successfully too (including correlations for $^{2,3}J(Si, C)$ couplings).

Wrackmeyer and Biffar⁶⁶ measured one-bond silicon–carbon couplings for non-cyclic organosilanes $CH_{4-n}(Si(CH_3)_3)_n$ ($n = 1-4$), $(CH_3)_{4-n}C(Si(CH_3)_3)_n$ ($n = 1, 3$) and cyclic organosilanes $((CH_3)_2SiCH_2)_n$ ($n = 2, 3$) and $(CH_3)_2Si(CH_2)_3$ **1**. Reduced couplings $^1K(^{29}Si, E)$, $^1K(^{13}C, E)$ and $^1K(^{119}Sn, E)$ ($E = ^1H, ^{11}B, ^{13}C, ^{29}Si, ^{119}Sn$) were compared for some of the silicon compounds above and for their analogs with silicon atom substituted by carbon or tin, respectively. The conclusions were that ratios of the reduced coupling constants studied are close to ratios of densities $\Psi_{sSi}(0)^2/\Psi_{sC}(0)^2$ (~ 2), $\Psi_{sSn}(0)^2/\Psi_{sSi}(0)^2$ (~ 4) and $\Psi_{sSn}(0)^2/\Psi_{sC}(0)^2$ (~ 8). This points to a dominant role of the Fermi contact term under the assumption that the term $c_E^2 c_E^2 / \Delta E$ from Equation (10) is considered as independent of the nuclei Sn, Si and C.



Kovačević and Maksić⁶⁷ calculated one-bond silicon–carbon couplings by maximum overlap approximation method assuming that the Fermi contact term

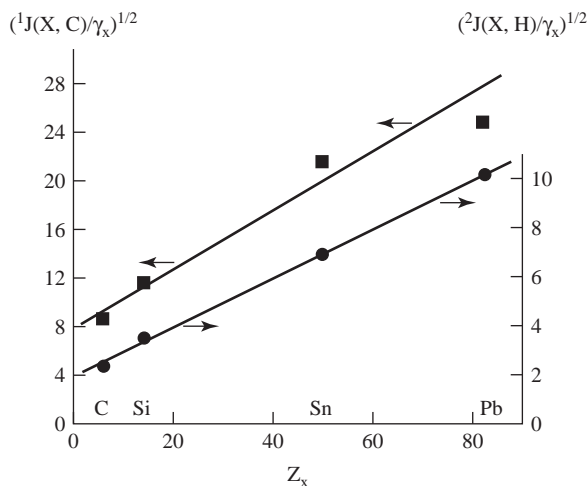


Figure 13 Reeves and Wells correlations of $^1K(X, C)$ (■) and $^2K(X-C-H)$ (●) reduced couplings in Me_4X set of compounds ($X = C, Si, Sn, Pb$) with Z_X atomic number. Reproduced with permission from ref. 64. Copyright 1968 American Chemical Society.

has a dominant effect using simplification in Equation (10). The authors computed the product $c_{\text{Si}}(0)^2 c_{\text{C}}(0)^2$ and fitted experimental data for six compounds by Levy et al.⁶⁸ with different carbon hybridization parameters (all sp³, sp² and sp carbon atom hybrids are presented by Me₄Si, Et₄Si, PhSiMe₃, ViSiMe₃, Vi₂SiMe₂ and Ph–C≡C–SiMe₃) into the relation (10) with result:

$$^1J(^{29}\text{Si}, ^{13}\text{C}) = 555.4c_{\text{Si}}^2c_{\text{C}}^2 + 18.2 \quad (\text{Hz}) \quad (11)$$

The correlation has standard deviation 2.2 Hz and is quite superior when considering the coarse approximations used, that is, average excitation energy approximation and charge dependence of $\Psi_{\text{Si}}(0)^2\Psi_{\text{C}}(0)^2$ value. Thus, the correlation appears to confirm that the Fermi contact contribution dominates the one-bond silicon–carbon coupling.

According to the Bent's rule,⁶⁹ another quantity influencing the s-character of the valence bond and consequently a value of spin–spin coupling is electronegativity of nearest neighbor substituent. Harris and Kimber⁷⁰ searched for such a substituent X electronegativity (χ_X) influence on $^1J(^{29}\text{Si}, ^{13}\text{C})$ in a series of 12 Me₃SiX compounds, and they found the correlation

$$|^1J(\text{Si}, \text{C})| = 7.90\chi_X + 31.5 \quad (\text{Hz}) \quad (12)$$

with correlation coefficient $r = 0.96$ and number of points $n = 12$ (see Figure 14). The authors then suggest that the Fermi contact term provides the dominant contribution to the coupling. This is confirmed by another correlation between $^1K(\text{Si}, \text{C})$ for the above-mentioned compound series and $^1K(\text{C}, \text{C})$ for analogous

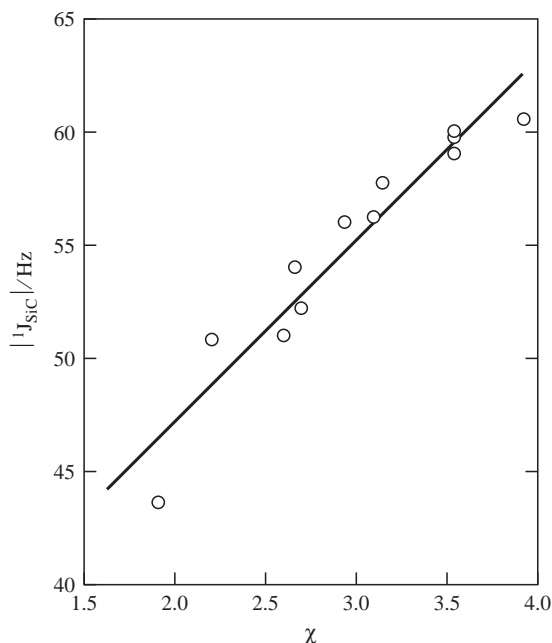


Figure 14 Dependence of $^1J(\text{Si}, \text{C})$ couplings in Me₃SiX compounds on the X substituent electronegativity χ_X . Reproduced from ref. 70 with permission from Elsevier Science.

series of Me_3CX compounds⁶⁸ (see Figure 15):

$$|{}^1K(\text{Si}, \text{C})| = 1.72|{}^1K(\text{C}, \text{C})| + 0.80, \quad r = 0.96, \quad n = 7 \quad (13)$$

The authors conclude that the same mechanism, that is, Fermi contact term, is taking place for ${}^1J(\text{Si}, \text{C})$ and ${}^1J(\text{C}, \text{C})$ couplings and that probably the silicon d orbitals do not participate to any great extent in the silicon–carbon bonding. They conclude also that the one-bond silicon–carbon coupling constants are generally negative because neither of the observed coupling constant magnitudes approaches zero (so it is supposed that there cannot be some of the couplings positive and other ones negative) and because ${}^1J(\text{Si}, \text{C})$ measured on Me_4Si ^{35,39,71} and later in other compounds (e.g. paper in ref. 42) was detected to have a negative sign.

In another work, Harris and Kimber⁷² studied a series of methylethoxysilanes $\text{Me}_n\text{Si}(\text{OEt})_{4-n}$, $n = 0-4$. One-bond silicon–carbon couplings increase strongly non-linearly with increased number of the ethoxy groups. The changes are so large that if only changes of s-character of atom orbitals are considered, then substantial changes in s-electron densities must be supposed in order to save Fermi contact interaction model. The measured values were satisfactorily fitted by an empirical quadratic fit by Ditchfield et al.⁷³

Dreeskamp and Hildebrand⁷⁴ studied a series of vinyl-, chlor- and chlormethyl-substituted tetramethylsilanes and concluded that magnitudes of ${}^1J(\text{Si}, \text{C})$ in these compounds are proportional to the s-character of atomic orbitals.

Beer and Grinter⁷⁵ calculated ${}^1J(\text{Si}, \text{C})$ coupling constants by finite perturbation theory at the INDO level of approximation for 20 simple silicon compounds

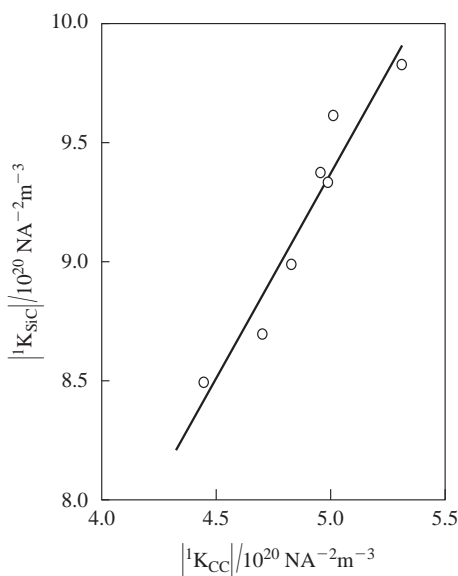


Figure 15 Dependence of ${}^1K(\text{Si}, \text{C})$ reduced couplings in Me_3SiX compounds on corresponding ${}^1K(\text{C}, \text{C})$ reduced couplings in Me_3CX compounds. Reproduced from ref. 70 with permission from Elsevier Science.

including sp^3 and sp^2 hybridized carbons bonded to the silicon and other different substituents at the silicon. The results testified that the spin–orbital and the spin–dipolar terms are negligible in magnitude relatively to the Fermi contact term and they even mutually cancel so that their combined effect is below 1% of the total coupling. Correlation coefficients with experimental data lie in a range 0.966–0.985. Silicon d orbitals were not required for the computations.

2.2.1 Silacyclobutanes and silacyclopentanes

In ref. 66, a surprisingly low value of $^1J(\text{Si}, \text{C}(\text{Me}))$ coupling in $(\text{CH}_3)_2\text{Si}(\text{CH}_2)_3$ (1) is discussed. It is inferred that $^1J(\text{Si}, \text{C}(\text{Me}_{\text{eq}})) > ^1J(\text{Si}, \text{C}(\text{Me}_{\text{ax}}))$ with the observed value being an average (due to ring flipping) from axial and equatorial positions. Value of $^1J(\text{Si}, \text{C}(\text{Me}_{\text{eq}}))$ is supposed to be close to value in linear silanes and lower value of $^1J(\text{Si}, \text{C}(\text{Me}_{\text{ax}}))$ should be the source of the averaged lower value of the detected coupling.

Krapivin et al.⁷⁶ studied a large number of silacyclobutanes and silacyclopentanes by ^{29}Si and ^{13}C NMR and by semi-empirical calculations. The authors concentrated to explanation of *endo*- and *exo*-silicon–carbon coupling constants in silacyclobutanes which have lower values when compared to silacyclopentanes or non-cyclic silanes. The influence of inclusion of silicon d atomic orbitals into a basic molecular orbital set was studied, so calculations with sp and spd hybrid orbitals were compared. First, influence of the product of bond-order parameters $c_{\text{Si}}^2 c_{\text{C}}^2$ from Equation (10) on $^1J(\text{Si}, \text{C})$ was tested. A better linear correlation between $^1J(\text{Si}, \text{C})$ and the product $c_{\text{Si}}^2 c_{\text{C}}^2$ was obtained for spd hybrid bases than for sp bases (see Figure 16) but different slopes for the fit lines in Figure 16 indicate that this approach is not sufficient. The authors then considered possible influence of geometrical deformations (bond lengths and angles) on the $c_{\text{Si}}^2 c_{\text{C}}^2$ values but the calculated values changed too slightly with the angles and distances varied for both sp and spd hybrid bases and thus the geometrical factor was ruled out. From other two remaining factors ΔE and $\Psi_{\text{Si}}(0)^2 \Psi_{\text{SC}}(0)^2$ in Equation (10), authors did not try to calculate ΔE but concentrated to values of the valence shell electronic densities at nuclei. They considered effective nuclear charge (Z^*) as the main source of $\Psi_{\text{Si}}(0)^2 \Psi_{\text{SC}}(0)^2$ changes and found that spd basis leads to the desirable decrease in the value of $\Psi_{\text{Si}}(0)^2 \Psi_{\text{SC}}(0)^2$ while the sp basis did not give any usable change. They conclude that the effect of d orbitals to NMR parameters is significant.

2.2.2 Aminosilanes

Kupče et al.⁷⁷ studied a series of cyclosilazoxanes $(\text{Me}_2\text{Si-X})_n$, $\text{X} = \text{O}, \text{NH}$, $n = 3\text{--}6$ (in detail see Table A9). It is concluded that $^1J(\text{Si}, \text{C})$ coupling values for $\text{N-SiMe}_2\text{-N}$ (62.3–64.5 Hz), $\text{N-SiMe}_2\text{-O}$ (68.2–69.8 Hz) and $\text{O-SiMe}_2\text{-O}$ (74.0–74.5 Hz) fragments lie in very narrow and non-overlapping regions which allows one to use them for analytical purposes.

Kupče and Lukevics⁷⁸ measured one-bond silicon–carbon couplings for about 40 simple aminosilanes and correlated $^1J(\text{Si}, \text{C})$ with $^1J(^{29}\text{Si}, ^{15}\text{N})$ (both couplings

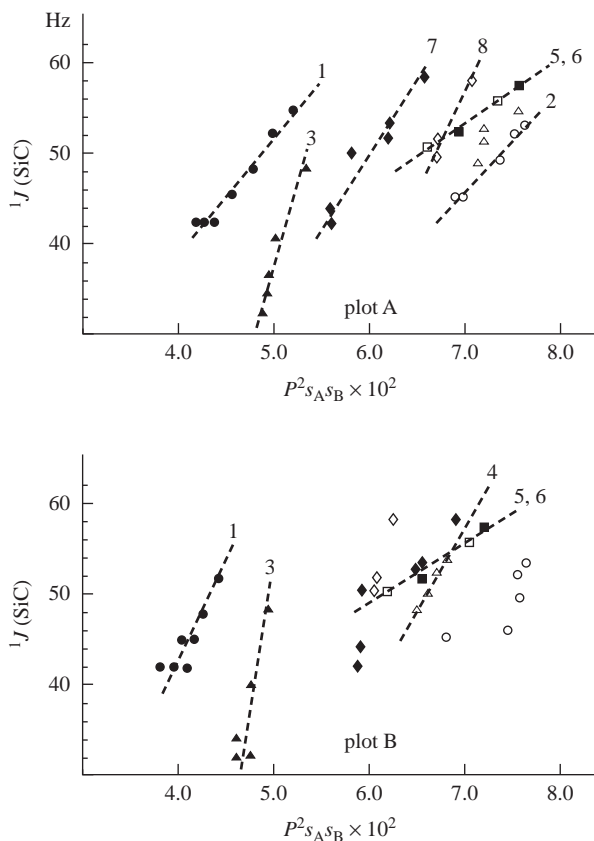


Figure 16 Dependence of $^1J(\text{Si}, \text{C})$ in cyclic carbosilanes on a calculated bond-order parameter $P^2 s_A s_B$. spd base (plot A) and sp base (plot B) were used for calculations. Different points corresponds to: (1, ●) $^1J(\text{Si}, \text{C}(2))$; (2, ○) $^1J(\text{Si}, \text{C}(\text{Me}))$ in xySi_5^{2-} ; (5, ■) $^1J(\text{Si}, \text{C}(2))$; (6, □) $^1J(\text{Si}, \text{C}(\text{Me}))$ in xySi_5^{2-} ; (3, ▲) $^1J(\text{Si}(\text{a}), \text{C}(2,4))$, $^1J(\text{Si}(\text{b}), \text{C}(2,4))$; (4, △) $^1J(\text{Si}(\text{a}), \text{C}(\text{Me}))$, $^1J(\text{Si}(\text{b}), \text{C}(\text{Me}))$ in $\text{xySi}(\text{a})_4^{2-}\text{Si}(\text{b})\text{Me}_2$; (7, ◆) $^1J(\text{Si}(\text{a}), \text{C}(2))$, $^1J(\text{Si}(\text{a}), \text{C}(5))$, $^1J(\text{Si}(\text{b}), \text{C}(2))$, $^1J(\text{Si}(\text{b}), \text{C}(4))$; (8, ◇) $^1J(\text{Si}(\text{a}), \text{C}(\text{Me}))$, $^1J(\text{Si}(\text{b}), \text{C}(\text{Me}))$ in $\text{X}(\text{Me})\text{Si}(\text{a})_4^{2-}\text{Si}(\text{b})\text{Me}_2$. Reproduced from ref. 76 with permission from Elsevier Science.

for the same molecule) for 7 picked up (unspecified) derivatives:

$$^1J(^{29}\text{Si}, ^{15}\text{N}) = 0.41^1J(\text{Si}, \text{C}) - 7.3, \quad r = 0.97 \quad (14)$$

The authors state that according to this correlation, $^1K(^{29}\text{Si}, ^{15}\text{N})$ and $^1K(\text{Si}, \text{C})$ are governed by the same mechanism, that is, by Fermi contact interaction and that $^1K(^{29}\text{Si}, ^{15}\text{N})$ must be positive due to the increase with electronegativity of the substituent on the silicon. Absolute values of both couplings are correlated in Equation (14).

The same procedure with the same conclusions was applied for few disilazanes⁷⁹ resulting in the following equation:

$$^1J(^{29}\text{Si}, ^{15}\text{N}) = 0.31^1J(\text{Si}, \text{C}) - 4.0, \quad r = 0.993 \quad (15)$$

The slope lower than that in Equation (14) is explained by lower electronegativities of substituents on the nitrogen.

A year later, Wrackmeyer et al.⁸⁰ found one more general correlation between $^1J(^{29}\text{Si}, ^{15}\text{N})$ and $^1J(\text{Si}, \text{C})$ but in this case a set of aminosilanes was compared with a set of compounds with N substituted by CH:

$$^1J(^{29}\text{Si}, ^{15}\text{N}) = -0.64^1J(\text{Si}, \text{C}) - 15.5 \quad (16)$$

The $^1J(^{29}\text{Si}, ^{15}\text{N})$ value on the left side of the above equation is taken from aminosilane while the $^1J(\text{Si}, \text{C})$ on the right is from the corresponding compound with CH replacing N. The negative sign of slope in Equation (16) is because signed values of couplings are considered.

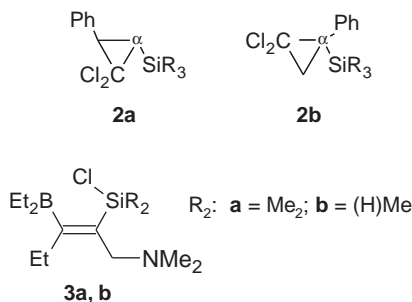
The Si–Br–Si bridging was detected⁸¹ in the trisilylamine $[\text{Me}_2(\text{Br})\text{Si}]_3\text{N}$ by unusually low value of one-bond silicon–carbon coupling (56.2 Hz) and by low value of silicon–nitrogen one-bond coupling. Three fluxional structures of the compound were proposed where on average the nitrogen and methyl groups are forced to move into pseudo-axial positions which lead on average to smaller couplings.

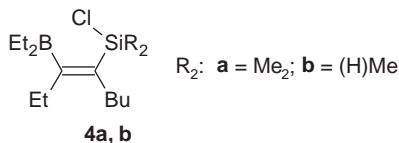
2.2.3 Si–C≡C fragments

Liepinš et al.⁸² studied substituent effects on α -silylstyrenes (*E*)- $\text{PhC}(\text{H})=\text{C}^z(\text{H})\text{SiR}_3$ (R_3 : $\text{Me}_n\text{Cl}_{3-n}$, $\text{Me}_n\text{Ph}_{3-n}$) and silyldichlorocyclopropanes **2a, b** (R_3 : $\text{Me}_n\text{Ph}_{3-n}$). The absolute values of $^1J(\text{Si}, \text{C}(\alpha))$, $^1J(\text{Si}, \text{C}(\text{Me}))$ and $^1J(\text{Si}, \text{C}(\text{Ph}))$ increase with increasing number of the phenyl substituent on the silicon which is explained by increased positive charge on the silicon atom. For α -silylstyrenes, the following equation between one-bond silicon–carbon couplings and a sum of Pauling electronegativities $\sum \Delta E$ was found:

$$^1J(\text{Si}, \text{C}) = -149.6 + 28.4 \sum \Delta E, \quad r = 0.987, \quad n = 7 \quad (17)$$

Wrackmeyer et al.⁸³ found increased values of $^1J(\text{Si}, \text{C})$ couplings in compounds **3a, b** compared to couplings in compounds **4a, b**. The phenomenon of increased coupling was interpreted as due to a coordinative bond between silicon and nitrogen in **3a, b**.





Kamińska-Trela et al.⁸⁴ measured $^1J(\text{Si}, \text{C})$ couplings on three *cis*- and three *trans*-1-trimethylsilyl-1,2-dihaloethanes ($\text{Me}_3\text{Si}-\text{C}(\text{X})=\text{C}(\text{H})\text{X}$, $\text{X} = \text{Cl}, \text{Br}, \text{I}$). They concluded that values of the $^1J(\text{Si}, \text{C})$ couplings clearly depend on the electronegativity of the substituents as expected, that is, with the increasing electronegativity of the substituents the $^1J(\text{Si}, \text{C})$ value also goes up.

Liepinš et al.⁸⁵ studied series of about 40 silaethylenes of types $\text{Me}_{3-n}\text{X}_n\text{Si}-\text{C}(\text{H})=\text{C}(\text{H})\text{Cl}$ (I = *trans*, II = *cis*), $\text{Me}_{3-n}\text{X}_n\text{Si}-\text{C}(\text{H})=\text{CCl}_2$ (III), $\text{Me}_{3-n}\text{X}_n\text{Si}-\text{C}(\text{Cl})=\text{CCl}_2$ (IV) and $\text{Me}_{3-n}\text{X}_n\text{Si}-\text{C}(\text{H})=\text{C}(\text{H})-\text{SiX}_n\text{Me}_{3-n}$ (V), where $n = 0-3$, $\text{X} = \text{Cl}, \text{MeO}, \text{EtO}$. For the values, see Tables B1.1, B1.4 and B1.5. Linear correlations were found between $^1J(\text{Si}, \text{C}(\text{C}=\text{C}))$ and the sum of electronegativities of substituents bonded to silicon ($\sum E$):

$$\text{I: } ^1J(\text{Si}, \text{C}(\text{C}=\text{C})) = -71.0 + 20.2 \sum E, \quad n = 8, r = 0.964 \quad (18a)$$

$$\text{II: } ^1J(\text{Si}, \text{C}(\text{C}=\text{C})) = -69.6 + 20.4 \sum E, \quad n = 8, r = 0.969 \quad (18b)$$

$$\text{III: } ^1J(\text{Si}, \text{C}(\text{C}=\text{C})) = -62.2 + 19.0 \sum E, \quad n = 6, r = 0.984 \quad (18c)$$

$$\text{IV: } ^1J(\text{Si}, \text{C}(\text{C}=\text{C})) = -89.7 + 23.5 \sum E, \quad n = 6, r = 0.987 \quad (18d)$$

The tight dependences on the $\sum E$ point to a major role of positive charge on $^1J(\text{Si}, \text{C}(\text{C}=\text{C}))$ couplings. Roughly linear correlation was found between $^1J(\text{Si}, \text{C}(\text{C}=\text{C}))$ and $^1J(\text{Si}, \text{C}(\text{Me}))$ in the same molecule for compounds studied (see Figure 17a) but a different slope emerged for Cl- and EtO-substituted compounds. More pronounced is this effect for correlation between $^1J(\text{Si}, \text{C}(\text{Me}))$ and $^2J(\text{Si}-\text{C}(\text{Me})-\text{H})$ shown in Figure 17b. The effect was partially explained by the expected stronger (p-d) π interaction between silicon and methyl carbon for EtO substituent than for Cl substituent. This interaction was inferred from a different behavior of the methyl carbon chemical shifts on X substitution. For increasing number of Cl substituents, the methyl carbon chemical shift increases while that for EtO substituent decreases. On the other hand, due to a lack of correlation between $^1J(\text{Si}, \text{C}(\text{C}=\text{C}))$ and $^2J(\text{Si}-\text{C}(\text{Me})-\text{H})$, this (p-d) π interaction cannot explain the effect completely and other (possibly steric) effects must be taken into account too.

The lone-pair effect was studied by Liepinš et al.⁸⁶ They compared one-bond silicon-carbon couplings in furylvinyl silanes **5** and **6** with the same couplings in phenylvinyl and thienylvinyl silanes **7-9** and with nitrogen-substituted heterocycles **10-15**. For couplings, see Tables 2a and 2b. The $^1J(\text{Si}, \text{C}(2))$ couplings in **5** and **6** largely differ from $^1J(\text{Si}, \text{C}(\text{Vi}))$ couplings in the same compound. By contrast, the differences in both one-bond silicon-carbon couplings to sp^2 carbon in **7-9** are negligible, which leads to the conclusion that the oxygen lone-pairs

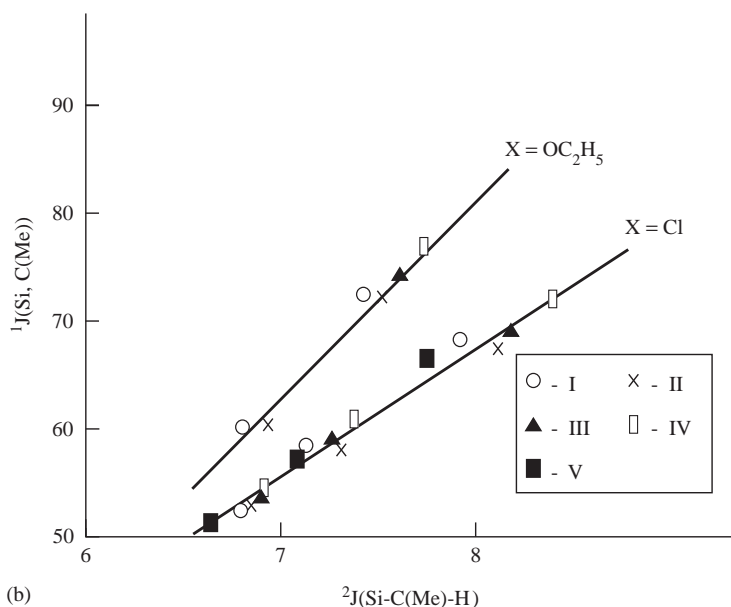
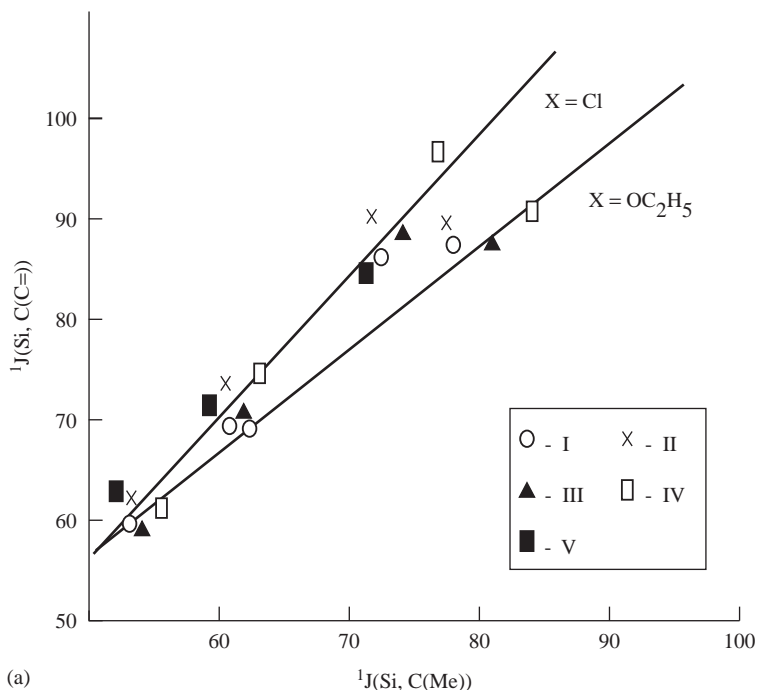


Figure 17 (a) Dependence of $^1J(\text{Si}, \text{C}(\text{C}\equiv))$ on $^1J(\text{Si}, \text{C}(\text{Me}))$ for compounds I–V (for their meaning, see text). For $\text{X} = \text{Cl}$ substituent on silicon, different fit was obtained ($^1J(\text{Si}, \text{C}(\text{C}\equiv)) = -13.7 + 1.39^1J(\text{Si}, \text{C}(\text{Me}))$, $r = 0.980$) than for $\text{X} = \text{EtO}$ substituent (formula not shown). Reproduced from ref. 85 with permission from Elsevier Science. (b) Dependence of $^1J(\text{Si}, \text{C}(\text{Me}))$ on $^2J(\text{Si}-\text{C}(\text{Me})-\text{H})$ for compounds I–V (for their meaning, see text). For $\text{X} = \text{Cl}$ substituent on silicon, different fit was obtained ($^1J(\text{Si}, \text{C}(\text{C}\equiv)) = -49.5 + 15.2^2J(\text{Si}-\text{C}(\text{Me})-\text{H})$, $r = 0.989$) than for $\text{X} = \text{EtO}$ substituent ($^1J(\text{Si}, \text{C}(\text{C}\equiv)) = -110.5 + 25.2^2J(\text{Si}-\text{C}(\text{Me})-\text{H})$, $r = 0.990$). Reproduced from ref. 85 with permission from Elsevier Science.

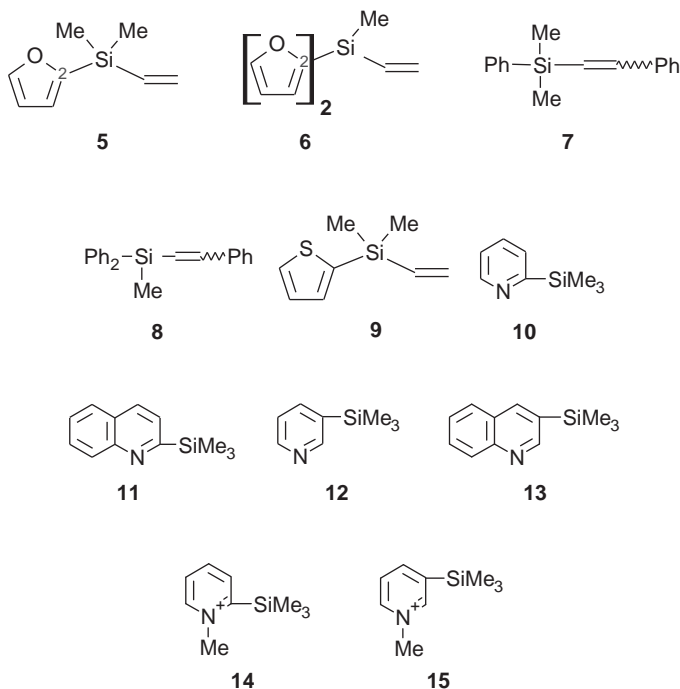
Table 2a Values of $^1J(\text{Si}, \text{C})$ couplings for compounds **5–9**

	Compound				
	5	6	7	8	9
$^1J(\text{Si}, \text{C}(\text{ring}))$	78.9	85.3	67.7	69.4	68.4
$^1J(\text{Si}, \text{C}(\text{Vi}))$	69.0	73.4	67.6	69.8	68.3

Table 2b Values of $^1J(\text{Si}, \text{C})$ couplings for compounds **10–14**

	Compound				
	10	11	12	13	14
$^1J(\text{Si}, \text{C}(\text{ring}))$	75.9	75.5	62.8	62.5	54.7

increase one-bond silicon–carbon couplings through the adjacent bond. Similar effect is demonstrated by comparing 2-silicon-substituted nitrogen heterocycles **10** and **11** with the structures **12–15** where the nitrogen lone-pair either does not exist or is more distant from the silicon–carbon bond.



Popelis and Lukevics⁸⁷ measured three sets of (2-furyl) and (2-thienyl) silanes. The first set consists of compounds $R_n\text{Si}(\text{CH}_3)_{4-n}$, $R_n\text{SiH}_{4-n}$, $R^1_n\text{Si}(\text{CH}_3)_{4-n}$, $R^1_n\text{SiH}_{4-n}$ and $R^1_n\text{SiCl}_{4-n}$. R and R^1 are furan and thienyl, respectively, bonded in a position 2 to the silicon. An increase of one-bond silicon–carbon couplings with a number of thienyl and furyl groups was observed with exception of Cl-substituted silanes where the opposite trend was found. The following correlation:

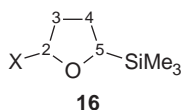
$$^1J(\text{Si}, \text{C}(2)) = 69.03 + 6.54 \sum \sigma^*, \quad r = 0.998, n = 8 \quad (19)$$

was found between one-bond silicon–C(2) carbon of furan ring coupling and the sum of inductive Taft constants σ^* of all substituents. A similar correlation was found for the thienyl rings:

$$^1J(\text{Si}, \text{C}(2)) = 60.50 + 5.96 \sum \sigma^*, \quad r = 0.999, n = 5 \quad (20)$$

The similarity of both dependencies (19) and (20) suggests a similar kind of electronic effects, that is, substituent inductive effect and it appears that $(\pi\text{--d})\pi$ bonding interaction does not come to light. The increase of $^1J(\text{Si}, \text{C})$ was explained mainly by an increase of the positive charge at silicon and partially by an increase of the s-character of the silicon–carbon bond. The second set of compounds in this chapter consists of 2-substituted 5-trimethylsilylfuranes **16** with 10 different substituents X. The linear correlation between reduced coupling $^1K(\text{Si}, \text{C}(5))$ and the Hammett substituent constant σ_p of the substituent was found:

$$^1K(\text{Si}, \text{C}(5)) = (221.2 - 31.0\sigma_p)10^{-16}, \quad r = 0.960, n = 10 \quad (21)$$



According to the authors, the bond order C(5)–Si increases from 1.0948 to 1.1336 when the substituent σ_p decreases, so the change is due to a redistribution of the s-character of the silicon orbitals which is connected with a redistribution of π -electron density within Si–C bond.

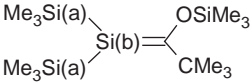
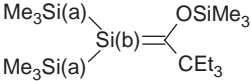
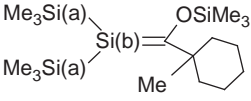
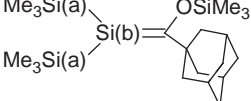
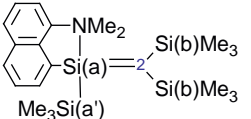
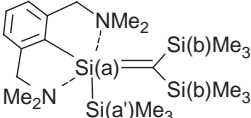
2.2.4 Si=C, Si=Si bonds

Some studies^{88,89} treated Si=C double bond and West⁹⁰ Si=Si double bond influence on one-bond silicon–carbon couplings. A brief summary of the studied compounds and the measured one-bond silicon–carbon couplings is to be found in Table 3. It is concluded in all three papers that the increase in the values of the silicon–carbon one-bond coupling constants is consistent with an increase of s-content of sp^2 hybridized silicon.

2.2.5 Hyperconjugation

An effect of hyperconjugation in connection with silicon–carbon coupling constants was studied by Delmulle and Van Der Keelen⁹¹ on a set of

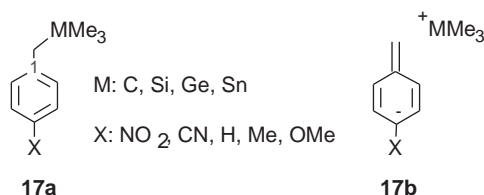
Table 3 Examples of $^1J(^{29}\text{Si}, ^{13}\text{C})$ coupling constants for compounds with sp^2 hybridized silicon

	$^1J(\text{Si(b)}, \text{C}(\text{C}=\text{C}))$	83.5	Ref. 88
	$^1J(\text{Si(a)}, \text{C}(\text{Me}))$	48.8	
	$^1J(\text{Si(b)}, \text{C}(\text{C}=\text{C}))$	83.9	Ref. 88
	$^1J(\text{Si(a)}, \text{C}(\text{Me}))$	48.0	
	$^1J(\text{Si(b)}, \text{C}(\text{C}=\text{C}))$	85.0	Ref. 88
	$^1J(\text{Si(a)}, \text{C}(\text{Me}))$	47.7	
	$^1J(\text{Si(b)}, \text{C}(\text{C}=\text{C}))$	84.4	Ref. 88
	$^1J(\text{Si(a)}, \text{C}(\text{Me}))$	47.6	
	$^1J(\text{Si(a)}, \text{C}(2))$	65.9	Ref. 89
	$^1J(\text{Si(a)}, \text{C}(\text{Ar}))$	55.9	
	$^1J(\text{Si(b)}, \text{C}(2))$	57.6	
	$^1J(\text{Si(b)}, \text{C}(2))$	55.3	
	$^1J(\text{Si(a')}, \text{C}(\text{Me}))$	45.2	
	$^1J(\text{Si(b)}, \text{C}(\text{Me}))$	49.5	
	$^1J(\text{Si(b)}, \text{C}(\text{Me}))$	49.1	
	$^2J(\text{Si(a')}, \text{C}(2))$	7.8	
	$^1J(\text{Si(a)}, \text{C}(2))$	68.6	Ref. 89
	$^1J(\text{Si(a)}, \text{C}(\text{Ar}))$	56.7	
	$^1J(\text{Si(b)}, \text{C}(2))$	56.6	
	$^1J(\text{Si(b)}, \text{C}(2))$	55.6	
	$^1J(\text{Si(a')}, \text{C}(\text{Me}))$	45.1	
	$^1J(\text{Si(b)}, \text{C}(\text{Me}))$	49.5	
	$^1J(\text{Si(b)}, \text{C}(\text{Me}))$	49.0	
	$^2J(\text{Si(a')}, \text{C}(2))$	7.6	
$(\text{Me}_3\text{Si})_2\text{Si(b)} = \text{C}(\text{O}-\text{SiMe}_3)\text{R}^{\text{a}}$	$^1J(\text{Si(b)}, \text{C})$	84.0	Ref. 90
$\text{Mes}_2\text{Si} = \text{SiMes}_2^{\text{b}}$	$^1J(\text{Si}, \text{C})$	90.0	Ref. 90

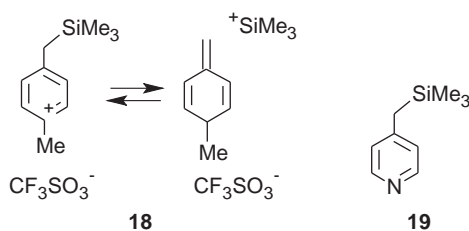
^aR = adamantyl.^bMes = 2,4,6-trimethylphenyl.

methylvinylsilanes $(\text{CH}_3)_4-n\text{Si}(\text{CH}=\text{CH}_2)_n$, $n = 0-4$. A behavior of proton–proton and one-bond proton–carbon couplings together with the increase of both silicon–carbon coupling constants with n is explained by $[\text{d}, \sigma^*-\pi]$ hyperconjugation between silicon d , σ^* and carbon π orbitals which results in decrease of ΔE .

Lambert and Singer⁹² studied an effect of neutral hyperconjugation on structures **17a**. They supposed existence of resonance structures **17b** (M and X have the same meaning as for **17a**) of these compounds. The expectation was confirmed by decreased $^1J(\text{M}, (\text{CH}_2))$ with increased electron-withdrawing power of the substituent X and by increased $^1J(\text{C}(1), \text{C}(\text{CH}_2))$ one-bond carbon–carbon coupling due to decreased and increased bond orders, respectively.



Similarly Happer et al.⁹³ studied hyperconjugation in *N*-methyl 4-trimethylsilylmethylpyridinium ion **18** by X-ray analysis and by inspecting silicon–carbon and carbon–carbon coupling constants. They compared the NMR results with NMR results for the trimethylsilyl-substituted picoline **19** ($^1J(\text{Si}, \text{C}(\text{CH}_2)) = 41.8$ Hz). Both measured compounds have smaller $^1J(\text{Si}, \text{C}(\text{CH}_2))$ than compounds **17a, b** studied by Lambert and Singer⁹² (see above); the ion **18** has distinctively lower silicon–carbon coupling ($^1J(\text{Si}, \text{C}(\text{CH}_2)) = 35.9$ Hz) than **19** which points to more electron-demanding ring in **18** and generally to a strong hyperconjugation in both these compounds.

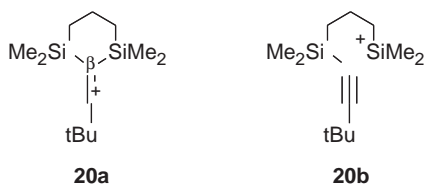


Müller et al.⁵⁹ studied vinyl cation **20a** stabilized by the counterion tetrakis(pentafluorophenyl)borate, $[\text{B}(\text{C}_6\text{F}_5)_4]^-$, or by the hexabromocarborane, $[\text{CB}_{11}\text{H}_6\text{Br}_6]^-$. The X-ray, ^{29}Si and ^{13}C NMR and IR analysis gave the compound as the resonance between **20a, b** Lewis structures. The silicon atoms are equivalent in the benzene and toluene solutions and coupling $^1J(^{29}\text{Si}, ^{13}\text{C}^\beta) = 15.7$ Hz is unusually low. Its value is explained by a very small s -orbital contribution to the $\text{Si}-\text{C}^\beta$ bond and consequently by a low Fermi contact contribution. This phenomenon is caused by the β -silyl hyperconjugation where $\text{Si}-\text{C}^\beta$ σ bond

Table 4 $^1J(\text{Si}, \text{C}^\beta)$ couplings for structures **21**

	R										
	H	4-Me	4-Et	2,4-Di-methyl	2,5-Di-methyl	3,5-Di-methyl	4-Ph	2-F	3-F	4-F	4-Cl
$J(\text{Si}, \text{C}^\beta)$	18.2	19.8	20.2	20.7	19.5	18.8	19.5	16.6	17.2	18.8	18.4

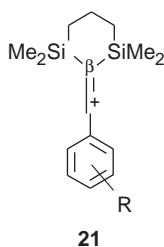
orbital is delocalized into (formally) vacant carbon 2p orbital.



The same β -silyl hyperconjugation effect was observed⁹⁴ for the substituted vinyl cations **21** (and two other vinyl compounds of similar structure) stabilized by the tetrakis(pentafluorophenyl)borate, $[\text{B}(\text{C}_6\text{F}_5)_4]^-$, in solution. The measured silicon–carbon couplings for structures **21** are summarized in Table 4 (complete silicon–carbon data sets are in Table B1.5). Six resonance structures were proposed, either due to the β -silyl hyperconjugation or by π -resonance via the aryl substituent. Values of $^1J(^{29}\text{Si}, ^{13}\text{C}^\beta)$ vs. Brown's substituent constant σ^+ for different *meta* and *para* substituents were correlated by

$$^1J(\text{Si}, \text{C}^\beta) = (-4.2 \pm 0.5)\sigma^+ + (18.6 \pm 0.1), \quad r = 0.96, n = 8 \quad (22)$$

(see Figure 18). The correlation suggests (together with silicon chemical shift correlation vs. σ^+ , not shown here) that the hyperconjugation becomes more pronounced as the π stabilization by the aryl substituent decreases.



2.2.6 Si–C \equiv C fragments

Kamieńska-Trela⁹⁵ studied $\text{Alk}_3\text{M}-\text{C}\equiv\text{CH}$ and $\text{Alk}_3\text{M}-\text{C}\equiv\text{C}-\text{MAlk}_3$ compounds with $\text{M} = \text{Si}, \text{Sn}$ and $\text{Alk} = \text{Et}, n\text{Bu}$. A very pronounced decrease of $^1J(\text{C}\equiv\text{C})$ was observed in acetylene with substitution of hydrogen by Alk_3M .

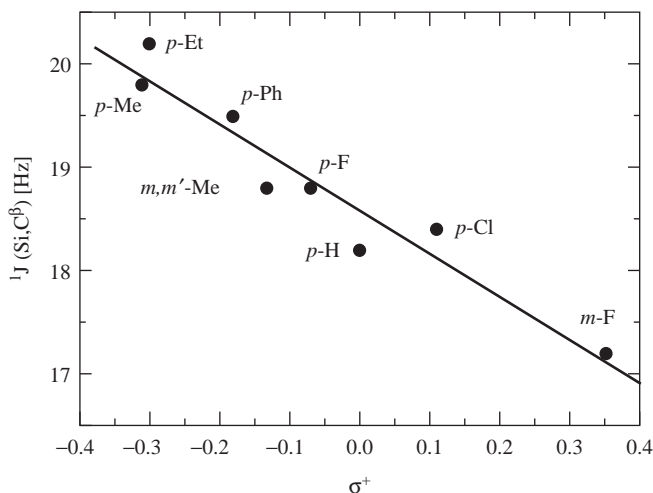


Figure 18 Correlation of $^1J(\text{Si}, \text{C}^\beta)$ with Brown substituent constants σ^+ for vinyl cations **21**. Reproduced with permission from ref. 94. Copyright 2005 American Chemical Society.

The effect was interpreted as a very strong p_π – d_π interaction between the carbon–carbon triple bond and the silicon atom. Such interaction introduces a very large contribution of the mesomeric form (B) into the structure:



This interaction almost should not influence the $^1J(\text{Si}, \text{C}(\equiv))$ but should affect markedly $^2J(\text{Si}-\text{C} \equiv \text{C})$. Really, it was found that on substitution of the second Alk_3M group into the $\text{Alk}_3\text{M}-\text{C} \equiv \text{CH}$, little changes below 2% were observed for $^1J(\text{Si}, \text{C}(\equiv))$ while $^2J(\text{Si}-\text{C} \equiv \text{C})$ decreased drastically to about 62% or 50% of the mono-substituted acetylene for $\text{M} = \text{Si}$ or Sn , respectively.

Kamieńska-Trela and Knieriem⁹⁶ performed finite perturbation calculations of $^1J(\text{Si}, \text{C})$ at INDO level approximation for three silyl derivatives of acetylene $\text{H}_3\text{Si}-\text{C} \equiv \text{CH}$, $\text{H}_3\text{Si}-\text{C} \equiv \text{C}-\text{SiH}_3$ and $(\text{H}_3\text{Si}-\text{C} \equiv \text{C})_2$. The computed values quite disagree with the experimental ones in this case (they are almost exactly one-half of the experimental values). The computed spin–orbital and the spin–dipolar contributions are of a negligible value with respect to the Fermi contact term but on the other hand the author states that the INDO method does not properly handle these terms.

About 12 values of $^1J(\text{Si}, \text{C}^\alpha)$ and $^2J(\text{Si}, \text{C}^\beta)$ were published⁹⁷ for X-substituted ethynylsilanes $\text{R}_3\text{Si}-\text{C}^\alpha \equiv \text{C}^\beta-\text{X}$ ($\text{R} = \text{Me}, \text{Et}$). The influence of the substituent X appeared to be complex and no simple relation describing, for example, influence of electronegativity of X was found.

A set of 22 ethynylsilanes $(\text{CH}_3)_3\text{Si}-\text{C}^\alpha \equiv \text{C}^\beta-\text{X}$ was measured and silicon–carbon couplings were discussed by Liepinš et al.⁹⁸ Correlation between

one-bond $^1J(\text{Si}, \text{C}^\alpha)$ and electronegativity σ_p of the substituent X was found

$$^1J(\text{Si}, \text{C}^\alpha) = 82.9 - 21.7\sigma_p, \quad r = 0.98, n = 12 \quad (23)$$

together with another correlation

$$^2J(\text{Si}, \text{C}^\beta) = -3.44 + 0.23^1J(\text{Si}, \text{C}^\alpha), \quad r = 0.94, n = 15 \quad (24)$$

($^1J(\text{Si}, \text{C}^{\alpha,\beta})$ in absolute values). So with increasing electronegativity of substituent X, both the (absolute) values decrease. The opposite but weak trend was observed for $^1J(\text{Si}, \text{C}(\text{Me}))$. A comparison with trends for analogous ethynylstanan derivatives gave Equations (25) and (26):

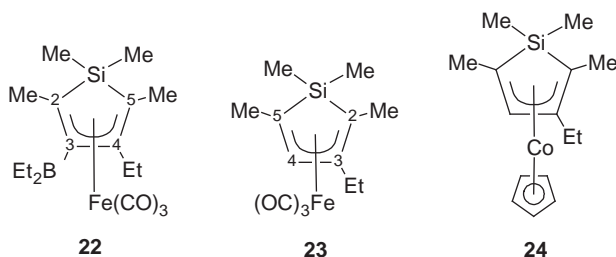
$$^1J(\text{Si}, \text{C}^\alpha) = 49.6 + 0.07^1J(^{119}\text{Sn}, \text{C}^\alpha), \quad r = 0.964, n = 13 \quad (25)$$

$$^2J(\text{Si}, \text{C}^\beta) = 5.57 + 0.11^2J(^{119}\text{Sn}, \text{C}^\beta), \quad r = 0.997, n = 8 \quad (26)$$

The slopes in the correlations are similar, thus pointing to a similar mechanism of the coupling. The authors conclude that the slopes in these equations should be much higher if Fermi contact term and consequently s-electron densities for silicon and tin play a major rule in the coupling building, so other contributions should take place.

2.2.7 Complexes

For the complexed siloles **22–24**, Köster et al.⁹⁹ briefly discussed higher values of couplings to quasi-equatorial methyls $^1J(\text{Si}, \text{C}(\text{exo-Me}))$ relatively to $^1J(\text{Si}, \text{C}(\text{endo-Me}))$ couplings to quasi-axial methyls; for the values see Table 5.

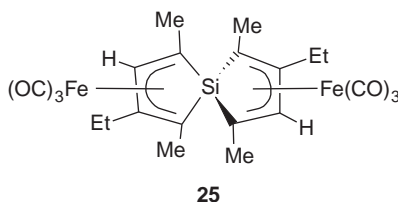


Köster et al.¹⁰⁰ noted similar effect for the diastereoisomers of complexed spirobisilole **25**. The silicon-bonded quasi-axial carbons have lower silicon–carbon

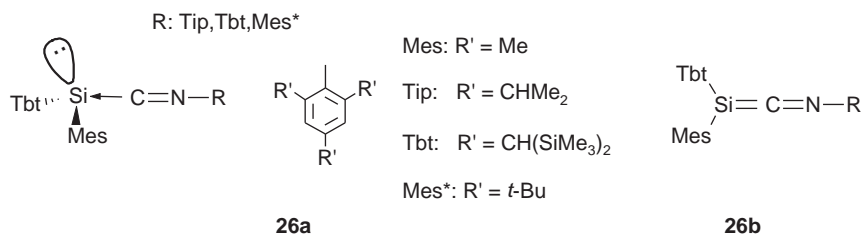
Table 5 One-bond silicon–carbon couplings for quasi-axial (*endo*) and quasi-equatorial (*exo*) silicon-bonded methyls in complexed siloles **22–24**

Compound	<i>endo</i>	<i>exo</i>
22	55.8	40.1
23	57.6	40.9
24	58.4	37.4

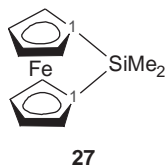
coupling (51.2–53.1 Hz) than the silicon-bonded quasi-equatorial carbons (72.4–73.3 Hz).



Takeda et al.⁶⁰ reported about three silylene–isocyanide complexes **26a**. Two possible basic electronic structures **26a**, **b** were supposed. ²⁹Si chemical shifts and low ¹J(Si, C(CN)) values (38.6 Hz, 22.1 Hz and 1.0 Hz (!) for *R* equal Tip, Tbt and Mes*, respectively) lead to the clear preference of the structure **26a**.



Relatively low value of ¹J(Si, C(1)) in **27** (57.8 Hz) when compared to the value ¹J(Si, C(1)) in 1,1'-bis(trimethylsilyl)ferrocene (73.6 Hz) led authors¹⁰¹ to the conclusion that C(1) carbon in the compound **27** has electron distribution close to that of sp³ hybridized carbons.



2.2.8 ¹J(Si, C) and isotope-induced chemical shifts

Some efforts were devoted to a search for possible relations between one-bond silicon–carbon couplings and the isotope-induced chemical shifts. Kupče et al.¹⁸ studied oxygen 18/16 one-bond isotope effects on ²⁹Si (¹Δ^{18/16}O(²⁹Si), change in the silicon chemical shift when ¹⁸O isotope is substituted by ¹⁶O isotope in the position directly bonded to the silicon) for a set of 11 simple siloxanes. They found that the isotope effect decreases with increase of the one-bond silicon–carbon coupling (in absolute value) caused by increased electronegativity of substituent on the silicon.

Liepinš et al.⁹⁸ studied ethynylsilanes $(\text{CH}_3)_3\text{Si}-\text{C}^\alpha\equiv\text{C}^\beta-\text{X}$ and found the correlations (27) and (28)

$$^1\Delta^{13/12}\text{C}(^{29}\text{Si}) = -49.69 + 0.41J(\text{Si}, \text{C}^\alpha), \quad r = 0.971, n = 16 \quad (27)$$

$$^2\Delta^{13/12}\text{C}(^{29}\text{Si}) = -17.60 + 0.82^2J(\text{Si}, \text{C}^\beta), \quad r = 0.93, n = 16 \quad (28)$$

(see Figures 19 and 20).

Wrackmeyer et al.¹⁰² studied $^1\Delta^{13/12}\text{C}(^{29}\text{Si})$ effect on some 2,5-dihydro-1,2,5azasilaboroles and silole and their tricarbonyliron complexes but the correlation with silicon–carbon coupling was found to be far from straightforward and the effect seems to be complex.

2.2.9 Assignments

The one-bond silicon–carbon coupling satellites in silicon or carbon spectra could serve as a simple and effective assignment tool as can be seen in a number of papers, for example, in refs. 103–105. The assignment procedure uses well-known fact that one-bond silicon–carbon couplings (in absolute value) are usually about one order larger than the silicon–carbon couplings over more bonds, so the presence of the silicon satellites (with the separation above 30 Hz) on the ^{13}C spectrum clearly indicates bonding to silicon. Comparison of values of silicon–carbon couplings found from carbon and silicon spectra can help in further

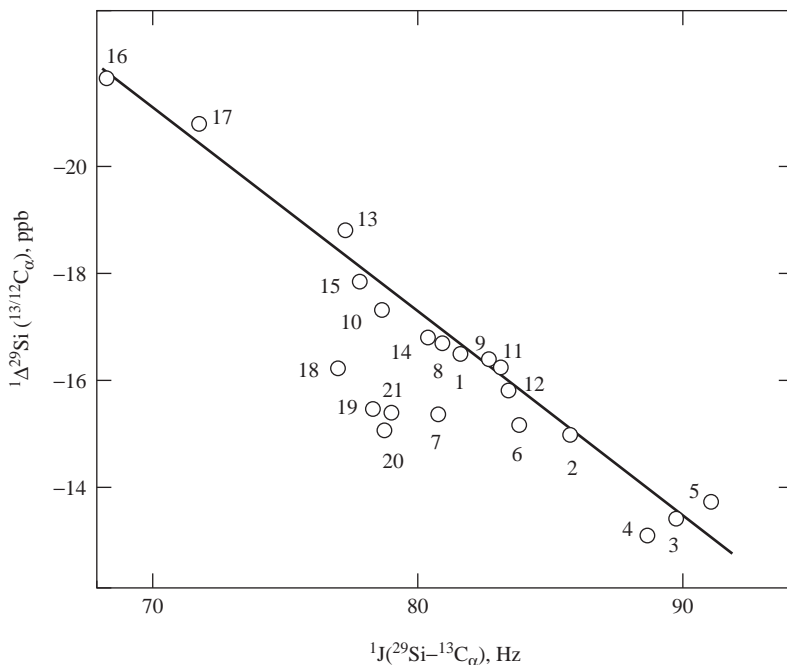


Figure 19 Correlation between the isotope shifts $^1\Delta^{29}\text{Si}(^{13/12}\text{C}^\alpha)$ and $^1J(^{29}\text{Si}, ^{13}\text{C}^\alpha)$ couplings in ethynylsilanes $(\text{CH}_3)_3\text{Si}-\text{C}^\alpha\equiv\text{C}^\beta-\text{X}$. Reproduced from ref. 98 with permission from Elsevier Science.

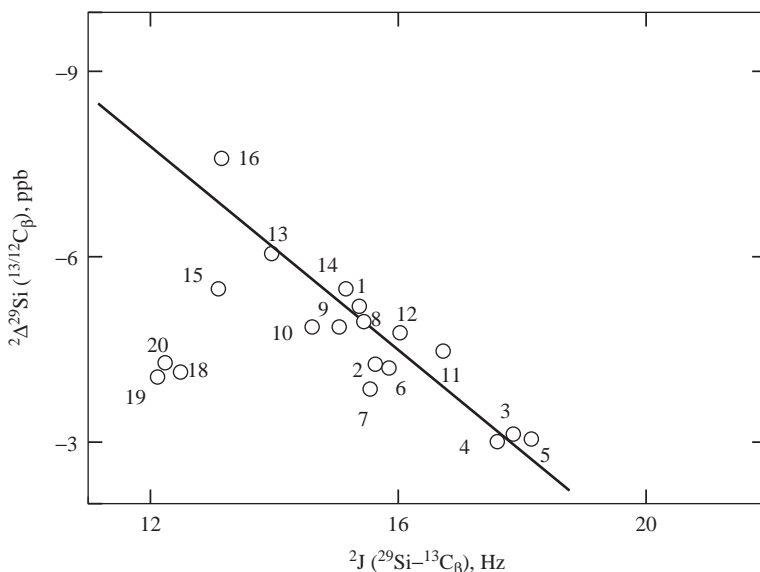


Figure 20 Correlation between the isotope shifts ${}^2\Delta^{29}\text{Si}({}^{13/12}\text{C}^\beta)$ and ${}^2J({}^{29}\text{Si}, {}^{13}\text{C}^\beta)$ couplings in ethynylsilanes $(\text{CH}_3)_3\text{Si}-\text{C}^\alpha\equiv\text{C}^\beta-\text{X}$. Reproduced from ref. 98 with permission from Elsevier Science.

assignment. In probably the first application,¹⁰⁶ authors tried to find presence of $\text{H}_3\text{Si}-\text{N}\equiv\text{C}$ and $\text{Me}_3\text{Si}-\text{N}\equiv\text{C}$ isomers in $\text{H}_3\text{Si}-\text{C}\equiv\text{N}$ and $\text{Me}_3\text{Si}-\text{C}\equiv\text{N}$. The presence of the isomers was deduced according to IR and microwave spectra. No trace of such isomers was found by NMR and direct silicon–carbon bond was confirmed by ${}^{13}\text{C}$ satellites splitting in ${}^{29}\text{Si}$ NMR spectra.

2.3 $J({}^{29}\text{Si}, {}^{13}\text{C})$ couplings over two and more bonds

2.3.1 ${}^nJ(\text{Si}, \text{C})$ signs

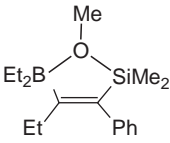
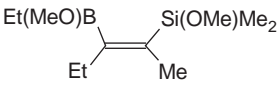
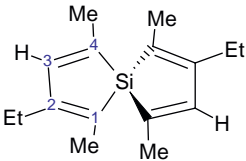
Only few works with two- or three-bond silicon–carbon coupling constants with their signs appeared in the literature; the results are shown in Table 6.

Kupče and Wrackmeyer^{45–47} found by Ψ -BIRD HMQC, Ψ -BIRD HSQC or BIS-HMQC experiment that the two-bond silicon–carbon couplings in measured compounds lie in a range from +2.5 Hz to –21.4 Hz.

Sign of ${}^2J(\text{Si}-\text{C}\equiv\text{C})$ in three substituted acetylenes was found negative by Wrackmeyer et al.¹⁰⁷ Absolute values of ${}^2J(\text{Si}-\text{C}\equiv\text{C})$ couplings usually lie within region from 10 Hz to 20 Hz and are given in Appendix C.

Köster et al.¹⁰⁰ detected $|{}^2J(\text{Si}, \text{C}(2))|$ and $|{}^2J(\text{Si}, \text{C}(3))|$ in some 1,1'-substituted spirobisiloles where both two- and three-bond interactions around the five-membered ring should take place. The negative sign of ${}^2J(\text{Si}, \text{C}(3))$ was determined for the spirobisilole (see Table 6) and domination of three-bond term in this coupling was stated.

Table 6 $^{2,3}J(\text{Si}, \text{C})$ couplings measured with signs

$\text{Et}_3\text{Si}-\text{O}-\text{SiEt}_3$	$^2J(\text{Si}-\text{C}-\text{C})$	+2.2	45
$\text{Me}_2(\text{Cl})\text{Si}-\text{Si}(\text{Cl})\text{Me}_2$	$^2J(\text{Si}-\text{Si}-\text{C})$	-8.6	45
$\text{Me}_2\text{Si}(\text{NEt}_2)_2$	$^2J(\text{Si}-\text{N}-\text{C})$	+1.5	47
$\text{Me}_3\text{Si}-\text{O}-\text{Me}$	$^2J(\text{Si}-\text{O}-\text{C})$	+1.7	46
$\text{Me}_3\text{Si}-\text{O}-\text{Et}$	$^2J(\text{Si}-\text{O}-\text{C})$	+1.7	50
	$^3J(\text{Si}-\text{O}-\text{C}-\text{C})$	-2.5	
	$^2J(\text{Si}-\text{O}-\text{C})$	+1.67	108
	$^3J(\text{Si}-\text{O}-\text{C}-\text{C})$	-2.46	
$\text{Me}_3\text{Si}-\text{O}-i\text{Pr}$	$^2J(\text{Si}-\text{O}-\text{C})$	+1.69	108
	$^3J(\text{Si}-\text{O}-\text{C}-\text{C})$	-1.62	
$\text{Me}_3\text{Si}-\text{O}-\text{CH}=\text{CH}-\text{CH}=\text{CH}_2$	$^2J(\text{Si}-\text{O}-\text{C})$	+1.7	50
	$^3J(\text{Si}-\text{O}-\text{C}=\text{C})$	-3.5	
$\text{Me}_3\text{Si}-\text{O}-\text{ChPh}_2$	$^2J(\text{Si}-\text{O}-\text{C})$	+1.40	108
	$^3J(\text{Si}-\text{O}-\text{C}-\text{C}(\text{Ph}))$	1.89	
$(\text{MeO})_3\text{Si}-\text{C}_6\text{H}_4-\text{Me}$	$^2J(\text{Si}-\text{O}-\text{C})$	+1.3	47
$(\text{MeO})_4\text{Si}$	$^2J(\text{Si}-\text{O}-\text{C})$	+1.2	45
	$^2J(\text{Si}-\text{O}-\text{C})$	+0.45	45
			
$\text{Me}_3\text{Si}-\text{SMe}$	$^2J(\text{Si}-\text{S}-\text{C})$	+1.5	45
$\text{Me}_3\text{Si}-\text{C}(=\text{O})\text{Me}$	$^2J(\text{Si}-\text{C}(\text{sp}^2)-\text{C})$	-21.4	45
	$^2J(\text{Si}-\text{O}-\text{C})$	+1.2	45
	$^2J(\text{Si}-\text{C}(\text{sp}^2)-\text{C}(\text{Me}))$	-10.1	
Ph_3SiH	$^2J(\text{Si}-\text{C}=\text{C})$	-4.7	45
	$^2J(\text{Si}-\text{C}=\text{C}(2))$	-8.0	100
	$^2J(\text{Si}-\text{C}=\text{C}(3))$	-9.0	
$\text{Et}_2\text{N}-\text{SiMe}_2-\text{C}(1) \equiv \text{C}(2)-\text{Me}$	$^2J(\text{Si}-\text{C} \equiv \text{C}(2))$	-17.7	107
$\text{Et}_2\text{N}-\text{Si}(\text{a})\text{Me}_2-\text{C}(1) \equiv \text{C}(2)-\text{Si}(\text{b})\text{Me}_3$	$^2J(\text{Si}(\text{a})-\text{C} \equiv \text{C}(2))$	-12.8	107
	$^2J(\text{Si}(\text{b})-\text{C} \equiv \text{C}(1))$	-13.8	
$\text{Me}_3\text{Si}-\text{C} \equiv \text{CH}$	$^2J(\text{Si}-\text{C} \equiv \text{C})$	-14.8	43
$\text{trans}-(\text{Et}_3\text{P})_2\text{Pt}(\text{C} \equiv \text{C}-\text{SiMe}_3)_2$	$^2J(\text{Si}-\text{C} \equiv \text{C})$	-14.3	43

Blechta and Schraml⁵⁰ and Sýkora et al.¹⁰⁸ published values of $^{2,3}J(\text{Si}, \text{C})$ couplings through Si–O–C and Si–O–C–C bonding pathways. The samples were measured by gHSQC-RELAY (P) or gHSQC-RELAY (D) pulse sequences. The measured signs of the couplings $^2J(\text{Si–O–C}) > 0$ and $^3J(\text{Si–O–C–C}) < 0$ are in agreement with numerical simulations.¹⁰⁸

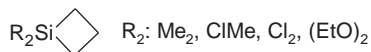
2.3.2 Values of $^nJ(\text{Si}, \text{C})$ couplings

Information about absolute values of two- and more-bond coupling constants is scattered through the literature, the numbers being usually by-product of the original work and usually quoted without any comment. The values are spread within appendix.

Della and Tsanaktsidis¹⁰⁹ measured absolute values of $^{1,2,3}J(\text{Si}, \text{C})$ couplings in a set of eight cyclic compounds (see Table 7). The absolute values of $^3J(\text{Si}, \text{C})$ couplings were shortly discussed in terms of dihedral angles.

Wrackmeyer and Biffar⁶⁶ found $^2J(\text{Si}, \text{C}(3))$ in **1** (16.4 Hz) to be too high if only additivity rule for two coupling pathways is used, so the authors supposed an influence of the bonding angle.

Krapivin et al.⁷⁶ detected large absolute values (16 Hz, 17 Hz and 19 Hz) of $|^2J(\text{Si}, \text{C})|$ in four silacyclobutanes **28** and attributed their magnitudes to through-space interaction Si(1)–C(3).

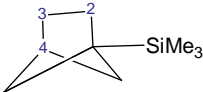


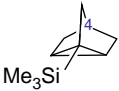

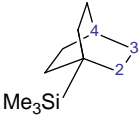
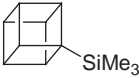



28

Unusually high values of two-bond couplings $^2J(\text{Si–Si–C})$ (between 34 Hz and 39 Hz) were found by Brook et al.⁸⁸ for a series of $(\text{Me}_3\text{Si})_3\text{Si–C(=O)–R}$ compounds (see Table B1.1).

Schraml and coworkers made a set of studies on absolute values of $^{2,3}J(\text{Si}, \text{C})$ couplings through Si–O–C and Si–O–C–C bonding pathway. First works were made on silylated sugars²¹ and silylated phenol–carboxylic acids.¹¹⁰ Much more recent work by Sýkora et al.¹¹¹ published extensive table of $|^{2,3,4,5}J(\text{Si}, \text{C})|$ (see Table A4) couplings to phenol carbons in 4-substituted silylated phenols $4\text{-X–C}_6\text{H}_4\text{–O–SiR}_3$, where $\text{R}_3 = \text{Me}_3, (\text{H})\text{Me}_2, (\text{tBu})\text{Me}_2, (\text{tBu})\text{Ph}_2$ and $\text{X} = \text{NO}_2, \text{CF}_3, \text{Cl}, \text{F}, \text{CH}_3, \text{CH}_3\text{O}$. The result is that $|^2J(\text{Si}, \text{C})|$ and $|^3J(\text{Si}, \text{C})|$ couplings fall into the region 1.4–2.7 Hz and $|^4J(\text{Si}, \text{C})|$ and $|^5J(\text{Si}, \text{C})|$ couplings fall into the distinct region 0–0.7 Hz. This can be utilized for the line assignments in ^{13}C and ^{29}Si NMR spectroscopy. Calculations of the couplings agreed with the two distinct regions of the experimental values of couplings for $^{2,3}J(\text{Si}, \text{C})$ and $^{4,5}J(\text{Si}, \text{C})$. The Fermi contact term is responsible for about 90% contribution to $^{2,3}J(\text{Si}, \text{C})$ couplings, thus playing the dominant role as it plays for one-bond silicon–carbon couplings. All the computed $^2J(\text{Si}, \text{C})$ couplings had positive sign while all computed $^3J(\text{Si}, \text{C})$ couplings had the sign negative. This can be further used for the line assignment when coupling sign-sensitive NMR pulse sequences are used. Sýkora et al.¹⁰⁸ studied series of $\text{Me}_3\text{Si–O–(CH}_2)_n\text{–Me}$, $n = 0\text{–}3$, $\text{Me}_3\text{Si–O–CH}_3\text{–}_n\text{–R}_n$, where $\text{R} = \text{Me}$ ($n = 0\text{–}3$), Ph ($n = 0\text{–}3$) or Vi ($n = 0\text{–}2$). Absolute values

Table 7 $|^{1,2,3}J(\text{Si}, \text{C})|$ in some cyclic compounds

	$^1J(\text{Si}, \text{C})$	62.89	109
	$^1J(\text{Si}, \text{C}(\text{Me}))$	50.46	
	$^2J(\text{Si}, \text{C}(2))$	3.22	
	$^3J(\text{Si}, \text{C}(3))$	4.04	
	$^3J(\text{Si}, \text{C}(4))$	10.46	
	$^1J(\text{Si}, \text{C})$	61.29	109
	$^1J(\text{Si}, \text{C}(\text{Me}))$	49.92	
	$^3J(\text{Si}, \text{C}(3))$	4.09	
	$^3J(\text{Si}, \text{C}(5))$	7.87	
	$^1J(\text{Si}, \text{C})$	61.70	109
	$^1J(\text{Si}, \text{C}(\text{Me}))$	50.30	
	$^2J(\text{Si}, \text{C}(2))$	1.63	
	$^3J(\text{Si}, \text{C}(3))$	4.90	
	$^3J(\text{Si}, \text{C}(4))$	6.22	
	$^1J(\text{Si}, \text{C})$	63.87	109
	$^1J(\text{Si}, \text{C}(\text{Me}))$	51.78	
	$^3J(\text{Si}, \text{C}(4))$	3.23	
	$^1J(\text{Si}, \text{C})$	59.76	109
	$^1J(\text{Si}, \text{C}(\text{Me}))$	50.00	
	$^3J(\text{Si}, \text{C}(3))$	5.35	
	$^3J(\text{Si}, \text{C}(5))$	4.98	
	$^3J(\text{Si}, \text{C}(6))$	4.98	
	$^1J(\text{Si}, \text{C})$	60.42	109
	$^1J(\text{Si}, \text{C}(\text{Me}))$	49.98	
	$^3J(\text{Si}, \text{C}(3))$	5.08	
	$^1J(\text{Si}, \text{C}(\text{Me}))$	50.57	109
	$^2J(\text{Si}, \text{C})$	2.44	
	$^3J(\text{Si}, \text{C})$	3.32	
	$^1J(\text{Si}, \text{C})$	58.89	109
	$^1J(\text{Si}, \text{C}(\text{Me}))$	49.80	
	$^3J(\text{Si}, \text{C})$	4.61	

of $^{2,3}J(\text{Si}, \text{C})$ couplings and their trends are illustrated in Figure 21. The chain length in the $\text{Me}_3\text{Si}-\text{O}-(\text{CH}_2)_n-\text{Me}$ series has no pronounced effect on absolute values. $^2J(\text{Si}, \text{C})$ and $^3J(\text{Si}, \text{C})$ couplings have values in a non-overlapping regions 1.6–1.8 Hz and 2.4–2.5 Hz, respectively. Branching on the carbon bonded through oxygen to silicon (C^α) leads to large changes in absolute values for both couplings. $^2J(\text{Si}, \text{C})$ couplings have a minimum for one or two substituents ($n = 1, 2$) at C^α and their values appreciably jump up for $n = 3$ to values

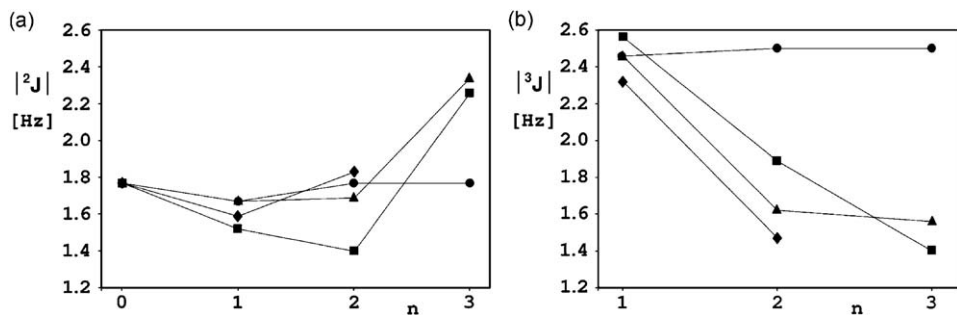
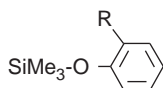


Figure 21 The dependencies of (a) $^2J(\text{Si-O-C})$ and (b) $^3J(\text{Si-O-C-C})$ couplings on chain length in $\text{Me}_3\text{Si-O}(\text{CH}_2)_n\text{-Me}$ (●), and on extent of branching in $\text{Me}_3\text{Si-O-CH}_2\text{-}_n\text{-R}_n$ ($\text{R} = \text{Me}$ (▲), Ph (■), Vi (◆)). Reproduced from ref. 108 with permission from Wiley & Sons Limited.

comparable with 3J for non-branched compounds. $^3J(\text{Si, C})$ couplings almost monotonically decrease with number of branching groups n to the region of values for $^2J(\text{Si, C})$ non-branched compounds. Number n of branching groups appears to be a substantial factor influencing magnitude of both couplings while the nature of substituent (Me , Ph , Vi) is less important. According to a numerical simulation, substantial contribution to values of the coupling constants gives the Fermi contact term. All the simulated two- and three-bond silicon–carbon couplings have positive and negative signs, respectively. It is in accord with experimentally detected signs for some of these compounds¹⁰⁸; see above. Consequently, it appears that $^{2,3}J(\text{Si, C})$ coupling signs can be exploited for structure assignment tasks.

Sychrovský et al.¹¹² reported absolute values of two-, three-, four- and five-bond silicon–carbon couplings for three compounds **29**; for numbers see Table A4. *Ab initio* calculations of all measured silicon–carbon coupling constants with and without considering solvent influence and internal molecular rotation were done with conclusions that inclusion of the internal molecular rotation improves substantially (tenths of percent) calculated values.



R : H , Me , $t\text{Bu}$

29

2.3.3 Structural studies

Schraml et al.¹¹³ showed how $(\text{Si, C, Si})\text{gHMQC}$ pulse sequence can help in the carbon line assignments by detecting multiple-bond silicon–carbon connectivities and absolute values of coupling constants on the example of silylated 7-hydroflavone, silylated ferullic acid and silylated quercetin.

Similarly Maloň et al.¹¹⁴ used their H(Si)C double-INEPT experiment to reveal silicon–carbon multiple-bond correlations (without silicon–carbon coupling value detection) for determination of silylated hydroxyl phenolic group positions.

ACKNOWLEDGMENTS

I sincerely appreciate Prof. Jan Schraml for consultations of structural and other features of this work and for its check. I thank Prof. Jan Čermák for the help with structural chemistry of complexes, Drs. Milan Kurfürst and Jan Sýkora for a help with other chemical aspects of this work and Jan Sýkora for a help with figures too. Financial support of the Czech Science Foundation (grant no. 203/06/0738) and the Grant Agency of ASCR (grant no. IAA 400720706) is gratefully appreciated.

REFERENCES

1. J. Schraml, 29Si NMR experiments in solutions of organosilicon compounds, in: *The Chemistry of Organosilicon Compounds*, Z. Rappoport and Y. Apeilg, eds., Vol. 3, Wiley, Chichester, 2001, p. 223.
2. R. K. Harris and B. E. Mann, *NMR and the Periodic Table*, Academic Press Inc. Ltd, London, 1978.
3. G. C. Levy and G. L. Nelson, in: *Carbon-13 Nuclear Magnetic Resonance for Organic Chemists*, Wiley, New York, NY, 1972.
4. C. Brevard and P. Granger, *Handbook of High Resolution Multinuclear NMR*, Wiley Interscience Publication, New York, NY, 1977.
5. H. Marsmann, 29Si-NMR spectroscopic results, in: *NMR Basic Principles and Progress*, P. Diehl, E. Fluck and R. Kosfeld, eds., Vol. 17, Springer-Verlag, Berlin, 1981, p. 66.
6. P. H. Bolton, *J. Magn. Reson.*, 1980, **41**, 287.
7. D. P. Burum and R. R. Ernst, *J. Magn. Reson.*, 1980, **39**, 163.
8. G. A. Morris, *J. Am. Chem. Soc.*, 1980, **102**, 428.
9. G. A. Morris and R. Freeman, *J. Am. Chem. Soc.*, 1979, **101**, 760.
10. D. M. Doddrell, D. T. Pegg and M. R. Bendall, *J. Magn. Reson.*, 1982, **48**, 323.
11. D. M. Doddrell, D. T. Pegg, W. Brooks and M. R. Bendall, *J. Am. Chem. Soc.*, 1981, **103**, 727.
12. J. Schraml, *Collect. Czech Chem. Commun.*, 1983, **48**, 3402.
13. A. Allerhand, R. E. Addlemand and D. Osman, *J. Am. Chem. Soc.*, 1985, **107**, 5809.
14. A. Allerhand and M. Dohrenwend, *J. Am. Chem. Soc.*, 1985, **107**, 6684.
15. A. Allerhand, R. E. Addlemand, D. Osman and M. Dohrenwend, *J. Magn. Reson.*, 1985, **65**, 361.
16. S. R. Maple and A. Allerhand, *J. Magn. Reson.*, 1986, **66**, 168.
17. E. Kupče and E. Lukevics, *J. Magn. Reson.*, 1988, **80**, 359.
18. E. Kupče, E. Liepiņš, I. Zicname and E. Lukevics, *J. Chem. Soc. Chem. Commun.*, 1989, 818.
19. B. Wrackmeyer and E. Kupče, *Z. Naturforsch.*, 1998, **53b**, 411.
20. J. Paast, J. Puskar, J. Schraml and E. Lipmaa, *Collect. Czech Chem. Commun.*, 1985, **50**, 2060.
21. J. Paast, J. Puskar, M. Alla, E. Lipmaa and J. Schraml, *Magn. Reson. Chem.*, 1985, **23**, 1076.
22. A. Bax, R. Freeman and S. P. Kempsell, *J. Magn. Reson.*, 1980, **41**, 349.
23. A. Bax, R. Freeman and S. P. Kempsell, *J. Am. Chem. Soc.*, 2008, **102**, 4849.
24. S. Berger, T. Fäcke and R. Wagner, *Magn. Reson. Chem.*, 1996, **34**, 4.
25. T. Fäcke, R. Wagner and S. Berger, *Concepts Magn. Reson.*, 1994, **6**, 293.
26. S. Berger, *J. Magn. Reson. A*, 1993, **101**, 329.
27. A. Bax, R. H. Griffey and B. L. Hawkins, *J. Am. Chem. Soc.*, 1983, **105**, 7188.
28. V. Blechta, J. Sýkora and J. Schraml, *Magn. Reson. Chem.*, 2004, **42**, 968.
29. V. Blechta and J. Schraml, *Magn. Reson. Chem.*, 2009, **47**, 511.
30. B. L. Corio, *Structure of High Resolution NMR Spectra*, Academic Press, New York, NY, 1967.
31. K. G. R. Pachler and P. L. Wessels, *J. Magn. Reson.*, 1973, **12**, 337.

32. S. Sørensen, R. S. Hansen and H. J. Jacobsen, *J. Magn. Reson.*, 1974, **14**, 243.
33. H. J. Jacobsen, S. A. A. Linde and S. Sørensen, *J. Magn. Reson.*, 1974, **15**, 385.
34. K. A. McLauchlan, *Mol. Phys.*, 1966, **11**, 303.
35. R. R. Dean and W. McFarlane, *Mol. Phys.*, 1967, **12**, 289.
36. W. McFarlane, *J. Chem. Soc. A: Inorg. Phys. Theor.*, 1967, 1275.
37. J. D. Kennedy, W. McFarlane, G. S. Pyne and B. Wrackmeyer, *J. Chem. Soc. Dalton Trans.*, 1975, 386.
38. C. Schumann and H. Dreeskamp, *J. Magn. Reson.*, 1970, **3**, 204.
39. H. Dreeskamp and G. Stegmeier, *Z. Naturforsch.*, 1967, **22a**, 1458.
40. A. Bax and R. Freeman, *J. Magn. Reson.*, 1981, **45**, 177.
41. R. R. Ernst, G. Bodenhausen and A. Wokaun, in: *Principles of Nuclear Magnetic Resonance in One and Two Dimensions*, R. Breslow, J. Halperin and J. S. Rowlinson, eds., Clarendon Press, Oxford, 1987.
42. B. Wrackmeyer and H. Zhou, *Spectrochim. Acta*, 1991, **47A**, 849.
43. B. Wrackmeyer, K. H. Locquenghien, E. Kupče and A. Sebald, *Magn. Reson. Chem.*, 1993, **31**, 45.
44. B. Wrackmeyer, H. Vollrath and S. Ali, *Inorg. Chim. Acta*, 1999, **296**, 26.
45. E. Kupče and B. Wrackmeyer, *Magn. Reson. Chem.*, 1992, **30**, 950.
46. E. Kupče and B. Wrackmeyer, *J. Magn. Reson.*, 1992, **99**, 343.
47. E. Kupče, E. Lukevics and B. Wrackmeyer, *Magn. Reson. Chem.*, 1994, **32**, 326.
48. H. Kessler, S. Mronga and G. Gemmecker, *Magn. Reson. Chem.*, 1991, **29**, 527.
49. E. J. M. Meier, W. Koźmiński and W. von Philipsborn, *Magn. Reson. Chem.*, 1996, **34**, 89.
50. V. Blechta and J. Schraml, *Magn. Reson. Chem.*, 2008, **46**, 734.
51. A. Bax and D. G. Davis, *J. Magn. Reson.*, 1985, **65**, 355.
52. L. Braunschweiler and R. R. Ernst, *J. Magn. Reson.*, 1983, **53**, 521.
53. B. Coleman, Applications of silicon-29 NMR spectroscopy, in: *NMR of Newly Accessible Nuclei*, P. Laszlo, ed., Vol. 2, Academic Press, Inc., New York, 1983, p. 197.
54. E. Kupče and E. Lukevics, Multinuclear and multipulse NMR of organosilicon compounds, in: *Isotopes in the Physical and Biomedical Science*, E. Buncel and J. R. Jones, eds., Vol. 2, Elsevier Science Publishers B.V., Amsterdam, 1991, p. 213.
55. Y. Takeuchi and T. Takayama, 29Si NMR spectroscopy of organosilicon compounds, in: *The Chemistry of Organic Silicon Compounds*, Z. Rappoport and Y. Apeilog, eds., Vol. 2, Wiley, Chichester, 1998, p. 267.
56. B. Wrackmeyer, Applications of 29Si NMR spectroscopy, in: *Annual Reports on NMR Spectroscopy*, G. A. Webb, ed., Vol. 57, Elsevier Ltd., Amsterdam, 2006, p. 255.
57. N. F. Ramsey, *Phys. Rev.*, 1953, **91**, 303.
58. A. J. Pople and D. P. Santry, *Mol. Phys.*, 1964, **8**, 1.
59. T. Müller, M. Juhasz and C. A. Reed, *Angew. Chem. Int. Ed.*, 2004, **43**, 1543.
60. N. Takeda, H. Suzuki, R. Tokitoh and R. Okazaki, *J. Am. Chem. Soc.*, 1997, **119**, 1456.
61. B. Wrackmeyer and O. L. Tok, *Z. Naturforsch.*, 2006, **61b**, 243.
62. L. W. Reeves and E. J. Wells, *Can. J. Chem.*, 1963, **41**, 2698.
63. J. Feeney, R. Hague and L. W. Reeves, *Can. J. Chem.*, 1968, **46**, 1389.
64. F. J. Weigert, M. Winokur and J. D. Roberts, *J. Am. Chem. Soc.*, 1968, **90**, 1566.
65. F. H. Köhler, W. A. Geike and N. Hertkorn, *J. Organomet. Chem.*, 1987, **334**, 359.
66. B. Wrackmeyer and W. Biffar, *Z. Naturforsch.*, 1979, **34b**, 1270.
67. K. Kovačević and Z. B. Maksič, *J. Mol. Struct.*, 1973, **17**, 203.
68. G. C. Levy, D. M. White and J. D. Cargioli, *J. Magn. Reson.*, 1972, **8**, 280.
69. H. A. Bent, *Chem. Rev.*, 1971, **61**, 275.
70. R. K. Harris and B. J. Kimber, *J. Magn. Reson.*, 1975, **17**, 174.
71. H. von Elser and H. Dreeskamp, *Ber. Bunsenges. Physik. Chem.*, 1969, **73**, 619.
72. R. K. Harris and B. J. Kimber, *Org. Magn. Reson.*, 1975, **7**, 460.
73. R. Ditchfield, M. A. Jensen and J. N. Murrell, *J. Chem. Soc. (A)*, 1967, 1674.
74. H. Dreeskamp and K. Hildebrand, *Liebigs Ann. Chem.*, 1975, **1975**, 712.
75. M. D. Beer and R. Grinter, *J. Magn. Reson.*, 1978, **31**, 187.
76. A. M. Krapivin, M. Mägi, V. I. Svergun, R. Z. Zaharjan, E. D. Babich and N. V. Ushakov, *J. Organomet. Chem.*, 1980, **190**, 9.

77. E. Kupče, E. Liepinš, E. Lukevics and B. Astapov, *J. Chem. Soc. Dalton Trans.*, 1987, 1593.
78. E. Kupče and E. Lukevics, *J. Magn. Reson.*, 1988, **76**, 63.
79. E. Kupče, E. Lukevics, Y. M. Varezkhin, A. N. Mikhailova and V. D. Sheludiyakov, *Organometallics*, 1988, **7**, 1649.
80. B. Wrackmeyer, C. Stader and H. Zhou, *Spectrochim. Acta*, 1989, **45A**, 1101.
81. B. Wrackmeyer, G. Kehr and D. Wettinger, *Magn. Reson. Chem.*, 1998, **36**, S157.
82. E. Liepinš, Yu. Goldberg, I. Iovel and E. Lukevics, *J. Organomet. Chem.*, 1987, **335**, 301.
83. B. Wrackmeyer, K. Shahid and S. Ali, *Appl. Organomet. Chem.*, 2005, **19**, 377.
84. K. Kamińska-Trela, L. Kania, J. Sitkowski and E. Bednarek, *J. Organomet. Chem.*, 1989, **364**, 29.
85. E. Liepinš, I. Birgele, E. Lukevics, V. D. Sheludiyakov and V. G. Lahtin, *J. Organomet. Chem.*, 1990, **385**, 185.
86. E. Liepinš, J. Popelis and E. Lukevics, *Izv. Akad. N. Latv. SSR, Ser. Khim.*, 1990, **2**, 233.
87. J. Popelis and E. Lukevics, *Khim. Geterotsykl. Soed.*, 1993, **7**, 879.
88. A. G. Brook, F. Abdesaken, G. Gutekunst and N. Plavac, *Organometallics*, 1982, **1**, 994.
89. B. Wrackmeyer and H. Oehme, *Z. Naturforsch.*, 2001, **56b**, 947.
90. R. West, *Pure Appl. Chem.*, 1984, **56**, 164.
91. L. Delmulle and G. P. Van Der Keelen, *J. Mol. Struct.*, 1980, **66**, 309.
92. J. B. Lambert and R. A. Singer, *J. Am. Chem. Soc.*, 1992, **114**, 10246.
93. A. Happer, N. G. Janice, B. Pool and J. White, *J. Organomet. Chem.*, 2002, **659**, 10.
94. T. Müller, D. Margraf and Y. Syha, *J. Am. Chem. Soc.*, 2005, **127**, 10852.
95. K. Kamińska-Trela, *J. Organomet. Chem.*, 1978, **159**, 15.
96. K. Kamińska-Trela and B. Knieriem, *J. Organomet. Chem.*, 1980, **198**, 25.
97. K. Kamińska-Trela, Z. Biedrzycka, R. Machinek, B. Knieriem and W. Lüttke, *Org. Magn. Reson.*, 1984, **22**, 317.
98. E. Liepinš, I. Birgele, E. Lukevics, E. T. Bogorodovsky and V. S. Zavgorodny, *J. Organomet. Chem.*, 1990, **393**, 11.
99. R. Köster, G. Seidel, J. Süß and B. Wrackmeyer, *Chem. Ber.*, 1993, **126**, 1107.
100. R. Köster, G. Seidel, I. Klopp, C. Krüger, G. Kehr, J. Süß and B. Wrackmeyer, *Chem. Ber.*, 1993, **126**, 1385.
101. B. Wrackmeyer, A. Ayazi, W. Milius and M. Herberhold, *J. Organomet. Chem.*, 2003, **682**, 180.
102. B. Wrackmeyer, G. Seidel and R. Köster, *Magn. Reson. Chem.*, 2000, **38**, 520.
103. B. Wrackmeyer, *Tetrahedron*, 1986, **5**, 1709.
104. B. Wrackmeyer, W. Milius, M. H. Bhatti and S. Ali, *J. Organomet. Chem.*, 2003, **665**, 196.
105. B. Wrackmeyer, H. E. Maisel, E. Molla, A. Mottalib, A. Badshah, M. H. Bhatti and S. Ali, *Appl. Organomet. Chem.*, 2003, **17**, 465.
106. D. E. J. Arnold, S. Cradock, E. A. V. Ebsworth, J. D. Murdoch, D. W. H. Rankin, D. C. J. Skea, R. K. Harris and B. J. Kimber, *J. Chem. Soc. Dalton Trans.*, 1981, 1349.
107. B. Wrackmeyer, J. Süß and W. Milius, *Chem. Ber.*, 1996, **129**, 147.
108. J. Sýkora, V. Blechta, L. Soukupová and J. Schraml, *Magn. Reson. Chem.*, 2008, **46**, 1112.
109. E. W. Della and J. Tsanaksidis, *Organometallics*, 1988, **7**, 1178.
110. J. Schraml, J. Paast, J. Puskar, T. Pekh, E. Lipmaa and R. Brežný, *Collect. Czech Chem. Commun.*, 1987, **52**, 1985.
111. J. Sýkora, V. Blechta, V. Sychrovský, J. Hetflejš, S. Šabata, L. Soukupová and J. Schraml, *Magn. Reson. Chem.*, 2006, **44**, 669.
112. V. Sychrovský, L. Benda, A. Prokop, V. Blechta, J. Schraml and V. Špirko, *J. Phys. Chem. A*, 2008, **112**, 5167.
113. J. Schraml, V. Blechta, J. Sýkora, L. Soukupová, P. Cuřínová, D. Proněk and J. Lachman, *Magn. Reson. Chem.*, 2005, **43**, 829.
114. M. Maloň, S. Takahashi and H. Koshino, *Tetrahedron Lett.*, 2007, **48**, 7586.
115. B. Wrackmeyer, G. Kehr, H. Zhou and S. Ali, *Magn. Reson. Chem.*, 1996, **34**, 921.
116. B. Wrackmeyer, E. V. Klimkina and Y. N. Bubnov, *J. Organomet. Chem.*, 2001, **620**, 51.
117. B. Wrackmeyer, O. L. Tok, M. H. Bhatti and S. Ali, *Appl. Organomet. Chem.*, 2003, **17**, 843.
118. U. Herzog, G. Rheinwald and H. Borrmann, *J. Organomet. Chem.*, 2002, **660**, 27.

119. K. G. Sharp, P. A. Sutor, E. A. Williams, J. D. Cargioli, T. C. Farrar and K. Ishibitsu, *J. Am. Chem. Soc.*, 1976, **98**, 1977.
120. H. C. Marsmann, W. Raml and E. Hengge, *Z. Naturforsch.*, 1980, **85b**, 1541.
121. U. Herzog and G. Rheinwald, *Eur. J. Inorg. Chem.*, 2001, **2001**, 3107.
122. B. Wrackmeyer and P. Bernatowicz, *J. Organomet. Chem.*, 1999, **579**, 133.
123. B. Wrackmeyer and B. Schwarze, *J. Organomet. Chem.*, 1997, **534**, 181.
124. B. Wrackmeyer, K. Schamel and M. Herberhold, *Z. Naturforsch.*, 1989, **44b**, 55.
125. B. Wrackmeyer, A. Pedall and J. Weidinger, *Z. Naturforsch.*, 2001, **56b**, 1009.
126. M. Herberhold, V. Tröbs, H. Zhou and B. Wrackmeyer, *Z. Naturforsch.*, 1997, **52b**, 1181.
127. B. Wrackmeyer, U. Klaus and W. Milius, *Inorg. Chim. Acta*, 1996, **250**, 327.
128. G. Engelhardt and R. Radeaglia, *J. Organomet. Chem.*, 1981, **212**, 51.
129. E. Kupče and B. Wrackmeyer, *J. Magn. Reson.*, 1992, **97**, 568.
130. B. Wrackmeyer, I. Ordnung and B. Schwarze, *Z. Naturforsch.*, 1997, **52b**, 427.
131. B. Wrackmeyer, A. Pedall and J. Weidinger, *J. Organomet. Chem.*, 2002, **649**, 225.
132. B. Wrackmeyer, J. Weidinger, A. Pedall and W. Milius, *Z. Anorg. Allg. Chem.*, 2003, **629**, 862.
133. B. Wrackmeyer, A. Pedall, W. Milius, O. L. Tok and Y. N. Bubnov, *J. Organomet. Chem.*, 2002, **649**, 232.
134. B. Wrackmeyer, W. Milius, H. E. Maisel, H. Vollrath and M. Herberhold, *Z. Anorg. Allg. Chem.*, 2003, **629**, 1169.
135. B. Wrackmeyer, W. Milius and S. Ali, *J. Organomet. Chem.*, 2003, **682**, 188.
136. B. Wrackmeyer, S. Ali, W. Storch and M. Vosteen, *Z. Naturforsch.*, 1999, **54b**, 1165.
137. E. Kupče, E. Liepinš, G. Lapsina, G. Zelcans and E. Lukevics, *J. Organomet. Chem.*, 1987, **333**, 1.
138. B. Wrackmeyer and H. Zhou, *Magn. Reson. Chem.*, 1990, **28**, 1066.
139. U. Herzog, K. Trommer and G. Roewer, *J. Organomet. Chem.*, 1998, **552**, 99.
140. B. Wrackmeyer, S. Kersch and H. E. Maisel, *Silicon Germanium Tin Lead Comp.*, 1998, **21**, 89.
141. G. Heckmann, G. Becker and H. Kraft, *Magn. Reson. Chem.*, 1999, **37**, 667.
142. E. Kupče and E. Lukevics, *Izv. Akad. N. Latv. SSR, Ser. Khim.*, 1987, **5**, 633.
143. V. A. Pestunovich, S. N. Tandura, M. G. Voronkov, V. P. Baryshok, G. I. Zelchan and V. I. Glukhikh, *Spectrosc. Lett.*, 1978, **11**, 339.
144. U. Herzog, N. Schulze, K. Trommer and G. Roewer, *J. Organomet. Chem.*, 1997, **547**, 133.
145. H. Lange and U. Herzog, *J. Organomet. Chem.*, 2002, **660**, 36.
146. H. Lange, U. Herzog, H. Borrmann and B. Walfort, *J. Organomet. Chem.*, 2004, **689**, 4897.
147. U. Herzog and H. Borrmann, *J. Organomet. Chem.*, 2003, **681**, 5.
148. U. Herzog and G. Rheinwald, *J. Organomet. Chem.*, 2001, **628**, 133.
149. C. Knopf, U. Herzog, G. Roewer, E. Brendler, G. Rheinwald and H. Lang, *J. Organomet. Chem.*, 2002, **662**, 14.
150. U. Herzog, R. Richter, E. Brendler and G. Roewer, *J. Organomet. Chem.*, 1996, **507**, 221.
151. U. Herzog and H. Borrmann, *J. Organomet. Chem.*, 2004, **689**, 564.
152. K. Trommer, U. Herzog and G. Roewer, *J. Organomet. Chem.*, 1997, **540**, 119.
153. B. Wrackmeyer and A. Berndt, *Magn. Reson. Chem.*, 2004, **42**, 490.
154. C. N. McMahon, S. G. Bott, L. B. Alemany, H. W. Roesky and A. R. Barron, *Organometallics*, 1999, **18**, 5395.
155. B. Wrackmeyer, I. Ordnung and B. Schwarze, *J. Organomet. Chem.*, 1997, **532**, 71.
156. B. Wrackmeyer, I. Ordnung and B. Schwarze, *J. Organomet. Chem.*, 1997, **527**, 163.
157. U. Herzog and H. Borrmann, *Inorg. Chem. Commun.*, 2003, **6**, 718.
158. B. Wrackmeyer, H. E. Maisel, W. Milius, M. H. Bhatti and S. Ali, *Z. Naturforsch.*, 2003, **58b**, 543.
159. R. Köster, G. Seidel and B. Wrackmeyer, *Chem. Ber.*, 1990, **124**, 1003.
160. U. Herzog and G. Rheinwald, *J. Organomet. Chem.*, 2001, **627**, 23.
161. U. Herzog and G. Rheinwald, *J. Organomet. Chem.*, 2002, **648**, 220.
162. U. Herzog, U. Böhme, G. Roewer, G. Rheinwald and H. Lang, *J. Organomet. Chem.*, 2000, **602**, 193.
163. R. L. Lambert and D. Seyferth, *J. Am. Chem. Soc.*, 1972, **94**, 9246.
164. U. Herzog, U. Böhme, E. Brendler and G. Rheinwald, *J. Organomet. Chem.*, 2001, **630**, 139.
165. U. Herzog, U. Böhme and G. Rheinwald, *J. Organomet. Chem.*, 2001, **627**, 144.

166. E. Kupče, E. Liepinš, A. Lapsina, I. Urtane, G. Zelvans and E. Lukevics, *J. Organomet. Chem.*, 1985, **279**, 343.
167. U. Herzog and H. Borrmann, *J. Organomet. Chem.*, 2003, **675**, 42.
168. R. Köster, G. Seidel and B. Wrackmeyer, *Chem. Ber.*, 1989, **122**, 1825.
169. B. Wrackmeyer, S. V. Gruener and A. S. Zolotareva, *Z. Naturforsch.*, 2003, **58b**, 1035.
170. B. Wrackmeyer and O. L. Tok, *Magn. Reson. Chem.*, 2002, **40**, 406.
171. B. Wrackmeyer, O. L. Tok and Y. N. Bubnov, *J. Organomet. Chem.*, 1999, **580**, 234.
172. R. Köster, G. Seidel, R. Boese and B. Wrackmeyer, *Chem. Ber.*, 1988, **121**, 597.
173. R. Köster, G. Seidel, B. Wrackmeyer and K. Horchler, *Chem. Ber.*, 1990, **123**, 1253.
174. R. Köster, G. Seidel, B. Wrackmeyer, K. Horchler and D. Schlosser, *Angew. Chem. Int. Ed. Engl.*, 1989, **28**, 918.
175. B. Wrackmeyer, G. Kehr and J. Süß, *Chem. Ber.*, 1993, **126**, 2221.
176. B. Wrackmeyer, G. Kehr, S. Willbold and S. Ali, *J. Organomet. Chem.*, 2002, **646**, 125.
177. B. Wrackmeyer, K. Shahid and S. Ali, *Z. Naturforsch.*, 2005, **60b**, 590.
178. B. Wrackmeyer and J. Süß, *Main Group Met. Chem.*, 1996, **19**, 39.
179. B. Wrackmeyer, O. L. Tok and W. Milius, *Appl. Organomet. Chem.*, 2006, **20**, 443.
180. N. S. Hosmane, N. N. Sirmokadan and M. N. Mollenhauer, *J. Organomet. Chem.*, 1985, **279**, 359.
181. B. Wrackmeyer, H. E. Maisel, W. Milius, M. H. Bhatti and S. Ali, *J. Organomet. Chem.*, 2003, **669**, 72.
182. B. Wrackmeyer, O. L. Tok, A. Khan and A. Badshah, *Appl. Organomet. Chem.*, 2005, **19**, 1249.
183. B. Wrackmeyer, O. L. Tok and Y. N. Bubnov, *Angew. Chem. Int. Ed.*, 1999, **38**, 124.
184. B. Wrackmeyer, O. L. Tok and Y. N. Bubnov, *Appl. Organomet. Chem.*, 2004, **18**, 43.
185. B. Wrackmeyer, O. L. Tok, A. Khan and A. Badshah, *Z. Naturforsch.*, 2004, **60b**, 251.
186. R. Köster, G. Seidel, R. Boese and B. Wrackmeyer, *Chem. Ber.*, 1986, **120**, 669.
187. E. V. Bakhmutova, A. Cruz, R. Ramirez-Trejo, R. Contreras and B. Wrackmeyer, *Magn. Reson. Chem.*, 2001, **39**, 739.
188. B. Wrackmeyer, H. E. Maisel, W. Milius, A. Badshah, E. Molla and A. Mottalib, *J. Organomet. Chem.*, 2000, **602**, 45.
189. B. Wrackmeyer, A. Badshah, E. Molla and A. Mottalib, *J. Organomet. Chem.*, 1999, **584**, 98.
190. B. Wrackmeyer, K. Wagner, A. Sebald, H. Merwin and R. Boese, *Magn. Reson. Chem.*, 1991, **29**, S3.
191. B. Wrackmeyer, *J. Organomet. Chem.*, 1989, **364**, 331.
192. B. Wrackmeyer, G. Kehr and R. Boese, *Chem. Ber.*, 1992, **125**, 643.
193. B. Wrackmeyer, H. Maisel, W. Milius and M. Herberhold, *J. Organomet. Chem.*, 2003, **680**, 271.
194. B. Wrackmeyer, M. H. Bhatti, S. Ali, O. L. Tok and Y. N. Bubnov, *J. Organomet. Chem.*, 2002, **657**, 146.
195. V. Wray and L. Ernst, *J. Magn. Reson.*, 1980, **40**, 55.
196. C. Beyer, U. Böhme, C. Pietzsch and G. Roewer, *J. Organomet. Chem.*, 2002, **654**, 187.
197. U. Herzog and R. West, *Macromolecules*, 1999, **32**, 2210.
198. V. I. Dodero, T. N. Mitchell and J. C. Podestá, *Organometallics*, 2003, **22**, 856.
199. E. Kupče, B. Wrackmeyer and P. Granger, *J. Magn. Reson.*, 1992, **100**, 401.
200. R. Köster, G. Seidel, R. Boese and B. Wrackmeyer, *Chem. Ber.*, 1988, **121**, 709.
201. R. Köster, G. Seidel and R. Boese, *Chem. Ber.*, 1990, **123**, 2109.
202. R. Köster, G. Seidel, R. Boese and B. Wrackmeyer, *Chem. Ber.*, 1988, **121**, 1955.
203. B. Wrackmeyer, O. L. Tok, M. H. Bhatti and S. Ali, *Collect. Czech Chem. Commun.*, 2002, **67**, 822.
204. B. Wrackmeyer, O. L. Tok, K. Shahid and S. Ali, *Inorg. Chim. Acta*, 2004, **357**, 1103.
205. B. Wrackmeyer, *Heteroatom Chem.*, 2006, **17**, 188.
206. B. Wrackmeyer, G. Kehr, J. Süß and E. Molla, *J. Organomet. Chem.*, 1999, **577**, 82.
207. B. Wrackmeyer, O. L. Tok, W. Milius, A. Khan and A. Badshah, *Appl. Organomet. Chem.*, 2006, **20**, 99.
208. B. Wrackmeyer, H. Maisel and W. Milius, *Chem. Ber.*, 1997, **130**, 1349.
209. B. Wrackmeyer, G. Kehr, J. Süß and E. Molla, *J. Organomet. Chem.*, 1998, **562**, 207.
210. M. Herberhold, S. Gerstmann and B. Wrackmeyer, *Phosphorus Sulfur Silicon*, 1998, **134/135**, 255.
211. M. Herberhold, S. Gerstmann and B. Wrackmeyer, *Phosphorus Sulfur Silicon*, 1996, **113**, 89.
212. M. Herberhold, S. Gerstmann and B. Wrackmeyer, *Z. Naturforsch.*, 1998, **53b**, 573.
213. B. Wrackmeyer, O. L. Tok, G. Guldner and S. V. Gruener, *Appl. Organomet. Chem.*, 2003, **17**, 860.

214. B. Wrackmeyer, *J. Organomet. Chem.*, 1979, **166**, 353.
215. F. Hölzl and B. Wrackmeyer, *J. Organomet. Chem.*, 1979, **179**, 397.
216. B. Wrackmeyer and G. Kehr, *Main Group Met. Chem.*, 1993, **16**, 305.
217. B. Wrackmeyer, G. Kehr, D. Wettinger and W. Milius, *Main Group Met. Chem.*, 1993, **16**, 445.
218. B. Wrackmeyer, O. L. Tok, M. H. Bhatti, K. Shahid and S. Ali, *Z. Naturforsch.*, 2003, **58b**, 607.
219. A. Sebald and B. Wrackmeyer, *Spectrochim. Acta*, 1981, **37A**, 365.
220. B. Wrackmeyer, W. Milius and A. Badshah, *J. Organomet. Chem.*, 2002, **656**, 97.
221. B. Wrackmeyer, G. Kehr and H. Zhou, *Main Group Met. Chem.*, 1992, **15**, 89.
222. B. Wrackmeyer and J. Süß, *Z. Naturforsch.*, 2002, **57b**, 741.
223. M. Herberhold, U. Berthold, W. Milius and B. Wrackmeyer, *Z. Naturforsch.*, 1996, **51b**, 1283.
224. F. J. Zuno-Cruz, A. L. Carrasco and M. J. Rosales-Hoz, *Polyhedron*, 2002, **21**, 1105.
225. B. Biernat and T. Szymańska-Buzar, *J. Organomet. Chem.*, 2005, **690**, 4656.
226. P. B. Hitchcock, M. F. Lappert and M. Layh, *Inorg. Chim. Acta*, 1998, **269**, 181.
227. P. B. Hitchcock, M. F. Lappert and S. Tian, *J. Organomet. Chem.*, 1997, **549**, 1.
228. M. M. Corradi, A. D. Frankland, P. B. Hitchcock, M. F. Lappert and G. A. Lawless, *Chem. Commun.*, 1996, 2323.
229. B. Wrackmeyer, H. E. Maisel and M. Herberhold, *J. Organomet. Chem.*, 2001, **637–639**, 727.
230. M. Herberhold, B. Distler, H. Maisel, W. Milius, B. Wrackmeyer and P. Zanello, *Z. Anorg. Allg. Chem.*, 1996, **622**, 1515.
231. B. Wrackmeyer, E. V. Klimkina and W. Milius, *Inorg. Chem. Commun.*, 2004, **7**, 412.
232. B. Wrackmeyer, E. V. Klimkina, W. Milius, O. L. Tok and M. Herberhold, *Inorg. Chim. Acta*, 2005, **358**, 1420.
233. B. Wrackmeyer, E. V. Klimkina, H. E. Maisel, W. Milius and M. Herberhold, *Inorg. Chim. Acta*, 2004, **357**, 1703.
234. B. Wrackmeyer, E. V. Klimkina and W. Milius, *Inorg. Chem. Commun.*, 2006, **9**, 716.
235. B. Wrackmeyer, E. V. Klimkina and W. Milius, *Struct. Chem.*, 2004, **15**, 333.
236. R. Köster, G. Seidel, B. Wrackmeyer and D. Schlosser, *Chem. Ber.*, 1989, **122**, 2055.

APPENDICES

The tables of coupling constants in this section summarize all types of coupling constants with two exceptions. Coupling constants to sp² hybridized silicon are in Table 3 and the multiple-bond coupling constants with signs are in Table 6.

Most of the values in the tables are written without sign. These couplings were measured in absolute value.

Where two numbers for one coupling in one reference are shown, the values were taken from both silicon and carbon spectra. Differences can be ascribed to different experimental conditions.

Few compounds were measured in several papers. Differences in the values of the couplings could be caused by a precision of detection, different solvents and concentrations of the samples and finally by different temperatures.

The precision of the coupling constant values is given as in the original papers.

The entries are sorted according to atomic weight of the compound (sorted from lightest to heaviest), then follows number of silicon atoms in the compound, number of bonds of silicon(s) to atoms different from carbon and kind of the atom(s) bonded to silicon(s). The “sorting weight” of the atoms bonded to silicon is in the following order: C, H, B, Si, Ge, Sn, Pb, N, P, O, S, Se, Te, F, Cl, Br and I.

Sometimes higher sorting classes are used: bond to a cycle, bond to a multi-cycle, bond within a cycle, bond within a multi-cycle, Si(sp³)–C(sp²) bond and finally Si(sp³)–C(sp). The size of the cycle and number of bonds of each kind are taken into account. These sorting criteria were not applied to the table “Complexes” in Appendix D.

The following abbreviations are used in the tables:

Me:	CH ₃
Et:	CH ₂ –CH ₃
Vi:	CH=CH ₂
Pr:	(CH ₂) ₂ –CH ₃
<i>i</i> Pr:	CH(CH ₃) ₂
All:	CH ₂ –CH=CH ₂
Bu, <i>n</i> Bu:	(CH ₂) ₃ –CH ₃
<i>t</i> Bu:	C(CH ₃) ₃
<i>i</i> Pent:	CH ₂ –CH ₂ –C(H)Me ₂
CN:	C≡N
CO:	C=O
Ph:	C ₆ H ₅

APPENDIX A

Tables of silicon–carbon coupling constants in molecules containing Si(sp³)–C(sp³) bonds only.

Table A1. Compounds with Si–C or Si–H bonds

Compound	Coupling	Coupling value	Reference
Me ₄ Si	¹ J(Si, C)	–50	71
	¹ J(Si, C)	–50	39
	¹ J(Si, C)	–52	35
	¹ J(Si, C)	50.3	68
	¹ J(Si, C)	50.7	91
	¹ J(Si, C)	51.0	72
	¹ J(Si, C)	50.8	70
	¹ J(Si, C)	51.0	66
	¹ J(Si, C)	50.845	14
Me ₃ Si–Pr	¹ J(Si, C(Pr))	51.4	80
Me ₃ Si–CH ₂ Cl	¹ J(Si, C(CH ₂))	51.3	74
	¹ J(Si, C(Me))	52.2	
Me ₃ Si– <i>t</i> Bu	¹ J(Si, C(<i>t</i> Bu))	57.0	66
	¹ J(Si, C(Me))	51.6	
Et ₄ Si	¹ J(Si, C)	50.2	68

Table A1 (Continued)

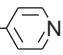
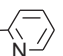
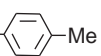
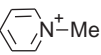
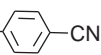
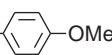
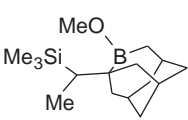
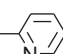
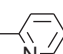
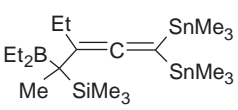
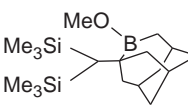
Compound	Coupling	Coupling value	Reference
$\text{Me}_3\text{Si}-\text{CH}_2-\text{Ph}$	$^1J(\text{Si}, \text{C}(\text{CH}_2))$	46.1	92
	$^1J(\text{Si}, \text{C}(\text{Me}))$	51.4	
	$^1J(\text{Si}, \text{C}(\text{CH}_2))$	47.8	80
$\text{Me}_3\text{Si}-\text{CH}_2-$ 	$^1J(\text{Si}, \text{C}(\text{CH}_2))$	41.8	93
	$^1J(\text{Si}, \text{C}(\text{Me}))$	51.9	
$\text{Me}_3\text{Si}-\text{CH}_2-$ 	$^1J(\text{Si}, \text{C}(\text{CH}_2))$	45.0	115
	$^1J(\text{Si}, \text{C}(\text{Me}))$	52.0	
$\text{Me}_3\text{Si}-\text{CH}_2-$ 	$^1J(\text{Si}, \text{C}(\text{CH}_2))$	46.5	92
	$^1J(\text{Si}, \text{C}(\text{Me}))$	51.3	
$\text{Me}_3\text{Si}-\text{C}(=\text{O})\text{Ph}$	$^1J(\text{Si}, \text{C}(\text{C}=\text{O}))$	63	88
$\text{Me}_3\text{Si}-\text{CH}_2-$ 	$^1J(\text{Si}, \text{C}(\text{CH}_2))$	35.9	93
	$^1J(\text{Si}, \text{C}(\text{Me}))$	52.7	
$\text{Me}_3\text{Si}-\text{CH}_2-$ 	$^1J(\text{Si}, \text{C}(\text{CH}_2))$	43.8	92
	$^1J(\text{Si}, \text{C}(\text{Me}))$	51.8	
$\text{Me}_3\text{Si}-\text{CH}_2-$ 	$^1J(\text{Si}, \text{C}(\text{CH}_2))$	46.9	92
	$^1J(\text{Si}, \text{C}(\text{Me}))$	51.3	
	$^1J(\text{Si}, \text{C}(\text{Me}))$	49.6	116
$\text{Me}_3\text{Si}-$ 	$^1J(\text{Si}, \text{C}(\text{CH}))$	47.0	115
$\text{Me}_3\text{Sn}-$ 	$^1J(\text{Si}, \text{C}(\text{Me}))$	52.0	
$\text{Me}_3\text{Si}-\text{CH}_2-\text{PbMe}_3$	$^1J(\text{Si}, \text{C}(\text{CH}_2))$	−51.2	42
	$^1J(\text{Si}, \text{C}(\text{Me}))$	−51.2	
$\text{Me}_3\text{Si}-\text{CH}_2-\text{PbEt}_3$	$^1J(\text{Si}, \text{C}(\text{CH}_2))$	−51.6	42
	$^1J(\text{Si}, \text{C}(\text{Me}))$	−51.2	
	$^1J(\text{Si}, \text{C}(\text{Me}))$	51.0	117
$\text{Me}_3\text{Si}-\text{C}(\text{PbMe}_3)_3$	$^1J(\text{Si}, \text{C}(\text{C}-\text{Si}))$	−39.1	42
	$^1J(\text{Si}, \text{C}(\text{Me}))$	−50.5	
$(\text{Me}_3\text{Si})_2\text{CH}_2$	$^1J(\text{Si}, \text{C}(\text{CH}_2))$	45.0	66
	$^1J(\text{Si}, \text{C}(\text{Me}))$	50.6	
	$^1J(\text{Si}, \text{C}(\text{Me}))$	50.5	116

Table A1 (Continued)

Compound	Coupling	Coupling value	Reference
(Me ₃ Si) ₂ CH–SnMe ₃	¹ J(Si, C(CH))	–41.2	42
	¹ J(Si, C(Me))	–50.4	
(Me ₃ Si) ₂ CH–PbMe ₃	¹ J(Si, C(CH))	–43.1	42
	¹ J(Si, C(Me))	–50.7	
(Me ₃ Si–CH ₂) ₂ PbMe ₂	¹ J(Si, C(CH ₂))	–50.1	42
	¹ J(Si, C(Me))	–51.2	
(Me ₃ Si–CH ₂) ₂ PbEt ₂	¹ J(Si, C(CH ₂))	–51.2	42
	¹ J(Si, C(Me))	–51.2	
(Me ₃ Si) ₃ CH	¹ J(Si, C(CH))	38.7	66
	¹ J(Si, C(Me))	50.6	81
	¹ J(Si, C(CH))	38.7	
	¹ J(Si, C(Me))	50.6	118
	¹ J(Si, C(CH))	37.6	
	¹ J(Si, C(Me))	51.0	
	¹ J(Si, C(C))	38.0	66
(Me ₃ Si) ₃ C–Me	¹ J(Si, C(Me))	51.2	42
	¹ J(Si, C(Sn))	–31.8	
(Me ₃ Si) ₃ C–SnMe ₃	¹ J(Si, C(Me))	–50.9	42
	¹ J(Si, C(Pb))	–35.8	
(Me ₃ Si) ₃ C–PbMe ₃	¹ J(Si, C(Me))	–50.8	42
	¹ J(Si, C(CH ₂))	–50.7	
(Me ₃ Si–CH ₂) ₃ Pb–Me	¹ J(Si, C(Me))	–51.0	42
	¹ J(Si, C(CH ₂))	–50.8	
(Me ₃ Si–CH ₂) ₃ Pb–Et	¹ J(Si, C(Me))	–51.2	42
	¹ J(Si, C(CSi ₄))	30.9	
(Me ₃ Si) ₄ C	¹ J(Si, C(Me))	51.5	66
	¹ J(Si, C(CSi ₄))	–30.0	42
	¹ J(Si, C(Me))	–51.6	
[(Me ₃ Si) ₂ CH] ₂ SnMe ₂	¹ J(Si, C(CH))	–40.3	42
	¹ J(Si, C(Me))	–50.7	
[(Me ₃ Si) ₂ CH] ₂ PbMe ₂	¹ J(Si, C(CH))	–42.5	42
	¹ J(Si, C(Me))	–51.2	
[(Me ₃ Si–CH ₂) ₄ Pb	¹ J(Si, C(CH ₂))	–50.1	42
	¹ J(Si, C(Me))	–50.7	
<i>Si–H bond</i>			
Me ₃ Si–H	¹ J(Si, C)	50.8	70

Table A2. Compounds with Si–Si or Si–Sn bonds and possible Si–H bonds

Me ₃ Si–SiMe ₃	¹ J(Si, C)	43.6	70
	² J(Si, C)	5.8	
(Me ₃ Si(a)) ₂ Si(b)Me ₂	¹ J(Si(a), C)	43.8	119
	¹ J(Si(b), C)	37.0	
(Me ₃ Si(a)) ₃ Si(b)Me	¹ J(Si(a), C(Me))	43.9	120
	¹ J(Si(b), C(Me))	33.4	
	² J(Si(b), C(Me))	5.0	
(Me ₃ Si) ₄ Si	¹ J(Si, C)	44.7	119
	¹ J(Si, C)	44.4	120
	¹ J(Si, C)	–49.0	42
(Me ₃ Si) ₃ Si–Si(SiMe ₃) ₃	¹ J(Si, C)	42.3	121
Me ₃ Si(a)–Si(b)Me ₂ H	¹ J(Si(a), C)	44.6	119
	¹ J(Si(b), C)	43.8	
(Me ₃ Si(a)) ₃ Si(b)H	¹ J(Si(a), C(Me))	45.3	120
	² J(Si(b), C(Me))	4.6	
(Me ₃ Sn) ₂ SiMe ₂	¹ J(Si, C)	–37.0	122
	² J(Si, C)	5.7	
(Me ₃ Sn) ₄ Si	² J(Si, C)	4.9	122

Table A3. Compounds with Si–N or Si–P bonds and possible Si–Si or Si–H bonds

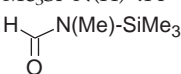
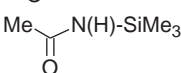
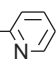
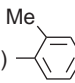
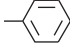
<i>Si–N bond(s)</i>			
Me ₃ Si–N(H)–Pr	¹ J(Si, C)	56.5	78
Me ₃ Si–N(H)– <i>i</i> Pr	¹ J(Si, C)	56.5	78
 H–C(=O)–N(Me)–SiMe ₃	¹ J(Si, C)	57.5	78
 Me–C(=O)–N(H)–SiMe ₃	¹ J(Si, C)	57.8	78
Me ₃ Si–N(H)– <i>t</i> Bu	¹ J(Si, C)	56.4	78
		56.5	80
Me ₃ Si–NEt ₂	¹ J(Si, C)	56.5	78
Me ₂ (<i>i</i> Pr)Si–N(H)– <i>i</i> Pr	¹ J(Si, C(<i>i</i> Pr))	60.0	80
	¹ J(Si, C(Me))	55.6	
Me ₂ (thex)Si–NH ₂	¹ J(Si, C(thex))	62.1	80
	¹ J(Si, C(Me))	55.3	
Me ₂ (<i>t</i> Bu)Si–N(H)–Et	¹ J(Si, C(<i>t</i> Bu))	61.0	80
	¹ J(Si, C(Me))	55.5	
Me ₃ Si–N(H)–C(Et)Me ₂	¹ J(Si, C)	55.7	80
Me ₃ Si–N(H)–Ph	¹ J(Si, C)	57.3	78
		56.7	80
Me ₃ Si–N(H)– 	¹ J(Si, C)	58.0	115
Me ₂ (<i>i</i> Pr)Si–N(H)– <i>t</i> Bu	¹ J(Si, C(<i>i</i> Pr))	60.0	80
	¹ J(Si, C(Me))	55.6	
Me ₂ (<i>t</i> Bu)Si–N(H)– <i>i</i> Pr	¹ J(Si, C(Me))	55.0	80
Me ₃ Si–NPr ₂	¹ J(Si, C)	56.7	78
 Me–C ₆ H ₄ –	¹ J(Si, C)	57.2	80
Me ₃ Si–N(H)– 			

Table A3 (Continued)

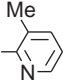
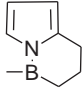
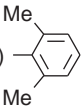
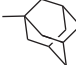
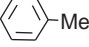

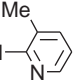
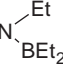
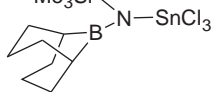
Me ₃ Si-N(H)- 	¹ J(Si, C)	58.6	115
Me ₂ (thex)Si-N(H)-Et	¹ J(Si, C(thex)) ¹ J(Si, C(Me))	61.6 55.5	80
Me ₃ Si-N(H)- 	¹ J(Si, C)	59.9	123
Me ₃ Si-N(H)- 	¹ J(Si, C)	57.2	80
Me ₂ (thex)Si-N(H)-iPr	¹ J(Si, C(thex)) ¹ J(Si, C(Me))	62.1 55.6	80
Me ₃ Si-N(H)-CMe ₂ -CH ₂ -N(H)-iPr	¹ J(Si, C)	57.8	80
SiMe ₃ -N(H)- 	¹ J(Si, C)	55.6	80
Me ₃ Si-N(H)-CH(Ph)Me	¹ J(Si, C)	55.9	80
Me ₃ Si-N(H)-P(<i>t</i> Bu) ₂	¹ J(Si, C)	58.8	124
Me ₃ Si-N(H)-SO ₂ - 	¹ J(Si, C)	58.5	78
Me ₃ Si-N(<i>t</i> Bu)-SnMe ₃	¹ J(Si, C)	55.2	125
Me ₃ Si-N()Me ₃ Sn	¹ J(Si, C)	56.2	115
Me ₃ Si-N()Me ₃ Sn	¹ J(Si, C)	56.2	115
Me ₃ Si-N(<i>t</i> Bu)-SnCl ₃	¹ J(Si, C) ² J(Si, C)	56.6 1.9	125
Me ₂ (<i>t</i> Bu)Si-N(H)-PbMe ₃	¹ J(Si, C(<i>t</i> Bu)) ¹ J(Si, C(Me))	58.9 53.4	126
Me ₃ Si-N()Me ₃ Sn	¹ J(Si, C)	55.6	127
Me ₃ Si-N()SnCl ₃	¹ J(Si, C)	57.2	125

Table A3 (Continued)

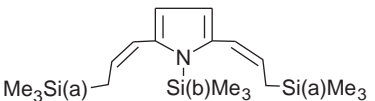
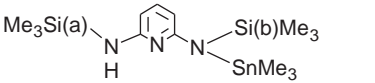
$\text{Me}_3\text{Si}-\text{N}(\text{S}-\text{iPr})-\text{BiPr}_2$	$^1J(\text{Si}, \text{C})$	55.0	127
$\text{Me}_3\text{Sn}-\text{N}(\text{S}-\text{iPr})-\text{BiPr}_2$	$^1J(\text{Si}, \text{C}) (-55^\circ\text{C})$	56.6	
	$^1J(\text{Si}, \text{C}) (-55^\circ\text{C})$	56.6	
$\text{Me}_3\text{Si}(\text{a})-\text{Si}(\text{b})\text{Me}_2-\text{NMe}_2$	$^1J(\text{Si}(\text{a}), \text{C})$	42.9	128
	$^1J(\text{Si}(\text{b}), \text{C})$	45.8	
$(\text{Me}_3\text{Si})_2\text{NH}$	$^1J(\text{Si}, \text{C})$	56.2	70
	$^1J(\text{Si}, \text{C})$	56.3	77
	$^1J(\text{Si}, \text{C})$	56.2	78
$(\text{Me}_3\text{Si})_2\text{NNa}$	$^1J(\text{Si}, \text{C})$	51.9	79
$\text{Me}_2(\text{tBu})\text{Si}(\text{a})-\text{N}(\text{H})-\text{Si}(\text{b})\text{Me}_3$	$^1J(\text{Si}(\text{a}), \text{C}(\text{tBu}))$	61.4	80
	$^1J(\text{Si}(\text{a}), \text{C}(\text{Me}))$	54.9	
	$^1J(\text{Si}(\text{b}), \text{C}(\text{Me}))$	56.2	
$[(\text{Me}_3\text{Si})_2\text{N}]_2\text{Ge}$	$^1J(\text{Si}, \text{C})$	55.85	129
$\text{Me}_2(\text{thex})\text{Si}(\text{a})-\text{N}(\text{H})-\text{Si}(\text{b})\text{Me}_3$	$^1J(\text{Si}(\text{a}), \text{C}(\text{thex}))$	62.1	80
	$^1J(\text{Si}(\text{a}), \text{C}(\text{Me}))$	55.0	
	$^1J(\text{Si}(\text{b}), \text{C}(\text{Me}))$	56.1	
$(\text{Me}_3\text{Si})_2\text{N}-\text{SnMe}_3$	$^1J(\text{Si}, \text{C})$	55.1	125
$(\text{Me}_3\text{Si})_2\text{N}-\text{SnCl}_3$	$^1J(\text{Si}, \text{C})$	56.4	125
	$^1J(\text{Si}, \text{C}(\text{CH}))$	45.2	130
	$^1J(\text{Si}(\text{a}), \text{C}(\text{Me}))$	52.0	
	$^1J(\text{Si}(\text{b}), \text{C}(\text{Me}))$	57.8	
$\text{Me}_2\text{Si}(\text{N}(\text{H})\text{Pr})_2$	$^1J(\text{Si}, \text{C})$	64.8	78
$\text{Me}_2\text{Si}[\text{N}(\text{H})\text{iPr}]_2$	$^1J(\text{Si}, \text{C})$	65.0	80
$\text{Me}_2\text{Si}[\text{N}(\text{H})\text{tBu}]_2$	$^1J(\text{Si}, \text{C})$	64.9	78
	$^1J(\text{Si}, \text{C})$	65.3	80
$\text{Me}_2\text{Si}(\text{N}(\text{H})\text{Ph})_2$	$^1J(\text{Si}, \text{C})$	67.0	78
$\text{Me}_3\text{Si}-\text{N}(\text{H})-\text{C}(=\text{O})-\text{N}(\text{H})-\text{SiMe}_3$	$^1J(\text{Si}, \text{C})$	57.7	78
$[\text{Me}_3\text{Si}-\text{N}(\text{H})-\text{CH}_2]_2$	$^1J(\text{Si}, \text{C})$	56.0	80
$\text{Me}_3\text{Si}(\text{a})-\text{N}(\text{H})-\text{CMe}_2-\text{CH}_2-\text{N}(\text{H})-\text{Si}(\text{b})\text{Me}_3$	$^1J(\text{Si}(\text{a}), \text{C})$	56.0	80
	$^1J(\text{Si}(\text{b}), \text{C})$	54.6	
$\text{Me}_3\text{Si}-\text{N}(\text{H})-\text{N}(\text{H})-\text{SiMe}_3$	$^1J(\text{Si}, \text{C})$	58.5	115
$[\text{Me}_2(\text{tBu})\text{Si}-\text{N}(\text{H})-\text{CH}_2]_2$	$^1J(\text{Si}, \text{C})$	55.6	80
$(\text{Me}_3\text{Si})_2\text{N}-\text{TiCl}_3$	$^1J(\text{Si}, \text{C})$	56.0	131
$[\text{Me}_3\text{Si}-\text{N}(\text{tBu})]_2\text{Sn}$	$^1J(\text{Si}, \text{C})$	53.8	132
	$^1J(\text{Si}(\text{a}), \text{C})$	58.1	115
	$^1J(\text{Si}(\text{b}), \text{C})$	56.7	
$[\text{Me}_3\text{Si}-\text{N}(\text{tBu})]_2\text{SnCl}_2$	$^1J(\text{Si}, \text{C})$	56.2	133,134
	$^nJ(\text{Si}, \text{C}(\text{tBu}))$	1.9	
$[\text{Me}_3\text{Si}-\text{N}(\text{tBu})]_2\text{Sn}[\text{C}\equiv\text{C}-\text{Me}]_2$	$^1J(\text{Si}, \text{C})$	55.6	133

Table A3 (Continued)

	$^1J(\text{Si}, \text{C})$	55.5	135
$[\text{Me}_3\text{Si}-\text{N}(\text{tBu})]_2\text{Sn}(\text{Cl})-\text{C}\equiv\text{C}-\text{Me}$	$^1J(\text{Si}, \text{C})$	55.8	133
	$^1J(\text{Si}, \text{C})$	56.5	136
	$^1J(\text{Si}, \text{C})$	56.5	136
$[\text{Me}_3\text{Si}-\text{N}(\text{tBu})]_2\text{P}$	$^1J(\text{Si}, \text{C})$	53.8	132
$[\text{Me}_3\text{Si}-\text{N}(\text{tBu})]_2-\text{Sn}(\text{Cl})-\text{C}\equiv\text{C}-\text{tBu}$	$^1J(\text{Si}, \text{C})$	55.9	133
	$^1J(\text{Si}, \text{C})$	54.8	132
	$^1J(\text{Si}, \text{C})$	56.2	115
	$^1J(\text{Si}, \text{C})$	57.9	133
	$^1J(\text{Si}, \text{C})$	56.1	133
	$^1J(\text{Si}, \text{C})$	56.5	133
	$^1J(\text{Si}, \text{C})$	54.9	132
	$^1J(\text{Si}, \text{C})$	56.3	133
	$^1J(\text{Si}, \text{C}(\text{Me}))$	55.6	133

Table A3 (Continued)

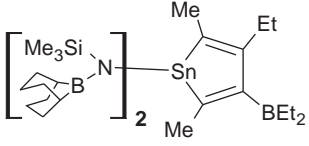
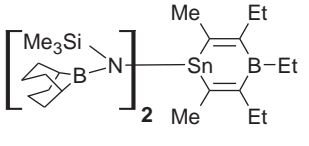
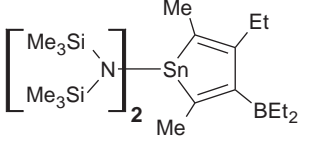
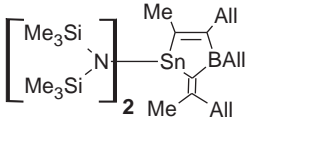
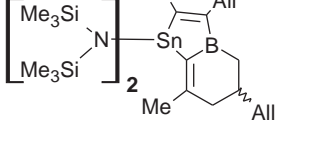
	$^1J(\text{Si}, \text{C}(\text{Me}))$	55.6	
	$^1J(\text{Si}, \text{C})$	55.6	133
(Et–N(H)–SiMe ₂) ₂	$^1J(\text{Si}, \text{C})$	47.2	80
Me ₃ Si–N ₃	$^1J(\text{Si}, \text{C})$	58.5	78
Me–Si[NMe ₂] ₃	$^1J(\text{Si}, \text{C})$	79.6	137
Me–Si(N(H)Pr) ₃	$^1J(\text{Si}, \text{C})$	75.3	78,137
Me–Si(N(H)Ph) ₃	$^1J(\text{Si}, \text{C})$	77.6	78
Me ₂ (Et ₃ Si–N(H))Si–N(H) <i>i</i> Pr	$^1J(\text{Si}, \text{C}(\text{Me}))$	56.1	80
(Me ₃ Si) ₃ N	$^1J(\text{Si}, \text{C})$	–56.8	138
	$^1J(\text{Si}, \text{C})$	56.1	81
[(Me ₃ Si) ₂ N] ₂ TiCl ₂	$^1J(\text{Si}, \text{C})$	56.8	131
[(Me ₃ Si) ₂ N] ₂ Sn	$^1J(\text{Si}, \text{C})$	54.7	132
[(Me ₃ Si) ₂ N] ₂ SnCl ₂	$^1J(\text{Si}, \text{C})$	56.3	133,134
[(Me ₃ Si) ₂ N] ₂ Sn[C≡C–Me] ₂	$^1J(\text{Si}, \text{C})$	55.7	133
[(Me ₃ Si) ₂ N] ₂ Pb	$^1J(\text{Si}, \text{C})$	54.4	132
[(Me ₃ Si) ₂ N] ₂ Sn[C≡C– <i>t</i> Bu] ₂	$^1J(\text{Si}, \text{C})$	55.7	133
	$^1J(\text{Si}, \text{C})$	55.2	133
	$^1J(\text{Si}, \text{C})$	55.6	133
	$^1J(\text{Si}, \text{C})$	55.3	133
	$^1J(\text{Si}, \text{C})$	55.3	
<i>Si–H bond</i>			
Me(H)Si[N(H)– <i>t</i> Bu] ₂	$^1J(\text{Si}, \text{C})$	64.3	80
<i>Si–Si bond(s)</i>			
Me ₃ Si(a)–Si(b)(NMe ₂)Me ₂	$^1J(\text{Si}(\text{a}), \text{C})$	42.9	128
	$^1J(\text{Si}(\text{b}), \text{C})$	45.8	

Table A3 (Continued)

$\text{Me}_3\text{Si(a)}-\text{Si(b)}(\text{NEt}_2)\text{Me}_2$	$^1J(\text{Si(a)}, \text{C})$	42.9	139
	$^1J(\text{Si(b)}, \text{C})$	46.9	
$[\text{Me}_2(\text{Et}_2\text{N})\text{Si}]_2$	$^1J(\text{Si}, \text{C})$	38.5	139
$(\text{Me}_3\text{Si(a)}-\text{Si(b)}\text{Me}_2)_2\text{NH}$	$^1J(\text{Si(a)}, \text{C})$	42	119
	$^1J(\text{Si(b)}, \text{C})$	46.6	
$(\text{Et}-\text{N(H)}-\text{Me}_2\text{Si})_2$	$^1J(\text{Si}, \text{C})$	47.2	80
$(i\text{Pr}-\text{N(H)}-\text{Me}_2\text{Si})_2$	$^1J(\text{Si}, \text{C})$	46.3	80
$(t\text{Bu}-\text{N(H)}-\text{Me}_2\text{Si})_2$	$^1J(\text{Si}, \text{C})$	47.0	80
$(\text{Me}-\text{CH}_2-\text{C(Me)H}-\text{N(H)}-\text{Me}_2\text{Si})_2$	$^1J(\text{Si}, \text{C})$	47.0	80
	$^1J(\text{Si}, \text{C})$	45.6	
$(\text{Ph}-\text{N(H)}-\text{Me}_2\text{Si})_2$	$^1J(\text{Si}, \text{C})$	47.0	80
$(\text{Me}_2(t\text{Bu})\text{Si}-\text{N(H)}-\text{Si(a)}\text{Me}_2)_2$	$^1J(\text{Si(a)}, \text{C})$	46.3	80
$[(i\text{Pr}-\text{N(H)})_2-\text{MeSi}]_2$	$^1J(\text{Si}, \text{C})$	52.8	80
$[(t\text{Bu}-\text{N(H)})_2-\text{SiMe}]_2$	$^1J(\text{Si}, \text{C})$	52.4	80
<i>Si-P bonds</i>			
$(\text{Me}_3\text{Si})_2\text{P}-\text{SnMe}_3$	$^1J(\text{Si}, \text{C})$	-49.3	140

Table A4. Compounds with Si-chalcogen bond(s) and possible Si-N or Si-Si bond(s)

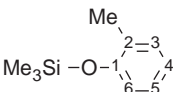
<i>Si-O bond(s)</i>			
$\text{Me}_3\text{Si}-\text{O}-\text{Me}$	$^1J(\text{Si}, \text{C})$	59.06	18
	$^2J(\text{Si}, \text{C})$	1.77	
$\text{Me}_3\text{Si}-\text{O}-\text{Et}$	$^1J(\text{Si}, \text{C})$	59.0	72,70
	$^1J(\text{Si}, \text{C})$	58.87	108
	$^2J(\text{Si}, \text{C})$	+1.67	
	$^3J(\text{Si}, \text{C})$	-2.46	
$\text{Me}_3\text{Si}-\text{O}-i\text{Pr}$	$^1J(\text{Si}, \text{C})$	58.84	108
	$^2J(\text{Si}, \text{C})$	+1.69	
	$^3J(\text{Si}, \text{C})$	-1.62	
$\text{Me}_3\text{Si}-\text{O}-t\text{Bu}$	$^1J(\text{Si}, \text{C})$	59.19	18
$\text{Me}_3\text{Si}-\text{O}-\text{Ph}$	$^1J(\text{Si}, \text{C})$	59.74	18
	$^2J(\text{Si}, \text{C})$	2.08	111
	$^3J(\text{Si}, \text{C})$	1.67	
	$^4J(\text{Si}, \text{C})$	0.33	
	$^5J(\text{Si}, \text{C})$	0.42	
$\text{Me}_3\text{Si}-\text{O}-\text{C}_6\text{H}_4-\text{Me}$	$^2J(\text{Si}, \text{C})$	2.12	111
	$^3J(\text{Si}, \text{C})$	1.64	
	$^4J(\text{Si}, \text{C})$	0.39	
	$^5J(\text{Si}, \text{C})$	0.49	
	$^2J(\text{Si}, \text{C(1)})$	2.12	112
	$^3J(\text{Si}, \text{C(2)})$	1.95	
	$^3J(\text{Si}, \text{C(6)})$	1.28	
	$^4J(\text{Si}, \text{C(3)})$	0.25	
	$^4J(\text{Si}, \text{C(5)})$	0.49	
	$^5J(\text{Si}, \text{C(4)})$	0.43	

Table A4 (Continued)

$\text{Me}_3\text{Si}-\text{O}-\text{C}_6\text{H}_4-\text{F}$	$^2J(\text{Si}, \text{C})$	2.12	111
	$^3J(\text{Si}, \text{C})$	1.62	
	$^4J(\text{Si}, \text{C})$	0.35	
	$^5J(\text{Si}, \text{C})$	0.48	
$\text{Me}_3\text{Si}-\text{O}-\text{C}_6\text{H}_4-\text{OMe}$	$^2J(\text{Si}, \text{C})$	2.15	111
	$^3J(\text{Si}, \text{C})$	1.58	
	$^4J(\text{Si}, \text{C})$	0.41	
	$^5J(\text{Si}, \text{C})$	0.53	
$\text{Me}_3\text{Si}-\text{O}-\text{C}_6\text{H}_4-\text{Cl}$	$^2J(\text{Si}, \text{C})$	2.15	111
	$^3J(\text{Si}, \text{C})$	1.67	
	$^4J(\text{Si}, \text{C})$	0.32	
	$^5J(\text{Si}, \text{C})$	0.63	
$\text{Me}_2(\text{tBu})\text{Si}-\text{O}-\text{C}_6\text{H}_5$	$^1J(\text{Si}, \text{C}(\text{tBu}))$	67.1	111
	$^1J(\text{Si}, \text{C}(\text{Me}))$	57.2	
	$^2J(\text{Si}, \text{C}(\text{Ph}))$	2.56	
	$^3J(\text{Si}, \text{C})$	1.53	
	$^4J(\text{Si}, \text{C})$	0.33	
	$^5J(\text{Si}, \text{C})$	0.41	
$i\text{Pr}_3\text{Si}-\text{O}-\text{C}\equiv\text{P}$	$^1J(\text{Si}, \text{C})$	51.3	141
	$^2J(\text{Si}, \text{C}(\text{C}\equiv))$	1.2	
$\text{Me}_3\text{Si}-\text{O}-\text{C}_6\text{H}_4-\text{NO}_2$	$^2J(\text{Si}, \text{C})$	2.01	111
	$^3J(\text{Si}, \text{C})$	1.87	
	$^4J(\text{Si}, \text{C})$	0.24	
	$^5J(\text{Si}, \text{C})$	0.37	
$\text{Me}_3\text{Si}-\text{O}-\text{C}_6\text{H}_4-\text{tBu}$	$^2J(\text{Si}, \text{C}(1))$	1.95	112
	$^3J(\text{Si}, \text{C}(2))$	2.69	
	$^3J(\text{Si}, \text{C}(6))$	1.83	
	$^4J(\text{Si}, \text{C}(3))$	0.25	
	$^4J(\text{Si}, \text{C}(5))$	0.20	
	$^5J(\text{Si}, \text{C}(4))$	0.25	
$\text{Me}_2(\text{tBu})\text{Si}-\text{O}-\text{C}_6\text{H}_4-\text{Me}$	$^1J(\text{Si}, \text{C}(\text{tBu}))$	67.1	111
	$^1J(\text{Si}, \text{C}(\text{Me}))$	57.2	
	$^2J(\text{Si}, \text{C}(\text{Ph}))$	2.56	
	$^3J(\text{Si}, \text{C})$	1.46	
	$^4J(\text{Si}, \text{C})$	0.39	
$\text{Me}_2(\text{tBu})\text{Si}-\text{O}-\text{C}_6\text{H}_4-\text{F}$	$^1J(\text{Si}, \text{C}(\text{tBu}))$	67.1	111
	$^1J(\text{Si}, \text{C}(\text{Me}))$	57.2	
	$^2J(\text{Si}, \text{C}(\text{Ph}))$	2.56	
	$^3J(\text{Si}, \text{C})$	1.46	
	$^4J(\text{Si}, \text{C})$	0.27	
	$^5J(\text{Si}, \text{C})$	0.45	
$\text{Me}_3\text{Si}-\text{O}-\text{C}_6\text{H}_4-\text{CF}_3$	$^2J(\text{Si}, \text{C})$	2.07	111
	$^3J(\text{Si}, \text{C})$	1.78	

Table A4 (Continued)

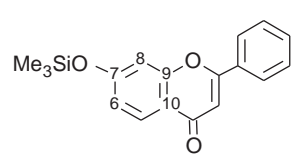
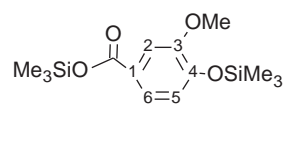
$\text{Me}_2(\text{tBu})\text{Si}-\text{O}-\text{C}_6\text{H}_4-\text{OMe}$	$^1J(\text{Si}, \text{C}(\text{tBu}))$	67.1	111
	$^1J(\text{Si}, \text{C}(\text{Me}))$	57.2	
	$^2J(\text{Si}, \text{C}(\text{Ph}))$	2.62	
	$^3J(\text{Si}, \text{C})$	1.40	
	$^4J(\text{Si}, \text{C})$	0.31	
	$^5J(\text{Si}, \text{C})$	0.39	
$\text{Me}_2(\text{tBu})\text{Si}-\text{O}-\text{C}_6\text{H}_4-\text{Cl}$	$^1J(\text{Si}, \text{C}(\text{tBu}))$	67.1	111
	$^1J(\text{Si}, \text{C}(\text{Me}))$	57.2	
	$^2J(\text{Si}, \text{C}(\text{Ph}))$	2.56	
	$^3J(\text{Si}, \text{C})$	1.53	
	$^4J(\text{Si}, \text{C})$	0.37	
	$^5J(\text{Si}, \text{C})$	0.52	
$\text{Me}_2(\text{tBu})\text{Si}-\text{O}-\text{C}_6\text{H}_4-\text{NO}_2$	$^1J(\text{Si}, \text{C}(\text{tBu}))$	67.8	111
	$^1J(\text{Si}, \text{C}(\text{Me}))$	57.2	
	$^2J(\text{Si}, \text{C}(\text{Ph}))$	2.56	
	$^3J(\text{Si}, \text{C})$	1.59	
$\text{Me}_3\text{Si}-\text{O}-\text{CHPh}_2$	$^1J(\text{Si}, \text{C})$	58.92	108
	$^2J(\text{Si}, \text{C})$	+1.40	
	$^3J(\text{Si}, \text{C}(\text{Ph}))$	1.89	
$\text{Me}_2(\text{tBu})\text{Si}-\text{O}-\text{C}_6\text{H}_4-\text{CF}_3$	$^1J(\text{Si}, \text{C}(\text{tBu}))$	67.1	111
	$^1J(\text{Si}, \text{C}(\text{Me}))$	57.2	
	$^2J(\text{Si}, \text{C}(\text{Ph}))$	2.56	
	$^3J(\text{Si}, \text{C})$	1.59	
	$^4J(\text{Si}, \text{C})$	0.37	
	$^5J(\text{Si}, \text{C})$	0.37	
	$^2J(\text{Si}, \text{C}(7))$	2.0	113
	$^3J(\text{Si}, \text{C}(6))$	1.8	
	$^3J(\text{Si}, \text{C}(8))$	1.8	
	$^4J(\text{Si}, \text{C}(9))$	0.4	
	$^5J(\text{Si}, \text{C}(10))$	0.4	
$\text{Me}_2\text{Si}(\text{OMe})_2$	$^1J(\text{Si}, \text{C})$	73.73	18
	$^2J(\text{Si}, \text{C})$	1.77	
$\text{Me}_2\text{Si}(\text{OEt})_2$	$^1J(\text{Si}, \text{C})$	73.0	72
$(\text{Me}_3\text{Si})_2\text{O}$	$^1J(\text{Si}, \text{C})$	60.0	70
	$^1J(\text{Si}, \text{C})$	59.5	77
	$^1J(\text{Si}, \text{C})$	59.60	17,142
	$^2J(\text{Si}, \text{C}(4))$	2.2	110
	$^2J(\text{Si}, \text{C}(\text{COO}))$	2.6	
	$^3J(\text{Si}, \text{C}(1))$	2.2	
	$^3J(\text{Si}, \text{C}(3))$	1.1	
	$^3J(\text{Si}, \text{C}(5))$	1.6	

Table A4 (Continued)

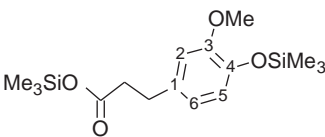
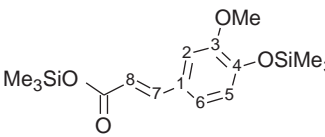
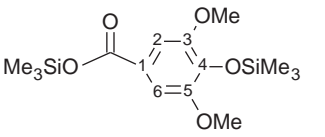
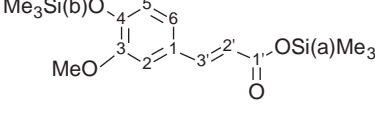
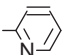
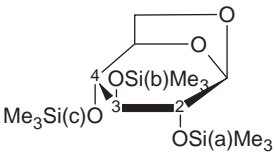
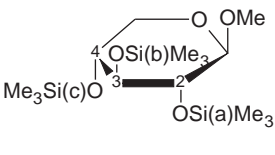
	$^2J(\text{Si}, \text{C}(4))$	2.4	110
	$^2J(\text{Si}, \text{C}(\text{CO}))$	3.0	
	$^3J(\text{Si}, \text{C}(3))$	1.3	
	$^3J(\text{Si}, \text{C}(5))$	1.5	
	$^3J(\text{Si}, \text{C}(\text{CH}_2))$	1.8	
	$^2J(\text{Si}, \text{C}(4))$	2.2	110
	$^2J(\text{Si}, \text{C}(\text{CO}))$	2.6	
	$^3J(\text{Si}, \text{C}(3))$	0.7	
	$^3J(\text{Si}, \text{C}(5))$	1.5	
	$^3J(\text{Si}, \text{C}(8))$	2.2	
	$^2J(\text{Si}, \text{C}(4))$	2.4	110
	$^2J(\text{Si}, \text{C}(\text{CO}))$	2.5	
	$^3J(\text{Si}, \text{C}(1))$	2.1	
	$^3J(\text{Si}, \text{C}(3, 5))$	1.2	
	$^2J(\text{Si}(\text{a}), \text{C}(1'))$	2.4	113
	$^2J(\text{Si}(\text{b}), \text{C}(4))$	2.4	
	$^3J(\text{Si}(\text{a}), \text{C}(2'))$	2.2	
	$^3J(\text{Si}(\text{b}), \text{C}(3))$	1.3	
	$^3J(\text{Si}(\text{b}), \text{C}(5))$	1.6	
	$^4J(\text{Si}(\text{a}), \text{C}(3'))$	0.4	
	$^4J(\text{Si}(\text{b}), \text{C}(2))$	0.5	
	$^4J(\text{Si}(\text{b}), \text{C}(6))$	0.5	
	$^5J(\text{Si}(\text{b}), \text{C}(1))$	0.5	
Me–Si(OMe) ₃	$^1J(\text{Si}, \text{C})$	97.15	18
	$^2J(\text{Si}, \text{C})$	1.32	
Me–Si(OEt) ₃	$^1J(\text{Si}, \text{C})$	96.2	72
	$^1J(\text{Si}, \text{C})$	97.0	
(EtO) ₃ Si–(CH ₂) ₂ – 	$^1J(\text{Si}, \text{C})$	96.6	144
	$^2J(\text{Si}(\text{a}), \text{C}(2))$	1.9–2.1	21
	$^2J(\text{Si}(\text{b}), \text{C}(3))$	1.9–2.1	
	$^2J(\text{Si}(\text{c}), \text{C}(4))$	1.9–2.1	
	$^3J(\text{Si}(\text{a}), \text{C}(3))$	2.4–2.6	
	$^3J(\text{Si}(\text{b}), \text{C}(3))$	1.2–1.4	
	$^3J(\text{Si}(\text{b}), \text{C}(4))$	1.2–1.4	
	$^2J(\text{Si}(\text{a}), \text{C}(2))$	1.9–2.1	21
	$^2J(\text{Si}(\text{b}), \text{C}(3))$	1.9–2.1	
	$^2J(\text{Si}(\text{c}), \text{C}(4))$	1.9–2.1	
	$^3J(\text{Si}(\text{a}), \text{C}(3))$	2.4–2.6	
	$^3J(\text{Si}(\text{b}), \text{C}(3))$	1.2–1.4	
	$^3J(\text{Si}(\text{b}), \text{C}(4))$	1.2–1.4	
	$^3J(\text{Si}(\text{c}), \text{C}(3))$	2.4–2.6	

Table A4 (Continued)

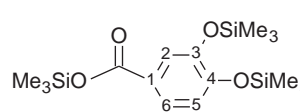
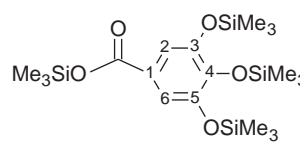
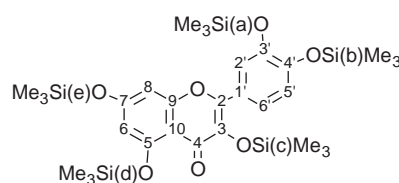
	$^2J(\text{Si}, \text{C}(3))$	2.1	110
	$^2J(\text{Si}, \text{C}(4))$	2.1	
	$^2J(\text{Si}, \text{C}(\text{COO}))$	2.6	
	$^3J(\text{Si}, \text{C}(1))$	2.2	
	$^3J(\text{Si}, \text{C}(2))$	1.5	
	$^3J(\text{Si}, \text{C}(3))$	1.8	
	$^3J(\text{Si}, \text{C}(4))$	1.8	
	$^3J(\text{Si}, \text{C}(5))$	1.5	
$(\text{MeO})_4\text{Si}$	$^2J(\text{Si}, \text{C})$	1.10	18
$(\text{EtO})_4\text{Si}$	$^2J(\text{Si}, \text{C})$	1.10	17,18,142
	$^3J(\text{Si}, \text{C})$	2.35	
$(\text{Me}_3\text{Si}(\text{a})-\text{O})_2\text{Si}(\text{b})\text{Me}_2$	$^1J(\text{Si}(\text{a}), \text{C})$	59.70	18
	$^1J(\text{Si}(\text{b}), \text{C})$	74.43	
	$^2J(\text{Si}, \text{C}(3, 5))$	2.1	110
	$^2J(\text{Si}, \text{C}(4))$	2.7	
	$^2J(\text{Si}, \text{C}(\text{COO}))$	2.8	
	$^3J(\text{Si}, \text{C}(1))$	2.2	
	$^3J(\text{Si}, \text{C}(2, 6))$	1.2	
	$^3J(\text{Si}, \text{C}(3, 5))$	1.4	
	$^3J(\text{Si}, \text{C}(4))$	2.3	
	$^2J(\text{Si}(\text{a}), \text{C}(3'))$	2.3	113
	$^2J(\text{Si}(\text{b}), \text{C}(4'))$	2.2	
	$^2J(\text{Si}(\text{c}), \text{C}(3))$	2.6	
	$^2J(\text{Si}(\text{d}), \text{C}(5))$	2.1	
	$^2J(\text{Si}(\text{e}), \text{C}(7))$	2.0	
	$^3J(\text{Si}(\text{a}), \text{C}(2'))$	1.3	
	$^3J(\text{Si}(\text{a}), \text{C}(4'))$	1.5	
	$^3J(\text{Si}(\text{b}), \text{C}(3'))$	1.8	
	$^3J(\text{Si}(\text{b}), \text{C}(5'))$	1.3	
	$^3J(\text{Si}(\text{c}), \text{C}(2))$	2.9	
	$^3J(\text{Si}(\text{c}), \text{C}(4))$	0.5	
	$^3J(\text{Si}(\text{d}), \text{C}(6))$	1.3	
	$^3J(\text{Si}(\text{d}), \text{C}(10))$	1.2	
	$^3J(\text{Si}(\text{e}), \text{C}(6))$	1.8	
	$^3J(\text{Si}(\text{e}), \text{C}(8))$	2.0	
	$^4J(\text{Si}(\text{a}), \text{C}(1'))$	0.5	
	$^4J(\text{Si}(\text{b}), \text{C}(6'))$	0.5	
	$^4J(\text{Si}(\text{c}), \text{C}(1'))$	0.5	
	$^4J(\text{Si}(\text{d}), \text{C}(7))$	0.6	
	$^4J(\text{Si}(\text{d}), \text{C}(4))$	0.2	
	$^4J(\text{Si}(\text{d}), \text{C}(9))$	0.5	
	$^5J(\text{Si}(\text{a}), \text{C}(6'))$	0.5	
	$^5J(\text{Si}(\text{b}), \text{C}(1'))$	0.5	
	$^5J(\text{Si}(\text{d}), \text{C}(8))$	0.5	
	$^6J(\text{Si}(\text{b}), \text{C}(2))$	0.5	
$(\text{Me}_3\text{Si}-\text{O})_4\text{Si}$	$^1J(\text{Si}, \text{C})$	59.8	70

Table A4 (Continued)

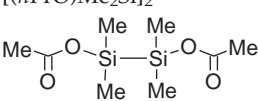
<i>Si–O and Si–H bond(s)</i>			
$\text{Me}_2(\text{H})\text{Si}-\text{O}-\text{C}_6\text{H}_5$	$^2J(\text{Si}, \text{C})$	2.20	111
	$^3J(\text{Si}, \text{C})$	2.41	
	$^4J(\text{Si}, \text{C})$	0.20	
	$^5J(\text{Si}, \text{C})$	0.43	
$\text{Me}_2(\text{H})\text{Si}-\text{O}-\text{C}_6\text{H}_4\text{Me}$	$^2J(\text{Si}, \text{C})$	2.20	111
	$^3J(\text{Si}, \text{C})$	2.30	
	$^4J(\text{Si}, \text{C})$	0.26	
	$^5J(\text{Si}, \text{C})$	0.49	
$\text{Me}_2(\text{H})\text{Si}-\text{O}-\text{C}_6\text{H}_4\text{F}$	$^2J(\text{Si}, \text{C})$	2.20	111
	$^3J(\text{Si}, \text{C})$	2.26	
$\text{Me}_2(\text{H})\text{Si}-\text{O}-\text{C}_6\text{H}_3(\text{OMe})_2$	$^2J(\text{Si}, \text{C})$	2.26	111
	$^3J(\text{Si}, \text{C})$	2.20	
	$^4J(\text{Si}, \text{C})$	0.29	
	$^5J(\text{Si}, \text{C})$	0.45	
$\text{Me}_2(\text{H})\text{Si}-\text{O}-\text{C}_6\text{H}_4\text{Cl}$	$^2J(\text{Si}, \text{C})$	2.14	111
	$^3J(\text{Si}, \text{C})$	2.35	
	$^4J(\text{Si}, \text{C})$	0.23	
	$^5J(\text{Si}, \text{C})$	0.49	
$\text{Me}_2(\text{H})\text{Si}-\text{O}-\text{C}_6\text{H}_4\text{NO}_2$	$^2J(\text{Si}, \text{C})$	2.01	111
	$^3J(\text{Si}, \text{C})$	2.68	
	$^5J(\text{Si}, \text{C})$	0.22	
$\text{Me}_2(\text{H})\text{Si}-\text{O}-\text{C}_6\text{H}_4\text{CF}_3$	$^2J(\text{Si}, \text{C})$	2.02	111
	$^3J(\text{Si}, \text{C})$	2.56	
<i>Si–O and Si–Si bond(s)</i>			
$\text{Me}_3\text{Si}(\text{a})-\text{Si}(\text{b})\text{Me}_2-\text{OMe}$	$^1J(\text{Si}(\text{a}), \text{C})$	43.9	128
	$^1J(\text{Si}(\text{b}), \text{C})$	48.0	
$\text{Me}_3\text{Si}(\text{a})-\text{Si}(\text{b})\text{Me}_2-\text{OEt}$	$^1J(\text{Si}(\text{a}), \text{C})$	43.6	128
	$^1J(\text{Si}(\text{b}), \text{C})$	48.0	
$\text{Me}_3\text{Si}(\text{a})-\text{Si}(\text{b})\text{Me}_2-\text{OnBu}$	$^1J(\text{Si}(\text{a}), \text{C})$	44.6	128
	$^1J(\text{Si}(\text{b}), \text{C})$	47.7	
$\text{Me}_3\text{Si}(\text{a})-\text{Si}(\text{b})\text{Me}_2-\text{OtBu}$	$^1J(\text{Si}(\text{a}), \text{C})$	44.0	128
	$^1J(\text{Si}(\text{b}), \text{C})$	47.6	
$(\text{Me}_3\text{Si}(\text{a}))_3\text{Si}(\text{b})-\text{OMe}$	$^1J(\text{Si}(\text{a}), \text{C}(\text{Me}))$	44.1	120
	$^2J(\text{Si}(\text{b}), \text{C}(\text{MeSi}))$	5.5	
$[(\text{MeO})\text{Me}_2\text{Si}]_2$	$^1J(\text{Si}, \text{C})$	48.4	128
$[(n\text{PrO})\text{Me}_2\text{Si}]_2$	$^1J(\text{Si}, \text{C})$	48.0	128
	$^1J(\text{Si}, \text{C})$	53.2	128
$[(i\text{PrO})\text{Me}_2\text{Si}]_2$	$^1J(\text{Si}, \text{C})$	48.0	128
$[(n\text{BuO})\text{Me}_2\text{Si}]_2$	$^1J(\text{Si}, \text{C})$	48.4	128
$[(t\text{BuO})\text{Me}_2\text{Si}]_2$	$^1J(\text{Si}, \text{C})$	47.7	128

Table A4 (Continued)

[(PhO)Me ₂ Si] ₂	¹ J(Si, C)	50.5	128
(Me ₃ Si(a)–Si(b)Me ₂) ₂ O	¹ J(Si(a), C)	43.8	119
	¹ J(Si(b), C)	48.0	
[(MeO) ₃ Si] ₃ Si(b)–OMe	² J(Si(b), C)	5.2	120
<i>Si–O and Si–N bond(s)</i>			
Me ₂ (EtO)Si–N(H)–Pr	¹ J(Si, C)	69.9	78
Me ₂ (EtO)Si–N(H)– <i>t</i> Bu	¹ J(Si, C)	69.5	78
Me ₂ (EtO)Si–N(H)–Ph	¹ J(Si, C)	70.6	78
Me ₂ (EtO)Si–NPr ₂	¹ J(Si, C)	70.2	78
Me ₃ Si(a)–O–NH–Si(b)Me ₃	¹ J(Si(a), C)	59.53	142
	¹ J(Si(b), C)	56.74	
	¹ J(Si(a), C)	59.53	17
	¹ J(Si(b), C)	56.74	
	¹ J(Si(a), C)	59.47	18
	¹ J(Si(b), C)	59.69	
	¹ J(Si(a), C)	59.5	79
	¹ J(Si(b), C)	56.7	
Me(EtO)Si(N(H)Ph) ₂	¹ J(Si, C)	82.8	78
Me(EtO) ₂ Si–N(H)– <i>t</i> Bu	¹ J(Si, C)	87.2	78
Me(EtO) ₂ Si–N(H)–Ph	¹ J(Si, C)	90.6	78
[Me ₃ Si–(OSiMe ₂) ₄ –O–Si(a)Me ₂] ₂ NH	¹ J(Si(a), C)	69.4	77
<i>Si–S bonds</i>			
(Me ₃ Si) ₂ S	¹ J(Si, C)	53.9	145
(Bu–S–Me ₂ Si) ₃ CH	¹ J(Si, C)	55.2	118
<i>Si–S and Si–Si bond(s)</i>			
Me ₃ Si(a)–Si(b)Me ₂ –SH	¹ J(Si(a), C)	44.5	145
	¹ J(Si(b), C)	42.8	
Me ₃ Si(a)–Si(b)Me ₂ –SLi	¹ J(Si(a), C)	41.3	145
	¹ J(Si(b), C)	42.3	
(Me ₃ Si(a)) ₂ Si(b)(Me)–SH	¹ J(Si(a), C)	45.2	145
	¹ J(Si(b), C)	35.9	
(Me ₃ Si(a)) ₂ Si(Me)–SK	¹ J(Si(a), C)	39.8	145
(Me ₃ Si(a)) ₃ Si–SH	¹ J(Si(a), C)	45.2	145
(Me ₃ Si(a)) ₃ Si–SK	¹ J(Si(a), C)	41.3	145
(Me ₃ Si(a)) ₃ Si–Si(SiMe ₃) ₂ –SK	¹ J(Si(a), C)	43.0	146
[Me(Bu–S) ₂ Si(a)] ₂ Si(b)Me ₂	¹ J(Si(b), C)	41.4	147
(Me ₃ Si(a)–Si(b)Me ₂) ₂ S	¹ J(Si(a), C)	46.6	145
	¹ J(Si(b), C)	44.4	
[(Me ₃ Si(a)) ₂ Si(b)Me] ₂ S	¹ J(Si(a), C)	46.5	145
	¹ J(Si(b), C)	39.1	
(Me ₃ Si(a)) ₃ Si–Si(Si(d)Me ₃) ₂ –S–SiMe ₃	¹ J(Si(a), C)	44.5	146
	¹ J(Si(d), C)	45.2	
[(Me ₃ Si(a)) ₃ Si–Si(SiMe ₃) ₂ –S] ₂ SiMe ₂	¹ J(Si(a), C)	44.7	146
<i>Si–Se bonds</i>			
(Me ₃ Si) ₂ Se	¹ J(Si, C)	52.5	145

Table A4 (Continued)

<i>Si–Se and Si–Si bond(s)</i>			
(Me ₃ Si(a)) ₂ Si(b)(Me)–SeH	¹ J(Si(a), C)	45.4	145
	¹ J(Si(b), C)	34.5	
(Me ₃ Si(a)) ₃ Si(b)–SeH	¹ J(Si(a), C)	46.2	145
(Me ₃ Si(a)) ₃ Si(b)–SeK	¹ J(Si(a), C)	42.3	145
(Me ₃ Si(a)–Si(b)Me ₂) ₂ Se	¹ J(Si(a), C)	45.2	145
	¹ J(Si(b), C)	42.0	
[(Me ₃ Si(a)) ₂ Si(b)Me] ₂ Se	¹ J(Si(a), C)	46.0	145
[(Me ₃ Si(a)) ₃ Si(b)] ₂ Se	¹ J(Si(a), C)	45.4	145
(Me ₃ Si(a)) ₃ Si(b)–Se–Si(c)Me ₂ –Si(d)Me ₃	¹ J(Si, C)	45.2	146
[(Me ₃ Si(a)) ₃ Si(b)–Se–Si(c)Me ₂] ₂	¹ J(Si, C)	45.2	146
<i>Si–Te bonds</i>			
(Me ₃ Si) ₂ Te	¹ J(Si, C)	51.0	145
<i>Si–Te and Si–Si bond(s)</i>			
(Me ₃ Si(a)) ₂ Si(b)(Me)–TeH	¹ J(Si(a), C)	46.2	145
	¹ J(Si(b), C)	32.6	
(Me ₃ Si(a)) ₂ Si(b)(Me)–TeK	¹ J(Si(a), C)	42.0	145
(Me ₃ Si(a)) ₃ Si(b)–TeH	¹ J(Si(a), C)	46.1	145
(Me ₃ Si(a)) ₃ Si(b)–TeK	¹ J(Si(a), C)	43.1	145
(Me ₃ Si(a)–Si(b)Me ₂) ₂ Te	¹ J(Si(b), C)	40.8	145
[(Me ₃ Si(a)) ₂ Si(b)Me] ₂ Te	¹ J(Si(a), C)	45.5	145
	¹ J(Si(b), C)	33.0	
[(Me ₃ Si(a)) ₃ Si(b)–Te–Si(c)Me ₂] ₂	¹ J(Si, C)	45.9	146

Table A5. Compounds with silicon bonded to halogens and possible silicon bonds to chalcogens, N, Si or H

<i>Si–Cl bond(s)</i>			
Me ₃ SiCl	¹ J(Si, C)	57.7	70
	¹ J(Si, C)	57.4	74
Me ₂ (Cl)Si–CH ₂ Cl	¹ J(Si, C(CH ₂))	61.2	74
	¹ J(Si, C(Me))	60.6	
Me ₂ (Cl)Si–CHCl ₂	¹ J(Si, C(CH ₂))	62.0	74
	¹ J(Si, C(Me))	62.0	
Me ₂ SiCl ₂	¹ J(Si, C)	68.3	74
(Me ₂ (Cl)Si) ₂ CH ₂	¹ J(Si, C(CH ₂))	49.1	148
	¹ J(Si, C(Me))	58.3	
(Me ₂ (Cl)Si(a)) ₂ –CH–Si(b)Me ₃	¹ J(Si(a), C(Me))	58.8	118
	¹ J(Si(b), C(Me))	52.5	
Cl ₃ Si–Me	¹ J(Si, C)	86.6	74
Cl ₃ Si–CH ₂ Cl	¹ J(Si, C)	97.6	74
(Me ₂ (Cl)Si) ₃ CH	¹ J(Si, C(CH))	39.5	118
	¹ J(Si, C(Me))	60.2	
(Cl ₂ MeSi) ₂ CH ₂	¹ J(Si, C(CH ₂))	59.9	148
	¹ J(Si, C(Me))	71.1	

Table A5 (Continued)

<i>Si-Cl and Si-Si bond(s)</i>			
Me ₃ Si(a)-Si(b)Me ₂ Cl	¹ J(Si(a), C)	46.2	119
	¹ J(Si(b), C)	45.9	
(Me ₃ Si) ₃ SiCl	¹ J(Si, C(Me))	45.8	120
[Me ₂ (Cl)Si] ₂	¹ J(Si, C)	49.1	128
	¹ J(Si, C)	48.7	149
(Me ₂ (Cl)Si(a)) ₂ Si(b)Me ₂	¹ J(Si(a), C)	47.0	150
	¹ J(Si(b), C)	41.5	
(Me ₂ (Cl)Si(a)-Si(b)Me ₂) ₂	¹ J(Si(a), C)	46.4	150
	¹ J(Si(b), C)	40.3	
Cl ₂ MeSi(a)-Si(b)(Cl)Me ₂	¹ J(Si(a), C)	54.7	150
	¹ J(Si(b), C)	51.5	
(Cl ₂ MeSi) ₂	¹ J(Si, C)	60.7	149
(Me ₂ (Cl)Si) ₂ SiCl ₂	¹ J(Si, C)	52.2	151
(Cl ₂ MeSi(a)) ₂ Si(b)Me ₂	¹ J(Si(a), C)	52.1	147
	¹ J(Si(b), C)	41.4	
(Cl ₂ MeSi(a)) ₃ Si(b)-Me	¹ J(Si(a), C)	56.0	150
	¹ J(Si(b), C)	40.1	
[(Me ₂ (Cl)Si) ₃ Si] ₂	¹ J(Si, C)	48.7	121
[(Cl ₂ MeSi(a)) ₂ Si(b)Me] ₂	¹ J(Si(a), C)	54.9	150
	¹ J(Si(b), C)	38.4	
<i>Si-Cl, possible Si-N, Si-O, Si-Si or Si-H bonds</i>			
Me-Si(H)Cl ₂	¹ J(Si, C)	-66	36
(Me ₂ (Cl)Si) ₂ NH	¹ J(Si, C)	68.1	77
Me(Et ₂ N) ₂ Si(a)-Si(b)Me(NEt ₂)Cl	¹ J(Si(b), C)	53.1	152
Me ₂ (Cl)Si-SiMe ₂ -O-Et	¹ J(Si, C)	52.1	128
	¹ J(Si, C)	49.1	
Me ₂ (Cl)Si-SiMe ₂ -O- <i>n</i> Pr	¹ J(Si, C)	51.1	128
	¹ J(Si, C)	49.1	
Me ₂ (Cl)Si-SiMe ₂ -O- <i>n</i> Bu	¹ J(Si, C)	51.3	128
	¹ J(Si, C)	47.7	
(Me ₂ (Cl)Si) ₂ O	¹ J(Si, C)	72.6	77
<i>Si-F, Si-Br, Si-I bond(s), possible Si-N, Si-Si bond(s)</i>			
Me ₃ SiF	¹ J(Si, C)	60.5	70
(Me ₃ Si(a)) ₃ Si(b)F	¹ J(Si(a), C(Me))	44.9	120
	² J(Si(b), C(Me))	5.9	
Me ₃ SiBr	¹ J(Si, C)	56.0	70
(Me ₃ Si(a)) ₃ Si(b)Br	¹ J(Si(a), C(Me))	46.3	120
	² J(Si(b), C(Me))	5.9	
(Me ₂ (Br)Si) ₃ CH	¹ J(Si, C(CH))	52.0	81
	¹ J(Si, C(Me))	63.0	
(Me ₂ (Br)Si) ₃ N	¹ J(Si, C)	56.2	81
Me ₃ SiI	¹ J(Si, C)	54.0	70
(Me ₃ Si) ₃ SiI	¹ J(Si, C(Me))	46.7	120

Table A6. Compounds with silicon(s) bonded to cycle(s) (silicon not within cycle)

	$^1J(\text{Si}, \text{C}(\text{CH}))$ $^1J(\text{Si}, \text{C}(\text{Me}))$	58.3 53.3	82
	$^1J(\text{Si}, \text{C}(\text{C}))$ $^1J(\text{Si}, \text{C}(\text{Me}))$	59.4 53.8	82
	$^1J(\text{Si}, \text{C})$	56.8	78
	$^1J(\text{Si}, \text{C})$	56.9	78
	$^1J(\text{Si}, \text{C}(4))$ $^1J(\text{Si}, \text{C}(\text{Me}))$	53.0, 53.2 51.9	153
	$^1J(\text{Si}, \text{C})$	56.2	127
	$^1J(\text{Si}, \text{C})$	59	154
	$^1J(\text{Si}, \text{C})$	59	154
	$^1J(\text{Si}(\text{a}), \text{C})$	59, 60	154
	$^1J(\text{Si}(\text{a}), \text{C})$ $^1J(\text{Si}(\text{b}), \text{C})$	59, 59 72	154
	$^1J(\text{Si}(\text{a}), \text{C})$ $^1J(\text{Si}(\text{b}), \text{C})$	59, 60 72	154

Table A6 (Continued)

	$^1J(\text{Si(a, c), C})$ $^1J(\text{Si(b), C})$	59, 60 72	154
	$^1J(\text{Si(a, c), C})$ $^1J(\text{Si(b), C})$	59, 59 73	154
	$^1J(\text{Si(a), C})$ $^1J(\text{Si(b), C})$	58 72	154
	$^1J(\text{Si(a), C})$ $^1J(\text{Si(b), C})$	58 72	154
	$^1J(\text{Si(a), C})$ $^1J(\text{Si(b, c), C})$	59 71, 74	154
	$^1J(\text{Si(a, d), C})$ $^1J(\text{Si(b, c), C})$	59, 59 72, 74	154
	$^1J(\text{Si(a), C})$ $^1J(\text{Si(b), C})$	58 72	154
	$^1J(\text{Si, C})$	47.3	103
	$^1J(\text{Si, C})$	56.3	78
	$^1J(\text{Si(a), C})$ $^1J(\text{Si(b), C(CH}_2)_2)$ $^1J(\text{Si(b), C(Me)})$	58.0 46.8 51.0	155, 156

Table A6 (Continued)

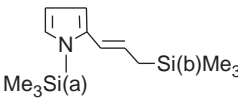
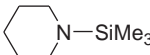
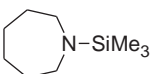
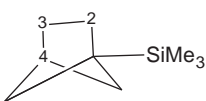
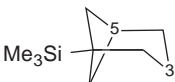
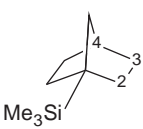
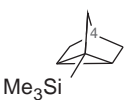
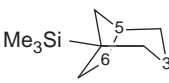
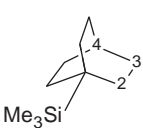
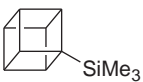
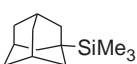
	$^1J(\text{Si(a)}, \text{C})$	58.1	155,156
	$^1J(\text{Si(b)}, \text{C}(\text{CH}_2))$	47.5	
	$^1J(\text{Si(b)}, \text{C}(\text{Me}))$	51.9	
	$^1J(\text{Si}, \text{C})$	56.6	78
	$^1J(\text{Si}, \text{C})$	56.4	78
	$^1J(\text{Si}, \text{C})$	62.89	109
	$^1J(\text{Si}, \text{C}(\text{Me}))$	50.46	
	$^2J(\text{Si}, \text{C}(2))$	3.22	
	$^3J(\text{Si}, \text{C}(3))$	4.04	
	$^3J(\text{Si}, \text{C}(4))$	10.46	
	$^1J(\text{Si}, \text{C})$	61.29	109
	$^1J(\text{Si}, \text{C}(\text{Me}))$	49.92	
	$^3J(\text{Si}, \text{C}(3))$	4.09	
	$^3J(\text{Si}, \text{C}(5))$	7.87	
	$^1J(\text{Si}, \text{C})$	61.70	109
	$^1J(\text{Si}, \text{C}(\text{Me}))$	50.30	
	$^2J(\text{Si}, \text{C}(2))$	1.63	
	$^3J(\text{Si}, \text{C}(3))$	4.90	
	$^3J(\text{Si}, \text{C}(4))$	6.22	
	$^1J(\text{Si}, \text{C})$	63.87	109
	$^1J(\text{Si}, \text{C}(\text{Me}))$	51.78	
	$^3J(\text{Si}, \text{C}(4))$	3.23	
	$^1J(\text{Si}, \text{C})$	59.76	109
	$^1J(\text{Si}, \text{C}(\text{Me}))$	50.00	
	$^3J(\text{Si}, \text{C}(3))$	5.35	
	$^3J(\text{Si}, \text{C}(5))$	4.98	
	$^3J(\text{Si}, \text{C}(6))$	4.98	
	$^1J(\text{Si}, \text{C})$	60.42	109
	$^1J(\text{Si}, \text{C}(\text{Me}))$	49.98	
	$^3J(\text{Si}, \text{C}(3))$	5.08	
	$^1J(\text{Si}, \text{C}(\text{Me}))$	50.57	109
	$^2J(\text{Si}, \text{C})$	2.44	
	$^3J(\text{Si}, \text{C})$	3.32	
	$^1J(\text{Si}, \text{C})$	58.89	109
	$^1J(\text{Si}, \text{C}(\text{Me}))$	49.80	
	$^3J(\text{Si}, \text{C})$	4.61	

Table A7. Compounds with silicon(s) within four-membered ring

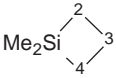
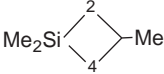
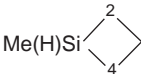
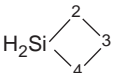
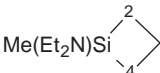
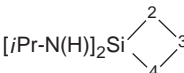
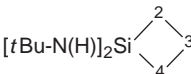
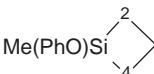
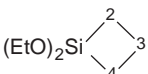
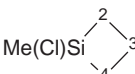
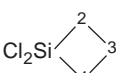
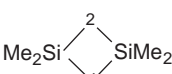
	$^1J(\text{Si}, \text{C}(2, 4))$	42.3	66
	$^1J(\text{Si}, \text{C}(\text{Me}))$	44.6	
	$^2J(\text{Si}, \text{C}(3))$	16.4	
	$^1J(\text{Si}, \text{C}(2, 4))$	42	
	$^1J(\text{Si}, \text{C}(\text{Me}))$	45	
	$^2J(\text{Si}, \text{C}(3))$	16	
	$^1J(\text{Si}, \text{C}(2, 4))$	43	76
	$^1J(\text{Si}, \text{C}(\text{Me}))$	46	
	$^1J(\text{Si}, \text{C}(\text{Me}))$	44	
	$^1J(\text{Si}, \text{C}(2, 4))$	42	76
	$^1J(\text{Si}, \text{C}(\text{Me}))$	45	
	$^1J(\text{Si}, \text{C}(2, 4))$	42	76
	$^2J(\text{Si}, \text{C}(3))$	17	
	$^1J(\text{Si}, \text{C}(2, 4))$	45	76
	$^1J(\text{Si}, \text{C}(\text{Me}))$	52	
	$^1J(\text{Si}, \text{C})$	48.5	80
	$^2J(\text{Si}, \text{C}(3))$	17.4	
	$^1J(\text{Si}, \text{C})$	50.1	80
	$^2J(\text{Si}, \text{C}(3))$	17.4	
	$^1J(\text{Si}, \text{C}(2, 4))$	47	76
	$^1J(\text{Si}, \text{C}(\text{Me}))$	54	
	$^1J(\text{Si}, \text{C})$	55	76
	$^2J(\text{Si}, \text{C}(3))$	19	
	$^1J(\text{Si}, \text{C}(2, 4))$	45	76
	$^1J(\text{Si}, \text{C}(\text{Me}))$	49	
	$^2J(\text{Si}, \text{C}(3))$	17	
	$^1J(\text{Si}, \text{C}(2, 4))$	52	76
	$^2J(\text{Si}, \text{C}(3))$	19	
	$^1J(\text{Si}, \text{C}(2, 4))$	34.7	66
	$^1J(\text{Si}, \text{C}(\text{Me}))$	48.3	
	$^1J(\text{Si}, \text{C}(2, 4))$	35	
	$^1J(\text{Si}, \text{C}(\text{Me}))$	49	

Table A7 (Continued)

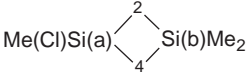
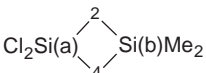
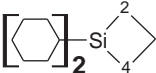
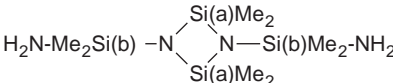
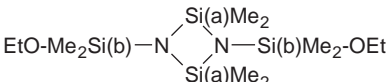
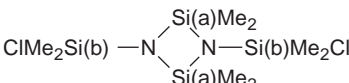
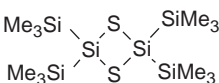
	$^1J(\text{Si(a)}, \text{C}(2, 4))$	40	76
	$^1J(\text{Si(b)}, \text{C}(2, 4))$	36	
	$^1J(\text{Si(a)}, \text{C}(\text{Me}))$	54	
	$^1J(\text{Si(b)}, \text{C}(\text{Me}))$	51	
	$^1J(\text{Si(a)}, \text{C}(2, 4))$	48	76
	$^1J(\text{Si(b)}, \text{C}(2, 4))$	32	
	$^1J(\text{Si}, \text{C}(\text{Me}))$	52	
	$^1J(\text{Si}, \text{C}(\text{CH}))$	48	76
	$^1J(\text{Si}, \text{C}(2, 4))$	41	
	$^1J(\text{Si(a)}, \text{C})$	60.9	79
	$^1J(\text{Si(b)}, \text{C})$	63.9	
	$^1J(\text{Si(a)}, \text{C})$	61.2	79
	$^1J(\text{Si(b)}, \text{C})$	68.1	
	$^1J(\text{Si(a)}, \text{C})$	61.9	79
	$^1J(\text{Si(b)}, \text{C})$	67.2	
	$^1J(\text{Si}, \text{C})$	46.2	157

Table A8. Compounds with silicon(s) within five-membered ring

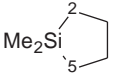
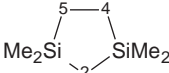
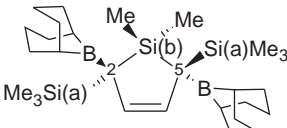
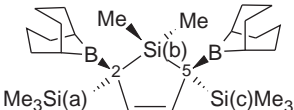
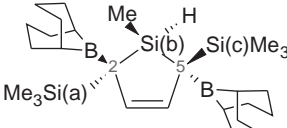
	$^1J(\text{Si}, \text{C}(2, 5))$	51	76
	$^1J(\text{Si}, \text{C}(\text{Me}))$	50	
	$^1J(\text{Si}, \text{C}(2))$	42	76
	$^1J(\text{Si}, \text{C}(4, 5))$	52	
	$^1J(\text{Si}, \text{C}(\text{Me}))$	50	
	$^1J(\text{Si(a)}, \text{C}(2, 5))$	31.2	158
	$^1J(\text{Si(b)}, \text{C}(2, 5))$	34.6	
	$^1J(\text{Si(a)}, \text{C}(\text{Me}))$	52.0	
	$^1J(\text{Si(b)}, \text{C}(\text{Me}))$	48.5	
	$^1J(\text{Si(a)}, \text{c}), \text{C}(\text{Me}))$	52.6	158
	$^1J(\text{Si(a)}, \text{c}), \text{C}(\text{Me}))$	51.9	
	$^1J(\text{Si(b)}, \text{C}(\text{Me}))$	48.5	
	$^1J(\text{Si(a)}, \text{C}(2))$	29.9	158
	$^1J(\text{Si(c)}, \text{C}(5))$	27.2	
	$^1J(\text{Si(a)}, \text{c}), \text{C}(\text{Me}))$	52.6, 51.9	
	$^1J(\text{Si(b)}, \text{C}(\text{Me}))$	48.7	

Table A8 (Continued)

	$^1J(\text{Si(a)}, \text{C(2)})$	28.5	158
	$^1J(\text{Si(b)}, \text{C(2)})$	37.6	
	$^1J(\text{Si(a, c)}, \text{C(Me)})$	52.6	
	$^1J(\text{Si(b)}, \text{C(Me)})$	49.3	
<i>Si–N bond(s), possible Si–Si bond</i>			
	$^1J(\text{Si}, \text{C(2, 5)})$	56	76
	$^1J(\text{Si}, \text{C(Me)})$	55	
$[\textit{i}\text{Pr-N(H)}]_2\text{Si}$	$^1J(\text{Si}, \text{C})$	63.2	80
$[\textit{t}\text{Bu-N(H)}]_2\text{Si}$	$^1J(\text{Si}, \text{C})$	64.3	80
	$^1J(\text{Si}, \text{C(CH}_2\text{)})$	55.7	131
	$^1J(\text{Si}, \text{C(Me)})$	55.7	
	$^1J(\text{Si}, \text{C(CH}_2\text{)})$	56.2	125
	$^1J(\text{Si}, \text{C(Me)})$	53.2	
	$^1J(\text{Si}, \text{C(CH}_2\text{)})$	56.7	125
	$^1J(\text{Si}, \text{C(Me)})$	57.0	
	$^1J(\text{Si(a)}, \text{C(CH}_2\text{)})$	54.9	131
	$^1J(\text{Si(a)}, \text{C(Me)})$	54.9	
	$^1J(\text{Si(b)}, \text{C})$	56.2	
	$^1J(\text{Si}, \text{C(Me)})$	56.7	131
	$^1J(\text{Si}, \text{C(Me)})$	55.1	
	$^1J(\text{Si}, \text{C(CH}_2\text{)})$	55.1	
	$^1J(\text{Si(a)}, \text{C(Me)})$	54.1	131
	$^1J(\text{Si(b)}, \text{C})$	55.4	
	$^1J(\text{Si(a)}, \text{C(CH}_2\text{)})$	54.9	131
	$^1J(\text{Si(a)}, \text{C(Me)})$	54.9	
	$^1J(\text{Si(b)}, \text{C})$	56.2	

Table A8 (Continued)

	$^1J(\text{Si(a), C(Me)})$	53.7	131
	$^1J(\text{Si(b), C})$	55.6	
	$^1J(\text{Si, C})$	−44.8	134
<i>Si–O bond(s)</i> 	$^1J(\text{Si, C(2, 5)})$	57	76
	$^1J(\text{Si, C(Me)})$	55	
	$^1J(\text{Si, C(C(H)Me)})$	60.1	107
	$^1J(\text{Si, C(Me)})$	57.1	
	$^1J(\text{Si, C(Me)})$	55.1	
	$^1J(\text{Si, C(C(H)Me)})$	60.1	
	$^1J(\text{Si, C(Me)})$	56.4	
	$^1J(\text{Si, C(Me)})$	55.1	
	$^1J(\text{Si, C(C(Ph)H)})$	56.3	159
	$^1J(\text{Si, C(Me)})$	57.2	
	$^1J(\text{Si, C(Me)})$	55.7	
	$^1J(\text{Si, C(C(H)Sn)})$	54.0	159
	$^1J(\text{Si, C(Me)})$	55.4	
	$^1J(\text{Si, C(Me)})$	56.8	
	$^1J(\text{Si, C(CH)})$	49.2	107
	$^1J(\text{Si, C(CH)})$	48.2	
	$^1J(\text{Si(a), C(Me)})$	59.0	
	$^1J(\text{Si(a), C(Me)})$	53.2	
	$^1J(\text{Si(b), C(Me)})$	50.2	
<i>Si–S and Si–Si bond(s)</i>			
	$^1J(\text{Si, C})$	46.6	160
	$^1J(\text{Si, C})$	46.2	160
	$^1J(\text{Si, C})$	46.9	161

Table A8 (Continued)

	$^1J(\text{Si}, \text{C})$	45.7	161
	$^1J(\text{Si}, \text{C})$	45.7	161
	$^1J(\text{Si(a)}, \text{C})$	46.5	162
	$^1J(\text{Si(b)}, \text{C})$	58.3	
	$^1J(\text{Si(a)}, \text{C})$	46.5	160
	$^1J(\text{Si(b)}, \text{C})$	58.3	
<i>Si-Se bonds, possible other bond(s)</i>			
	$^1J(\text{Si(a)}, \text{C})$	44.7	160
	$^1J(\text{Si(b)}, \text{C})$	45.6	
	$^1J(\text{Si(c)}, \text{C})$	56.4	
	$^1J(\text{Si}, \text{C})$	45.2	160
	$^1J(\text{Si}, \text{C})$	44.7	160
	$^1J(\text{Si}, \text{C})$	44.7	161
	$^1J(\text{Si(a)}, \text{C})$	45.2	160
	$^1J(\text{Si(b)}, \text{C})$	54.0	
<i>Si-Te bonds, possible other bonds</i>			
	$^1J(\text{Si(a)}, \text{C})$	43.7	160
	$^1J(\text{Si(b)}, \text{C})$	45.2	
	$^1J(\text{Si(c)}, \text{C})$	53.4	
	$^1J(\text{Si(a)}, \text{C})$	42.8	160
	$^1J(\text{Si(b)}, \text{C})$	44.7	
	$^1J(\text{Si(c)}, \text{C})$	50.0	
	$^1J(\text{Si}, \text{C})$	42.3	160
	$^1J(\text{Si(a)}, \text{C})$	42.8	160
	$^1J(\text{Si(b)}, \text{C})$	47.6	

Table A8 (Continued)

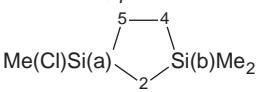
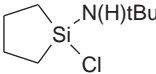
<i>Si–Cl bond, possible Si–N bond</i>			
	$^1J(\text{Si(a)}, \text{C(2)})$	50	76
	$^1J(\text{Si(b)}, \text{C(2)})$	43	
	$^1J(\text{Si}, \text{C(5)})$	58	
	$^1J(\text{Si}, \text{C(4)})$	53	
	$^1J(\text{Si(a)}, \text{C(Me)})$	58	
	$^1J(\text{Si(b)}, \text{C(Me)})$	51	
	$^1J(\text{Si}, \text{C})$	68.7	80

Table A9. Compounds with silicon(s) within six-membered and larger rings

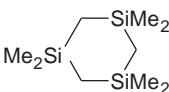
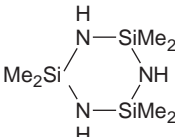
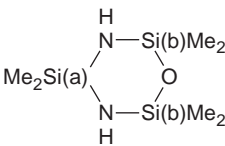
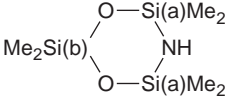
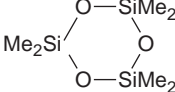
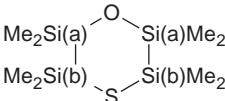
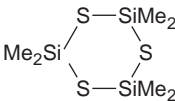
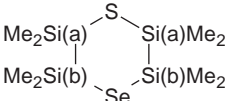
	$^1J(\text{Si}, \text{C(CH}_2\text{)})$	44.0	66
	$^1J(\text{Si}, \text{C(Me)})$	50.8	
	$^1J(\text{Si}, \text{C})$	63.0	77
	$^1J(\text{Si(a)}, \text{C})$	62.3	77
	$^1J(\text{Si(b)}, \text{C})$	68.5	
	$^1J(\text{Si(a)}, \text{C})$	68.4	77
	$^1J(\text{Si(b)}, \text{C})$	74.0	
	$^1J(\text{Si}, \text{C})$	74.2	77
	$^1J(\text{Si(a)}, \text{C})$	58.3	160
	$^1J(\text{Si(b)}, \text{C})$	43.7	
	$^1J(\text{Si}, \text{C})$	59.6	160
	$^1J(\text{Si(a)}, \text{C})$	45.7	160
	$^1J(\text{Si(b)}, \text{C})$	45.7	

Table A9 (Continued)

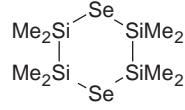
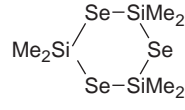
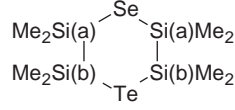
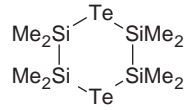
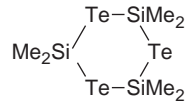
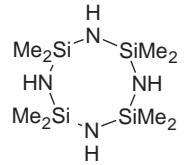
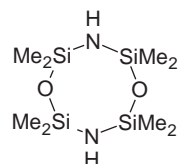
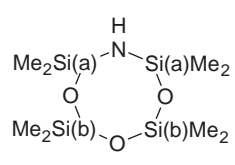
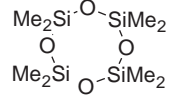
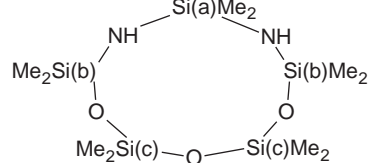
	$^1J(\text{Si}, \text{C})$	44.1	160
	$^1J(\text{Si}, \text{C})$	55.4	160
	$^1J(\text{Si(a)}, \text{C})$ $^1J(\text{Si(b)}, \text{C})$	44.5 41.8	160
	$^1J(\text{Si}, \text{C})$	42.3	160
	$^1J(\text{Si}, \text{C})$	49.5	160
	$^1J(\text{Si}, \text{C})$	64.0	77
	$^1J(\text{Si}, \text{C})$	69.8	77
	$^1J(\text{Si(a)}, \text{C})$ $^1J(\text{Si(b)}, \text{C})$	69.7 75.4	77
	$^1J(\text{Si}, \text{C})$ $^1J(\text{Si}, \text{C})$	75.4 75.58	77 18
	$^1J(\text{Si(a)}, \text{C})$ $^1J(\text{Si(b)}, \text{C})$ $^1J(\text{Si(c)}, \text{C})$	64.5 69.4 74.9	77

Table A9 (Continued)

	$^1J(\text{Si(a, b), C})$	69.6	77
	$^1J(\text{Si(a, b), C})$	69.3	
	$^1J(\text{Si(c), C})$	74.7	
	$^1J(\text{Si, C})$	69.2	77

Table A10. Compounds with silicon(s) within two rings

	$^1J(\text{Si, C(2, 4)})$	45	76
	$^1J(\text{Si, C(Me)})$	50	
	$^1J(\text{Si, C(2, 4)})$	48	76
	$^1J(\text{Si, C(Me)})$	53	
	$^1J(\text{Si, C(CH2)})$	55.2	131
	$^1J(\text{Si, C(Me)})$	55.2	
	$^1J(\text{Si, C(CH2)})$	54.9	131
	$^1J(\text{Si, C(Me)})$	54.9	
	$^1J(\text{Si, C(CH2)})$	56.7	133
	$^1J(\text{Si, C(Me)})$	54.3	
	$^1J(\text{Si, C(CH2)})$	56.1	133
	$^1J(\text{Si, C(Me)})$	53.8	
	$^1J(\text{Si, C(CH2)})$	56.0	133
	$^1J(\text{Si, C(Me)})$	53.9	

Table A10 (Continued)

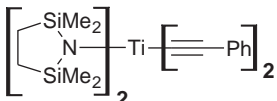
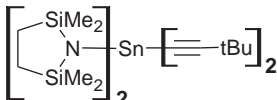
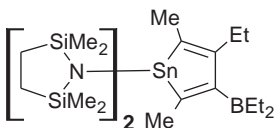
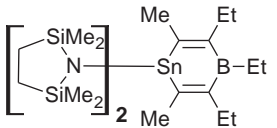
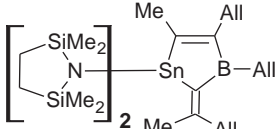
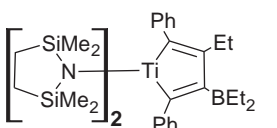
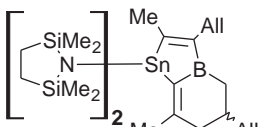
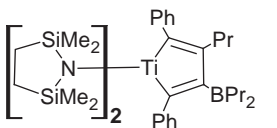
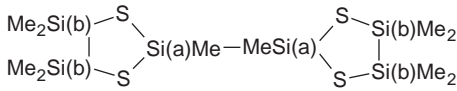
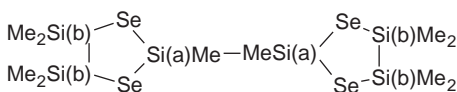
	$^1J(\text{Si}, \text{C}(\text{CH}_2))$	54.9	131
	$^1J(\text{Si}, \text{C}(\text{Me}))$	54.9	
	$^1J(\text{Si}, \text{C}(\text{CH}_2))$	56.1	133
	$^1J(\text{Si}, \text{C}(\text{Me}))$	53.8	
	$^1J(\text{Si}, \text{C}(\text{CH}_2))$	56.1	133
	$^1J(\text{Si}, \text{C}(\text{Me}))$	53.4	
	$^1J(\text{Si}, \text{C}(\text{Me}))$	53.4	
	$^1J(\text{Si}, \text{C}(\text{CH}_2))$	56.5	133
	$^1J(\text{Si}, \text{C}(\text{Me}))$	53.4	
	$^1J(\text{Si}, \text{C}(\text{CH}_2))$	56.0	133
	$^1J(\text{Si}, \text{C}(\text{Me}))$	53.4	
	$^1J(\text{Si}, \text{C}(\text{Me}))$	54.1	131
	$^1J(\text{Si}, \text{C}(\text{CH}_2))$	55.6	133
	$^1J(\text{Si}, \text{C}(\text{CH}_2))$	55.6	
	$^1J(\text{Si}, \text{C}(\text{Me}))$	53.6	
	$^1J(\text{Si}, \text{C}(\text{Me}))$	53.2	
	$^1J(\text{Si}, \text{C}(\text{Me}))$	53.2	
	$^1J(\text{Si}, \text{C}(\text{Me}))$	53.2	
	$^1J(\text{Si}, \text{C}(\text{Me}))$	54.2	131
	$^1J(\text{Si}(\text{a}), \text{C})$	48.6	162
	$^1J(\text{Si}(\text{b}), \text{C})$	42.6	
	$^1J(\text{Si}(\text{a}), \text{C})$	48.6	160
	$^1J(\text{Si}(\text{b}), \text{C})$	46.2	
	$^1J(\text{Si}(\text{b}), \text{C})$	43.2	160

Table A11. Compounds with silicon(s) within bi-cycles and multi-cycles

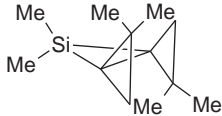

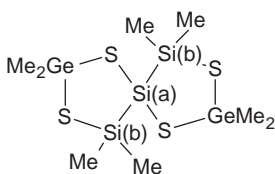
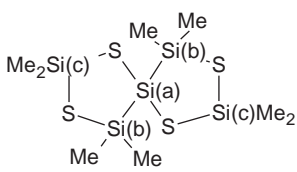
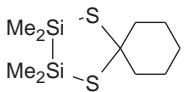
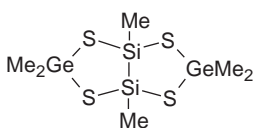
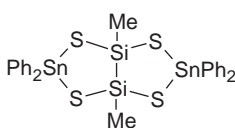
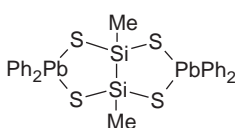
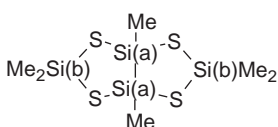
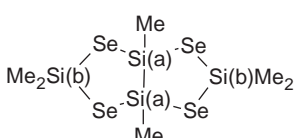
	$^1J(\text{Si}, \text{C}(\text{Me}))$	58	163
	$^1J(\text{Si}, \text{C})$	37	76
	$^1J(\text{Si}(\text{b}), \text{C})$ $^1J(\text{Si}(\text{b}), \text{C})$	49.5 47.5	151
	$^1J(\text{Si}(\text{b}), \text{C})$ $^1J(\text{Si}(\text{b}), \text{C})$ $^1J(\text{Si}(\text{c}), \text{C})$ $^1J(\text{Si}(\text{c}), \text{C})$	50.6 47.6 59.1 57.5	151
	$^1J(\text{Si}, \text{C})$	47.1	160
	$^1J(\text{Si}, \text{C})$	51.5	164
	$^1J(\text{Si}, \text{C})$	49.8	161,164
	$^1J(\text{Si}, \text{C})$	48.3	161
	$^1J(\text{Si}(\text{a}), \text{C})$ $^1J(\text{Si}(\text{b}), \text{C})$	52.2 58.7	162,164
	$^1J(\text{Si}(\text{b}), \text{C})$	53.9	164

Table A11 (Continued)

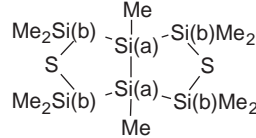
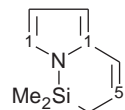
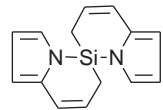
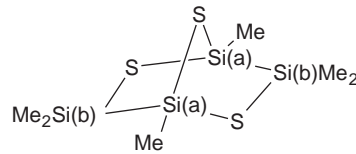
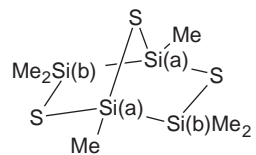
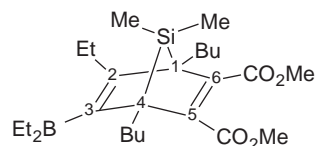
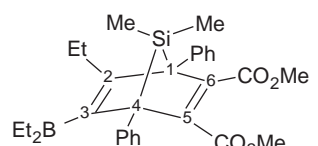
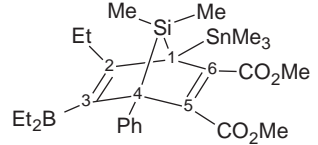
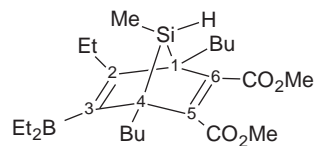
	$^1J(\text{Si}(\text{b}), \text{C})$	45.2	162
	$^1J(\text{Si}, \text{C}(\text{CH}_2))$ $^1J(\text{Si}, \text{C}(\text{Me}))$ $^2J(\text{Si}, \text{C}(1))$ $^2J(\text{Si}, \text{C}(5))$	56.7 57.7 7.8 4.5	155
	$^1J(\text{Si}, \text{C})$	66.5	155
	$^1J(\text{Si}(\text{a}), \text{C})$	48.6	165
	$^1J(\text{Si}(\text{a}), \text{C})$ $^1J(\text{Si}(\text{b}), \text{C})$	47.6 46.6	162
	$^1J(\text{Si}, \text{C}(1))$ $^1J(\text{Si}, \text{C}(4))$ $^1J(\text{Si}, \text{C}(\text{Me}))$ $^1J(\text{Si}, \text{C}(\text{Me}))$ $^2J(\text{Si}, \text{C}(2))$ $^2J(\text{Si}, \text{C}(5))$ $^2J(\text{Si}, \text{C}(6))$	50.2 49.7 45.6 41.3 4.5 3.4 3.4	104
	$^1J(\text{Si}, \text{C}(1))$ $^1J(\text{Si}, \text{C}(4))$ $^1J(\text{Si}, \text{C}(\text{Me}))$ $^1J(\text{Si}, \text{C}(\text{Me}))$	46.9 46.9 45.5 47.9	104
	$^1J(\text{Si}, \text{C}(1))$ $^1J(\text{Si}, \text{C}(4))$ $^1J(\text{Si}, \text{C}(\text{Me}))$ $^1J(\text{Si}, \text{C}(\text{Me}))$	39.1 43.4 43.5 48.1	104
	$^1J(\text{Si}, \text{C}(1))$ $^1J(\text{Si}, \text{C}(4))$ $^1J(\text{Si}, \text{C}(\text{Me}))$ $^2J(\text{Si}, \text{C}(2))$ $^2J(\text{Si}, \text{C}(6))$	51.0 51.3 39.7 4.9 3.7	104

Table A11 (Continued)

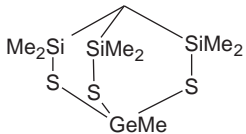
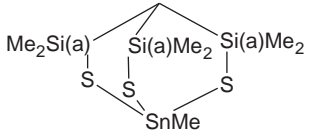
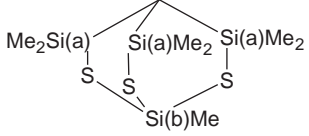
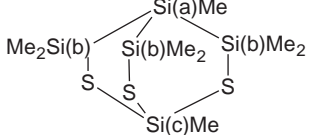
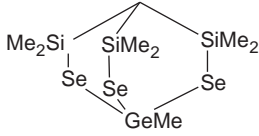
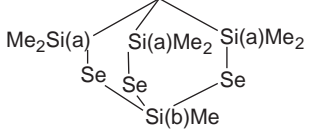
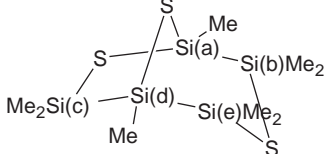
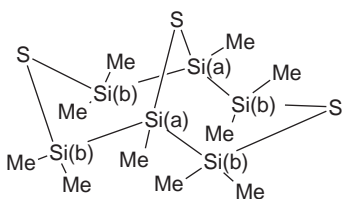
	$^1J(\text{Si}, \text{C})$	55.9	118
	$^1J(\text{Si(a)}, \text{C})$	55.2	118
	$^1J(\text{Si(a)}, \text{C})$	57.0	118
	$^1J(\text{Si(a)}, \text{C})$	36.9	162
	$^1J(\text{Si(b)}, \text{C})$	46.2	
	$^1J(\text{Si(c)}, \text{C})$	66.0	
	$^1J(\text{Si}, \text{C})$	53.5	118
	$^1J(\text{Si(a)}, \text{C})$	55.2	118
	$^1J(\text{Si(b)}, \text{C})$	57.0	
	$^1J(\text{Si(a)}, \text{C})$	44.7	162
	$^1J(\text{Si(c)}, \text{C})$	46.8	
	$^1J(\text{Si(e)}, \text{C})$	46.6	
	$^1J(\text{Si(b)}, \text{C})$	46.1	151

Table A11 (Continued)

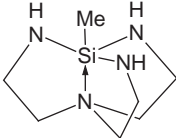
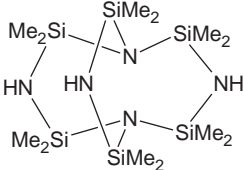
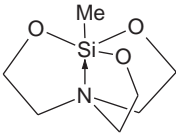
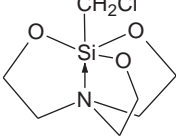
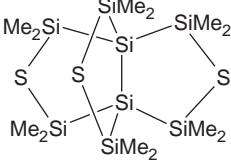
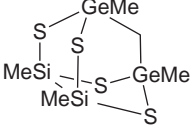
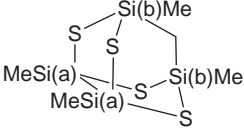
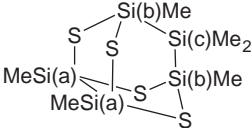
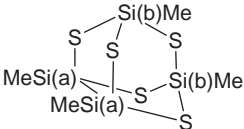
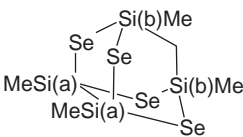
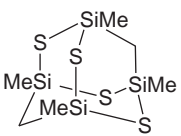
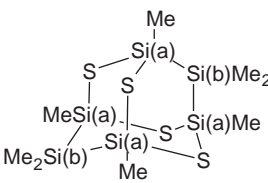
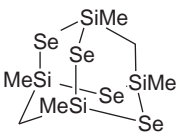
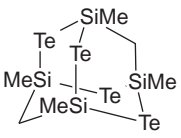
	$^1J(\text{Si}, \text{C})$	66.2	137
	$^1J(\text{Si}, \text{C})$	64.1	79
	$^1J(\text{Si}, \text{C})$ $^1J(\text{Si}, \text{C})$	106.9 106.5 (CDCl_3) 107.0 (DMSO)	143 166
	$^1J(\text{Si}, \text{C})$	115.7 (CDCl_3) 114.0 (DMSO)	166
	$^1J(\text{Si}, \text{C})$	47.5	121
	$^1J(\text{Si}, \text{C})$	52.2	167
	$^1J(\text{Si}(\text{b}), \text{C}(\text{CH}_2))$ $^1J(\text{Si}(\text{a}), \text{C})$ $^1J(\text{Si}(\text{b}), \text{C}(\text{Me}))$	51.9 51.9 59.9	148
	$^1J(\text{Si}(\text{a}), \text{C})$ $^1J(\text{Si}(\text{b}), \text{C})$ $^1J(\text{Si}(\text{c}), \text{C})$	51.0 45.2 41.8	147
	$^1J(\text{Si}(\text{a}), \text{C})$ $^1J(\text{Si}(\text{b}), \text{C})$	53.0 65.6	167 148

Table A11 (Continued)

	$^1J(\text{Si(b), C(CH}_2\text{)})$	49.1	148
	$^1J(\text{Si(a), C})$	46.4	
	$^1J(\text{Si(b), C(Me)})$	55.4	
	$^1J(\text{Si, C(CH}_2\text{)})$	51.9	148
	$^1J(\text{Si, C(Me)})$	62.3	
	$^1J(\text{Si(b), C})$	43.2	147
	$^1J(\text{Si, C(Me)})$	57.3	148
	$^1J(\text{Si, C(CH}_2\text{)})$	43.3	148
	$^1J(\text{Si, C(Me)})$	50.5	

APPENDIX B1

Tables of silicon–carbon coupling constants in molecules containing Si(sp³)–C(sp²) bonds to (usually substituted) vinyl or C=O group.

Table B1.1. Silicon bonded only to carbons

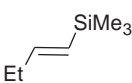
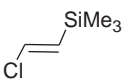
Vi–SiMe ₃	$^1J(\text{Si, C(C=)})$	64	68
	$^1J(\text{Si, C(C=)})$	64.0	91
	$^1J(\text{Si, C(Me)})$	52.0	
	$^1J(\text{Si, C(C=)})$	64.16	85
	$^1J(\text{Si, C(Me)})$	52.25	
	$^1J(\text{Si, C(C=)})$	65.4	82
	$^1J(\text{Si, C(Me)})$	54.0	
	$^1J(\text{Si, C(C=)})$	59.32	85
	$^1J(\text{Si, C(Me)})$	53.33	
	$^2J(\text{Si, C})$	5.76	

Table B1.1 (Continued)

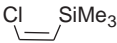
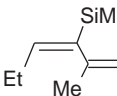
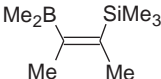
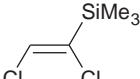
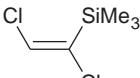
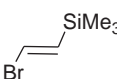
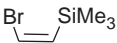
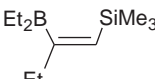
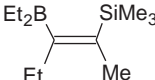
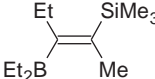
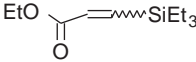
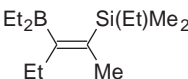
	$^1J(\text{Si}, \text{C}(\text{HC}=\text{}))$ $^1J(\text{Si}, \text{C}(\text{Me}))$	61.82 53.49	85
	$^1J(\text{Si}, \text{C}(\text{Me}))$	51.7	168
	$^1J(\text{Si}, \text{C}(\text{Me}))$	50.6	168
$\text{Cl}_2\text{C}=\text{C}(\text{H})-\text{SiMe}_3$	$^1J(\text{Si}, \text{C}(\text{C}=\text{}))$ $^1J(\text{Si}, \text{C}(\text{Me}))$	58.60 54.24	85
	$^1J(\text{Si}, \text{C}(\text{C}=\text{}))$	62.3	84
	$^1J(\text{Si}, \text{C}(\text{C}=\text{}))$	62.3	84
	$^1J(\text{Si}, \text{C}(\text{C}=\text{}))$ $^1J(\text{Si}, \text{C}(\text{Me}))$ $^2J(\text{Si}, \text{C})$	57.10 53.05 4.91	85
	$^1J(\text{Si}, \text{C}(\text{C}=\text{}))$ $^1J(\text{Si}, \text{C}(\text{Me}))$	62.19 53.48	85
	$^1J(\text{Si}, \text{C}(\text{C}=\text{}))$	69.7	168
$\text{Cl}_2\text{C}=\text{C}(\text{Cl})-\text{SiMe}_3$	$^1J(\text{Si}, \text{C}(\text{C}=\text{}))$ $^1J(\text{Si}, \text{C}(\text{Me}))$ $^2J(\text{Si}, \text{C})$	60.81 55.49 6.07	85
	$^1J(\text{Si}, \text{C}(\text{C}=\text{}))$ $^1J(\text{Si}, \text{C}(\text{Me}))$ $^3J(\text{Si}, \text{C}(\text{Et}))$ $^1J(\text{Si}, \text{C}(\text{C}=\text{}))$ $^1J(\text{Si}, \text{C}(\text{Me}))$	70.9 51.2 7.6 70.2 50.6	103 168
	$^1J(\text{Si}, \text{C}(\text{C}=\text{}))$ $^1J(\text{Si}, \text{C}(\text{Me}))$	69.8 51.2	103
	$^1J(\text{Si}, \text{C}(\text{C}=\text{}))$ $^1J(\text{Si}, \text{C}(\text{Et}))$ $^2J(\text{Si}, \text{C}(\text{C}=\text{}))$	57.86 53.48 8.28	85
	$^1J(\text{Si}, \text{C}(\text{Me}))$	49.9	168

Table B1.1 (Continued)

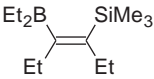
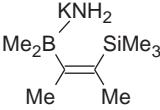
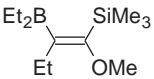
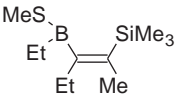
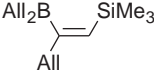
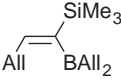
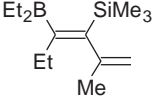
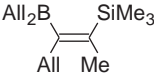
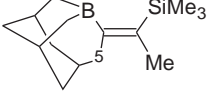
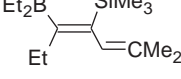
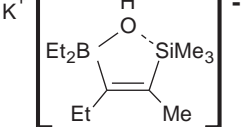
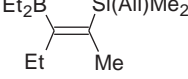
	$^1J(\text{Si}, \text{C}(\text{C}=\text{}))$ $^1J(\text{Si}, \text{C}(\text{Me}))$	70.2 49.9	168
	$^1J(\text{Si}, \text{C}(\text{Me}))$	53.2	168
	$^1J(\text{Si}, \text{C}(\text{C}=\text{}))$ $^1J(\text{Si}, \text{C}(\text{Me}))$ $^2J(\text{Si}, \text{C}(\text{C}=\text{}))$	80.7 51.6 14.0	169
	$^1J(\text{Si}, \text{C}(\text{C}=\text{}))$ $^1J(\text{Si}, \text{C}(\text{Me}))$ $^3J(\text{Si}, \text{C}(\text{Et}))$	64.0 50.8 8.7	170
	$^1J(\text{Si}, \text{C}(\text{C}=\text{}))$ $^1J(\text{Si}, \text{C}(\text{Me}))$ $^2J(\text{Si}, \text{C}(\text{C}=\text{}))$	67.9 51.5 9.1	171
	$^1J(\text{Si}, \text{C}(\text{Me}))$ $^2J(\text{Si}, \text{C}(\text{C}=\text{}))$	51.8 8.8	171
	$^1J(\text{Si}, \text{C}(\text{Me}))$ $^1J(\text{Si}, \text{C}(\text{C}=\text{}))$ $^1J(\text{Si}, \text{C}(\text{Me}))$	51.0 68.1 50.9	172,168 170
	$^1J(\text{Si}, \text{C}(\text{C}=\text{}))$ $^1J(\text{Si}, \text{C}(\text{Me}))$	68.5 50.5	171
	$^1J(\text{Si}, \text{C}(\text{C}=\text{}))$ $^1J(\text{Si}, \text{C}(\text{Me}))$ $^3J(\text{Si}, \text{C}(5))$	71.1, 71.2 49.6, 49.9 7.6	116
	$^1J(\text{Si}, \text{C}(\text{C}=\text{}))$ $^1J(\text{Si}, \text{C}(\text{Me}))$	68.0 50.9	168
	$^1J(\text{Si}, \text{C}(\text{C}=\text{}))$ $^1J(\text{Si}, \text{C}(\text{Me}))$	76.2 48.7	173
	$^1J(\text{Si}, \text{C}(\text{C}=\text{}))$ $^1J(\text{Si}, \text{C}(\text{All}))$ $^1J(\text{Si}, \text{C}(\text{Me}))$	70.9 51.3 46.1	168

Table B1.1 (Continued)

	$^1J(\text{Si}, \text{C}(\text{C}=\text{}))$ $^1J(\text{Si}, \text{C}(\text{Me}))$	70.0 50.2	83
	$^1J(\text{Si}, \text{C}(\text{C}=\text{}))$ $^1J(\text{Si}, \text{C}(\text{Me}))$	59.3 55.0	84
	$^1J(\text{Si}, \text{C}(\text{C}=\text{}))$ $^1J(\text{Si}, \text{C}(\text{Me}))$	60.3 55.2	84
	$^1J(\text{Si}, \text{C}(\text{C}=\text{}))$ $^1J(\text{Si}, \text{C}(\text{Me}))$ $^1J(\text{Si}, \text{C}(\text{Me}))$ $^2J(\text{Si}, \text{C}(\text{Me}))$ $^3J(\text{Si}, \text{C}(5))$	70.8 50.4, 50.5 50.5 6.4 7.0	116
	$^1J(\text{Si}, \text{C}(\text{C}=\text{}))$ $^1J(\text{Si}, \text{C}(\text{Me}))$ $^2J(\text{Si}, \text{C}(\text{Me}))$ $^3J(\text{Si}, \text{C}(5))$	71.7 50.5 6.4 7.9	116
	$^1J(\text{Si}, \text{C}(\text{Et}))$ $^1J(\text{Si}, \text{C}(\text{Me}))$	52.6 52.0	173
	$^1J(\text{Si}, \text{C}(\text{C}=\text{}))$	81.0	168,174
	$^1J(\text{Si}, \text{C}(\text{C}=\text{}))$ $^1J(\text{Si}, \text{C}(\text{Me}))$	64.1 51.1	168
	$^1J(\text{Si}, \text{C}(\text{C}=\text{}))$ $^1J(\text{Si}, \text{C}(\text{Me}))$	69.3 50.0	168
	$^1J(\text{Si}, \text{C}(\text{C}=\text{}))$ $^1J(\text{Si}, \text{C}(\text{Me}))$	68.9 50.4	168
	$^1J(\text{Si}, \text{C}(\text{Me}))$	48.7	173

Table B1.1 (Continued)

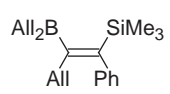
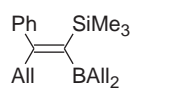
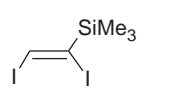
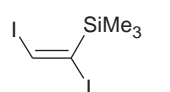
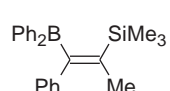
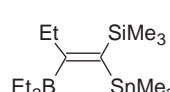
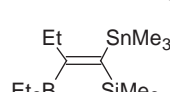
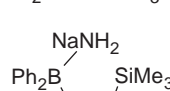
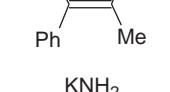
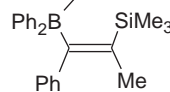
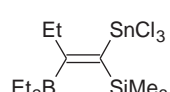
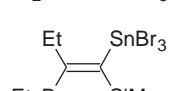
	$^1J(\text{Si}, \text{C}(\text{C}=\text{}))$ $^1J(\text{Si}, \text{C}(\text{Me}))$	64.9 51.9	171
	$^1J(\text{Si}, \text{C}(\text{Me}))$	51.9	171
	$^1J(\text{Si}, \text{C}(\text{C}=\text{}))$ $^1J(\text{Si}, \text{C}(\text{Me}))$	55.4 54.3	84
	$^1J(\text{Si}, \text{C}(\text{C}=\text{}))$ $^1J(\text{Si}, \text{C}(\text{Me}))$	57.6 54.6	84
	$^1J(\text{Si}, \text{C}(\text{Me}))$	50.9	168
	$^1J(\text{Si}, \text{C}(\text{Me}))$	50.7	103,175
	$^1J(\text{Si}, \text{C}(\text{C}=\text{}))$ $^1J(\text{Si}, \text{C}(\text{Me}))$	59.2 50.7	103
	$^1J(\text{Si}, \text{C}(\text{Me}))$	51.5	168
	$^1J(\text{Si}, \text{C}(\text{Me}))$	51.0	168
	$^1J(\text{Si}, \text{C}(\text{C}=\text{}))$ $^1J(\text{Si}, \text{C}(\text{Me}))$	58.1 52.3	176
	$^1J(\text{Si}, \text{C}(\text{C}=\text{}))$ $^1J(\text{Si}, \text{C}(\text{Me}))$	58.0 52.5	176
	$^1J(\text{Si}, \text{C}(\text{Me}))$	51.3	117

Table B1.1 (Continued)

	$^1J(\text{Si}, \text{C}(\text{C}=\text{)))}$	66.5	117
$\text{Me}_3\text{Si}-(\text{H})\text{C}=\text{C}(\text{H})-\text{SiMe}_3$	$^1J(\text{Si}, \text{C}(\text{C}=\text{)))}$	63.34	85
	$^1J(\text{Si}, \text{C}(\text{Me}))$	51.89	
Vi_2SiMe_2	$^1J(\text{Si}, \text{C}(\text{C}=\text{)))}$	66	68
	$^1J(\text{Si}, \text{C}(\text{C}=\text{)))}$	66.0	91
	$^1J(\text{Si}, \text{C}(\text{Me}))$	53.7	
	$^1J(\text{Si}, \text{C}(\text{C}=\text{)))}$	56.9	105
	$^1J(\text{Si}, \text{C}(\text{Me}))$	52.9	
	$^1J(\text{Si}(\text{a}), \text{C}(\text{C}=\text{)))}$	53.4	103
	$^1J(\text{Si}(\text{b}), \text{C}(\text{C}=\text{)))}$	55.9	
	$^1J(\text{Si}(\text{a}), \text{C}(\text{Me}))$	49.8	
	$^1J(\text{Si}(\text{b}), \text{C}(\text{Me}))$	50.1	
	$^3J(\text{Si}, \text{C}(\text{Et}))$	11.7	
	$^1J(\text{Si}(\text{b}), \text{C}(\text{C}=\text{)))}$	65.7	177
	$^1J(\text{Si}, \text{C}(\text{Me}))$	51.6	
	$^1J(\text{Si}, \text{C}(\text{Me}))$	50.7	
	$^1J(\text{Si}(\text{a}), \text{C}(\text{C}=\text{)))}$	42.2	177
	$^1J(\text{Si}(\text{b}), \text{C}(\text{C}=\text{)))}$	65.2	
	$^1J(\text{Si}, \text{C}(\text{Me}))$	51.5	
	$^1J(\text{Si}, \text{C}(\text{Me}))$	50.9	
	$^1J(\text{Si}, \text{C}(\text{C}=\text{)))}$	55.3	116
	$^1J(\text{Si}, \text{C}(\text{Me}))$	49.6, 49.9	
	$^1J(\text{Si}, \text{C}(\text{Me}))$	49.6, 49.5	
	$^1J(\text{Si}, \text{C}(\text{C}=\text{)))}$	71.9	178
	$^1J(\text{Si}, \text{C}(\text{Me}))$	50.8	
	$^1J(\text{Si}, \text{C}(\text{C}=\text{)))}$	69.3	179
	$^1J(\text{Si}, \text{C}(\text{Me}))$	50.9	
	$^2J(\text{Si}, \text{C}(12))$	4.6	
	$^3J(\text{Si}, \text{C}(\text{CBr}_2))$	4.8	
	$^3J(\text{Si}, \text{C}(\text{C}3))$	7.0	
Vi_3SiMe	$^1J(\text{Si}, \text{C}(\text{C}=\text{)))}$	70	68
	$^1J(\text{Si}, \text{C}(\text{C}=\text{)))}$	68.0	91
	$^1J(\text{Si}, \text{C}(\text{Me}))$	55.9	

Table B1.1 (Continued)

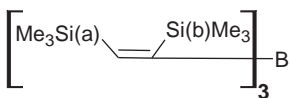
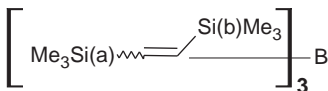
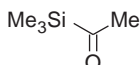
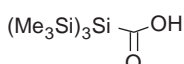
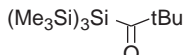
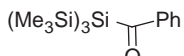
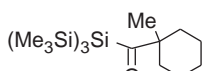
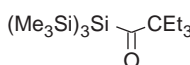
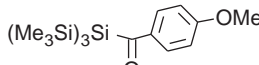
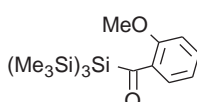
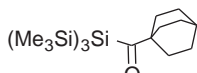
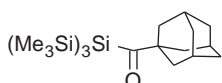
Vi ₄ Si	¹ J(Si, C)	70	74
	¹ J(Si, C)	72.8	91
	¹ J(Si(a), C(C=))	63.4	103
	¹ J(Si(b), C(C=))	57.3	
	¹ J(Si(a), C(Me))	51.1	
	¹ J(Si(b), C(Me))	51.1	
	¹ J(Si(a), C(C=))	65	180
	¹ J(Si(b), C(C=))	50	
	¹ J(Si, C(Me))	52	
	¹ J(Si, C(Me))	51	
	² J(Si(b), C(C=))	45	
<i>Si-C=O bonds</i>			
	¹ J(Si, C(C=O))	-62.3	45
	¹ J(Si, C(Me))	-51.3	
	² J(Si, C(Me))	-21.4	
	¹ J(Si, C(Me))	45.9	88
	² J(Si, C(C=O))	37.6	
	¹ J(Si, C(Me))	45.9	88
	² J(Si, C(C=O))	34.3	
	¹ J(Si, C(Me))	46.3	88
	² J(Si, C(C=O))	38.5	
	¹ J(Si, C(Me))	45.4	88
	² J(Si, C(C=O))	34.8	
	¹ J(Si, C(Me))	44.9	88
	² J(Si, C(C=O))	34.3	
	¹ J(Si, C(Me))	45.4	88
	² J(Si, C(C=O))	37.0	
	¹ J(Si, C(Me))	45.4	88
	² J(Si, C(C=O))	36.7	
	¹ J(Si, C(Me))	45.8	88
	² J(Si, C(C=O))	33.8	
	¹ J(Si, C(C=O))	63.6	88
	¹ J(Si, C(Me))	44.9	
	² J(Si, C(C=O))	34.2	

Table B1.2. Silicon(s) bonded to carbons and hydrogen(s)

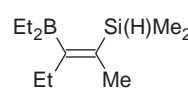
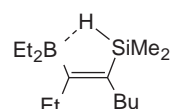
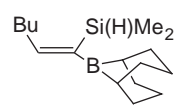
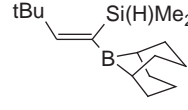
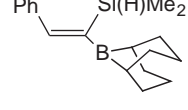
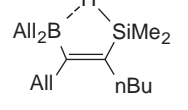
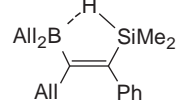
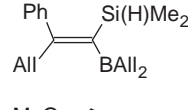
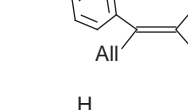
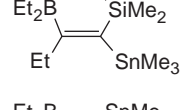
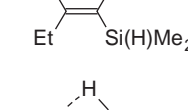
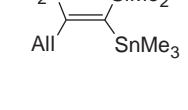
	$^1J(\text{Si}, \text{C}(\text{C}=\text{)))}$ $^1J(\text{Si}, \text{C}(\text{Me}))$ $^2J(\text{Si}, \text{C}(\text{Me}))$	71.4 49.7 6.5	168
	$^1J(\text{Si}, \text{C}(\text{C}=\text{)))}$ $^1J(\text{Si}, \text{C}(\text{Me}))$ $^3J(\text{Si}, \text{C}(\text{Et}))$	71.1 49.4 8.8	83,170
	$^1J(\text{Si}, \text{C}(\text{C}=\text{)))}$ $^1J(\text{Si}, \text{C}(\text{Me}))$	57.9 50.3	181
	$^1J(\text{Si}, \text{C}(\text{C}=\text{)))}$ $^1J(\text{Si}, \text{C}(\text{Me}))$	57.6 51.0	181
	$^1J(\text{Si}, \text{C}(\text{C}=\text{)))}$ $^1J(\text{Si}, \text{C}(\text{Me}))$	55.8 51.1	181
	$^1J(\text{Si}, \text{C}(\text{C}=\text{)))}$ $^1J(\text{Si}, \text{C}(\text{Me}))$	64.4 49.4	61
	$^1J(\text{Si}, \text{C}(\text{C}=\text{)))}$ $^1J(\text{Si}, \text{C}(\text{Me}))$ $^2J(\text{Si}, \text{C}(\text{Ph}))$ $^3J(\text{Si}, \text{C}(\text{All}))$	66.7 51.3 5.2 7.9	61
	$^1J(\text{Si}, \text{C}(\text{Me}))$ $^3J(\text{Si}, \text{C}(\text{All}))$ $^3J(\text{Si}, \text{C}(\text{Ph}))$	51.5 7.6 5.1	61
	$^1J(\text{Si}, \text{C}(\text{Me}))$ $^3J(\text{Si}, \text{C}(\text{All}))$	51.5 7.6	61
	$^1J(\text{Si}, \text{C}(\text{C}=\text{)))}$ $^1J(\text{Si}, \text{C}(\text{Me}))$ $^3J(\text{Si}, \text{C}(\text{Et}))$	58.6 50.6 14.5	182
	$^1J(\text{Si}, \text{C}(\text{C}=\text{)))}$ $^1J(\text{Si}, \text{C}(\text{Me}))$ $^3J(\text{Si}, \text{C}(\text{Et}))$	58.8 49.7 12.3	182
	$^1J(\text{Si}, \text{C}(\text{C}=\text{)))}$ $^1J(\text{Si}, \text{C}(\text{Me}))$ $^3J(\text{Si}, \text{C}(\text{All}))$	56.6 50.5 14.5	182

Table B1.2 (Continued)

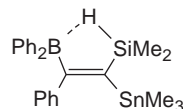
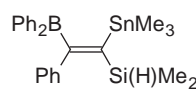
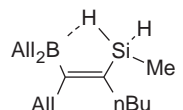
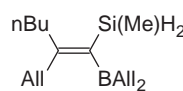
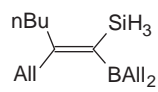
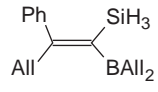
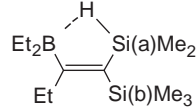
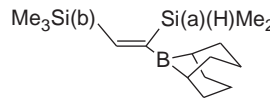
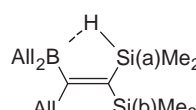
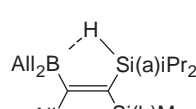
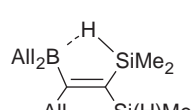
	$^1J(\text{Si}, \text{C}(\text{C}=\text{)))}$	55.7	182
	$^1J(\text{Si}, \text{C}(\text{Me}))$	50.6	
	$^1J(\text{Si}, \text{C}(\text{C}=\text{)))}$	52.6	182
	$^1J(\text{Si}, \text{C}(\text{Me}))$	50.3	
	$^nJ(\text{Si}, \text{C}(\text{Ph}))$	8.6	
	$^1J(\text{Si}, \text{C}(\text{C}=\text{)))}$	68.1	61
	$^1J(\text{Si}, \text{C}(\text{Me}))$	49.4	
	$^3J(\text{Si}, \text{C}(\text{All}))$	7.8	
	$^1J(\text{Si}, \text{C}(\text{Me}))$	51.1	61
	$^3J(\text{Si}, \text{C}(\text{All}))$	8.4	
	$^3J(\text{Si}, \text{C}(\text{All}))$	8.4	61
	$^nJ(\text{Si}, \text{C}(\text{nBu}))$	8.4	
	$^3J(\text{Si}, \text{C}(\text{All}))$	8.2	61
	$^3J(\text{Si}, \text{C}(\text{Ph}))$	5.6	
	$^1J(\text{Si}, \text{C}(\text{C}=\text{)))}$	56.5	183
	$^1J(\text{Si}(\text{a}), \text{C}(\text{Me}))$	49.7	
	$^1J(\text{Si}(\text{b}), \text{C}(\text{Me}))$	50.2	
	$^1J(\text{Si}(\text{a}), \text{C}(\text{C}=\text{)))}$	55.4	181
	$^1J(\text{Si}(\text{b}), \text{C}(\text{C}=\text{)))}$	64.0	
	$^1J(\text{Si}(\text{a}), \text{C}(\text{Me}))$	49.9	
	$^1J(\text{Si}(\text{b}), \text{C}(\text{Me}))$	51.1	
	$^1J(\text{Si}, \text{C}(\text{C}=\text{)))}$	56.5	183
	$^1J(\text{Si}(\text{a}), \text{C}(\text{Me}))$	49.3	
	$^1J(\text{Si}(\text{b}), \text{C}(\text{Me}))$	50.8	
	$^1J(\text{Si}, \text{C}(\text{C}=\text{)))}$	56.5	
	$^1J(\text{Si}, \text{C}(\text{C}=\text{)))}$	57.7	184
	$^1J(\text{Si}(\text{a}), \text{C}(\text{iPr}))$	51.0	
	$^1J(\text{Si}(\text{b}), \text{C}(\text{Me}))$	50.8	
	$^3J(\text{Si}, \text{C}(\text{All}))$	13.6	
	$^3J(\text{Si}, \text{C}(\text{All}))$	6.9	
	$^1J(\text{Si}, \text{C}(\text{C}=\text{)))}$	56.1	183
	$^1J(\text{Si}, \text{C}(\text{Me}))$	50.4	
	$^1J(\text{Si}, \text{C}(\text{Me}))$	49.6	

Table B1.2 (Continued)

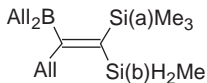
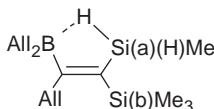
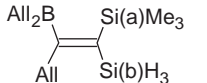
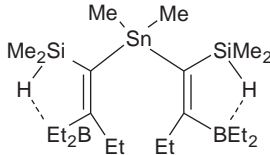
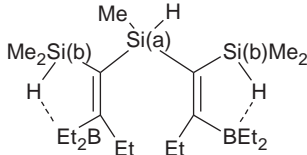
	$^1J(\text{Si}, \text{C}(\text{C}=\text{)))}$	55.4	184
	$^1J(\text{Si}, \text{C}(\text{C}=\text{)))}$	52.4	
	$^1J(\text{Si}(\text{a}), \text{C}(\text{Me}))$	50.2	
	$^1J(\text{Si}(\text{b}), \text{C}(\text{Me}))$	50.9	
	$^3J(\text{Si}, \text{C}(\text{All}))$	12.9	
	$^3J(\text{Si}, \text{C}(\text{All}))$	11.0	
	$^1J(\text{Si}, \text{C}(\text{C}=\text{)))}$	53.9	184
	$^1J(\text{Si}(\text{a}), \text{C}(\text{Me}))$	49.1	
	$^1J(\text{Si}(\text{b}), \text{C}(\text{Me}))$	50.9	
	$^3J(\text{Si}, \text{C}(\text{All}))$	8.2	
	$^1J(\text{Si}, \text{C}(\text{C}=\text{)))}$	55.8	184
	$^1J(\text{Si}, \text{C}(\text{C}=\text{)))}$	52.7	
	$^1J(\text{Si}(\text{a}), \text{C}(\text{Me}))$	51.3	
	$^3J(\text{Si}, \text{C}(\text{All}))$	13.8	
	$^3J(\text{Si}, \text{C}(\text{All}))$	10.3	
	$^1J(\text{Si}, \text{C}(\text{Me}))$	50.2	182
	$^1J(\text{Si}(\text{a}), \text{C}(\text{C}=\text{)))}$	51.2	185
	$^1J(\text{Si}(\text{b}), \text{C}(\text{C}=\text{)))}$	63.4	
	$^1J(\text{Si}(\text{a}), \text{C}(\text{Me}))$	47.6	
	$^1J(\text{Si}(\text{b}), \text{C}(\text{Me}))$	51.8	
	$^1J(\text{Si}(\text{b}), \text{C}(\text{Me}))$	51.8	

Table B1.3. Silicon(s) bonded to nitrogen(s) and carbon(s)

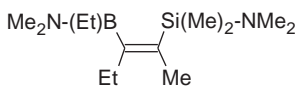
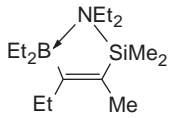
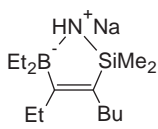
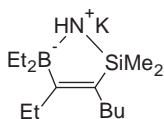
	$^1J(\text{Si}, \text{C}(\text{C}=\text{)))}$	78.0	168
	$^1J(\text{Si}, \text{C}(\text{Me}))$	56.2	
	$^1J(\text{Si}, \text{C}(\text{C}=\text{)))}$	82.7	107
	$^1J(\text{Si}, \text{C}(\text{Me}))$	52.2	
	$^2J(\text{Si}, \text{C}(\text{Me}))$	-9.8	
	$^1J(\text{Si}, \text{C}(\text{Me}))$	47.8	186
	$^1J(\text{Si}, \text{C}(\text{Me}))$	47.8	186

Table B1.3 (Continued)

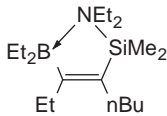
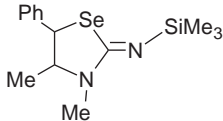
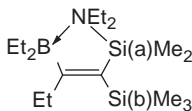
	$^1J(\text{Si}, \text{C}(\text{C}=\text{C}))$	81.7	107
	$^1J(\text{Si}, \text{C}(\text{Me}))$	52.2	
	$^1J(\text{Si}, \text{C})$	56.8	187
$\text{Me}(\text{Vi})\text{Si}[\text{N}(\text{H})i\text{Pr}]_2$	$^1J(\text{Si}, \text{C}(\text{Vi}))$	80.6	80
	$^1J(\text{Si}, \text{C}(\text{Me}))$	67.1	
$\text{Me}(\text{Vi})\text{Si}[\text{N}(\text{H})t\text{Bu}]_2$	$^1J(\text{Si}, \text{C}(\text{Vi}))$	80.7	80
	$^1J(\text{Si}, \text{C}(\text{Me}))$	67.0	
$\text{Vi}-\text{Si}[\text{NMe}_2]_3$	$^1J(\text{Si}, \text{C})$	97.7	137
$\text{Vi}-\text{Si}[\text{N}(\text{H})\text{Pr}]_3$	$^1J(\text{Si}, \text{C})$	92.3	78,137
	$^1J(\text{Si}, \text{C}(\text{C}=\text{C}))$	63.0	107
	$^1J(\text{Si}, \text{C}(\text{C}=\text{C}))$	61.0	
	$^1J(\text{Si}(\text{a}), \text{C}(\text{Me}))$	51.2	
	$^1J(\text{Si}(\text{b}), \text{C}(\text{Me}))$	49.2	

Table B1.4. Silicon bonded to oxygen(s) and carbon(s)

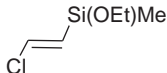

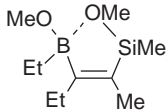
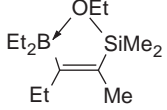
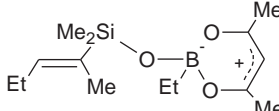
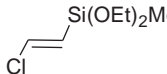
	$^1J(\text{Si}, \text{C}(\text{C}=\text{C}))$	68.20	85
	$^1J(\text{Si}, \text{C}(\text{Me}))$	62.64	
	$^2J(\text{Si}, \text{C}(\text{C}=\text{C}))$	7.06	
	$^1J(\text{Si}, \text{C}(\text{C}=\text{C}))$	71.24	85
	$^1J(\text{Si}, \text{C}(\text{Me}))$	62.64	
	$^1J(\text{Si}, \text{C}(\text{C}=\text{C}))$	82.4	172
	$^1J(\text{Si}, \text{C}(\text{Me}))$	56.0	
	$^1J(\text{Si}, \text{C}(\text{C}=\text{C}))$	87.5	107
	$^1J(\text{Si}, \text{C}(\text{Me}))$	54.1	
	$^2J(\text{Si}, \text{C}(\text{Me}))$	-11.8	
	$^3J(\text{Si}, \text{C}(\text{Et}))$	8.9	
	$^1J(\text{Si}, \text{C}(\text{Me}))$	59	172
	$^1J(\text{Si}, \text{C}(\text{C}=\text{C}))$	86.90	85
	$^1J(\text{Si}, \text{C}(\text{Me}))$	78.38	
	$^2J(\text{Si}, \text{C})$	7.01	

Table B1.4 (Continued)

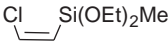
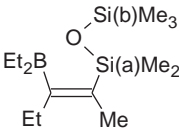
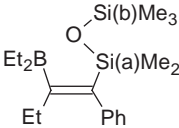
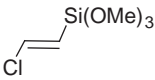
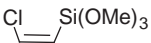
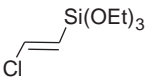
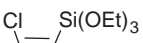
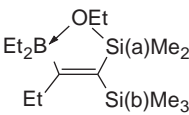
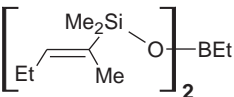
	$^1J(\text{Si}, \text{C}(\text{C}=\text{)))}$ $^1J(\text{Si}, \text{C}(\text{Me}))$	89.68 78.54	85
$\text{Cl}_2\text{C}=\text{C}(\text{H})-\text{Si}(\text{OEt})_2\text{Me}$	$^1J(\text{Si}, \text{C}(\text{C}=\text{)))}$ $^1J(\text{Si}, \text{C}(\text{Me}))$	87.35 81.19	85
$\text{Cl}_2\text{C}=\text{C}(\text{Cl})-\text{Si}(\text{OEt})_2\text{Me}$	$^1J(\text{Si}, \text{C}(\text{C}=\text{)))}$ $^1J(\text{Si}, \text{C}(\text{Me}))$ $^2J(\text{Si}, \text{C}(\text{C}=\text{)))}$	91.30 84.34 8.64	85
	$^1J(\text{Si}(\text{a}), \text{C}(\text{C}=\text{)))}$ $^1J(\text{Si}(\text{a}), \text{C}(\text{Me}))$ $^1J(\text{Si}(\text{b}), \text{C})$	84.6 59.2 57.9	159
	$^1J(\text{Si}(\text{a}), \text{C}(\text{C}=\text{)))}$ $^1J(\text{Si}(\text{a}), \text{C}(\text{Me}))$ $^1J(\text{Si}(\text{b}), \text{C})$	81.1 57.8 59.1	159
	$^1J(\text{Si}, \text{C}(\text{C}=\text{)))}$ $^2J(\text{Si}, \text{C}(\text{C}=\text{)))}$	115.68 8.05	85
	$^1J(\text{Si}, \text{C}(\text{C}=\text{)))}$	116.74	85
	$^1J(\text{Si}, \text{C}(\text{C}=\text{)))}$ $^2J(\text{Si}, \text{C}(\text{C}=\text{)))}$	114.56 7.79	85
	$^1J(\text{Si}, \text{C}(\text{C}=\text{)))}$	117.08	85
$\text{Cl}_2\text{C}=\text{C}(\text{H})-\text{Si}(\text{OEt})_3$	$^1J(\text{Si}, \text{C}(\text{C}=\text{)))}$	115.67	85
$\text{Cl}_2\text{C}=\text{C}(\text{Cl})-\text{Si}(\text{OEt})_3$	$^1J(\text{Si}, \text{C}(\text{C}=\text{)))}$ $^2J(\text{Si}, \text{C}(\text{C}=\text{)))}$	127.28 9.75	85
	$^1J(\text{Si}, \text{C}(\text{C}=\text{)))}$ $^1J(\text{Si}, \text{C}(\text{C}=\text{)))}$ $^1J(\text{Si}(\text{a}), \text{C}(\text{Me}))$ $^1J(\text{Si}(\text{b}), \text{C}(\text{Me}))$	66.9 61.0 55.1 51.2	107
	$^1J(\text{Si}, \text{C}(\text{C}=\text{)))}$ $^1J(\text{Si}, \text{C}(\text{Me}))$	79.3 61.0	172
$(\text{EtO})_3\text{Si}-\text{C}(\text{H})=\text{C}(\text{H})-\text{Si}(\text{OEt})_3$	$^1J(\text{Si}, \text{C}(\text{C}=\text{)))}$	115.96	85

Table B1.5. Silicon(s) bonded to chlor(s) and carbon(s) and possibly to hydrogen(s)

	$^1J(\text{Si}, \text{C}(\text{C}=\text{}))$ $^1J(\text{Si}, \text{C}(\text{Me}))$	76.5 59.8	82
	$^1J(\text{Si}, \text{C}(\text{C}=\text{}))$ $^1J(\text{Si}, \text{C}(\text{Me}))$ $^2J(\text{Si}, \text{C})$	69.87 60.69 7.42	85
	$^1J(\text{Si}, \text{C}(\text{C}=\text{}))$ $^1J(\text{Si}, \text{C}(\text{Me}))$	73.02 60.49	85
$\text{Cl}_2\text{C}=\text{C}(\text{H})-\text{Si}(\text{Cl})\text{Me}_2$	$^1J(\text{Si}, \text{C}(\text{C}=\text{}))$ $^1J(\text{Si}, \text{C}(\text{Me}))$	70.19 61.77	85
$\text{Cl}_2\text{C}=\text{C}(\text{Cl})-\text{Si}(\text{Cl})\text{Me}_2$	$^1J(\text{Si}, \text{C}(\text{C}=\text{}))$ $^1J(\text{Si}, \text{C}(\text{Me}))$ $^2J(\text{Si}, \text{C}(\text{C}=\text{}))$	74.80 63.82 8.08	85
	$^1J(\text{Si}, \text{C}(\text{C}=\text{}))$ $^1J(\text{Si}, \text{C}(\text{Me}))$	78.3 57.0	172
	$^1J(\text{Si}, \text{C}(\text{Me}))$	59.0	172
	$^1J(\text{Si}, \text{C}(\text{C}=\text{}))$ $^1J(\text{Si}, \text{C}(\text{Me}))$ $^3J(\text{Si}, \text{C}(\text{Et}))$	80.2 56.0 9.1	83
	$^1J(\text{Si}, \text{C}(\text{C}=\text{}))$ $^1J(\text{Si}, \text{C}(\text{Me}))$ $^2J(\text{Si}, \text{C}(\text{CH}_2))$ $^3J(\text{Si}, \text{C}(\text{Et}))$	86.6 60.3 7.4 9.9	83
	$^1J(\text{Si}, \text{C}(\text{C}=\text{}))$ $^1J(\text{Si}, \text{C}(\text{Me}))$	80.2 57.1	83
	$^1J(\text{Si}, \text{C}(\text{C}=\text{}))$ $^1J(\text{Si}, \text{C}(\text{Me}))$	64.5 56.9	181
	$^1J(\text{Si}, \text{C}(\text{Me}))$ $^1J(\text{Si}, \text{C}(\text{C}=\text{}))$ $^1J(\text{Si}, \text{C}(\text{Me}))$	57.7 66.0 57.9	188 181
	$^1J(\text{Si}, \text{C}(\text{C}=\text{}))$ $^1J(\text{Si}, \text{C}(\text{Me}))$	63.5 57.2	181

Table B1.5 (Continued)

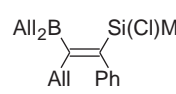
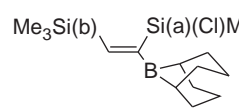
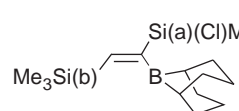
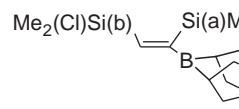
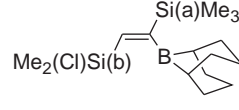
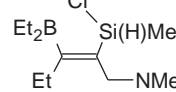
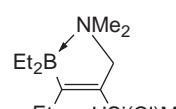
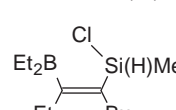
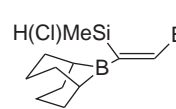
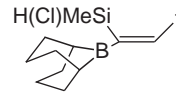
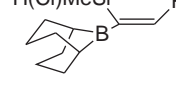
	$^1J(\text{Si}, \text{C}(\text{Me}))$	58.6	171
$\text{Me}_2(\text{Cl})\text{C}(\text{H})=\text{C}(\text{H})\text{Si}(\text{Cl})\text{Me}_2$	$^1J(\text{Si}, \text{C}(\text{C}=\text{}))$ $^1J(\text{Si}, \text{C}(\text{Me}))$	71.11 59.30	85
	$^1J(\text{Si}(\text{a}), \text{C}(\text{C}=\text{}))$ $^1J(\text{Si}(\text{b}), \text{C}(\text{C}=\text{}))$ $^1J(\text{Si}(\text{a}), \text{C}(\text{Me}))$ $^1J(\text{Si}(\text{b}), \text{C}(\text{Me}))$	64.5 62.7 56.5 52.1	181
	$^1J(\text{Si}(\text{b}), \text{C}(\text{C}=\text{}))$ $^1J(\text{Si}(\text{a}), \text{C}(\text{Me}))$ $^1J(\text{Si}(\text{b}), \text{C}(\text{Me}))$	62.8 58.5 51.5	181
	$^1J(\text{Si}(\text{b}), \text{C}(\text{C}=\text{}))$ $^1J(\text{Si}(\text{a}), \text{C}(\text{Me}))$ $^1J(\text{Si}(\text{b}), \text{C}(\text{Me}))$	76.3 51.1 58.0	181
	$^1J(\text{Si}(\text{b}), \text{C}(\text{C}=\text{}))$ $^1J(\text{Si}(\text{a}), \text{C}(\text{Me}))$ $^1J(\text{Si}(\text{b}), \text{C}(\text{Me}))$	75.0 52.3 56.4	181
	$^1J(\text{Si}, \text{C}(\text{C}=\text{}))$ $^1J(\text{Si}, \text{C}(\text{Me}))$ $^2J(\text{Si}, \text{C}(\text{CH}_2))$ $^3J(\text{Si}, \text{C}(\text{Et}))$	94.3 63.7 4.7 11.5	83
	$^1J(\text{Si}, \text{C}(\text{C}=\text{}))$ $^1J(\text{Si}, \text{C}(\text{Me}))$ $^2J(\text{Si}, \text{C}(\text{CH}_2))$ $^3J(\text{Si}, \text{C}(\text{Et}))$	80.6 59.0 12.3 8.0	83
	$^1J(\text{Si}, \text{C}(\text{C}=\text{}))$ $^1J(\text{Si}, \text{C}(\text{Me}))$	80.0 55.8	83
	$^1J(\text{Si}, \text{C}(\text{C}=\text{}))$ $^1J(\text{Si}, \text{C}(\text{Me}))$	64.1 56.1	181
	$^1J(\text{Si}, \text{C}(\text{C}=\text{}))$ $^1J(\text{Si}, \text{C}(\text{Me}))$	65.6 56.9	181
	$^1J(\text{Si}, \text{C}(\text{C}=\text{}))$ $^1J(\text{Si}, \text{C}(\text{Me}))$	64.7 57.3	181

Table B1.5 (Continued)

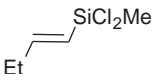
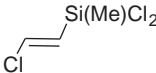
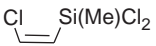
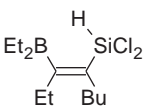
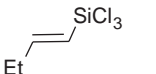
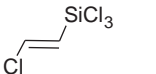

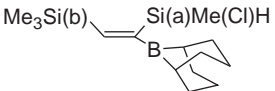
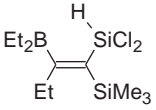
Vi(Me)SiCl_2	$^1J(\text{Si}, \text{C}(\text{C}=\text{}))$	92	74
	$^1J(\text{Si}, \text{C}(\text{Me}))$	71	
	$^1J(\text{Si}, \text{C}(\text{C}=\text{}))$	89.70	85
	$^1J(\text{Si}, \text{C}(\text{Me}))$	70.40	
	$^1J(\text{Si}, \text{C}(\text{C}=\text{}))$	93.1	82
	$^1J(\text{Si}, \text{C}(\text{Me}))$	71.3	
	$^1J(\text{Si}, \text{C}(\text{C}=\text{}))$	86.11	85
	$^1J(\text{Si}, \text{C}(\text{Me}))$	73.00	
	$^2J(\text{Si}, \text{C})$	9.03	
	$^1J(\text{Si}, \text{C}(\text{C}=\text{}))$	89.62	85
	$^1J(\text{Si}, \text{C}(\text{Me}))$	72.28	
$\text{Cl}_2\text{C}=\text{C}(\text{H})\text{--Si}(\text{Me})\text{Cl}_2$	$^1J(\text{Si}, \text{C}(\text{C}=\text{}))$	87.81	85
	$^1J(\text{Si}, \text{C}(\text{Me}))$	74.37	
$\text{Cl}_2\text{C}=\text{C}(\text{Cl})\text{--Si}(\text{Me})\text{Cl}_2$	$^1J(\text{Si}, \text{C}(\text{C}=\text{}))$	96.77	85
	$^1J(\text{Si}, \text{C}(\text{Me}))$	77.58	
	$^2J(\text{Si}, \text{C}(\text{C}=\text{}))$	10.72	
	$^1J(\text{Si}, \text{C}(\text{C}=\text{}))$	94.2	177
Vi--SiCl_3	$^1J(\text{Si}, \text{C})$	113	74
	$^1J(\text{Si}, \text{C})$	118.1	82
	$^1J(\text{Si}, \text{C})$	112.40	85
	$^1J(\text{Si}, \text{C})$	111.86	85
	$^2J(\text{Si}, \text{C})$	11.54	
	$^1J(\text{Si}, \text{C})$	115.58	85
$\text{Cl}_2\text{C}=\text{C}(\text{H})\text{--SiCl}_3$	$^1J(\text{Si}, \text{C})$	114.62	85
$\text{Cl}_2\text{C}=\text{C}(\text{Cl})\text{--SiCl}_3$	$^1J(\text{Si}, \text{C})$	130.77	85
	$^2J(\text{Si}, \text{C})$	13.42	
$\text{Cl}_3\text{Si--CH}=\text{CH--SiCl}_3$	$^1J(\text{Si}, \text{C})$	107.46	85
	$^1J(\text{Si}(\text{a}), \text{C}(\text{C}=\text{}))$	64.2	181
	$^1J(\text{Si}(\text{b}), \text{C}(\text{C}=\text{}))$	61.0	
	$^1J(\text{Si}(\text{a}), \text{C}(\text{Me}))$	56.0	
	$^1J(\text{Si}(\text{b}), \text{C}(\text{Me}))$	52.0	
	$^1J(\text{Si}, \text{C}(\text{C}=\text{}))$	71.0	177
	$^1J(\text{Si}, \text{C}(\text{C}=\text{}))$	55.6	
	$^1J(\text{Si}, \text{C}(\text{Me}))$	51.2	

Table B1.5 (Continued)

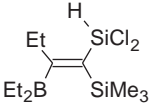
	$^1J(\text{Si}, \text{C})$	68.2	177
	$^1J(\text{Si}, \text{C})$	55.1	
	$^1J(\text{Si}, \text{C}(\text{Me}))$	51.4	
	$^3J(\text{Si}, \text{C}(\text{Et}))$	17.4	
	$^3J(\text{Si}, \text{C}(\text{Et}))$	9.6	
$\text{Cl}_2(\text{Me})\text{Si}-\text{CH}=\text{CH}-\text{Si}(\text{Me})\text{Cl}_2$	$^1J(\text{Si}, \text{C}(\text{C}=\text{C}))$	84.42	85
	$^1J(\text{Si}, \text{C}(\text{Me}))$	71.01	

Table B1.6. Silicon bonded to ring(s) or within ring(s) by $\text{Si}(\text{sp}^3)-\text{C}(\text{sp}^3)$ bond(s)

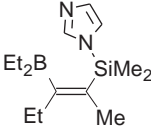
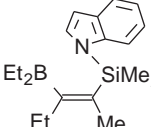
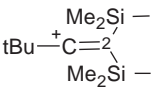
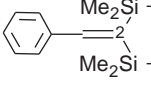
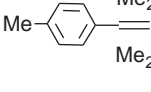
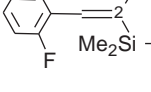
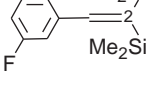
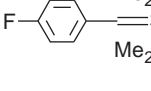
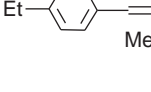
	$^1J(\text{Si}, \text{C}(\text{C}=\text{C}))$	82.6	107
	$^1J(\text{Si}, \text{C}(\text{Me}))$	46.0	
	$^1J(\text{Si}, \text{C}(\text{C}=\text{C}))$	80.7	107
	$^1J(\text{Si}, \text{C}(\text{Me}))$	57.1	
	$^1J(\text{Si}, \text{C}(2))$	15.7	59
	$^1J(\text{Si}, \text{C}(4, 6))$	56.2	
	$^1J(\text{Si}, \text{C}(\text{Me}))$	55.7, 55.3	
	$^1J(\text{Si}, \text{C}(2))$	18.2	94
	$^1J(\text{Si}, \text{C}(4, 6, \text{Me}))$	55.0	
	$^1J(\text{Si}, \text{C}(2))$	19.8	94
	$^1J(\text{Si}, \text{C}(4, 6, \text{Me}))$	54.7	
	$^1J(\text{Si}, \text{C}(2))$	16.6	94
	$^1J(\text{Si}, \text{C}(4, 6, \text{Me}))$	55.2	
	$^1J(\text{Si}, \text{C}(2))$	17.2	94
	$^1J(\text{Si}, \text{C}(4, 6, \text{Me}))$	55.5	
	$^1J(\text{Si}, \text{C}(2))$	18.8	94
	$^1J(\text{Si}, \text{C}(4, 6, \text{Me}))$	55.9	
	$^1J(\text{Si}, \text{C}(2))$	20.2	94
	$^1J(\text{Si}, \text{C}(4, 6, \text{Me}))$	55.7	

Table B1.6 (Continued)

	$^1J(\text{Si}, \text{C}(2))$ $^1J(\text{Si}, \text{C}(4, 6, \text{Me}))$	20.7 55.7	94
	$^1J(\text{Si}, \text{C}(2))$ $^1J(\text{Si}, \text{C}(4, 6, \text{Me}))$	19.5 55.5	94
	$^1J(\text{Si}, \text{C}(2))$ $^1J(\text{Si}, \text{C}(4, 6, \text{Me}))$	18.8 55.6	94
	$^1J(\text{Si}, \text{C}(2))$ $^1J(\text{Si}, \text{C}(4, 6, \text{Me}))$	18.4 55.7	94
	$^1J(\text{Si}, \text{C}(2))$ $^1J(\text{Si}, \text{C}(4, 6, \text{Me}))$	19.5 55.6	94
	$^1J(\text{Si}, \text{C}(2))$ $^1J(\text{Si}, \text{C}(4, 6, \text{Me}))$	19.6, 19.9 55.7	94
	$^1J(\text{Si}, \text{C}(\text{C}=\text{C}))$ $^1J(\text{Si}, \text{C}(\text{Me}))$ $^3J(\text{Si}, \text{C}(\text{Bu}))$	61.9 53.4 8.9	189
	$^1J(\text{Si}(\text{a}), \text{C})$	56.0	118
	$^1J(\text{Si}(\text{a}), \text{C})$	53.8	118
	$^1J(\text{Si}, \text{C})$	77.6	137

APPENDIX B2

Tables of silicon–carbon coupling constants in molecules containing Si bonded by Si(sp³)–C(sp²) bond to ring(s).

Table B2.1. Compounds with silicon bonded to one five-membered ring

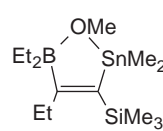
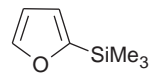
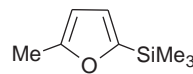
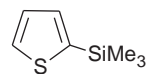
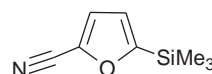
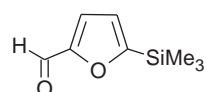
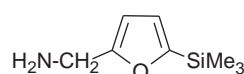
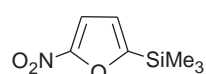
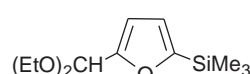
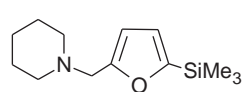
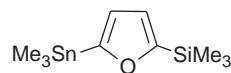
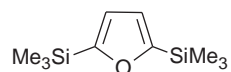
	$^1J(\text{Si}, \text{C}(\text{Me}))$	51.6	190
	$^1J(\text{Si}, \text{C}(\text{C}=\text{O}))$ $^1J(\text{Si}, \text{C}(\text{Me}))$	76.2 53.7	87
	$^1J(\text{Si}, \text{C}(\text{C}=\text{O}))$ $^1J(\text{Si}, \text{C}(\text{Me}))$	77.9 53.8	87
	$^1J(\text{Si}, \text{C}(\text{C}=\text{O}))$ $^1J(\text{Si}, \text{C}(\text{Me}))$	66.1 53.5	87
	$^1J(\text{Si}, \text{C}(\text{C}=\text{O}))$ $^1J(\text{Si}, \text{C}(\text{Me}))$	69.0 54.4	87
	$^1J(\text{Si}, \text{C}(\text{C}=\text{O}))$ $^1J(\text{Si}, \text{C}(\text{Me}))$	69.4 54.3	87
	$^1J(\text{Si}, \text{C}(\text{C}=\text{O}))$ $^1J(\text{Si}, \text{C}(\text{Me}))$	76.4 53.9	87
	$^1J(\text{Si}, \text{C}(\text{C}=\text{O}))$ $^1J(\text{Si}, \text{C}(\text{Me}))$	66.8 54.7	87
	$^1J(\text{Si}, \text{C}(\text{C}=\text{O}))$ $^1J(\text{Si}, \text{C}(\text{Me}))$	75.7 54.0	87
	$^1J(\text{Si}, \text{C}(\text{C}=\text{O}))$ $^1J(\text{Si}, \text{C}(\text{Me}))$	76.7 53.9	87
	$^1J(\text{Si}, \text{C}(\text{C}=\text{O}))$ $^1J(\text{Si}, \text{C}(\text{Me}))$	75.9 53.7	87
	$^1J(\text{Si}, \text{C}(\text{C}=\text{O}))$ $^1J(\text{Si}, \text{C}(\text{Me}))$	75.7 53.9	87

Table B2.1 (Continued)

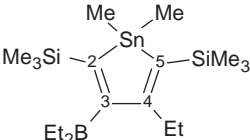
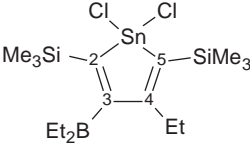
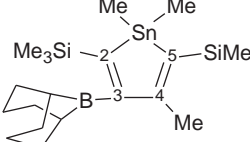
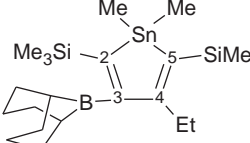
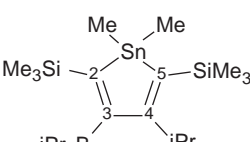
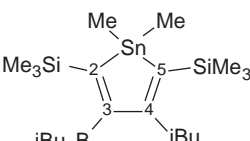
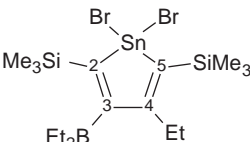
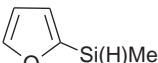
	$^1J(\text{Si}, \text{C}(2))$ $^1J(\text{Si}, \text{C}(5))$ $^1J(\text{Si}, \text{C}(\text{Me}))$ $^1J(\text{Si}, \text{C}(\text{Me}))$ $^{2,3}J(\text{Si}, \text{C}(4))$	65.0 63.6 51.9 51.9 11.6	191,192
	$^1J(\text{Si}, \text{C}(2))$ $^1J(\text{Si}, \text{C}(5))$	63.6 62.0	176
	$^1J(\text{Si}, \text{C}(2))$ $^1J(\text{Si}, \text{C}(5))$ $^1J(\text{Si}, \text{C}(\text{Me}))$ $^1J(\text{Si}, \text{C}(\text{Me}))$	65.1 64.2 52.3 52.3	191
	$^1J(\text{Si}, \text{C}(2))$ $^1J(\text{Si}, \text{C}(5))$ $^1J(\text{Si}, \text{C}(\text{Me}))$ $^1J(\text{Si}, \text{C}(\text{Me}))$ $^{2,3}J(\text{Si}, \text{C}(4))$ $^{2,3}J(\text{Si}, \text{C}(4))$	65.4 64.3 52.3 52.3 14.1 10.5	191
	$^1J(\text{Si}, \text{C}(2))$ $^1J(\text{Si}, \text{C}(5))$ $^1J(\text{Si}, \text{C}(\text{Me}))$ $^1J(\text{Si}, \text{C}(\text{Me}))$	65.5 64.0 51.2 51.2	191
	$^1J(\text{Si}, \text{C}(2))$ $^1J(\text{Si}, \text{C}(5))$ $^1J(\text{Si}, \text{C}(\text{Me}))$ $^1J(\text{Si}, \text{C}(\text{Me}))$	65.3 63.8 52.0 52.0	191
	$^1J(\text{Si}, \text{C}(2))$ $^1J(\text{Si}, \text{C}(5))$	63.5 62.8	176
<i>Si-H bond(s)</i>			
	$^1J(\text{Si}, \text{C}(\text{C}=\text{O}))$	80.2	86

Table B2.1 (Continued)

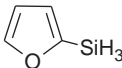
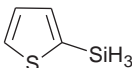
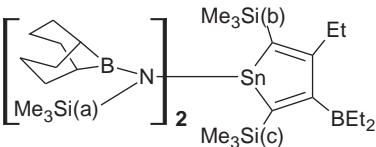
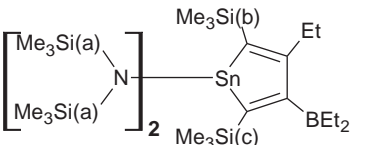
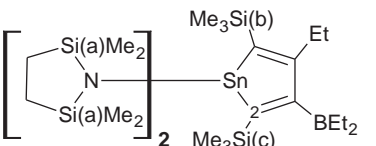
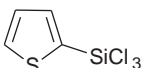
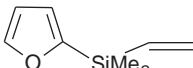
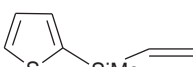
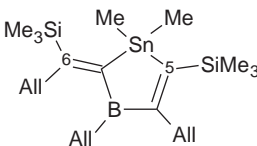
	$^1J(\text{Si}, \text{C})$	84.0	87
	$^1J(\text{Si}, \text{C})$	73.2	87
<i>Si–N bonds</i>			
	$^1J(\text{Si(a)}, \text{C(Me)})$	56.0	133
	$^1J(\text{Si(a)}, \text{C(Me)})$	56.1	
	$^1J(\text{Si(b, c)}, \text{C(Me)})$	52.4	
	$^1J(\text{Si(b, c)}, \text{C(Me)})$	51.6	
	$^1J(\text{Si(a)}, \text{C(Me)})$	55.3	133,193
	$^1J(\text{Si(b, c)}, \text{C(Me)})$	52.3	
	$^1J(\text{Si(b, c)}, \text{C(Me)})$	51.8	
	$^1J(\text{Si(a)}, \text{C(CH}_2\text{)})$	63.6	133
	$^1J(\text{Si(a)}, \text{C(Me)})$	53.5	
	$^1J(\text{Si(a)}, \text{C(Me)})$	53.5	
	$^1J(\text{Si(b, c)}, \text{C(Me)})$	51.2	
	$^1J(\text{Si(b, c)}, \text{C(Me)})$	51.2	
<i>Si–Cl bonds</i>			
	$^1J(\text{Si}, \text{C})$	129.4	87
<i>Si–Vi bond</i>			
	$^1J(\text{Si}, \text{C(OC=)})$	78.0	86
	$^1J(\text{Si}, \text{C(Vi)})$	69.0	
	$^1J(\text{Si}, \text{C(SC=)})$	68.4	86
	$^1J(\text{Si}, \text{C(Vi)})$	68.3	
	$^1J(\text{Si}, \text{C(5)})$	55.7	194
	$^1J(\text{Si}, \text{C(6)})$	61.8	
	$^1J(\text{Si}, \text{C(Me)})$	50.9	
	$^1J(\text{Si}, \text{C(Me)})$	50.9	

Table B2.2. Compounds with silicon bonded to more five-membered rings

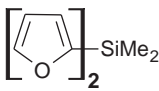
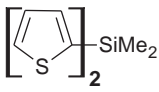
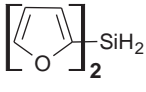
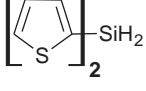
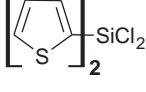
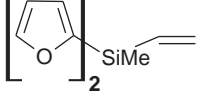
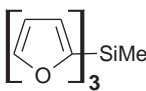
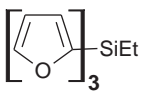
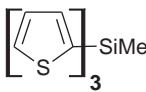
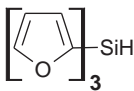
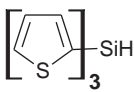
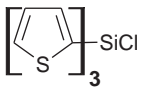
	$^1J(\text{Si}, \text{C}(\text{C}=\text{O}))$	83.0	87
	$^1J(\text{Si}, \text{C}(\text{Me}))$	57.1	
	$^1J(\text{Si}, \text{C}(\text{C}=\text{O}))$	71.5	87
	$^1J(\text{Si}, \text{C}(\text{Me}))$	56.6	
	$^1J(\text{Si}, \text{C})$	87.8	87
	$^1J(\text{Si}, \text{C})$	75.4	87
	$^1J(\text{Si}, \text{C})$	108.6	87
	$^1J(\text{Si}, \text{C}(\text{OC}=\text{O}))$	85.3	86
	$^1J(\text{Si}, \text{C}(\text{Vi}))$	73.4	
	$^1J(\text{Si}, \text{C}(\text{C}=\text{O}))$	90.3	87
	$^1J(\text{Si}, \text{C}(\text{Me}))$	60.5	
	$^1J(\text{Si}, \text{C}(\text{C}=\text{O}))$	89.8	86
	$^1J(\text{Si}, \text{C}(\text{C}=\text{O}))$	77.1	87
	$^1J(\text{Si}, \text{C}(\text{Me}))$	59.6	
	$^1J(\text{Si}, \text{C})$	92.0	87
	$^1J(\text{Si}, \text{C})$	78.7	87
	$^1J(\text{Si}, \text{C})$	93.7	87

Table B2.2 (Continued)

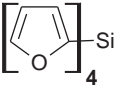
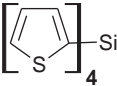
	$^1J(\text{Si}, \text{C})$	97.3	87
	$^1J(\text{Si}, \text{C})$	82.7	87

Table B2.3. Compounds with silicon bonded to six-membered ring(s)

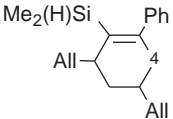
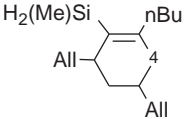
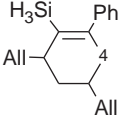
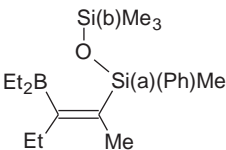
Me_3SiPh	$^1J(\text{Si}, \text{C}(\text{Ph}))$	66.5	68
	$^1J(\text{Si}, \text{C})$	52.2	70
	$^1J(\text{Si}, \text{C}(\text{Me}))$	51.0	61
	$^1J(\text{Si}, \text{C}(\text{Me}))$	50.5	
	$^3J(\text{Si}, \text{C}(4))$	5.3	
	$^3J(\text{Si}, \text{C}(\text{Ph}))$	4.5	
	$^1J(\text{Si}, \text{C}(\text{Me}))$	50.0	61
	$^2J(\text{Si}, \text{C}(\text{C}=\text{C}))$	8.2	
	$^3J(\text{Si}, \text{C}(4))$	7.6	
	$^2J(\text{Si}, \text{C}(\text{C}=\text{C}))$	3.0	61
	$^3J(\text{Si}, \text{C}(4))$	5.6	
	$^3J(\text{Si}, \text{C}(\text{Ph}))$	5.6	
$\text{H}_3\text{Si-Ph}$	$^1J(\text{Si}, \text{C})$	71.6	195
	$^2J(\text{Si}, \text{C})$	4.88	
	$^3J(\text{Si}, \text{C})$	6.09	
$\text{Me}_2(\text{Ph})\text{Si}(\text{b})-\text{Si}(\text{a})\text{Me}_3$	$^1J(\text{Si}(\text{a}), \text{C})$	44.1	119
	$^1J(\text{Si}(\text{b}), \text{C})$	44.8	
$\text{Me}_2(\text{Ph})\text{Si}-\text{N}(\text{H})\text{Et}$	$^1J(\text{Si}, \text{C}(\text{Ph}))$	71.9	80
	$^1J(\text{Si}, \text{C}(\text{Me}))$	58.3	
$\text{Me}_2(\text{Ph})\text{Si}-\text{N}(\text{H})i\text{Pr}$	$^1J(\text{Si}, \text{C}(\text{Ph}))$	72.4	80
	$^1J(\text{Si}, \text{C}(\text{Me}))$	57.8	
$\text{Me}(\text{Ph})\text{Si}[\text{N}(\text{H})i\text{Pr}]_2$	$^1J(\text{Si}, \text{C}(\text{Ph}))$	81.7	80
	$^1J(\text{Si}, \text{C}(\text{Me}))$	67.0	
$\text{Me}(\text{Ph})\text{Si}[\text{N}(\text{H})t\text{Bu}]_2$	$^1J(\text{Si}, \text{C}(\text{Ph}))$	81.6	80
	$^1J(\text{Si}, \text{C}(\text{Me}))$	66.5	
$\text{Ph-Si}(\text{N}(\text{H})\text{Pr})_3$	$^1J(\text{Si}, \text{C})$	92.9	137,78
	$^1J(\text{Si}(\text{a}), \text{C}(\text{Ph}))$	73.3	159
	$^1J(\text{Si}(\text{a}), \text{C}(\text{Me}))$	59.5	
	$^1J(\text{Si}(\text{b}), \text{C})$	59.1	

Table B2.3 (Continued)

	$^1J(\text{Si}, \text{C}(\text{Me}))$	59.9, 59.8	196
	$^1J(\text{Si}, \text{C}(\text{Me}))$	59.4, 59.83	196
$\text{Ph}(\text{CH}_3-(\text{CH}_2)_2)\text{SiCl}_2$	$^1J(\text{Si}, \text{C}(\text{CH}_2))$	71	197
$\text{Ph}(\text{CH}_3-(\text{CH}_2)_5)\text{SiCl}_2$	$^1J(\text{Si}, \text{C}(\text{CH}_2))$	71	197
$\text{Ph}(\text{CH}_3-(\text{CH}_2)_7)\text{SiCl}_2$	$^1J(\text{Si}, \text{C}(\text{CH}_2))$	71	197
$\text{MeO}-\text{C}_6\text{H}_4-\text{SiCl}_2-(\text{CH}_2)_5-\text{Me}$	$^1J(\text{Si}, \text{C}(\text{CH}_2))$	71	197
$\text{Ph}-\text{SiCl}_3$	$^1J(\text{Si}, \text{C})$	~ 117	195
$(\text{Me}_2(\text{Ph})\text{Si}-\text{CH}_2)_2\text{SnCl}_2$	$^3J(\text{Si}, \text{C})$	9.1	
	$^1J(\text{Si}, \text{C}(\text{Me}))$	54.4	198
	$^1J(\text{Si}, \text{C}(\text{C}=\text{N}))$	38.6	60
	$^1J(\text{Si}, \text{C}(\text{C}=\text{N}))$	1.0	60
	$^1J(\text{Si}, \text{C}(\text{C}=\text{N}))$	22.1	60
$\text{Ph}_2(\text{Me})\text{Si}-\text{NH}_2$	$^1J(\text{Si}, \text{C}(\text{Ph}))$	74.4	79
	$^1J(\text{Si}, \text{C}(\text{Me}))$	59.8	
$\text{Ph}_2(\text{Me})\text{Si}-\text{N}(\text{H})\text{Ph}$	$^1J(\text{Si}, \text{C}(\text{Ph}))$	76.1	78
	$^1J(\text{Si}, \text{C}(\text{Me}))$	60.6	
$(\text{Me}_2(\text{Ph})\text{Si})_2\text{NH}$	$^1J(\text{Si}, \text{C}(\text{Ph}))$	72.2	79
	$^1J(\text{Si}, \text{C}(\text{Me}))$	58.2	
	$^1J(\text{Si}, \text{C}(\text{Ph}))$	74.4	111
	$^1J(\text{Si}, \text{C}(\text{tBu}))$	69.4	
	$^2J(\text{Si}, \text{C}(\text{OPh}))$	2.63	
	$^3J(\text{Si}, \text{C}(\text{OPh}))$	2.02	

Table B2.3 (Continued)

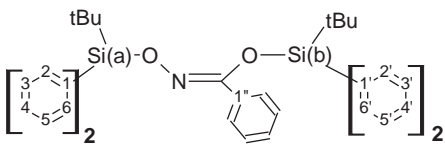
$\text{Ph}_2(\text{tBu})\text{Si}-\text{O}-\text{C}_6\text{H}_4-\text{Me}$	$^1J(\text{Si}, \text{C}(\text{Ph}))$	74.0	111
	$^1J(\text{Si}, \text{C}(\text{tBu}))$	69.4	
	$^2J(\text{Si}, \text{C}(\text{OPh}))$	2.62	
	$^3J(\text{Si}, \text{C}(\text{OPh}))$	2.06	
$\text{Ph}_2(\text{tBu})\text{Si}-\text{O}-\text{C}_6\text{H}_4-\text{F}$	$^1J(\text{Si}, \text{C}(\text{Ph}))$	74.8	111
	$^1J(\text{Si}, \text{C}(\text{tBu}))$	69.4	
	$^2J(\text{Si}, \text{C}(\text{OPh}))$	2.56	
	$^3J(\text{Si}, \text{C}(\text{OPh}))$	2.08	
$\text{Ph}_2(\text{tBu})\text{Si}-\text{O}-\text{C}_6\text{H}_4-\text{OMe}$	$^1J(\text{Si}, \text{C}(\text{Ph}))$	74.8	111
	$^1J(\text{Si}, \text{C}(\text{tBu}))$	69.4	
	$^2J(\text{Si}, \text{C}(\text{OPh}))$	2.56	
	$^3J(\text{Si}, \text{C}(\text{OPh}))$	1.99	
$\text{Ph}_2(\text{tBu})\text{Si}-\text{O}-\text{C}_6\text{H}_4-\text{Cl}$	$^1J(\text{Si}, \text{C}(\text{Ph}))$	74.8	111
	$^1J(\text{Si}, \text{C}(\text{tBu}))$	69.4	
	$^2J(\text{Si}, \text{C}(\text{OPh}))$	2.63	
	$^3J(\text{Si}, \text{C}(\text{OPh}))$	2.08	
$\text{Ph}_2(\text{tBu})\text{Si}-\text{O}-\text{C}_6\text{H}_4-\text{NO}_2$	$^1J(\text{Si}, \text{C}(\text{Ph}))$	74.8	111
	$^1J(\text{Si}, \text{C}(\text{tBu}))$	69.4	
	$^2J(\text{Si}, \text{C}(\text{OPh}))$	2.69	
	$^3J(\text{Si}, \text{C}(\text{OPh}))$	2.07	
$\text{Ph}_2(\text{tBu})\text{Si}-\text{O}-\text{C}_6\text{H}_4-\text{CF}_3$	$^1J(\text{Si}, \text{C}(\text{Ph}))$	74.0	111
	$^1J(\text{Si}, \text{C}(\text{tBu}))$	69.4	
	$^2J(\text{Si}, \text{C}(\text{OPh}))$	2.66	
	$^3J(\text{Si}, \text{C}(\text{OPh}))$	2.08	
$\left[\text{F}-\text{C}_6\text{H}_4 \right]_2-\text{Si}(\text{Cl})\text{Me}$	$^1J(\text{Si}, \text{C}(\text{Me}))$	61.5	196
$(\text{Me}_2(\text{Ph})\text{Si}-\text{CH}_2)_3\text{SnH}$	$^1J(\text{Si}, \text{C}(\text{Me}))$	52.5	198
$(\text{Me}_2(\text{Ph})\text{Si}-\text{CH}_2)_4\text{Sn}$	$^1J(\text{Si}, \text{C}(\text{CH}_2))$	33.9	198
	$^1J(\text{Si}, \text{C}(\text{Me}))$	52.5	
$(\text{Ph}_2(\text{Me})\text{Si})_2\text{NH}$	$^1J(\text{Si}, \text{C}(\text{Ph}))$	74.6	79
	$^1J(\text{Si}, \text{C}(\text{Me}))$	60.0	
	$^2J(\text{Si}(\text{a}), \text{C}(2,6))$	3.5	28
	$^2J(\text{Si}(\text{b}), \text{C}(2',6'))$	3.7	
	$^2J(\text{Si}(\text{b}), \text{C}(\text{C}=\text{N}))$	4.6	
	$^3J(\text{Si}(\text{a}), \text{C}(3,5))$	5.3	
	$^3J(\text{Si}(\text{a}), \text{C}(\text{C}=\text{N}))$	4.9	
	$^3J(\text{Si}(\text{b}), \text{C}(3',5'))$	5.6	
	$^3J(\text{Si}(\text{b}), \text{C}(1'))$	2.3	
	$^4J(\text{Si}(\text{a}), \text{C}(4))$	~ 1	
	$^4J(\text{Si}(\text{b}), \text{C}(4'))$	~ 1	
$[(\text{Me}_2(\text{Ph})\text{Si}-\text{CH}_2)_3\text{Sn}]_2$	$^1J(\text{Si}, \text{C}(\text{CH}_2))$	26	198
	$^1J(\text{Si}, \text{C}(\text{Me}))$	51.5	

Table B2.4. Compounds with silicon bonded by Si(sp³)–C(sp²) bond(s) to six-membered ring(s) and by Si(sp³)–X(sp³) bond(s) to or within other cycles

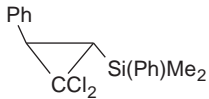
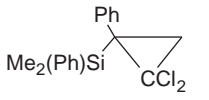
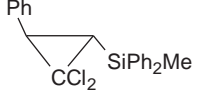
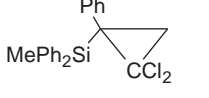
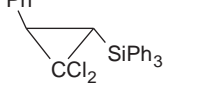
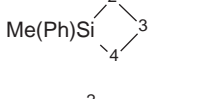
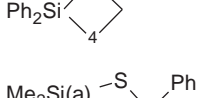
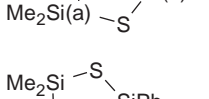
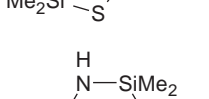
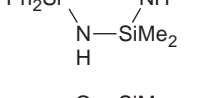
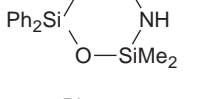
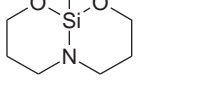
	¹ J(Si, C(Ph)) ¹ J(Si, C(HC)) ¹ J(Si, C(Me))	69.1 59.9 55.2	82
	¹ J(Si, C(Ph)) ¹ J(Si, C) ¹ J(Si, C(Me))	69.2 58.8 55.2	82
	¹ J(Si, C(Ph)) ¹ J(Si, C(HC)) ¹ J(Si, C(Me))	70.7 62.4 56.9	82
	¹ J(Si, C(Ph)) ¹ J(Si, C(C)) ¹ J(Si, C(Me))	70.9 63.2 57.6	82
	¹ J(Si, C(Ph)) ¹ J(Si, C(HC))	73.1 64.4	82
	¹ J(Si, C(Ph)) ¹ J(Si, C(2,4)) ¹ J(Si, C(Me))	60 43 46	76
	¹ J(Si, C(Ph)) ¹ J(Si, C(2,4))	62 44	76
	¹ J(Si(b), C(Ph)) ¹ J(Si(a), C) ¹ J(Si(b), C(Me))	76.8 46.7 60.3	162
	¹ J(Si, C(Ph))	46.7	162
	¹ J(Si, C(Ph)) ¹ J(Si, C(Me))	83.8 63.1	79
	¹ J(Si, C)	68.2	77
	¹ J(Si, C)	117.3	78

Table B2.4 (Continued)

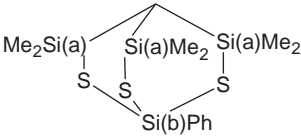
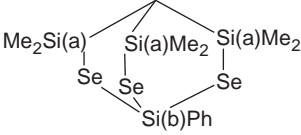
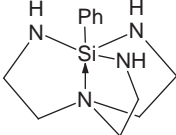
	$^1J(\text{Si(a)}, \text{C})$	56.4	118
	$^1J(\text{Si(a)}, \text{C})$	53.5	118
	$^1J(\text{Si}, \text{C})$	76.0	137

Table B2.5. Compounds with silicon bonded by Si(sp³)–C(sp²) bond to six-membered ring(s) and to substituted vinyl(s) or C=O

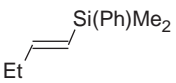
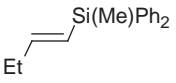
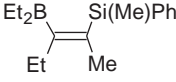
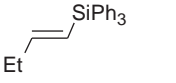
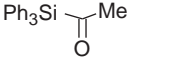
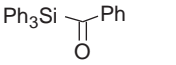
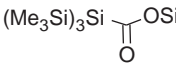
	$^1J(\text{Si}, \text{C(Ph)})$	67.7	82
	$^1J(\text{Si}, \text{C(HC=)})$	67.6	
	$^1J(\text{Si}, \text{C(Me)})$	54.2	
Ph-CH=CH-Si(Ph)Me ₂	$^1J(\text{Si}, \text{C(Ph)})$	67.7	86
	$^1J(\text{Si}, \text{C(HC=)})$	67.6	
	$^1J(\text{Si}, \text{C(Ph)})$	69.4	82
	$^1J(\text{Si}, \text{C(HC=)})$	69.8	
	$^1J(\text{Si}, \text{C(Me)})$	55.5	
Ph-CH=CH-Si(Me)Ph ₂	$^1J(\text{Si}, \text{C(Ph)})$	69.4	86
	$^1J(\text{Si}, \text{C(HC=)})$	69.8	
	$^1J(\text{Si}, \text{C(Me)})$	52.9	168
	$^1J(\text{Si}, \text{C(Ph)})$	71.2	82
	$^1J(\text{Si}, \text{C(HC=)})$	72.2	
	$^1J(\text{Si}, \text{C(C=O)})$	64	88
	$^1J(\text{Si}, \text{C(C=O)})$	64.0	88
	$^1J(\text{Si}, \text{C(Me)})$	45.8	88
	$^2J(\text{Si}(\text{SiMe}_3), \text{C})$	37.0	

Table B2.5 (Continued)

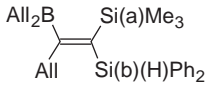
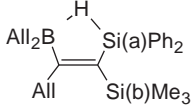
	$^1J(\text{Si}(\text{b}), \text{C}(\text{Ph}))$	76.7	184
	$^1J(\text{Si}, \text{C}(\text{C}=\text{C}))$	57.2	
	$^1J(\text{Si}(\text{a}), \text{C}(\text{Me}))$	51.5	
	$^3J(\text{Si}, \text{C}(\text{All}))$	11.0	
	$^1J(\text{Si}(\text{a}), \text{C}(\text{Ph}))$	76.3	184
	$^1J(\text{Si}, \text{C}(\text{C}=\text{C}))$	57.2	
	$^1J(\text{Si}(\text{b}), \text{C}(\text{Me}))$	50.5	
	$^3J(\text{Si}, \text{C}(\text{All}))$	14.8	
	$^3J(\text{Si}, \text{C}(\text{All}))$	7.6	

Table B2.6. Compounds with silicon bonded to heteroaromatic rings

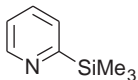
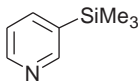
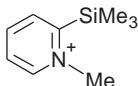
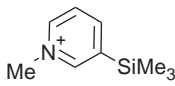
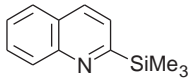
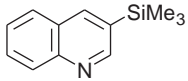
	$^1J(\text{Si}, \text{C}(\text{C}=\text{N}))$	75.9	86
	$^1J(\text{Si}, \text{C}(\text{C}=\text{N}))$	62.8	86
	$^1J(\text{Si}, \text{C}(\text{C}=\text{N}))$	54.7	86
	$^1J(\text{Si}, \text{C}(\text{C}=\text{N}))$	57.0	86
	$^1J(\text{Si}, \text{C}(\text{C}=\text{N}))$	75.5	86
	$^1J(\text{Si}, \text{C}(\text{C}=\text{N}))$	62.5	86

Table B2.7. Compounds with silicon bonded to spiro structures or to other bi-cycles

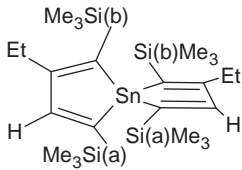
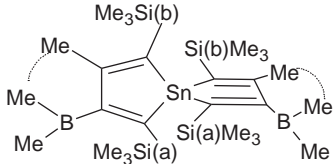
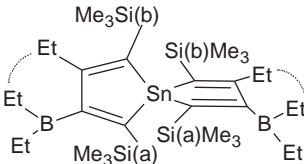
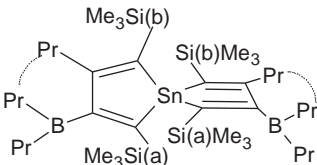
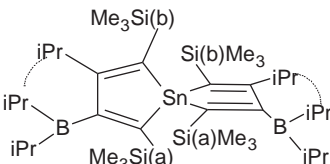
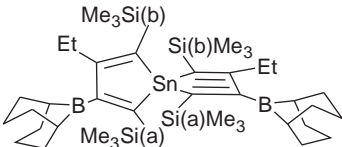
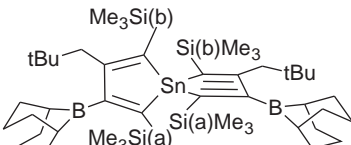
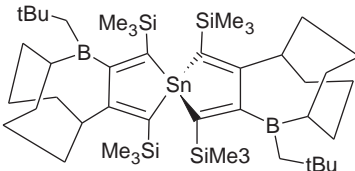
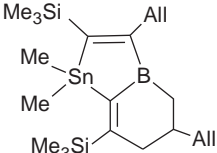
	$^1J(\text{Si}(\text{a}), \text{C}(\text{C}=\text{C}))$	61.6	192
	$^1J(\text{Si}(\text{b}), \text{C}(\text{C}=\text{C}))$	64.2	
	$^1J(\text{Si}, \text{C}(\text{Me}))$	52.2	
	$^1J(\text{Si}, \text{C}(\text{Me}))$	52.2	
	$^1J(\text{Si}(\text{a}), \text{C}(\text{C}=\text{C}))$	64.2	192
	$^1J(\text{Si}(\text{b}), \text{C}(\text{C}=\text{C}))$	63.8	
	$^1J(\text{Si}, \text{C}(\text{Me}))$	52.2	
	$^1J(\text{Si}, \text{C}(\text{Me}))$	52.2	

Table B2.7 (Continued)

	$^1J(\text{Si(a)}, \text{C}(\text{C}=\text{C}))$	64.4	192
	$^1J(\text{Si(b)}, \text{C}(\text{C}=\text{C}))$	63.3	
	$^1J(\text{Si}, \text{C}(\text{Me}))$	51.4	
	$^1J(\text{Si}, \text{C}(\text{Me}))$	52.0	
	$^{2,3}J(\text{Si}, \text{C}(\text{EtC}=\text{C}))$	11.3	
	$^1J(\text{Si(a)}, \text{C}(\text{C}=\text{C}))$	64.4	
	$^1J(\text{Si(b)}, \text{C}(\text{C}=\text{C}))$	63.4	
	$^1J(\text{Si(a)}, \text{C}(\text{C}=\text{C}))$	64.9	192
	$^1J(\text{Si(b)}, \text{C}(\text{C}=\text{C}))$	63.4	
	$^1J(\text{Si(a)}, \text{C}(\text{C}=\text{C}))$	64.9	192
	$^1J(\text{Si(b)}, \text{C}(\text{C}=\text{C}))$	63.8	
	$^1J(\text{Si(a)}, \text{C}(\text{C}=\text{C}))$	64.3	192
	$^1J(\text{Si(b)}, \text{C}(\text{C}=\text{C}))$	63.8	
	$^1J(\text{Si}, \text{C}(\text{Me}))$	53.2	
	$^1J(\text{Si}, \text{C}(\text{Me}))$	51.2	
	$^{2,3}J(\text{Si}, \text{C}(\text{EtC}=\text{C}))$	10.3	
	$^1J(\text{Si(a)}, \text{C}(\text{C}=\text{C}))$	65.3	192
	$^1J(\text{Si(b)}, \text{C}(\text{C}=\text{C}))$	64.1	
	$^1J(\text{Si}, \text{C}(\text{Me}))$	51.9	
	$^1J(\text{Si}, \text{C}(\text{Me}))$	51.9	
	$^1J(\text{Si}, \text{C}(\text{C}=\text{C}))$	64.4	193
	$^1J(\text{Si}, \text{C}(\text{C}=\text{C}))$	63.3	
	$^1J(\text{Si}, \text{C}(\text{Me}))$	52.0	
	$^1J(\text{Si}, \text{C}(\text{Me}))$	51.4	
	$^1J(\text{Si}, \text{C}(\text{Me}))$	51.0	194
	$^1J(\text{Si}, \text{C}(\text{Me}))$	50.5	

APPENDIX B3

Tables of silicon–carbon coupling constants in molecules containing Si bonded by Si(sp³)–C(sp²) bond within ring(s).

Table B3.1. Compounds with silicon within four-membered ring

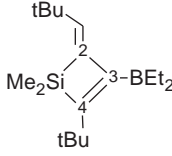
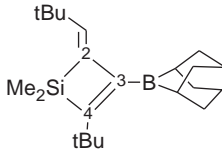
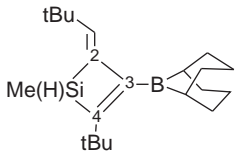
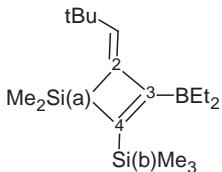
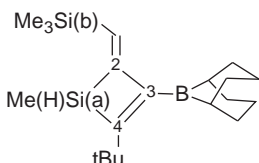
	$^1J(\text{Si}, \text{C}(2))$	50.8	105
	$^1J(\text{Si}, \text{C}(4))$	54.1	
	$^1J(\text{Si}, \text{C}(\text{Me}))$	45.9	
	$^{2,3}J(\text{Si}, \text{C}(\text{tBuC}(4)))$	5.3, <2	
	$^{3,4}J(\text{Si}, \text{C}(\text{tBuC}=\text{)))}$	3.6, 8.0	
	$^1J(\text{Si}, \text{C}(2))$	52.6	105
	$^1J(\text{Si}, \text{C}(4))$	54.1	
	$^1J(\text{Si}, \text{C}(\text{Me}))$	44.6	
	$^1J(\text{Si}, \text{C}(4))$	54.0	105
	$^1J(\text{Si}, \text{C}(\text{Me}))$	45.0	
	$^1J(\text{Si}(\text{a}), \text{C}(2))$	49.9	105
	$^1J(\text{Si}(\text{a}), \text{C}(4))$	40.5	
	$^1J(\text{Si}(\text{b}), \text{C}(4))$	64.9	
	$^1J(\text{Si}(\text{a}), \text{C}(\text{Me}))$	51.3	
	$^1J(\text{Si}(\text{b}), \text{C}(\text{Me}))$	51.4	
	$^3J(\text{Si}(\text{b}), \text{C}(2))$	15.8	
	$^1J(\text{Si}(\text{a}), \text{C}(2))$	54.4	105
	$^1J(\text{Si}(\text{a}), \text{C}(4))$	53.5	
	$^1J(\text{Si}(\text{b}), \text{C}(\text{C}=\text{)))}$	70.4	
	$^1J(\text{Si}(\text{a}), \text{C}(\text{Me}))$	44.1	
	$^1J(\text{Si}(\text{b}), \text{C}(\text{Me}))$	51.6	

Table B3.2. 1-Azonia-2-sila-5-boratoles

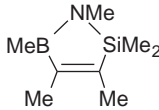
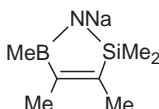
	$^1J(\text{Si}, \text{C}(\text{C}=\text{)))}$	77.5	168
	$^1J(\text{Si}, \text{C}(\text{Me}))$	52.5	
	$^1J(\text{Si}, \text{C}(\text{C}=\text{)))}$	70.2	168
	$^1J(\text{Si}, \text{C}(\text{Me}))$	48.8	

Table B3.2 (Continued)

$\text{Na}^+ \left[\begin{array}{c} \text{H} \\ \diagup \quad \diagdown \\ \text{Me}_2\text{B} \quad \text{SiMe}_2 \\ \diagdown \quad \diagup \\ \text{Me} \quad \text{Me} \end{array} \right]^-$	$^1J(\text{Si}, \text{C}(\text{Me}))$	46.8	168
$\begin{array}{c} \text{NMe} \\ \diagup \quad \diagdown \\ \text{EtB} \quad \text{SiMe}_2 \\ \diagdown \quad \diagup \\ \text{Et} \quad \text{Me} \end{array}$	$^1J(\text{Si}, \text{C}(\text{C}=\text{O}))$ $^1J(\text{Si}, \text{C}(\text{Me}))$	76.0 52.0	168,172
$\begin{array}{c} \text{H} \\ \diagup \quad \diagdown \\ \text{EtB} \quad \text{Si}(\text{Et})\text{Me} \\ \diagdown \quad \diagup \\ \text{Et} \quad \text{Me} \end{array}$	$^1J(\text{Si}, \text{C}(\text{C}=\text{O}))$ $^1J(\text{Si}, \text{C}(\text{Me}))$	75.7 51.8	168
$\begin{array}{c} \text{NMe} \\ \diagup \quad \diagdown \\ \text{ClB} \quad \text{SiMe}_2 \\ \diagdown \quad \diagup \\ \text{Et} \quad \text{Me} \end{array}$	$^1J(\text{Si}, \text{C}(\text{C}=\text{O}))$ $^1J(\text{Si}, \text{C}(\text{Me}))$	74.7 54.0	168,172
$\begin{array}{c} \text{NMe} \\ \diagup \quad \diagdown \\ \text{EtB} \quad \text{Si}(\text{Et})\text{Me} \\ \diagdown \quad \diagup \\ \text{Et} \quad \text{Me} \end{array}$	$^1J(\text{Si}, \text{C}(\text{C}=\text{O}))$ $^1J(\text{Si}, \text{C}(\text{Et}))$ $^1J(\text{Si}, \text{C}(\text{Me}))$	76.0 55.8 51.8	168
$\begin{array}{c} \text{NMe} \\ \diagup \quad \diagdown \\ \text{EtB} \quad \text{SiMe}_2 \\ \diagdown \quad \diagup \\ \text{Et} \quad \text{Et} \end{array}$	$^1J(\text{Si}, \text{C}(\text{C}=\text{O}))$ $^1J(\text{Si}, \text{C}(\text{Me}))$	76.6 52.2	168
$\begin{array}{c} \text{NMe} \\ \diagup \quad \diagdown \\ \text{EtO-B} \quad \text{SiMe}_2 \\ \diagdown \quad \diagup \\ \text{Et} \quad \text{Me} \end{array}$	$^1J(\text{Si}, \text{C}(\text{C}=\text{O}))$ $^1J(\text{Si}, \text{C}(\text{Me}))$	75.1 53.5	168
$\begin{array}{c} \text{NMe} \\ \diagup \quad \diagdown \\ \text{Me}_2\text{N-B} \quad \text{SiMe}_2 \\ \diagdown \quad \diagup \\ \text{Et} \quad \text{Me} \end{array}$	$^1J(\text{Si}, \text{C}(\text{Me}))$	53.9	168
$\begin{array}{c} \text{NMe} \\ \diagup \quad \diagdown \\ \text{Et-O-B} \quad \text{SiMe}_2 \\ \diagdown \quad \diagup \\ \text{Et} \quad \text{Me} \end{array}$	$^1J(\text{Si}, \text{C}(\text{C}=\text{O}))$ $^1J(\text{Si}, \text{C}(\text{Me}))$	75.1 53.7	172
$\begin{array}{c} \text{NNa} \\ \diagup \quad \diagdown \\ \text{EtB} \quad \text{Si}(\text{Et})\text{Me} \\ \diagdown \quad \diagup \\ \text{Et} \quad \text{Me} \end{array}$	$^1J(\text{Si}, \text{C}(\text{C}=\text{O}))$ $^1J(\text{Si}, \text{C}(\text{Et}))$ $^1J(\text{Si}, \text{C}(\text{Me}))$	70.2 50.9 47.8	168

Table B3.2 (Continued)

	$^1J(\text{Si}, \text{C}(\text{C}=\text{)))}$	70.2	168
	$^1J(\text{Si}, \text{C}(\text{Me}))$	48.8	
	$^1J(\text{Si}, \text{C}(\text{C}=\text{)))}$	75.4	172
	$^1J(\text{Si}, \text{C}(\text{Me}))$	53.3	
	$^1J(\text{Si}, \text{C}(\text{C}=\text{)))}$	75.4	
	$^1J(\text{Si}, \text{C}(\text{Me}))$	53.2	
	$^1J(\text{Si}, \text{C}(\text{C}=\text{)))}$	76.0	186
	$^1J(\text{Si}, \text{C}(\text{Me}))$	53.7	
	$^1J(\text{Si}, \text{C}(\text{C}=\text{)))}$	76.4	168
	$^1J(\text{Si}, \text{C}(\text{Me}))$	52.5	
	$^1J(\text{Si}, \text{C}(\text{C}=\text{)))}$	73.2	168
	$^1J(\text{Si}, \text{C}(\text{Me}))$	53.7	
	$^1J(\text{Si}, \text{C}(\text{C}=\text{)))}$	73.2	172
	$^1J(\text{Si}, \text{C}(\text{Me}))$	53.7	
	$^1J(\text{Si}, \text{C}(\text{C}=\text{)))}$	76.0	186
	$^1J(\text{Si}, \text{C}(\text{Me}))$	52.0	
$\text{Na}^+ \left[\begin{array}{c} \text{H} \\ \\ \text{Et}_2\text{B} \text{---} \text{N} \text{---} \text{Si}(\text{Et})\text{Me} \\ \quad \quad \\ \text{Et} \quad \quad \text{Me} \end{array} \right]^-$	$^1J(\text{Si}, \text{C}(\text{Me}))$	48.1	168
$\text{Na}^+ \left[\begin{array}{c} \text{H} \\ \\ \text{Et}_2\text{B} \text{---} \text{N} \text{---} \text{SiMe}_2 \\ \quad \quad \\ \text{Et} \quad \quad \text{Et} \end{array} \right]^-$	$^1J(\text{Si}, \text{C}(\text{Me}))$	46.8	168
$\text{K}^+ \left[\begin{array}{c} \text{H} \\ \\ \text{Et}_2\text{B} \text{---} \text{N} \text{---} \text{SiMe}_2 \\ \quad \quad \\ \text{Et} \quad \quad \text{Me} \end{array} \right]^-$	$^1J(\text{Si}, \text{C}(\text{Me}))$	47.8	168

Table B3.2 (Continued)

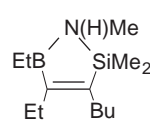
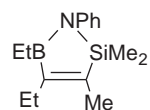
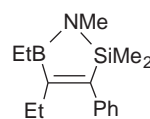
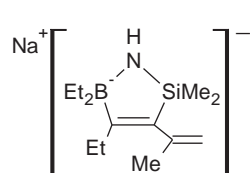
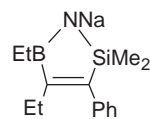
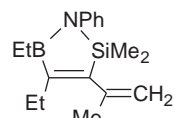
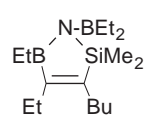
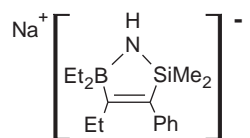
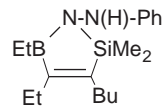
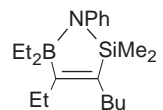
	$^1J(\text{Si}, \text{C}(\text{Me}))$	53.3	186
	$^1J(\text{Si}, \text{C}(\text{C}=\text{}))$ $^1J(\text{Si}, \text{C}(\text{Me}))$	76.3 53.4	168
	$^1J(\text{Si}, \text{C}(\text{C}=\text{}))$ $^1J(\text{Si}, \text{C}(\text{Me}))$	75.4 53.3	168
	$^1J(\text{Si}, \text{C}(\text{Me}))$	48.8	172
	$^1J(\text{Si}, \text{C}(\text{Me}))$	49.6	168
	$^1J(\text{Si}, \text{C}(\text{C}=\text{}))$ $^1J(\text{Si}, \text{C}(\text{Me}))$	73.6 54.5	168
	$^1J(\text{Si}, \text{C}(\text{C}=\text{}))$ $^1J(\text{Si}, \text{C}(\text{Me}))$	75.4 54.0	186
	$^1J(\text{Si}, \text{C}(\text{Me}))$	49.8	168
	$^1J(\text{Si}, \text{C}(\text{C}=\text{}))$ $^1J(\text{Si}, \text{C}(\text{Me}))$	75.1 54.0	186
	$^1J(\text{Si}, \text{C}(\text{C}=\text{}))$ $^1J(\text{Si}, \text{C}(\text{Me}))$	76.3 53.4	186

Table B3.2 (Continued)

	$^1J(\text{Si}, \text{C}(\text{C}=\text{}))$ $^1J(\text{Si}, \text{C}(\text{Me}))$	73.5 52.5	186
	$^1J(\text{Si}, \text{C}(\text{C}=\text{}))$ $^1J(\text{Si}, \text{C}(\text{Me}))$	74.0 54.0	186
	$^1J(\text{Si}, \text{C}(\text{Me}))$	52.9	186
	$^1J(\text{Si}, \text{C}(\text{C}=\text{}))$ $^1J(\text{Si}, \text{C}(\text{Me}))$	74.8 52.7	186
	$^1J(\text{Si}, \text{C}(\text{Me}))$	54	186
	$^1J(\text{Si}, \text{C}(\text{C}=\text{}))$ $^1J(\text{Si}, \text{C}(\text{Me}))$	76.3 54.0	186
	$^1J(\text{Si}(\text{a}), \text{C}(\text{C}=\text{}))$ $^1J(\text{Si}(\text{a}), \text{C}(\text{Me}))$ $^1J(\text{Si}(\text{b}), \text{C}(\text{Me}))$	74.8 52.8, 52.7 56.4	186
	$^1J(\text{Si}, \text{C}(\text{C}=\text{}))$ $^1J(\text{Si}, \text{C}(\text{Me}))$	76.2 52.1	102
	$^1J(\text{Si}, \text{C}(\text{C}=\text{}))$ $^1J(\text{Si}, \text{C}(\text{Me}))$	76.8 52.3	102
	$^1J(\text{Si}, \text{C}(\text{C}=\text{}))$ $^1J(\text{Si}, \text{C}(\text{Me}))$	75.5 53.4	102

Table B3.2 (Continued)*Si-H bond*

$\text{Na}^+ \left[\begin{array}{c} \text{H} \\ \diagup \quad \diagdown \\ \text{Et}_2\text{B} \quad \text{Si(H)Me} \\ \diagdown \quad \diagup \\ \text{Et} \quad \text{Me} \end{array} \right]^-$	$^1J(\text{Si}, \text{C}(\text{Me}))$	48.8	168
---	---------------------------------------	------	-----

Si-Ph bond

$\begin{array}{c} \text{H} \\ \diagup \quad \diagdown \\ \text{EtB} \quad \text{Si(Ph)Me} \\ \diagdown \quad \diagup \\ \text{Et} \quad \text{Me} \end{array}$	$^1J(\text{Si}, \text{C}(\text{MeC}=\text{}))$	78.8	168
	$^1J(\text{Si}, \text{C}(\text{Me}))$	55.4	
	$^1J(\text{Si}, \text{C}(3))$	79.5	199
	$^1J(\text{Si}, \text{C}(\text{Me}))$	56.2	

$\begin{array}{c} \text{NMe} \\ \diagup \quad \diagdown \\ \text{EtB} \quad \text{Si(Ph)Me} \\ \diagdown \quad \diagup \\ \text{Et} \quad \text{Me} \end{array}$	$^1J(\text{Si}, \text{C}(\text{MeC}=\text{}))$	79.3	168
	$^1J(\text{Si}, \text{C}(\text{Me}))$	54.3	

$\begin{array}{c} \text{NNa} \\ \diagup \quad \diagdown \\ \text{EtB} \quad \text{Si(Ph)Me} \\ \diagdown \quad \diagup \\ \text{Et} \quad \text{Me} \end{array}$	$^1J(\text{Si}, \text{C}(\text{Me}))$	50.2	168
--	---------------------------------------	------	-----

$\begin{array}{c} \text{NH}_2 \\ \diagup \quad \diagdown \\ \text{Et}_2\text{B} \quad \text{Si(Ph)Me} \\ \diagdown \quad \diagup \\ \text{Et} \quad \text{Me} \end{array}$	$^1J(\text{Si}, \text{C}(\text{MeC}=\text{}))$	86.5	168
	$^1J(\text{Si}, \text{C}(\text{Me}))$	53.9	

$\text{Na}^+ \left[\begin{array}{c} \text{H} \\ \diagup \quad \diagdown \\ \text{Et}_2\text{B} \quad \text{Si(Ph)Me} \\ \diagdown \quad \diagup \\ \text{Et} \quad \text{Me} \end{array} \right]^-$	$^1J(\text{Si}, \text{C}(\text{MeC}=\text{}))$	81.0	168
	$^1J(\text{Si}, \text{C}(\text{Ph}))$	60.3	
	$^1J(\text{Si}, \text{C}(\text{Me}))$	50.2	

$\text{K}^+ \left[\begin{array}{c} \text{H} \\ \diagup \quad \diagdown \\ \text{Et}_2\text{B} \quad \text{Si(Ph)Me} \\ \diagdown \quad \diagup \\ \text{Et} \quad \text{Me} \end{array} \right]^-$	$^1J(\text{Si}, \text{C}(\text{Me}))$	49.8	168
---	---------------------------------------	------	-----

Two cycles

$\begin{array}{c} \text{Me} \quad \text{Me} \\ \diagdown \quad \diagup \\ \text{Bu} \text{---} \text{Si} \quad \text{Si} \text{---} \text{Bu} \\ \diagup \quad \diagdown \quad \diagup \quad \diagdown \\ \text{Et} \quad \text{B} \text{---} \text{N} \text{---} (\text{CH}_2)_2 \text{---} \text{N} \text{---} \text{B} \text{---} \text{Et} \\ \diagdown \quad \diagup \quad \diagdown \quad \diagup \\ \text{Et} \quad \text{Et} \end{array}$	$^1J(\text{Si}, \text{C}(\text{Me}))$	52.0	186
---	---------------------------------------	------	-----

$\begin{array}{c} \text{Me} \quad \text{Me} \\ \diagdown \quad \diagup \\ \text{Bu} \text{---} \text{Si} \quad \text{Si} \text{---} \text{Bu} \\ \diagup \quad \diagdown \quad \diagup \quad \diagdown \\ \text{Et} \quad \text{B} \text{---} \text{N} \text{---} \text{C}_6\text{H}_4 \text{---} \text{N} \text{---} \text{B} \text{---} \text{Et} \\ \diagdown \quad \diagup \quad \diagdown \quad \diagup \\ \text{Et} \quad \text{Et} \end{array}$	$^1J(\text{Si}, \text{C}(\text{Me}))$	53.4	186
--	---------------------------------------	------	-----

Table B3.2 (Continued)

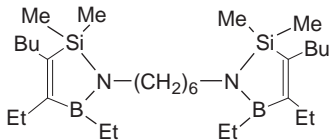
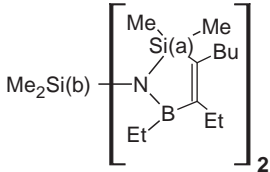
	$^1J(\text{Si}, \text{C}(\text{Me}))$	52.3	186
	$^1J(\text{Si}(\text{a}), \text{C}(\text{C}=\text{)))}$	76.9	186
	$^1J(\text{Si}(\text{a}), \text{C}(\text{Me}))$	53.1	
	$^1J(\text{Si}(\text{b}), \text{C}(\text{Me}))$	62.9	

Table B3.3. 1-Oxonia-2-sila-5-boratoles

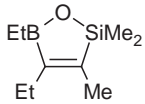
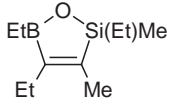
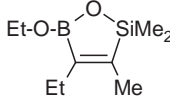
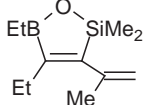
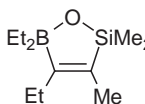
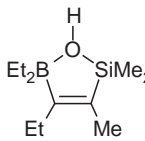
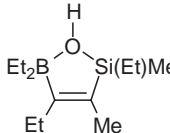
	$^1J(\text{Si}, \text{C}(\text{C}=\text{)))}$	73.2	172
	$^1J(\text{Si}, \text{C}(\text{Me}))$	57.4	
	$^1J(\text{Si}, \text{C}(\text{C}=\text{)))}$	71.9	159
	$^1J(\text{Si}, \text{C}(\text{Et}))$	59.0	
	$^1J(\text{Si}, \text{C}(\text{Me}))$	56.5	
	$^1J(\text{Si}, \text{C}(\text{C}=\text{)))}$	74.5	172
	$^1J(\text{Si}, \text{C}(\text{Me}))$	58.7	
	$^1J(\text{Si}, \text{C}(\text{C}=\text{)))}$	73.2	172
	$^1J(\text{Si}, \text{C}(\text{Me}))$	57.4	
	$^1J(\text{Si}, \text{C}(\text{C}=\text{)))}$	73.2	159
	$^1J(\text{Si}, \text{C}(\text{Me}))$	57.4	
	$^1J(\text{Si}, \text{C}(\text{C}=\text{)))}$	86.4	159
	$^1J(\text{Si}, \text{C}(\text{Me}))$	53.3	159

Table B3.3 (Continued)

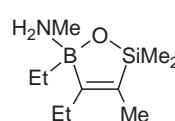
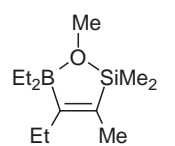
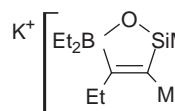
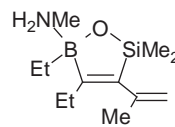
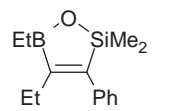
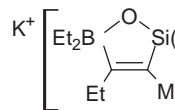
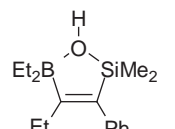
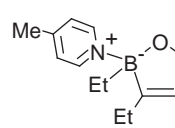
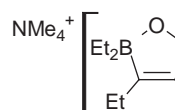
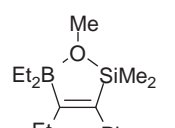
	$^1J(\text{Si}, \text{C}(\text{C}=\text{}))$	79.5	172
	$^1J(\text{Si}, \text{C}(\text{Me}))$	55.0	
	$^1J(\text{Si}, \text{C}(\text{Me}))$	55.5	159
	$^1J(\text{Si}, \text{C}(\text{C}=\text{}))$	87.9	
	$^1J(\text{Si}, \text{C}(\text{C}=\text{}))$	82.3	173
	$^1J(\text{Si}, \text{C}(\text{Me}))$	51.9	
	$^1J(\text{Si}, \text{C}(\text{C}=\text{}))$	79.5	172
	$^1J(\text{Si}, \text{C}(\text{Me}))$	55.6	
	$^1J(\text{Si}, \text{C}(\text{C}=\text{}))$	71.6	159
	$^1J(\text{Si}, \text{C}(\text{Me}))$	58.3	
	$^1J(\text{Si}, \text{C}(\text{C}=\text{}))$	81.6	173
	$^1J(\text{Si}, \text{C}(\text{Me}))$	51.4	
	$^1J(\text{Si}, \text{C}(\text{Me}))$	56.8	159
	$^1J(\text{Si}, \text{C}(\text{Me}))$	56.1	172
	$^1J(\text{Si}, \text{C}(\text{Me}))$	51.5	173
	$^1J(\text{Si}, \text{C}(\text{C}=\text{}))$	85.4	159
	$^1J(\text{Si}, \text{C}(\text{Me}))$	56.0	

Table B3.3 (Continued)

$\text{K}^+ \left[\begin{array}{c} \text{Et}_2\text{B} \quad \text{O} \quad \text{SiMe}_2 \\ \diagdown \quad \diagup \\ \text{Et} \quad \text{Ph} \end{array} \right]^-$	$^1J(\text{Si}, \text{C}(=\text{C}))$ $^1J(\text{Si}, \text{C}(\text{Me}))$	78.8 53.3	173
$\begin{array}{c} \text{AlCl}_3 \\ \\ \text{EtB} \quad \text{O} \quad \text{SiMe}_2 \\ \diagdown \quad \diagup \\ \text{Et} \quad \text{Me} \end{array}$	$^1J(\text{Si}, \text{C}(\text{Me}))$	61	172
$\text{N}(\text{H})\text{Me}_3^+ \left[\begin{array}{c} \text{Et}_2\text{B} \quad \text{O} \quad \text{SiMe}_2 \\ \diagdown \quad \diagup \\ \text{Et} \quad \text{Ph} \end{array} \right]^-$	$^1J(\text{Si}, \text{C}(\text{Me}))$	55.8	173
$\text{NMe}_4^+ \left[\begin{array}{c} \text{Et}_2\text{B} \quad \text{O} \quad \text{SiMe}_2 \\ \diagdown \quad \diagup \\ \text{Et} \quad \text{Ph} \end{array} \right]^-$	$^1J(\text{Si}, \text{C}(\text{Me}))$	53.0	173
<i>Si–Ph bond</i>			
$\begin{array}{c} \text{O} \\ \\ \text{EtB} \quad \text{Si}(\text{Ph})\text{Me} \\ \diagdown \quad \diagup \\ \text{Et} \quad \text{Me} \end{array}$	$^1J(\text{Si}, \text{C}(=\text{C}))$ $^1J(\text{Si}, \text{C}(\text{Me}))$	75.1 59.3	159
$\begin{array}{c} \text{Me} \\ \\ \text{O} \\ \\ \text{Et}_2\text{B} \quad \text{Si}(\text{Ph})\text{Me} \\ \diagdown \quad \diagup \\ \text{Et} \quad \text{Me} \end{array}$	$^1J(\text{Si}, \text{C}(\text{Ph}))$ $^1J(\text{Si}, \text{C}(=\text{C}))$ $^1J(\text{Si}, \text{C}(\text{Me}))$	73.7 89.9 57.8	159
$\text{K}^+ \left[\begin{array}{c} \text{Et}_2\text{B} \quad \text{O} \quad \text{Si}(\text{Ph})\text{Me} \\ \diagdown \quad \diagup \\ \text{Et} \quad \text{Me} \end{array} \right]^-$	$^1J(\text{Si}, \text{C}(\text{Me}))$	55.0	173

Table B3.4. 1-Thionia-2-sila-5-boratoles and 1-selenia-2-sila-5-boratoles

<i>Si–S</i>			
$\begin{array}{c} \text{S} \\ \\ \text{EtB} \quad \text{SiMe}_2 \\ \diagdown \quad \diagup \\ \text{Et} \quad \text{Me} \end{array}$	$^1J(\text{Si}, \text{C}(\text{Me}))$	51.9	200
$\begin{array}{c} \text{S} \\ \\ \text{EtB} \quad \text{SiMe}_2 \\ \diagdown \quad \diagup \\ \text{Et} \quad \text{C}=\text{C} \\ \\ \text{Me} \end{array}$	$^1J(\text{Si}, \text{C}(=\text{C}))$ $^1J(\text{Si}, \text{C}(\text{Me}))$	67.6 51.9	200

Table B3.4 (Continued)

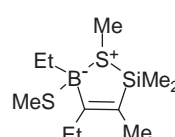
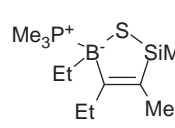
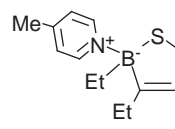
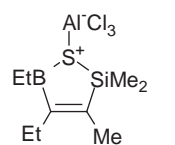
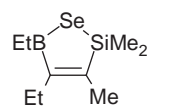
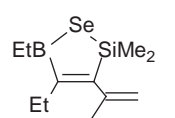
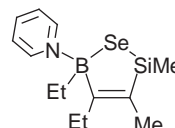
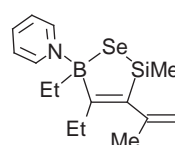
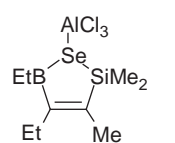
	$^1J(\text{Si}, \text{C}(\text{C}=\text{O}))$	76.3	201
	$^1J(\text{Si}, \text{C}(\text{Me}))$	52.7	
	$^1J(\text{Si}, \text{C}(\text{Me}))$	51.9	
	$^1J(\text{Si}, \text{C}(\text{Me}))$	50.2	200
	$^1J(\text{Si}, \text{C}(\text{C}=\text{O}))$	72.4	200
	$^1J(\text{Si}, \text{C}(\text{Me}))$	50.1	
	$^1J(\text{Si}, \text{C}(\text{Me}))$	53.9	200
<i>Si-Se</i>			
	$^1J(\text{Si}, \text{C}(\text{C}=\text{O}))$	68.1, 68.2	202
	$^1J(\text{Si}, \text{C}(\text{Me}))$	50.4, 50.7	
	$^2J(\text{Si}, \text{C}(\text{Me}))$	8.2	
	$^3J(\text{Si}, \text{C}(\text{Et}))$	8.2	
	$^1J(\text{Si}, \text{C}(\text{C}=\text{O}))$	65.0, 65.7	202
	$^1J(\text{Si}, \text{C}(\text{Me}))$	51.5, 51.5	
	$^1J(\text{Si}, \text{C}(\text{C}=\text{O}))$	71.4	202
	$^1J(\text{Si}, \text{C}(\text{Me}))$	49.5	
	$^1J(\text{Si}, \text{C}(\text{Me}))$	48.8	
	$^1J(\text{Si}, \text{C}(\text{C}=\text{O}))$	67.8	202
	$^1J(\text{Si}, \text{C}(\text{Me}))$	50.7	
	$^1J(\text{Si}, \text{C}(\text{Me}))$	49.7	
	$^1J(\text{Si}, \text{C}(\text{Me}))$	53.1	202

Table B3.4 (Continued)

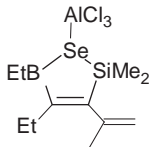
	$^1J(\text{Si}, \text{C}(\text{C}=\text{C}))$	53.3	202
---	---	------	-----

Table B3.5. 1-Sila-2, 4-cyclopentadienes

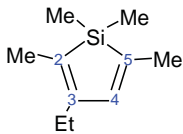
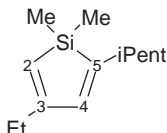
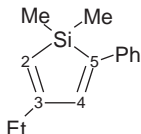
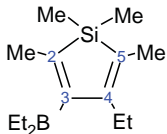
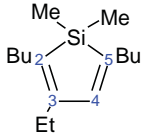
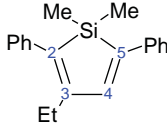
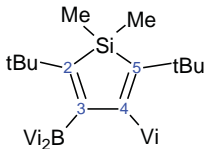
	$^1J(\text{Si}, \text{C}(2))$	67.8	99
	$^1J(\text{Si}, \text{C}(5))$	62.7	
	$^1J(\text{Si}, \text{C}(\text{Me}))$	48.7	
	$^{2,3}J(\text{Si}, \text{C}(3))$	8.7	
	$^{2,3}J(\text{Si}, \text{C}(4))$	9.3	
	$^1J(\text{Si}, \text{C}(2))$	67.7	102
	$^1J(\text{Si}, \text{C}(5))$	62.8	
	$^1J(\text{Si}, \text{C}(\text{Me}))$	48.7	
	$^1J(\text{Si}, \text{C}(2))$	68.5	175
	$^1J(\text{Si}, \text{C}(5))$	60.8	
	$^1J(\text{Si}, \text{C}(\text{Me}))$	49.4	
	$^2J(\text{Si}, \text{C}(3))$	6.0	
	$^2J(\text{Si}, \text{C}(4))$	8.8	
	$^1J(\text{Si}, \text{C}(2))$	68.5	175
	$^1J(\text{Si}, \text{C}(5))$	62.1	
	$^1J(\text{Si}, \text{C}(\text{Me}))$	50.4	
	$^2J(\text{Si}, \text{C}(3))$	5.8	
	$^2J(\text{Si}, \text{C}(4))$	8.8	
	$^1J(\text{Si}, \text{C}(2))$	65.9	99
	$^1J(\text{Si}, \text{C}(5))$	68.7	
	$^1J(\text{Si}, \text{C}(\text{Me}))$	47.2	
	$^2J(\text{Si}, \text{C}(4))$	11.0	
	$^1J(\text{Si}, \text{C}(2))$	66.5	99
	$^1J(\text{Si}, \text{C}(5))$	63.6	
	$^1J(\text{Si}, \text{C}(\text{Me}))$	47.9	
	$^2J(\text{Si}, \text{C}(3))$	8.8	
	$^2J(\text{Si}, \text{C}(4))$	9.8	
	$^1J(\text{Si}, \text{C}(\text{Me}))$	50.0	99
	$^1J(\text{Si}, \text{C}(2))$	63.1	203
	$^1J(\text{Si}, \text{C}(5))$	68.2	
	$^1J(\text{Si}, \text{C}(\text{Me}))$	47.6	
	$^2J(\text{Si}, \text{C}(4))$	10.6	

Table B3.5 (Continued)

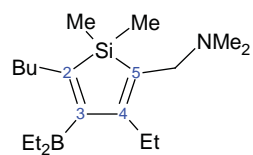
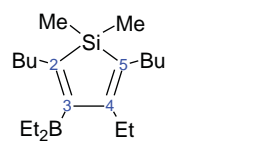
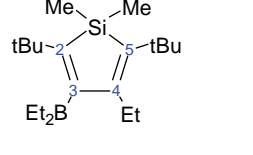
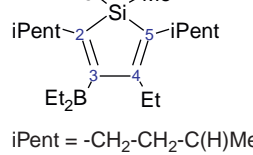
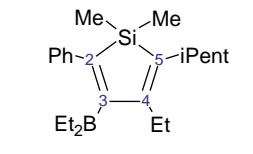
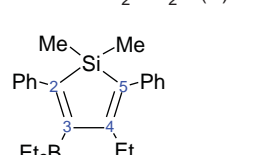
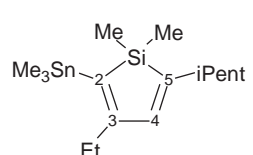
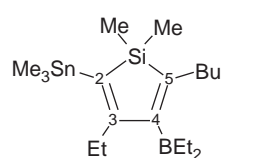
	$^3J(\text{Si}, \text{C}(\text{Vi}))$	7.1	
	$^nJ(\text{Si}, \text{C}(t\text{Bu}))$	6.6	
	$^nJ(\text{Si}, \text{C}(t\text{Bu}))$	6.1	
	$^1J(\text{Si}, \text{C}(2))$	68.1	204
	$^1J(\text{Si}, \text{C}(5))$	70.0	
	$^1J(\text{Si}, \text{C}(\text{Me}))$	48.0	
	$^2J(\text{Si}, \text{C}(4))$	< 10	
	$^2J(\text{Si}, \text{C}(\text{NCH}_2))$	12.4	
	$^1J(\text{Si}, \text{C}(2))$	64.1	99
	$^1J(\text{Si}, \text{C}(5))$	68.2	
	$^1J(\text{Si}, \text{C}(\text{Me}))$	47.3	
	$^2J(\text{Si}, \text{C}(4))$	10.7	
	$^1J(\text{Si}, \text{C}(2))$	64.1	99
	$^1J(\text{Si}, \text{C}(5))$	67.5	
	$^1J(\text{Si}, \text{C}(\text{Me}))$	47.0	
	$^2J(\text{Si}, \text{C}(4))$	11.7	
	$^1J(\text{Si}, \text{C}(2))$	65.9	99
	$^1J(\text{Si}, \text{C}(5))$	68.8	
	$^1J(\text{Si}, \text{C}(\text{Me}))$	48.5	
	$^2J(\text{Si}, \text{C}(4))$	9.8	
	$i\text{Pent} = -\text{CH}_2-\text{CH}_2-\text{C}(\text{H})\text{Me}_2$		
	$^1J(\text{Si}, \text{C}(2))$	63.5	99
	$^1J(\text{Si}, \text{C}(5))$	67.1	
	$^1J(\text{Si}, \text{C}(\text{Me}))$	48.2	
	$^2J(\text{Si}, \text{C}(4))$	10.4	
	$i\text{Pent} = -\text{CH}_2-\text{CH}_2-\text{C}(\text{H})\text{Me}_2$		
	$^1J(\text{Si}, \text{C}(\text{Me}))$	49.3	99
	$^2J(\text{Si}, \text{C}(4))$	9.8	
	$^1J(\text{Si}, \text{C}(2))$	52.8	175
	$^1J(\text{Si}, \text{C}(5))$	59.6	
	$^1J(\text{Si}, \text{C}(\text{Me}))$	48.4	
	$^2J(\text{Si}, \text{C}(3))$	3.9	
	$^2J(\text{Si}, \text{C}(4))$	11.7	
	$^1J(\text{Si}, \text{C}(2))$	53.9	175
	$^1J(\text{Si}, \text{C}(5))$	60.0	
	$^1J(\text{Si}, \text{C}(\text{Me}))$	47.8	
	$^2J(\text{Si}, \text{C}(3))$	6.6	

Table B3.5 (Continued)

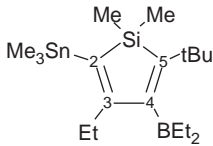
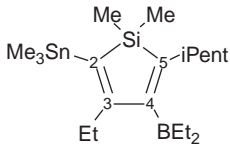
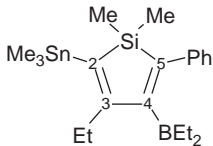
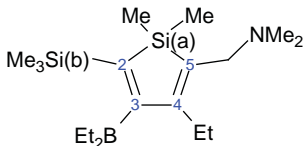
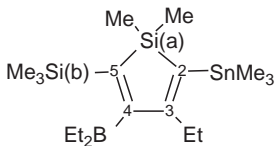
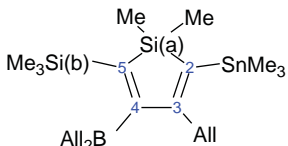
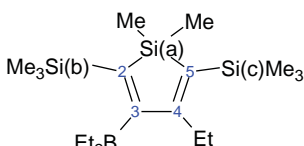
	$^1J(\text{Si}, \text{C}(2))$	53.4	175
	$^1J(\text{Si}, \text{C}(5))$	62.1	
	$^1J(\text{Si}, \text{C}(\text{Me}))$	47.4	
	$^2J(\text{Si}, \text{C}(3))$	4.4	
	$^1J(\text{Si}, \text{C}(2))$	54.5	175
	$^1J(\text{Si}, \text{C}(5))$	60.5	
	$^1J(\text{Si}, \text{C}(\text{Me}))$	48.0	
	$^2J(\text{Si}, \text{C}(3))$	6.5	
	$^1J(\text{Si}, \text{C}(2))$	53.4	175
	$^1J(\text{Si}, \text{C}(5))$	58.6	
	$^1J(\text{Si}, \text{C}(\text{Me}))$	48.6	
	$^2J(\text{Si}, \text{C}(3))$	5.0	
	$^1J(\text{Si}, \text{C}(2, 5))$	65.0	204
	$^1J(\text{Si}, \text{C}(2, 5))$	64.1	
	$^1J(\text{Si}, \text{C}(2, 5))$	53.5	
	$^1J(\text{Si}(\text{a}), \text{C}(\text{Me}))$	48.3	
	$^1J(\text{Si}(\text{b}), \text{C}(\text{Me}))$	51.3	
	$^2J(\text{Si}, \text{C}(4))$	< 10	
	$^1J(\text{Si}(\text{a}), \text{C}(2))$	51.8	175
	$^1J(\text{Si}(\text{a}), \text{C}(5))$	44.0	
	$^1J(\text{Si}(\text{a}), \text{C}(\text{Me}))$	47.4	
	$^1J(\text{Si}(\text{b}), \text{C}(\text{Me}))$	50.9	
	$^2J(\text{Si}(\text{a}), \text{C}(3))$	9.0	205
	$^1J(\text{Si}(\text{a}), \text{C}(\text{C}2))$	44.2	
	$^1J(\text{Si}(\text{a}), \text{C}(\text{C}5))$	51.8	
	$^1J(\text{Si}(\text{b}), \text{C}(\text{C}5))$	63.9	
	$^1J(\text{Si}(\text{a}), \text{C}(\text{Me}))$	47.4	
	$^1J(\text{Si}(\text{b}), \text{C}(\text{Me}))$	51.2	
	$^1J(\text{Si}, \text{C}(2))$	55.6	194
	$^1J(\text{Si}, \text{C}(5))$	13.7	
	$^1J(\text{Si}(\text{a}), \text{C}(\text{Me}))$	51.2	
	$^1J(\text{Si}(\text{b}), \text{C}(\text{Me}))$	47.2	
	$^{2,3}J(\text{Si}, \text{C}(3))$	11.0	
	$^{2,3}J(\text{Si}, \text{C}(3))$	9.3	
	$^1J(\text{Si}, \text{C}(\text{Me}))$	51.4	99
	$^1J(\text{Si}, \text{C}(\text{Me}))$	50.9	
	$^1J(\text{Si}, \text{C}(\text{Me}))$	47.0	
	$^{2,3}J(\text{Si}, \text{C}(4))$	11.7	
	$^{2,3}J(\text{Si}, \text{C}(4))$	8.6	

Table B3.5 (Continued)

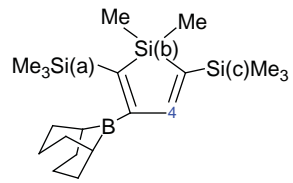
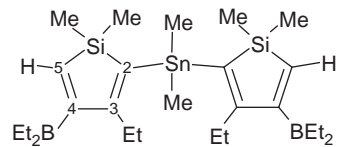
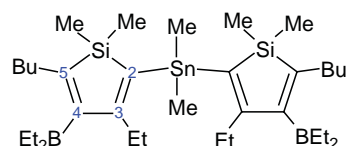
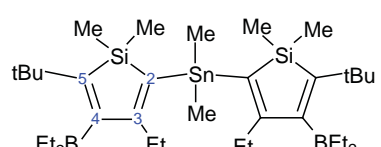
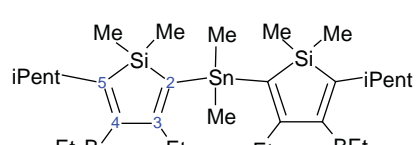
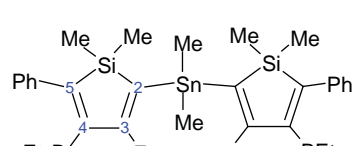
	$^1J(\text{Si}, \text{C}(2))$	62.4	194
	$^1J(\text{Si}, \text{C}(2))$	43.8	
	$^1J(\text{Si}, \text{C}(5))$	61.5	
	$^1J(\text{Si}, \text{C}(5))$	48.9	
	$^1J(\text{Si}(a), \text{C}(\text{Me}))$	47.2	
	$^1J(\text{Si}(b,c), \text{C}(\text{Me}))$	51.1	
	$^1J(\text{Si}(b,c), \text{C}(\text{Me}))$	50.7	
	$^{2,3}J(\text{Si}, \text{C}(4))$	11.4	
	$^{2,3}J(\text{Si}, \text{C}(4))$	8.9	
	$^1J(\text{Si}(a), \text{C}(2))$	62.4	158
	$^1J(\text{Si}(b), \text{C}(2))$	45.9	
	$^1J(\text{Si}(b), \text{C}(5))$	60.4	
	$^1J(\text{Si}(c), \text{C}(5))$	60.6	
	$^1J(\text{Si}(a), \text{C}(\text{Me}))$	51.1	
	$^1J(\text{Si}(b), \text{C}(\text{Me}))$	47.6	
	$^1J(\text{Si}(c), \text{C}(\text{Me}))$	51.9	
	$^2J(\text{Si}(b), \text{C}(4))$	12.0	
	$^2J(\text{Si}(c), \text{C}(4))$	11.9	
	$^3J(\text{Si}(a), \text{C}(4))$	8.1	
	$^1J(\text{Si}, \text{C}(2))$	53.1	206
	$^1J(\text{Si}, \text{C}(5))$	60.1	
	$^1J(\text{Si}, \text{C}(\text{Me}))$	47.2	
	$^1J(\text{Si}, \text{C}(2))$	53.8	206
	$^1J(\text{Si}, \text{C}(5))$	59.6	
	$^1J(\text{Si}, \text{C}(\text{Me}))$	47.8	
	$^1J(\text{Si}, \text{C}(2))$	52.3	206
	$^1J(\text{Si}, \text{C}(5))$	59.9	
	$^1J(\text{Si}, \text{C}(\text{Me}))$	47.4	
	$^1J(\text{Si}, \text{C}(2))$	54.0	206
	$^1J(\text{Si}, \text{C}(5))$	59.4	
	$^1J(\text{Si}, \text{C}(\text{Me}))$	47.8	
	$^1J(\text{Si}, \text{C}(2))$	51.9	206
	$^1J(\text{Si}, \text{C}(5))$	59.9	
	$^1J(\text{Si}, \text{C}(\text{Me}))$	48.0	

Table B3.5 (Continued)

	$^1J(\text{Si}, \text{C}(2))$	65.4	206
	$^1J(\text{Si}, \text{C}(2))$	44.0	
	$^1J(\text{Si}, \text{C}(5))$	51.3	
	$^2J(\text{Si}, \text{C}(3))$	11.7	
	$^2J(\text{Si}, \text{C}(3))$	8.9	
	$^1J(\text{Si}, \text{C}(2))$	50.3	206
	$^1J(\text{Si}, \text{C}(5))$	60.8	
	$^1J(\text{Si}(\text{a}), \text{C}(\text{Me}))$	47.2	
	$^1J(\text{Si}(\text{b}), \text{C}(\text{Me}))$	51.2	
	$^2J(\text{Si}, \text{C}(3))$	11.8	
<i>Si-H</i>			
	$^1J(\text{Si}, \text{C}(2))$	63.3	203
	$^1J(\text{Si}, \text{C}(5))$	68.1	
	$^1J(\text{Si}, \text{C}(\text{Me}))$	48.3	
	$^2J(\text{Si}, \text{C}(3))$	9.1	
	$^2J(\text{Si}, \text{C}(4))$	8.4	
	$^1J(\text{Si}, \text{C}(2))$	62.6	203
	$^1J(\text{Si}, \text{C}(5))$	68.1	
	$^1J(\text{Si}, \text{C}(\text{Me}))$	48.0	
	$^2J(\text{Si}, \text{C}(4))$	11.0	
	$^nJ(\text{Si}, \text{C}(\text{Bu}))$	7.7	
	$^nJ(\text{Si}, \text{C}(\text{Bu}))$	7.0	
	$^1J(\text{Si}, \text{C}(2))$	63.3	203
	$^1J(\text{Si}, \text{C}(5))$	67.2	
	$^1J(\text{Si}, \text{C}(\text{Me}))$	47.5	
	$^2J(\text{Si}, \text{C}(4))$	12.5	
	$^nJ(\text{Si}, \text{C}(\text{tBu}))$	6.5	
	$^nJ(\text{Si}, \text{C}(\text{tBu}))$	6.3	
	$^1J(\text{Si}, \text{C}(2))$	68.8	204
	$^1J(\text{Si}, \text{C}(5))$	70.7	
	$^1J(\text{Si}, \text{C}(\text{Me}))$	48.2	
	$^2J(\text{Si}, \text{C}(4))$	< 10	
	$^2J(\text{Si}, \text{C}(\text{NCH}_2))$	12.0	
	$^1J(\text{Si}, \text{C}(2))$	64.4	203
	$^1J(\text{Si}, \text{C}(5))$	69.0	
	$^1J(\text{Si}, \text{C}(\text{Me}))$	47.5	
	$^2J(\text{Si}, \text{C}(4))$	11.6	
	$^1J(\text{Si}, \text{C}(2))$	64.2	203
	$^1J(\text{Si}, \text{C}(5))$	68.1	
	$^1J(\text{Si}, \text{C}(\text{Me}))$	47.3	
	$^2J(\text{Si}, \text{C}(4))$	12.3	

Table B3.5 (Continued)

	$^1J(\text{Si}, \text{C}(\text{HC}=\text{}))$	60.0	182
	$^1J(\text{Si}, \text{C}(\text{SnC}=\text{}))$	53.1	
	$^1J(\text{Si}, \text{C}(\text{Me}))$	43.9	
	$^2J(\text{Si}, \text{C}(\text{EtC}=\text{}))$	5.4	
	$^3J(\text{Si}, \text{C}(\text{Et}))$	9.6	
	$^1J(\text{Si}, \text{C}(2, 5))$	65.4	204
	$^1J(\text{Si}, \text{C}(2, 5))$	64.5	
	$^1J(\text{Si}, \text{C}(2, 5))$	53.2	
	$^1J(\text{Si}(\text{a}), \text{C}(\text{Me}))$	47.9	
	$^1J(\text{Si}(\text{b}), \text{C}(\text{Me}))$	51.2	
	$^2J(\text{Si}, \text{C}(4))$	5.2	
	$^1J(\text{Si}, \text{C}(2))$	42.7	203
	$^1J(\text{Si}, \text{C}(5))$	48.9	
	$^1J(\text{Si}(\text{a}), \text{C}(\text{Me}))$	47.5	
	$^1J(\text{Si}(\text{b}, \text{c}), \text{C}(\text{Me}))$	52.1	
	$^1J(\text{Si}(\text{b}, \text{c}), \text{C}(\text{Me}))$	51.6	
	$^{2,3}J(\text{Si}, \text{C}(4))$	11.0	
	$^{2,3}J(\text{Si}, \text{C}(4))$	9.1	
	$^1J(\text{Si}, \text{C}(2))$	43.7	203
	$^1J(\text{Si}, \text{C}(5))$	49.4	
	$^1J(\text{Si}(\text{a}), \text{C}(\text{Me}))$	46.7	
	$^1J(\text{Si}(\text{b}, \text{c}), \text{C}(\text{Me}))$	51.6	
	$^1J(\text{Si}(\text{b}, \text{c}), \text{C}(\text{Me}))$	51.3	
	$^{2,3}J(\text{Si}, \text{C}(4))$	11.2	
	$^{2,3}J(\text{Si}, \text{C}(4))$	8.6	
	$^1J(\text{Si}(\text{a}), \text{C}(2))$	45.9	185
	$^1J(\text{Si}(\text{b}), \text{C}(2))$	63.0	
	$^1J(\text{Si}(\text{a}), \text{C}(5))$	50.7	
	$^1J(\text{Si}(\text{c}), \text{C}(5))$	62.7	
	$^1J(\text{Si}(\text{a}), \text{C}(\text{Me}))$	48.0	
	$^1J(\text{Si}(\text{b}, \text{c}), \text{C}(\text{Me}))$	51.3	
	$^1J(\text{Si}(\text{b}, \text{c}), \text{C}(\text{Me}))$	51.3	
	$^{2,3}J(\text{Si}(\text{a}, \text{c}), \text{C}(4))$	7.7	
	$^3J(\text{Si}(\text{b}), \text{C}(4))$	12.4	
	$^1J(\text{Si}(\text{a}), \text{C}(2))$	45.7	185
	$^1J(\text{Si}(\text{b}), \text{C}(2))$	64.2	
	$^1J(\text{Si}(\text{a}), \text{C}(5))$	50.7	
	$^1J(\text{Si}(\text{c}), \text{C}(5))$	62.6	
	$^1J(\text{Si}(\text{a}), \text{C}(\text{Me}))$	47.3	
	$^1J(\text{Si}(\text{b}, \text{c}), \text{C}(\text{Me}))$	51.6	
	$^1J(\text{Si}(\text{b}, \text{c}), \text{C}(\text{Me}))$	51.6	
	$^1J(\text{Si}(\text{b}, \text{c}), \text{C}(\text{Me}))$	51.4	
	$^1J(\text{Si}(\text{b}, \text{c}), \text{C}(\text{Me}))$	51.4	
	$^2J(\text{Si}(\text{a}, \text{c}), \text{C}(4))$	7.9	
	$^3J(\text{Si}(\text{b}), \text{C}(4))$	12.3	

Table B3.6. Silacyclopenta-2-enes

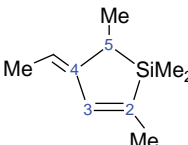
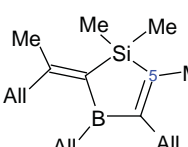
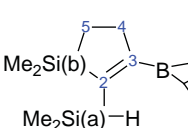
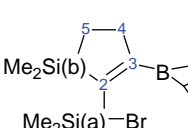
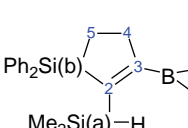
	$^1J(\text{Si}, \text{C}(2))$	59.0	99
	$^1J(\text{Si}, \text{C}(5))$	54.8	
	$^1J(\text{Si}, \text{C}(\text{Me}))$	49.9	
	$^1J(\text{Si}, \text{C}(\text{Me}))$	48.6	
	$^2J(\text{Si}, \text{C}(3))$	7.0	
	$^1J(\text{Si}, \text{C}(5))$	65.3	194
	$^1J(\text{Si}, \text{C}(\text{Me}))$	48.2	
	$^1J(\text{Si}(\text{a}), \text{C}(2))$	61.4	207
	$^1J(\text{Si}(\text{b}), \text{C}(2))$	49.7	
	$^1J(\text{Si}(\text{b}), \text{C}(5))$	51.8	
	$^1J(\text{Si}(\text{a}), \text{C}(\text{Me}))$	51.0	
	$^1J(\text{Si}(\text{b}), \text{C}(\text{Me}))$	48.2	
	$^{2,3}J(\text{Si}, \text{C}(4))$	12.0	
	$^{2,3}J(\text{Si}, \text{C}(4))$	6.4	
	$^1J(\text{Si}(\text{a}), \text{C}(2))$	67.8	207
	$^1J(\text{Si}(\text{b}), \text{C}(2))$	47.5	
	$^1J(\text{Si}(\text{b}), \text{C}(5))$	51.9	
	$^1J(\text{Si}(\text{a}), \text{C}(\text{Me}))$	55.3	
	$^1J(\text{Si}(\text{b}), \text{C}(\text{Me}))$	49.0	
	$^{2,3}J(\text{Si}, \text{C}(4))$	13.6	
	$^{2,3}J(\text{Si}, \text{C}(4))$	5.5	
	$^1J(\text{Si}(\text{a}), \text{C}(2))$	65.7	207
	$^1J(\text{Si}(\text{b}), \text{C}(2))$	45.2	
	$^1J(\text{Si}(\text{b}), \text{C}(5))$	54.0	
	$^1J(\text{Si}(\text{a}), \text{C}(\text{Me}))$	51.1	
	$^1J(\text{Si}(\text{b}), \text{C}(\text{Ph}))$	65.6	
	$^{2,3}J(\text{Si}, \text{C}(4))$	11.8	
	$^{2,3}J(\text{Si}, \text{C}(4))$	10.1	

Table B3.7. Silacyclohexa-2-enes

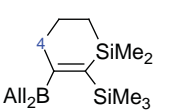

	$^1J(\text{Si}, \text{C}(\text{C}=\text{C}))$	51.9	183
	$^1J(\text{Si}, \text{C}(\text{CH}_2))$	50.4	
	$^1J(\text{Si}, \text{C}(\text{Me}))$	50.3	
	$^1J(\text{Si}, \text{C}(\text{Me}))$	49.6	
	$^1J(\text{Si}, \text{C}(\text{C}=\text{C}))$	51.9	
	$^1J(\text{Si}, \text{C}(\text{C}=\text{C}))$	51.9	184
	$^1J(\text{Si}(\text{a}), \text{C}(\text{CH}_2))$	50.4	
	$^3J(\text{Si}, \text{C}(4))$	12.6	
	$^3J(\text{Si}, \text{C}(4))$	11.0	

Table B3.7 (Continued)

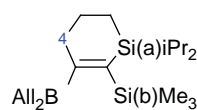
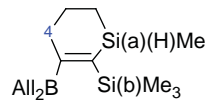
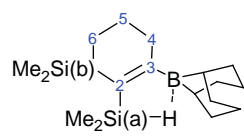
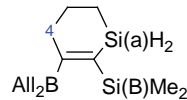
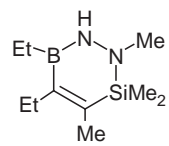
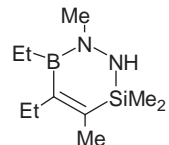
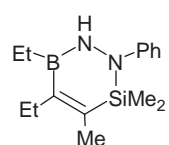
	$^1J(\text{Si}, \text{C}(\text{C}=\text{C}))$	52.0	184
	$^1J(\text{Si}, \text{C}(\text{C}=\text{C}))$	48.9	
	$^1J(\text{Si}(\text{a}), \text{C}(\text{iPr}))$	51.0	
	$^1J(\text{Si}(\text{a}), \text{C}(\text{CH}_2))$	47.7	
	$^1J(\text{Si}(\text{b}), \text{C}(\text{Me}))$	46.3	
	$^3J(\text{Si}, \text{C}(4))$	10.5	
	$^3J(\text{Si}, \text{C}(4))$	10.5	
	$^1J(\text{Si}, \text{C}(\text{C}=\text{C}))$	57.6	184
	$^1J(\text{Si}, \text{C}(\text{C}=\text{C}))$	49.4	
	$^1J(\text{Si}(\text{a}), \text{C}(\text{CH}_2))$	50.2	
	$^1J(\text{Si}(\text{a}), \text{C}(\text{Me}))$	50.2	
	$^1J(\text{Si}(\text{b}), \text{C}(\text{Me}))$	49.8	
	$^3J(\text{Si}, \text{C}(4))$	12.3	
	$^3J(\text{Si}, \text{C}(4))$	9.9	
	$^1J(\text{Si}(\text{a}), \text{C}(2))$	57.0	207
	$^1J(\text{Si}(\text{b}), \text{C}(2))$	53.1	
	$^1J(\text{Si}(\text{b}), \text{C}(6))$	51.2	
	$^1J(\text{Si}(\text{a}), \text{C}(\text{Me}))$	49.2	
	$^1J(\text{Si}(\text{b}), \text{C}(\text{Me}))$	50.4	
	$^{2,4}J(\text{Si}, \text{C}(5))$	< 3	
	$^3J(\text{Si}, \text{C}(4))$	11.6	
	$^1J(\text{Si}, \text{C}(\text{C}=\text{C}))$	58.2	184
	$^1J(\text{Si}, \text{C}(\text{C}=\text{C}))$	49.1	
	$^1J(\text{Si}(\text{a}), \text{C}(\text{CH}_2))$	50.2	
	$^1J(\text{Si}(\text{b}), \text{C}(\text{Me}))$	50.7	
	$^3J(\text{Si}, \text{C}(4))$	12.7	
	$^3J(\text{Si}, \text{C}(4))$	9.7	
	$^1J(\text{Si}, \text{C}(\text{C}=\text{C}))$	72.1	186
	$^1J(\text{Si}, \text{C}(\text{Me}))$	56.6	
	$^1J(\text{Si}, \text{C}(\text{Me}))$	56.6	186
	$^1J(\text{Si}, \text{C}(\text{C}=\text{C}))$	74.5	186
	$^1J(\text{Si}, \text{C}(\text{Me}))$	57.4	

Table B3.7 (Continued)

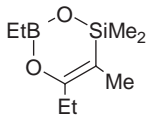
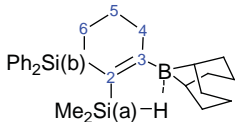
	$^1J(\text{Si}, \text{C}(\text{C}=\text{O}))$	70.4	172
	$^1J(\text{Si}, \text{C}(\text{Me}))$	61.0	
	$^1J(\text{Si}(\text{b}), \text{C}(\text{Ph}))$	67.1	207
	$^1J(\text{Si}, \text{C}(2))$	58.6	
	$^1J(\text{Si}, \text{C}(2))$	56.7	
	$^1J(\text{Si}(\text{b}), \text{C}(6))$	52.6	
	$^1J(\text{Si}(\text{a}), \text{C}(\text{Me}))$	50.0	
	$^2J(\text{Si}, \text{C}(5))$	<3	
	$^2J(\text{Si}(\text{b}), \text{C}(\text{Ph}))$	3.8	
	$^3J(\text{Si}(\text{b}), \text{C}(\text{Ph}))$	4.9	
	$^3J(\text{Si}, \text{C}(4))$	11.7	
	$^3J(\text{Si}, \text{C}(4))$	9.6	

Table B3.8. Silacyclohepta-2-enes and disilacycloheptadienes

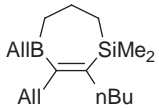
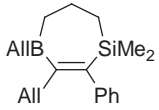
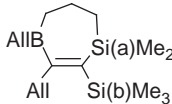
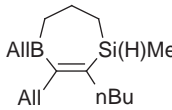
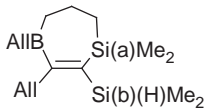
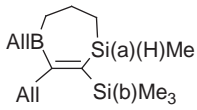
	$^1J(\text{Si}, \text{C}(\text{C}=\text{O}))$	63.7	61
	$^1J(\text{Si}, \text{C}(\text{CH}_2))$	51.3	
	$^1J(\text{Si}, \text{C}(\text{Me}))$	50.1	
	$^3J(\text{Si}, \text{C}(\text{All}))$	7.2	
	$^1J(\text{Si}, \text{C}(\text{C}=\text{O}))$	61.5	61
	$^1J(\text{Si}, \text{C}(\text{CH}_2))$	51.3	
	$^1J(\text{Si}, \text{C}(\text{Me}))$	51.5	
	$^3J(\text{Si}, \text{C}(\text{All}))$	6.7	
	$^1J(\text{Si}(\text{a}), \text{C}(\text{Me}))$	50.2	183
	$^1J(\text{Si}(\text{b}), \text{C}(\text{Me}))$	49.7	
	$^1J(\text{Si}, \text{C}(\text{C}=\text{O}))$	64.4	61
	$^1J(\text{Si}, \text{C}(\text{CH}_2))$	51.1	
	$^1J(\text{Si}, \text{C}(\text{Me}))$	49.4	
	$^3J(\text{Si}, \text{C}(\text{All}))$	10.3	
	$^1J(\text{Si}, \text{C}(\text{C}=\text{O}))$	51.9	183
	$^1J(\text{Si}, \text{C}(\text{CH}_2))$	49.8	
	$^1J(\text{Si}(\text{a}), \text{C}(\text{Me}))$	49.7	
	$^1J(\text{Si}(\text{a}), \text{C}(\text{Me}))$	50.6	
	$^1J(\text{Si}, \text{C}(\text{C}=\text{O}))$	55.0	184
	$^1J(\text{Si}, \text{C}(\text{C}=\text{O}))$	50.7	
	$^1J(\text{Si}(\text{a}), \text{C}(\text{CH}_2))$	50.0	
	$^1J(\text{Si}(\text{a}), \text{C}(\text{Me}))$	49.7	
	$^1J(\text{Si}(\text{b}), \text{C}(\text{Me}))$	50.4	
	$^3J(\text{Si}, \text{C}(\text{All}))$	12.1	

Table B3.8 (Continued)

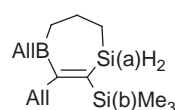
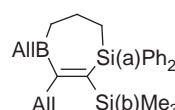
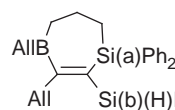
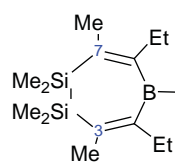
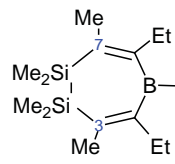
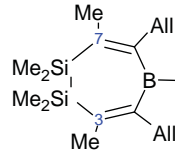
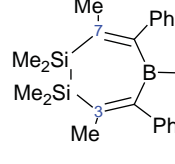
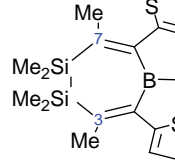
	$^1J(\text{Si}, \text{C}(\text{C}=\text{O}))$	54.7	184
	$^1J(\text{Si}, \text{C}(\text{C}=\text{O}))$	49.1	
	$^1J(\text{Si}(\text{a}), \text{C}(\text{CH}_2))$	50.2	
	$^1J(\text{Si}(\text{b}), \text{C}(\text{Me}))$	50.9	
	$^3J(\text{Si}, \text{C}(\text{All}))$	10.1	
	$^1J(\text{Si}, \text{C}(\text{C}=\text{O}))$	54.6	184
	$^1J(\text{Si}, \text{C}(\text{C}=\text{O}))$	52.7	
	$^1J(\text{Si}(\text{a}), \text{C}(\text{CH}_2))$	52.2	
	$^1J(\text{Si}(\text{b}), \text{C}(\text{Me}))$	50.8	
	$^3J(\text{Si}, \text{C}(\text{All}))$	10.9	
	$^1J(\text{Si}, \text{C}(\text{Ph}))$	54.4	184
	$^1J(\text{Si}, \text{C}(\text{Ph}))$	54.0	
	$^1J(\text{Si}, \text{C}(\text{C}=\text{O}))$	66.3	
	$^1J(\text{Si}(\text{a}), \text{C}(\text{CH}_2))$	52.9	
	$^3J(\text{Si}, \text{C}(\text{All}))$	10.3	
	$^1J(\text{Si}, \text{C}(3, 7))$	62.3	208
	$^1J(\text{Si}, \text{C}(\text{Me}))$	43.2	
	$^2J(\text{Si}, \text{C}(3, 7))$	6.0	
	$^1J(\text{Si}, \text{C}(3, 7))$	61.6	208
	$^1J(\text{Si}, \text{C}(\text{Me}))$	43.5	
	$^1J(\text{Si}, \text{C}(\text{Me}))$	43.5	
	$^2J(\text{Si}, \text{C}(3, 7))$	6.0	
	$^1J(\text{Si}, \text{C}(\text{Me}))$	43.4	171
	$^1J(\text{Si}, \text{C}(3, 7))$	60.2	208
	$^1J(\text{Si}, \text{C}(\text{Me}))$	43.5	
	$^2J(\text{Si}, \text{C}(3, 7))$	6.0	
	$^1J(\text{Si}, \text{C}(3, 7))$	59.6	208
	$^1J(\text{Si}, \text{C}(\text{Me}))$	43.5	
	$^1J(\text{Si}, \text{C}(\text{Me}))$	43.0	
	$^2J(\text{Si}, \text{C}(3, 7))$	6.0	

Table B3.8 (Continued)

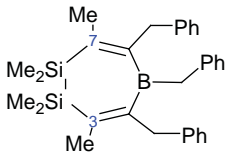
	$^1J(\text{Si}, \text{C}(3, 7))$	60.4	208
	$^1J(\text{Si}, \text{C}(\text{Me}))$	43.5	
	$^2J(\text{Si}, \text{C}(3, 7))$	6.0	

Table B3.9. Bi-cycles

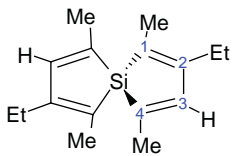
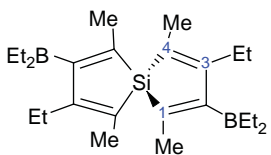
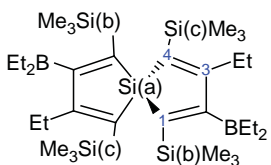
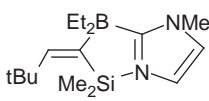
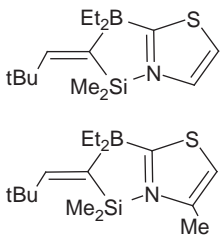
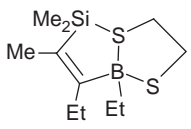
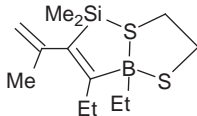
	$^1J(\text{Si}, \text{C}(1))$	62.0	100
	$^1J(\text{Si}, \text{C}(4))$	66.4	
	$^2J(\text{Si}, \text{C}(2))$	9.0	
	$^2J(\text{Si}, \text{C}(3))$	8.0	
	$^1J(\text{Si}, \text{C}(1))$	61.0	100
	$^1J(\text{Si}, \text{C}(4))$	65.5	
	$^2J(\text{Si}, \text{C}(3))$	10.0	
	$^1J(\text{Si}(\text{a}), \text{C}(1))$	63.4	100
	$^1J(\text{Si}(\text{a}), \text{C}(4))$	62.6	
	$^1J(\text{Si}(\text{b}), \text{C}(1))$	40.2	
	$^1J(\text{Si}(\text{c}), \text{C}(4))$	46.6	
	$^{2,3}J(\text{Si}, \text{C}(3))$	11.2	
	$^{2,3}J(\text{Si}, \text{C}(3))$	7.2	
	$^1J(\text{Si}, \text{C}(\text{Me}))$	54.0	
	$^1J(\text{Si}, \text{C}(\text{C}=\text{}))$	67.3	188,189
	$^1J(\text{Si}, \text{C}(\text{Me}))$	53.7	
	$^1J(\text{Si}, \text{C}(\text{C}=\text{}))$	68.2	189
	$^1J(\text{Si}, \text{C}(\text{Me}))$	53.3	
	$^2J(\text{Si}, \text{C}(\text{C}=\text{}))$	4.5	
	$^1J(\text{Si}, \text{C}(\text{C}=\text{}))$	77.1	201
	$^1J(\text{Si}, \text{C}(\text{Me}))$	52.5	
	$^1J(\text{Si}, \text{C}(\text{Me}))$	51.5	
	$^1J(\text{Si}, \text{C}(\text{Me}))$	52.1	201
	$^1J(\text{Si}, \text{C}(\text{Me}))$	52.1	

Table B3.9 (Continued)

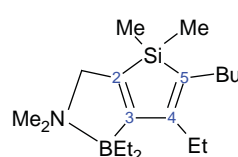
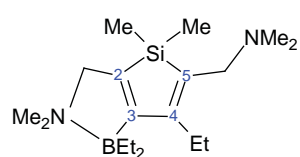
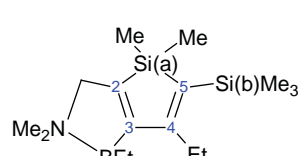
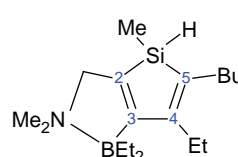
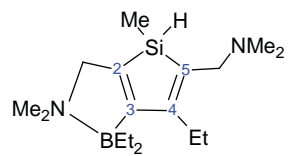
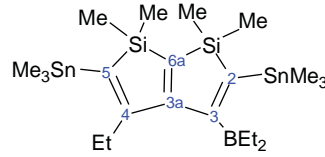
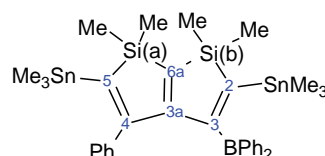
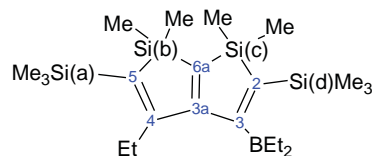
	$^1J(\text{Si}, \text{C}(2))$	62.6	204
	$^1J(\text{Si}, \text{C}(5))$	69.7	
	$^1J(\text{Si}, \text{C}(\text{Me}))$	49.2	
	$^2J(\text{Si}, \text{C}(4))$	< 10	
	$^1J(\text{Si}, \text{C}(2))$	65.7	204
	$^1J(\text{Si}, \text{C}(5))$	71.0	
	$^1J(\text{Si}, \text{C}(\text{Me}))$	49.5	
	$^2J(\text{Si}, \text{C}(4))$	7.9	
	$^2J(\text{Si}, \text{C}(\text{NCH}_2))$	11.8	
	$^3J(\text{Si}, \text{C}(\text{Et}))$	5.8	
	$^1J(\text{Si}, \text{C}(2,5))$	64.4	204
	$^1J(\text{Si}, \text{C}(2,5))$	46.0	
	$^1J(\text{Si}(a), \text{C}(2, 5))$	67.0	
	$^1J(\text{Si}(a), \text{C}(\text{Me}))$	48.3	
	$^1J(\text{Si}(b), \text{C}(\text{Me}))$	50.8	
	$^1J(\text{Si}, \text{C}(2))$	62.6	204
	$^1J(\text{Si}, \text{C}(5))$	69.7	
	$^1J(\text{Si}, \text{C}(\text{Me}))$	48.4	
	$^2J(\text{Si}, \text{C}(4))$	< 10	
	$^1J(\text{Si}, \text{C}(2))$	66.3	204
	$^1J(\text{Si}, \text{C}(5))$	71.8	
	$^1J(\text{Si}, \text{C}(\text{Me}))$	49.6	
	$^2J(\text{Si}, \text{C}(4))$	< 10	
	$^2J(\text{Si}, \text{C}(\text{NCH}_2))$	11.9	
	$^1J(\text{Si}, \text{C}(2))$	44.4	209
	$^1J(\text{Si}, \text{C}(5))$	49.1	
	$^1J(\text{Si}, \text{C}(6a))$	59.0	
	$^1J(\text{Si}, \text{C}(6a))$	57.0	
	$^1J(\text{Si}, \text{C}(\text{Me}))$	48.8	
	$^1J(\text{Si}, \text{C}(\text{Me}))$	48.8	
	$^1J(\text{Si}, \text{C}(2))$	43.0	209
	$^1J(\text{Si}, \text{C}(5))$	46.8	
	$^1J(\text{Si}, \text{C}(6a))$	77.8	
	$^1J(\text{Si}, \text{C}(6a))$	68.6	
	$^1J(\text{Si}(b), \text{C}(\text{Me}))$	40.7	
	$^1J(\text{Si}, \text{C}(2))$	62.0	209
	$^1J(\text{Si}, \text{C}(2))$	43.9	
	$^1J(\text{Si}, \text{C}(5))$	62.9	
	$^1J(\text{Si}, \text{C}(5))$	46.7	

Table B3.9 (Continued)

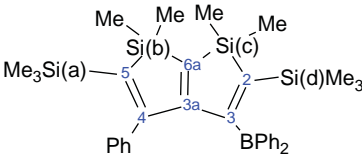
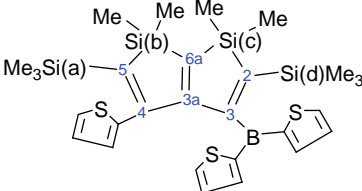
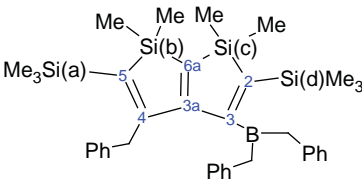
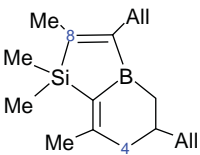
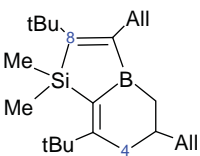
	$^1J(\text{Si}, \text{C}(6a))$	58.2	
	$^1J(\text{Si}, \text{C}(6a))$	58.2	
	$^1J(\text{Si}(b,c), \text{C}(\text{Me}))$	48.6	
	$^1J(\text{Si}(b,c), \text{C}(\text{Me}))$	48.6	
	$^1J(\text{Si}(a,d), \text{C}(\text{Me}))$	51.5	
	$^1J(\text{Si}(a,d), \text{C}(\text{Me}))$	50.5	
	$^nJ(\text{Si}, \text{C}(4))$	9.6	
	$^1J(\text{Si}, \text{C}(2))$	60.9	209
	$^1J(\text{Si}, \text{C}(2))$	43.7	
	$^1J(\text{Si}, \text{C}(5))$	60.9	
	$^1J(\text{Si}, \text{C}(5))$	45.4	
	$^1J(\text{Si}, \text{C}(6a))$	57.4	
	$^1J(\text{Si}, \text{C}(6a))$	57.4	
	$^1J(\text{Si}(a), \text{C}(\text{Me}))$	51.3	
	$^1J(\text{Si}(d), \text{C}(\text{Me}))$	51.7	
	$^1J(\text{Si}, \text{C}(2))$	61.0	
	$^1J(\text{Si}, \text{C}(2))$	42.1	
	$^1J(\text{Si}, \text{C}(5))$	59.9	209
	$^1J(\text{Si}, \text{C}(5))$	44.6	
	$^1J(\text{Si}, \text{C}(6a))$	57.8	
	$^1J(\text{Si}, \text{C}(6a))$	56.6	
	$^1J(\text{Si}(a), \text{C}(\text{Me}))$	51.7	
	$^1J(\text{Si}(c), \text{C}(\text{Me}))$	49.2	
	$^1J(\text{Si}(d), \text{C}(\text{Me}))$	52.1	
	$^1J(\text{Si}, \text{C}(2))$	61.7	
	$^1J(\text{Si}, \text{C}(2))$	42.8	
	$^1J(\text{Si}, \text{C}(5))$	61.0	
	$^1J(\text{Si}, \text{C}(5))$	47.0	209
	$^1J(\text{Si}, \text{C}(6a))$	58.6	
	$^1J(\text{Si}, \text{C}(6a))$	56.8	
	$^{2,3}J(\text{Si}, \text{C}(3a))$	11.2	
	$^{2,3}J(\text{Si}, \text{C}(3a))$	9.8	
	$^{2,3}J(\text{Si}, \text{C}(3a))$	7.7	
	$^nJ(\text{Si}, \text{C}(4))$	9.8	
	$^nJ(\text{Si}, \text{C}(4))$	3.9	
	$^1J(\text{Si}, \text{C}(8))$	44.8	
	$^1J(\text{Si}, \text{C}(\text{Me}))$	48.6	
	$^1J(\text{Si}, \text{C}(\text{Me}))$	48.2	194
	$^3J(\text{Si}, \text{C}(4))$	7.4	
	$^1J(\text{Si}, \text{C}(8))$	66.5	
	$^1J(\text{Si}, \text{C}(\text{Me}))$	49.3	
	$^1J(\text{Si}, \text{C}(\text{Me}))$	49.3	194
	$^3J(\text{Si}, \text{C}(4))$	6.8	
	$^3J(\text{Si}, \text{C}(4))$	6.8	

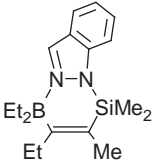
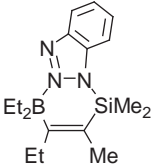
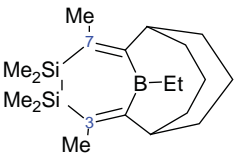
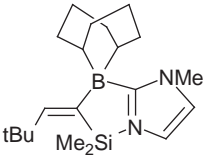
Table B3.9 (Continued)

	$^1J(\text{Si}, \text{C}(8))$	66.3	194
	$^1J(\text{Si}, \text{C}(\text{Me}))$	50.1	
	$^nJ(\text{Si}, \text{C}(\text{tBu}))$	9.1	
	$^3J(\text{Si}, \text{C}(4))$	8.4	
	$^1J(\text{Si}, \text{C}(5))$	64.1	194
	$^1J(\text{Si}, \text{C}(8))$	63.2	
	$^1J(\text{Si}, \text{C}(8))$	51.4	
	$^1J(\text{Si}(a), \text{C}(\text{Me}))$	43.0	
	$^1J(\text{Si}(a), \text{C}(\text{Me}))$	43.0	
	$^1J(\text{Si}(b,c), \text{C}(\text{Me}))$	50.7	
	$^1J(\text{Si}(b,c), \text{C}(\text{Me}))$	50.7	
	$^nJ(\text{Si}, \text{C}(4))$	7.6	
	$^1J(\text{Si}, \text{C}(5))$	52.2	194
	$^1J(\text{Si}, \text{C}(8))$	62.5	
	$^1J(\text{Si}(a), \text{C}(\text{Me}))$	46.2	
	$^1J(\text{Si}(b,c), \text{C}(\text{Me}))$	50.8	
	$^1J(\text{Si}(b,c), \text{C}(\text{Me}))$	50.7	
	$^nJ(\text{Si}, \text{C}(4))$	8.1	
	$^1J(\text{Si}, \text{C}(\text{C}=\text{}))$	85.6	107
	$^1J(\text{Si}, \text{C}(\text{Me}))$	56.1	
	$^2J(\text{Si}, \text{C}(\text{Me}))$	-9.5	
	$^3J(\text{Si}, \text{C}(\text{Et}))$	7.0	
	$^1J(\text{Si}, \text{C}(\text{C}=\text{}))$	86.6	107
	$^1J(\text{Si}, \text{C}(\text{Me}))$	56.1	
	$^1J(\text{Si}, \text{C}(\text{Me}))$	52.7	201
	$^1J(\text{Si}, \text{C}(\text{Me}))$	49.6	
	$^1J(\text{Si}, \text{C}(\text{Me}))$	52.3	201
	$^1J(\text{Si}, \text{C}(\text{Me}))$	51.4	

Table B3.10. Tri-cycles and tetra-cycle

	$^1J(\text{Si}, \text{C}(\text{Me}))$	57	186
	$^1J(\text{Si}, \text{C}(2))$	49.0	206
	$^1J(\text{Si}, \text{C}(5))$	61.6	
	$^1J(\text{Si}, \text{C}(5))$	42.5	
	$^1J(\text{Si}, \text{C}(6a))$	57.0	
	$^1J(\text{Si}, \text{C}(6a))$	57.0	
	$^1J(\text{Si}, \text{C}(7a))$	57.3	
	$^1J(\text{Si}, \text{C}(7a))$	56.5	
	$^1J(\text{Si}(a), \text{C}(\text{Me}))$	49.1	
	$^1J(\text{Si}(b), \text{C}(\text{Me}))$	50.0	
	$^1J(\text{Si}(c), \text{C}(\text{Me}))$	50.0	
	$^1J(\text{Si}, \text{C}(\text{Me}))$	56.2	188
	$^1J(\text{Si}, \text{C}(\text{Me}))$	51.4	201
	$^1J(\text{Si}, \text{C}(\text{Me}))$	52.8	
	$^1J(\text{Si}, \text{C}(5))$	63.5	194
	$^1J(\text{Si}, \text{C}(8))$	55.1	
	$^1J(\text{Si}, \text{C}(8))$	52.0	
	$^1J(\text{Si}(a,b), \text{C}(\text{C}=\text{C}))$	61.3	
	$^1J(\text{Si}(a,b), \text{C}(\text{C}=\text{C}))$	49.0	
	$^1J(\text{Si}(a,d), \text{C}(\text{Me}))$	52.0	
	$^1J(\text{Si}(a,d), \text{C}(\text{Me}))$	51.2	
	$^1J(\text{Si}(b,c), \text{C}(\text{Me}))$	51.2	
	$^1J(\text{Si}(b,c), \text{C}(\text{Me}))$	50.3	
	$^1J(\text{Si}(b,c), \text{C}(\text{Me}))$	48.5	
	$^1J(\text{Si}(b,c), \text{C}(\text{Me}))$	48.5	
	$^7J(\text{Si}, \text{C}(4))$	8.8	
	$^1J(\text{Si}, \text{C}(2))$	49.7	206
	$^1J(\text{Si}, \text{C}(6))$	53.1	
	$^1J(\text{Si}, \text{C}(6))$	53.1	
	$^1J(\text{Si}, \text{C}(7a))$	56.9	
	$^1J(\text{Si}, \text{C}(7a))$	42.6	
	$^1J(\text{Si}, \text{C}(8a))$	59.9	
	$^1J(\text{Si}, \text{C}(8a))$	56.1	
	$^1J(\text{Si}(a), \text{C}(\text{Me}))$	51.7	
	$^1J(\text{Si}(a), \text{C}(\text{Me}))$	50.0	
	$^1J(\text{Si}(b), \text{C}(\text{Me}))$	50.0	

Table B3.10 (Continued)

	$^1J(\text{Si(b)}, \text{C(Me)})$	49.1	
	$^1J(\text{Si(c)}, \text{C(Me)})$	50.0	
	$^1J(\text{Si(c)}, \text{C(Me)})$	50.0	
	$^nJ(\text{Si}, \text{C}(\text{CH}_2(\text{Et}-\text{C}(5))))$	10.3	
	$^nJ(\text{Si}, \text{C}(\text{CH}_2(\text{Et}-\text{C}(5))))$	10.3	
	$^1J(\text{Si}, \text{C}(\text{C}=\text{O}))$	85.2	107
	$^1J(\text{Si}, \text{C}(\text{C}=\text{O}))$	86.6	107
	$^1J(\text{Si}, \text{C(Me)})$	56.1	
	$^1J(\text{Si}, \text{C}(3,7))$	61.0	208
	$^1J(\text{Si}, \text{C(Me)})$	43.6	
	$^1J(\text{Si}, \text{C(Me)})$	42.6	
	$^2J(\text{Si}, \text{C}(3,7))$	6.0	
	$^1J(\text{Si}, \text{C(Me)})$	54.0	188

APPENDIX B4**Table B4.1.** Silicon bonded to X = Y = Z fragment(s)

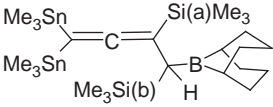
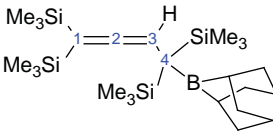
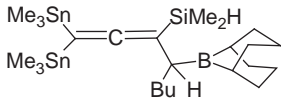
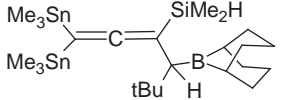
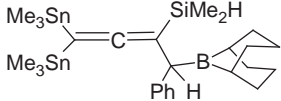
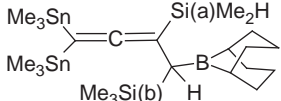
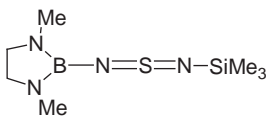
	$^1J(\text{Si(a)}, \text{C}(\text{C}=\text{O}))$	63.0	117
	$^1J(\text{Si(a)}, \text{C(Me)})$	52.1	
	$^1J(\text{Si(b)}, \text{C(Me)})$	51.0	
	$^1J(\text{Si}, \text{C}(1))$	51.8	177
	$^1J(\text{Si}, \text{C}(4))$	33.3	
	$^1J(\text{Si}, \text{C(Me)})$	52.4	
	$^1J(\text{Si}, \text{C(Me)})$	51.6	
	$^nJ(\text{Si}, \text{C}(2))$	< 2	
	$^nJ(\text{Si}, \text{C}(3))$	< 2	

Table B4.1 (Continued)

	$^1J(\text{Si}, \text{C}(\text{C}=\text{)))}$	64.9	117
	$^1J(\text{Si}, \text{C}(\text{Me}))$	52.8	
	$^1J(\text{Si}, \text{C}(\text{Me}))$	52.5	
	$^1J(\text{Si}, \text{C}(\text{C}=\text{)))}$	64.3	117
	$^1J(\text{Si}, \text{C}(\text{Me}))$	52.8	
	$^1J(\text{Si}, \text{C}(\text{Me}))$	52.0	
	$^1J(\text{Si}, \text{C}(\text{C}=\text{)))}$	64.5	117
	$^1J(\text{Si}, \text{C}(\text{Me}))$	52.7	
	$^1J(\text{Si}, \text{C}(\text{Me}))$	52.5	
	$^1J(\text{Si}(\text{a}), \text{C}(\text{C}=\text{)))}$	65.0	117
	$^1J(\text{Si}(\text{a}), \text{C}(\text{Me}))$	52.4	
	$^1J(\text{Si}(\text{a}), \text{C}(\text{Me}))$	52.0	
	$^1J(\text{Si}(\text{b}), \text{C}(\text{Me}))$	51.1	
$(\text{Me}_3\text{Si}(\text{a}))_2\text{C}=\text{C}=\text{N}-\text{Si}(\text{b})\text{Me}_3$	$^1J(\text{Si}(\text{a}), \text{C}(\text{C}=\text{)))}$	53.95	19
	$^1J(\text{Si}(\text{a}), \text{C}(\text{Me}))$	53.30	
	$^2J(\text{Si}(\text{a}), \text{C}(\text{C}=\text{)))}$	0.20	
	$^3J(\text{Si}(\text{a}), \text{C}(\text{Si}(\text{a})\text{Me}))$	0.62	
	$^3J(\text{Si}(\text{b}), \text{C}(\text{C}=\text{)))}$	4.43	
	$^5J(\text{Si}(\text{a}), \text{C}(\text{Si}(\text{b})\text{Me}))$	0.32	
	$^1J(\text{Si}, \text{C})$	56.5	210
$(\text{Me}_3\text{Si}-\text{N}=\text{S}=\text{N})_2\text{B}-\text{NEt}_2$	$^1J(\text{Si}, \text{C})$	59.1	210
$(\text{Me}_3\text{Si}-\text{N}=\text{S}=\text{N})_2\text{Sn}n\text{Bu}_2$	$^1J(\text{Si}, \text{C})$	57.8	211
$(\text{Me}_3\text{Si}-\text{N}=\text{S}=\text{N})_2\text{Sn}t\text{Bu}_2$	$^1J(\text{Si}, \text{C})$	56.7	211
$\text{MeSi}(\text{N}=\text{S}=\text{N}t\text{Bu})_3$	$^1J(\text{Si}, \text{C})$	61.0	211
$\text{MeSi}(\text{N}=\text{S}=\text{N}-\text{SiMe}_3)_3$	$^1J(\text{Si}, \text{C})$	58.0	211
	$^1J(\text{Si}, \text{C})$	57.5	
$t\text{BuSi}(\text{N}=\text{S}=\text{N}-\text{SiMe}_3)_3$	$^1J(\text{Si}, \text{C})$	57.8	211
$\text{Si}(\text{N}=\text{S}=\text{N}-\text{SiMe}_3)_4$	$^1J(\text{Si}, \text{C})$	57.8	212
$\text{Me}_3\text{Si}-\text{N}=\text{C}=\text{O}$	$^1J(\text{Si}, \text{C})$	58.6	78

APPENDIX C

Tables of silicon–carbon coupling constants in molecules containing Si(sp³)–C(sp) bond.

Table C1. One Si–C≡C fragment in molecule

Me ₃ Si–C≡CH	¹ J(Si, C(C≡))	81.47	98
	¹ J(Si, C(Me))	56.28	
	² J(Si, C(C≡))	15.41	
	¹ J(Si, C≡)	–79.4	
	¹ J(Si, C(Me))	–55.1	
Me ₃ Si–C≡C–Me	² J(Si–C≡C)	–14.8	43
	¹ J(Si, C(C≡))	88.9	
	² J(Si, C(C≡))	17.6	
	¹ J(Si, C(C≡))	85.75	
	¹ J(Si, C(Me))	56.28	
	² J(Si, C(C≡))	15.74	
	¹ J(Si, C(C≡))	80.9	
Me ₃ Si–C≡C–Me	¹ J(Si, C(Me))	57.5	102
	² J(Si, C(C≡))	15.6	
	¹ J(Si, C(C≡))	68.10	
	¹ J(Si, C(Me))	57.27	
	² J(Si, C(C≡))	13.14	
Me ₃ Si–C≡CCl	¹ J(Si, C(C≡))	84.0	97
	² J(Si, C(C≡))	17.1	
Et ₃ Si–C≡CH	¹ J(Si, C(C≡))	78.7	97
	² J(Si, C(C≡))	13.5	
	¹ J(Si, C(C≡))	75.0	
	¹ J(Si, C(Et))	57.0	
	² J(Si, C(C≡))	18.6	
Me ₃ Si–C≡C–S–Me	¹ J(Si, C(C≡))	82.63	98
	¹ J(Si, C(Me))	56.44	
	² J(Si, C(C≡))	15.54	
Me ₃ Si–C≡C–CH ₂ Cl	¹ J(Si, C(C≡))	80.77	98
	¹ J(Si, C(Me))	56.53	
	² J(Si, C(C≡))	15.42	
Et ₃ Si–C≡C–Me	¹ J(Si, C(C≡))	85.2	97
	² J(Si, C(C≡))	15.5	
Me ₃ Si–C≡C– <i>t</i> Bu	¹ J(Si, C(C≡))	88.2	97
	² J(Si, C(C≡))	16.7	
Me ₃ Si–C≡C–CH ₂ –NEt ₂	¹ J(Si, C(C≡))	83.84	98
	¹ J(Si, C(Me))	56.24	
	² J(Si, C(C≡))	15.75	
Me ₃ Si–C≡C–CH ₂ –O–Et	¹ J(Si, C(C≡))	80.57	98
	¹ J(Si, C(Me))	56.41	
	² J(Si, C(C≡))	15.49	
Me ₃ Si–C≡C–S–Et	¹ J(Si, C(C≡))	82.73	98
	¹ J(Si, C(Me))	56.39	
	² J(Si, C(C≡))	16.67	

Table C1 (Continued)

$\text{Me}_3\text{Si}-\text{C}\equiv\text{C}-\text{CF}_3$	$^1J(\text{Si}, \text{C}(\text{C}\equiv))$	71.77	98
	$^1J(\text{Si}, \text{C}(\text{Me}))$	57.33	
$\text{Et}_3\text{Si}-\text{C}\equiv\text{C}-\text{Et}$	$^1J(\text{Si}, \text{C}(\text{C}\equiv))$	84.9	97
	$^2J(\text{Si}, \text{C}(\text{C}\equiv))$	15.2	
$\text{Me}_3\text{Si}-\text{C}\equiv\text{C}-\text{Ph}$	$^1J(\text{Si}, \text{C}(\text{C}\equiv))$	83.12	98
	$^1J(\text{Si}, \text{C}(\text{Me}))$	56.28	
$\text{Me}_3\text{Si}-\text{C}\equiv\text{C}-\text{NEt}_2$	$^2J(\text{Si}, \text{C}(\equiv\text{C}))$	16.01	
	$^1J(\text{Si}, \text{C}(\text{C}\equiv))$	96.5	
$\text{Me}_3\text{Si}-\text{C}\equiv\text{C}-\text{NEt}_2$	$^1J(\text{Si}, \text{C}(\text{Me}))$	55.9	213
	$^2J(\text{Si}, \text{C}(\equiv\text{C}))$	20.2	
$\text{Me}_3\text{Si}-\text{C}\equiv\text{C}-\text{Br}$	$^1J(\text{Si}, \text{C}(\text{C}\equiv))$	81.6	97
	$^2J(\text{Si}, \text{C}(\text{C}\equiv))$	15.5	
$\text{Me}_3\text{Si}-\text{C}\equiv\text{C}-\text{Br}$	$^1J(\text{Si}, \text{C}(\text{C}\equiv))$	80.22	98
	$^1J(\text{Si}, \text{C}(\text{Me}))$	56.68	
$\text{Et}_3\text{Si}-\text{C}\equiv\text{C}-i\text{Pr}$	$^2J(\text{Si}, \text{C}(\text{C}\equiv))$	15.05	
	$^1J(\text{Si}, \text{C}(\text{C}\equiv))$	84.5	
$\text{Me}_3\text{Si}-\text{C}\equiv\text{C}-i\text{Pr}$	$^2J(\text{Si}, \text{C}(\text{C}\equiv))$	14.9	97
	$^1J(\text{Si}, \text{C}(\text{C}\equiv))$	88.7	
$\text{Me}_3\text{Si}-\text{C}\equiv\text{C}-\text{C}_6\text{H}_{13}$	$^2J(\text{Si}, \text{C}(\text{C}\equiv))$	17.3	
	$^1J(\text{Si}, \text{C}(\text{C}\equiv))$	84.4	
$\text{Et}_3\text{Si}-\text{C}\equiv\text{C}-t\text{Bu}$	$^2J(\text{Si}, \text{C}(\text{C}\equiv))$	14.7	97
	$^1J(\text{Si}, \text{C}(\text{C}\equiv))$	78.25	
$\text{Me}_3\text{Si}-\text{C}\equiv\text{C}-\text{GeMe}_3$	$^1J(\text{Si}, \text{C}(\text{Me}))$	56.09	98
	$^2J(\text{Si}, \text{C}(\equiv\text{C}))$	12.20	
$\text{Me}_3\text{Si}-\text{C}\equiv\text{C}-\text{Cl}$	$^1J(\text{Si}, \text{C}(\text{C}\equiv))$	78.4	97
	$^2J(\text{Si}, \text{C}(\text{C}\equiv))$	13.3	
$\text{Me}_3\text{Si}-\text{C}\equiv\text{C}-\text{Cl}$	$^1J(\text{Si}, \text{C}(\text{C}\equiv))$	77.73	98
	$^1J(\text{Si}, \text{C}(\text{Me}))$	56.49	
$\text{Me}_3\text{Si}-\text{C}\equiv\text{C}-\text{CH}_2-\text{GeMe}_3$	$^2J(\text{Si}, \text{C}(\equiv\text{C}))$	13.15	
	$^1J(\text{Si}, \text{C}(\text{C}\equiv))$	88.31	
$\text{Me}_3\text{Si}-\text{C}\equiv\text{C}-\text{CH}_2-\text{GeMe}_3$	$^1J(\text{Si}, \text{C}(\text{Me}))$	56.01	98
	$^2J(\text{Si}, \text{C}(\equiv\text{C}))$	17.69	
$\text{Me}_3\text{Si}-\text{C}\equiv\text{C}-\text{GeEt}_3$	$^1J(\text{Si}, \text{C}(\text{C}\equiv))$	78.30	98
	$^1J(\text{Si}, \text{C}(\text{Me}))$	55.99	
$\text{Me}_3\text{Si}-\text{C}\equiv\text{C}-\text{GeEt}_3$	$^2J(\text{Si}, \text{C}(\text{C}\equiv))$	12.30	
	$^1J(\text{Si}, \text{C}(\text{C}\equiv))$	77.0	
$\text{Me}_3\text{Si}-\text{C}\equiv\text{C}-\text{SnMe}_3$	$^1J(\text{Si}, \text{C}(\text{Me}))$	56.2	214
	$^2J(\text{Si}, \text{C}(\equiv\text{C}))$	10.8	
$\text{Me}_3\text{Si}-\text{C}\equiv\text{C}-\text{SnMe}_3$	$^1J(\text{Si}, \text{C}(\text{C}\equiv))$	79.0	97
	$^1J(\text{Si}, \text{C}(\text{Me}))$	55.8	
$\text{Me}_3\text{Si}-\text{C}\equiv\text{C}-\text{SnMe}_3$	$^2J(\text{Si}, \text{C}(\text{C}\equiv))$	11.6	
	$^1J(\text{Si}, \text{C}(\text{C}\equiv))$	78.83	
$\text{Me}_3\text{Si}-\text{C}\equiv\text{C}-\text{C}_6\text{F}_5$	$^1J(\text{Si}, \text{C}(\text{Me}))$	55.92	98
	$^1J(\text{Si}, \text{C}(\text{C}\equiv))$	77.62	
$\text{Me}_3\text{Si}-\text{C}\equiv\text{C}-\text{C}_6\text{F}_5$	$^1J(\text{Si}, \text{C}(\text{Me}))$	56.57	98
	$^2J(\text{Si}, \text{C}(\text{C}\equiv))$	14.00	
$\text{Me}_3\text{Si}-\text{C}\equiv\text{C}-\text{C}\equiv\text{C}-\text{SnMe}_3$	$^1J(\text{Si}, \text{C}(\text{C}\equiv))$	82.0	215
	$^1J(\text{Si}, \text{C}(\text{Me}))$	57.2	
$\text{Me}_3\text{Si}-\text{C}\equiv\text{C}-\text{C}\equiv\text{C}-\text{SnMe}_3$	$^2J(\text{Si}, \text{C}(\text{C}\equiv))$	12.6	

Table C1 (Continued)

$\text{Me}_3\text{Si}-\text{C}\equiv\text{C}-\text{S}-\text{C}_6\text{F}_5$	$^1J(\text{Si}, \text{C}(\text{C}\equiv))$	78.50	98
	$^1J(\text{Si}, \text{C}(\text{Me}))$	56.70	
	$^2J(\text{Si}, \text{C}(\text{C}\equiv))$	14.61	
$\text{Me}_3\text{Si}-\text{C}\equiv\text{C}-\text{SnCl}_3$	$^1J(\text{Si}, \text{C}(\text{Me}))$	57.2	216,176
$\text{Me}_3\text{Si}-\text{C}\equiv\text{C}-\text{Sn}(\text{C}\equiv\text{C}-\text{Me})_3$	$^1J(\text{Si}, \text{C}(\text{C}\equiv))$	73.9	217
	$^2J(\text{Si}, \text{C}(\text{C}\equiv))$	11.2	
$\text{Me}_3\text{Si}-\text{C}\equiv\text{C}-\text{Sn}t\text{Bu}_3$	$^1J(\text{Si}, \text{C}(\text{C}\equiv))$	78.66	98
	$^1J(\text{Si}, \text{C}(\text{Me}))$	55.79	
$\text{Me}_3\text{Si}-\text{C}\equiv\text{C}-\text{Sn}(\text{Me})(\text{C}\equiv\text{C}-t\text{Bu})_2$	$^1J(\text{Si}, \text{C}(\text{C}\equiv))$	76.9	217
	$^1J(\text{Si}, \text{C}(\text{Me}))$	56.6	
	$^2J(\text{Si}, \text{C}(\text{C}\equiv))$	11.3	
$\text{Me}_3\text{Si}-\text{C}\equiv\text{C}-\text{Sn}(\text{C}\equiv\text{C}-t\text{Bu})_3$	$^1J(\text{Si}, \text{C}(\text{C}\equiv))$	74.8	217
	$^1J(\text{Si}, \text{C}(\text{Me}))$	56.2	
	$^2J(\text{Si}, \text{C}(\text{C}\equiv))$	10.8	
$\text{Me}_3\text{Si}-\text{C}\equiv\text{C}-\text{CH}_2-\text{Sn}t\text{Bu}_3$	$^1J(\text{Si}, \text{C}(\text{C}\equiv))$	90.80	98
	$^1J(\text{Si}, \text{C}(\text{Me}))$	55.91	
	$^2J(\text{Si}, \text{C}(\text{C}\equiv))$	18.02	
$\text{Me}_3\text{Si}-\text{C}\equiv\text{C}-\text{SnBr}_3$	$^1J(\text{Si}, \text{C}(\text{C}\equiv))$	66.6	176
	$^1J(\text{Si}, \text{C}(\text{Me}))$	57.0	
	$^2J(\text{Si}, \text{C}(\text{C}\equiv))$	9.3	
$\text{Me}_3\text{Si}(\text{a})-\text{C}\equiv\text{C}-\text{CH}_2-\text{SiMe}_3$	$^1J(\text{Si}(\text{a}), \text{C}(\text{C}\equiv))$	89.54	98
	$^1J(\text{Si}(\text{a}), \text{C}(\text{Me}))$	56.06	
	$^2J(\text{Si}(\text{a}), \text{C}(\text{C}\equiv))$	17.86	
<i>Si-H bond(s)</i>			
$\text{Me}_2(\text{H})\text{Si} \equiv \text{C} - \text{C}_6\text{H}_4\text{OMe}$	$^1J(\text{Si}, \text{C}(\text{C}\equiv))$	87.0	61
	$^1J(\text{Si}, \text{C}(\text{Me}))$	56.0	
$\text{Me}_2(\text{H})\text{Si}-\text{C}\equiv\text{C}-\text{SnMe}_3$	$^2J(\text{Si}, \text{C}(\text{C}\equiv))$	16.9	
	$^1J(\text{Si}, \text{C}(\text{C}\equiv))$	79.8	182
	$^1J(\text{Si}, \text{C}(\text{Me}))$	55.7	
$\text{H}_2(\text{Me})\text{Si}-\text{C}\equiv\text{C}-n\text{Bu}$	$^2J(\text{Si}, \text{C}(\text{C}\equiv))$	12.0	
	$^1J(\text{Si}, \text{C}(\text{C}\equiv))$	92.0	61
	$^1J(\text{Si}, \text{C}(\text{Me}))$	56.2	
$\text{H}_3\text{Si}-\text{C}\equiv\text{CH}$	$^2J(\text{Si}, \text{C}(\text{C}\equiv))$	17.7	
	$^1J(\text{Si}, \text{C})$	75.0	95
	$^2J(\text{Si}, \text{C})$	18.6	
$\text{H}_3\text{Si}-\text{C}\equiv\text{C}-n\text{Bu}$	$^1J(\text{Si}, \text{C}(\text{C}\equiv))$	97.9	61
	$^2J(\text{Si}, \text{C}(\text{C}\equiv))$	19.2	
$\text{H}_3\text{Si}-\text{C}\equiv\text{C}-\text{Ph}$	$^1J(\text{Si}, \text{C}(\text{C}\equiv))$	94.9	61
	$^2J(\text{Si}, \text{C}(\text{C}\equiv))$	18.1	
	$^3J(\text{Si}, \text{C}(\text{Ph}))$	11.5	
<i>Si-N bond</i>			
$\text{Et}_2\text{N}-\text{SiMe}_2-\text{C}\equiv\text{C}-\text{Me}$	$^1J(\text{Si}, \text{C}(\text{C}\equiv))$	93.5	107
	$^1J(\text{Si}, \text{C}(\text{Me}))$	64.0	
	$^2J(\text{Si}, \text{C}(\text{C}\equiv))$	-18.7	
$\text{Et}_2\text{N}-\text{SiMe}_2-\text{C}\equiv\text{C}-n\text{Bu}$	$^1J(\text{Si}, \text{C}(\text{C}\equiv))$	93.5	107
	$^1J(\text{Si}, \text{C}(\text{Me}))$	64.0	
	$^2J(\text{Si}, \text{C}(\text{C}\equiv))$	-17.7	

Table C1 (Continued)*Si–halogen, optional Si–N and Si–H bond(s)*

$\text{Me}_2(\text{Cl})\text{Si}-\text{C}\equiv\text{C}-\text{Bu}$	$^1J(\text{Si}, \text{C}(\text{C}\equiv))$	105.7	175,218
	$^1J(\text{Si}, \text{C}(\text{Me}))$	65.4	
$\text{Me}_2(\text{Cl})\text{Si}-\text{C}\equiv\text{C}-t\text{Bu}$	$^2J(\text{Si}, \text{C}(\equiv\text{C}))$	21.8	175
	$^1J(\text{Si}, \text{C}(\text{C}\equiv))$	105.7	
	$^1J(\text{Si}, \text{C}(\text{Me}))$	65.4	
$\text{Me}_2(\text{Cl})\text{Si}-\text{C}\equiv\text{C}-\text{CH}_2-\text{NMe}_2$	$^2J(\text{Si}, \text{C}(\equiv\text{C}))$	20.7	218
	$^1J(\text{Si}, \text{C}(\text{C}\equiv))$	102.8	
	$^1J(\text{Si}, \text{C}(\text{Me}))$	65.8	
$\text{Me}_2(\text{Cl})\text{Si}-\text{C}\equiv\text{C}-i\text{Pent}$	$^2J(\text{Si}, \text{C}(\equiv\text{C}))$	19.4	99,175
	$^1J(\text{Si}, \text{C}(\text{C}\equiv))$	106.8	
	$^1J(\text{Si}, \text{C}(\text{Me}))$	64.9	
$\text{Me}_2(\text{Cl})\text{Si}-\text{C}\equiv\text{C}-\text{Ph}$	$^2J(\text{Si}, \text{C}(\equiv\text{C}))$	22.3	175
	$^1J(\text{Si}, \text{C}(\text{C}\equiv))$	102.5	
	$^1J(\text{Si}, \text{C}(\text{Me}))$	65.4	
$\text{Me}(\text{H})\text{SiCl}-\text{C}\equiv\text{C}-n\text{Bu}$	$^2J(\text{Si}, \text{C}(\equiv\text{C}))$	20.7	61
	$^1J(\text{Si}, \text{C}(\text{C}\equiv))$	108.2	
	$^1J(\text{Si}, \text{C}(\text{Me}))$	64.6	
$\text{Me}(\text{H})\text{SiCl}-\text{C}\equiv\text{C}-\text{Bu}$	$^2J(\text{Si}, \text{C}(\equiv\text{C}))$	22.4	218
	$^1J(\text{Si}, \text{C}(\text{C}\equiv))$	108.2	
	$^1J(\text{Si}, \text{C}(\text{Me}))$	64.6	
$\text{Me}(\text{H})\text{SiCl}-\text{C}\equiv\text{C}-\text{CH}_2-\text{NMe}_2$	$^2J(\text{Si}, \text{C}(\equiv\text{C}))$	22.4	204,218
	$^1J(\text{Si}, \text{C}(\text{C}\equiv))$	105.4	
	$^1J(\text{Si}, \text{C}(\text{Me}))$	64.6	
$\text{Cl}_2(\text{H})\text{Si}-\text{C}\equiv\text{C}-\text{Bu}$	$^2J(\text{Si}, \text{C}(\equiv\text{C}))$	21.2	177
	$^1J(\text{Si}, \text{C}(\text{C}\equiv))$	136.9	
	$^2J(\text{Si}, \text{C}(\equiv\text{C}))$	28.3	
$\text{Cl}_3\text{Si}-\text{C}\equiv\text{C}-n\text{Bu}$	$^1J(\text{Si}, \text{C}(\text{C}\equiv))$	177.1	61
	$^2J(\text{Si}, \text{C}(\equiv\text{C}))$	35.3	
	$^1J(\text{Si}(\text{a}), \text{C}(\text{C}\equiv))$	86.5	
$\text{HC}\equiv\text{C}-\text{Si}(\text{a})\text{Me}_2-\text{N}[\text{Si}(\text{b})(\text{Br})\text{Me}_2]_2$	$^1J(\text{Si}(\text{a}), \text{C}(\text{Me}))$	65.4	81
	$^1J(\text{Si}(\text{b}), \text{C}(\text{Me}))$	67.6	
	$^2J(\text{Si}, \text{C}(\text{C}\equiv))$	16.7	

Si bonded to substituted vinyl(s)

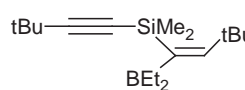
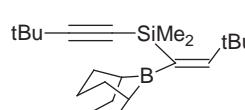
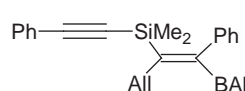
	$^1J(\text{Si}, \text{C}(\text{C}\equiv))$	86.5	105
	$^1J(\text{Si}, \text{C}(\text{C}=\text{}))$	60.9	
	$^1J(\text{Si}, \text{C}(\text{Me}))$	56.7	
	$^2J(\text{Si}, \text{C}(\text{C}\equiv))$	15.8	
	$^1J(\text{Si}, \text{C}(\text{C}\equiv))$	87.0	105
	$^1J(\text{Si}, \text{C}(\text{Me}))$	57.0	
	$^2J(\text{Si}, \text{C}(\text{C}\equiv))$	15.8	
	$^1J(\text{Si}, \text{C}(\text{C}\equiv))$	81.4	194
	$^1J(\text{Si}, \text{C}(\text{C}=\text{}))$	66.7	
	$^1J(\text{Si}, \text{C}(\text{Me}))$	57.5	
	$^2J(\text{Si}, \text{C}(\text{C}\equiv))$	15.2	

Table C1 (Continued)

$\begin{array}{c} \text{tBu}-\equiv-\text{SiMe}_2-\text{Et} \\ \quad \quad \quad \diagup \quad \diagdown \\ \quad \quad \text{SnMe}_3 \quad \text{BEt}_2 \end{array}$	$^1J(\text{Si}, \text{C}(\text{Me}))$	53.4	175
$\begin{array}{c} \text{Ph}-\equiv-\text{SiMe}_2-\text{Et} \\ \quad \quad \quad \diagup \quad \diagdown \\ \quad \quad \text{SnMe}_3 \quad \text{BEt}_2 \end{array}$	$^1J(\text{Si}, \text{C}(\text{Me}))$	53.4	175
$\begin{array}{c} \text{Me} \\ \\ \equiv-\text{SiH}-\text{Et} \\ \quad \quad \diagdown \\ \text{Me}_3\text{Sn} \quad \text{BEt}_2 \end{array}$	$^1J(\text{Si}, \text{C}(\text{C}\equiv))$	82.8	182
	$^1J(\text{Si}, \text{C}(\text{C}=\))$	62.5	
	$^1J(\text{Si}, \text{C}(\text{Me}))$	54.6	
	$^2J(\text{Si}, \text{C}(\text{C}\equiv))$	15.0	
	$^3J(\text{Si}, \text{C}(\text{Et}))$	14.0	
$\begin{array}{c} \text{Me} \\ \\ \text{Ph}-\equiv-\text{SiH}-\text{Ph} \\ \quad \quad \diagdown \\ \text{All} \quad \text{BALL}_2 \end{array}$	$^1J(\text{Si}, \text{C}(\text{C}\equiv))$	83.9	194
	$^1J(\text{Si}, \text{C}(\text{Me}))$	57.7	
	$^2J(\text{Si}, \text{C}(\text{C}\equiv))$	14.8	
	$^2J(\text{Si}, \text{C}(\text{All}))$	8.1	
$\begin{array}{c} \text{Me}_3\text{Si(a)}-\equiv-\text{S}-\text{Et} \\ \quad \quad \quad \diagup \quad \diagdown \\ \quad \quad \text{Me}_3\text{Si(b)} \quad \text{BEt}_2 \end{array}$	$^1J(\text{Si(a)}, \text{C}(\text{C}\equiv))$	86.0	178
	$^1J(\text{Si(b)}, \text{C}(\text{C}=\))$	71.4	
	$^1J(\text{Si(a)}, \text{C}(\text{Me}))$	56.7	
	$^1J(\text{Si(b)}, \text{C}(\text{Me}))$	52.8	
	$^2J(\text{Si}, \text{C}(\text{C}\equiv))$	15.0	

Table C2. Two Si-C \equiv C fragments in molecule

(HC \equiv C) $_2$ SiMe $_2$	$^1J(\text{Si}, \text{C}(\text{C}\equiv))$	100.0	219
	$^2J(\text{Si}, \text{C}(\text{C}\equiv))$	20.4	
(Me-C \equiv C) $_2$ SiMe $_2$	$^1J(\text{Si}, \text{C}(\text{C}\equiv))$	98.6	99
	$^1J(\text{Si}, \text{C}(\text{Me}))$	62.5	
	$^1J(\text{Si}, \text{C}(\text{C}\equiv))$	98.8	102
	$^1J(\text{Si}, \text{C}(\text{Me}))$	62.2	
	$^2J(\text{Si}, \text{C}(\text{C}\equiv))$	19.8	
	$^3J(\text{Si}, \text{C}(\text{Me}))$	1.8	
Bu-C(1) \equiv C(2)-SiMe $_2$ -C(4) \equiv C(5)H	$^1J(\text{Si}, \text{C}(2))$	101.9	175
	$^1J(\text{Si}, \text{C}(4))$	93.2	
	$^1J(\text{Si}, \text{C}(\text{Me}))$	62.1	
	$^2J(\text{Si}, \text{C}(1))$	20.1	
	$^2J(\text{Si}, \text{C}(5))$	18.6	
<i>t</i> Bu-C(1) \equiv C(2)-SiMe $_2$ -C(4) \equiv C(5)H	$^1J(\text{Si}, \text{C}(2))$	101.4	175
	$^1J(\text{Si}, \text{C}(4))$	93.2	
	$^1J(\text{Si}, \text{C}(\text{Me}))$	62.7	
	$^2J(\text{Si}, \text{C}(1))$	19.1	
	$^2J(\text{Si}, \text{C}(5))$	18.5	
<i>i</i> Pent-C(1) \equiv C(2)-SiMe $_2$ -C(4) \equiv C(5)H	$^1J(\text{Si}, \text{C}(2))$	101.9	175
	$^1J(\text{Si}, \text{C}(4))$	93.2	
	$^1J(\text{Si}, \text{C}(\text{Me}))$	62.1	
	$^2J(\text{Si}, \text{C}(1))$	19.6	

Table C2 (Continued)

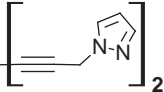
Ph–C(1)≡C(2)–SiMe ₂ –C(4)≡C(5)H	² J(Si, C(5))	18.5	175
	¹ J(Si, C(2))	97.0	
	¹ J(Si, C(4))	94.8	
	¹ J(Si, C(Me))	62.1	
	² J(Si, C(1))	19.6	
(Bu–C≡C) ₂ SiMe ₂	² J(Si, C(5))	17.4	99,218
	¹ J(Si, C(C≡))	100.3	
	¹ J(Si, C(Me))	61.0	
(tBu–C≡C) ₂ SiMe ₂	² J(Si, C(C≡))	20.2	99
	¹ J(Si, C(C≡))	99.2	
	¹ J(Si, C(Me))	62.1	
Bu–C(1)≡C(2)–SiMe ₂ –C(4)≡C(5)–CH ₂ –NMe ₂	² J(Si, C(C≡))	19.1	204
	¹ J(Si, C(2))	100.2	
	¹ J(Si, C(4))	96.5	
	¹ J(Si, C(Me))	62.1	
	² J(Si, C(1))	19.5	
(Me ₂ N–CH ₂ –C≡C) ₂ SiMe ₂	² J(Si, C(5))	18.9	204,218
	¹ J(Si, C(C≡))	98.3	
	¹ J(Si, C(Me))	61.9	
(iPent–C≡C) ₂ SiMe ₂	² J(Si, C(C≡))	19.5	99
	¹ J(Si, C(C≡))	99.2	
	¹ J(Si, C(Me))	61.6	
(Ph–C≡C) ₂ SiMe ₂	² J(Si, C(C≡))	19.5	99
	¹ J(Si, C(C≡))	97.0	
	¹ J(Si, C(Me))	61.9	
iPent–C(1)≡C(2)–SiMe ₂ –C(4)≡C(5)–Ph	¹ J(Si, C(2))	100.2	99
	¹ J(Si, C(4))	96.5	
	¹ J(Si, C(Me))	62.1	
	² J(Si, C(1))	20.2	
	² J(Si, C(5))	19.6	
Me ₂ Si 	¹ J(Si, C(C≡))	95.5	218
	¹ J(Si, C(Me))	62.6	
	² J(Si, C(C≡))	20.1	
Me ₃ Sn–C(1)≡C(2)–SiMe ₂ –C(4)≡C(5)–Bu	¹ J(Si, C(2))	88.2	175
	¹ J(Si, C(4))	100.3	
	¹ J(Si, C(Me))	61.6	
	² J(Si, C(1))	13.1	
	² J(Si, C(5))	19.6	
Me ₃ Sn–C(1)≡C(2)–SiMe ₂ –C(4)≡C(5)–tBu	¹ J(Si, C(2))	89.4	175
	¹ J(Si, C(4))	99.7	
	¹ J(Si, C(Me))	61.6	
	² J(Si, C(1))	13.6	
	² J(Si, C(5))	19.1	
Me ₃ Sn–C(1)≡C(2)–SiMe ₂ –C(4)≡C(5)–iPent	¹ J(Si, C(2))	89.4	175
	¹ J(Si, C(4))	100.3	
	¹ J(Si, C(Me))	62.1	
	² J(Si, C(1))	13.0	

Table C2 (Continued)

$\text{Me}_3\text{Sn}-\text{C}(1)\equiv\text{C}(2)-\text{SiMe}_2-\text{C}(4)\equiv\text{C}(5)-\text{Ph}$	$^2J(\text{Si}, \text{C}(5))$	19.6	175
	$^1J(\text{Si}, \text{C}(2))$	89.4	
	$^1J(\text{Si}, \text{C}(4))$	97.3	
	$^1J(\text{Si}, \text{C}(\text{Me}))$	62.1	
$\text{Me}_3\text{Si}-\text{C}\equiv\text{C}-\text{SiMe}_3$	$^2J(\text{Si}, \text{C}(1))$	13.6	95
	$^2J(\text{Si}, \text{C}(5))$	18.5	
	$^1J(\text{Si}, \text{C}(\text{C}\equiv))$	74.8	214
	$^2J(\text{Si}, \text{C})$	11.5	
	$^1J(\text{Si}, \text{C}(\text{C}\equiv))$	79.0	
	$^1J(\text{Si}, \text{C}(\text{Me}))$	56.1	
	$^2J(\text{Si}, \text{C}(\text{C}\equiv))$	13.6	98
	$^1J(\text{Si}, \text{C}(\text{C}\equiv))$	76.75	
$\text{Me}_3\text{Si}-\text{C}\equiv\text{C}-\text{C}\equiv\text{C}-\text{SiMe}_3$	$^1J(\text{Si}, \text{C}(\text{Me}))$	56.13	215
	$^2J(\text{Si}, \text{C}(\text{C}\equiv))$	12.37	
	$^1J(\text{Si}, \text{C}(\text{C}\equiv))$	80.1	215
	$^1J(\text{Si}, \text{C}(\text{Me}))$	57.2	
	$^2J(\text{Si}, \text{C}(\text{C}\equiv))$	14.3	107
	$^1J(\text{Si}(\text{a}), \text{C}(1))$	77.8	
$\text{Et}_2\text{N}-\text{Si}(\text{a})\text{Me}_2-\text{C}(1)\equiv\text{C}(2)-\text{Si}(\text{b})\text{Me}_3$	$^1J(\text{Si}(\text{b}), \text{C}(2))$	82.7	
	$^1J(\text{Si}(\text{a}), \text{C}(\text{Me}))$	64.9	
	$^1J(\text{Si}(\text{b}), \text{C}(\text{Me}))$	57.1	
	$^2J(\text{Si}(\text{a}), \text{C}(2))$	-12.8	
	$^2J(\text{Si}(\text{b}), \text{C}(1))$	-13.8	178
	$^1J(\text{Si}, \text{C}(\text{C}\equiv))$	79.7	
$(\text{Me}_3\text{Si}-\text{C}\equiv\text{C})_2\text{S}$	$^1J(\text{Si}, \text{C}(\text{Me}))$	56.7	
	$^2J(\text{Si}, \text{C}(\text{C}\equiv))$	14.2	
$\text{Et}_3\text{Si}-\text{C}\equiv\text{C}-\text{SiEt}_3$	$^1J(\text{Si}, \text{C}(\text{C}\equiv))$	74.8	95
	$^1J(\text{Si}, \text{C}(\text{Et}))$	56.0	
	$^2J(\text{Si}, \text{C}(\equiv\text{C}))$	11.5	217
$(\text{Me}_3\text{Si}-\text{C}\equiv\text{C})_2\text{Sn}(\text{Me})_2$	$^1J(\text{Si}, \text{C}(\text{C}\equiv))$	76.3	
	$^1J(\text{Si}, \text{C}(\text{Me}))$	56.2	
	$^2J(\text{Si}, \text{C}(\text{C}\equiv))$	11.2	
$(\text{Me}_3\text{Si}-\text{C}\equiv\text{C})_2\text{SnCl}_2$	$^1J(\text{Si}, \text{C}(\text{Me}))$	56.7	176,216
	$^2J(\text{Si}, \text{C}\equiv)$	9.8	
$(\text{Me}_3\text{Si}-\text{C}\equiv\text{C})_2\text{Sn}(\text{C}\equiv\text{C}-\text{Me})_2$	$^1J(\text{Si}, \text{C}(\text{C}\equiv))$	73.9	217
	$^2J(\text{Si}, \text{C}(\text{C}\equiv))$	10.4	
$(\text{Me}_3\text{Si}-\text{C}\equiv\text{C})_2\text{Sn}(\text{Me})(\text{C}\equiv\text{C}-i\text{Bu})$	$^1J(\text{Si}, \text{C}(\text{C}\equiv))$	74.5	217
	$^1J(\text{Si}, \text{C}(\text{Me}))$	56.6	
	$^2J(\text{Si}, \text{C}(\text{C}\equiv))$	11.3	
$(\text{Me}_3\text{Si}-\text{C}\equiv\text{C})_2\text{SnBr}_2$	$^1J(\text{Si}, \text{C}(\text{C}\equiv))$	68.6	176
	$^1J(\text{Si}, \text{C}(\text{Me}))$	56.7	
	$^2J(\text{Si}, \text{C}(\text{C}\equiv))$	9.9	
$(\text{Me}_3\text{Si}-\text{C}\equiv\text{C})_2\text{Sn}(\text{C}\equiv\text{C}-i\text{Bu})_2$	$^1J(\text{Si}, \text{C}(\text{C}\equiv))$	74.3	217
	$^1J(\text{Si}, \text{C}(\text{Me}))$	56.2	
	$^2J(\text{Si}, \text{C}(\text{C}\equiv))$	11.7	
<i>trans</i> -(Et_3P) $_2\text{Pt}(\text{C}\equiv\text{C}-\text{SiMe}_3)_2$	$^1J(\text{Si}, \text{C}\equiv)$	-90.0	43
	$^1J(\text{Si}, \text{C}(\text{Me}))$	-54.6	
	$^2J(\text{Si}-\text{C}\equiv)$	-14.3	

Table C2 (Continued)

<i>cis</i> -(Ph ₂ P–CH ₂ –CH ₂ –PPh ₂)Pt(C≡C–SiMe ₃) ₂	¹ J(Si, C(Me))	–55.0	43
<i>Si–H bond(s)</i>			
(Bu–C≡C) ₂ Si(H)Me	¹ J(Si, C(C≡))	102.2	204,218
	¹ J(Si, C(Me))	61.6	
	² J(Si, C(C≡))	20.2	
Me ₂ N–CH ₂ –C(1)≡C(2)–Si(H)Me–C(4)≡C(5)–Bu	¹ J(Si, C(2))	101.6	204
	¹ J(Si, C(4))	102.2	
	¹ J(Si, C(Me))	61.4	
	² J(Si, C(1))	19.4	
	² J(Si, C(5))	20.0	
(Me ₂ N–CH ₂ –C≡C) ₂ Si(H)Me	¹ J(Si, C(C≡))	102.5	204,218
	¹ J(Si, C(Me))	62.1	
	² J(Si, C(C≡))	19.4	
(Et ₂ N–C≡C) ₂ Si(H)Me	¹ J(Si, C(C≡))	110.0	213
	¹ J(Si, C(Me))	61.0	
	² J(Si, C(C≡))	24.4	
Me ₃ Sn–C(1)≡C(2)–Si(H)Me–C(4)≡C(5)H	¹ J(Si, C(2))	92.9	182
	¹ J(Si, C(4))	96.2	
	¹ J(Si, C(Me))	61.7	
	² J(Si, C(1))	14.2	
	² J(Si, C(5))	19.1	
Me ₃ Si(a)–C≡C–Si(b)(H)Me ₂	¹ J(Si(a), C(C≡))	79.3	184
	¹ J(Si(b), C(C≡))	76.2	
	² J(Si(a), C(C≡))	12.6	
	² J(Si(b), C(C≡))	12.2	
Me ₂ (H)Si(a)–C≡C–Me ₂ Si(b)–CH ₂ –CH=CH ₂	¹ J(Si(a), C(C≡))	77.0	207
	¹ J(Si(b), C(C≡))	84.9	
	¹ J(Si(b), C(CH ₂))	53.6	
	¹ J(Si(a), C(Me))	56.1	
	¹ J(Si(b), C(Me))	55.8	
	² J(Si(a), C(C≡))	12.6	
	² J(Si(b), C(C≡))	14.0	
	³ J(Si(b), C(C≡))	5.6	
Me ₃ Si(a)–C≡C–Si(b)(H) <i>i</i> Pr ₂	¹ J(Si(a), C(C≡))	75.1	184
	¹ J(Si(b), C(C≡))	76.3	
	² J(Si(a), C(C≡))	14.5	
	² J(Si(b), C(C≡))	11.9	
Me ₂ (H)Si–C≡C–Si(H)Me ₂	¹ J(Si, C(C≡))	78.8	209
	¹ J(Si, C(Me))	56.1	
	² J(Si, C(C≡))	12.6	
Me ₃ Si(a)–C≡C–Si(b)(Me)H ₂	¹ J(Si(a), C(C≡))	82.1	184
	¹ J(Si(b), C(C≡))	75.1	
	¹ J(Si(a), C(Me))	56.3	
	¹ J(Si(b), C(Me))	56.1	
	² J(Si(a), C(C≡))	13.2	
	² J(Si(b), C(C≡))	12.4	
(Me ₂ (H)Si–C≡C) ₂ SnMe ₂	¹ J(Si, C(C≡))	79.8	182
	¹ J(Si, C(Me))	50.5	
	² J(Si, C(C≡))	13.2	

Table C2 (Continued)

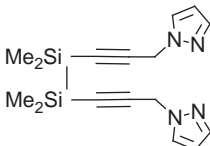
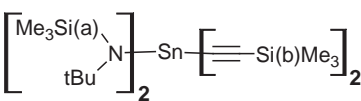
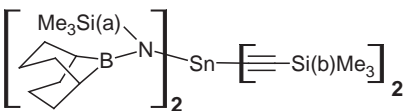
$\text{Me}_3\text{Si(a)}-\text{C}\equiv\text{C}-\text{Si(b)}\text{H}_3$	$^1J(\text{Si(a)}, \text{C}(\text{C}\equiv))$	87.0	184
	$^1J(\text{Si(b)}, \text{C}(\text{C}\equiv))$	75.1	
	$^1J(\text{Si(a)}, \text{C}(\text{Me}))$	56.3	
	$^2J(\text{Si(a)}, \text{C}(\text{C}\equiv))$	13.8	
	$^2J(\text{Si(b)}, \text{C}(\text{C}\equiv))$	12.2	
<i>Si-Si bond</i>			
$(\text{HC}(1)\equiv\text{C}(2)-\text{SiMe}_2)_2$	$^1J(\text{Si}, \text{C}(2))$	79.0	208
	$^1J(\text{Si}, \text{C}(\text{Me}))$	59.4	
	$^2J(\text{Si}, \text{C}(1))$	15.2	
	$^2J(\text{Si}, \text{C}(2))$	7.4	
	$^2J(\text{Si}, \text{C}(\text{Me}))$	5.8	
$(\text{Me}-\text{C}\equiv\text{C}-\text{SiMe}_2)_2$	$^1J(\text{Si}, \text{C}(\text{C}\equiv))$	79.0	218
	$^2J(\text{Si}, \text{C}(\text{C}\equiv))$	15.2	
	$^1J(\text{Si}, \text{C}(\text{Me}))$	49.4	
$(\text{Me}_2\text{N}-\text{CH}_2-\text{C}\equiv\text{C}-\text{SiMe}_2)_2$	$^1J(\text{Si}, \text{C}(\text{C}\equiv))$	76.6	218
	$^1J(\text{Si}, \text{C}(\text{Me}))$	49.4	
	$^2J(\text{Si}, \text{C}(\text{C}\equiv))$	13.7	
	$^1J(\text{Si}, \text{C}(\text{C}\equiv))$	74.0	218
	$^1J(\text{Si}, \text{C}(\text{Me}))$	50.5	
	$^2J(\text{Si}, \text{C}(\text{C}\equiv))$	13.7	
<i>Si-N bond(s)</i>			
$\text{Me}_3\text{Si(a)}-\text{C}\equiv\text{C}-\text{Si(b)}\text{Me}_2-\text{NEt}_2$	$^1J(\text{Si(a)}, \text{C}(\text{C}\equiv))$	82.7	107
	$^1J(\text{Si(b)}, \text{C}(\text{C}\equiv))$	77.8	
	$^1J(\text{Si(a)}, \text{C}(\text{Me}))$	57.1	
	$^1J(\text{Si(b)}, \text{C}(\text{Me}))$	64.9	
	$^2J(\text{Si(a)}, \text{C}(\text{C}\equiv))$	13.8	
	$^2J(\text{Si(b)}, \text{C}(\text{C}\equiv))$	12.8	
	$^1J(\text{Si(b)}, \text{C}(\text{C}\equiv))$	75.2	133
	$^1J(\text{Si(a)}, \text{C})$	55.8	
	$^1J(\text{Si(b)}, \text{C}(\text{Me}))$	56.1	
	$^2J(\text{Si(b)}, \text{C}(\text{C}\equiv))$	10.6	
	$^1J(\text{Si(b)}, \text{C}(\text{C}\equiv))$	74.5	133
	$^1J(\text{Si(a)}, \text{C})$	56.3	
	$^1J(\text{Si(b)}, \text{C}(\text{Me}))$	56.3	
	$^2J(\text{Si(b)}, \text{C}(\text{C}\equiv))$	10.8	
$[(\text{Me}_3\text{Si(a)})_2\text{N}]_2\text{Sn}(\text{C}\equiv\text{C}-\text{Si(b)}\text{Me}_3)_2$	$^1J(\text{Si(b)}, \text{C}(\text{C}\equiv))$	73.9	133,193
	$^1J(\text{Si(a)}, \text{C})$	55.8	
	$^1J(\text{Si(b)}, \text{C}(\text{Me}))$	56.0	
	$^2J(\text{Si(b)}, \text{C}(\text{C}\equiv))$	10.4	
<i>Si-halogen bond(s) with possible Si-N and Si-H bond(s)</i>			
$\text{Me}_3\text{Si(a)}-\text{C}\equiv\text{C}-\text{Si(b)}(\text{Cl})\text{Me}_2$	$^1J(\text{Si(a)}, \text{C}(\text{C}\equiv))$	73.4	175
	$^1J(\text{Si(b)}, \text{C}(\text{C}\equiv))$	94.9	
	$^1J(\text{Si(a)}, \text{C}(\text{Me}))$	64.6	
	$^1J(\text{Si(b)}, \text{C}(\text{Me}))$	56.7	

Table C2 (Continued)

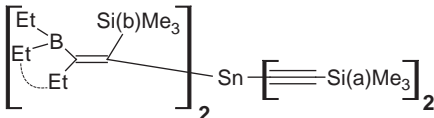
	$^2J(\text{Si(a)}, \text{C}(\text{C}\equiv))$	16.6	
	$^2J(\text{Si(b)}, \text{C}(\text{C}\equiv))$	12.7	
$\text{Me}_3\text{Si(a)}-\text{C}\equiv\text{C}-\text{Si(b)}(\text{H})\text{MeCl}$	$^1J(\text{Si(a)}, \text{C}(\text{C}\equiv))$	72.7	184
	$^1J(\text{Si(b)}, \text{C}(\text{C}\equiv))$	96.9	
	$^1J(\text{Si(a)}, \text{C}(\text{Me}))$	56.3	
	$^1J(\text{Si(b)}, \text{C}(\text{Me}))$	64.6	
	$^2J(\text{Si(a)}, \text{C}(\text{C}\equiv))$	16.6	
	$^2J(\text{Si(b)}, \text{C}(\text{C}\equiv))$	11.6	
$\text{Me}_2(\text{Cl})\text{Si}-\text{C}\equiv\text{C}-\text{Si}(\text{Cl})\text{Me}_2$	$^1J(\text{Si}, \text{C}(\text{C}\equiv))$	89.6	209
	$^1J(\text{Si}, \text{C}(\text{Me}))$	64.1	
	$^2J(\text{Si}, \text{C}(\text{C}\equiv))$	14.8	
$\text{Cl}_2(\text{H})\text{Si(a)}-\text{C}\equiv\text{C}-\text{Si(b)}\text{Me}_3$	$^1J(\text{Si(a)}, \text{C}(\text{C}\equiv))$	122.9	177
	$^1J(\text{Si(b)}, \text{C}(\text{C}\equiv))$	69.3	
	$^1J(\text{Si}, \text{C}(\text{Me}))$	56.9	
	$^2J(\text{Si(a)}, \text{C}(\text{C}\equiv))$	21.8	
	$^2J(\text{Si(b)}, \text{C}(\text{C}\equiv))$	11.1	
$\text{Me}_3\text{Si(a)}-\text{C}\equiv\text{C}-\text{Si(b)}\text{Cl}_3$	$^1J(\text{Si(a)}, \text{C}(\text{C}\equiv))$	68.2	184
	$^1J(\text{Si(b)}, \text{C}(\text{C}\equiv))$	160.7	
	$^1J(\text{Si(a)}, \text{C}(\text{Me}))$	56.7	
	$^2J(\text{Si(a)}, \text{C}(\text{C}\equiv))$	26.7	
	$^2J(\text{Si(b)}, \text{C}(\text{C}\equiv))$	11.2	
$(\text{HC}\equiv\text{C}-\text{Si(a)}\text{Me}_2)_2\text{N}-\text{Si(b)}(\text{Br})\text{Me}_2$	$^1J(\text{Si(a)}, \text{C}(\text{C}\equiv))$	86.8	81
	$^1J(\text{Si(a)}, \text{C}(\text{Me}))$	64.7	
	$^1J(\text{Si(b)}, \text{C}(\text{Me}))$	67.9	
	$^2J(\text{Si(a)}, \text{C}(\text{C}\equiv))$	16.7	
$\text{Me}_2(\text{Br})\text{Si}-\text{C}\equiv\text{C}-\text{Si}(\text{Br})\text{Me}_2$	$^1J(\text{Si}, \text{C}(\text{C}\equiv))$	91.6	209
	$^1J(\text{Si}, \text{C}(\text{Me}))$	66.0	
	$^2J(\text{Si}, \text{C}(\text{C}\equiv))$	14.8	
<i>Si bonded to (substituted) vinyl(s)</i>			
$\text{Me}_2(\text{H})\text{Si(a)}-\text{C}\equiv\text{C}-\text{Si(b)}\text{Me}_2-\text{CH}=\text{CH}_2$	$^1J(\text{Si(a)}, \text{C}(\text{C}\equiv))$	78.6	207
	$^1J(\text{Si(b)}, \text{C}(\text{C}\equiv))$	79.0	
	$^1J(\text{Si(b)}, \text{C}(\text{C}=\text{)))}$	71.7	
	$^1J(\text{Si(a)}, \text{C}(\text{Me}))$	56.1	
	$^1J(\text{Si(b)}, \text{C}(\text{Me}))$	57.5	
	$^2J(\text{Si(a)}, \text{C}(\text{C}\equiv))$	12.6	
	$^2J(\text{Si(b)}, \text{C}(\text{C}\equiv))$	12.9	
	$^4J(\text{Si(b)}, \text{C}(\text{Me}))$	7.4	
$(\text{Me}_3\text{Si}-\text{C}\equiv\text{C})_2\text{C}=\text{CBr}_2$	$^1J(\text{Si}, \text{C}(\text{C}\equiv))$	79.9	179
	$^1J(\text{Si}, \text{C}(\text{Me}))$	56.6	
	$^2J(\text{Si}, \text{C}(\text{C}\equiv))$	15.1	
$\text{Me}_3\text{Si}-\text{C}\equiv\text{C}-\text{SiMe}_2-\text{C}(\text{Et})=\text{C}(\text{Me}_3\text{Sn})(\text{BEt}_2)$	$^1J(\text{Si}, \text{C}(\text{Me}))$	53.5	175
	$^1J(\text{Si(a)}, \text{C}(\text{C}\equiv))$	75.2	192
	$^1J(\text{Si(b)}, \text{C}(\text{C}=\text{)))}$	60.0	
	$^1J(\text{Si(a)}, \text{C}(\text{Me}))$	55.6	
	$^1J(\text{Si(b)}, \text{C}(\text{Me}))$	50.1	

Table C2 (Continued)

	$^1J(\text{Si(a)}, \text{C}(\text{C}\equiv))$	78.5	192
	$^1J(\text{Si(b)}, \text{C}(\text{C}\equiv))$	57.8	
	$^1J(\text{Si(a)}, \text{C}(\text{Me}))$	56.1	
	$^1J(\text{Si(b)}, \text{C}(\text{Me}))$	52.3	
	$^2J(\text{Si(a)}, \text{C}(\text{C}\equiv))$	11.4	

Table C3. More than two Si–C≡C fragments in molecule

(MeC≡C) ₃ SiMe	$^1J(\text{Si}, \text{C}(\text{C}\equiv))$	112.2	102
	$^1J(\text{Si}, \text{C}(\text{Me}))$	68.9	
	$^2J(\text{Si}, \text{C}(\text{C}\equiv))$	22.8	
	$^3J(\text{Si}, \text{C}(\text{Me}))$	1.9	
HC(1)≡C(2)–Si(a)Me ₂ –C(4)≡C(5)–Si(b)Me ₃	$^1J(\text{Si(a)}, \text{C(2)})$	93.9	175
	$^1J(\text{Si(a)}, \text{C(4)})$	91.0	
	$^1J(\text{Si(b)}, \text{C(5)})$	79.2	
	$^1J(\text{Si(a)}, \text{C(Me)})$	62.6	
	$^1J(\text{Si(b)}, \text{C(Me)})$	56.7	
	$^2J(\text{Si(a)}, \text{C(1)})$	18.6	
	$^2J(\text{Si(a)}, \text{C(5)})$	12.7	
	$^2J(\text{Si(b)}, \text{C(4)})$	12.7	
Me ₂ N–CH ₂ –C(1)≡C(2)–SiMe ₂ –C(4)≡C(5)–SiMe ₃	$^1J(\text{Si}, \text{C(2)})$	98.3	204
	$^1J(\text{Si}, \text{C(4)})$	89.5	
	$^1J(\text{Si}, \text{C(5)})$	76.0	
	$^1J(\text{Si}, \text{C(Me)})$	62.1	
	$^2J(\text{Si}, \text{C(1)})$	18.8	
	$^2J(\text{Si}, \text{C(5)})$	14.8	
	$^2J(\text{Si}, \text{C(4)})$	12.4	
	$^2J(\text{Si}, \text{C(2)})$	12.2	
Me ₃ Sn–C(1)≡C(2)–Si(a)Me ₂ –C(4)≡C(5)–Si(b)Me ₃	$^1J(\text{Si(a)}, \text{C(2)})$	90.5	175
	$^1J(\text{Si(a)}, \text{C(4)})$	89.0	
	$^1J(\text{Si(b)}, \text{C(5)})$	77.3	
	$^1J(\text{Si(a)}, \text{C(Me)})$	61.4	
	$^1J(\text{Si(b)}, \text{C(Me)})$	56.2	
	$^2J(\text{Si(a)}, \text{C(1)})$	13.7	
	$^2J(\text{Si(a)}, \text{C(5)})$	14.7	
	$^2J(\text{Si(b)}, \text{C(4)})$	12.2	
(HC≡C–SiMe ₂) ₃ CH	$^1J(\text{Si}, \text{C}(\text{C}\equiv))$	80.3	81
	$^1J(\text{Si}, \text{C}(\text{CH}))$	42.0	
	$^1J(\text{Si}, \text{C}(\text{Me}))$	58.0	
	$^2J(\text{Si}, \text{C}(\text{C}\equiv))$	15.3	
(Me ₃ Si–C≡C) ₃ SnMe	$^1J(\text{Si}, \text{C}(\text{C}\equiv))$	74.5	217
	$^1J(\text{Si}, \text{C}(\text{Me}))$	56.6	
	$^2J(\text{Si}, \text{C}(\text{C}\equiv))$	10.0	
(Me ₃ Si–C≡C) ₃ SnCl	$^1J(\text{Si}, \text{C}(\text{C}\equiv))$	70.5	176,216
	$^1J(\text{Si}, \text{C}(\text{Me}))$	56.5	
	$^2J(\text{Si}, \text{C}(\text{C}\equiv))$	10.3	

Table C3 (Continued)

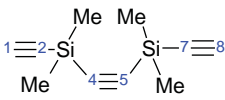
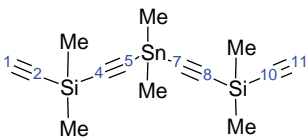
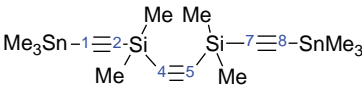
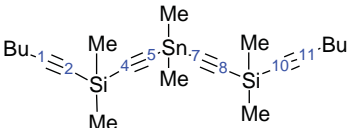
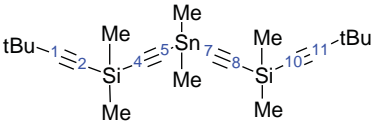
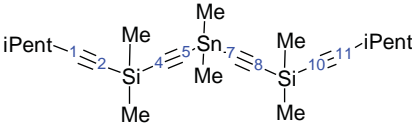
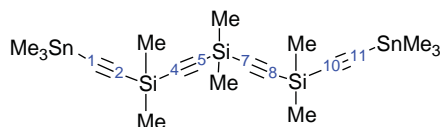
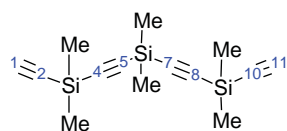
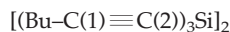
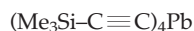
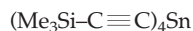
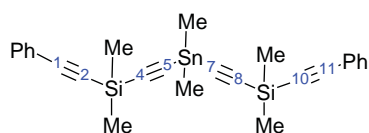
$(\text{Me}_3\text{Si}-\text{C}\equiv\text{C})_3\text{Sn}-\text{C}\equiv\text{C}-\text{Me}$	$^1J(\text{Si}, \text{C}(\text{C}\equiv))$	73.1	217
	$^2J(\text{Si}, \text{C}(\text{C}\equiv))$	10.4	
$(\text{Me}_3\text{Si}-\text{C}\equiv\text{C})_3\text{SnBr}$	$^1J(\text{Si}, \text{C}(\text{C}\equiv))$	70.7	176
	$^1J(\text{Si}, \text{C}(\text{Me}))$	56.3	
	$^2J(\text{Si}, \text{C}(\text{C}\equiv))$	9.8	
$(\text{Me}_3\text{Si}-\text{C}\equiv\text{C})_3\text{Sn}-\text{C}\equiv\text{C}-t\text{Bu}$	$^1J(\text{Si}, \text{C}(\text{C}\equiv))$	73.4	217
	$^1J(\text{Si}, \text{C}(\text{Me}))$	56.2	
	$^2J(\text{Si}, \text{C}(\text{C}\equiv))$	10.8	
$(\text{Me}-\text{C}\equiv\text{C})_4\text{Si}$	$^1J(\text{Si}, \text{C})$	117.8	102
	$^2J(\text{Si}, \text{C})$	26.5	
	$^3J(\text{Si}, \text{C}(\text{Me}))$	1.5	
	$^1J(\text{Si}, \text{C})$	127.0	220
	$^2J(\text{Si}, \text{C})$	26.5	
	$^3J(\text{Si}, \text{C}(\text{Me}))$	1.5	
	$^1J(\text{Si}, \text{C}(2,7))$	94.3	209
	$^1J(\text{Si}, \text{C}(4,5))$	88.8	
	$^1J(\text{Si}, \text{C}(\text{Me}))$	62.2	
	$^2J(\text{Si}, \text{C}(1,8))$	18.3	
	$^2J(\text{Si}, \text{C}(4,5))$	15.0	
	$^1J(\text{Si}, \text{C}(2,10))$	94.3	206
	$^1J(\text{Si}, \text{C}(4,8))$	88.6	
	$^1J(\text{Si}, \text{C}(\text{Me}))$	62.0	
	$^2J(\text{Si}, \text{C}(1,11))$	19.7	
	$^2J(\text{Si}, \text{C}(5,7))$	13.8	
	$^1J(\text{Si}, \text{C}(2,7))$	90.3	209
	$^1J(\text{Si}, \text{C}(4,5))$	88.0	
	$^1J(\text{Si}, \text{C}(\text{Me}))$	61.4	
	$^2J(\text{Si}, \text{C}(1,8))$	14.0	
	$^2J(\text{Si}, \text{C}(4,5))$	14.6	
	$^1J(\text{Si}, \text{C}(2,10))$	94.3	206
	$^1J(\text{Si}, \text{C}(4,8))$	88.5	
	$^1J(\text{Si}, \text{C}(\text{Me}))$	62.2	
	$^2J(\text{Si}, \text{C}(1,11))$	20.7	
	$^2J(\text{Si}, \text{C}(5,7))$	13.6	
	$^1J(\text{Si}, \text{C}(2,10))$	99.9	206
	$^1J(\text{Si}, \text{C}(4,8))$	88.0	
	$^1J(\text{Si}, \text{C}(\text{Me}))$	62.1	
	$^2J(\text{Si}, \text{C}(1,11))$	18.9	
	$^2J(\text{Si}, \text{C}(5,7))$	13.0	
	$^1J(\text{Si}, \text{C}(2,10))$	100.3	206
	$^1J(\text{Si}, \text{C}(4,8))$	87.7	
	$^1J(\text{Si}, \text{C}(\text{Me}))$	62.2	
	$^2J(\text{Si}, \text{C}(1,11))$	20.2	
	$^2J(\text{Si}, \text{C}(5,7))$	13.6	

Table C3 (Continued)

$^1J(\text{Si}, \text{C}(2,10))$	97.1	206
$^1J(\text{Si}, \text{C}(4,8))$	87.6	
$^1J(\text{Si}, \text{C}(\text{Me}))$	62.1	
$^2J(\text{Si}, \text{C}(1,11))$	19.5	
$^2J(\text{Si}, \text{C}(5,7))$	13.6	
$^1J(\text{Si(a)}, \text{C}(\text{C}\equiv))$	76.3	99
$^1J(\text{Si(b)}, \text{C}(\text{C}\equiv))$	90.0	
$^1J(\text{Si(a)}, \text{C}(\text{Me}))$	56.7	
$^1J(\text{Si(b)}, \text{C}(\text{Me}))$	61.6	
$^2J(\text{Si(a)}, \text{C}(\text{C}\equiv))$	12.7	
$^2J(\text{Si(b)}, \text{C}(\text{C}\equiv))$	15.2	
$^1J(\text{Si(a)}, \text{C}(\text{C}\equiv))$	76.8	204
$^1J(\text{Si(b)}, \text{C}(\text{C}\equiv))$	90.0	
$^1J(\text{Si}, \text{C}(\text{Me}))$	61.1	
$^2J(\text{Si(a)}, \text{C}(\text{C}\equiv))$	12.2	
$^2J(\text{Si(b)}, \text{C}(\text{C}\equiv))$	15.2	
$^1J(\text{Si}, \text{C}(\text{Me}))$	56.1	192
$^2J(\text{Si}, \text{C})$	9.8	
$^1J(\text{Si}, \text{C}(\text{C}\equiv))$	73.1	216,221
$^1J(\text{Si}, \text{C}(\text{Me}))$	56.1	
$^2J(\text{Si}, \text{C})$	9.8	
$^1J(\text{Si}, \text{C}(\text{C}\equiv))$	73.1	217
$^2J(\text{Si}, \text{C}(\text{C}\equiv))$	10.4	
$^1J(\text{Si}, \text{C}(\text{C}\equiv))$	72.7	217
$^1J(\text{Si}, \text{C}(\text{Me}))$	56.2	
$^1J(\text{Si}, \text{C}(2))$	108.0	220
$^2J(\text{Si}, \text{C}(1))$	21.3	
$^2J(\text{Si}, \text{C}(2))$	9.4	
$^3J(\text{Si}, \text{C}(1))$	3.0	
$^nJ(\text{Si}, \text{C}(\text{Bu}))$	1.9	
$^1J(\text{Si}, \text{C}(2,10))$	94.3	206
$^1J(\text{Si}, \text{C}(4,8))$	89.3	
$^1J(\text{Si}, \text{C}(5,7))$	88.8	
$^1J(\text{Si}, \text{C}(\text{Me}))$	62.8	
$^1J(\text{Si}, \text{C}(\text{Me}))$	62.0	
$^1J(\text{Si}, \text{C}(\text{Me}))$	62.0	
$^2J(\text{Si}, \text{C}(1,11))$	19.0	
$^2J(\text{Si}, \text{C}(4,8))$	15.0	
$^2J(\text{Si}, \text{C}(5,7))$	15.0	
$^1J(\text{Si}, \text{C}(2,10))$	89.1	206
$^1J(\text{Si}, \text{C}(4,8))$	87.3	
$^1J(\text{Si}, \text{C}(5,7))$	89.0	
$^1J(\text{Si}, \text{C}(\text{Me}))$	62.0	
$^1J(\text{Si}, \text{C}(\text{Me}))$	61.5	
$^1J(\text{Si}, \text{C}(\text{Me}))$	61.5	
$^2J(\text{Si}, \text{C}(1,11))$	13.4	
$^2J(\text{Si}, \text{C}(4,8))$	15.0	
$^2J(\text{Si}, \text{C}(5,7))$	14.5	

Table C3 (Continued)

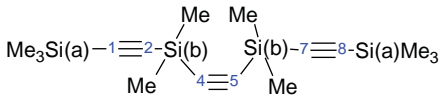
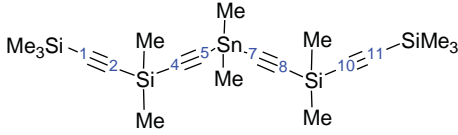
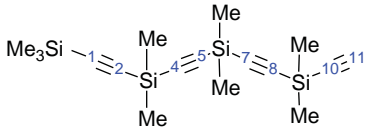
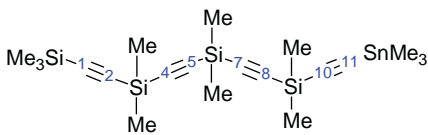
	$^1J(\text{Si}, \text{C}(1,8))$	75.8	209
	$^1J(\text{Si}, \text{C}(2,7))$	90.6	
	$^1J(\text{Si}, \text{C}(4,5))$	88.6	
	$^1J(\text{Si}(\text{a}), \text{C}(\text{Me}))$	56.1	
	$^1J(\text{Si}(\text{b}), \text{C}(\text{Me}))$	61.0	
	$^2J(\text{Si}, \text{C}(1,8))$	14.8	
	$^2J(\text{Si}, \text{C}(2,7))$	11.8	
	$^2J(\text{Si}, \text{C}(4,5))$	14.8	
	$^1J(\text{Si}, \text{C}(1,11))$	78.0	206
	$^1J(\text{Si}, \text{C}(2,10))$	89.8	
	$^1J(\text{Si}, \text{C}(4,8))$	88.5	
	$^1J(\text{Si}, \text{C}(\text{Me}))$	61.4	
	$^2J(\text{Si}, \text{C}(1,11))$	13.9	
	$^2J(\text{Si}, \text{C}(2,10))$	12.2	
	$^2J(\text{Si}, \text{C}(5,7))$	13.6	
	$^1J(\text{Si}, \text{C}(1))$	75.3	206
	$^1J(\text{Si}, \text{C}(2))$	89.0	
	$^1J(\text{Si}, \text{C}(4))$	88.0	
	$^1J(\text{Si}, \text{C}(5))$	88.7	
	$^1J(\text{Si}, \text{C}(7))$	88.0	
	$^1J(\text{Si}, \text{C}(8))$	88.5	
	$^1J(\text{Si}, \text{C}(10))$	93.7	
	$^1J(\text{Si}, \text{C}(\text{Me}))$	82.0	
	$^1J(\text{Si}, \text{C}(\text{Me}))$	62.0	
	$^1J(\text{Si}, \text{C}(\text{Me}))$	61.5	
	$^2J(\text{Si}, \text{C}(1))$	15.0	
	$^2J(\text{Si}, \text{C}(2))$	12.5	
	$^2J(\text{Si}, \text{C}(4))$	14.0	
	$^2J(\text{Si}, \text{C}(5))$	14.8	
	$^2J(\text{Si}, \text{C}(7))$	15.0	
	$^2J(\text{Si}, \text{C}(8))$	14.8	
	$^2J(\text{Si}, \text{C}(11))$	18.3	
	$^1J(\text{Si}, \text{C}(1))$	76.0	206
	$^1J(\text{Si}, \text{C}(2))$	90.4	
	$^1J(\text{Si}, \text{C}(4))$	88.8	
	$^1J(\text{Si}, \text{C}(5))$	88.9	
	$^1J(\text{Si}, \text{C}(7))$	89.6	
	$^1J(\text{Si}, \text{C}(8))$	87.9	
	$^1J(\text{Si}, \text{C}(10))$	90.6	
	$^1J(\text{Si}, \text{C}(\text{Me}))$	63.0	
	$^1J(\text{Si}, \text{C}(\text{Me}))$	62.0	
	$^1J(\text{Si}, \text{C}(\text{Me}))$	61.8	
	$^2J(\text{Si}, \text{C}(1))$	15.5	
	$^2J(\text{Si}, \text{C}(2))$	12.3	
	$^2J(\text{Si}, \text{C}(4))$	14.8	
	$^2J(\text{Si}, \text{C}(5))$	15.0	
	$^2J(\text{Si}, \text{C}(7))$	14.7	
	$^2J(\text{Si}, \text{C}(8))$	15.0	
	$^2J(\text{Si}, \text{C}(11))$	13.7	

Table C4 (Continued)

	$^1J(\text{Si(a)}, \text{C}(\text{C}\equiv))$ $^1J(\text{Si(b)}, \text{C}(\text{C}\equiv))$ $^1J(\text{Si(c)}, \text{C}(\text{C}\equiv))$ $^1J(\text{Si(d)}, \text{C}(\text{C}\equiv))$ $^2J(\text{Si(a)}, \text{C}(\text{C}\equiv))$	78.5 57.8 65.4 63.2 7.6	192
	$^1J(\text{Si}, \text{C}(2))$ $^1J(\text{Si}, \text{C}(2))$	61.7 43.9	209
	$^1J(\text{Si(a)}, \text{C}(\text{Me}))$	55.4	209
	$^1J(\text{Si}, \text{C}(2))$	72.0	206
	$^1J(\text{Si}, \text{C}(2))$ $^1J(\text{Si}, \text{C}(6a))$	71.7 60.0	206
	$^1J(\text{Si}, \text{C}(\text{C}\equiv))$ $^1J(\text{Si}, \text{C}(1))$ $^1J(\text{Si}, \text{C}(2))$ $^1J(\text{Si}, \text{C}(4))$ $^2J(\text{Si}, \text{C}(\text{C}\equiv))$ $^2J(\text{Si}, \text{C}(1))$ $^2J(\text{Si}, \text{C}(3))$	83.9 50.9 77.8 46.7 11.0 5.8 6.1	222
	$^1J(\text{Si(c)}, \text{C}(\text{C}\equiv))$ $^1J(\text{Si(a)}, \text{C}(\text{CH}_2))$ $^1J(\text{Si(a)}, \text{C}(\text{Me}))$ $^1J(\text{Si(b)}, \text{C})$ $^1J(\text{Si(c)}, \text{C}(\text{Me}))$ $^2J(\text{Si(c)}, \text{C}(\text{C}\equiv))$	73.7 55.0 55.0 56.3 55.7 9.1	131

Table C4 (Continued)

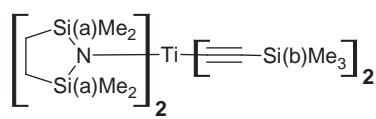
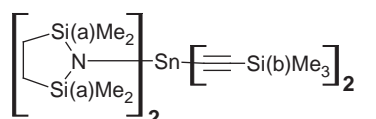
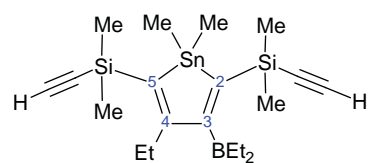
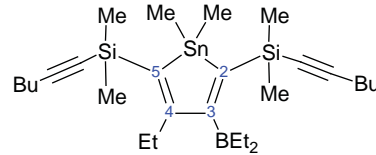
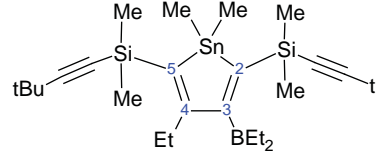
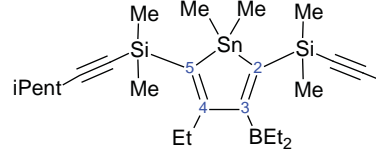
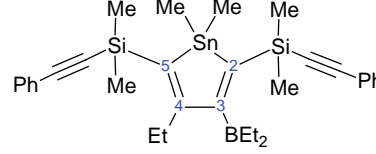
	$^1J(\text{Si}(\text{b}), \text{C}(\text{C}\equiv))$	73.7	131
	$^1J(\text{Si}(\text{a}), \text{C}(\text{CH}_2))$	55.0	
	$^1J(\text{Si}(\text{a}), \text{C}(\text{Me}))$	55.0	
	$^1J(\text{Si}(\text{b}), \text{C}(\text{Me}))$	55.9	
	$^2J(\text{Si}(\text{b}), \text{C}(\text{C}\equiv))$	9.1	
	$^1J(\text{Si}(\text{b}), \text{C}(\text{C}\equiv))$	73.6	133
	$^1J(\text{Si}(\text{a}), \text{C}(\text{CH}_2))$	56.2	
	$^1J(\text{Si}(\text{a}), \text{C}(\text{Me}))$	53.8	
	$^1J(\text{Si}(\text{b}), \text{C}(\text{Me}))$	56.0	
	$^2J(\text{Si}(\text{b}), \text{C}(\text{C}\equiv))$	10.5	
	$^1J(\text{Si}, \text{C}(2))$	71.1	206
	$^1J(\text{Si}, \text{C}(5))$	72.3	
	$^{2,3}J(\text{Si}, \text{C}(4))$	11.8	
	$^1J(\text{Si}, \text{C}(2))$	72.4	206
	$^1J(\text{Si}, \text{C}(5))$	72.3	
	$^{2,3}J(\text{Si}, \text{C}(4))$	12.7	
	$^1J(\text{Si}, \text{C}(2))$	72.1	206
	$^1J(\text{Si}, \text{C}(5))$	74.1	
	$^{2,3}J(\text{Si}, \text{C}(4))$	13.1	
	$^1J(\text{Si}, \text{C}(2))$	72.6	206
	$^1J(\text{Si}, \text{C}(5))$	71.5	
	$^{2,3}J(\text{Si}, \text{C}(4))$	13.0	
	$^1J(\text{Si}, \text{C}(2))$	70.9	206
	$^1J(\text{Si}, \text{C}(5))$	70.5	
	$^{2,3}J(\text{Si}, \text{C}(4))$	11.6	
$\text{Me}_3\text{Si}(\text{a})-\text{C}\equiv\text{C}-\text{Si}(\text{b})(\text{H})\text{Ph}_2$	$^1J(\text{Si}(\text{a}), \text{C}(\text{C}\equiv))$	86.6	184
	$^1J(\text{Si}(\text{b}), \text{C}(\text{C}\equiv))$	74.6	
	$^1J(\text{Si}(\text{b}), \text{C}(\text{Ph}))$	76.3	
	$^1J(\text{Si}(\text{a}), \text{C}(\text{Me}))$	56.3	
	$^2J(\text{Si}(\text{a}), \text{C}(\text{C}\equiv))$	13.4	
	$^2J(\text{Si}(\text{b}), \text{C}(\text{C}\equiv))$	12.2	

Table C4 (Continued)

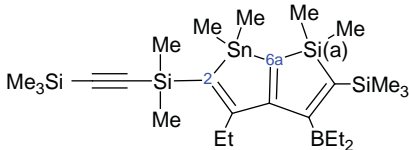
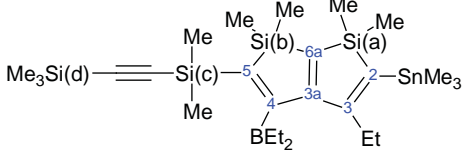
$\text{Me}_2(\text{H})\text{Si}(\text{a})-\text{C}\equiv\text{C}-\text{Si}(\text{b})\text{Ph}_2-\text{CH}_2-\text{CH}=\text{CH}_2$	$^1J(\text{Si}(\text{a}), \text{C}(\text{C}\equiv))$	77.4	207
	$^1J(\text{Si}(\text{b}), \text{C}(\text{C}\equiv))$	85.3	
	$^1J(\text{Si}(\text{b}), \text{C}(\text{Ph}))$	75.5	
	$^1J(\text{Si}(\text{b}), \text{C}(\text{CH}_2))$	54.9	
	$^1J(\text{Si}(\text{a}), \text{C}(\text{Me}))$	55.8	
	$^2J(\text{Si}(\text{a}), \text{C}(\text{C}\equiv))$	12.5	
	$^2J(\text{Si}(\text{b}), \text{C}(\text{C}\equiv))$	12.7	
	$^2J(\text{Si}(\text{b}), \text{C}(\text{Ph}))$	4.0	
	$^3J(\text{Si}(\text{b}), \text{C}(\text{Ph}))$	5.8	
	$^3J(\text{Si}(\text{b}), \text{C}(\text{C}\equiv))$	5.4	
	$^1J(\text{Si}(\text{a}), \text{C}(\text{C}\equiv))$	77.4	
	$^1J(\text{Si}(\text{b}), \text{C}(\text{C}\equiv))$	87.2	
	$^1J(\text{Si}(\text{b}), \text{C}(\text{Ph}))$	77.1	
$\text{Me}_2(\text{H})\text{Si}(\text{a})-\text{C}\equiv\text{C}-\text{Si}(\text{b})(\text{Vi})\text{Ph}_2$	$^1J(\text{Si}(\text{b}), \text{C}(\text{Vi}))$	75.5	207
	$^1J(\text{Si}(\text{a}), \text{C}(\text{Me}))$	55.4	
	$^2J(\text{Si}(\text{a}), \text{C}(\text{C}\equiv))$	12.4	
	$^2J(\text{Si}(\text{b}), \text{C}(\text{C}\equiv))$	13.2	
	$^1J(\text{Si}, \text{C}(\text{C}\equiv))$	83.9	
	$^2J(\text{Si}, \text{C}(\text{C}\equiv))$	13.1	
	$^1J(\text{Si}, \text{C}(2))$	70.7	
	$^1J(\text{Si}, \text{C}(6\text{a}))$	57.8	
	$^1J(\text{Si}(\text{a}), \text{C}(\text{Me}))$	47.4	
	$^1J(\text{Si}(\text{c}), \text{C}(\text{C}\equiv))$	77.5	
	$^1J(\text{Si}(\text{d}), \text{C}(\text{C}\equiv))$	77.8	
	$^1J(\text{Si}, \text{C}(2))$	49.0	
	$^1J(\text{Si}, \text{C}(5))$	69.7	
$\text{Ph}_2(\text{H})\text{Si}-\text{C}\equiv\text{C}-\text{Si}(\text{H})\text{Ph}_2$	$^1J(\text{Si}, \text{C}(5))$	43.8	184
	$^1J(\text{Si}, \text{C}(6\text{a}))$	58.8	
	$^1J(\text{Si}, \text{C}(6\text{a}))$	56.1	
	$^1J(\text{Si}(\text{a}), \text{C}(\text{Me}))$	50.2	
	$^1J(\text{Si}(\text{b}), \text{C}(\text{Me}))$	49.5	
	$^1J(\text{Si}(\text{c}), \text{C}(\text{Me}))$	56.6	
	$^1J(\text{Si}(\text{d}), \text{C}(\text{Me}))$	56.1	
	$^2J(\text{Si}(\text{c}), \text{C}(\text{C}\equiv))$	12.1	
	$^2J(\text{Si}(\text{d}), \text{C}(\text{C}\equiv))$	12.3	
	$^1J(\text{Si}(\text{a}, \text{b}), \text{C}(\text{C}\equiv))$	76.3	
	$^1J(\text{Si}(\text{a}, \text{b}), \text{C}(\text{C}\equiv))$	78.9	
	$^1J(\text{Si}, \text{C}(5))$	70.1	
	$^1J(\text{Si}, \text{C}(8))$	60.0	
	$^1J(\text{Si}, \text{C}(2))$	49.0	206
	$^1J(\text{Si}, \text{C}(5))$	69.7	
	$^1J(\text{Si}, \text{C}(5))$	43.8	
	$^1J(\text{Si}, \text{C}(6\text{a}))$	58.8	
	$^1J(\text{Si}, \text{C}(6\text{a}))$	56.1	
	$^1J(\text{Si}(\text{a}), \text{C}(\text{Me}))$	50.2	
	$^1J(\text{Si}(\text{b}), \text{C}(\text{Me}))$	49.5	
	$^1J(\text{Si}(\text{c}), \text{C}(\text{Me}))$	56.6	
	$^1J(\text{Si}(\text{d}), \text{C}(\text{Me}))$	56.1	
	$^2J(\text{Si}(\text{c}), \text{C}(\text{C}\equiv))$	12.1	
	$^2J(\text{Si}(\text{d}), \text{C}(\text{C}\equiv))$	12.3	
	$^1J(\text{Si}(\text{a}, \text{b}), \text{C}(\text{C}\equiv))$	76.3	
	$^1J(\text{Si}(\text{a}, \text{b}), \text{C}(\text{C}\equiv))$	78.9	
	$^1J(\text{Si}, \text{C}(8))$	46.7	194
	$^1J(\text{Si}(\text{b}, \text{c}), \text{C}(\text{Me}))$	51.2	
	$^1J(\text{Si}(\text{b}, \text{c}), \text{C}(\text{Me}))$	50.3	
	$^1J(\text{Si}(\text{b}, \text{c}), \text{C}(\text{Me}))$	50.8	
	$^1J(\text{Si}(\text{b}, \text{c}), \text{C}(\text{Me}))$	48.5	
	$^1J(\text{Si}(\text{a}, \text{b}), \text{C}(\text{C}\equiv))$	76.3	
	$^1J(\text{Si}(\text{a}, \text{b}), \text{C}(\text{C}\equiv))$	78.9	
	$^1J(\text{Si}, \text{C}(5))$	70.1	
	$^1J(\text{Si}, \text{C}(8))$	60.0	
	$^1J(\text{Si}, \text{C}(8))$	46.7	
	$^1J(\text{Si}(\text{b}, \text{c}), \text{C}(\text{Me}))$	51.2	
	$^1J(\text{Si}(\text{b}, \text{c}), \text{C}(\text{Me}))$	50.3	
	$^1J(\text{Si}(\text{b}, \text{c}), \text{C}(\text{Me}))$	50.8	
	$^1J(\text{Si}(\text{b}, \text{c}), \text{C}(\text{Me}))$	48.5	

Table C4 (Continued)

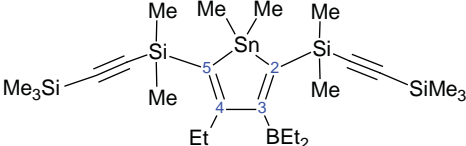
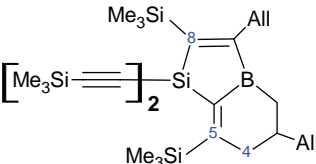
	$^1J(\text{Si(a,d), C(Me)})$	56.4	206
	$^1J(\text{Si(a,d), C(Me)})$	54.7	
	$^2J(\text{Si(a,b), C(C}\equiv\text{)})$	11.9	
	$^2J(\text{Si(a,b), C(C}\equiv\text{)})$	12.3	
	$^nJ(\text{Si, C(4)})$	9.7	
	$^1J(\text{Si, C(2)})$	66.4	
	$^1J(\text{Si, C(5)})$	71.9	
	$^{2,3}J(\text{Si, C(4)})$	12.8	
	$^1J(\text{Si, C(5)})$	60.3	194
	$^1J(\text{Si, C(8)})$	65.3	
	$^1J(\text{Si, C(8)})$	54.8	
	$^1J(\text{Si, C(Me)})$	56.4	
	$^1J(\text{Si, C(Me)})$	56.2	
	$^1J(\text{Si, C(Me)})$	51.3	
	$^1J(\text{Si, C(Me)})$	51.1	
	$^nJ(\text{Si, C(C}\equiv\text{)})$	12.2	
	$^nJ(\text{Si, C(C}\equiv\text{)})$	11.8	
	$^nJ(\text{Si, C(4)})$	8.9	

Table C5. $\text{X}_3\text{Si}-\text{C}\equiv\text{N}$ structures

$\text{Me}_3\text{Si}-\text{C}\equiv\text{N}$	$^1J(\text{Si, C(C}\equiv\text{)})$	-53.3	106
$\text{H}_3\text{Si}-\text{C}\equiv\text{N}$	$^1J(\text{Si, C})$	-62.5	106

APPENDIX D

Table D1. Complexes

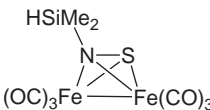
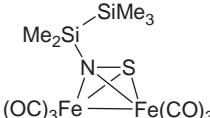
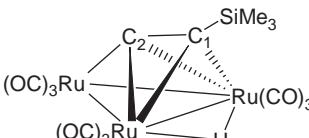
	$^1J(\text{Si, C})$	57.1	223
	$^1J(\text{Si, C(Me}_2\text{)})$	46.8	223
	$^1J(\text{Si, C(Me}_3\text{)})$	45.7	
	$^1J(\text{Si, C(1)})$	64.0	224
	$^1J(\text{Si, C(Me)})$	55.6	

Table D1. (Continued)

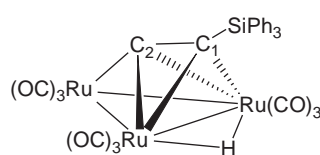
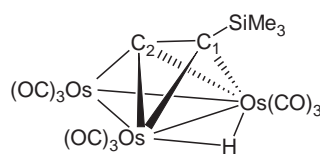
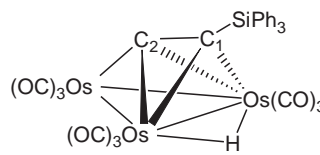
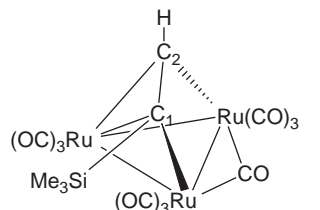
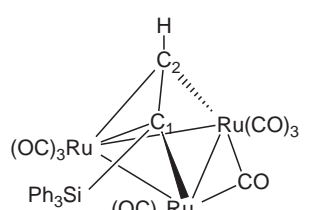
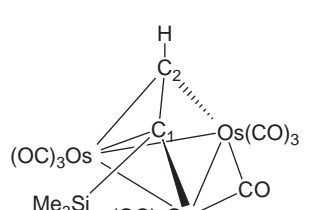
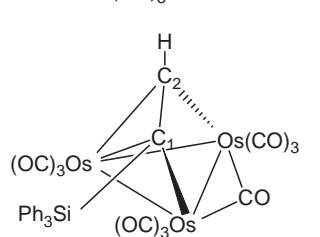
	$^1J(\text{Si}, \text{C}(1))$	71.7	224
	$^1J(\text{Si}, \text{C}(1))$ $^1J(\text{Si}, \text{C}(\text{Me}))$	63.2 55.3	224
	$^1J(\text{Si}, \text{C}(1))$	73.2	224
	$^1J(\text{Si}, \text{C}(1))$ $^1J(\text{Si}, \text{C}(\text{Me}))$	65.5 53.7	224
	$^1J(\text{Si}, \text{C}(1))$	70.5	224
	$^1J(\text{Si}, \text{C}(1))$ $^1J(\text{Si}, \text{C}(\text{Me}))$	64.5 53.4	224
	$^1J(\text{Si}, \text{C}(1))$	72.2	224

Table D1. (Continued)

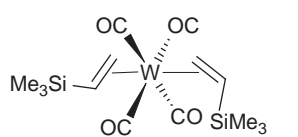
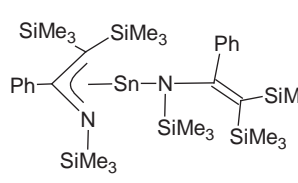
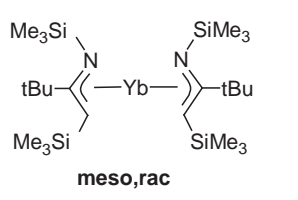
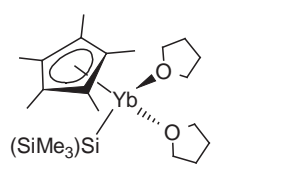
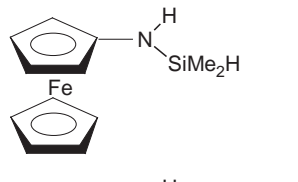
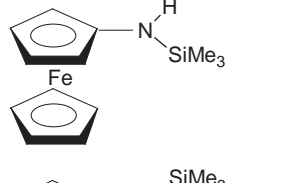
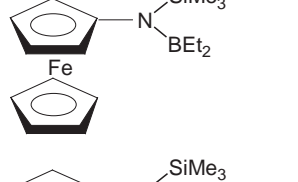
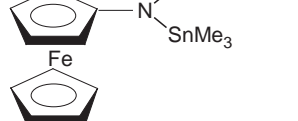
 <p>meso, rac</p>	$^1J(\text{Si}, \text{C}(\text{Me}))$ $^1J(\text{Si}, \text{C}(\text{Me}))$	52 50	225
	$^1J(\text{Si}(\text{N}), \text{C}(\text{Me}))$ $^1J(\text{Si}(\text{C}=\text{N}), \text{C}(\text{Me}))$ $^1J(\text{Si}(\text{C}=\text{N}), \text{C}(\text{Me}))$	56.6 52 49.3	226
 <p>meso, rac</p>	$^1J(\text{Si}, \text{C}(\text{C}=\text{N}))$	64.6	227
	$^1J(\text{Si}, \text{C}(\text{Me}))$ $^2J(\text{Si}, \text{C}(\text{Me}))$	40 8	228
	$^1J(\text{Si}, \text{C})$	57.1	229
	$^1J(\text{Si}, \text{C})$	57.0	229, 230
	$^1J(\text{Si}, \text{C})$	57.8	229
	$^1J(\text{Si}, \text{C})$	56.2	229

Table D1. (Continued)

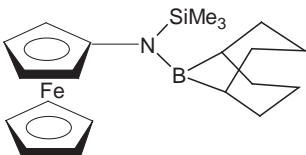
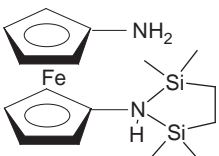
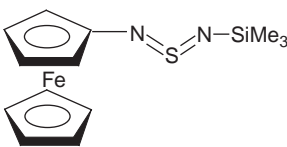
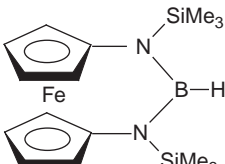
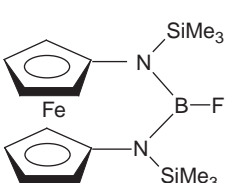
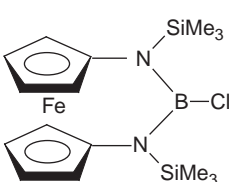
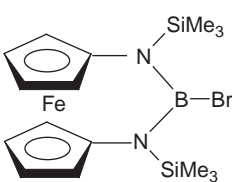
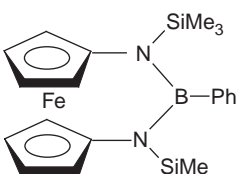
	$^1J(\text{Si}, \text{C})$	58.0	229
	$^1J(\text{Si}, \text{C}(\text{CH}_2))$ $^1J(\text{Si}, \text{C}(\text{Me}))$	58.5 54.4	231
	$^1J(\text{Si}, \text{C})$	57.4	230
	$^1J(\text{Si}, \text{C})$	57.2	232
	$^1J(\text{Si}, \text{C})$	57.5	232
	$^1J(\text{Si}, \text{C})$	58	232
	$^1J(\text{Si}, \text{C})$	58.5	232
	$^1J(\text{Si}, \text{C})$	57.7	232

Table D1. (Continued)

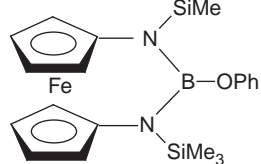
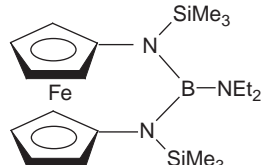
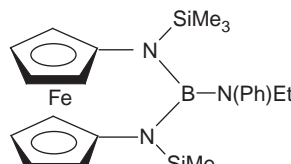
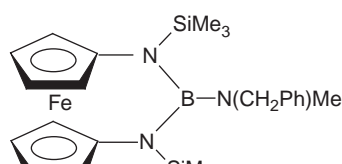
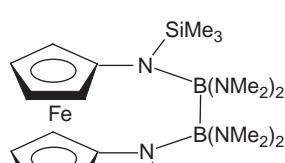
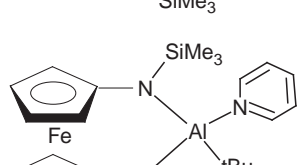
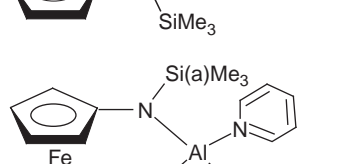
	$^1J(\text{Si}, \text{C})$	57.7	232
	$^1J(\text{Si}, \text{C})$	57.0	233
	$^1J(\text{Si}, \text{C}) (+23^\circ\text{C})$ $^1J(\text{Si}, \text{C}) (-30^\circ\text{C})$	57.7 57.3	233
	$^1J(\text{Si}, \text{C}) (+23^\circ\text{C})$ $^1J(\text{Si}, \text{C}) (-50^\circ\text{C})$ $^1J(\text{Si}, \text{C}) (-50^\circ\text{C})$	56.5 56.8 56.8	233
	$^1J(\text{Si}, \text{C})$	57.0	232
	$^1J(\text{Si}, \text{C})$	55.6, 55.7	234
	$^1J(\text{Si(a)}, \text{C})$ $^1J(\text{Si(b)}, \text{C(Me)})$ $^1J(\text{Si(b)}, \text{C(CH)})$	55.8, 55.7 49.6, 49.7 18.1	234

Table D1. (Continued)

	$^1J(\text{Si}(\text{SiN}), \text{C})$ $^1J(\text{Si}(\text{SiSi}), \text{C}(\text{Me}))$	56.0, 55.9 42.9, 42.7	234
	$^1J(\text{Si}, \text{C})$	57.0	134
	$^1J(\text{Si}, \text{C})$	56.1	193
	$^1J(\text{Si}(\text{b}), \text{C}(\text{C}\equiv))$ $^1J(\text{Si}(\text{a}), \text{C})$ $^1J(\text{Si}(\text{b}), \text{C}(\text{Me}))$ $^2J(\text{Si}(\text{b}), \text{C}(\text{C}\equiv))$	73.7 56.5 56.1 10.6	193
	$^1J(\text{Si}, \text{C})$	56.1	193
	$^1J(\text{Si}(\text{b}), \text{C}(2))$ $^1J(\text{Si}(\text{c}), \text{C}(5))$ $^1J(\text{Si}(\text{b}), \text{C}(\text{Me}))$ $^1J(\text{Si}(\text{c}), \text{C}(\text{Me}))$ $^1J(\text{Si}(\text{a}), \text{C})$	64.4 64.4 52.0 52.0 56.1	193
	$^1J(\text{Si}, \text{C})$	71.72	235

Table D1. (Continued)

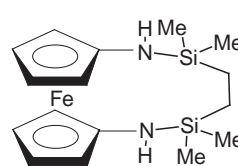
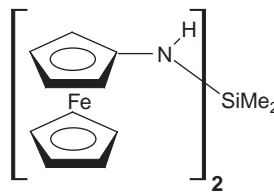
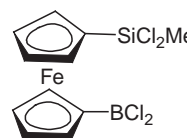
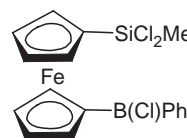
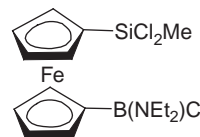
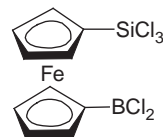
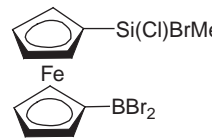
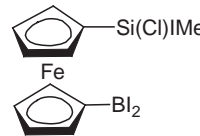
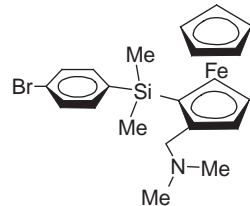
	$^1J(\text{Si}, \text{C})$	56.7	231
	$^1J(\text{Si}, \text{C})$	61.0	229
	$^1J(\text{Si}, \text{C}(\text{Ferr}))$ $^1J(\text{Si}, \text{C}(\text{Me}))$ $^2J(\text{Si}, \text{C}(\text{Ferr}))$	99.6 72.8 8.1	101
	$^1J(\text{Si}, \text{C}(\text{Ferr}))$ $^1J(\text{Si}, \text{C}(\text{Me}))$	100.6 72.9	101
	$^1J(\text{Si}, \text{C}(\text{Ferr}))$ $^1J(\text{Si}, \text{C}(\text{Me}))$	101.8 72.8	101
	$^1J(\text{Si}, \text{C})$ $^2J(\text{Si}, \text{C})$ $^3J(\text{Si}, \text{C})$	127.8 10.1 7.3	101
	$^1J(\text{Si}, \text{C}(\text{Me}))$	70.1	101
	$^1J(\text{Si}, \text{C}(\text{Me}))$	66.5	101
	$^1J(\text{Si}, \text{C}(\text{Me}))$	61.23	196

Table D1. (Continued)

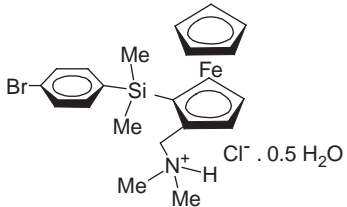
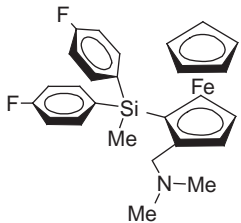
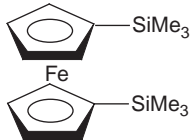
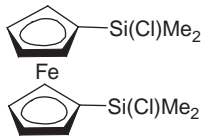
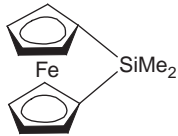
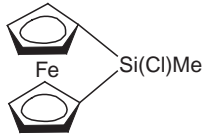
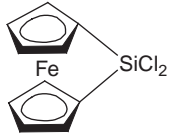
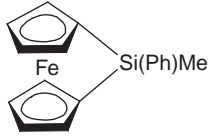
	$^1J(\text{Si}, \text{C}(\text{Me}))$	55.40	196
	$^1J(\text{Si}, \text{C}(\text{Me}))$	56.7	196
	$^1J(\text{Si}, \text{C}(\text{Ferr}))$ $^1J(\text{Si}, \text{C}(\text{Me}))$ $^2J(\text{Si}, \text{C})$ $^3J(\text{Si}, \text{C})$	71.6 52.6 5.5 4.4	65
	$^1J(\text{Si}, \text{C}(\text{Ferr}))$ $^1J(\text{Si}, \text{C}(\text{Me}))$ $^2J(\text{Si}, \text{C})$	83.1 60.3 6.7	101
	$^1J(\text{Si}, \text{C}(\text{Ferr}))$ $^1J(\text{Si}, \text{C}(\text{Me}))$	57.8 56.0	101
	$^1J(\text{Si}, \text{C}(\text{Ferr}))$ $^1J(\text{Si}, \text{C}(\text{Me}))$ $^2J(\text{Si}, \text{C})$	73.4 62.3 8.7	101
	$^1J(\text{Si}, \text{C})$ $^2J(\text{Si}, \text{C})$ $^3J(\text{Si}, \text{C})$	99.1 8.6 6.7	101
	$^1J(\text{Si}, \text{C}(\text{Ferr}))$ $^1J(\text{Si}, \text{C}(\text{Ph}))$ $^1J(\text{Si}, \text{C}(\text{Me}))$	50.6 73.7 56.4	101

Table D1. (Continued)

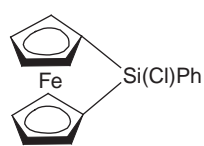
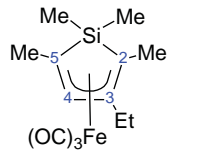
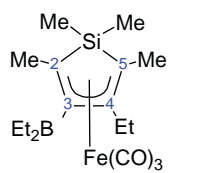
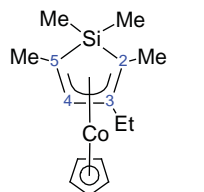
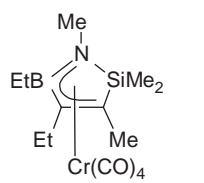
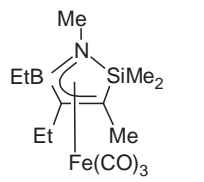
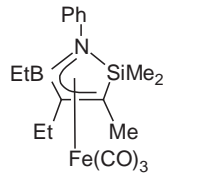
	$^1J(\text{Si}, \text{C}(\text{Ferr}))$	77.0	101
	$^2J(\text{Si}, \text{C}(\text{Ferr}))$	8.5	
	$^2J(\text{Si}, \text{C}(\text{Ferr}))$	8.2	
	$^1J(\text{Si}, \text{C}(2))$	63.9	99
	$^1J(\text{Si}, \text{C}(5))$	63.0	
	$^1J(\text{Si}, \text{C}(\text{Me-endo}))$	57.6	
	$^1J(\text{Si}, \text{C}(\text{Me-exo}))$	40.9	
	$^2J(\text{Si}, \text{C}(3))$	10.8	
	$^2J(\text{Si}, \text{C}(4))$	9.4	
	$^1J(\text{Si}, \text{C}(\text{C}=\text{O}))$	63.7	
	$^1J(\text{Si}, \text{C}(\text{Me-endo}))$	40.8	
	$^1J(\text{Si}, \text{C}(\text{Me-exo}))$	57.4	
	$^1J(\text{Si}, \text{C}(2))$	64.6	99
	$^1J(\text{Si}, \text{C}(5))$	62.8	
	$^1J(\text{Si}, \text{C}(\text{Me}))$	55.8	
	$^1J(\text{Si}, \text{C}(\text{Me}))$	40.1	
	$^2J(\text{Si}, \text{C}(4))$	9.9	
	$^1J(\text{Si}, \text{C}(2))$	66.4	99
	$^1J(\text{Si}, \text{C}(5))$	65.8	
	$^1J(\text{Si}, \text{C}(\text{Me-endo}))$	58.4	
	$^1J(\text{Si}, \text{C}(\text{Me-exo}))$	37.4	
	$^2J(\text{Si}, \text{C}(3))$	11.0	
	$^2J(\text{Si}, \text{C}(4))$	9.2	
	$^1J(\text{Si}, \text{C}(\text{C}=\text{O}))$	78.2	236
	$^1J(\text{Si}, \text{C}(\text{Me-exo}))$	50.6	
	$^1J(\text{Si}, \text{C}(\text{Me-endo}))$	59.5	
	$^1J(\text{Si}, \text{C}(\text{C}=\text{O}))$	77.2	236
	$^1J(\text{Si}, \text{C}(\text{Me-exo}))$	47.8	
	$^1J(\text{Si}, \text{C}(\text{Me-endo}))$	57.8	
	$^1J(\text{Si}, \text{C}(\text{Me, exo}))$	57.6	
	$^1J(\text{Si}, \text{C}(\text{Me, endo}))$	47.7	
	$^1J(\text{Si}, \text{C}(\text{Me-exo}))$	47.8	236
	$^1J(\text{Si}, \text{C}(\text{Me-endo}))$	59.9	

Table D1. (Continued)

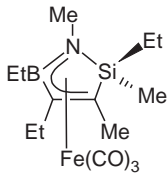
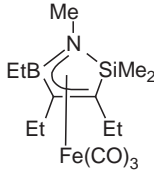
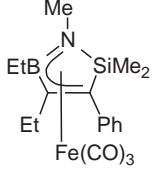
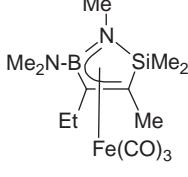
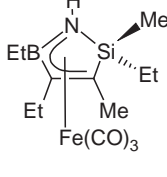
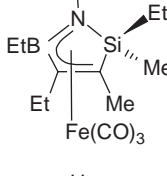
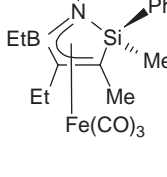
	$^1J(\text{Si}, \text{C}(\text{Me}))$	56.8	236
	$^1J(\text{Si}, \text{C}(\text{C}=\text{}))$	76.8	236
	$^1J(\text{Si}, \text{C}(\text{Me-}exo))$	48.7	
	$^1J(\text{Si}, \text{C}(\text{Me-}endo))$	56.1	
	$^1J(\text{Si}, \text{C}(\text{C}=\text{}))$	76.9	102
	$^1J(\text{Si}, \text{C}(\text{Me}, \text{exo}))$	57.5	
	$^1J(\text{Si}, \text{C}(\text{Me}, \text{endo}))$	47.5	
	$^1J(\text{Si}, \text{C}(\text{C}=\text{}))$	74.1	236
	$^1J(\text{Si}, \text{C}(\text{Me-}exo))$	49.4	
	$^1J(\text{Si}, \text{C}(\text{Me-}endo))$	58.5	
	$^1J(\text{Si}, \text{C}(\text{C}=\text{}))$	74.4	102
	$^1J(\text{Si}, \text{C}(\text{Me}, \text{exo}))$	53.1	
	$^1J(\text{Si}, \text{C}(\text{Me}, \text{endo}))$	48.9	
	$^1J(\text{Si}, \text{C}(\text{Me-}exo))$	46.8	236
	$^1J(\text{Si}, \text{C}(\text{Me-}endo))$	58.0	
	$^1J(\text{Si}, \text{C}(\text{C}=\text{}))$	75.8	236
	$^1J(\text{Si}, \text{C}(\text{Et-}endo))$	60.0	
	$^1J(\text{Si}, \text{C}(\text{Me-}exo))$	47.8	
	$^1J(\text{Si}, \text{C}(\text{C}=\text{}))$	76.3	236
	$^1J(\text{Si}, \text{C}(\text{Et-}exo))$	49.8	
	$^1J(\text{Si}, \text{C}(\text{Me-}endo))$	58.0	
	$^1J(\text{Si}, \text{C}(\text{C}=\text{}))$	79.9	236
	$^1J(\text{Si}, \text{C}(\text{Ph-}exo))$	60.5	
	$^1J(\text{Si}, \text{C}(\text{Me-}endo))$	58.5	

Table D1. (Continued)

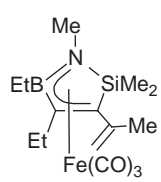
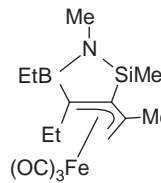
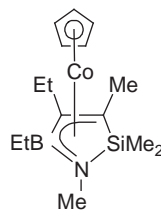
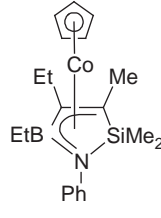
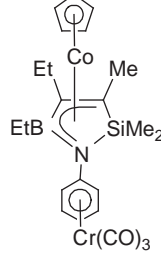
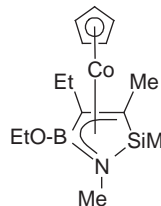
	$^1J(\text{Si}, \text{C}(\text{Me-}exo))$	48.4	236
	$^1J(\text{Si}, \text{C}(\text{Me-}endo))$	58.8	
	$^1J(\text{Si}, \text{C}(\text{Me-}exo))$	56.6	236
	$^1J(\text{Si}, \text{C}(\text{Me-}endo))$	53.0	
	$^1J(\text{Si}, \text{C}(\text{C}=\text{}))$	79.1	236
	$^1J(\text{Si}, \text{C}(\text{Me-}exo))$	44.9	
	$^1J(\text{Si}, \text{C}(\text{Me-}endo))$	58.3	
	$^1J(\text{Si}, \text{C}(\text{Me-}exo))$	46.3	236
	$^1J(\text{Si}, \text{C}(\text{Me-}endo))$	60.1	
	$^1J(\text{Si}, \text{C}(\text{C}=\text{}))$	79.3	236
	$^1J(\text{Si}, \text{C}(\text{Me-}exo))$	45.8	
	$^1J(\text{Si}, \text{C}(\text{Me-}endo))$	58.8	
	$^1J(\text{Si}, \text{C}(\text{C}=\text{}))$	78.8	236
	$^1J(\text{Si}, \text{C}(\text{Me-}exo))$	44.3	
	$^1J(\text{Si}, \text{C}(\text{Me-}endo))$	66.9	

Table D1. (Continued)

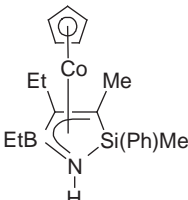
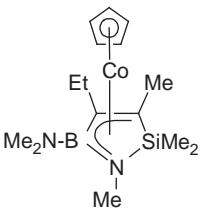
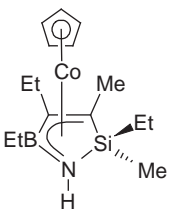
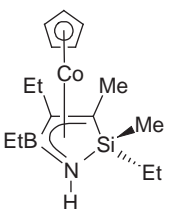
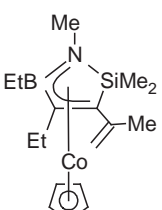
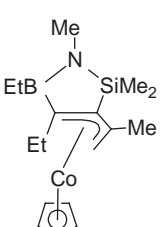
	$^1J(\text{Si}, \text{C}(\text{C}=\text{}))$	81.4	236
	$^1J(\text{Si}, \text{C}(\text{Ph-}exo, \text{endo}))$	60.6	
	$^1J(\text{Si}, \text{C}(\text{Me-}endo, \text{exo}))$	61.4	
	$^1J(\text{Si}, \text{C}(\text{Me-}exo))$	43.7	236
	$^1J(\text{Si}, \text{C}(\text{Me-}endo))$	58.5	236
	$^1J(\text{Si}, \text{C}(\text{Et-}endo))$	60.3	236
	$^1J(\text{Si}, \text{C}(\text{Me-}exo))$	44.1	
	$^1J(\text{Si}, \text{C}(\text{Me-}exo))$	45.0	236
	$^1J(\text{Si}, \text{C}(\text{Me-}endo))$	60.0	
	$^1J(\text{Si}, \text{C}(\text{C}=\text{}))$	79.3	236
	$^1J(\text{Si}, \text{C}(\text{Me-}exo))$	51.3	
	$^1J(\text{Si}, \text{C}(\text{Me-}endo))$	55.0	

Table D1. (Continued)

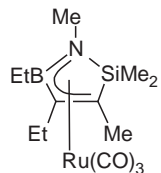
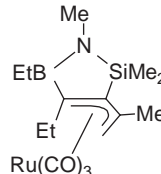
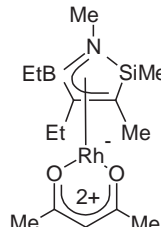
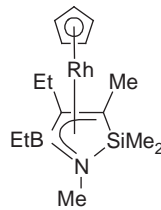
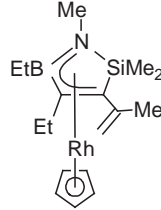
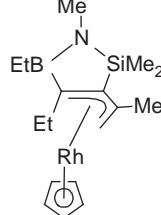
	$^1J(\text{Si}, \text{C}(\text{C}=\text{}))$	78.1	236
	$^1J(\text{Si}, \text{C}(\text{Me-}exo))$	47.8	
	$^1J(\text{Si}, \text{C}(\text{Me-}endo))$	58.0	
	$^1J(\text{Si}, \text{C}(\text{C}=\text{}))$	74.3	236
	$^1J(\text{Si}, \text{C}(\text{C}=\text{}))$	78.5	236
	$^1J(\text{Si}, \text{C}(\text{Me-}exo))$	48.0	
	$^1J(\text{Si}, \text{C}(\text{Me-}endo))$	57.1	
	$^1J(\text{Si}, \text{C}(\text{Me-}exo))$	43.3	236
	$^1J(\text{Si}, \text{C}(\text{Me-}endo))$	58.1	
	$^1J(\text{Si}, \text{C}(\text{Me-}exo))$	42.5	236
	$^1J(\text{Si}, \text{C}(\text{Me-}endo))$	58.5	
	$^1J(\text{Si}, \text{C}(\text{Me-}exo))$	52.3	236
	$^1J(\text{Si}, \text{C}(\text{Me-}endo))$	56.1	

Table D1. (Continued)

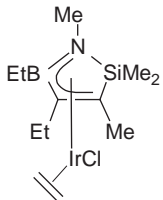
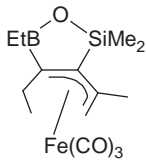
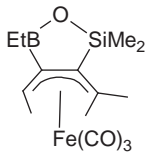
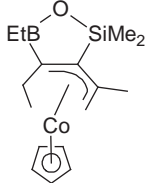
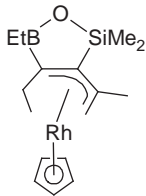
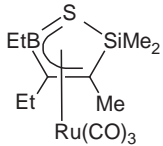
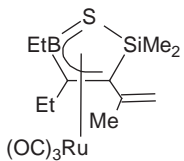
	$^1J(\text{Si}, \text{C}(\text{Me-}exo))$	49.5	236
	$^1J(\text{Si}, \text{C}(\text{Me-}endo))$	56.3	
	$^1J(\text{Si}, \text{C}(\text{C}=\text{O}))$	71.4	172
	$^1J(\text{Si}, \text{C}(\text{Me}))$	61.7	
	$^1J(\text{Si}, \text{C}(\text{Me}))$	58.0	
	$^1J(\text{Si}, \text{C}(\text{C}=\text{O}))$	71.4	172
	$^1J(\text{Si}, \text{C}(\text{Me}))$	60.3	
	$^1J(\text{Si}, \text{C}(\text{Me}))$	55.4	
	$^1J(\text{Si}, \text{C}(\text{C}=\text{O}))$	73.4	172
	$^1J(\text{Si}, \text{C}(\text{Me}))$	60.6	
	$^1J(\text{Si}, \text{C}(\text{Me}))$	57.2	
	$^1J(\text{Si}, \text{C}(\text{C}=\text{O}))$	73.0	172
	$^1J(\text{Si}, \text{C}(\text{Me}))$	61.5	
	$^1J(\text{Si}, \text{C}(\text{Me}))$	56.6	
	$^1J(\text{Si}, \text{C}(\text{Me}))$	53.9	200
	$^1J(\text{Si}, \text{C}(\text{Me}))$	45.8	
	$^1J(\text{Si}, \text{C}(\text{Me}))$	56.0	200
	$^1J(\text{Si}, \text{C}(\text{Me}))$	46.8	

Table D1. (Continued)

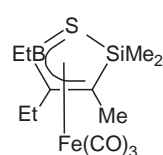
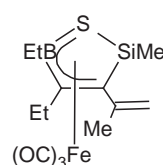
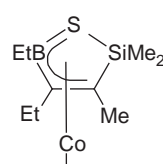
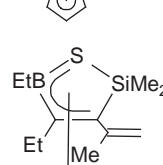
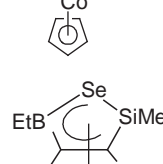
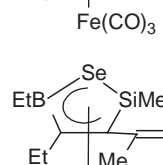
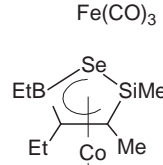
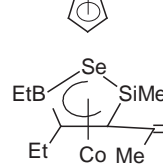
	$^1J(\text{Si}, \text{C}(\text{C}=\text{}))$	71.9	200
	$^1J(\text{Si}, \text{C}(\text{Me}))$	53.9	
	$^1J(\text{Si}, \text{C}(\text{Me}))$	47.8	
	$^1J(\text{Si}, \text{C}(\text{Me}))$	55.9	200
	$^1J(\text{Si}, \text{C}(\text{Me}))$	47.8	
	$^1J(\text{Si}, \text{C}(\text{Me}))$	56.0	200
	$^1J(\text{Si}, \text{C}(\text{Me}))$	43.7	
	$^1J(\text{Si}, \text{C}(\text{Me}))$	58.0	200
	$^1J(\text{Si}, \text{C}(\text{Me}))$	43.8	
	$^1J(\text{Si}, \text{C}(\text{C}=\text{}))$	70.9	202
	$^1J(\text{Si}, \text{C}(\text{Me}))$	53.4	
	$^1J(\text{Si}, \text{C}(\text{Me}))$	45.8	
	$^2J(\text{Si}, \text{C}(\text{Me}))$	6.4	
	$^3J(\text{Si}, \text{C}(\text{Et}))$	4.5	
	$^1J(\text{Si}, \text{C}(\text{C}=\text{}))$	66.4	202
	$^1J(\text{Si}, \text{C}(\text{Me}))$	55.1	
	$^1J(\text{Si}, \text{C}(\text{Me}))$	45.8	
	$^1J(\text{Si}, \text{C}(\text{C}=\text{}))$	72.9, 73.4	202
	$^1J(\text{Si}, \text{C}(\text{Me}))$	54.6, 54.8	
	$^1J(\text{Si}, \text{C}(\text{Me}))$	42.1, 42.2	
	$^1J(\text{Si}, \text{C}(\text{Me}))$	57.4	202
	$^1J(\text{Si}, \text{C}(\text{Me}))$	42.4	

Table D1. (Continued)

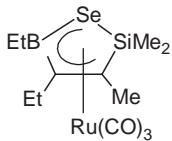
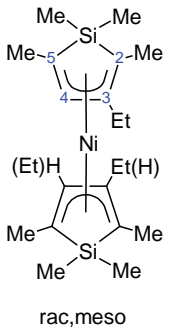
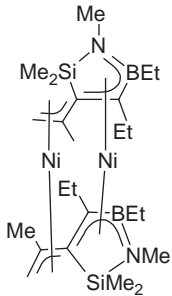
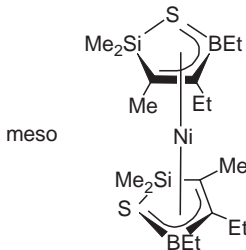
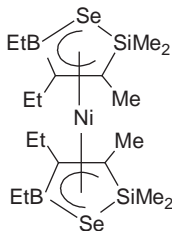
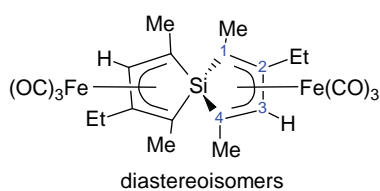
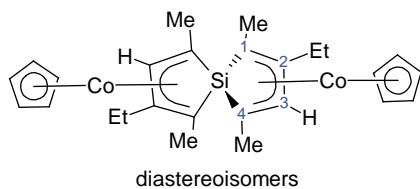
	$^1J(\text{Si}, \text{C}(\text{C}=\text{C}))$	70.7	202
	$^1J(\text{Si}, \text{C}(\text{Me}))$	53.2	
	$^1J(\text{Si}, \text{C}(\text{Me}))$	45.0	
 rac,meso	$^1J(\text{Si}, \text{C}(2))$	66.0	99
	$^1J(\text{Si}, \text{C}(5))$	64.0	
	$^2J(\text{Si}, \text{C}(3))$	11.1	
	$^2J(\text{Si}, \text{C}(4))$	9.2	
	$^1J(\text{Si}, \text{C}(2))$	66.5	
	$^1J(\text{Si}, \text{C}(5))$	68.5	
	$^2J(\text{Si}, \text{C}(3))$	9.8	
	$^2J(\text{Si}, \text{C}(4))$	9.2	
	$^1J(\text{Si}, \text{C}(2))$	68.3	
	$^1J(\text{Si}, \text{C}(5))$	66.0	
	$^2J(\text{Si}, \text{C}(3))$	11.8	
	$^2J(\text{Si}, \text{C}(4))$	9.2	
	$^1J(\text{Si}, \text{C}(2))$	64.7	
	$^1J(\text{Si}, \text{C}(5))$	66.6	
 meso	$^1J(\text{Si}, \text{C}(\text{Me-}exo))$	48.8	236
	$^1J(\text{Si}, \text{C}(\text{Me-}endo))$	57.4	
 meso	$^1J(\text{Si}, \text{C}(\text{C}=\text{C}))$	70.8	200
	$^1J(\text{Si}, \text{C}(\text{Me}))$	55.6	
	$^1J(\text{Si}, \text{C}(\text{Me}))$	46.8	
 meso	$^1J(\text{Si}, \text{C}(\text{C}=\text{C}))$	69.6	202
	$^1J(\text{Si}, \text{C}(\text{Me}))$	54.8	
	$^1J(\text{Si}, \text{C}(\text{Me}))$	46.4	

Table D1. (Continued)

$^1J(\text{Si}, \text{C}(1))$	53.1	100
$^1J(\text{Si}, \text{C}(4))$	73.3	
$^2J(\text{Si}, \text{C}(2))$	8.9	
$^2J(\text{Si}, \text{C}(3))$	11.2	
$^1J(\text{Si}, \text{C}(1))$	52.4	
$^1J(\text{Si}, \text{C}(4))$	72.3	
$^2J(\text{Si}, \text{C}(2))$	8.9	
$^2J(\text{Si}, \text{C}(3))$	10.8	
$^1J(\text{Si}, \text{C}(1))$	52.1	
$^1J(\text{Si}, \text{C}(4))$	73.3	
$^2J(\text{Si}, \text{C}(2))$	9.8	
$^2J(\text{Si}, \text{C}(3))$	9.8	
$^1J(\text{Si}, \text{C}(1))$	52.2	
$^1J(\text{Si}, \text{C}(4))$	72.4	
$^2J(\text{Si}, \text{C}(2))$	9.8	
$^2J(\text{Si}, \text{C}(3))$	9.8	



$^1J(\text{Si}, \text{C}(1))$	51.9	100
$^1J(\text{Si}, \text{C}(4))$	76.2	
$^2J(\text{Si}, \text{C}(2))$	8.9	
$^2J(\text{Si}, \text{C}(3))$	11.5	
$^1J(\text{Si}, \text{C}(1))$	52.7	
$^1J(\text{Si}, \text{C}(4))$	75.8	
$^2J(\text{Si}, \text{C}(2))$	10.0	
$^2J(\text{Si}, \text{C}(3))$	11.5	
$^1J(\text{Si}, \text{C}(1))$	51.9	
$^1J(\text{Si}, \text{C}(4))$	75.4	
$^2J(\text{Si}, \text{C}(2))$	8.9	
$^2J(\text{Si}, \text{C}(3))$	10.0	

CHAPTER 3

1D Double Quantum Filter NMR Studies

N. Chandrakumar

Contents		
	1. Introduction and General Principles	266
	1.1 The characteristics of multiple quantum coherences	267
	1.2 INADEQUATE	268
	1.3 Double quantum filters in the solid state and in ordered phases	271
	1.4 Double quantum filters in spatially resolved NMR	271
	1.5 Specialized DQF experiments	271
	1.6 2D MQ experiments	272
	2. Implementation of DQF Experiments	272
	2.1 Preparation	272
	2.2 Evolution	283
	2.3 Reconversion	285
	3. Applications of DQF Experiments	297
	3.1 Solution state	297
	3.2 Solid state	306
	3.3 Spatially resolved NMR	316
	4. Conclusions	325
	Acknowledgments	325
	References	325

Abstract

NMR spectra are rich in information content, but are often crowded severely, except for the simplest systems. A generic approach to address this problem is spectral simplification by suitable editing. Editing procedures are in turn most frequently rooted in the manipulation of spins by means of their couplings, be they scalar, dipolar, or quadrupolar. In this connection, creation of a double quantum state to filter spectra has proven to be an especially fruitful strategy. In this contribution, we discuss the principles, implementation, and typical applications of one-dimensional double quantum filter NMR experiments in solution state, solid state, and spatially resolved NMR.

Department of Chemistry, Indian Institute of Technology-Madras, Chennai 600036, Tamil Nadu, India

Annual Reports on NMR Spectroscopy, Volume 67
ISSN 0066-4103, DOI 10.1016/S0066-4103(09)06703-9

© 2009 Elsevier Ltd.
All rights reserved.

Keywords: Double quantum coherences; double quantum filters; spectral editing; creation of DQC; two- or three-pulse sandwich; non-exponential relaxation; dipolar recoupling; transition selective reconversion; time reversed reconversion; spin-1/2 systems; quadrupolar systems; DQF spectroscopy; *in vivo* DQF NMR; DQF imaging; DQ diffusion studies

1. INTRODUCTION AND GENERAL PRINCIPLES

Multiple quantum coherences (MQCs) involve the superposition of spin states that differ in their magnetic quantum number by a quantity other than one unit.^{1,2} They may be prepared with reasonable efficiency in pulse FT NMR mode by the application of a non-selective two-pulse sandwich, normally supplemented by a π pulse in the middle of the delay between the two pulses, in order to refocus shifts and inhomogeneities.^{3,4}

Generation of MQCs requires the presence of a coupling involving the spins: scalar, dipolar, or quadrupolar. The spin system is normally prepared for the generation of MQCs by coherent evolution under such a coupling.^a

Consequently, MQCs may be employed as filters to distinguish the spectral responses of coupled spins from those of uncoupled spins. This normally results in spectral simplification (by the suppression of signals from isolated spins (which are not coupled to other spins)) and also frequently permits identification of the partners in coupling. Further, on systems of rare spins, it permits the measurement of homonuclear couplings, which is otherwise a difficult undertaking: the satellite transitions due to homonuclear couplings among rare spins have but a fraction of the intensity of the main peak arising from the corresponding isolated rare spin — and would therefore be generally masked by the main peak unless the latter were suppressed.

Clearly, these are powerful capabilities that are much applied in diverse areas addressed by NMR. However, all this may be accomplished only in indirect mode, since MQCs are not directly observable in pulse FT NMR and need to be converted to transverse magnetization components (single quantum coherences, SQCs) for purposes of detection.^{1,2}

While a multiple quantum filter experiment permits one to distinguish responses of coupled spins from those of isolated spins — which are suppressed — the penalty paid is in general an attenuation of the responses of coupled spins as well, owing to the successive coherence transformations that are required in performing such an experiment.

How does a multiple quantum filter permit distinction between coupled and isolated spins? It may be recalled that n quantum coherences sense n times the resonance offset (or chemical shift), phase shift, or field gradient applied.¹⁻⁴ These are the properties that enable their discrimination from one another.

^aIt may be noted, however, that under suitable conditions non-exponential relaxation processes involving such a coupling could also play this role, even if the relevant coupling is unresolved and averages to zero.

Special interest pertains to double quantum coherences (DQCs), especially in the context of the NMR of nuclei with spin-1/2. DQCs normally involve relatively light penalties in terms of the attenuation of desired responses.

In this overview, we summarize the principles and recent advances in this area of NMR and attempt to capture the flavor of the applications of double quantum filter (DQF) studies in NMR.

1.1 The characteristics of multiple quantum coherences

MQC may be defined in terms of the density matrix element $|M\rangle\langle M'|$. Here, $|M\rangle$ and $|M'\rangle$ are eigenstates of the total z component of spin, I_z , with eigenvalues M and M' , respectively; $\Delta M = (M - M')$ is the order of the coherence.

From these definitions, the effect of a phase shift may be inferred as follows:

$$\begin{aligned}
 I_z|M\rangle &= M|M\rangle \\
 I_z|M'\rangle &= M'|M'\rangle \\
 \Rightarrow e^{-iI_z\varphi}|M\rangle &= e^{-iM\varphi}|M\rangle \\
 \langle M'|e^{iI_z\varphi} &= e^{iM'\varphi}\langle M'| \\
 \therefore e^{-iI_z\varphi}|M\rangle\langle M'|e^{iI_z\varphi} &= e^{-iM\varphi}|M\rangle\langle M'|e^{iM'\varphi} \\
 &= e^{-i(M-M')\varphi}|M\rangle\langle M'| = e^{-i\Delta M\varphi}|M\rangle\langle M'|
 \end{aligned} \tag{1}$$

In other words, the coherence is phase shifted in proportion to its order.

In entirely similar vein, the effect of resonance offsets Ω and field gradients \mathbf{G} may also be inferred to be in proportion to the coherence order:

$$e^{-i\Omega I_z t}|M\rangle\langle M'|e^{i\Omega I_z t} = e^{-i(M-M')\Omega t}|M\rangle\langle M'| = e^{-i\Delta M\Omega t}|M\rangle\langle M'| \tag{2}$$

$$e^{-i\gamma(\vec{\mathbf{G}}\cdot\vec{\mathbf{r}})I_z t}|M\rangle\langle M'|e^{i\gamma(\vec{\mathbf{G}}\cdot\vec{\mathbf{r}})I_z t} = e^{-i(M-M')\gamma(\vec{\mathbf{G}}\cdot\vec{\mathbf{r}})t}|M\rangle\langle M'| = e^{-i\Delta M\gamma(\vec{\mathbf{G}}\cdot\vec{\mathbf{r}})t}|M\rangle\langle M'| \tag{3}$$

In Equation (3), \mathbf{r} is the position vector of any given point in the sample.

It may be noted in particular that zero quantum coherence (ZQC) is not affected by phase shifts, resonance offsets, or gradients.

The phase cycling of the double quantum preparation sandwich $P(\tau)$ in 90° steps (see Sections 1.2 and 2.1.1) exploits this dependence on coherence order, and results in a phase shift of DQC — and hence of the reconverted single quantum signal — in steps of 180° . We have:

$$\begin{aligned}
 P(\tau)I_zP^{-1}(\tau) &= c(\tau) \\
 e^{-iI_z\varphi}P e^{iI_z\varphi}I_z e^{-iI_z\varphi}P^{-1} e^{iI_z\varphi} &= e^{-iI_z\varphi}PI_zP^{-1} e^{iI_z\varphi} = e^{-iI_z\varphi}c(\tau) e^{iI_z\varphi} = e^{-ip\varphi}c(\tau)
 \end{aligned} \tag{4}$$

Here, $c(\tau)$ represents DQC and p is the coherence order (± 2) that is prepared by the sandwich P . Clearly then, a 90° phase shift generates a 180° phase shift of DQC, that is, negates its sign.

The phase cycling of the reconversion pulse (or sandwich) (see Section 1.2) may also be understood in similar light, although it is perhaps a little more

subtle. We denote the reconversion sequence by R and the resulting (single quantum) signal by S . We have:

$$R(\text{DQC})R^{-1} = S \quad (5)$$

The effect of a phase shift of the reconversion sequence may be found by evaluating the following expression:

$$e^{-iI_z\varphi} R e^{iI_z\varphi} (\text{DQC}) e^{-iI_z\varphi} R^{-1} e^{iI_z\varphi} \quad (6)$$

If a 90° phase shift is employed, we find:

$$\begin{aligned} e^{-i(\pi/2)I_z} R e^{i(\pi/2)I_z} (\text{DQC}) e^{-i(\pi/2)I_z} R^{-1} e^{i(\pi/2)I_z} &= -e^{-i(\pi/2)I_z} R (\text{DQC}) R^{-1} e^{i(\pi/2)I_z} \\ &= -e^{-i(\pi/2)I_z} S e^{i(\pi/2)I_z} = -e^{-i(\pi/2)} S \\ &\equiv e^{-i\pi} e^{-i(\pi/2)} S = e^{-i(3\pi/2)} S \end{aligned} \quad (7)$$

Since the phase of a SQC such as the signal S is shifted by 90° given a 90° phase shift of the reconversion segment^b, we notice that the overall phase shift that the signal accumulates amounts to 270° , including the sign change of DQC under these conditions. However, a 180° phase shift of the reconversion segment results in no phase change of the DQC and therefore results merely in reversal of the signal S . For a 270° phase shift of the reconversion segment on the other hand, the overall phase shift of the signal is 90° .

To complete this picture, we need to look at the effect of the reconversion sequence phase on $(\pm)z$ magnetization, on which the reconversion operates in the case of isolated spins:

$$\begin{aligned} e^{-i(\pi/2)I_z} R e^{i(\pi/2)I_z} I_z e^{-i(\pi/2)I_z} R^{-1} e^{i(\pi/2)I_z} &= e^{-i(\pi/2)I_z} R I_z R^{-1} e^{i(\pi/2)I_z} \\ &= e^{-i(\pi/2)I_z} S' e^{i(\pi/2)I_z} = e^{-i(\pi/2)} S' \end{aligned} \quad (8)$$

In other words, the (single quantum) signal S' arising from z magnetization suffers the standard phase shift of any SQC, that is, it is shifted in phase by φ given a phase shift of φ .^b In summary then, the signal from isolated spins and that from the double quantum pathway relevant for coupled spin pairs cycle in the opposite sense to each other when the reconversion sequence is cycled through the xy plane: the sense of cycling of the former being the same as that of the reconversion segment itself.

1.2 INADEQUATE

One of the early applications of the idea of double quantum filtering is in the area of ^{13}C NMR at natural abundance (*ca.* 1.1%), by way of the Incredible Natural Abundance Double QUAntum Transfer Experiment (INADEQUATE).⁵

^bNote that if the detected coherence order were to be deemed as -1 , the signal suffers a phase shift of $-\varphi$, given a phase shift of φ . This still results in the opposite sense of shift of the signal from DQC and that from z magnetization, following the detailed arguments above.

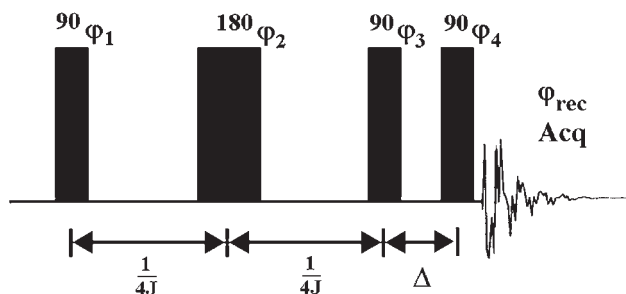


Figure 1 1D INADEQUATE pulse sequence. The unobservable double quantum coherence generated at the end of the second 90° pulse is converted to observable SQCs by the final 90° pulse after a short delay Δ . The optimum preparation time is $(2J)^{-1}$. Double quantum pathway selection may be achieved by either phase cycling, as indicated in the figure, or gradient-controlled coherence pathway selection.

This experiment is designed to permit a spectral display of scalar coupled ^{13}C resonances at natural abundance. Because one-bond C–C couplings ($^1J_{\text{CC}}$) have a well-defined range of values (which depend on the state of hybridization of carbon), an INADEQUATE experiment that is based on the generation of DQC mediated by one-bond couplings permits the visualization of the molecular carbon skeleton: this is probably the closest NMR ever gets to directly visualizing molecular-bonding topology. Working at natural abundance has the twin advantages of not requiring any synthetic isotope labeling and of dealing with the simplest spin coupled systems, *viz.*, a pair of spins: but of course results in poor sensitivity, the intensity of each of the ^{13}C doublet components at natural abundance being essentially 0.55% of the intensity of the resonance due to an isolated ^{13}C at the same site in the molecule.

The INADEQUATE pulse sequence is shown in Figure 1 and involves DQ preparation, followed essentially immediately by reconversion to detectable SQC. It may be noted that the optimal preparation period τ , ignoring relaxation, is given by $(2J)^{-1}$. In standard implementation, broadband ^1H decoupling (typically with composite pulse trains) is performed right through the experiment, resulting in ^1H decoupled ^{13}C spectra with signal enhancement by the NOE. Discrimination between signals from isolated ^{13}C spins and those that are coupled may in principle be achieved by either phase cycling or gradient-controlled coherence pathway selection.

Phase cycling in turn may involve one or a combination of several strategies:

- (i) Keeping the reconversion pulse phase ϕ_4 fixed, the double quantum preparation sandwich (phases ϕ_1 , ϕ_2 , and ϕ_3 , which may all be set equal) may be phase rotated from scan to scan in increments of 90° with concomitant receiver-phase alternation (phase ϕ_{rec}). This approach is based on the response of DQC to phase shifts (see Section 1.1), *viz.*, a given phase shift applied to the spin system results in double the phase shift of DQC: a 90° phase shift of the preparation sandwich as a whole therefore

results in 180° rotation of the DQC created, which then leads to phase reversal of the reconverted SQC.

- (ii) Keeping the phase of the preparation sandwich fixed, the reconversion pulse phase φ_4 and receiver phase φ_{rec} may be rotated in opposite senses in 90° increments on successive scans (see Section 1.1).
- (iii) Phase alternation of the 180° pulse of the preparation sandwich (phase φ_2) may be introduced in addition, keeping the receiver phase constant, compensating for imperfections in the refocusing pulse.
- (iv) A 90° phase shift of the 180° pulse of the preparation sandwich (phase φ_2) may be introduced as well, with concomitant receiver-phase alternation.
- (v) Phase alternation of the first 90° pulse (phase φ_1) of the preparation sandwich may also be introduced, accompanied by receiver-phase alternation.
- (vi) Standard four-step CYCLOPS may be superimposed on all of the above, resulting in an expanded $4 \times 4 \times 2 \times 2 \times 4$ phase cycle, that is, a 512-step procedure, or a suitable subset thereof.

It is to be remarked that essentially no delay Δ (in practice, $\leq 10 \mu\text{s}$) is required between the end of the preparation sandwich and the reconversion pulse for the phase-cycling procedure; in turn, only a short delay corresponding to the receiver dead time is required between the end of the reconversion pulse and start of acquisition.

Gradient-controlled pathway selection⁶ may on the other hand be performed on a single scan basis by inserting a pair of gradient pulses just before and after the reconversion pulse, with amplitude ratio 1:2 to register the 'echo' component. Under the influence of a gradient of unit amplitude, DQC undergoes two units of dephasing (see Section 1.1) and may be rephased by a gradient of two units amplitude acting on the reconverted SQC, the reconversion pulse effecting a change in sign of the coherence order as well, for the echo component. The delay between the preparation sandwich and reconversion pulse on the one hand and that between the reconversion pulse and start of acquisition on the other now needs to be extended however to *ca.* 1 ms each in order to allow for the dephasing/rephasing gradient pulse to be ramped up, to settle, and to be ramped down, and for the eddy current effects of the gradient pulses to decay. Note also that half the signal is lost per scan in the gradient-controlled procedure owing to the selection of one pathway out of two for coherence reconversion (e.g., the echo pathway *or* the anti-echo pathway).

The resulting signals by either procedure bear the stamp of the filter experiment in that a series of anti-phase (AP) doublets result in the INADEQUATE spectrum.^c

^cThe term 'AP doublets' refers to doublets whose individual components have equal, but opposite intensity. For example, while an in-phase (IP) doublet of spin #1 may be represented in operator notation (i.e., algebraically) as I_{1x} , the corresponding AP doublet may be represented by the operator $2I_{1x}I_{2z}$, clearly indicating that the sign of the individual peak of the doublet due to spin #1 is related to the spin state of the coupled spin #2. As this operator indicates, the two peaks of spin #1 now have equal but opposite intensity since the spin state of the coupled spin #2 takes on the two values $\pm 1/2$, given that its spin is $1/2$.

It is possible to generate doublets that have the natural IP intensity pattern by supplementing the INADEQUATE sequence with a refocusing delay after the reconversion pulse. This approach may be generalized to the design of a symmetric filter experiment and is related to the idea of mixing that is conjugate to the preparation. Uniform excitation and detection may be achieved by running such a symmetrized version of INADEQUATE,⁷ averaging over a range of τ values.^d

Strong coupling effects cause sub-optimal excitation of DQC with the conventional choice of τ . This may be remedied: a reasonable compromise value of the preparation period is found to be $3/(2J)$.⁸

In the INADEQUATE experiment applied to rare spins such as ^{13}C , ^{29}Si ,^{9–14} ^{183}W ,^{15–18} $^{119/117}\text{Sn}$,^{18a,18b} etc., to detect their respective homonuclear couplings, the spin at each chemical shift exhibits in principle a pair of responses due to its coupling to a second spin. Because the prospect of finding a third spin coupled to either/both of the first two is further attenuated by the natural abundance factor, INADEQUATE spectra have a relatively simple structure, exhibiting at each chemical shift one AP doublet per coupled partner.

1.3 Double quantum filters in the solid state and in ordered phases

DQFs may also be configured for systems of dipole coupled or quadrupole coupled spins in ordered phases. For such ordered phases, recoupling^{19–23} is often invoked under magic angle spinning (MAS) conditions, since standard acquisition under MAS would average out the dipolar (or quadrupolar) interaction. The J coupled version is also possible in such systems when resolution permits.^{13,24}

1.4 Double quantum filters in spatially resolved NMR

The DQF experiment is invaluable not only in the context of spectroscopy *in vitro*, but also for spatially resolved NMR, including *in vivo* experiments, as well as for NMR diffusion measurements, microscopy, and imaging.^{25–27}

The double (and when appropriate the triple) quantum filter experiment has been explored as a means to distinguish between ‘mobile’ species and species with ‘restricted mobility,’ such as Na^+ in biological systems, for example, in cells.

In the context of imaging, DQF procedures result in unique image contrast, by a variety of mechanisms including molecule selectivity, T_2 contrast, etc.

1.5 Specialized DQF experiments

The DQF experiment that INADEQUATE represents is however by no means limited to detecting homonuclear couplings among rare spins-1/2.

^dThe INADEQUATE experiment becomes ‘symmetric’ when refocusing is included, in the sense that the preparation sandwich is then essentially repeated for reconversion, except for the final 90° pulse. By averaging over τ , which is now both the preparation and the reconversion time, a $\sin^2 \pi/\tau$ dependence is introduced in the signal, which averages to 1/2 when τ is varied over a number of steps. The resulting signal intensities are then independent of the value of J ; however, phase anomalies could remain that need to be removed by a suitable strategy: see, for example, ref. 7.

In general, filter experiments may be broadly classified, in analogy with electrical engineering terminology, into highpass filter experiments and bandpass filter experiments in the spin number domain, corresponding respectively to n quantum filtration and n spin filtration for spins- $1/2$.⁷ If an n spin filter experiment were applied to a ^1H network, for example, **only** the response from a network of n coupled protons would remain in the resulting spectrum. If an n quantum filter experiment were applied to the same system on the other hand, responses from networks of n **or more** coupled protons would remain in the spectrum. Furthermore, there has been some effort in the direction of topology-selective filtration, which would distinguish, to give a simple example, between linear and non-linear three-spin- $1/2$ networks.^{28–30} Such filter experiments in general lead to the possibility of spin chromatography,³¹ that is, the separation of the NMR responses of different species in a mixture into different sub-spectra, without physically separating the mixture into its components.

In addition, filter experiments may of course be employed on nuclei with spin $> 1/2$.

1.6 2D MQ experiments

It is clear that the 1D filter experiment introduced above may be expanded into a 2D experiment, most simply by acquiring a series of spectra with systematic incrementation of the period between MQC preparation and reconversion. This expanded and incremented period would then permit evolution of MQC, so that the MQ frequency spectrum may be inferred by double Fourier transformation of the resulting two-dimensional dataset.

In the case of INADEQUATE, for example, the 2D version³² would displace to different extents along the vertical spectral axis (which corresponds to F_1 , the frequency dimension that is related to the evolution time t_1) all doublets at a given chemical shift that result from coupling to different chemically shifted 'second' spins.

Here again, 2D double quantum spectra of both rare spins, as well as ^1H ,³¹ have been investigated, as also DQS of systems with spin $> 1/2$. [In addition, DQF may be incorporated in standard 2D experiments such as COSY^{31a}. In this context, RF gradients have also been employed for coherence pathway selection^{31b–d}.]

The 2D version in solid state is the popular MQ-MAS experiment,³³ while the imaging analog involves phase-encoding MQCs that are generated in the preparation period.^{34–36}

2. IMPLEMENTATION OF DQF EXPERIMENTS

2.1 Preparation

2.1.1 Solution state

In a system with three or more energy levels, MQCs may be prepared by a single RF pulse if one commences operations from a non-equilibrium state of

the first kind¹ (i.e., a spin state where the populations deviate from their equilibrium values).

In the more common case where the initial state corresponds to thermal equilibrium, the preparation sandwich that may be employed to this end has been referred to earlier in Section 1. In general, the basic sequence for generation of even-order coherence comprises two 90° pulses with either the same phase or a phase difference of 180°, there being a refocusing 180° pulse in the middle of this pulse sandwich. We shall briefly examine below the effect of the relative phase of the two 90° pulses in the preparation sandwich.

Considering a homonuclear system of n weakly coupled spins-1/2, we have the following forms of the Hamiltonian H in the rotating frame and the equilibrium density matrix σ_{eq} . We may now establish the nature of the effect on the spin system of a preparation sandwich 90° _{ϕ} – $\tau/2$ – 180° _{ϕ} – $\tau/2$ – 90° _{$\phi+\psi$} (with propagator P):

$$\begin{aligned}
 H &= \sum_{i=1}^n \delta_i I_{iz} + \sum_{i<} \sum_j 2\pi J_{ij} I_{iz} I_{jz} \\
 \sigma_{\text{eq}} &\sim \sum_{i=1}^n I_{iz} \equiv I_z \\
 I_\phi &= \sum_{i=1}^n I_{i\phi} \\
 P &= e^{-i(\pi/2)I_{\phi+\psi}} e^{-iH(\tau/2)} e^{-i\pi I_\phi} e^{-iH(\tau/2)} e^{-i(\pi/2)I_\phi} \\
 &= e^{-i(\pi/2)I_{\phi+\psi}} e^{-iH(\tau/2)} e^{-i\tilde{H}(\tau/2)} e^{-3i(\pi/2)I_\phi} \\
 \tilde{H} &= -\sum_{i=1}^n \delta_i I_{iz} + \sum_{i<} \sum_j 2\pi J_{ij} I_{iz} I_{jz} \\
 \therefore P &= e^{-i(\pi/2)I_{\phi+\psi}} e^{-i\tau \left(\sum_{i<} \sum_j 2\pi J_{ij} I_{iz} I_{jz} \right)} e^{i(\pi/2)I_\phi} \quad (9)
 \end{aligned}$$

The first term (on the right extreme) of this propagator clearly serves to establish transverse magnetization of the spin system, in phase quadrature to the corresponding first pulse of the sandwich. The second term of the propagator describes the effect of scalar spin–spin couplings on this transverse state. The simple property that allows tracking of the effect of a series of weak couplings to a given spin is that these couplings commute. Every additional coupling to an (additional) spin may therefore be considered one at a time, sequentially in arbitrary order — and generates a new state that involves an AP component in phase quadrature (+90° in phase) with respect to the initial state that it acts on. This implies that the phase of the AP magnetization that results after the cascade of couplings to $(n-1)$ spins is equal — or opposite — to the initial phase if n is odd, while the phase changes by $\pm 90^\circ$ if n is even. If the phase increment ψ of the final pulse of the preparation sandwich is 0°, this state is converted to

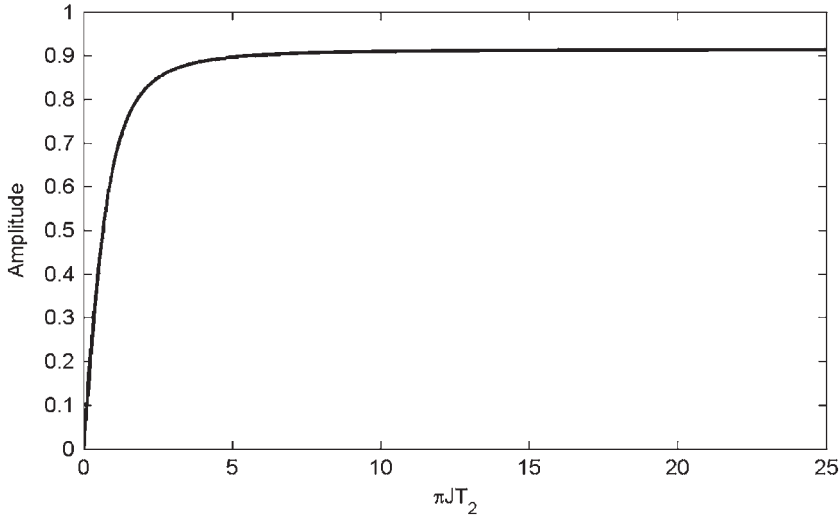


Figure 2 The plot of the amplitude A given in Equation (11) against πJT_2 .

even-order coherence, regardless of n being odd or even. If, on the other hand, the phase increment ψ of the final pulse of the preparation sandwich is 90° , the final state generated corresponds to odd-order coherence regardless of the parity of n .

The preparation time τ is split by the refocusing pulse in two equal durations $\tau/2$, τ being set to $(2J)^{-1}$ in the case of weak scalar coupling,^e ignoring relaxation effects. When spin–spin relaxation effects are taken into account, the optimal preparation time changes. In general, for a weakly coupled two-spin-1/2 system that exhibits equal relaxation rates for the two coupled spins, we have:

$$\tau_{\text{opt}} = \frac{1}{\pi J} \tan^{-1}(\pi JT_2) = \frac{1}{\pi J} \tan^{-1}\left(\frac{J}{\Delta\nu_{1/2}}\right) \quad (10)$$

Here, a Lorentzian lineshape has been assumed and the linewidth (i.e., full width at half height) has been denoted $\Delta\nu_{1/2}$. This expression clearly reduces to the nominal value of the preparation time when the coupling constant J is very much greater than the linewidth. It may be noted that unequal relaxation rates of the two coupled spins results in the generation of some ZQC in addition.

Taking into account the decay of transverse components due to relaxation (in the case of equal relaxation rates of the two coupled spins), the optimum amplitude A also gets reduced from 1 to:

$$A = \sin[\tan^{-1}(\pi JT_2)] \exp\left[-\frac{\tan^{-1}(\pi JT_2)}{\pi JT_2}\right] \quad (11)$$

This is illustrated in Figure 2, where the amplitude function A is plotted against πJT_2 .

^eIn presence of strong coupling effects, on the other hand, with $\Delta\delta/J < \sqrt{3}$, the optimum preparation time amounts to $3(2J)^{-1}$.⁸

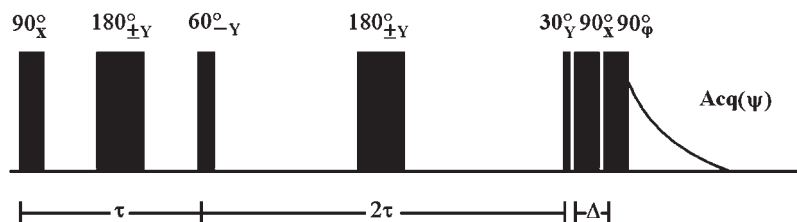


Figure 3 Basic J -compensated INADEQUATE pulse sequence. The reconversion pulse phase φ and receiver phase ψ are cycled through as usual.

The phase of the DQC created in spin-1/2 systems with a standard preparation pulse sandwich (of phase x , y , $-x$, or $-y$) is $\pm y$, although rotation of the phase of the sandwich by 45° would result in creation of the $\pm x$ phase of DQC.⁶ Note however that for scalar coupled spin-1 systems in solution state, there is an interesting difference in this respect between two-spin-1 DQC and one-spin-1 DQC: the latter is generated with x -phase employing the standard preparation sequence.³⁷

As seen from Equation (11), the amplitude of DQC prepared is thus a function of J , which does not of course in general have one unique value, even in a given molecule. A J -compensated preparation sequence has therefore been introduced.³⁸ The sequence was designed by analogy to composite pulses,³⁹ with the J coupling playing the role of the RF field. The basic version is shown in Figure 3.

This sequence may be readily seen to compensate for a range of J values by introducing a time dependence that includes the third harmonic term in π/τ , thereby partially flattening out the sine dependence. Unlike the three-pulse sandwich however, this sequence does create DQC of phase x in addition to that of phase y when τ deviates from $(2J)^{-1}$; however, the x -phase DQC is not converted to signal by the 90° read pulse of standard phase ($\varphi = \pm x, \pm y$). The $J\tau$ dependence of the amplitudes of DQC_y , DQC_x , and their resultant generated by this sequence is shown in Figure 4, and compared with the DQC_y amplitude generated by the standard preparation sequence.

The authors introduced a slightly modified equivalent version of their basic sequence, based on practical considerations. Their final experimental sequence also involves thrice the standard preparation time as shown in Figure 5.

Torres et al.³⁸ also introduced an offset-compensated INADEQUATE sequence for moderate offset ranges, which they termed C-INADEQUATE, as distinct from a version introduced earlier by Levitt and Ernst,⁴⁰ which operates better at large offsets. Further, Torres et al.³⁸ introduced a J -compensated as well as offset-compensated version, JC-INADEQUATE.

An INEPT sequence has been employed as a front-end module to enhance the sensitivity of INADEQUATE.⁴¹ The two segments of this pulse sequence may be concatenated in two alternative versions, shown in Figure 6.

⁶The 'phase of the preparation sandwich' refers to the phase of each of the individual pulses of the sandwich when all three pulses have the same phase (*vide* Section 1.2).

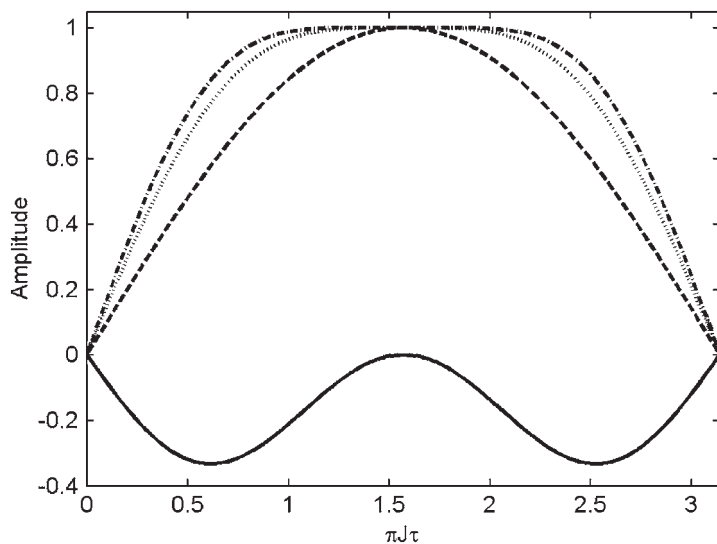


Figure 4 Plot of the amplitude of DQC of phase y (dot), phase x (solid), and the resultant (dot-dash) generated by the J -compensated sequence, compared with the DQC of phase y (dash) generated by the standard preparation sequence.

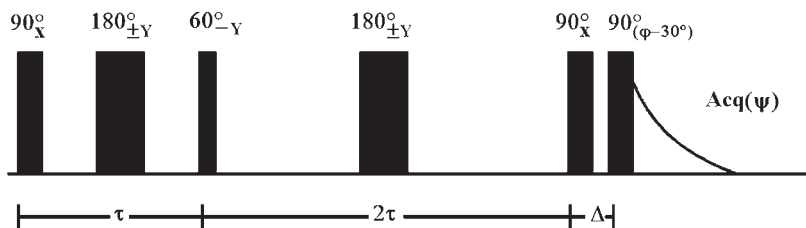


Figure 5 J -compensated INADEQUATE pulse sequence. The reconversion pulse phase is now set to $(\varphi - 30^\circ)$; the variable reconversion pulse phase term φ and receiver phase ψ are cycled through in the usual manner.

The second version involves omission of two refocusing pulses. In both versions, τ_1 is set to $(4J_{\text{CH}})^{-1}$. In the first version, $(\tau_2 + \tau_3)$ is set to $(4J_{\text{CC}})^{-1}$, while τ_4 is set to this value in the second version. In turn, τ_2 may be set to $(4J_{\text{CH}})^{-1}$ for CH systems, while a shorter compromise value of this setting satisfies all CH_n multiplicities. The phase of the 90° (a) pulse is in quadrature to the normal INADEQUATE setting, since refocusing of the CH coupling during τ_2 results in a 90° rotation of carbon magnetization vectors. Either version of this experiment aims to deliver sensitivity that is an improvement in relation to the standard NOE-enhanced version, both because the maximum INEPT signal could be four times the normal ^{13}C signal (as compared to at most three times the normal ^{13}C signal for the NOE experiment) and also because the repetition rate of the experiment would now depend on ^1H T_1 , which could be shorter than ^{13}C T_1 .

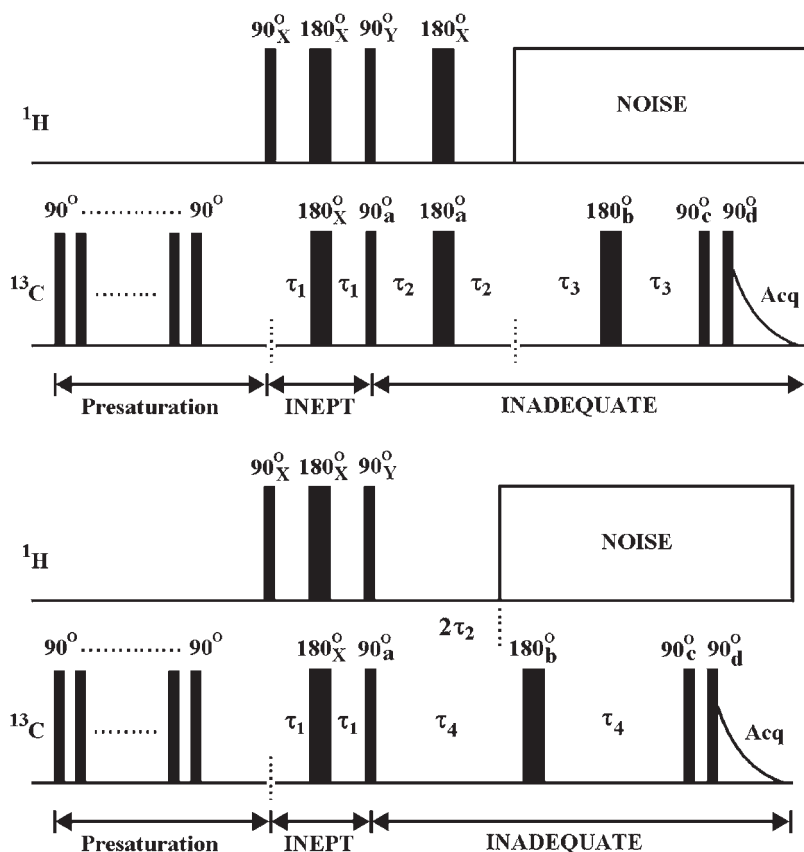


Figure 6 Two versions of the INEPT INADEQUATE pulse sequence, with difference in concatenation of the two segments. The version at the bottom involves fewer RF pulses.

DEPT polarization transfer has also been carried out for INADEQUATE, by Sparks and Ellis⁴²; Podkorytov⁴³ proposed a seven-pulse DEPT INADEQUATE pulse sequence. This is a simplification of the original eight-pulse sequence proposed by Sparks and Ellis.⁴²

2.1.2 Solid state

'Double quantum pulses' have been employed on quadrupolar spin systems in the solid state to directly excite DQC in such systems. These studies dealt with static single crystals and polycrystalline solids. DQCs are directly excited, for example, when a spin-1 system (such as ^2H) with quadrupolar coupling is irradiated at its Larmor frequency ω_0 with an RF field amplitude ω_1 that is much weaker than the quadrupolar splitting $2\omega_Q$.^{44–46} The effective nutation frequency under such a pulse is ω_1^2/ω_Q and has been observed in quadrupolar nuclei such as ^{27}Al ($I = 5/2$) as well.^{47,48}

It may also be noted that direct cross-polarization of multiple quantum transitions of spin-1 and spin-3/2 systems in solid state from spin-1/2 sources

(typically, from abundant spins such as ^1H) has been discussed in the literature as well^{49,50} (see Section 3.2.5).

While weak ('selective') pulses analogous to the double quantum pulses referred to above^{44–48} may be employed to create MQC in a multi-level system, a suitable sandwich constructed from standard hard pulses constitutes the normal preparation strategy.

In principle, the preparation segment of solid state experiments that rely on the J coupling could be run in the manner indicated above for solution state work, with the provision that MAS be employed to average out dipolar couplings and chemical shift anisotropy in the solid state, so that the remaining interactions resemble those in the liquid state. It may be noted that while inhomogeneous interactions such as chemical shift anisotropy, quadrupolar interactions, and heteronuclear dipolar interactions may be averaged out by MAS at moderate speeds (5–15 kHz), homonuclear dipolar interactions among abundant high γ spins require the use of ultrafast MAS (40–70 kHz) to do so. It is often of interest on the other hand to generate MQCs between groups of spins that are dipole coupled; when MAS has successfully 'removed' dipolar interactions, the generation of MQCs governed by these interactions is of course a contradiction in terms. Much effort has therefore been devoted to 'recoupling' for these purposes the dipolar interactions removed by MAS, typically in a 2D framework: the acquisition dimension retains the full dipolar decoupling under MAS, while one seeks to reintroduce dipolar couplings in the virtual time dimension.

It may be recalled that the average dipolar coupling between a pair of spins vanishes over a rotor period owing to the **spatial** averaging under MAS. This may be partially undone by two different approaches: (i) introducing a suitable **spin** manipulation during each rotor cycle or (ii) setting up 'rotational resonance' (R^2) conditions, where a multiple of the rotor frequency is set equal to the chemical shift difference between a pair of spins.

Rotor-driven experiments may be categorized physically as experiments where the dipolar flip-flop terms are re-introduced between a pair of spins by making up, with rotor quanta, the energy difference between the two chemically shifted species. It has proved possible to generate under rotational resonance conditions the ZQC of a pair of spins, starting from a non-equilibrium longitudinal state. This ZQC may then be transformed into DQC by applying a selective inversion pulse at one of the chemical shifts.⁵¹

As an example of the spin manipulation strategy, REDOR¹⁹ was an early pulse sequence that re-introduced heteronuclear dipolar couplings by the insertion of a π pulse on one of the coupled spins every half MAS rotor cycle; TEDOR¹⁹ is an extension of REDOR that involves a coherence transfer between the two coupled heterospins. For homonuclear couplings, RFDR²⁰ and SEDRA²⁰ involve the insertion of a π pulse at the mid-point of each rotor cycle and may be viewed as RF-driven experiments where the refocusing pulse allows the dipolar flip-flop terms to remain active.

DRAMA was the first pulse sequence⁵² that achieved direct recoupling for homonuclear systems, resulting in an average dipolar Hamiltonian that does not vanish over a rotor cycle. While a number of modifications of and alternatives to

this approach have been reported in the subsequent literature, the basic principles may be well illustrated with this sequence. The basic DRAMA sequence consists of a pair of 90° pulses of opposite phase issued every rotor cycle, with the interval between the two pulses being set to one-half the rotor period. The tolerance of this basic sequence to offset and shift anisotropy effects is considerably improved by an extended sequence, both shown in Figure 7.

It may be readily shown that under these conditions the dipolar coupling is of the zz form ($3I_{1z}I_{2z} - \vec{I}_1 \cdot \vec{I}_2$) for half the rotor period, but changes to the xx form ($3I_{1x}I_{2x} - \vec{I}_1 \cdot \vec{I}_2$) for the remaining half (the pulse phases being y and $-y$), thus undoing the spatial averaging (which of course requires that the spin part remain constant over the rotor cycle).

This may be easily demonstrated for the two-pulse DRAMA sequence in the zeroth-order average Hamiltonian \bar{H}_d for a dipole coupled two-spin-1/2 system. We may calculate the sequence propagator U as follows:

$$\begin{aligned}
 H_d &= -D_{zz}(3I_{1z}I_{2z} - \vec{I}_1 \cdot \vec{I}_2); & D_{zz} &= \frac{1}{2} \left(\frac{\mu_0}{4\pi} \right) \frac{\gamma_1 \gamma_2 \hbar}{r_{12}^3} (3 \cos^2 \theta - 1) \\
 U &= \exp\left(-iH_d \frac{\tau_R}{4}\right) \exp\left(i\frac{\pi}{2}I_y\right) \exp\left(-iH_d \frac{\tau_R}{2}\right) \exp\left(-i\frac{\pi}{2}I_y\right) \exp\left(-iH_d \frac{\tau_R}{4}\right) \\
 &\Rightarrow U = \exp\left(-iH_d \frac{\tau_R}{4}\right) \exp\left(-i\tilde{H}_d \frac{\tau_R}{2}\right) \exp\left(-iH_d \frac{\tau_R}{4}\right) \\
 \tilde{H}_d &= \exp\left(i\frac{\pi}{2}I_y\right) H_d \exp\left(-i\frac{\pi}{2}I_y\right) = -D_{zz}(3I_{1x}I_{2x} - \vec{I}_1 \cdot \vec{I}_2)
 \end{aligned} \tag{12}$$

At the same time, the spatial part of the Hamiltonian, D_{zz} , is rendered time dependent by MAS:

$$D_{zz}(t) = d \left(-\frac{1}{\sqrt{2}} \sin 2\beta \cos(\omega_R t + \gamma) + \frac{1}{2} \sin^2 \beta \cos(2(\omega_R t + \gamma)) \right) \tag{13}$$

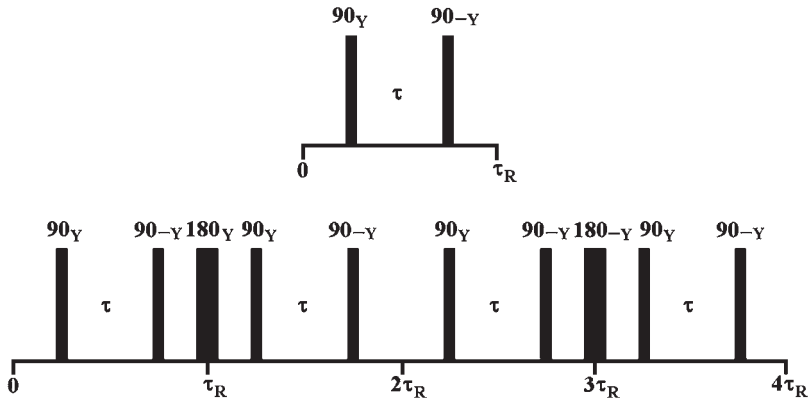


Figure 7 Two-pulse DRAMA sequence (top); extended DRAMA sequence (bottom) that averages out CSA and resonance offset effects over two rotor periods.

Here, d is the dipolar coupling constant ($d = (\mu_0/4\pi)(\gamma_1\gamma_2\hbar/r_{12}^3)$), while β and γ are Euler angles that describe the rotation of the dipolar tensor principal axis frame into the rotor-fixed frame R and ω_R the rotor frequency.

The dipolar Hamiltonian then averages over the rotor period to:

$$\begin{aligned}
 \int_0^{\tau_R} H_{ii}(t)dt &= - \int_0^{\tau_R} D_{zz}(t) \left[3I_{1i}I_{2i} - \vec{I}_1 \cdot \vec{I}_2 \right] dt \\
 &= - \left[3I_{1z}I_{2z} - \vec{I}_1 \cdot \vec{I}_2 \right] \int_0^{\tau_R/4} D_{zz}(t)dt \\
 &\quad - \left[3I_{1x}I_{2x} - \vec{I}_1 \cdot \vec{I}_2 \right] \int_{\tau_R/4}^{3\tau_R/4} D_{zz}(t)dt - \left[3I_{1z}I_{2z} - \vec{I}_1 \cdot \vec{I}_2 \right] \int_{3\tau_R/4}^{\tau_R} D_{zz}(t)dt \\
 \int D_{zz}(t)dt &= d \left[-\frac{1}{\sqrt{2}} \sin 2\beta \int \cos(\omega_R t + \gamma) dt \right. \\
 &\quad \left. + \frac{1}{2} \sin^2 \beta \int \cos(2(\omega_R t + \gamma)) dt \right] \\
 \Rightarrow \bar{H}_d &= \frac{1}{\tau_R} \int_0^{\tau_R} H_{ii}(t)dt = \frac{1}{\sqrt{2}\pi} d \sin 2\beta \cos \gamma (3(I_{1z}I_{2z} - I_{1x}I_{2x})) \quad (14)
 \end{aligned}$$

The DRAMA sequence — or other improved variants — may be employed to generate DQCs. This may be accomplished by inserting n cycles of DRAMA (in n rotor periods) into the interval between a 90° pulse pair with opposite phases, whose phases are in turn in quadrature with the DRAMA pulse phases. This generates an average Hamiltonian of the form:

$$\bar{H}_d = \frac{1}{\tau_R} \int_0^{\tau_R} H_{ii}(t)dt = \frac{1}{\sqrt{2}\pi} d \sin 2\beta \cos \gamma (3(I_{1y}I_{2y} - I_{1x}I_{2x})) \quad (15)$$

More refined sequences for homonuclear dipolar recoupling have since been designed, including DRAWS^{53,54} (see Section 3.2.2) as well as the C_n^N and R_n^N families of sequences.^{55–57} The latter rely, respectively, on suitable cycles of pairs of 2π and π pulses. Here, n is the number of pulse sets (e.g., $(2\pi)_\varphi(2\pi)_{-\varphi}$) issued in N periods of the rotor. For example, the C_7 sequence may be viewed as continuous phase-modulated irradiation with the nutation frequency being a multiple of seven times the rotation frequency. A compensated C_7 sequence that is considerably more tolerant to RF inhomogeneity, as well as isotropic and anisotropic chemical shift offsets, has been introduced by Hohwy et al.⁵⁸ by cyclically permuting the $(2\pi)_\varphi(2\pi)_{\varphi+\pi}$ element to $(\pi/2)_\varphi(2\pi)_{\varphi+\pi}(3\pi/2)_\varphi$.

A popular sequence that is robust at high MAS speeds is the BABA sequence,^{59,60} comprising back-to-back two-pulse sandwiches of suitably phase-shifted $\pi/2$ pulses (see, e.g., Section 3.2.1). The BABA sequence (see Section 3.2.1, Figure 27) may be readily seen to give rise to the average Hamiltonian:

$$\bar{H}_d = \frac{1}{\tau_R} \int_0^{\tau_R} H_{ii}(t)dt = \frac{1}{\sqrt{2}\pi} d \sin 2\beta \sin \gamma (3(I_{1x}I_{2x} - I_{1y}I_{2y})) \quad (16)$$

Optimal control theory has been employed to generate sequences for recoupling that may be used for DQF work; one important advantage in comparison to sequences such as C_7 is that far lower RF power deposition in the sample is called into play. An optimal control version of HORROR,⁶¹ termed $^{\text{OC}}$ HORROR, has been developed for homonuclear recoupling,⁶² as also double quantum planar and isotropic dipolar recoupling sequences.⁶³ Heteronuclear recoupling sequences based on optimal control have also been designed, for example, for ^{15}N - ^{13}C applications.⁶⁴ In general, optimal control sequences attempt to achieve short coherence transfer times with moderate RF amplitudes for applications on powder samples undergoing MAS, under conditions of RF field inhomogeneity. For example, $^{\text{OC}}$ HORROR has been shown to achieve on 2,3- $^{13}\text{C}_2$ -L-alanine a robust DQF efficiency of 73%, employing less than one-fourth the RMS average RF field required by C_7 at 10 kHz MAS, as shown in Figure 8.

Karlsson et al.⁵¹ discussed efficient DQ excitation under rotational resonance. Rotational resonance implies that the difference of two isotropic chemical shifts equals a small integral multiple of the spinning frequency. The approach of the authors involves the preparation of non-equilibrium longitudinal states involving difference magnetization of the two spins, followed by their conversion under rotational resonance conditions to ZQC. This is then followed by frequency-selective spin inversion to transform ZQC to DQC. These processes may be represented in terms of the following transformations of

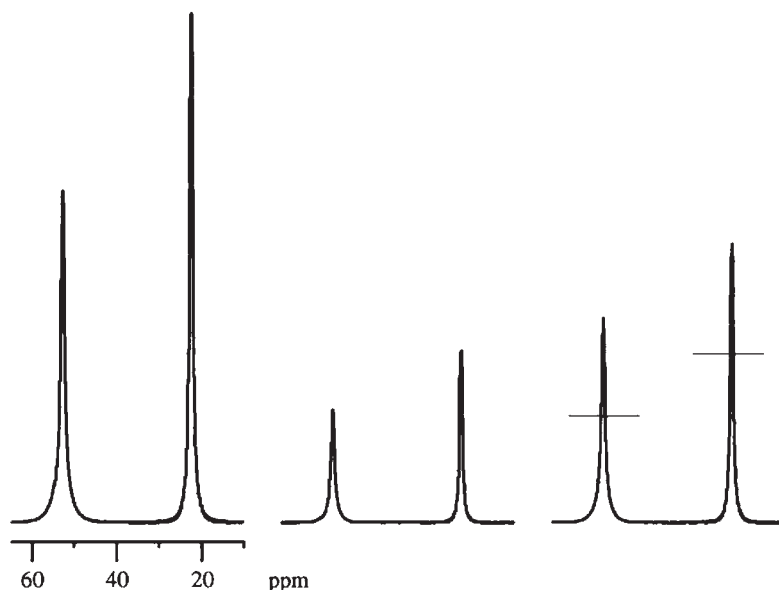


Figure 8 Experimental data on $^{13}\text{C}_2$ - $^{13}\text{C}_3$ -L-alanine obtained using: CP-MAS (left), HORROR DQF CP-MAS (middle), and $^{\text{OC}}$ HORROR DQF CP-MAS (right). The horizontal bars on the $^{\text{OC}}$ HORROR spectrum at right indicate the corresponding intensities (heights) of the HORROR signals. Reproduced with permission from ref. 62; Copyright Elsevier.

the spin states:

$$(I_{1z} - I_{2z}) \xrightarrow{\omega_D(I_{1x}I_{2x} + I_{1y}I_{2y})t} (I_{1z} - I_{2z}) \cos \omega_D t + 2(I_{1x}I_{2y} - I_{1y}I_{2x}) \sin \omega_D t$$

$$(I_{1x}I_{2y} - I_{1y}I_{2x}) \xrightarrow{\pi_x(I_2)} -(I_{1x}I_{2y} + I_{1y}I_{2x})$$
(17)

Here, $\omega_D = (\mu_0/4\pi)(\gamma^2\hbar(3\cos^2\theta - 1)/2r^3)$, r being the distance between the two spins 1 and 2, while θ is the angle that the internuclear vector makes with the magnetic field. The excitation process is reversed for reconversion: frequency-selective inversion transforms DQC to ZQC, and rotational resonance then converts ZQC to longitudinal difference magnetization. This is then followed finally by a $\pi/2$ pulse for readout. Spectral peaks obtained under rotational resonance conditions are however broadened or split by homonuclear dipolar couplings.

These authors also introduced pulse-assisted rotational resonance DQ excitation.⁶⁵ Here, the spinning frequency is displaced from rotational resonance. RF cycles are then inserted, as in rotational resonance echo schemes. Most of the spin evolution is still performed without RF fields, reducing problems associated with ^1H decoupling. Signal detection, being performed off rotational resonance, improves resolution and sensitivity.

Dusold and Sebal⁶⁶ discussed DQ filtration under rotational resonance conditions. Overall efficiencies of this procedure⁵¹ decrease when CSA is significant. Bechmann et al. concluded⁶⁷ that a pulse scheme of Nielsen et al.⁶⁸ is less prone to these effects.

More recently, a broadband rotary resonance recoupling sequence (B^2R^3) has been introduced by Duma et al.⁶⁹ for efficient ^{13}C – ^{13}C correlations, involving phase-alternated irradiation on the ^1H channel during the mixing time, with an RF amplitude close to the spinning frequency. No ^{13}C irradiation is involved during the mixing time.

In general, the operation of recoupling sequences for rare spin double quantum filtering applications is normally associated with the use of species with site-selective isotope labeling so that a large number of dipolar couplings would not be involved, which would complicate the analysis of the results.

The analysis of the generation of DQCs as a function of the preparation time is a common, fruitful approach in determining the relevant dipolar coupling constant information. For this purpose, the double quantum filtered signal intensity is analyzed as a function of the double quantum excitation time.

It may also be pointed out here that conjugate mixing, that is, a time-reversed reconversion pulse sequence, is to be preferred in such recoupling studies to avoid intensity cancellation owing to phase shifts among the different DQCs prepared (see Section 2.3.4). In the DQ case, the time-reversed reconversion pulse sequence is created simply by employing once again the excitation sequence, but with a 90° phase shift.

2.1.3 Creation of MQC under conditions of multi-exponential relaxation

As an important example of this case, we shall briefly discuss ^{23}Na .⁷⁰ This isotope has spin $3/2$ and involves three degenerate transitions in the absence of a

resolved quadrupolar coupling. The central transition (CT) ($1/2 \leftrightarrow -1/2$) has a different (slower) transverse relaxation rate (R_{2S}) as compared to the two outer transitions ($3/2 \leftrightarrow 1/2$ and $-1/2 \leftrightarrow -3/2$; R_{2F}) when the extreme narrowing condition is not satisfied. A 90° pulse applied to the spin system generates transverse magnetization, which corresponds to a first rank tensor of order 1; this gets transformed to third rank tensor components of order 1 under the influence of multi-exponential relaxation effects. (Note that second rank tensor components are not generated unless the quadrupole interaction is not averaged to zero, or unless the outer transitions were to decay with unequal rates.) The third rank component of order 1 thus generated may then be transformed to one of order 2 (i.e., DQC) by a subsequent pulse of the same (or opposite) phase as the initial pulse, while it may be transformed to one of order 3 (i.e., triple quantum coherence, TQC) by a pulse phase shifted by 90° with respect to the initial pulse. Thus, the standard MQC preparation sandwich functions in this case as well, free evolution during the preparation sandwich being under the influence of multi-exponential relaxation.

2.2 Evolution

2.2.1 Spin filtering

As noted earlier, the phase-cycled DQF experiment involves an infinitesimal evolution period of the DQC created at the end of the preparation sequence. In the case of gradient-controlled pathway selection, DQC evolves for a short duration of the order of 1 ms. This 'high pass' DQF already acts as a 'bandpass' two-spin filter when one is dealing with rare spins, such as ^{13}C . When one is dealing with abundant spins such as ^1H , the 'high pass' DQF may be transformed into what approaches a 'bandpass' filter, that is, in this case a two-spin filter, by introducing a variable evolution time, split in two equal halves with a refocusing pulse. The DQC of a two-spin- $1/2$ system does not evolve during this period; however, DQC of an n -spin- $1/2$ system ($n > 2$) does evolve under coupling. By variation of the evolution period over a cycle in terms of the relevant double quantum coupling frequency, therefore, such n -spin DQC contributions ($n > 2$) would average to zero, except where there is a central component in the spin multiplet of the DQC — which of course does not evolve in time.²⁸

2.2.2 Spectral editing

The SEMINA sequence has been proposed by Sørensen et al.^{71,72} for facilitation of the assignment of direct and long-range ^{13}C - ^{13}C couplings by identifying the total proton multiplicity for pairs of coupled ^{13}C spins. This is achieved by incorporating a SEMUT type editing⁷³ or double editing, following preparation of DQC. SEMINA sequences with a single-step and a two-step editing are shown in Figures 9 and 10, respectively.

The SEMINA sequences distinguish between $C_A H_n^A - C_B H_m^B$ systems with $m+n$ odd or even. This results because the SEMUT editing step during the double quantum evolution period ($2\tau_1$) confers a phase factor $(-1)^{m+n}$ on the ^{13}C DQC

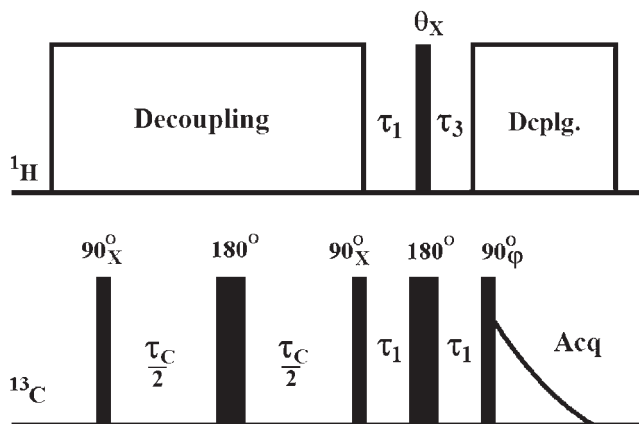


Figure 9 SEMINA-1 sequence for SEMUT edited INADEQUATE. $\tau_C = (2J_{CC})^{-1}$. To generate two sub-spectra with $n+m$ being odd or even (see text), θ may be chosen as 0° or 180° ; τ_1 may be set equal to τ_3 . In turn, τ_1 is chosen to be $(2J)^{-1}$, J being the sum of the one- and two-bond J_{CH} couplings in the fragment under consideration (see text).

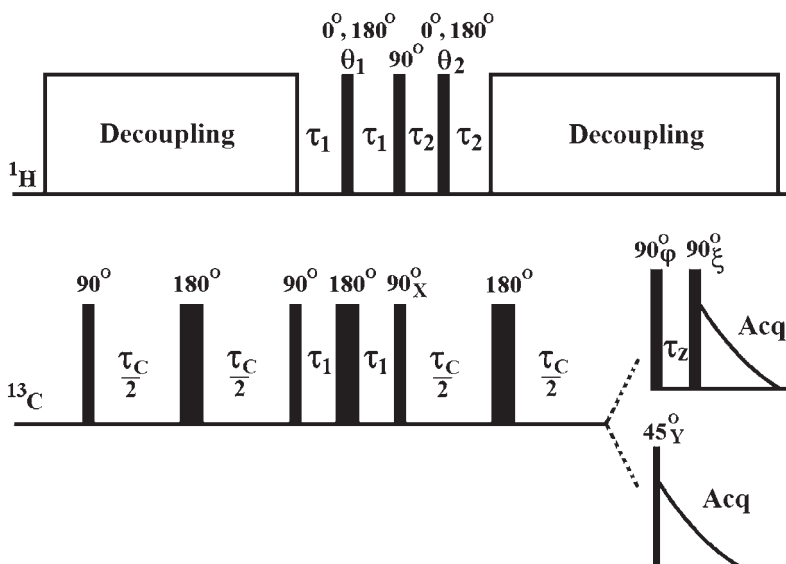


Figure 10 SEMINA-2 pulse sequence. A final 45_Y pulse or preferably a z filter serves to remove anti-phase components. τ_1 and τ_2 are ideally set to $(2J_{CH})^{-1}$. τ_C is set as for the sequence of Figure 9.

for a ^1H editing pulse flip angle of π , the $\text{CH}_n\text{--CH}_m$ fragment behaving in this respect much like a hypothetical CH_{n+m} system would in a SEMUT experiment. The second editing pulse on the ^1H channel in SEMINA-2 then serves to distinguish the parity of n and m , the second editing pulse flip angle also being 0 or π .

2.3 Reconversion

The standard reconversion strategy for a DQF experiment is to employ a 90° pulse. Such a pulse — with phase x , y , $-x$, or $-y$ — reconverts exclusively DQC of phase y for spin-1/2 systems. (It may be noted however that this is not true of scalar (or dipole) coupled spin-1 systems, where one-spin-1 DQC of phase x is also reconverted by such a pulse. It may be recalled that under conditions of scalar or dipolar coupling between two spins-1, the standard preparation sandwich produces spin states of the type $I_y^2 S_z$, which include DQC of x -phase (cf. Section 3.1.2). Clearly, such a state may be converted to states of the type $I_y^2 S_x$ or $I_z^2 S_y$ depending on the 90° reconversion pulse phase, these states being observable.^{74,75})

It has already been noted earlier that reconversion may be supplemented by a refocusing period allowing the AP SQC after reconversion to rephase, with a delay τ that includes a refocusing 180° pulse to generate IP signals; uniform excitation–detection may then be accomplished by supplementing this with τ averaging.

It may be mentioned that in the corresponding DQS experiments such as 2D INADEQUATE,³² $45^\circ/135^\circ$ or $60^\circ/120^\circ$ reconversion pulses have been employed. The former choice ensures optimum suppression of quad image peaks in the F_1 dimension with improved sensitivity (compared to the 90° reconversion pulse in this 2D context). The latter choice on the other hand ensures optimum sensitivity with a slight trade-off against quad image peak suppression in F_1 . These reconversion pulses convert both the x - and y -phase DQC in spin-1/2 systems, albeit with unequal amplitudes and unequal flip angle dependencies.^{1,2}

2.3.1 CR reconversion

More recently, there has been considerable interest in the sensitivity enhancement of such experiments, especially in the context of INADEQUATE-type sequences as applied to rare spins. In particular, it has been recognized that the upper bound on coherence transfer in two-spin-1/2 systems may be attained in practical implementations of coherence transfer from DQC to SQC.^{76–79} In fact, reconversion pulse sequences that involve ‘composite refocusing’ (CR) have been designed for 2D INADEQUATE that optimally convert DQC to SQC in either an echo type of transfer or an anti-echo type of transfer. In these experiments, optimal sensitivity is obtained by transition-selective reconversion to one of the doublet components, employing a non-selective pulse sequence.

The approach to the design of the CR sequence is briefly summarized below. The maximum unitary transfer efficiency a_{\max} from DQC to SQC may be calculated based on the singular value decomposition of the respective matrix representations of the initial state B and final state A , arranging the respective singular values as a vector Σ in descending (or ascending) order for each of the states, and calculating:

$$a_{\max} = \frac{\Sigma^A \cdot \Sigma^B}{\Sigma^A \cdot \Sigma^A} \quad (18)$$

For the transfer from $I_1^- I_2^-$ to the observable state $(I_1^- + I_2^-)$, this value turns out to be $\sqrt{2}/4$ for a two-spin-1/2 system. It turns out that this value may be reached by transforming the DQC in question to a single transition on each of the coupled spins. This is equivalent to a transformation of the state $|\alpha\alpha\rangle$ to the states $|\alpha\beta\rangle$ and $|\beta\alpha\rangle$, which in turn is equivalent to a rotation of $\pi/\sqrt{2}$ by the operator $(I_{1x}I_2^z + I_1^zI_{2x})$, that is, an inversion in an equivalent three-level spin-1 system. Here, I_i^z represents $(1/2)(1+2I_{iz})$. The required rotation may therefore be written in terms of non-selective elements as $(\pi/2\sqrt{2})(I_{1x} + I_{2x} + 2I_{1x}I_{2z} + 2I_{1z}I_{2x})$. Such a rotation is realized in terms of the pulse sequence shown in Figure 11, two additional versions of the CR sequence being shown in Figures 12 and 13. The first two versions are phase-cycled implementations, while the third is a gradient-controlled alternative.

Here, the values of the phases are a function of the coherence transfer pathway chosen (echo or anti-echo), as well as the doublet component of choice (α or β spin state of the coupled nucleus). One possible set of choices for the respective phases for the sequence of Figure 11, ϕ_1 – ϕ_6 , which leads to the β component and the anti-echo pathway is: 0, 0, $\pi/2$, 0, $3\pi/2$, $\pi/2$.

The functioning of the CR sequence of Figure 11 for the 1D case may be readily appreciated by following the spin state transformations that it leads to, of y -phase DQC and x -phase DQC. We track first the fate of y -DQC under the

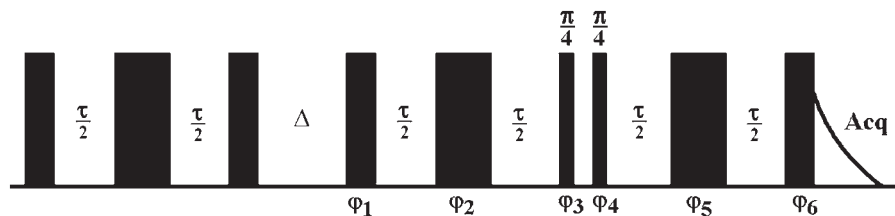


Figure 11 A one-dimensional version of INADEQUATE with composite refocusing (CR). τ is set to $(2J_{CC})^{-1}$. The thickest bars represent 180° pulses, while 90° pulses are thinner, the thinnest being 45° pulses. See text for one possible choice of pulse phases. Pulse phases are cycled in the customary INADEQUATE fashion.

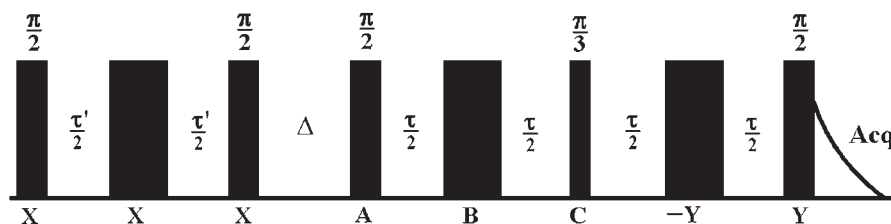


Figure 12 A one-dimensional version of INADEQUATE with composite refocusing (CR). The thickest bars represent 180° pulses. τ is set to $(2J_{CC})^{-1}$. This version consolidates the sequence with one fewer pulse and may be employed on modern spectrometers with digital phase shifters that can set essentially arbitrary phases. See text for one possible choice of pulse phases.

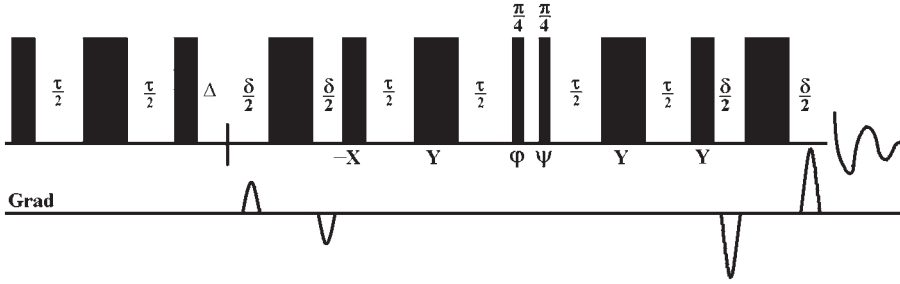


Figure 13 A one-dimensional version of INADEQUATE with composite refocusing (CR) and with gradient-controlled (echo) pathway selection. τ is set to $(2J_{CC})^{-1}$. See text for one possible choice of pulse phases.

sequence, starting at the end of the preparation sandwich:

$$\begin{aligned}
 2(I_{1x}I_{2y} + I_{1y}I_{2x}) &\xrightarrow{90^\circ_x} 2(I_{1x}I_{2z} + I_{1z}I_{2x}) \xrightarrow{180^\circ_x} -2(I_{1x}I_{2z} + I_{1z}I_{2x}) \\
 &\xrightarrow{\tau=(2J)^{-1}} -(I_{1y} + I_{2y}) \xrightarrow{45^\circ_y} -(I_{1y} + I_{2y}) \xrightarrow{45^\circ_x} -\frac{1}{\sqrt{2}}[(I_{1y} + I_{2y}) + (I_{1z} + I_{2z})] \\
 &\xrightarrow{180^\circ_{-y}} -\frac{1}{\sqrt{2}}[(I_{1y} + I_{2y}) - (I_{1z} + I_{2z})] \\
 &\xrightarrow{\tau=(2J)^{-1}} \sqrt{2}(I_{1x}I_{2z} + I_{1z}I_{2x}) + \frac{1}{\sqrt{2}}(I_{1z} + I_{2z}) \\
 &\xrightarrow{90^\circ_y} -\sqrt{2}(I_{1x}I_{2z} + I_{1z}I_{2x}) + \frac{1}{\sqrt{2}}(I_{1x} + I_{2x}) \\
 &\equiv \frac{1}{\sqrt{2}}(I_{1x}(1 - 2I_{2z}) + (1 - 2I_{1z})I_{2x}) \quad (19)
 \end{aligned}$$

If the period indicated by Δ in the 1D sequence is long enough to allow free precession of the DQC of y -phase that is generated by the preparation sandwich, as in a 2D experiment, x -phase DQC is produced as well. Its evolution under the sequence is described in turn as follows:

$$\begin{aligned}
 2(I_{1x}I_{2x} - I_{1y}I_{2y}) &\xrightarrow{90^\circ_x} 2(I_{1x}I_{2x} - I_{1z}I_{2z}) \xrightarrow{180^\circ_x} 2(I_{1x}I_{2x} - I_{1z}I_{2z}) \\
 &\xrightarrow{\tau=(2J)^{-1}} 2(I_{1x}I_{2x} - I_{1z}I_{2z}) \xrightarrow{45^\circ_y} -2(I_{1x}I_{2z} + I_{1z}I_{2x}) \\
 &\xrightarrow{45^\circ_x} -\sqrt{2}(I_{1x}I_{2z} + I_{1z}I_{2x}) + \sqrt{2}(I_{1x}I_{2y} + I_{1y}I_{2x}) \\
 &\xrightarrow{180^\circ_{-y}} -\sqrt{2}(I_{1x}I_{2z} + I_{1z}I_{2x}) - \sqrt{2}(I_{1x}I_{2y} + I_{1y}I_{2x}) \\
 &\xrightarrow{\tau=(2J)^{-1}} -\frac{1}{\sqrt{2}}(I_{1y} + I_{2y}) - \sqrt{2}(I_{1x}I_{2y} + I_{1y}I_{2x}) \\
 &\xrightarrow{90^\circ_y} -\frac{1}{\sqrt{2}}(I_{1y} + I_{2y}) + \sqrt{2}(I_{1z}I_{2y} + I_{1y}I_{2z}) \\
 &\equiv -\frac{1}{\sqrt{2}}(I_{1y}(1 - 2I_{2z}) + (1 - 2I_{1z})I_{2y}) \quad (20)
 \end{aligned}$$

An alternative version of the CR sequence requires one fewer pulse, but phase shifts other than 0° , 90° , 180° , and 270° . This sequence is shown in Figure 12. One possible set of choices for the phases A , B , and C , leading to the β component and the anti-echo pathway, is, respectively: $(3\pi/2)+2\mu$, $\pi/2+2\mu$, and μ , where μ is the magic angle (54.74°).

Phase cycles employed for the standard INADEQUATE experiment may be employed for these CR versions, implementing the phase cycle of the INADEQUATE reconversion pulse on the entire CR mixing sequence.

A gradient-controlled version of the CR sequence is displayed in Figure 13.

In this sequence, the phases φ and ψ correspond to $-y$ and $-x$, respectively, for selection of the anti-echo β component. A gradient-controlled version of the CR sequence with one fewer pulse is also known.

It may be noted that the CR sequences reconvert DQC of both phase x and phase y into transition-selective SQCs. The 2D INADEQUATE CR sequences are examples of coherence order and spin state-selective (COS^3) transformations.

2.3.2 LBR reversion

In the standard filter mode, only y -phase DQC is created at the end of the preparation time. It is therefore possible to design a simplified reconversion sandwich⁸⁰ whose efficiency at transforming y -phase DQC to single transition SQC matches the coherence transfer bound.^{77,78} The INADEQUATE sequence incorporating such an LBR reconversion sandwich is shown in Figure 14.

As compared to the CR sequence, this three-pulse sandwich has the advantage of a shorter duration as well as fewer pulses, and larger resulting J bandwidth. The LBR sequence, so called because it includes rotations under linear and bilinear spin operators, functions basically as follows.

DQC of y -phase is partially reconverted to AP SQC, whereupon it is allowed to evolve under coupling for a duration corresponding to $(2J)^{-1}$, the shifts being refocused; **in a two-spin-1/2 system — and in a quadrupole coupled spin-1**

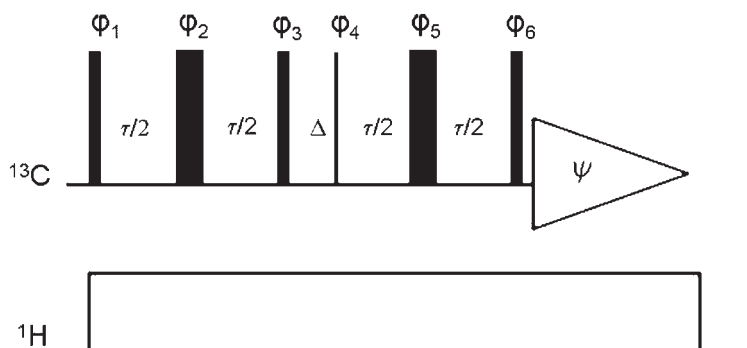


Figure 14 The 1D INADEQUATE LBR pulse sequence. The thinnest bar indicates a θ pulse (45° in the standard version), while thicker bars are 90° pulses, the thickest bars representing 180° pulses. Pulse phases φ_4 and φ_6 need to be in quadrature for single transition selection (see text for details of phase choices and phase cycling).

system — the remaining DQC does not evolve during this time; at the end of this interval of $(2J)^{-1}$, the AP SQC components have precessed by $\pm 90^\circ$ and have become IP; at this time, a 90° RF pulse is issued that has the same phase as the IP SQC and reconverts the remaining y -phase DQC quantitatively into AP SQC. The resulting superposition of IP and AP SQC leads to a single transition at each chemical shift provided their amplitudes match. Barring relaxation effects, transition selectivity is thus clearly optimal if the first reconversion pulse of the sandwich results in equal amplitudes of AP SQC and remnant DQC. This results in the choice of a 45° pulse.

A simple density matrix calculation, given below, clearly reveals the functioning of the LBR sequence in its role of converting $(\text{DQC})_y$ to single transitions at each chemical shift:

$$\begin{aligned}
 2(I_{1x}I_{2y} + I_{1y}I_{2x}) &\xrightarrow{\theta_y} 2c_\theta(I_{1x}I_{2y} + I_{1y}I_{2x}) - 2s_\theta(I_{1z}I_{2y} + I_{1y}I_{2z}) \\
 &\xrightarrow{\pi_y} -2c_\theta(I_{1x}I_{2y} + I_{1y}I_{2x}) + 2s_\theta(I_{1z}I_{2y} + I_{1y}I_{2z}) \\
 &\xrightarrow{2\pi J\tau I_{1z}I_{2z}} -2c_\theta(I_{1x}I_{2y} + I_{1y}I_{2x}) + 2c_J s_\theta(I_{1z}I_{2y} + I_{1y}I_{2z}) - s_J s_\theta(I_{1x} + I_{2x}) \\
 &\xrightarrow{90_x^\circ} -2c_\theta(I_{1x}I_{2z} + I_{1z}I_{2x}) - 2c_J s_\theta(I_{1z}I_{2y} + I_{1y}I_{2z}) - s_J s_\theta(I_{1x} + I_{2x}) \quad (21)
 \end{aligned}$$

Here, $c_\theta = \cos \theta$, $s_\theta = \sin \theta$, $c_J = \cos \pi J\tau$, and $s_J = \sin \pi J\tau$. Clearly then, for $\tau = (2J)^{-1}$, the final state σ_f of the two-spin system is given by:

$$\sigma_f = -2c_\theta(I_{1x}I_{2z} + I_{1z}I_{2x}) - s_\theta(I_{1x} + I_{2x}) \quad (22)$$

For the choice $\theta = \pi/4$, this final state obviously represents a single transition at each shift.

The high- or low-field component of the doublet may be selected by a number of alternative strategies:

- reversal of phase φ_4 of the initial θ reconversion pulse;
- change of the refocusing π pulse phase φ_5 in the reconversion sandwich by $\pm \pi/2$;
- reversal of phase φ_6 of the final 90° reconversion pulse;
- first reconversion pulse flip angle: $\theta = 3\pi/4$ or $\pi/4$.

The propagator of the sequence $\theta_\psi - \tau - \pi_\varphi - \tau - (\pi/2)_\chi$ may be written as:

$$U = e^{-i(\pi/2)I_\chi} e^{-i\pi I_\varphi} e^{-4\pi i J\tau I_{1z}I_{2z}} e^{-i\theta I_\psi} \quad (23)$$

We have for the density matrix evolution under this propagator:

$$\sigma(2\tau) = e^{-i(\pi/2)I_\chi} e^{-i\pi I_\varphi} e^{-4\pi i J\tau I_{1z}I_{2z}} e^{-i\theta I_\psi} \sigma(0) e^{i\theta I_\psi} e^{4\pi i J\tau I_{1z}I_{2z}} e^{i\pi I_\varphi} e^{i(\pi/2)I_\chi} \quad (24)$$

This may be rewritten employing phase shift operators as:

$$\begin{aligned}
 \sigma(2\tau) &= e^{-i\chi I_z} e^{-i(\pi/2)I_x} e^{i\chi I_z} e^{-i\varphi I_z} e^{-i\pi I_x} e^{i\varphi I_z} e^{-4\pi i J\tau I_{1z}I_{2z}} e^{-i\psi I_z} e^{-i\theta I_x} e^{i\psi I_z} \\
 &\sigma(0) e^{-i\psi I_z} e^{i\theta I_x} e^{i\psi I_z} e^{4\pi i J\tau I_{1z}I_{2z}} e^{-i\varphi I_z} e^{i\pi I_x} e^{i\varphi I_z} e^{-i\chi I_z} e^{i(\pi/2)I_x} e^{i\chi I_z} \quad (25)
 \end{aligned}$$

As noted earlier, the first pulse and last pulse must be in phase quadrature to generate a single transition instead of a doublet. In other words, the phase angles

χ and ψ must differ by $\pm\pi/2$. Taking the first pulse phase as $\pi/2$, the last pulse phase must therefore be 0 or π . Since the last pulse does not affect the IP transverse magnetization — being parallel with it in the rotating frame — but does change the sign of the AP magnetization created from the remaining DQC, phase reversal of the last pulse results in switching the selection of the single transition from one doublet component to the other.

Alternating the phase of the first pulse on the other hand does not affect the phase of the remaining DQC, but does reverse the sign of the AP magnetization — and eventually the IP magnetization — that is generated. This again results in switching the selected single transition.

Alternating the phase ϕ of the refocusing pulse does not switch the transition, but phase shifting it by $\pm\pi/2$ does. This may be readily understood on noting that any of the phases $\pm x$, $\pm y$ reverses the sign of the DQC remaining after the first pulse; however, when the refocusing pulse has the same (or opposite) phase as the first pulse, the sign of the AP magnetization generated by the first pulse is reversed as well. When the phase of the refocusing pulse is in quadrature ($\pm\pi/2$) with respect to the first pulse, however, the sign of the AP magnetization remains unchanged, which then results in switching the transition.

Relaxation effects during the LBR sandwich lead however to a different situation as compared to the preparation period. The equation to be satisfied for generation of a single transition is an equality of the amplitudes of IP and AP magnetization components of the same phase at the start of data detection. Assuming equal spin–spin relaxation rates of the two spins in question, this equality is given by:

$$A_{SQ} \sin(\pi J \tau) \exp\left(\frac{-\tau}{T_2^{SQ}}\right) = A_{DQ} \exp\left(\frac{-\tau}{T_2^{DQ}}\right) \quad (26)$$

Here, A_{SQ} and A_{DQ} are the amplitudes of AP transverse magnetization and DQC ($\sin\theta$ and $\cos\theta$, respectively), immediately after the first reconversion pulse. In other words, $\tau = (2J)^{-1}$ is the optimal reconversion time if the single quantum and double quantum amplitudes as well as relaxation rates are equal to each other. If, on the other hand, the relaxation rates are unequal, one may still operate at the same ‘ideal’ value of τ , but compensate for the differential relaxation rate by employing a suitable first reconversion pulse flip angle θ that generates a larger initial amplitude of the coherence which relaxes more rapidly. In this case, the equation to be satisfied is:

$$\tan \theta = \frac{\exp(-\tau/T_2^{DQ})}{\exp(-\tau/T_2^{SQ})} = \exp\left(-\frac{1}{2J} \left(\frac{1}{T_2^{DQ}} - \frac{1}{T_2^{SQ}}\right)\right) \quad (27)$$

When the DQ relaxation rate is higher than the SQ relaxation rate, the right-hand side is less than 1, implying that $\theta < \pi/4$. If on the other hand the DQ relaxation rate is lower than the SQ relaxation rate, the right-hand side is more than 1, leading to $\theta > \pi/4$. Examples of the two kinds of behavior are,

respectively, ^{13}C DQC at natural abundance (especially when heteronuclear dipolar interactions with ^1H dominate the ^{13}C relaxation) and spin-1 DQC (e.g., of ^2H) in lyotropic systems. For $\tau = (2J)^{-1}$, the single transition intensity with this optimal flip angle is given approximately, to first order in the relevant exponential factors, by:

$$\frac{1}{\sqrt{2}} \left[1 - \frac{1}{4J} \left(\frac{1}{T_2^{\text{SQ}}} + \frac{1}{T_2^{\text{DQ}}} \right) \right] \quad (28)$$

which reduces to $1/\sqrt{2}$ when the coupling is much larger than $\sim 78.5\%$ of the sum of the single and double quantum linewidths.

On the other hand, to maximize reconversion sensitivity at $\tau = (2J)^{-1}$, the criterion is to maximize the total intensity function:

$$\sin \theta \exp\left(\frac{-1}{2JT_2^{\text{SQ}}}\right) + \cos \theta \exp\left(\frac{-1}{2JT_2^{\text{DQ}}}\right) \quad (29)$$

The condition on θ is then readily obtained as:

$$\begin{aligned} \cos \theta \exp\left(\frac{-1}{2JT_2^{\text{SQ}}}\right) &= \sin \theta \exp\left(\frac{-1}{2JT_2^{\text{DQ}}}\right) \\ \Rightarrow \tan \theta &= \exp\left(\frac{1}{2J} \left(\frac{1}{T_2^{\text{DQ}}} - \frac{1}{T_2^{\text{SQ}}} \right) \right) \end{aligned} \quad (30)$$

For $\tau = (2J)^{-1}$, the single transition intensity with this optimal flip angle is now also given approximately, to first order in the relevant exponential factors, by:

$$\frac{1}{\sqrt{2}} \left[1 - \frac{1}{4J} \left(\frac{1}{T_2^{\text{SQ}}} + \frac{1}{T_2^{\text{DQ}}} \right) \right] \quad (31)$$

A multi-parameter optimization in terms of both τ and T_2 may also be performed.

The J dependence of the transfer function Z_a characterizing the selected component (excluding dispersive contributions, but including the combined effect of preparation and reconversion segments) is given for the CR sequence by:

$$Z_{a,\text{CR}} = \frac{1}{2\sqrt{2}} (\sin^2[\pi J\tau] + \sin^3[\pi J\tau]) \quad (32)$$

On the other hand, for the LBR sequence, it is given by:

$$Z_{a,\text{LBR}} = \frac{1}{2\sqrt{2}} (\sin[\pi J\tau] + \sin^2[\pi J\tau]) \quad (33)$$

In comparison, the basic INADEQUATE has the following J dependence, through its preparation sandwich:

$$Z_{a,\text{INADEQUATE}} = \frac{1}{2} \sin[\pi J\tau] \quad (34)$$

The J -bandwidth of the LBR sequence compares favorably with that of the CR sequence. This is readily seen on comparing the transfer functions of the 1D

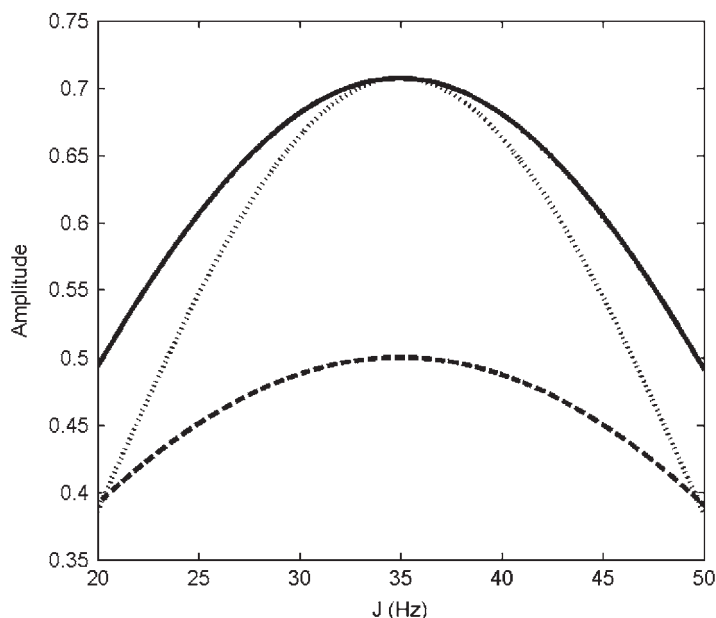


Figure 15 Amplitude of the absorptive component of the selected transition as a function of coupling constant, for INADEQUATE (bottom curve, dash), INADEQUATE CR (middle curve, dot), and INADEQUATE LBR (top curve, solid). Ref. 80; Copyright John Wiley & Sons.

INADEQUATE, 1D INADEQUATE CR, and 1D INADEQUATE LBR sequences which are plotted in Figure 15. Here, the nominal coupling constant J is set as 35 Hz. The intensity of the signal is plotted against J , in a range corresponding to $\pm 40\%$ variation of J .

From the plot, it may be noted that the 'flat' bandwidth of the 1D INADEQUATE LBR sequence is considerably higher than that of the 1D INADEQUATE CR sequence. At 40% deviation of the coupling constant from its nominal value, 1D INADEQUATE LBR results in a signal intensity of 1.04 units, whereas 1D INADEQUATE CR affords 0.86 units signal intensity. Signal intensity with 1D INADEQUATE under the same conditions amounts to only 0.8 units.

Typical practical results obtained employing INADEQUATE, as well as the CR and LBR versions are detailed in Figure 16, which displays the spectra that result working with a sample of sucrose.

Couplings in sucrose vary in the range from 38 to 53 Hz. Quantitative comparisons of the data displayed in Figure 16 show that the LBR spectra have 31% higher sensitivity as compared to standard INADEQUATE, while also being 18% higher in sensitivity compared to CR, when averaged over all the sites in the molecule.

The INADEQUATE LBR sequence is an example of spin state-selective (S^3) transformations.

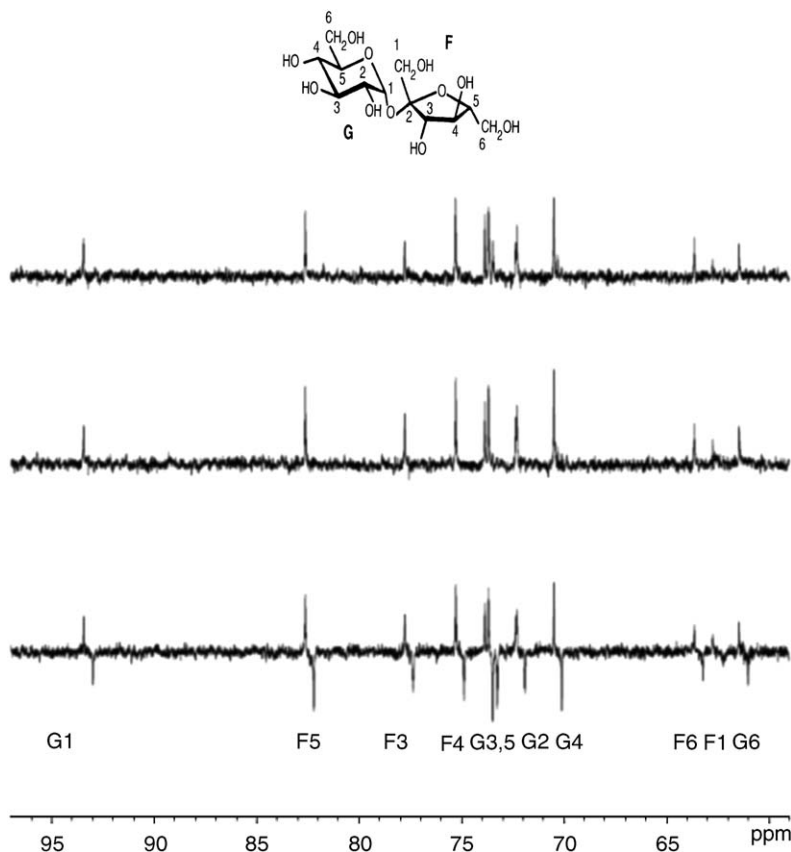


Figure 16 Expansion plots, in sequence, of 1D INADEQUATE (bottom trace), INADEQUATE LBR (middle trace), and INADEQUATE CR (top trace) spectra of a 0.5 M sucrose sample, recorded on a 400 MHz spectrometer. A total of 17k scans were acquired for each of the spectra, with a spectral width of 6,756.76 Hz and 8k data points; the delay (D1+AQ): 1.03 s. τ was set to 12.195 ms.

2.3.3 Detuned LBR sequence

The LBR sequence may be deliberately 'detuned'⁸⁰ to generate fractional intensity of the 'wrong' component of the doublet, while still enhancing the intensity of the selected component. This may be readily accomplished by altering the flip angle of the first pulse of the reconversion sandwich. The intensity variation of the two doublet components as a function of the first pulse flip angle is shown in Figure 17.

The utility of the detuned LBR sequence is that it permits measurement of the coupling and the chemical shift, while still resulting in enhanced sensitivity of the chosen component. A practical demonstration of this on sucrose is shown in Figure 18.

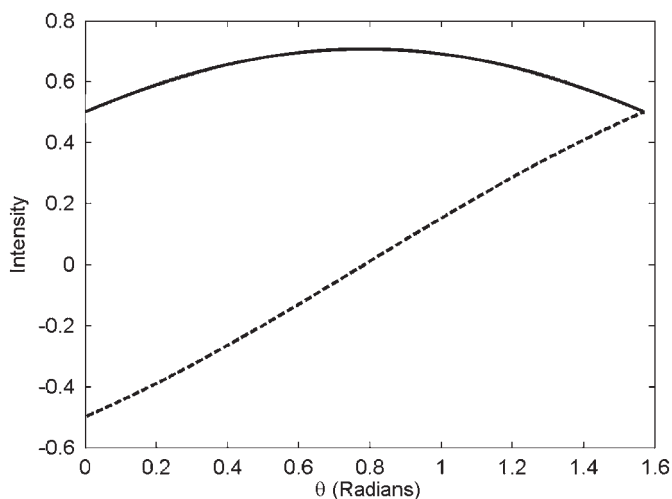


Figure 17 Plot of doublet component intensity for the detuned LBR sequence as a function of the first reconversion pulse flip angle θ , corresponding to the expressions $(\sin \theta + \cos \theta)$ (solid) and $(\sin \theta - \cos \theta)$ (dash). Ref. 80; Copyright John Wiley & Sons.

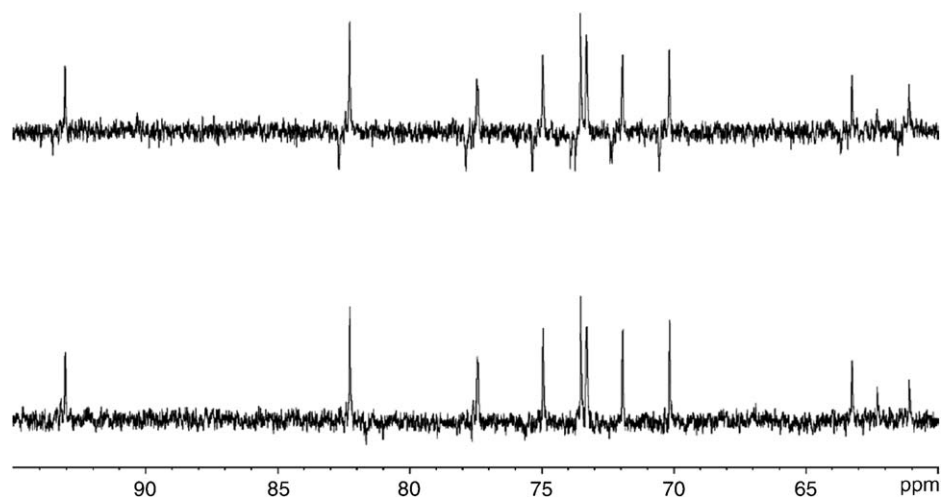


Figure 18 Expansion plots, in sequence, of 1D INADEQUATE LBR (bottom trace) and INADEQUATE LBR 22.5 (top trace) spectra of a 0.5 M sucrose sample, recorded on a 400 MHz spectrometer. A total of 17k scans were acquired for each of the spectra, with a spectral width of 4,761.9 Hz and 6k data points; the delay (D1+AQ) was set to 1.35 s. τ was set as for the spectra in Figure 16. Ref. 80; Copyright John Wiley & Sons.

2.3.4 Reconversion in the solid state

As pointed out in Section 2.1.2, reconversion of MQCs in the solid state (where one frequently works with powder samples at that) requires the special strategy

that the reconversion sequence be related to the preparation sequence by time reversal.⁴ We shall briefly summarize the case for this approach in the following.

We shall consider the spin system being prepared in a state of MQC starting from thermal equilibrium. For convenience, we shall consider that at the end of reconversion, the system is back in a longitudinal state as well — the signal arising from which may then be read out simply by the application of a suitable pulse. The state σ of the spin system following the chain of events (equilibrium \rightarrow preparation (τ) \rightarrow evolution (t_1) \rightarrow reconversion (τ')) is therefore given by:

$$I_z \xrightarrow{P(\tau)} I_z(\tau) \equiv P I_z P^\dagger \xrightarrow{E(t_1)} e^{-iH_1 t_1} P I_z P^\dagger e^{iH_1 t_1} \xrightarrow{R(\tau')} R e^{-iH_1 t_1} P I_z P^\dagger e^{iH_1 t_1} R^\dagger \quad (35)$$

The propagators P and R involve exponential operators such as $e^{-iH_P t}$ and $e^{-iH_R t}$, respectively, where H_P and H_R denote effective Hamiltonians (e.g., average Hamiltonians) for the respective processes. This form is explicitly shown above in the case of the propagator describing evolution of the system during t_1 , where H_1 is the Hamiltonian effective during this time. It may be recalled that the propagators are unitary, that is, their adjoint equals their inverse.

The expectation value of the ‘observable,’ $\langle I_z \rangle$, is therefore given by:

$$\text{Tr}(I_z \sigma) = \text{Tr}(I_z R e^{-iH_1 t_1} P I_z P^\dagger e^{iH_1 t_1} R^\dagger) = \text{Tr}((R^\dagger I_z R e^{-iH_1 t_1})(P I_z P^\dagger e^{iH_1 t_1})) \quad (36)$$

The invariance of the trace to cyclic permutations has been employed in the above. We may evaluate the trace in any convenient basis set; we choose the basis in which the Hamiltonian during the evolution time, H_1 , is diagonal. We now have:

$$\begin{aligned} \text{Tr}(I_z \sigma) &= \sum_{a,b} (R^\dagger I_z R e^{-iH_1 t_1})_{ba} (P I_z P^\dagger e^{iH_1 t_1})_{ab} \\ &= \sum_{a,b} (I_z(-\tau') e^{-iH_1 t_1})_{ba} (I_z(\tau) e^{iH_1 t_1})_{ab} \\ &= \sum_{a,b} (I_z(-\tau') e^{-i\omega_a t_1})_{ba} (I_z(\tau) e^{i\omega_b t_1})_{ab} \\ &= \sum_{a,b} (I_z(-\tau'))_{ba} (I_z(\tau))_{ab} e^{-i(\omega_a - \omega_b)t_1} \end{aligned} \quad (37)$$

It is to be noted that the transformations of I_z under the preparation and reconversion (or mixing) propagators (P and R , respectively) would in general involve complex coefficients since multiple quantum processes are involved — unlike, for example, a situation where transverse I_x magnetization (a single quantum state) is produced by their action. The above equation indicates therefore the interference of a number of different closely spaced frequencies ($\omega_a - \omega_b$) with different phase factors, which is bad news for the signal strength. The way out is to ensure that the reconversion propagator R is the adjoint of the preparation propagator P (i.e., its inverse, owing to the fact that time propagators such as R are unitary) — which requires also that τ' be set equal to τ . It is because the exponent (H_P) t in the propagator R now changes sign with respect to the exponent in the propagator P that this is termed time reversal.

Under this condition, we have:

$$\begin{aligned}
 R = P^\dagger &\Rightarrow \text{Tr}(I_z \sigma) = \sum_{a,b} (I_z(-\tau'))_{ba} (I_z(\tau))_{ab} e^{-i(\omega_a - \omega_b)t_1} \\
 &= \sum_{a,b} (R^\dagger I_z R)_{ba} (P I_z P^\dagger)_{ab} e^{-i(\omega_a - \omega_b)t_1} \\
 &= \sum_{a,b} (P I_z P^\dagger)_{ba} (P I_z P^\dagger)_{ab} e^{-i(\omega_a - \omega_b)t_1} \\
 &= \sum_{a,b} |(P I_z P^\dagger)_{ab}|^2 e^{-i(\omega_a - \omega_b)t_1} \quad (38)
 \end{aligned}$$

In the above, we have used the property that the operator I_z is Hermitian and remains so under a unitary transformation with the propagator P (or R), which has the consequence that $[I_z(\tau)]_{ab} = [I_z(\tau)]_{ba}^*$.

With the amplitude of each frequency term now being positive (or zero), signal cancellation owing to different phase factors associated with different frequencies of the oscillatory terms is minimized — and the signal strength maximized. As noted earlier in Section 2.1.2, in the DQ case time reversal is most simply accomplished by employing the same sequence for reconversion as for preparation, but with a 90° phase shift.

2.3.5 Signal resulting on reconversion of MQC mediated by multi-exponential relaxation

In this case, characteristic lineshapes result that correspond to the Fourier transform of the difference of two exponentially decaying functions of time, leading to a pseudo ‘second derivative’ type lineshape.^{70,81} The form of the time evolution during signal acquisition in the time domain may be written as:

$$f(t) \sim \frac{\sqrt{6}}{5} [\exp(R_1^{(1)*} t) - \exp(R_2^{(1)*} t)] \quad (39)$$

Here, $R_i^{(1)*}$ are apparent transverse relaxation rates ($i = 1$: outer transitions; $i = 2$: inner transition), while the corresponding $R_i^{(1)}$ are transverse relaxation rates given in terms of the relevant spectral density functions J for the respective single quantum transitions by:

$$\begin{aligned}
 R_1^{(1)} &= -C(J_0 + J_1) \\
 R_2^{(1)} &= -C(J_1 + J_2) \\
 C &= \frac{1}{40} \left(\frac{e^2 q Q}{\hbar} \right)^2 \left(1 + \frac{\eta^2}{3} \right) \quad (40)
 \end{aligned}$$

Here $e^2 q Q$ represents the quadrupolar coupling, while η is the asymmetry parameter. In turn, the spectral density functions are given in terms of the Larmor frequency ω_0 and the motional correlation time τ_c by:

$$J_n = \frac{2\tau_c}{1 + (n\omega_0\tau_c)^2} \quad (41)$$

Taking into account the MQC creation during the refocused preparation time τ , as well as time evolution of SQC during the acquisition time t , we find for the signal amplitude in terms of the equilibrium magnetization M_0 :

$$M(t, \tau) = \frac{3}{20} M_0 \left[\exp\left(\frac{-\tau}{T_{2S}^*}\right) - \exp\left(\frac{-\tau}{T_{2F}^*}\right) \right] \left[\exp\left(\frac{-t}{T_{2S}^*}\right) - \exp\left(\frac{-t}{T_{2F}^*}\right) \right] \quad (42)$$

The resulting spectral lineshape is clearly the difference of two Lorentzians of equal area, characterized by two different linewidths corresponding to the fast and slow decay time constants T_{2F}^* and T_{2S}^* .

3. APPLICATIONS OF DQF EXPERIMENTS

3.1 Solution state

Double quantum filtered experiments have been extensively developed and applied to solution state NMR. We categorize the applications broadly into spin-1/2 related and spin-1/spin-3/2 related.

3.1.1 Spin-1/2 systems

Hore et al.⁸² introduced the ‘double quantum transitions for finding unresolved lines’ (DOUBTFUL) experiment to identify two-spin systems with a specific double quantum frequency. The experiment is especially useful for proton NMR. It involves the same pulse sequence as 1D INADEQUATE, except for averaging over a range of values of the DQF delay t_1 (which occurs in place of Δ , the short delay between end of DQ preparation and start of reconversion). Averaging is performed typically over half a dozen or more systematically incremented values of t_1 so as to average out all DQCs that precess during t_1 — except the selected DQC that remains unmodulated during t_1 since the transmitter is placed at the center of the desired AB/AX spectrum, so that the algebraic sum of the relevant offsets becomes zero. AP signals result from the chosen spin pair. The authors demonstrated the experiment on an equimolar mixture of β -nicotinamide adenine dinucleotide (NADH) and NADH *c*-2'-phosphate (NADPH) in D_2O .

Bain et al.⁸³ discussed the selectivity of multiplet selection by the DOUBTFUL experiment. The authors discussed a variant of DOUBTFUL that incorporates a spin echo at the end of the basic sequence to generate IP doublets. They showed that in the limit of large n and small t the signal amplitude of this experiment varies as:

$$\frac{\sin(\omega t_f)}{\omega t_f} \quad (43)$$

where $t_f = nt$, n being the number of steps of variation of the DQ filter delay, the step size being t , and ω the angular frequency of double quantum precession relative to the carrier. The selectivity of the experiment may therefore be defined as the zero crossing frequency of the sinc function, that is, π/t_f in angular

frequency units. Any multiplet whose DQ frequency lies within $\pm \nu_f = \pm 1/(2t_f)$ Hz of the carrier will therefore be detected as positive signals by DOUBTFUL. Multiplets whose DQ frequencies lie between ν_f and $2\nu_f$ will also be detected, however, as negative signals of reduced amplitude. The authors demonstrated these effects on the triribonucleotide diphosphate UpUpC.

Bolton⁸⁴ demonstrated that in proton NMR, identification of all neighbors of a particular spin *A* may be achieved as follows: selective saturation of spin *A* is first performed followed by DQF. A difference spectrum is then constructed with and without saturation of *A*. This serves to identify signals only from *A* and its neighbors. The multiplet pattern of the neighbor spin corresponds to the difference between the sub-spectra associated with the two spin states of spin *A*. This approach was demonstrated on cytidine.

Novič et al.⁸⁵ described *z*-filtered DQ NMR spectra and their automated analysis by pattern recognition. Their sequence, valuable for systems with four or more spins, involves a two-pulse DQ reconversion strategy, with the flip angles being β_y (*ca.* 40°) and β' (*ca.* 20°), separated by a short delay to allow phase shifting.

Nakai and McDowell⁸⁶ presented 1D and pure-phase 2D versions of INADEQUATE with refocusing. They illustrated their approach with applications to hexanoic acid and hexadecanoic acid.

INADEQUATE has also been performed in indirect detection mode, various versions of this experiment having been developed by Keller and Vogele,⁸⁷ Weigelt and Otting,⁸⁸ Reif et al.,⁸⁹ Meissner et al.,⁹⁰ and Kövér and Forgó,⁹¹ the latter being a *J*-modulated version of ADEQUATE.⁸⁹

A double *J*-modulated (DJM) proton-detected INEPT INADEQUATE experiment has been described by Pham et al.⁹² The experiment permits simultaneous correlation of directly bonded carbons as well as those separated by multiple bonds, while also providing the values of all the J_{CC} couplings. Two intervals during which carbon-carbon couplings evolve are also incremented in concert with the DQ evolution period. The method has been demonstrated on a monosaccharide.

Jin et al.^{93,94} have developed ¹³C-detected IPAP INADEQUATE, as well as ¹H-detected IPAP DEPT INADEQUATE and IPAP RINEPT INADEQUATE for the measurement of long-range ¹³C-¹³C couplings. Both versions employ BEBOP and BIBOP pulses derived by optimal control procedures⁹⁵⁻⁹⁷ for reducing the duration of broadband excitation and inversion/refocusing pulses, respectively, with limited RF amplitude. The efficiency of the indirect detection version of these experiments has been further improved by incorporating the refocusing of ¹*J*_{CH} couplings prior to the preparation of DQCs, as well as by proton decoupling during the long evolution period. IP or AP doublets are generated and subsequently edited suitably to yield accurate values of small ¹³C-¹³C couplings. The methods have been illustrated on mono- and di-saccharide samples.

3.1.2 Spin-1 and spin-3/2 systems

Indirect detection of spin-1 DQC in liquids has been described by Yen and Weitekamp.⁹⁸ The authors excited spin-1 DQC of ¹⁴N (spin 5) in solution state

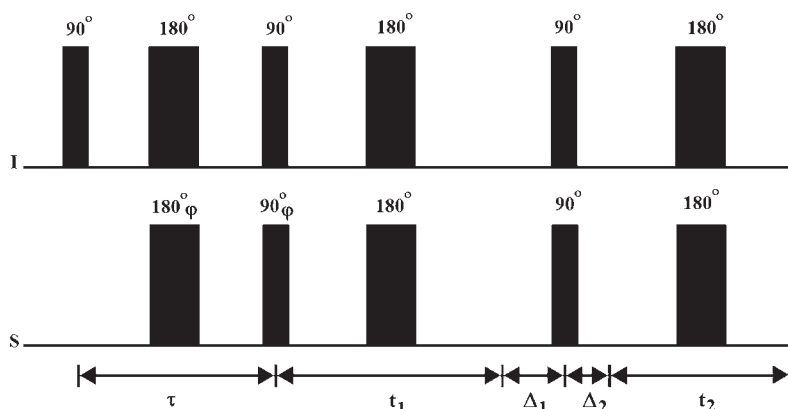


Figure 19 Pulse sequence for heteronuclear MQS, for example, for indirect excitation/detection of ^{14}N DQS in solution, via non-vanishing J_{NH} . The phase $\varphi = \Delta\omega t_1$ in accordance with the TPPI procedure. The echo top is sampled at the end of t_2 .

employing its resolved heteronuclear scalar coupling to ^1H (spins I) in the NH_4^+ ion as the means to do so. The pulse sequence is shown in Figure 19. They carried out this investigation on 8M NH_4NO_3 in acidified aqueous solution and chose the delay periods Δ_1 and Δ_2 for observation of the coherence transfer echo on the proton channel: $2\gamma_S\Delta_1 = \gamma_I\Delta_2$. It may be noted that spin-1 DQC is generated in this experiment despite the absence of ^{14}N quadrupolar coupling.

The propagator of the preparation segment of this sequence may be readily shown to be:

$$U = \exp\left(-2\pi i J \tau_p S_y \left(\sum_{i=1}^4 I_{iy}\right)\right) \exp\left(i \frac{\pi}{2} S_x\right) \quad (44)$$

The state of the spin system at the end of the preparation period may therefore be shown to be:

$$\begin{aligned} & \sum_{i=1}^4 (I_{iz}(1 + S_y^2(\cos 2\pi J \tau_p - 1)) + I_{ix}S_y \sin 2\pi J \tau_p) \\ & \equiv I_z(1 + S_y^2(\cos 2\pi J \tau_p - 1)) + I_x S_y \sin 2\pi J \tau_p \\ & \quad \text{with} \\ & I_z = \sum_{i=1}^4 I_{iz}, \quad I_x = \sum_{i=1}^4 I_{ix} \end{aligned} \quad (45)$$

For the choice of preparation time τ_p as $(2J)^{-1}$, therefore, one-spin DQC of the spin-1 system S is maximized, while two-spin heteronuclear MQC of the spin-1/2–spin-1 system vanishes.

The resulting ^{14}N DQC, if allowed to evolve, generates on indirect detection a (1, 1, 0, 1, 1) quintet with splittings $2J$ and with the central line missing, as shown in Figure 20. In order to effect indirect detection, a 90° pulse pair is clearly required following t_1 .

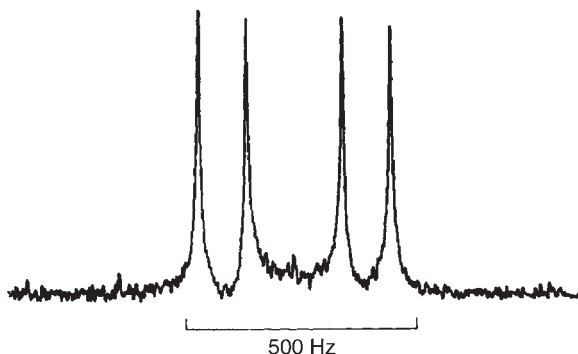


Figure 20 The 185 MHz ^1H -detected ^{14}N DQS of 8 M NH_4NO_3 in acidified aqueous solution. TPPI/ t_1 refocusing; $\tau = t_2 = 10$ ms; ^1H carrier on resonance; ^{14}N carrier 0.85 kHz off resonance; $\Delta t_1 = 200$ μs , $\Delta_1 = 11.327$ ms, $\Delta_2 = 1.618$ ms, satisfying the relation for coherence transfer echo filtering. Reproduced with permission from ref. 98; Copyright Elsevier.

Chandrakumar³⁷ showed in the same vein that homonuclear DQCs of spin-1 systems in solution state may also be excited and indirectly detected in the absence of quadrupolar couplings, given a homonuclear scalar coupling to another spin-1. The standard preparation sequence $(\pi/2)_{\varphi}-\tau/2-(\pi)_{\varphi}-\tau/2-(\pi/2)_{\varphi+\psi}$ when applied to such a scalar coupled two-spin-1 system leads, with $\varphi = x$ and $\psi = 0$, to the following state σ of the spin system:

$$\sigma = s_{2J}(I_y S_x + I_x S_y) + (c_{2J} - 1)(I_y^2 S_z + I_z S_y^2) + (I_z + S_z) \quad (46)$$

This state of the system clearly includes two-spin DQC of phase y (first term on the right) as well as one-spin DQC of phase x (contained in the second term), besides longitudinal magnetization (third term).

On the other hand, with $\varphi = x$ and $\psi = 90^\circ$, we find for the state of the spin system:

$$\sigma = s_{2J}(I_x S_z + I_z S_x) + (I_y + S_y) + (c_{2J} - 1)(I_x^2 S_y + I_y S_x^2) \quad (47)$$

This state includes two-spin TQC of phase y (contained in the third term on the right), besides AP and IP transverse magnetization of the two spins (first two terms).

It has been shown by Chandrakumar⁹⁹ and Chandrakumar et al.¹⁰⁰ that one-spin DQC in a scalar coupled two-spin-1 system gives rise to a DQ multiplet that is a doublet with splitting $4J$, while two-spin DQC in such a system gives rise to a DQ multiplet that is a triplet with splitting J . Further, one-spin DQC has a smaller relaxation rate⁹⁹ than either SQC or two-spin DQC.

These features are exemplified by the spectra of $[3,3' \text{-}^2\text{H}_2]\text{norcamphor}$ shown in Figure 21. This system has a ^2H - ^2H geminal coupling of 0.35 Hz, which is barely resolved in 1D mode after applying a resolution enhancement filter. In the

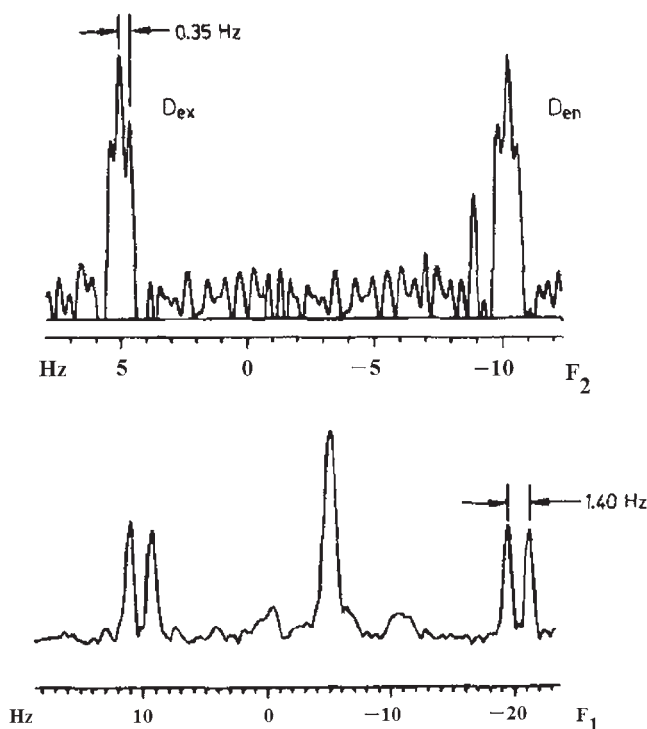


Figure 21 61.42 MHz ^2H NMR spectrum of $[3,3'\text{-}^2\text{H}_2]\text{norcamphor}$. (Top trace) The corresponding resolution-enhanced 1D ^2H spectrum. (Bottom trace) F_1 projection of a ^2H , ^2H double quantum spectrum run in pure phase (TPPI) mode with ^1H decoupling; the complete resolution of the one-spin double quantum multiplet is to be contrasted against the total lack of resolution of the two-spin double quantum multiplet. Adapted from ref. 100; Copyright John Wiley & Sons.

2D double quantum spectrum on the other hand, the F_1 dimension clearly displays the expected magnification of the coupling, as well as line narrowing, resulting in complete resolution of the doublet structure, as shown in the F_1 projection displayed in Figure 21.

Venkata Raman and Chandrakumar¹⁰¹ have exploited this difference in behavior under coupling to separate the two types of DQC from one another, by a J filter experiment; the pulse sequence is shown in Figure 22.

For a given J value, a finite evolution time with a refocusing pulse at the mid-point permits separation of one-spin-1 DQC responses from two-spin-1 DQC responses with an appropriate choice of the evolution time: no t_1 averaging is involved, unlike in standard spin filtering. This has been demonstrated on two-spin-1/2 mimics of spin-1 and an example is shown in Figure 23.

Ramesh and Chandrakumar⁸⁰ demonstrated that the LBR sequence may be applied to spin-1 systems in phases with residual order, such as lyotropics, for transition-selective reconversion of one-spin-1 DQC in such systems. In this application as well, shown in Figure 24, it turns out that the LBR sequence results

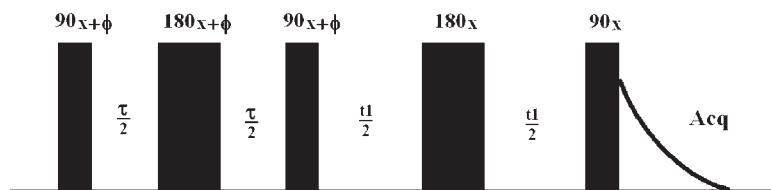


Figure 22 Pulse sequence for DQJ filter experiment. ϕ is stepped through the standard double quantum phase cycle with concomitant phase alternation of the receiver.

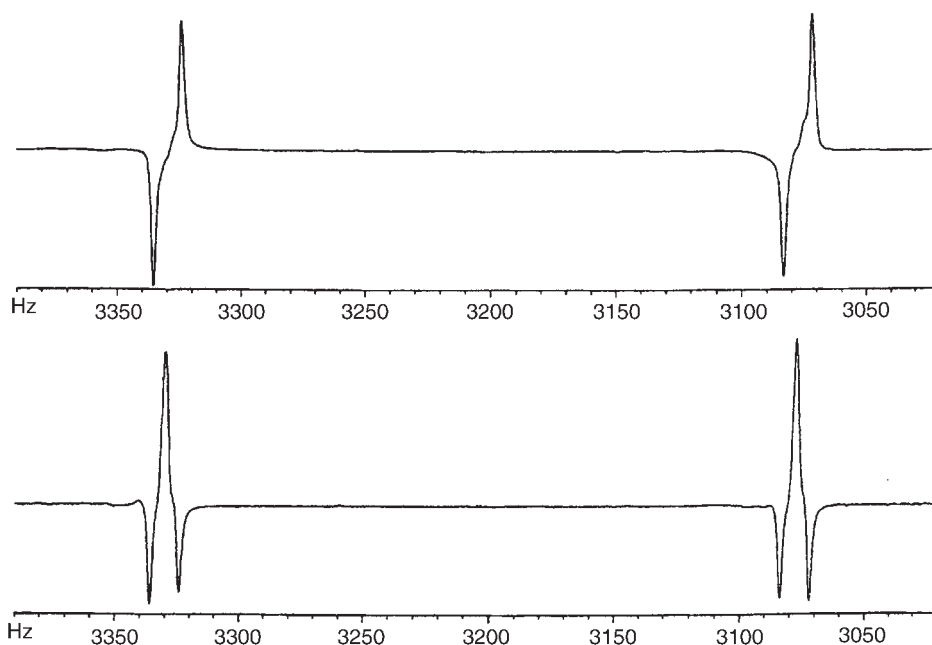


Figure 23 Experimental ^1H spectra of the DQJ filter experiment on 2-aminoethanol. The top trace corresponds to two-spin DQC selection obtained with $t_1 = 21.78 \text{ ms } (8J)^{-1}$, while the bottom trace corresponds to one-spin DQC selection resulting from the choice of $t_1 = 87 \text{ ms } (2J)^{-1}$. Ref. 101; Copyright Taylor & Francis.

in 32% sensitivity gain over standard INADEQUATE, 58% over refocused INADEQUATE, and 14% over the CR version — and in fact 5% over the corresponding single 90° pulse experiment with signal averaging!

Studies of dissolution of structured surfactant using localized DQF and cyclic J cross-polarization editing were described by Ciampi et al.¹⁰² Liquid crystalline phases form at the water-surfactant interface. The anisotropic motion of D_2O in the liquid crystalline phases offers a selective visualization of the surfactant/water interface, the quadrupolar splittings offering a quantitative measure of surfactant concentration. The composition of the liquid crystalline phase may be

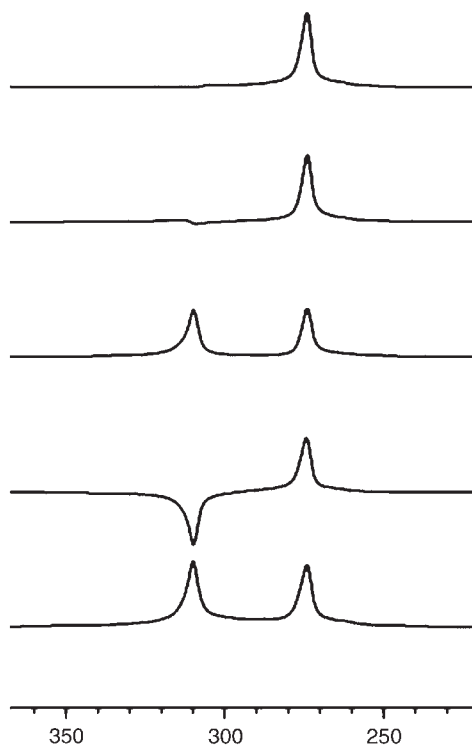


Figure 24 1D expansion plots, in sequence, of single pulse spectrum (90° pulse excitation, bottom trace) and DQF, refocused DQF, DQF CR, and DQF LBR (top trace) spectra of a 1.2 molal CTAB/ D_2O sample, recorded on a 400 MHz spectrometer. Two hundred and fifty-six scans were acquired for each of the spectra, with 4,058.44 Hz spectral width and 8k data points. Relaxation delay was set to 1 s. Ref. 80; Copyright John Wiley & Sons.

followed as a function of time at different sample locations, by comparison with completely dissolved samples at different water concentrations.

Sharf et al.¹⁰³ showed that DQF spectra of cartilage are the result of anisotropic motion of D_2O due to binding to fibrous collagen in the tissue. DQF lineshapes obtained as a function of preparation time could be fitted to obtain the average residual quadrupolar interaction (110 Hz, unresolved), its standard deviation (73 Hz), and the transverse relaxation rate (63 s^{-1}).

Discrimination between different compartments of sciatic nerve by 2H DQF NMR has been described by Shinar et al.¹⁰⁴ Rat sciatic nerve equilibrated with deuterated saline gives rise to three quadrupolar split water signals. Based on the time course of their shift by Co salts, they were assigned to epineurium (120 Hz quadrupolar splitting), endoneurium (470 Hz), and intra-axonal compartments (9 Hz). The DQF pulse sequence eliminated the signal of bulk water which experiences isotropic motion. Different preparation times maximize the three different compartmental water signals, and shift reagents may therefore be avoided in the DQF pulse sequence.

Multiple quantum filtered quadrupole echo sequences were proposed for ^2H and ^{23}Na by Eliav and Navon.¹⁰⁵ They demonstrated applications to cartilage and showed that the difference between relaxation rates determined by the multiple quantum filtered echo technique and the standard multiple quantum filtered spectroscopy is diagnostic of the anisotropic motion that leads to residual quadrupolar interactions.

Jelicks and Gupta¹⁰⁶ investigated the DQF NMR of ^{23}Na in cells and tissues and the quenching of extracellular coherence by paramagnetic species. They concluded that DQF NMR of cells and tissues allows detection of biexponentially relaxing $^{23}\text{Na}^+$. However, they showed that the signal detected is not solely due to intracellular $^{23}\text{Na}^+$ but contains a significant contribution from extracellular $^{23}\text{Na}^+$ which may be quenched by interaction with a paramagnetic reagent such as dysprosium bis(tripolyphosphate), $[\text{Dy}(\text{PPP}_i)_2]^{7-}$.

Hutchison et al.¹⁰⁷ carried out an evaluation of DQF for measurement of intracellular ^{23}Na concentration, the system studied being BSA in water. The authors concluded that this approach will not provide a useful measure of intracellular sodium in *in vivo* tissue samples.

Measurement of intracellular sodium in perfused rat mandibular salivary gland by DQF ^{23}Na NMR at 8.45 T was reported by Seo et al.¹⁰⁸ They observed signals from intracellular and interstitial ^{23}Na at 25°C. The resonance due to intracellular ^{23}Na consisted of two Lorentzian components, a sharp component from the CT and a broad component from the outer transitions, with the T_2 being, respectively, 95 and $1,360\text{ s}^{-1}$. The signal from interstitial ^{23}Na had longer relaxation times (corresponding to 71.1 and 42.8 s^{-1}) and disappeared on administration of dysprosium triethylenetetramine-*N,N,N',N'',N''',N'''*-hexaacetic acid (TTHA).

Reddy et al.¹⁰⁹ analyzed the influence of inhomogeneous RF fields on DQF and TQF experiments on spin-3/2 nuclei undergoing biexponential relaxation. The authors showed that the on resonance, three-pulse triple quantum filter without the 2θ refocusing pulse is 100% more sensitive than the corresponding DQF. Used with surface coils, the three-pulse as well as four-pulse filters (which include the 2θ pulse) act as depth pulses, yielding spatial localization. The three-pulse filter is more sensitive than the four-pulse filter. The authors went on to experimentally verify their predictions employing a homogeneous RF field with a cosine coil.

The *in vivo* NMR of Na^+ ions in ordered environments has been investigated by Kemp-Harper et al.¹¹⁰ DQF experiments with 54.7° pulses and the Jeener-Broekaert sequence were employed to investigate systems with residual quadrupolar couplings in excised tissues, cell suspensions, and *in vivo*. The authors demonstrated this approach with a surface coil to observe the ^{23}Na signal in anisotropic environments in human nasal cartilage.

Tauskela et al.¹¹¹ reported an extracellular (anisotropic, second rank tensor) contribution to the DQF ^{23}Na signal in isolated perfused rat hearts. As compared to single quantum experiments, MQF ^{23}Na NMR results, in general, in superior resolution of intra- and extracellular resonances, and significantly better sensitivity to increases in intracellular Na^+ , the MQF spectra being acquired

without the addition of shift or relaxation reagents. Further, DQF ^{23}Na NMR is a very sensitive technique to detect motional anisotropy, the presence of a residual quadrupole coupling having been reported for bovine cartilage, intra- and extracellular environments of erythrocytes, as well as brain tissue. Residual quadrupolar coupling results in a second rank tensor contribution to the observed ^{23}Na signal (*cf.* Section 2.1.3). A $90^\circ-\tau/2-180^\circ-\tau/2-\theta-t_1-\theta-\text{Acq.}$ sequence was employed for double quantum filtered and triple quantum filtered experiments, t_1 being a short delay of *ca.* 20 μs . For the triple quantum filtered case, θ was set to 90° ; for the double quantum filtered experiment the choice of $\theta = 54.7^\circ$ permits the acquisition of signals from the second rank tensor pathway alone, while for $\theta = 90^\circ$ both second and third rank tensor contributions to the signal are acquired, with opposite phase. The authors concluded that under certain DQ preparation conditions, it would be possible to estimate the intracellular Na^+ concentration of isolated perfused rat hearts by DQF ^{23}Na NMR without having to add shift or relaxation reagents.

Mouaddab et al.⁸¹ described the absolute quantification of the bound fraction of $^{23}\text{Na}^+$ by DQ filtered ^{23}Na spectroscopy. They performed a deconvolution of the lineshape resulting from the biexponential decay in such systems, where MQ creation is controlled by multi-exponential relaxation (see Section 2.3.5); an experimental spectrum from their work is shown in Figure 25. They showed further that the area under the positive Lorentzian component resulting on deconvolution of the signal closely matches the area between the zero derivative points (minima) of the composite lineshape. Their method was validated on a cationic exchange resin that had a quantitatively controlled number of Na^+ binding sites. The authors showed that absolute quantification of bound and free fractions of Na^+ is possible. This is of considerable interest as determining factors in the characterization of salted/brined/dried food products.

The lineshape resulting from Fourier transformation of the biexponential decay function that results after reconversion of DQC generated under

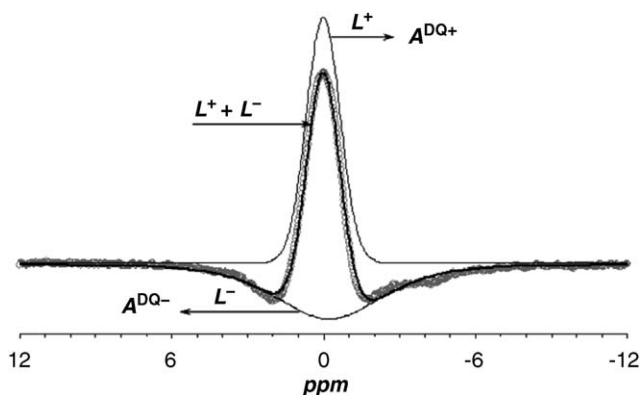


Figure 25 Experimental DQ spectrum (gray circles) of resin sample ($[\text{Na}^+] = 0.71\text{ M}$). The lines L^+ and L^- (of area $A^{\text{DQ}+}$ and $A^{\text{DQ}-}$) and their sum (thick line) result from experimental data processing. Reproduced with permission from ref. 81; Copyright Elsevier.

non-exponential relaxation conditions, as described earlier, may be analyzed for its components (denoted L^+ and L^- in the figure) by deconvolution, permitting quantitative analysis. This has been found to yield similar results as an approximate analysis based on the area under the line profile between the signal minima, thus validating the approximate analysis.

3.2 Solid state

3.2.1 ^1H studies

2D ^{15}N edited ^1H DQ MAS spectra were obtained by Schnell et al.¹¹² Recoupled polarization transfer (REPT) was employed to run an ^{15}N - ^1H HSQC experiment in indirect detection mode; this REPT-HSQC module also provides a filter for ^1H DQ signals. The technique has been demonstrated on hydrogen-bonded dimers of ^{15}N -labeled 2-ureido-4[^1H]-pyrimidinone.

DQF spin diffusion ^1H MAS NMR was employed by Cherry et al.¹¹³ to investigate domain size in polymer membranes. Sulfonated Diels-Alder poly(phenylene) polymer membranes were investigated by ^1H NMR at high MAS speeds, the proton environments of the sulfonic acid and phenylene polymer backbone being then resolved. The rotor-synchronized back-to-back BABA sequence was used. This allowed selective suppression of the sulfonic proton environment. This DQ filter in conjunction with a spin diffusion experiment was used to measure the domain size of the sulfonic acid component within the membrane.

Bechmann et al.¹¹⁴ discussed DQF ^1H MAS spectra and showed that this experiment permits the estimation of the minimum number of ^1H spins in a cluster. This could be an alternative to multiple quantum NMR experiments for the characterization of moderately sized clusters. The authors have demonstrated this approach on a carboxyl di-deuterated maleic acid sample at 10 kHz MAS speeds, employing a standard DQF COSY-like 1D sequence. They showed that the experimental sideband pattern lineshapes are best reproduced by a model incorporating a network of four nearest neighbor protons in addition to the basic maleic acid olefinic spin pair.

Buda et al.¹¹⁵ characterized the complex morphology of nylon-6 fibers by spin diffusion experiments that employ a dipolar filter based on DQ excitation. The authors also employed this approach to measure the distribution of residual dipolar couplings of lecithin molecules grafted on sub-micrometer cylindrical pore walls. The distribution of the orientation of collagen fibrils in Achilles tendon has also been estimated by ^1H DQF studies. Further, these authors also employed a DQ dipolar filtered spin diffusion ^1H NMR experiment to determine domain thickness in HDPE.¹¹⁶ A suitable pulse sequence is shown in Figure 26.

NMR studies of the proton conducting polymers Nafion and S-PEEK were reported by Ye et al.¹¹⁷ employing high-resolution ^1H solid state NMR under fast MAS. Homonuclear DQF spectra from rotor-synchronized BABA experiments were employed to disclose the nature of hydrogen-bonding interactions in the polymers. BABA allows recoupling of spins that are rigid on the time scale of the sequence. The intensity of DQC depends on the product of the dipolar coupling

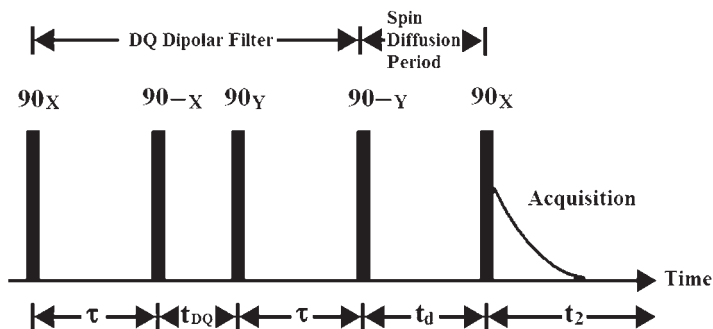


Figure 26 Four-pulse double quantum filter, which is followed by a 90°_X detection pulse after the spin diffusion time t_d .

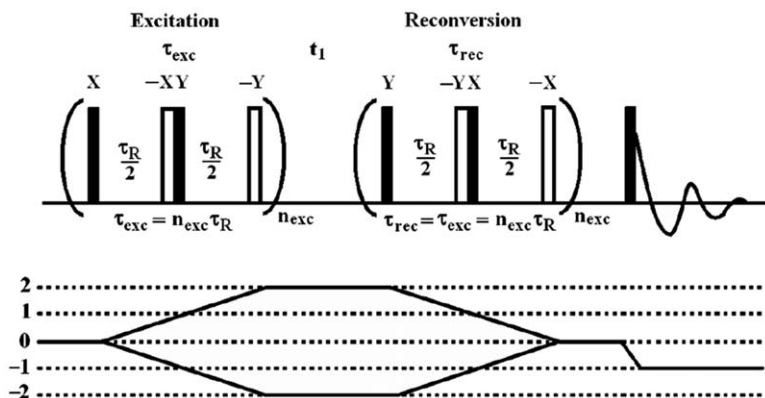


Figure 27 Homonuclear double quantum filtering with excitation and reconversion by back-to-back (BABA) pulse sequences, time reversed relative to each other. All pulses are $\pi/2$ pulses.

strength and the recoupling/excitation time. Fast tumbling of molecules (leading to the residual dipolar coupling) or long internuclear distances manifest as weak dipolar couplings. Proton interactions may therefore be detected and their relative mobilities gauged by employing the BABA sequence. Relative mobilities may be ascertained by comparing ^1H MAS NMR spectra with ^1H DQF MAS NMR spectra: mobile protons will be absent from the DQF MAS NMR spectrum. The pulse sequence is shown in Figure 27.

Ye et al.¹¹⁸ also employed the rotor-synchronized homonuclear ^1H DQF sequence to determine differential ^1H mobilities in polyvinazene (PV). They employed the BABA homonuclear DQF sequence for this work as well, to distinguish mobile from immobile protons at high MAS speeds (≥ 25 kHz). The basis of this work once again is that protons that undergo dynamics on a timescale faster than the rotor period exhibit motional averaging of their dipolar coupling. The pulse sequence of Figure 27 is again suitable.

3.2.2 ^{13}C , ^{15}N , ^{29}Si studies

Menger et al.¹¹⁹ studied the ^{13}C CP-DQF spectra and CP-DQS spectra of a single crystal of 9% doubly labeled glycine. Dipolar couplings were thus investigated in the static situation, the resulting AP DQF spectrum exhibiting clean suppression of the signals from unlabeled (natural abundance) species. It has been shown more recently that sensitivity-enhanced DQF spectra of static powder samples may be readily obtained by employing a detection scheme with a CPMG train.^{119a}

Menger et al.¹²⁰ also observed the ^{13}C – ^{13}C connectivities via dipolar couplings in rotating solids, employing the two-pulse Jeener experiment, as well as DQF spectra. For the latter case, a DQ preparation time τ (200 μs) was used that was significantly shorter than the rotor period (500 μs). Experiments were performed on a doubly labeled sample of glycine. The customary refocusing π pulse is omitted during the DQ preparation under MAS conditions, because it would scramble the magnetization vectors of nuclei in different crystallites, preventing the occurrence of rotational echoes.

A DQF for rotating solids was discussed by Meier and Earl.¹²¹ Doubly ^{13}C -labeled zinc acetate was employed. A time reversal pulse sequence was employed to generate DQC. The authors observed the ^{13}C – ^{13}C scalar coupling between the carboxyl and methyl resonances, as well as a shift of 31 Hz in the center of both resonances, arising from the homonuclear dipolar coupling.

Tycko and Dabbagh¹²² showed that spectral simplification and molecular structure determination is possible employing the DRAMA sequences to generate non-zero dipolar couplings under MAS and thence acquire a DQF spectrum. The authors demonstrated this approach in the ^{13}C MAS spectra of two experimental systems that were mixtures of organic compounds: one in which the resonances of doubly ^{13}C -labeled $(\text{CH}_3)_2\text{COHSO}_3\text{Na}$ were retained while filtering out the natural abundance responses from unlabeled *N*-acetyl-L-valine; and a second in which the resonances of the β and γ as well as the *S*-methyl positions of methionine $\cdot \text{HCl}$ labeled with ^{13}C at the *S*-methyl position were retained, while suppressing the natural abundance responses from unlabeled *N*-acetyl-L-valine.

^{13}C DQF MAS NMR has been applied to correlate pairs of ^{13}C nuclei in synthetically labeled DNA oligomers by Gregory et al.¹²³ and in proteins and peptides by Bower et al.¹²⁴ DQ-DRAWS, a modification of DRAMA, was introduced for this purpose, improving the performance in the presence of large chemical shift offsets and anisotropies. The sequence, shown in Figure 28, is named for 'dipolar recovery with a windowless sequence' and has been adapted to create DQC as well as to perform conjugate mixing down to SQC. It has been shown that the mutual orientation of two or more CSA tensors may be determined with high accuracy employing this sequence.

Gregory et al.¹²⁵ have shown that inter-strand distances in fibrillar β -amyloid peptides (the primary components of the plaques associated with Alzheimer's disease) could be determined with DRAWS, with only a single isotope label. Figure 29 shows CP/MAS and DQ-DRAWS spectra for two $1\text{-}^{13}\text{C}\text{-Val-A}\beta_{(10-35)}$ samples, one prepared as fibrils and another isolated as an ether precipitate. The ether precipitate shows no evidence of a ^{13}C – ^{13}C coupling, the DQ efficiency measured being 3.8%. The fibrillized amyloid sample, on the other hand,

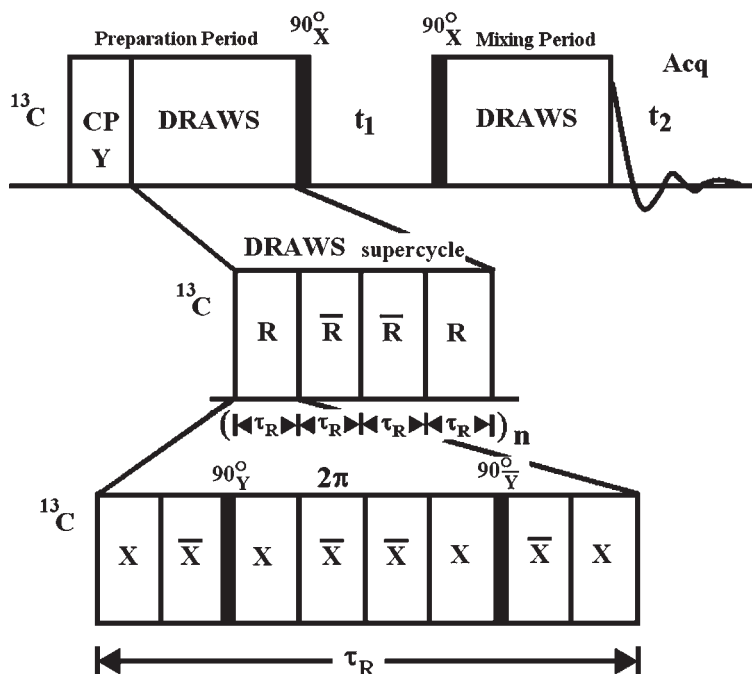


Figure 28 Double quantum MAS pulse sequence using DRAWS for preparation and reconversion (DQ-DRAWS). Preparation of DQC is performed with an initial state of transverse magnetization of the ^{13}C spin pair, generated by cross-polarization from ^1H ; protons are subsequently decoupled throughout the experiment at a higher power level off Hartmann–Hahn match.

exhibits a DQ efficiency of 13.2%, establishing the presence of an intermolecular dipolar contact in this case. The corresponding distance is estimated to be 4–6 Å.

The structure of surface-immobilized peptides, covalently bound to alkane thiolates that are self-assembled as monolayers on colloidal gold nanoparticles, was determined by Bower et al.¹²⁶ Secondary structure was quantified with the Ramachandran angles φ and ψ . These were determined by measuring the distance between backbone carbonyl ^{13}C spins, with DQF dipolar recoupled spectra employing a windowless sequence (DRAWS/DQ-DRAWS), and by determination of relative orientation of CSA tensors of carbonyl ^{13}C spins on adjacent peptide planes by DQ CP MAS spectra.

Heteronuclear DQ MAS NMR in dipolar solids was discussed by Saalwächter et al.¹²⁷ SYNCHRON4 is the pulse sequence applied to both spin channels (essentially, a 90° pulse pair with refocusing pulse in the middle on each channel, the 90° pulse spacing being half the rotor period). Reconversion is symmetric with the excitation, but is supplemented with a z filter prior to detection. The authors showed that the heteronuclear double quantum spinning sidebands that result are sensitive to heteronuclear distance, as well as the relative orientations of the chemical shift and dipolar tensors. The technique was demonstrated on the model system of deuterated ammonium formate, which comprises an isolated

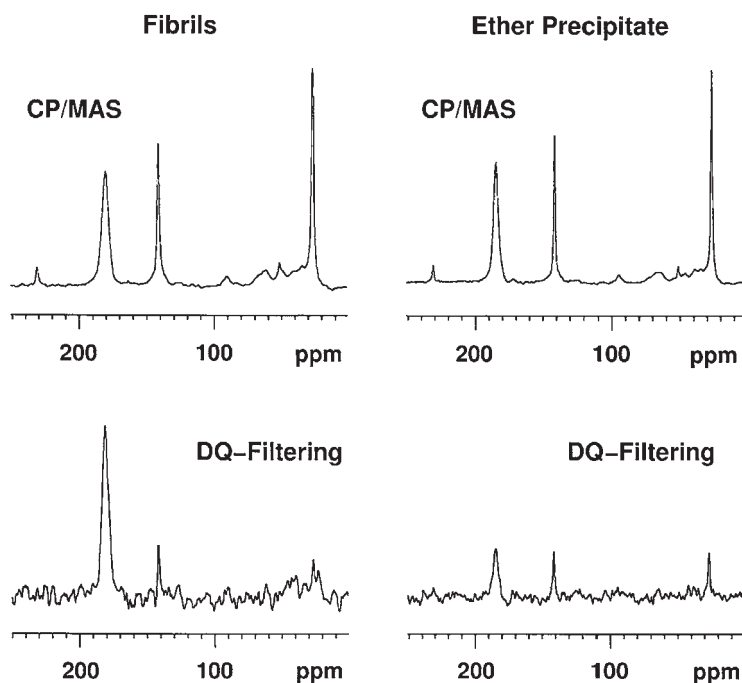


Figure 29 Solid state ^{13}C NMR spectra of $1\text{-}^{13}\text{C}\text{-Val}_{18}\text{-A}\beta_{(10-35)}$ mixed with a small amount of hexamethylbenzene (HMB). HMB resonances appear at 132 and 16 ppm. The broad resonance at 170 ppm in spectra at the left results from fibrils and the corresponding resonance at 175 ppm in the spectra on the right results from ether precipitate. The spectra at the top are CP-MAS spectra, while those at the bottom are DQF CP-MAS spectra employing the DQ-DRAWS sequence. Reproduced with permission from ref. 125; Copyright Elsevier.

$^{13}\text{C}\text{-}^1\text{H}$ spin pair at natural abundance of ^{13}C . The pulse sequence may also be used as a heteronuclear DQF that provides information about heteronuclear couplings. This allows differentiation of quaternary and CH_n -bonded carbons. Bisphenol A polycarbonate with ^{13}C at natural abundance was employed to demonstrate the elucidation of $^{13}\text{C}\text{-}^1\text{H}$ dipolar proximities by this method.

Verel et al.¹²⁸ demonstrated the application of the transition-selective INADEQUATE CR sequence for J -mediated DQF in the solid state. The authors investigated $[1,2\text{-}^{13}\text{C}_2]\text{glycine}$ -enriched *N. madagascariensis* drag line silk and further characterized the behavior of the sequence for this application, on $[2,3\text{-}^{13}\text{C}_2]\text{sodium propionate}$. They also developed subsequently¹²⁹ an S^3 version of the INADEQUATE experiment and demonstrated its application on protein systems, significantly improving the spectral resolution of the crowded $\text{C}'\text{-C}^\alpha$ region of two peptides, ubiquitin and HET-s(218–289), owing to the avoidance of J splittings in both dimensions of the 2D experiment.

Heindrichs et al.¹³⁰ discussed MAS DQ filtered dipolar shift correlation spectroscopy. This experiment is useful at establishing through-bond connectivities. Diagonal peak intensities are significantly reduced even with $\text{U-}^{13}\text{C}$ -labeled model amino acid systems.

Peptide backbone conformations have been obtained in powders under ^{13}C MAS by Blanco and Tycko¹³¹ using DQCSA on doubly (or more highly) labeled samples. They employed constant time double quantum evolution, which occurs at the sum of the anisotropic chemical shifts, resulting in characteristic ^{13}C sideband intensity patterns that reflect the relative orientation of the CSA tensors; these in turn reflect dihedral angles of the peptide backbone. The authors employed RF-driven recoupling for DQ excitation.

Mueller et al.¹³² demonstrated a uniform-sign cross-peak double quantum filtered COSY experiment for ^{13}C in solid state, as a through-bond correlation method for disordered solids. This is a refocused version of the DQF COSY experiment in solution state and yields doubly absorptive lineshapes. The authors showed that it is robust when performed even under 30 kHz MAS and at natural abundance of ^{13}C .

Dipolar dephasing of DQCs was investigated by auf der G nne¹³³ to determine effective dipolar couplings as well as homonuclear distances and dipolar lattice sums between spin-1/2 nuclei. It was shown that constant time data sampling can be combined with dipolar dephasing to compensate for relaxation effects and only two experimental data points are necessary for a distance measurement. The approach has been demonstrated on [$^{13}\text{C}_3$]-alanine.

Riedel et al.¹³⁴ showed that broadband homonuclear DQF C-13 shift correlation is possible with moderate RF fields of *ca.* 40 kHz at high MAS speeds of *ca.* 20 kHz with an RFDR zero quantum dipolar recoupling sequence. The authors demonstrated this approach on a sample of histidine, in both double quantum filtered COSY and double quantum spectral modes.

Homonuclear scalar couplings in solids have been measured by Cadars et al.¹³⁵ in isotope-enriched species employing a *z* filter. The approach was tested on ^{13}C -labeled polycrystalline L-alanine. The procedure is also valid for fully or partially enriched liquid or solid samples and has been applied with a selective DQ filter to ^{29}Si -enriched surfactant-templated layered silicates that lack long-range 3D crystallinity. The pulse sequence that may be employed to this end is shown in Figure 30.

Matsuoka and Schaefer¹³⁶ described DQF rotational echo double resonance. ^{13}C - ^{15}N REDOR coincident with ^{13}C - ^{13}C *J* evolution for DQF was employed. This removes the natural abundance ^{13}C background.

Matsuoka and Schaefer¹³⁷ have introduced, further, a ^{13}C dipolar DQF (D-DQF) rotational echo $^{13}\text{C}\{^2\text{H}\}$ double resonance experiment (REDOR) as well. D-DQF excitation and reconversion precede the REDOR evolution period. The homonuclear dipolar coupling of a directly bonded ^{13}C - ^{13}C pair has been used to create a dipolar DQF to remove natural abundance ^{13}C background in $^{13}\text{C}\{^2\text{H}\}$ REDOR. The efficiency of this approach is at its best when D-DQF excitation and reconversion precede the REDOR evolution period. The technique was demonstrated on a test sample of mixed recrystallized labeled alanines.

Oyler and Tycko¹³⁸ have discussed the conformational constraints obtained on uniformly ^{15}N , ^{13}C -labeled polypeptides from double single-quantum-filtered (DSQ)-REDOR experiments. Here, the term 'double single quantum' refers to a sum of heteronuclear zero and DQCs of the type I_yS_y . In this experiment,

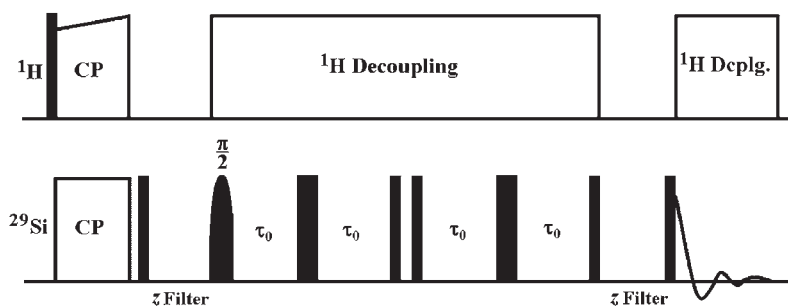


Figure 30 Pulse sequence for selective through-bond DQF. After CP, the magnetization is stored longitudinally to enable subsequent selective excitation of the desired resonance. The transverse magnetization of the selected spin is then transferred through homonuclear J couplings to bonded neighbors via a refocused INADEQUATE block. The length of the τ_0 delay is experimentally determined for optimized through-bond transfer.

frequency-selective REDOR is employed to prepare DSQ coherences involving directly bonded backbone ^{13}C O and ^{15}NH sites, dephase these coherences under longer range ^{15}NH – ^{13}C O dipolar couplings in a conformation-dependent manner, and convert the remaining DSQ coherences to detectable transverse ^{13}C magnetization. At least two sequential residues need to be uniformly labeled for application of this strategy. The technique has been demonstrated by the authors on two isotopically labeled systems, the helical peptide MB($i+4$)EK and the amyloid forming peptide A β_{11-25} .

Lopez et al.¹³⁹ employed DQF homonuclear MAS NMR ^{13}C correlation spectra to investigate membrane proteins. They combined double quantum filtering with ^{13}C – ^{13}C dipolar-assisted rotational resonance (DARR) experiments to yield correlation spectra free of natural abundance contributions, which would otherwise result in detrimental diagonal peak intensities. They investigated both DQ filtering prior to evolution (DOPE) and after mixing (DOAM), demonstrating their approach on ^{13}C -*cys*-labeled proteorhodopsin, a 27 kDa membrane protein. Their studies demonstrate that DQF DARR experiments allow through space constraints to be obtained for structural studies on ligands bound to membrane receptors, or on small fragments within large proteins.

DQF ^{13}C NMR studies of a series of doubly ^{13}C -labeled rhodopsins have been undertaken by Concistrè et al.¹⁴⁰ at MAS speeds of 7 kHz and temperatures below 120 K, before and after illumination at 420 nm for 10 h. The DQF strategy results in clean suppression of the natural abundance ^{13}C signals from the protein and lipid. The spectra obtained after illumination have at least one peak that is clearly split compared to the spectrum before illumination, indicating the formation of bathorhodopsin.

3.2.3 ^{31}P studies

Kubo et al.¹⁴¹ presented INADEQUATE driven by either spin diffusion or J coupling in solids under MAS, employing a simple solution state-like

preparation strategy commencing with cross-polarization. They demonstrated these experiments on the two-spin ^{31}P systems of sodium pyrophosphate decahydrate, $\text{Na}_4\text{P}_2\text{O}_7 \cdot 10\text{H}_2\text{O}$, and tetraphenyldiphosphine-1-oxide $(\text{C}_6\text{H}_5)_2\text{PP}(\text{O})(\text{C}_6\text{H}_5)_2$.

Franke et al.¹⁴² discussed the X–Y heteronuclear DQ MAS NMR experiment for crystalline inorganic solids. The experiment involves the generation of heteronuclear DQCs of abundant ^{31}P spins and rare ^{113}Cd , ^{77}Se , or ^{29}Si spins. The method relies on the presence of heteronuclear J coupling between these spins. Chemical shift evolution of heteronuclear DQC is involved, thus indirectly reporting on the rare spin resonance. The pulse sequence also acts as a DQF, offering heteronuclear correlation and spectral editing capability. The authors reported their investigations of three crystalline solids by this technique, *viz.*, CdSiP_2 , CdGeP_2 , and Ag_7PSe_6 .

Franke et al.¹⁴³ showed that in aprotic solids, ceramics, and glasses, cross-polarization and heteronuclear DQF MAS involving nuclei other than ^1H (such as ^{31}P) permit spectral editing and site resolution in semiconductor alloys. Once again, this experiment relies on scalar heteronuclear J coupling.

Auf der Günne and Eckert¹⁴⁴ reported high-resolution ^{31}P DQ NMR for the structural study of crystalline and glassy thiophosphates. DQC was created — and reconverted — under MAS conditions by the C_7 sequence. DQ excitation dynamics distinguish clearly between orthothiophosphate, pyrothiophosphate, and hexahypothiophosphate, owing to the difference in the strengths of ^{31}P homonuclear dipolar couplings.

Double quantum filtered 2D exchange, rotational resonance, and heteronuclear cross-polarization spectroscopies have been employed by auf der Günne et al.¹⁴⁵ on ^{31}P to generate information on local environments around ^{31}P sites in LiP_5 .

Bechmann et al.¹⁴⁶ reported the ^{31}P MAS and DQF MAS NMR near the rotational resonance condition with $n = 0$, as well as off-magic angle spinning (OMAS) of polycrystalline Pt(II) phosphine–thiolate complexes.

Tseng et al.¹⁴⁷ have discussed DQF heteronuclear correlation experiments. The DQ excitation profile is measured in a series of 2D experiments. Van Vleck second moment measurements may be made in this mode. The technique has been demonstrated on the model compounds hydroxyapatite and brushite. The ^{31}P homonuclear second moment of the apatite component in rat dentin has been characterized, based on the results obtained for the model compounds. The method may be used for the characterization of bone, enamel, and dentin.

3.2.4 ^{129}Xe studies

Brouwer et al.¹⁴⁸ have reported a DQF ^{129}Xe experiment to probe Xe in multiply occupied cavities in solid state inclusion compounds. Weak ^{129}Xe – ^{129}Xe dipolar couplings are recoupled under MAS. Because of weak dipolar interaction and strong CSA, a robust recoupling sequence was essential, and $\text{SR26}_4^{11,149}$ was employed. Experiments were performed on the xenon clathrate of Dianin's compound. The authors showed that the DQF NMR method is useful for peak assignment in ^{129}Xe NMR spectra because peaks arising from different types of

absorption/inclusion sites or from different levels of occupancy of single sites can be distinguished.

3.2.5 Studies on quadrupolar nuclei

Vega et al.⁴⁹ discussed cross-polarization in a spin-1/2 (S)–spin-1 (I) system and focused attention on the direct cross-polarization of the double quantum transition of the spin-1 nucleus. Irradiating at the center of the quadrupolar doublet, the Hartmann–Hahn match condition for double quantum cross-polarization (DQCP) is given by:

$$\frac{\omega_{1I}^2}{\omega_Q} = \omega_{1S} \quad (48)$$

DQCP is more efficient — as measured by proton order destruction — in both spin lock and adiabatic ADRF modes, as compared to normal single quantum cross-polarization. Further, Hartmann–Hahn matching is less critical for DQCP. Finally, the ADRF mode leads to a higher CP efficiency than the spin lock mode for DQCP as well. The authors reported ¹H–²H measurements on dilute solid benzene-*d*₁.

Vega⁵⁰ also described the cross-polarization processes between an abundant spin-1/2 system and spin-3/2 system in solid state, and derived conditions for single, double, and triple quantum cross-polarization of the spin-3/2 system. Experimental verifications of the various Hartmann–Hahn conditions were performed for ²³Na–¹H spin lock cross-polarization on a single crystal of sodium ammonium tartarate tetrahydrate.

In some early work, Eckman et al.¹⁵⁰ demonstrated double quantum NMR of ²H under MAS conditions, working with polycrystalline 28% randomly deuterated ferrocene-*d*₁₀, rotating at 1.11 kHz. They employed an evolution time increment that equaled the rotor period and showed that the DQ spectrum is far less sensitive to the accuracy and stability of the magic angle setting than is the standard single quantum spectrum.

Chandrakumar et al.¹⁵¹ showed that in selectively deuterated plastic crystal-line powders rotating at the magic angle, essentially clean separation of the double quantum chemical shift from the quadrupolar coupling could be obtained by a rotor-synchronized experiment in which the start of the scan is synchronized with the rotor and the evolution increment equals the rotor period; in turn, rotation speeds were kept much smaller than the quadrupolar coupling, so that DQC may be prepared by the standard preparation sequence. While the quadrupolar coupling is essential to prepare DQC, the evolution of DQC is however independent of the first-order quadrupolar interaction. Recall that for spin-1 systems, we have:

$$\begin{aligned} [I_z^2, I_x] &= i[I_y, I_z]_+; & i[I_z^2, [I_y, I_z]_+] &= I_x \\ \Rightarrow e^{-i\omega_Q I_z^2 \tau} I_x e^{i\omega_Q I_z^2 \tau} &= I_x \cos \omega_Q \tau + [I_y, I_z]_+ \sin \omega_Q \tau \end{aligned} \quad (49)$$

Here, $[I_i, I_j]_+ = I_i I_j + I_j I_i$.

With a second 90° pulse of the same — or opposite — phase as the first, therefore, a state of DQC of phase y is created, *viz.*, $\pm[I_x, I_y]_+$.

On the other hand, we have:

$$[I_z^2, [I_x, I_y]_+] = 0 \quad (50)$$

As a consequence, DQC does not evolve under the first-order quadrupolar interaction.

The authors thus demonstrated with their experiments on 3,3'- d_2 -norcamphor and 3,3'- d_2 -camphor that this QUADSHIFT experiment permits the separation of sites that are as close in chemical shift as 0.2 ppm, and allows correlating the shifts with their respective quadrupolar couplings. The F_2 trace at the *endo* site of the camphor species, shown in Figure 31, reveals strikingly the nature of the AP patterns that would result on double quantum filtering. It may be noted that since the quadrupolar interaction is traceless, the parallel and perpendicular couplings are of opposite sign, having a 2:–1 ratio. Consequently, the intense inner set of sidebands from the perpendicular orientations reveals an AP pattern that is the negative of the AP pattern from the weaker outer set of sidebands from the parallel orientation.

Man¹⁵² described the detection of DQC in spin-5/2 systems, excited by spin lock sequences. First-order quadrupolar interaction was taken into account. Predictions were made and experimentally verified on a static single crystal sample of corundum ($\alpha\text{-Al}_2\text{O}_3$) for ^{27}Al . In such experiments, MQCs excited by the first pulse are detected at the end of the spin lock pulse as single quantum transitions.

Double quantum filtered satellite transition MAS experiments have also been proposed by Kwak and Gan.¹⁵³ A CT-selective π pulse converts the first satellite transition (ST₁) SQC to DQC, by inversion of the $\pm 1/2$ energy levels, while

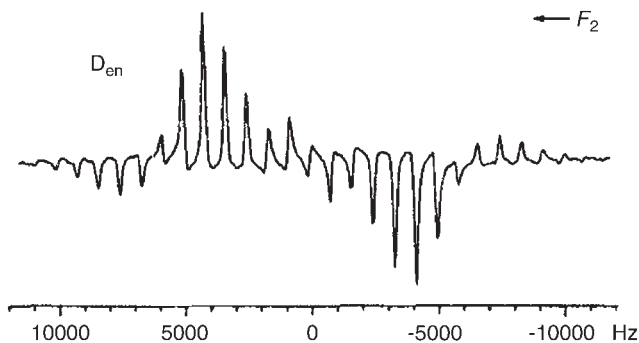


Figure 31 An F_2 trace from a 2D ^2H QUADSHIFT experiment run at 46.1 MHz on $[3,3'\text{-}^2\text{H}_2]\text{camphor}$. The F_2 trace with the sideband pattern observed for the *endo* site is displayed; scale relative to the transmitter offset. Spectral widths: 400 Hz (F_1) and 50 kHz (F_2); 96 points in t_1 , each with 240 scans repeated every 5 s, zero filled to 512 points; 1k points in t_2 , zero filled to 2k points. Preparation time: 90 μs ; MAS speed: 0.8 kHz. Estimated quadrupolar splitting $2\nu_Q$ is of the order of 8 kHz for the *endo* site in this molecule. Adapted from ref. 151; Copyright John Wiley & Sons.

leaving other spin states undisturbed. Clean ST MAS spectra of $I = 3/2$ and $5/2$ have been obtained, respectively, on RbNO_3 and AlPO_4 -berlinite, with efficient suppression of diagonal peaks and other unwanted peaks (e.g., $\text{ST}_{\pm 2} \rightarrow \text{CT}$).

Painter and Duer¹⁵⁴ showed that, working with CTs, dipolar interactions between quadrupolar nuclei with half-integer spin permit DQCs of the CTs to be excited without recoupling sequences even under MAS conditions. They demonstrated applications to 2D DQF correlation spectra of three distinct ^{23}Na sites in Na_2ZrO_3 . DQ excitation was accomplished by a 90° pulse pair, or by a single pulse under which rotational resonance is achieved for the sum or difference of nutation frequencies of the two spins.

Ashbrook and Wimper¹⁵⁵ demonstrated rotor-synchronized acquisition of DQF satellite transition spectra of quadrupolar nuclei with half-integer spin. In their work, a CT-selective π pulse was used to effect DQ excitation as well as reconversion.

Hwang et al.¹⁵⁶ demonstrated DQF ^2H experiments on water in MCM-41. Long soft RF pulses were used for $T_{2\rho}$ DQF NMR, followed by an observe pulse. It was found that the residual quadrupolar interaction dominates the signal decay.

Mali et al.¹⁵⁷ have shown that DQF spectra of half-integer quadrupolar nuclei show substantial dependence on magnitudes and relative orientations of the dipolar and quadrupolar coupling tensors. Employing symmetry-based recoupling schemes on the aluminophosphate molecular sieve AlPO_4 -14, they showed that symmetric schemes involving incrementation of both excitation and reconversion periods are good at providing distance information, while asymmetric procedures involving incrementation of the excitation period alone provide information on relative tensor orientation.

3.3 Spatially resolved NMR

3.3.1 *In vivo* studies

Thomas et al.¹⁵⁸ described localized ^1H DQF spectroscopy to obtain localized, water-suppressed spectra of J -coupled metabolites. Their work was done in ISIS mode, which is basically an eight-step procedure to achieve volume localization. The authors analyzed the behavior of AX and AX_3 systems under this experiment. They presented results on phantoms of carnosine, alanine, and ethanol in aqueous solution.

Jung and Lutz¹⁵⁹ described single shot localized DQF spectroscopy for spectral editing of human *in vivo* ^1H spectra. The sequence, shown in Figure 32, was implemented on a 1.5 T whole-body imager.

All four RF pulses of this sequence are slice selective. In the experiments, results of which are shown in Figure 33, a body coil was employed for excitation, while a Helmholtz coil was used for signal detection. 100 millimolar calcium lactate and 400 mmolal acetic acid were used in a phantom. The voxel size was $(13\text{ mm})^3$. Gradients were set to 0.002 mT/m. In the double quantum filtered spectra, notice the suppression of the acetic acid signal and the appearance of the methine proton signal at low field; spectrum (a) is the normal double spin echo spectrum with an echo time TE of 145 ms; spectrum (b) was acquired with the

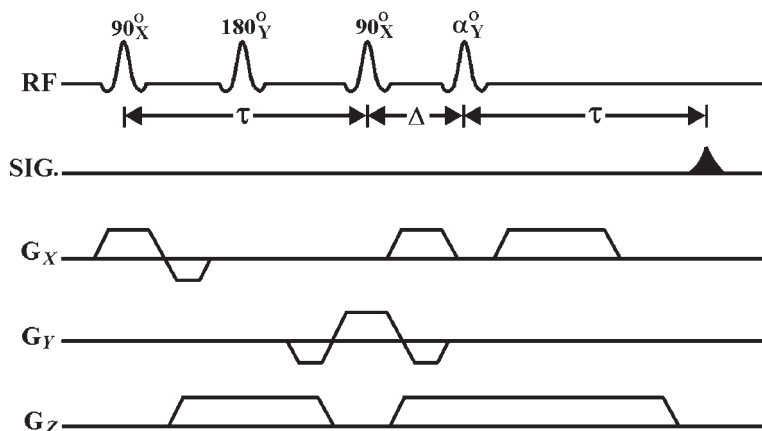


Figure 32 Localized single shot double quantum filter. The first three RF pulses create DQC at the time $\tau = (2J)^{-1}$, which evolves during the time Δ under the switched field gradients. The α pulse reconverts the DQC back into observable SQC so that an echo occurs at 2Δ after the α pulse because at this time the effect of the gradients is compensated for this coherence pathway. With $\tau = 2\Delta = (2J)^{-1}$, the doublets of an AX system are in phase. Uncoupled signals are eliminated by this process.

echo time set to 145 ms ($(J)^{-1}$), while spectrum (c) was obtained with the echo time mis-set to 100 ms and exhibits phase anomalies. Measurements were also successfully carried out on normal volunteers as well as on a patient who had chondroblastoma in the distal femur, 14 days after chemotherapy.

γ -Aminobutyric acid (GABA) is the major inhibitory neurotransmitter for the normal function of mammalian and human brain. However, owing to low concentration and spectral overlap with other signals, especially those from creatine (Cr), glutathione (GSH), as well as macromolecules, GABA is relatively difficult to detect. DQF experiments have therefore turned out to be of considerable significance for this application.

Yield enhancement of DQF designed for edited detection of GABA has been described by Wilman and Allen.¹⁶⁰ The GABA A_2 multiplet (triplet at 3 ppm) is edited from the Cr singlet in the proton spectroscopy of brain. The signal-to-noise ratio of the DQF is significantly enhanced primarily by significant reduction in transverse relaxation losses, accomplished by shortening the filter sequence by *ca.* 70%, shortening the initial preparation period and eliminating the refocusing time prior to start of acquisition, as well as by employing a selective read pulse. The acquisition of AP magnetization is possible in this case since the two-spin AP components are separated by $2J$, as opposed to the three-spin AP term which involves a separation of only J . The filter design was verified *in vitro* on phantoms of GABA in D_2O , and the suppression of Cr by more than a factor of 1,600 was demonstrated on rat brain extracts.

Lei and Peeling¹⁶¹ described simultaneous spectral editing for GABA and taurine by DQ coherence transfer (similar J values). A dual band coherence read pulse was employed. The pulse sequence is shown in Figure 34. It was

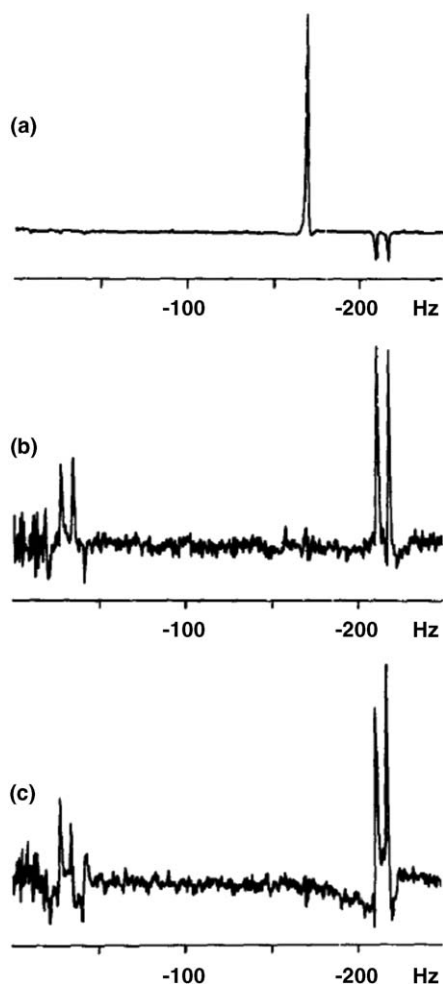


Figure 33 Volume localized ^1H spectra of a solution of 100 mmolal calcium lactate and 400 mmolal acetic acid in water. Cubic voxel: 2.197 ml; the irradiation was done with a body coil, while signal reception was performed with a Helmholtz coil, operating on a 1.5 T (63.57 MHz) whole-body MRI system. (a) Spectrum acquired employing a point resolved spectroscopy (double spin echo, PRESS) sequence: water suppression was performed by frequency-selective saturation, the echo time TE being 145 ms, with a repetition time TR of 6 s. The lactate CH_3 doublet is inverted w.r.t. the acetic acid singlet because $\text{TE} = (J)^{-1}$. (b) DQF spectrum obtained with: $2\tau = 145 \text{ ms} = (J)^{-1}$, $\alpha = 120^\circ$, $\Delta = 20 \text{ ms}$, TR = 10 s. The edited spectrum was suitably phase corrected to absorption mode. (c) DQF spectrum obtained with: $2\tau = 100 \text{ ms}$, other parameters as in (b). In comparison with (b), phase anomalies exist because $\tau \neq (2J)^{-1}$. Reproduced with permission from ref. 159; Copyright Elsevier.

implemented on a 7 T/21 cm system, with a 3 cm diameter saddle coil for transmission and reception. Results were demonstrated on a 2.5 cm diameter cylindrical phantom composed of 15 mM Cr, and 20 mM each of choline, GABA, and taurine in saline solution. The peaks indicated in spectrum A of Figure 35 are

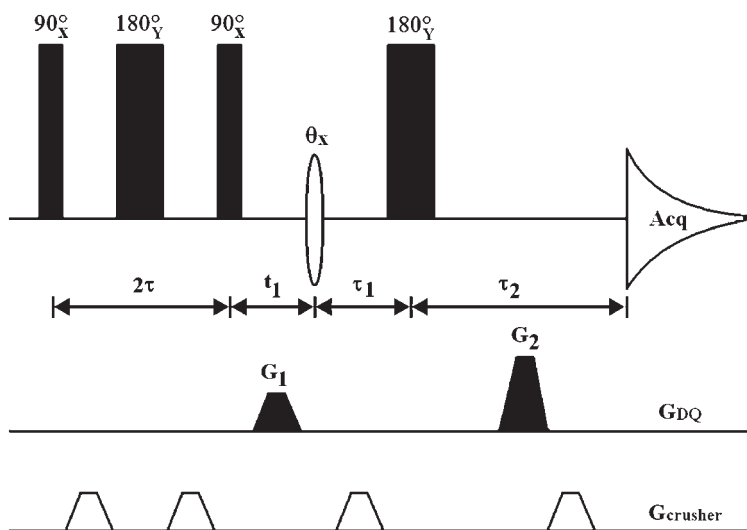


Figure 34 A double quantum coherence transfer pulse sequence for spectral editing. G_1 and G_2 are gradient pulses with equal duration (typically, 1 ms) and with 1:2 amplitude ratio for selection of the DQC pathway (G_{DQ}), G_1 being 32 mT/m. $\tau_1 = \tau - t_1$ and $\tau_2 = \tau + t_1$.

assigned as: 1 – choline (β -CH₂); 2 – Cr (CH₂); 3 – choline (α -CH₂); 4 – taurine (S-CH₂); 5 – taurine (N-CH₂); 6 – choline (CH₃); 7 – Cr (CH₃)+GABA (γ -CH₂); 8 – GABA (α -CH₂); and 9 – GABA (β -CH₂). The authors applied their experiment to rat brain tissue *in vitro* as well.

Du et al.¹⁶² described the sensitivity-enhanced detection of GABA *in vivo* by localized DQF. The authors demonstrated their DQF editing with selective DANTE readout at 4.1 T, resulting in robust suppression of Cr and GSH signals, the efficiency of editing being 40–50% on a phantom comprising 50 mM GABA and 61 mM choline. At the long echo time employed (77 ms), macromolecular signal contaminations were negligible. Applied to healthy volunteers, the mean GABA level was measured as 1.12 mM concentration in the occipital lobe, as compared to 7.1 mM Cr concentration. A volume-selective DQF sequence based on point resolved spectroscopy (PRESS) was employed and is shown in Figure 36.

3.3.2 Studies on soft materials

Schneider et al.¹⁶³ reported dipolar-encoded longitudinal magnetization, as well as DQ and TQ filters as contrast filters for ¹H imaging of residual dipolar couplings in elastomers. The authors demonstrated these experiments on commercial 1,4-*cis*-poly(isoprene), employing a spin echo imaging procedure following the preparation module to generate the desired contrast.

Wiesmath et al.¹⁶⁴ described DQF NMR signals in inhomogeneous magnetic fields, applied with the NMR MOBILE Universal Surface Explorer (MOUSE). A mismatched excitation reconversion sequence, MERE, was employed. The sequence involves a mismatched reconversion time, τ' , as shown in Figure 37. θ and 2θ pulses are employed, as customary with surface coils. τ is set to the maximum of the DQ

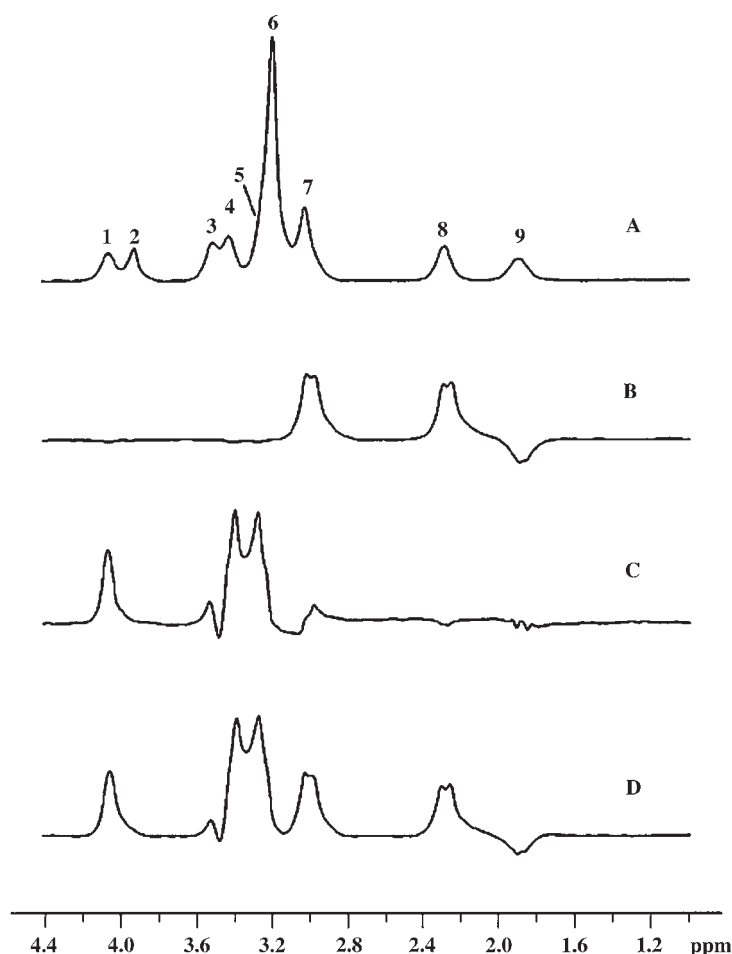


Figure 35 Spectra acquired from the solution phantom without spectral editing (A), with GABA editing (B), with taurine editing (C), and with GABA and taurine editing (D). Spectra B, C, and D have been scaled $\times 2$ relative to A. Reproduced with permission from ref. 161; Copyright Elsevier.

buildup curve; t_1 is a short, constant duration; τ' is varied keeping $\omega_D \tau' \ll 1$, $\tau' \ll T_{2,\text{eff}}$. Here, ω_D is the dipolar coupling expressed in angular frequency units.

The authors recorded the DQ buildup and decay curves for a series of cross-linked natural rubber samples. DQ decay curves turn out to have a better signal-to-noise ratio in the initial time regime than DQ buildup curves. Quantitative ratios of the total proton residual dipolar couplings are obtained from the curves, in good agreement with measurements in homogeneous fields. A linear dependence was found of these ratios on the sulfur-accelerator content.

3.3.3 Diffusion studies

An experiment designed to measure the apparent diffusion coefficient (ADC) of lactic acid *in vivo* has been reported using DQ coherence transfer spectroscopy by

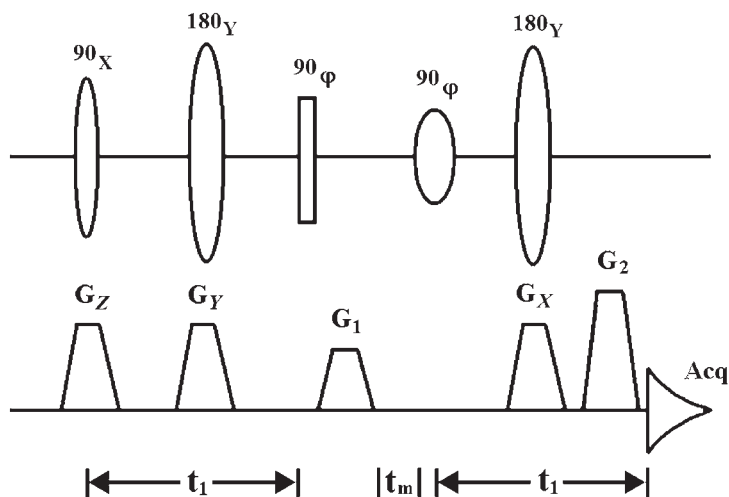


Figure 36 A modified PRESS sequence which generates MQC following the first three pulses, preceded by a water suppression sequence (not shown in the figure). The gradients G_1 and G_2 have the amplitude ratio 1:2. The delays t_1 and t_m are for preparation of MQC and MQC evolution, respectively. The 90° reconversion pulse may be chosen to selectively detect the peaks of interest, for example, by employing a suitable DANTE train to select the GABA β -CH₂ signal.

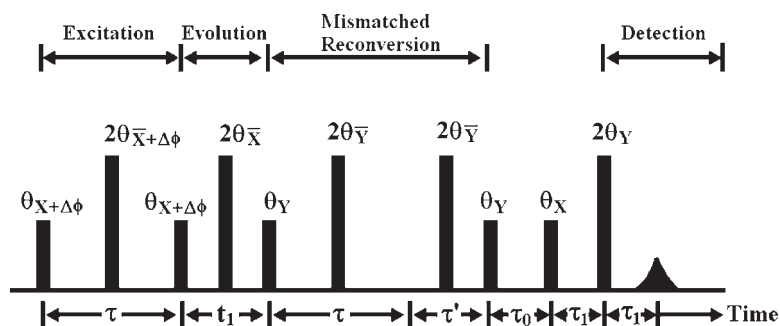


Figure 37 A five-pulse sequence with an arbitrary flip angle θ , including a z filter (of duration τ_0) at the end and supplemented by partially refocusing 2θ pulses for measuring DQF coherence decay curves. A short, constant DQ evolution time t_1 is employed. The preparation time τ is also kept fixed at the optimum DQ buildup time, while τ' is varied to measure the DQ decay curve.

Sotak.¹⁶⁵ The pulse sequence is shown in Figure 38. In addition to the molecule selectivity inherent to the method (e.g., discrimination from strong lipid signals), it is to be noted that the effective γ of the nuclear spin concerned gets doubled under these conditions, owing to the twofold sensitivity of DQCs to field gradients as noted earlier (see Section 1.1). The diffusion-controlled echo attenuation has the well-known $\exp(-\gamma^2 g^2 D \delta (\Delta - \delta/3))$ dependence, implying that for a given diffusion encode/decode gradient amplitude g , the exponent is

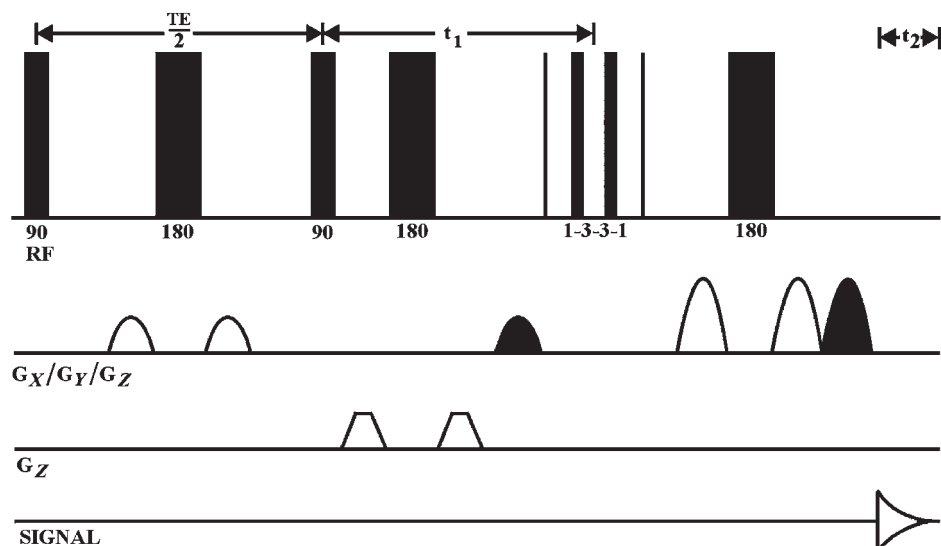


Figure 38 MQCs are prepared by the standard three-pulse sandwich, with the effects of pulse imperfections of the refocusing 180° pulse being minimized by the spoiler gradients that flank it. A frequency-selective 1-3-3-1 pulse is employed to achieve selective reversion of MQC. Coherence order selection is achieved by the darkened gradient pair, the members of which have a 1:2 amplitude ratio for DQC. G_z indicates the diffusion encode–decode gradient pair.

consequently multiplied by a factor of four. In their experiments, Sotak et al. applied the diffusion encode and decode gradients along the z direction during the DQ evolution time t_1 , symmetrically around a refocusing 180° pulse. The authors employed the model system of *N*-acetylalanine to validate the method and went on to perform it on a nude mouse on which a human tumor xenograft was implanted subcutaneously on the back.

Heteronuclear DQC selection by gradients in diffusion experiments was described by Kuchel and Chapman.¹⁶⁶ They demonstrated their approach on the ^1H – ^{31}P coupled system of neutralized phosphorous acid ($\text{HPO}(\text{OH})_2$) in water. This approach results in a 3.5-fold reduction of gradient amplitude for ^{31}P PGSE, the sum of γ of the two nuclei involved in the DQC being 1.4 relative to 1 for ^1H (ca. 0.4 for ^{31}P).

Sendhil Velan and Chandrakumar¹⁶⁷ demonstrated a diffusion experiment which excites MQC in solution state (e.g., two-spin DQC of the ethyl group in ethanol), diffusion encodes it during an incrementable refocused free precession period t_1 , finally reconverts it into SQC, and decodes the diffusion with a rephase gradient, followed by refocusing to form a spin echo whose second half is read out. On Fourier transforming with respect to the systematically incremented refocused free precession period, the multiple quantum J spectrum results. By running two such experiments with and without diffusion encode/decode (or in principle with two different pairs of gradient amplitudes for encode/decode), the effects of diffusion are manifested as an additional line broadening in this

dimension, which has a small spectral width — as determined by the couplings alone. This circumstance permits an accurate evaluation of the diffusion coefficient. On Fourier transforming with respect to t_1 , the F_1 linewidth in magnitude mode is given by:

$$\Delta\nu_{1/2, \text{MQ}} = \frac{\sqrt{3}}{\pi} \left(\frac{1}{T_2} + n^2 \gamma^2 g^2 \delta^2 D \right) \quad (51)$$

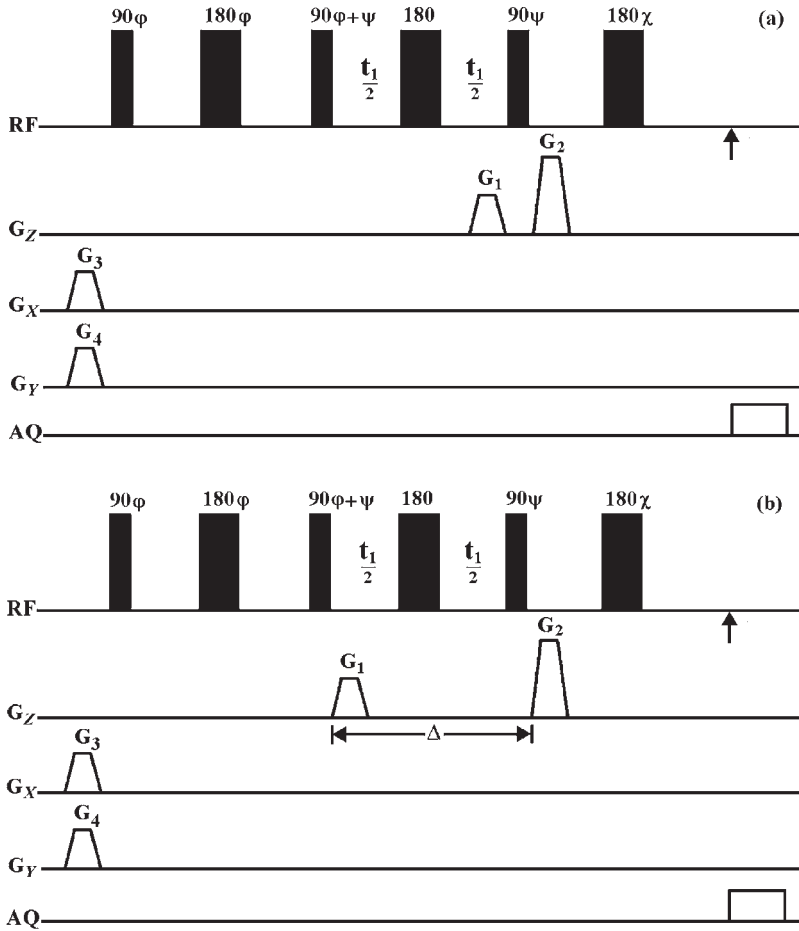


Figure 39 (a) Pulse sequence for multiple quantum J spectroscopy. The coherence selection gradients (G_1 and G_2 , in the amplitude ratio 1:2) are given immediately before and after the 90° reconversion pulse. G_3 and G_4 are spoilers. The arrow indicates the start of data acquisition from the echo maximum. The phase ψ equals 0° for even quantum excitation. χ is 0° for the odd quantum case and 90° for the even quantum case. (b) Pulse sequence for multiple quantum J spectroscopy with diffusion encoding in the F_1 dimension. The coherence selection gradient G_1 is given immediately after the preparation sandwich and G_2 is given after the 90° reconversion pulse. G_1 and G_2 also serve diffusion encode and decode purposes, respectively. All other symbols are as in (a).

The diffusion coefficient D may then be easily retrieved by comparing the pair of experiments. Values of D obtained by this procedure are in satisfactory accord with standard values in test cases. The pulse sequence is shown in Figure 39.

One advantage of the multiple quantum version is that the n quantum linewidth has an n^2 dependence on D , thereby facilitating the measurement of smaller D values; alternatively, the diffusion encode gradient, which is issued during the n quantum evolution time, needs to be only $(1/n)$ th of the normal single quantum diffusion encode gradient.

As an example from their work, a simple application to ethanol is shown in Figure 40.

Momot and Kuchel¹⁶⁸ described phase-sensitive convection compensating diffusion experiments with gradient selected homonuclear DQ filtering. In this application, DQF may be used for either solvent suppression or spectral editing. The method has been demonstrated on 3.16% (w/w) of propofol in chloroform and 1% (w/w) propofol and 10% (w/w) solutol HS15 in D_2O -saline. The technique is expected to offer advantages in diffusion measurements on spectrally crowded systems, for example, small molecules solubilized in colloidal solutions or bound to macromolecules.

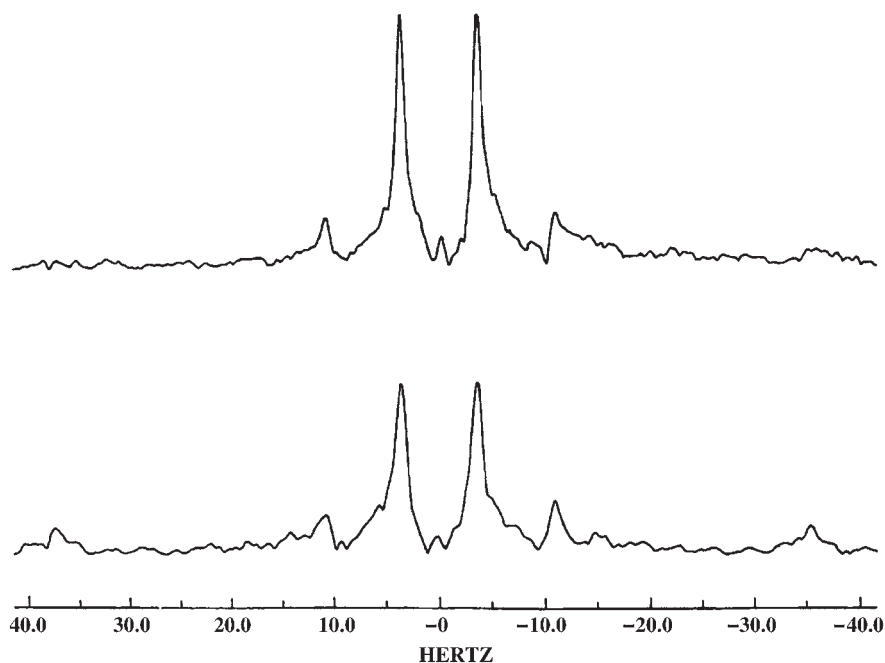


Figure 40 Double quantum J spectrum of ethanol (A_2X_3 spin system), arising from the AX DQC. Upper trace shows the maximum intensity column corresponding to the peaks at $\pm J/2$, with a linewidth of 1.14 Hz in the absence of diffusion encoding. The lower trace shows the corresponding column of the diffusion-encoded peaks, with a linewidth of 1.47 Hz, the dephasing gradient being 4.66 G/cm. The experiments were carried out at 300 MHz with an actively shielded microimaging probe head. Ref. 167; Copyright Indian Academy of Sciences.

4. CONCLUSIONS

DQF NMR studies — as the name implies — serve to simplify NMR spectra by filtering out certain responses of the spin system under investigation, which are not of relevance in the context of the study being undertaken. The excitation and reconversion of double quantum transitions lie at the heart of 1D DQF NMR studies, while their evolution in the intermediate period gives rise to 2D double quantum experiments. The strategies for excitation of DQCs are remarkably different in solution state under scalar couplings and in solid state under dipolar (or quadrupolar) couplings. While the venerable two-pulse sandwich — augmented if required with a refocusing pulse — may be used for excitation in solution state or with static solids, a variety of recoupling schemes have been introduced to generate DQCs mediated by anisotropic interactions under MAS conditions. Multi-exponential relaxation offers yet another avenue for generation of MQCs, especially in partially ordered quadrupolar spin systems when extreme narrowing conditions of relaxation are not fulfilled. Recent DQ reconversion strategies have involved COS³ approaches or S³ experiments, while reconversion that is ‘time reversed’ relative to the preparation is the norm in the solid state. An overview of a variety of applications of 1D DQF experiments in solution state, solid state, as well as in spatially resolved NMR has been included, addressing spin-1/2 systems as well as quadrupolar nuclei. Double quantum filtered NMR will undoubtedly remain a fertile ground for further research, developments, and applications, given especially the relatively widespread availability at present of cryoprobes^{169,170} for solution state work as well as for microimaging and small-animal MRI, and not only in the context of rare spin NMR, but also for proton work.

ACKNOWLEDGMENTS

It is a great pleasure to thank Ms. Samanwita Pal and Ms. Christy George for help with the literature search. The author owes CG special thanks for her skilled, energetic, and cheerful inputs in bringing the manuscript to shape.

REFERENCES

1. R. R. Ernst, G. Bodenhausen and A. Wokaun, *Principles of Nuclear Magnetic Resonance in One and Two Dimensions*, Clarendon, Oxford, 1987.
2. N. Chandrakumar and S. Subramanian, *Modern Techniques in High-Resolution FT-NMR*, Springer-Verlag, New York, NY, 1987.
3. G. Drobny, A. Pines, S. Sinton, D. P. Weitekamp and D. Wemmer, *Faraday Symp. Chem. Soc.*, 1978, **13**, 49.
4. D. P. Weitekamp, *Adv. Magn. Reson.*, 1983, **11**, 111.
5. A. Bax, R. Freeman and S. P. Kempsell, *J. Am. Chem. Soc.*, 1980, **102**, 4849.
6. R. E. Hurd, *J. Magn. Reson.*, 1990, **87**, 422.
7. O. W. Sørensen, M. H. Levitt and R. R. Ernst, *J. Magn. Reson.*, 1983, **55**, 104.
8. A. Bax and R. Freeman, *J. Magn. Reson.*, 1980, **41**, 507.
9. E. Hengge and F. Schrank, *J. Organomet. Chem.*, 1989, **362**, 11.

10. U. Pöschl, H. Siegl and K. Hassler, *J. Organomet. Chem.*, 1996, **506**, 93.
11. J. Maxka, B. R. Adams and R. West, *J. Am. Chem. Soc.*, 1989, **111**, 3447.
12. C. A. Fyfe, Y. Feng, H. Gies, H. Grondey and G. T. Kokotailo, *J. Am. Chem. Soc.*, 1990, **112**, 3264.
13. C. A. Fyfe, H. Grondey, Y. Feng and G. T. Kokotailo, *J. Am. Chem. Soc.*, 1990, **112**, 8812.
14. D. H. Brouwer, P. E. Kristiansen, C. A. Fyfe and M. H. Levitt, *J. Am. Chem. Soc.*, 2005, **127**, 542.
15. C. Brevard, R. Schimpf, G. Tourne and C. M. Tourne, *J. Am. Chem. Soc.*, 1983, **105**, 7059.
16. P. J. Domaille, *J. Am. Chem. Soc.*, 1984, **106**, 7677.
17. R. G. Finke, B. Rapko, R. J. Saxton and P. J. Domaille, *J. Am. Chem. Soc.*, 1986, **108**, 2947.
18. T. L. Jorris, M. Kozik, N. Casan-Pastor, P. J. Domaille, R. G. Finke, W. K. Miller and L. C. W. Baker, *J. Am. Chem. Soc.*, 1987, **109**, 7402.
- 18a. B. Wrackmeyer, *Ann. Rep. NMR Spectrosc.*, 1999, **38**, 203.
- 18b. I. D. Gay, C. H. W. Jones and R. D. Sharma, *J. Magn. Reson.*, 1991, **91**, 186.
19. J. Schaefer, REDOR & TEDOR, in: *Encyclopedia of NMR*, D. M. Grant and R. K. Harris, eds., Vol. 6, Wiley, New York, NY, 1996, p. 377.
20. J. M. Griffiths, A. E. Bennett and R. G. Griffin, Homonuclear Recoupling Schemes in MAS NMR, in: *Encyclopedia of NMR*, D. M. Grant and R. K. Harris, eds., Vol. 4, Wiley, New York, NY, 1996, p. 2390.
21. S. O. Smith, Rotational resonance in biology, in: *Encyclopedia of NMR*, D. M. Grant and R. K. Harris, eds., Vol. 7, Wiley, New York, NY, 1996, p. 4185.
22. M. J. Duer, *Introduction to Solid-State NMR Spectroscopy*, Blackwell Publishing, UK, 2004.
23. I. Schnell, *Prog. NMR Spectrosc.*, 2004, **45**, 145.
24. R. Benn, H. Grondey, C. Brevard and A. Pagelot, *J. Chem. Soc., Chem. Commun.*, 1988, 102.
25. P. T. Callaghan, *Principles of NMR Microscopy*, Clarendon, Oxford, 1991.
26. R. Kimmich, *NMR. Tomography, Diffusometry, Relaxometry*, Springer-Verlag, New York, NY, 1997.
27. B. Blümich, *NMR Imaging of Materials (Monographs on the Physics and Chemistry of Materials 57)*, Oxford Science Publications, Oxford, 2000.
28. M. H. Levitt and R. R. Ernst, *Chem. Phys. Lett.*, 1983, **100**, 119.
29. M. H. Levitt and R. R. Ernst, *J. Chem. Phys.*, 1985, **83**, 3297.
30. C. Radloff and R. R. Ernst, *Mol. Phys.*, 1989, **66**, 161.
31. L. Braunschweiler, G. Bodenhausen and R. R. Ernst, *Mol. Phys.*, 1983, **48**, 535.
- 31a. M. Rance, O. W. Sørensen, G. Bodenhausen, G. Wagner, R. R. Ernst and K. Wüthrich, *Biochem. Biophys. Res. Commun.*, 1983, **117**, 479.
- 31b. C. J. R. Counsell, M. H. Levitt and R. R. Ernst, *J. Magn. Reson.*, 1985, **64**, 470.
- 31c. D. G. Cory, F. H. Laukien and W. E. Maas, *J. Magn. Reson.*, 1993, **A105**, 223.
- 31d. D. G. Cory, F. H. Laukien and W. E. Maas, *Chem. Phys. Lett.*, 1993, **212**, 487.
32. T. H. Mareci and R. Freeman, *J. Magn. Reson.*, 1982, **48**, 158.
33. L. Frydman and J. S. Harwood, *J. Am. Chem. Soc.*, 1995, **117**, 5367.
34. A. N. Garroway, J. Baum, M. G. Munowitz and A. Pines, *J. Magn. Reson.*, 1984, **60**, 337.
35. S. Wimperis and B. Wood, *J. Magn. Reson.*, 1991, **95**, 428.
36. N. Chandrakumar and S. S. Velan, *J. Magn. Reson. A*, 1993, **104**, 115.
37. N. Chandrakumar, *J. Am. Chem. Soc.*, 1993, **115**, 3780.
38. A. M. Torres, T. T. Nakashima, R. E. D. McClung and D. R. Muhandiram, *J. Magn. Reson.*, 1992, **99**, 99.
39. M. H. Levitt, *Prog. NMR Spectrosc.*, 1986, **18**, 61.
40. M. H. Levitt and R. R. Ernst, *Mol. Phys.*, 1983, **50**, 1109.
41. O. W. Sørensen, R. Freeman, T. Frenkiel, T. H. Mareci and R. Schuck, *J. Magn. Reson.*, 1982, **46**, 180.
42. S. W. Sparks and P. D. Ellis, *J. Magn. Reson.*, 1985, **62**, 1.
43. I. S. Podkorytov, *J. Magn. Reson.*, 1990, **89**, 129.
44. A. Pines, D. J. Ruben, S. Vega and M. Mehring, *Phys. Rev. Lett.*, 1976, **36**, 110.
45. S. Vega, T. W. Shattuck and A. Pines, *Phys. Rev. Lett.*, 1976, **37**, 43.
46. S. Vega and A. Pines, *J. Chem. Phys.*, 1977, **66**, 5624.
47. H. Hatanaka, T. Terao and T. Hashi, *J. Phys. Soc. Jpn.*, 1975, **39**, 835.
48. H. Hatanaka and T. Hashi, *J. Phys. Soc. Jpn.*, 1975, **39**, 1139.

49. S. Vega, T. W. Shattuck and A. Pines, *Phys. Rev. A*, 1980, **22**, 638.
50. S. Vega, *Phys. Rev. A*, 1981, **23**, 3152.
51. T. Karlsson, M. Edén, H. Luthman and M. H. Levitt, *J. Magn. Reson.*, 2000, **145**, 95.
52. R. Tycko and G. Dabbagh, *Chem. Phys. Lett.*, 1990, **173**, 461.
53. D. M. Gregory, D. J. Mitchell, J. A. Stringer, S. Kiihne, J. C. Shiels, J. Callahan, M. A. Mehta and G. P. Drobny, *Chem. Phys. Lett.*, 1995, **246**, 654.
54. D. M. Gregory, M. A. Mehta, J. C. Shiels and G. P. Drobny, *J. Chem. Phys.*, 1997, **107**, 28.
55. Y. K. Lee, N. D. Kurur, M. Helmle, O. G. Johannessen, N. C. Nielsen and M. H. Levitt, *Chem. Phys. Lett.*, 1995, **242**, 304.
56. M. Carravetta, M. Edén, X. Zhao, A. Brinkmann and M. H. Levitt, *Chem. Phys. Lett.*, 2000, **321**, 205.
57. A. Brinkmann, M. Edén and M. H. Levitt, *J. Chem. Phys.*, 2000, **112**, 8539.
58. M. Hohwy, H. J. Jakobsen, M. Edén, M. H. Levitt and N. C. Nielsen, *J. Chem. Phys.*, 1998, **108**, 2686.
59. M. Feike, D. E. Demco, R. Graf, J. Gottwald, S. Hafner and H. W. Spiess, *J. Magn. Reson. A*, 1996, **122**, 214.
60. I. Schnell and H. W. Spiess, *J. Magn. Reson.*, 2001, **151**, 153.
61. N. C. Nielsen, H. Bildsøe, H. J. Jakobsen and M. H. Levitt, *J. Chem. Phys.*, 1994, **101**, 1805.
62. C. Kehlet, T. Vosegaard, N. Khaneja, S. J. Glaser and N. C. Nielsen, *Chem. Phys. Lett.*, 2005, **414**, 204.
63. Z. Tošner, S. J. Glaser, N. Khaneja and N. C. Nielsen, *J. Chem. Phys.*, 2006, **125**, 184502.
64. C. T. Kehlet, A. C. Sivertsen, M. Bjerring, T. O. Reiss, N. Khaneja, S. J. Glaser and N. C. Nielsen, *J. Am. Chem. Soc.*, 2004, **126**, 10202.
65. T. Karlsson, C. E. Hughes, J. S. Günne and M. H. Levitt, *J. Magn. Reson.*, 2001, **148**, 238.
66. S. Dusold and A. Sebald, *J. Magn. Reson.*, 2000, **145**, 340.
67. M. Bechmann, X. Helluy and A. Sebald, *J. Magn. Reson.*, 2001, **152**, 14.
68. N. C. Nielsen, F. Cruzet, R. G. Griffin and M. H. Levitt, *J. Chem. Phys.*, 1992, **96**, 5668.
69. L. Duma, D. Abergel, F. Ferrage, P. Pelupessy, P. Tekely and G. Bodenhausen, *Chem. Phys. Chem.*, 2008, **9**, 1104.
70. G. Jaccard, S. Wimperis and G. Bodenhausen, *J. Chem. Phys.*, 1986, **85**, 6282.
71. O. W. Sørensen, U. B. Sørensen and H. J. Jakobsen, *J. Magn. Reson.*, 1984, **59**, 332.
72. U. B. Sørensen, H. J. Jakobsen and O. W. Sørensen, *J. Magn. Reson.*, 1985, **61**, 382.
73. H. Bildsøe, S. Dønstrup, H. J. Jakobsen and O. W. Sørensen, *J. Magn. Reson.*, 1983, **53**, 154.
74. O. W. Sørensen, G. W. Eich, M. H. Levitt, G. Bodenhausen and R. R. Ernst, *Prog. NMR Spectrosc.*, 1984, **16**, 163.
75. N. Chandrakumar, *J. Magn. Reson.*, 1984, **60**, 28.
76. N. C. Nielsen, H. Thøgersen and O. W. Sørensen, *J. Am. Chem. Soc.*, 1995, **117**, 11365.
77. J. Stoustrup, O. Schedletsky, S. J. Glaser, C. Griesinger, N. C. Nielsen and O. W. Sørensen, *Phys. Rev. Lett.*, 1995, **74**, 2921.
78. N. C. Nielsen, H. Thøgersen and O. W. Sørensen, *J. Chem. Phys.*, 1996, **105**, 3962.
79. A. Meissner and O. W. Sørensen, *Concepts Magn. Reson.*, 2002, **14**, 141.
80. V. Ramesh and N. Chandrakumar, *Magn. Reson. Chem.*, 2006, **44**, 936.
81. M. Mouaddab, L. Foucat, J. P. Donnat, J. P. Renou and J. M. Bonny, *J. Magn. Reson.*, 2007, **189**, 151.
82. P. J. Hore, E. R. P. Zuiderweg, K. Nicolay, K. Dijkstra and R. Kaptein, *J. Am. Chem. Soc.*, 1982, **104**, 4286.
83. A. D. Bain, D. W. Hughes, J. M. Coddington and R. A. Bell, *J. Magn. Reson.*, 1984, **58**, 490.
84. P. H. Bolton, *J. Am. Chem. Soc.*, 1984, **106**, 4299.
85. M. Novič, H. Oschkinat, P. Pfändler and G. Bodenhausen, *J. Magn. Reson.*, 1987, **73**, 493.
86. T. Nakai and C. A. McDowell, *J. Magn. Reson. A*, 1993, **104**, 146.
87. P. J. Keller and K. E. Vogele, *J. Magn. Reson.*, 1986, **68**, 389.
88. J. Weigelt and G. Otting, *J. Magn. Reson. A*, 1995, **113**, 128.
89. B. Reif, M. Köck, R. Kerssebaum, H. Kang, W. Fenical and C. Griesinger, *J. Magn. Reson. A*, 1996, **118**, 282.
90. A. Meissner, D. Moskau, N. C. Nielsen and O. W. Sørensen, *J. Magn. Reson.*, 1997, **124**, 245.

91. K. E. Kövér and P. Forgó, *J. Magn. Reson.*, 2004, **166**, 47.
92. T. N. Pham, K. E. Kövér, L. Jin and D. Uhrin, *J. Magn. Reson.*, 2005, **176**, 199.
93. L. Jin and D. Uhrin, *Magn. Reson. Chem.*, 2007, **45**, 628.
94. L. Jin, K. E. Kövér, M. R. Lenoir and D. Uhrin, *J. Magn. Reson.*, 2008, **190**, 171.
95. T. E. Skinner, T. O. Reiss, B. Luy, N. Khaneja and S. J. Glaser, *J. Magn. Reson.*, 2004, **167**, 68.
96. T. E. Skinner, T. O. Reiss, B. Luy, N. Khaneja and S. J. Glaser, *J. Magn. Reson.*, 2005, **172**, 17.
97. B. Luy, K. Kobzar, T. E. Skinner, N. Khaneja and S. J. Glaser, *J. Magn. Reson.*, 2005, **176**, 179.
98. Y. S. Yen and D. P. Weitekamp, *J. Magn. Reson.*, 1982, **47**, 476.
99. N. Chandrakumar, *Spin-1 NMR*, Springer-Verlag, Berlin, Heidelberg, 1996.
100. N. Chandrakumar, H. E. Mons, D. Hüls and H. Günther, *Magn. Reson. Chem.*, 1996, **34**, 715.
101. S. V. Raman and N. Chandrakumar, *Mol. Phys.*, 1997, **90**, 855.
102. E. Ciampi, U. Goerke, P. J. McDonald, J. Chambers and B. Newling, *Magn. Reson. Imag.*, 2001, **19**, 572.
103. Y. Sharf, U. Eliav, H. Shinar and G. Navon, *J. Magn. Reson. B*, 1995, **107**, 60.
104. H. Shinar, Y. Seo and G. Navon, *J. Magn. Reson.*, 1997, **129**, 98.
105. U. Eliav and G. Navon, *J. Magn. Reson. A*, 1995, **115**, 241.
106. L. A. Jelicks and R. K. Gupta, *J. Magn. Reson.*, 1989, **81**, 586.
107. R. B. Hutchison, D. Malhotra, R. E. Hendrick, L. Chan and J. I. Shapiro, *J. Biol. Chem.*, 1990, **265**, 15506.
108. Y. Seo, M. Murakami and H. Watari, *Biochim. Biophys. Acta*, 1990, **1034**, 142.
109. R. Reddy, M. Shinnar, Z. Wang and J. S. Leigh, *J. Magn. Reson. B*, 1994, **104**, 148.
110. R. Kemp-Harper, S. P. Brown, P. Styles and S. Wimperis, *J. Magn. Reson. B*, 1994, **105**, 199.
111. J. S. Tauskela, J. M. Dizon, P. J. Cannon and J. Katz, *J. Magn. Reson. B*, 1995, **108**, 165.
112. I. Schnell, B. Langer, S. H. M. Söntjens, M. H. P. van Genderen, R. P. Sijbesma and H. W. Spiess, *J. Magn. Reson.*, 2001, **150**, 57.
113. B. R. Cherry, C. H. Fujimoto, C. J. Cornelius and T. M. Alam, *Macromolecules*, 2005, **38**, 1201.
114. M. Bechmann, H. Foerster, H. Maisel and A. Sebald, *Solid State NMR*, 2005, **27**, 174.
115. A. A. Buda, D. E. Demco, M. Bertmer and B. Blümich, *C. R. Chimie*, 2006, **9**, 346.
116. C. Hedesiu, D. E. Demco, R. Kleppinger, A. A. Buda, B. Blümich, K. Remerie and V. M. Litvinov, *Polymer*, 2007, **48**, 763.
117. G. Ye, N. Janzen and G. R. Goward, *Macromolecules*, 2006, **39**, 3283.
118. G. Ye, B. F. McGill, J. W. Traer, A. Czardybon and G. R. Goward, *Macromol. Chem. Phys.*, 2007, **208**, 2076.
119. E. M. Menger, S. Vega and R. G. Griffin, *J. Magn. Reson.*, 1984, **56**, 338.
- 119a. K. H. Lim, T. Nguyen, T. Mazur, D. E. Wemmer and A. Pines, *J. Magn. Reson.*, 2002, **157**, 160.
120. E. M. Menger, S. Vega and R. G. Griffin, *J. Am. Chem. Soc.*, 1986, **108**, 2215.
121. B. H. Meier and W. L. Earl, *J. Am. Chem. Soc.*, 1987, **109**, 7937.
122. R. Tycko and G. Dabbagh, *J. Am. Chem. Soc.*, 1991, **113**, 9444.
123. D. M. Gregory, G. M. Wolfe, T. P. Jarvie, J. C. Sheils and G. P. Drobny, *Mol. Phys.*, 1996, **89**, 1835.
124. P. V. Bower, N. Oyler, M. A. Mehta, J. R. Long, P. S. Stayton and G. P. Drobny, *J. Am. Chem. Soc.*, 1999, **121**, 8373.
125. D. M. Gregory, T. L. S. Benzinger, T. S. Burkoth, H. Miller-Auer, D. G. Lynn, S. C. Meredith and R. E. Botto, *Solid State NMR*, 1998, **13**, 149.
126. P. V. Bower, E. A. Louie, J. R. Long, P. S. Stayton and G. P. Drobny, *Langmuir*, 2005, **21**, 3002.
127. K. Saalwächter, R. Graf, D. E. Demco and H. W. Spiess, *J. Magn. Reson.*, 1999, **139**, 287.
128. R. Verel, J. D. van Beek and B. H. Meier, *J. Magn. Reson.*, 1999, **140**, 300.
129. R. Verel, T. Manolikas, A. B. Siemer and B. H. Meier, *J. Magn. Reson.*, 2007, **184**, 322.
130. A. S. D. Heindrichs, H. Geen and J. J. Titman, *J. Magn. Reson.*, 2000, **147**, 68.
131. F. J. Blanco and R. Tycko, *J. Magn. Reson.*, 2001, **149**, 131.
132. L. J. Mueller, D. W. Elliott, G. M. Leskowitz, J. Struppe, R. A. Olsen, K. C. Kim and C. A. Reed, *J. Magn. Reson.*, 2004, **168**, 327.
133. J. S. Günné, *J. Magn. Reson.*, 2006, **180**, 186.
134. K. Riedel, C. Herbst, J. Leppert, O. Ohlenschläger, M. Görlach and R. Ramachandran, *Chem. Phys. Lett.*, 2006, **424**, 178.

135. S. Cadars, A. Lesage, N. Hedin, B. F. Chmelka and L. Emsley, *J. Phys. Chem. B*, 2006, **110**, 16982.
136. S. Matsuoka and J. Schaefer, *J. Magn. Reson.*, 2006, **183**, 252.
137. S. Matsuoka and J. Schaefer, *Magn. Reson. Chem.*, 2007, **45**, S61.
138. N. A. Oyler and R. Tycko, *Magn. Reson. Chem.*, 2007, **45**, S101.
139. J. J. Lopez, C. Kaiser, S. Shastri and C. Glaubitz, *J. Biomol. NMR*, 2008, **41**, 97.
140. M. Concistrè, A. Gansmüller, N. McLean, O. G. Johannessen, I. M. Montesinos, P. H. M. Bovee-Geurts, P. Verdegem, J. Lugtenburg, R. C. D. Brown, W. J. DeGrip and M. H. Levitt, *J. Am. Chem. Soc.*, 2008, **130**, 10490.
141. A. Kubo, A. Root and C. A. McDowell, *J. Chem. Phys.*, 1990, **93**, 5462.
142. D. Franke, C. Hudalla and H. Eckert, *Solid State NMR*, 1992, **1**, 33.
143. D. Franke, C. Hudalla and H. Eckert, *Solid State NMR*, 1992, **1**, 297.
144. J. S. Günne and H. Eckert, *Chem. Eur. J.*, 1998, **4**, 1762.
145. J. S. Günne, S. Kaczmarek, L. van Wüllen, H. Eckert, D. Paschke, A. J. Foecker and W. Jeitschko, *J. Solid State Chem.*, 1999, **147**, 341.
146. M. Bechmann, S. Dusold, F. Geipel, A. Sebald and D. Sellmann, *J. Phys. Chem. A*, 2005, **109**, 5275.
147. Y. H. Tseng, Y. L. Tsai, T. W. T. Tasi, C. P. Lin, S. H. Huang, C. Y. Mou and J. C. C. Chan, *Solid State NMR*, 2007, **31**, 55.
148. D. H. Brouwer, S. Alavi and J. A. Ripmeester, *Phys. Chem. Chem. Phys.*, 2007, **9**, 1093.
149. P. E. Kristiansen, M. Carravetta, W. C. Lai and M. H. Levitt, *Chem. Phys. Lett.*, 2004, **390**, 1.
150. R. Eckman, L. Müller and A. Pines, *Chem. Phys. Lett.*, 1980, **74**, 376.
151. N. Chandrakumar, G. von Fircks and H. Günther, *Magn. Reson. Chem.*, 1994, **32**, 433.
152. P. P. Man, *J. Magn. Reson. A*, 1995, **113**, 40.
153. H. T. Kwak and Z. Gan, *J. Magn. Reson.*, 2003, **164**, 369.
154. A. J. Painter and M. J. Duer, *J. Chem. Phys.*, 2002, **116**, 710.
155. S. E. Ashbrook and S. Wimperis, *J. Magn. Reson.*, 2005, **177**, 44.
156. D. W. Hwang, W. J. Jhao and L. P. Hwang, *J. Magn. Reson.*, 2005, **172**, 214.
157. G. Mali, V. Kaučič and F. Taulelle, *J. Chem. Phys.*, 2008, **128**, 204503.
158. M. A. Thomas, H. P. Hetherington, D. J. Meyerhoff and D. B. Twieg, *J. Magn. Reson.*, 1991, **93**, 485.
159. W. I. Jung and O. Lutz, *J. Magn. Reson.*, 1991, **94**, 587.
160. A. H. Wilman and P. S. Allen, *J. Magn. Reson. B*, 1995, **109**, 169.
161. H. Lei and J. Peeling, *J. Magn. Reson.*, 2000, **143**, 95.
162. F. Du, W. J. Chu, B. Yang, J. A. D. Hollander and T. C. Ng, *Magn. Reson. Imag.*, 2004, **22**, 103.
163. M. Schneider, D. E. Demco and B. Blümich, *J. Magn. Reson.*, 1999, **140**, 432.
164. A. Wiesmath, C. Filip, D. E. Demco and B. Blümich, *J. Magn. Reson.*, 2001, **149**, 258.
165. C. H. Sotak, *J. Magn. Reson.*, 1990, **90**, 198.
166. P. W. Kuchel and B. E. Chapman, *J. Magn. Reson. A*, 1993, **101**, 53.
167. S. S. Velan and N. Chandrakumar, *Proc. Indian Acad. Sci.*, 1994, **106**, 1661.
168. K. I. Momot and P. W. Kuchel, *J. Magn. Reson.*, 2005, **174**, 229.
169. P. Styles, N. F. Soffe, C. A. Scott, D. A. Cragg, F. Row, D. J. White and P. C. J. White, *J. Magn. Reson.*, 1984, **60**, 397.
170. D. Marek, US Patent 5,247,256: RF receiver coil arrangement for NMR spectrometers.

CHAPTER 4

Analyses of Proton NMR Spectra of Strongly and Weakly Dipolar Coupled Spins: Special Emphasis on Spectral Simplification, Chiral Discrimination, and Discerning of Degenerate Transitions

Bikash Baishya¹, Uday Ramesh Prabhu^{1,2} and N. Suryaprakash¹

Contents		
	1. Introduction	333
	2. Molecules Aligned in the Liquid Crystalline Phase	334
	2.1 Hamiltonian of an oriented system	335
	2.2 Chemical shift in isotropic phase	335
	2.3 Chemical shift in anisotropic media	336
	2.4 The dipole–dipole coupling	336
	2.5 Quadrupolar interaction	338
	2.6 The order parameter of a probe molecule aligned in nematic phase	339
	2.7 Orienting the molecule	341
	2.8 Nomenclature of the spin system	341
	3. Analyses of the Spectra	342
	4. Techniques to Aid the Analyses of the Complex ¹ H NMR Spectra	345
	4.1 Specific deuteration with high power deuterium decoupling	345
	4.2 Determination of anisotropic chemical shift	345
	4.3 Energy level connectivity and Z-COSY technique	346
	4.4 Order parameter from natural abundance ² H NMR	349
	4.5 Multiple quantum (MQ) NMR	349
	4.6 Second-order spectra and estimation of an element of ordering matrix	357

¹NMR Research Centre, Indian Institute of Science, Bangalore 560012, India

²Solid State and Structural Chemistry Unit, Indian Institute of Science, Bangalore 560012, India

Annual Reports on NMR Spectroscopy, Volume 67

ISSN 0066-4103, DOI 10.1016/S0066-4103(09)06704-0

© 2009 Elsevier Ltd.
All rights reserved.

5. Analyses of Complex ^1H NMR Spectra of Weakly Dipolar Coupled Spins	363
5.1 Thermotropic liquid crystals providing first-order spectra	364
5.2 Orientation in bicelles	364
6. NMR Studies of Chiral Molecules	367
6.1 Chiral liquid crystal solvent and differential ordering effect (DOE)	368
6.2 Desired properties of the PBLG solvent	368
6.3 Order sensitive NMR parameters and chiral discrimination	369
7. Existing NMR Experiments for Chiral Discrimination	369
7.1 ^{13}C NMR in natural abundance	369
7.2 ^2H NMR in natural abundance	370
7.3 Advantages of proton NMR for chiral analyses	371
7.4 The first-order analyses of NMR spectra in PBLG solvent	371
7.5 Earlier ^1H experimental methods for chiral discrimination	374
8. Double Quantum Selective Refocusing (DQSERF): A Novel Concept	375
8.1 Dynamics of nuclear spins in SERF and DQSERF sequences	376
8.2 Behavior of magnetization in a SERF experiment	376
8.3 Dynamics of spin system in a DQSERF pulse sequence	377
8.4 Total separation by DQSERF in a strongly coupled A_3 spin system	379
8.5 Appearance of 2D SERF spectrum	379
8.6 Optimization of τ delay in DQSERF sequence	381
8.7 DQSERF and the measure of enantiomeric excess (ee)	384
8.8 Analyses of DQ-SERF spectra of A_3X , A_3MX , and A_3MPX spin systems	384
8.9 Advantages of DQSERF over SERF	385
8.10 Simplification of the analyses of complex ^1H NMR spectra	385
9. Spin State Selective Coherence Transfer: A Novel Conceptual Development of Methodology	386
9.1 Spin state selective coherence transfer and enantiomeric discrimination	386
9.2 Spin selective 3Q-SQ spectra of A_3X , A_3MX , and A_3MPX spin systems	387
9.3 Removal of B_0 field inhomogeneity at higher quantum	390
9.4 Totality of the coupling information from the overlapped and unresolved spectra of enantiomers	390
9.5 Spin selective higher quantum and the relative signs of the couplings	394
9.6 Advantages of higher quantum-single quantum correlation method	394
10. Binuclear Spin State Selection for Chiral Discrimination	395
10.1 Theoretical description of the pulse sequence	396
10.2 The interpretation of ^{13}C edited 3Q-SQ spectrum of (<i>R/S</i>)-3-butyn-2-ol	397
10.3 The interpretation of ^{13}C edited 3Q-SQ spectrum of (<i>R/S</i>)-propylene carbonate	399
11. Single Quantum Spin Selective Correlation: A Method for Chiral Discrimination and Achieving Incredible Resolution	402
11.1 Analysis of the spectrum of (<i>R/S</i>)-3-butyn-2-ol	403

11.2 Analyses of the spectra of (<i>R/S</i>)-propylene carbonate and (<i>R/S</i>)-propylene oxide	403
11.3 Advantages and limitations of the spin selected correlation experiments	410
11.4 Spin selective correlation experiment and quantification of ee	411
12. Band Selective Small Flip Angle COSY (BASE- β -COSY)	411
12.1 BASE- β -COSY and the simplification of ^1H NMR spectrum of (<i>R/S</i>)-3-butyn-2-ol	412
12.2 Analyses of 2D proton BASE- β -COSY spectrum of (<i>R/S</i>)- β -butyrolactone	414
12.3 Advantages of the BASE- β -COSY technique over other methods	414
12.4 BASE- β -COSY and the relative signs of the couplings	417
13. Conclusions	417
References	419

Abstract

The ^1H NMR spectra of partially aligned molecules become rapidly complex with the increase in the number of interacting spins and the decrease in the symmetry of the molecules. In the strongly orienting thermotropic liquid crystals, the analyses of the complex spectra are very challenging due to their second-order character. The numerical iterative calculations that are generally employed for such analyses are tedious and time consuming. On the other hand, in weakly ordering media such as bicelles or in chiral liquid crystal solvent poly- γ -benzyl-L-glutamate (PBLG), the spin systems are weakly coupled and the first-order analysis is generally possible. However, for the chiral molecules aligned in the chiral liquid crystal medium, the ^1H NMR spectra are not only complex, but also broad and featureless due to large number of pair-wise interactions of nuclear spins resulting in degenerate or near-degenerate transitions, in addition to an indistinguishable overlap of the spectra of enantiomers. This enormous loss of resolution severely hampers the analyses of proton spectra, even for spin systems with five to six interacting protons, thereby restricting its routine application. In this chapter, we report the diverse methods available to circumvent the difficulties in the analyses of such spectra, in both strongly and weakly orienting media. The discussion is devoted to recent methodological developments in the context of spectral simplification, chiral discrimination, and the discerning of the degenerate transitions.

Keywords: dipolar couplings; spectral simplification; chiral discrimination; discerning of degenerate transitions; sign of the couplings; enantiomeric excess; PBLG; DQSERF; multiple quantum; Soft-COSY; BASE- β -COSY

1. INTRODUCTION

The alignment of molecules in thermotropic liquid crystals to derive structural information is extensively employed since its discovery.¹ Several books,

comprehensive reviews, and biennial reports provide the details of the methodology and an account of the available literature.^{2–16} The object of this chapter is to give the detailed discussion on the current developments in the field to aid the analyses of complex ^1H NMR spectra of both strongly and weakly dipolar coupled spins. The chapter has been divided into two parts. In the first part, the methodological developments in the field to simplify the analyses of complex spectra of strongly dipolar coupled spin systems are discussed. In the second part, the attention is given to the analyses of the ^1H NMR spectra of weakly dipolar coupled spins, *viz.*, molecules aligned in bicelles, in chiral organic solvent poly- γ -benzyl-L-glutamate (PBLG). Particularly in the chiral organic solvent PBLG, where the differential ordering results in chiral discrimination, though ^1H NMR spectra are generally first order, there is a significant loss of resolution due to several short- and long-distance dipolar couplings experienced by each coupled spin in addition to indistinguishable overlap of the spectra from the enantiomers. The recent developments of the methods for overcoming such difficulties with emphasis on the unambiguous discrimination of the spectra for each enantiomer, achieving enhanced resolution, spectral simplification, and discerning of the degenerate transitions are discussed. The discussion is restricted to studies on small molecules.

2. MOLECULES ALIGNED IN THE LIQUID CRYSTALLINE PHASE

Since its discovery,¹ the technique of deriving the structural information by aligning the molecules in liquid crystals has been extensively practiced. For a small solute molecule dissolved in a nematic phase, the anisotropic environment of the liquid crystal provides an orientational order and a high degree of mobility, that is, a translational disorder. Consequences of these phenomena are the presence of finite intramolecular dipolar couplings among the spins and the averaging of all inter-molecular dipolar couplings to zero. The proton NMR spectrum of such a sample generally consists of sharp resonances from dissolved molecules riding over a broad background of a large number of resonances arising from the liquid crystal protons. The consequence of the orientation of the director in the magnetic field is the sharp lines for the solute molecules. However, it should be pointed out that not all liquid crystals align in the magnetic field. There are situations when broad lines are observed. An example could be a smectic A liquid crystal possessing a high temperature nematic. Initially the solute molecules give rise to broad lines. When the sample is heated and cooled to the nematic phase, keeping the sample in the magnet results in sharp lines for the dissolved solute molecule. Furthermore, in general, the degree of order of the solvent is high and that of solute is an order of magnitude lower. Thus, the spectra of the solute molecules clearly emerge out into sharp, well-resolved transitions from the background of the solvent. There is an unusual example where the dissolved solute molecule exhibits high order comparable to that of a solvent.¹⁷ Even in such a case, sharp resonances are observed. This fundamental difference of obtaining well-resolved transitions dominated by intramolecular

dipolar couplings, when compared to solids and liquids, is the basis for advancement of NMR spectroscopy of molecules aligned in liquid crystals.

2.1 Hamiltonian of an oriented system

For spin (1/2) nuclei, the Hamiltonian governing the NMR spectra of aligned molecules is given by the following equation:

$$H = - \sum_k (1 - \sigma_k - \sigma_k^a) \nu_0 I_{zk} + \sum_{k < l} \sum (J_{kl} + 2D_{kl}) I_{zk} I_{zl} + \frac{1}{2} \sum_{k < l} \sum (J_{kl} - D_{kl}) (I_k^+ I_l^- + I_k^- I_l^+) \quad (1)$$

In the above equation, J_{kl} and σ_k represent one-third of the traces of the corresponding tensors and are identical to the indirect spin-spin couplings and chemical shifts measured in the high-resolution NMR in the isotropic media. σ_k^a correspond to the shielding constant observed in the anisotropic media. D_{kl} is the direct dipolar coupling. The Hamiltonian for the oriented systems differs from that of the isotropic ones in that there are additional terms, *viz.*, chemical shift anisotropy and the dipolar couplings. These parameters are finite in the anisotropic media. Thus, in Equation (1), the substitution of $(1 - \sigma_k)$ for $(1 - \sigma_k - \sigma_k^a)$ and J_{kl} for $(J_{kl} + 2D_{kl})$ and $(J_{kl} - D_{kl})$ provides the total Hamiltonian for an isotropic system. The parameter J_{kl} also has the anisotropic part and contributes significantly in some cases. However, of the various parameters in the anisotropic media, the dipolar interaction is of significant relevance in the structure determination and has been the choice of measurement in many structure calculations. While dealing with the molecules aligned in chiral liquid crystals the chemical shift anisotropy, and for nucleus with spin $> 1/2$ the quadrupolar couplings are important. Therefore, a brief discussion on these interaction parameters is given below.

2.2 Chemical shift in isotropic phase

In isotropic liquid, the molecules undergo rapid tumbling motion to cause orientational disorder. This leads to motional averaging of the chemical shift Hamiltonian and is given as

$$\hat{H}_k^{\text{CS,iso}} \cong -\gamma_k \hbar B_0 \delta_k^{\text{iso}} \hat{I}_{kz} \quad (2)$$

where $\delta_k^{\text{iso}} = (1/3)(\delta_{xx}^k + \delta_{yy}^k + \delta_{zz}^k)$ is the motional average of overall molecular orientations. The chemical shift in terms of Larmor frequency can be written as:

$$\omega_k^0 = -\gamma_k \hbar B_0 (1 + \delta_k^{\text{iso}}) \quad (3)$$

In terms of interaction Hamiltonian, one can write:

$$[\hat{H}_k^0 = \hat{H}_k^{\text{static}} + \hat{H}_k^{\text{CS,iso}}] \quad (4)$$

2.3 Chemical shift in anisotropic media

There is a translational disorder and orientational order for the molecules in anisotropic liquid. The orientational order leads to non-zero ensemble average.

The chemical shift interaction of spin I_k is:

$$\hat{H}_k^{\text{CS}} \cong -\gamma_k \hbar \overline{\delta_{zz}^k(\theta)} B_0 \hat{I}_{kz} \quad (5)$$

The $\overline{\delta_{zz}^k(\theta)}$ is the motional average of the tensor element $\delta_{zz}^k(\theta)$ of the above equation and is given as

$$\overline{\delta_{zz}^k(\theta)} = \int d\theta \delta_{zz}^k(\theta) p(\theta) \quad (6)$$

where $p(\theta)d\theta$ is the probability that the molecule can be found with an orientation in the range θ to $\theta + d\theta$. However, $\overline{\delta_{zz}^k(\theta)}$ is not equal to δ_k^{iso} . The anisotropic effect results in the shifting of peaks from their isotropic positions.

2.4 The dipole–dipole coupling

Each nuclear spin produces a small local field around it. The magnitude and direction of the spin magnetic moment determine the strength and direction of the local magnetic field. A second nuclear spin in the vicinity interacts with this small local field. The nature of the interaction is mutual. The interaction is through space without the involvement of a chemical bond. The secular part of the dipole–dipole coupling Hamiltonian for homonuclear spin system is given by¹⁸:

$$\hat{H}_{kl}^{\text{DD}}(\theta_{kl}) = D_{kl}(3\hat{I}_{kz}\hat{I}_{lz} - \hat{I}_k \cdot \hat{I}_l) \quad (7)$$

$$\hat{H}_{kl}^{\text{DD}}(\theta_{kl}) = D_{kl} \frac{1}{2} (2\hat{I}_{kz}\hat{I}_{lz} - \frac{1}{2}(\hat{I}_{k+}\hat{I}_{l-} + \hat{I}_{k-}\hat{I}_{l+})) \quad (8)$$

where

$$D_{kl} = a_{kl} \frac{1}{2} (3 \cos^2 \theta_{kl} - 1) \quad (9)$$

and

$$a_{kl} = -\frac{\mu_0 \gamma_k \gamma_l \hbar}{4\pi r_{kl}^3} \quad (10)$$

Here r_{kl} is the internuclear distance between the nuclei k and l as depicted in Figure 1 and γ_k and γ_l are the magnetogyric ratios

$$\cos \theta_{kl} = e_{kl} \cdot e_z \quad (11)$$

Here e_{kl} is the unit vector along the line joining the center of the two nuclei as shown in Figure 1 and e_z is the direction of the magnetic field (B_0). In the heteronuclear case, the secular part of the dipole–dipole coupling Hamiltonian is given by:

$$\hat{H}_{kl}^{\text{DD}}(\theta_{kl}) = D_{kl} \hat{I}_{kz} \hat{I}_{lz} \quad (12)$$

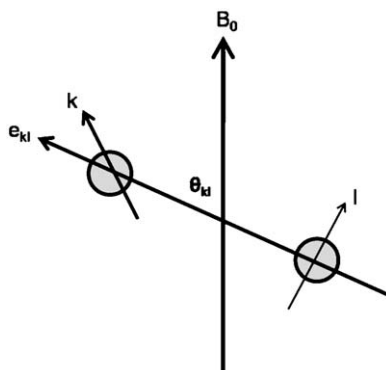


Figure 1 The orientation of inter-nuclear vector with respect to the applied static field B_0 .

2.4.1 Effect of dipolar coupling on spin system and its energy levels

The dipolar Hamiltonian can be written as a sum of two terms A and B , where

$$A = \hat{I}_{kz} \hat{I}_{lz} \quad \text{and} \quad B = (\hat{I}_{k+} \hat{I}_{l-} + \hat{I}_{k-} \hat{I}_{l+}) \quad (13)$$

The term A causes the first-order shift in energy to all the states as:

$$\langle \alpha\alpha | \hat{I}_{kz} \hat{I}_{lz} | \alpha\alpha \rangle \quad (14)$$

The eigenfunctions of these product operators are simply the product Zeeman states $|\alpha\alpha\rangle$, $|\alpha\beta\rangle$, $|\beta\alpha\rangle$, and $|\beta\beta\rangle$. As far as term B is concerned, there are non-vanishing matrix elements in the matrix representation of this operator in the Zeeman basis:

$$B = D_{kl} \begin{pmatrix} 0 & 0 & 0 & 0 \\ 0 & 0 & 1 & 0 \\ 0 & 1 & 0 & 0 \\ 0 & 0 & 0 & 0 \end{pmatrix}$$

This term mixes $|\alpha\beta\rangle$ and $|\beta\alpha\rangle$ states and hence eigenfunctions of B are linear combination of $|\alpha\beta\rangle$ and $|\beta\alpha\rangle$ functions. The consequence of this is a range of frequencies and homogeneous line broadening. In heteronuclear system, only the A part is responsible for the first-order shift in energy to all the states. The heteronuclear and homonuclear dipolar coupling Hamiltonians do not commute and it is difficult to remove heteronuclear coupling in the presence of homonuclear coupling.

2.4.2 Dipolar coupling in isotropic liquids

In isotropic liquids, there is no orientational order as the molecules undergo rapid molecular motion. The secular part of the intramolecular dipole-dipole couplings averages to zero:

$$\int_0^\pi d\theta_{kl} \sin \theta_{kl} (3 \cos^2 \theta_{kl} - 1) = 0 \quad (15)$$

where $\sin \theta_{kl}$ is a probability factor.

Thus

$$\hat{H}_{kl}^{\text{DD}} \cong 0 \quad (16)$$

2.4.3 Dipolar coupling in anisotropic phase

As a consequence of anisotropic liquids possessing orientational order and translational disorder, the intramolecular dipole–dipole couplings are not averaged to zero. The secular part of the dipole–dipole coupling is

$$D_{kl} = a_{kl} \frac{1}{2} \overline{(3 \cos^2 \theta_{kl} - 1)} \quad (17)$$

where $\overline{(3 \cos^2 \theta_{kl} - 1)}$ is an ensemble average and a_{kl} is discussed in Equation (10).

2.4.4 Pseudo-dipolar coupling (J_{kl}^a)

The experimentally determined dipolar coupling is the sum of the dipolar coupling and the anisotropic contribution of the indirect spin–spin coupling (J_{kl}^a). The multiplier of the spin operator for J_{kl}^a has the same functional dependence as that of the dipolar coupling and hence J_{kl}^a is also called pseudo-dipolar coupling. The dipolar couplings obtained from the NMR spectra ($D_{kl}(\text{expt})$) are, therefore, $D_{kl} + J_{kl}^a$. For a pair of protons, J_{kl}^a is usually negligible since the major contribution to J_{kl}^a comes from the spherically symmetric Fermi contact term. In such cases, the measured direct dipolar couplings straightaway provide the geometric information. For heavy nuclei such as fluorine, the contributions from J_{kl}^a , however, could be significant.¹⁶

2.5 Quadrupolar interaction

Quadrupolar interaction dominates the spectra of nuclear spins with spin angular momentum I greater than $1/2$. Since the impetus in this chapter is on the methods to simplify the analyses of proton NMR spectra of dipolar coupled spins, this interaction term was not introduced in the expression for the Hamiltonian given in Equation (1). This interaction, unlike other interactions discussed earlier which are magnetic, arises due to interaction between the electric quadrupole moment of the nucleus and the electric field gradient. The interaction is intramolecular. The quadrupolar interaction and Zeeman interaction always compete to orient the same magnetic moment in different directions. This leads to quadrupole perturbed Zeeman interaction in high B_0 fields and Zeeman perturbed quadrupole interaction in low B_0 fields. When Zeeman interaction is very large compared to the strength of quadrupolar interaction, the secular approximation can be employed. The secular quadrupolar interaction can be written as:

$$\hat{H}_k^{\text{Q}} \cong \omega_k^{\text{Q}} (3\hat{I}_{kz}^2 - \hat{I}_k \cdot \hat{I}_k) \quad (18)$$

Here ω_k^{Q} is the quadrupolar frequency.

2.5.1 Quadrupolar interaction in anisotropic liquids

The quadrupolar frequency in an anisotropic medium is given by:

$$\omega_k^Q = \frac{3eQ_k}{4I_k(2I_k - 1)} \overline{V_{zz}^k} \quad (19)$$

Here Q_k is the electric quadrupole moment of the nucleus, e the charge of the proton, and $\overline{V_{zz}^k}$ a component of the electric field gradient at the nucleus I_k . $\overline{V_{zz}^k}$ is an ensemble average over all molecular orientations weighted by the probability of occurrence of each molecular orientation in the liquid crystalline phase:

$$\overline{V_{zz}^k} = \int d\theta V_{zz}^k(\theta) p(\theta) \quad (20)$$

Because of the orientational order in liquid crystal, $\omega_k^Q \neq 0$.

2.5.2 Quadrupolar interaction in isotropic liquids

In an isotropic liquid, because of orientational disorder, $\omega_k^Q = 0$. Hence, the resonance position is unaffected. However, the relaxation is strongly influenced by this interaction and affects line intensities and line widths.

2.6 The order parameter of a probe molecule aligned in nematic phase

The dipolar Hamiltonian for the homonuclear spins is given by:

$$\hat{H}_{kl}^{DD}(\theta_{kl}) = D_{kl} \frac{1}{2} \left\{ 2\hat{I}_{kz}\hat{I}_{lz} - \frac{1}{2}(\hat{I}_{k+}\hat{I}_{l-} + \hat{I}_{k-}\hat{I}_{l+}) \right\} \quad (21)$$

In a liquid crystal

$$D_{kl} = -\frac{\mu_0}{4\pi} \frac{\gamma_k \gamma_l \hbar}{r_{kl}^3} \frac{1}{2} (3 \cos^2 \theta_{kl} - 1) \quad (22)$$

$$D_{kl} = -a_{kl} \cdot \frac{1}{2} \langle (3 \cos^2 \theta_{kl} - 1) \rangle \quad (23)$$

with

$$a_{kl} = \frac{\mu_0}{4\pi} \frac{\gamma_k \gamma_l \hbar}{r_{kl}^3} \quad (24)$$

D_{kl} is the Cartesian second rank tensor and describes the orientation dependence of the interaction. If there is no correlation between inter-nuclear distance and $\langle (3 \cos^2 \theta_{kl} - 1) \rangle$, then

$$D_{kl} = -a_{kl} \cdot \frac{1}{2} \langle (3 \cos^2 \theta_{kl} - 1) \rangle \left\langle \frac{1}{r_{kl}^3} \right\rangle \quad (25)$$

For rigid solutes

$$\left\langle \frac{1}{r_{kl}^3} \right\rangle = \frac{1}{r_{kl}^3} \quad (26)$$

Thus, Equation (25) can be written as:

$$D_{kl} = -\frac{a_{kl}}{r_{kl}^3} (S_{kl}) \quad (27)$$

where $S_{kl} = \langle (1/2)(3 \cos^2 \theta_{kl} - 1) \rangle$ is the orientation or order parameter of the axis passing through the center of the nuclei k and l . The values of S_{kl} vary between -0.5 and 1.0 . The S values along different molecular axes are found to be interdependent. Most often we encounter the situation where the director of the liquid crystal is assumed parallel to the magnetic field direction and the orthogonal X , Y , and Z axes are the molecule fixed coordinate frame. In this coordinate system, θ_x , θ_y , and θ_z are the angles between the molecular axes and the magnetic field direction and the definition of the element of the ordering matrix is given by:

$$S_{kl} = \frac{1}{2} \langle (3 \cos \theta_m \cos \theta_n - \delta_{mn}) \rangle, \quad m, n = x, y, z \quad (28)$$

The matrix S_{kl} is explicitly written as

$$S_{kl} = \begin{vmatrix} S_{xx} & S_{xy} & S_{xz} \\ S_{yx} & S_{yy} & S_{yz} \\ S_{zx} & S_{zy} & S_{zz} \end{vmatrix} \quad (29)$$

where δ_{mn} is the Kronecker delta ($\delta_{mn} = 1$, for $m = n$ and $\delta_{mn} = 0$, for $m \neq n$).

The above ordering matrix is symmetric and traceless and has five independent elements, viz., S_{XX} , S_{YY} , S_{XY} , S_{XZ} , and S_{YZ} .

2.6.1 Order parameter and the molecular symmetry

Depending on the symmetry of the molecule and the suitable choice of the coordinate system, the number of independent elements of the ordering matrix required to describe the orientation of the molecule varies from zero to five.

Molecules with tetrahedral or cubic symmetry do not orient (S value is zero) even in an anisotropic environment and hence the dipolar couplings in such systems average to zero. However, in actual practice, the anisotropic environment causes minor distortions in the symmetry providing dipolar splitting of the transitions.^{19,20} Molecules possessing point group symmetry, viz., D_{2d} , C_{3v} , and higher axis of symmetry require only one independent element of the ordering matrix to describe their orientation. For molecules possessing C_{2v} , D_{2v} , and D_{2h} point group symmetry, the number of independent elements required to describe the orientation reduces to two. For the molecules possessing only a plane of symmetry and if the two coordinate axes are chosen to be in the plane of the symmetry, three independent elements of the ordering matrix are required to

describe their orientation. For molecules without a plane of symmetry, all the five elements of the ordering matrix are essential to describe their orientation.

2.6.2 Order parameter and experimental conditions

The ordering of the molecule in the nematic phase depends on the temperature and solute concentration. As the concentration of the solute is increased the ordering generally decreases, unless the solvent interacts with solutes. Similarly, ordering generally increases with the decrease of temperature. In a study on the molecule methanol oriented in the liquid crystal 4-*n*-octyloxybenzoic acid, an unusual orientational behavior has been observed.²¹ When the order parameter was measured as a function of temperature and at two different concentrations, there was no steady increase of the order parameter with decrease of temperature; instead, the plot of the order parameter as a function of temperature passed through a maximum. This unusual behavior of methanol is interpreted as due to association. Any change in the order parameter because of different experimental conditions results in the change of the strength of the dipolar interaction. Hence, the spectra of the given molecule in a particular liquid crystal are not identical when recorded at different temperatures or concentrations.

2.7 Orienting the molecule

Solutions are prepared by mixing the appropriate amounts of solute and solvent. Solute concentration is maintained such that the liquid crystallinity is not destroyed and it is usually less than 4–5% (w/w). The solutions are homogenized by repeated heating of the mixtures to the isotropic phase and then cooling back to the nematic phase, with physical shaking or vortex mixing. It should be noted that the inhomogeneities as a result of temperature or concentration gradient within the sample provide spectra with differential line broadening. This differential line broadening is over and above the inhomogeneity of the external magnetic field. In superconducting magnets, the inhomogeneity due to external static magnetic field can be reduced by spinning the sample about the vertical axis without destroying the orientation. Typical line widths around 2–3 Hz have been obtained for the proton spectra, depending on the choice of the liquid crystal, experimental conditions, and preparation of the sample. It is appropriate to mention that when the nematic liquid crystal ZLI-1167 (a eutectic mixture of propyl, pentyl, and heptyl bicyclohexyl carbonitrile) is used, sharp lines are generally observed.

2.8 Nomenclature of the spin system

As far as the nomenclature of the NMR spectra is concerned, it is identical to that followed in the conventional high-resolution NMR studies in liquids. However, the definition of weak and strong coupling in the spectra of oriented molecules depends on the ratio of the sum of dipolar couplings and the indirect spin–spin couplings with the chemical shifts, unlike the ratio of the strength of only the indirect spin–spin coupling to the chemical shift in the isotropic phase.

The strength of the dipolar couplings may usually vary from few hertz to few kilohertz. The spectra may, therefore, be very complex with a spread of several kilohertz and are generally strongly coupled particularly in the thermotropic nematic liquid crystals normally employed unless heteronuclei are involved.^{22–24} The second important difference is that a group which is magnetically equivalent and provides a single resonance line in the isotropic phase gives rise to multiplet pattern in oriented systems. For example, in benzene, in the isotropic phase, all the six protons have the same chemical shift and also the indirect spin–spin couplings do not influence the spectrum giving rise to a single resonance line compared to a complex spectrum in the oriented phase. The spectrum of benzene is designated as $AA'A''A'''A''''A'''''$. Further, if all the nuclei within a magnetically equivalent group are equally coupled to one another, the group is called ‘fully equivalent.’ Such a group is denoted as A_n , where n is the number of fully equivalent spin 1/2 nuclei. In oriented molecules, even the fully equivalent groups such as A_n give rise to multiplicity of ‘ n ’ transitions with a separation equal to $3D_{ij}$ between adjacent transitions. The intensity distribution of the transitions corresponds to coefficients of the binomial expansion. For example, the methyl protons of CH_3CN , a fully equivalent group, give rise to a singlet in the isotropic phase because indirect spin couplings between the equivalent protons of the methyl group do not influence the spectrum. In the anisotropic phase, the nomenclature of the spin system is A_3 . Nevertheless, the dipolar couplings between the protons of the methyl group, although identical between any two methyl protons, result in a triplet with the intensity ratio of 1:2:1.

The molecules with a ‘tetrahedral (Td)’ or higher symmetry, in general, should not orient and must give single resonance line in either the isotropic phase or the oriented phase. However, as discussed earlier, there are unusual examples where the multiplicity of spectral lines is observed in such systems in the oriented phase.^{19,20}

3. ANALYSES OF THE SPECTRA

For N interacting spin 1/2 nuclei, the number of theoretically allowed transitions is given by $2^N C_{N-1}$. As an example, for systems with five, six, seven, and eight interacting spins, there are 210, 792, 3,003, and 11,440 allowed transitions, respectively. It implies that the addition of each interacting spin enhances the complexity of the spectrum and the number of allowed transitions increases by nearly a factor of four. Beyond eight interacting spins, the spectra usually become too complicated and the analysis becomes tedious. However, there are reports in the literature where the complex spectra of several interacting spins have been analyzed.^{25–33} The first-order analyses of the spectra similar to that of liquids are generally not possible and one has to diagonalize the Hamiltonian numerically, adapting the least-square-fit techniques, using computers. Several iterative computer programs, suitably modified by the inclusion of the dipolar coupling parameters, are commonly used.

The program normally employed for iterative calculations is named LAOCOONOR.³⁴ The numerical analysis requires the values of chemical shifts (ν_i), the indirect spin–spin couplings (J_{ij}), and the direct dipolar couplings to use as the starting parameters. All these parameters are unknown for an oriented system. Generally the chemical shifts and the indirect spin–spin couplings obtained from the isotropic spectra are employed as the starting parameters. The dipolar couplings are calculated assuming the molecular geometry and with certain guessed values for the orientational tensor components.

The normally practiced method is to simulate the spectrum. The trial spectrum simulated should closely resemble the experimental spectrum such that sufficient number of transitions can be assigned for subsequent iteration and refinement of parameters. Then certain specific experimental lines are assigned to theoretical ones and all the parameters are varied iteratively. The iterative procedure is continued until all the experimental lines are assigned to the simulated ones and the root-mean-square (RMS) error between the calculated and experimental line positions reaches an acceptable global minimum. When the spectra are very complex and the starting parameters are far from real values, the iterative analysis can get captured in the local minimum, making further analysis very tedious. Basic ingenuity lies in the judicious choice of the initial starting parameters. However, there are several difficulties in choosing the initial parameters. There are anisotropic contributions to the chemical shifts which depend on the chemical shift tensor components scaled by the order parameters along the respective axes. In addition to the scant knowledge available about proton chemical shift tensors, the magnitude and sign of the order parameter are unknown and consequently it is very difficult to predict the chemical shifts in the oriented phase. These values can vary very much from the isotropic values. Therefore, choosing the correct starting parameters of the chemical shifts is one of the bottlenecks in the analysis.

There are also anisotropic contributions to the indirect spin–spin couplings, and due to similar functional dependence, they are reflected in the dipolar couplings. For the precise determination of dipolar couplings, these contributions must be subtracted from the experimental values of dipolar couplings. As far as the proton–proton couplings are concerned, such contributions are shown to be negligible¹⁶ and the isotropic values are employed as the starting parameters and are kept constant during the initial iterations.

The D_{ij} , on the other hand, are dependent on the molecular geometry and the elements of the ordering matrix in the coordinate frame employed to define the orientation of the molecule. A prior knowledge about the geometry and symmetry of the molecule is necessary in order to obtain the guessed dipolar couplings so that the iterative calculation is accelerated. The strategy adapted for the analyses of the spectra is given as a flow chart in Figure 2. The iterative analyses can be tedious and time consuming when the spectra are very complex.

To overcome the tedium of such analyses, the program called DANSOM^{35,36} has been developed for the automatic analysis using an alternative strategy which does not require any line assignments. The program utilizes the full

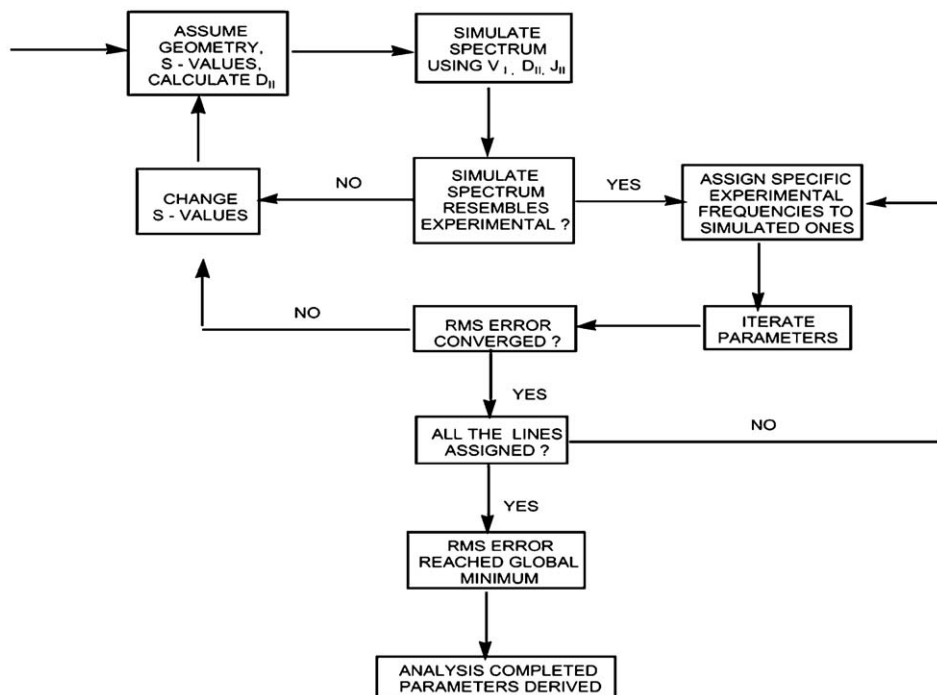


Figure 2 Flow chart depicting the strategy adopted for the analyses of the NMR spectra of oriented molecules.

information content of an NMR spectrum, that is, the total line shape. This information is supplied to the computer as the n -dimensional vector S of digitized signal intensities S_i which are ordered according to increasing or decreasing discrete frequencies ω_i . The basic algorithm relies on a matrix method derivable from a generalized formulation of the least-squares problem. The details of the theoretical basis of this automatic analysis are available in the literature.³⁷ However, it is important to note that these programs circumvent the tedium of line assignments and in many instances found to yield satisfactory results. The programs dedicated to NMR instrument called WIN-DAISY^{38,39} and PERCH⁴⁰ were also available. These programs call the experimental spectra directly on to the computer from the spectrometer and the automatic analysis is carried out by varying over a wide range, iteratively, all the parameters affecting the spectrum.

Due to several limitations, automatic analysis is not routinely employed and most of the published works in the literature utilize computer program requiring manual intervention proving it to be more robust. Thus, development of novel methods which provide additional information to aid the analyses of the complex spectra finds potential application.

4. TECHNIQUES TO AID THE ANALYSES OF THE COMPLEX ^1H NMR SPECTRA

The analyses of the spectra would be tedious when the number of interacting spins exceeds 10 and especially when the molecules lack any higher symmetry element. Several one- and two-dimensional techniques have, therefore, been developed and are being developed to aid the analysis of the complex spectrum. All the developed methodologies can be broadly classified into two groups: (a) the experimental techniques to derive additional information for subsequent analyses of complex ^1H spectra and (b) methods to simplify the complexity of the spectra amenable for easy analyses.

Some of the methods available in the literature are Z-COSY technique,⁴¹ natural abundance ^2H NMR,⁴² use of liquid crystals with low-order parameters,⁴³ multiple quantum (MQ) methodologies,^{44–55} multiple pulse sequences,^{56–59} specific deuteration,⁶⁰ two-dimensional inverse experiments,^{61–63} low-order orientation using bicelles,⁶⁴ proton-detected local field,^{65,66} use of low-power Lee Goldburg (LG) decoupling,⁶⁷ spin decoupling,^{68,69} spin echo technique,^{70,71} and near magic angle spinning.^{72,73} Though the application of the above techniques has been demonstrated on several spin systems, each of the above techniques has its own limitations and is not routinely employed. Thus, the studies are generally restricted to 8–10 interacting spins, beyond which the spectra become too complex and the analysis is tedious. Automatic analyses^{74–79} of the spectra have also been reported which do not require any line assignments. Before hopping on to the recently developed techniques, a couple of existing methods (not all the reported techniques) in the literature for simplifying the analyses of complex spectra will be discussed.

4.1 Specific deuteration with high power deuterium decoupling

In this study,⁶⁰ for the molecule investigated, all the proton sites except a pair of protons are deuterated. Subsequently the proton spectrum is acquired under broadband deuterium decoupling. A doublet is detected in the observed spectrum drastically simplifying the spectral analysis. The derived dipolar couplings are employed to determine molecular structure. However, the drawback of this method is requirement of specific deuteration, which is tedious and uneconomical.

4.2 Determination of anisotropic chemical shift

The individual proton chemical shifts in the anisotropic phase are unknown. If the knowledge of this information is available, they can be kept constant during the iterative analyses. To obtain the anisotropic chemical shift, it is necessary to eliminate the homonuclear dipolar couplings among protons. For this purpose, the use of multiple pulse techniques⁸⁰ is an excellent choice. Multipulse techniques have been employed earlier to achieve partial dipolar

decoupling and to simplify the spectra by scaling the dipolar couplings.^{56,57} The two-dimensional versions of the experiment on oriented samples have been utilized to demonstrate the scaling achieved. The multipulse experiments are, in general, technically demanding. On the other hand, the use of off-resonance LG decoupling⁸¹ is a simple and convenient means of removing homonuclear dipolar couplings which is widely employed in recent times in solid state studies and its implementation is easy. There are many LG sequences reported in the literature such as flip flop Lee Goldburg (FFLG),⁸² frequency switched Lee Goldburg (FSLG),^{83,84} phase modulated Lee Goldburg (PMLG),⁸⁵ and Lee Goldburg cross-polarization (LGCP).^{86,87} These LG sequences are designed to remove homonuclear dipolar couplings and find extensive applications in the separated local field (SLF) experiments involving liquid crystals and weak aligning media such as bicelles.^{88–90} In a review, both PMLG and FSLG sequences are referred as FFLG.⁹¹

In a report, the proton chemical shifts of the molecules in the oriented phase have been determined by adapting a two-dimensional approach, wherein during the t_1 period FSLG sequence is employed to suppress the homonuclear dipolar couplings and only the anisotropic proton chemical shifts are retained in the t_2 dimension.⁹² The designed pulse sequence for such an experiment is reported in Figure 3. It is demonstrated that in the case of the molecule *cis,cis*-mucononitrile, the chemical shifts obtained by this method are very nearly the same as the chemical shifts obtained by the conventional iterative analysis of the one-dimensional proton spectrum. It may be pointed out that for the conventional iterative analysis, the isotropic chemical shifts were used as the starting parameters. The method has also been applied to obtain the chemical shifts and for the subsequent iterative analyses of the proton spectrum of a seven spin system, 1-iodopropane.⁹² The complex one-dimensional spectrum of 1-iodopropane and its two-dimensional spectrum with LG decoupling in the F_1 dimension are also reported in Figure 3. It is evident from the projection of the 2D spectrum taken along F_1 dimension that the chemical shift differences obtained in the anisotropic phase are very much different from those of the isotropic phase. The knowledge of these values from the 2D spectrum significantly simplified the analyses of the one-dimensional spectrum.

4.3 Energy level connectivity and Z-COSY technique

The two-dimensional Z-COSY experiment provides information on the direct connectivity between the transitions which in turn yield the energy level connectivity. The techniques have been applied to oriented acetone and *cis,cis*-mucononitrile.⁴¹ The molecule *cis,cis*-mucononitrile has C_{2h} symmetry, requires three elements of the ordering matrix to define its orientation, and the protons of the molecule form an AA'BB' spin system. The Z-COSY spectrum shown in Figure 4 identified two groups of transitions; two of them had only two transitions each. However, the AA'BB' spin system has only two domains, symmetric and antisymmetric. The COSY spectrum resolved this ambiguity by

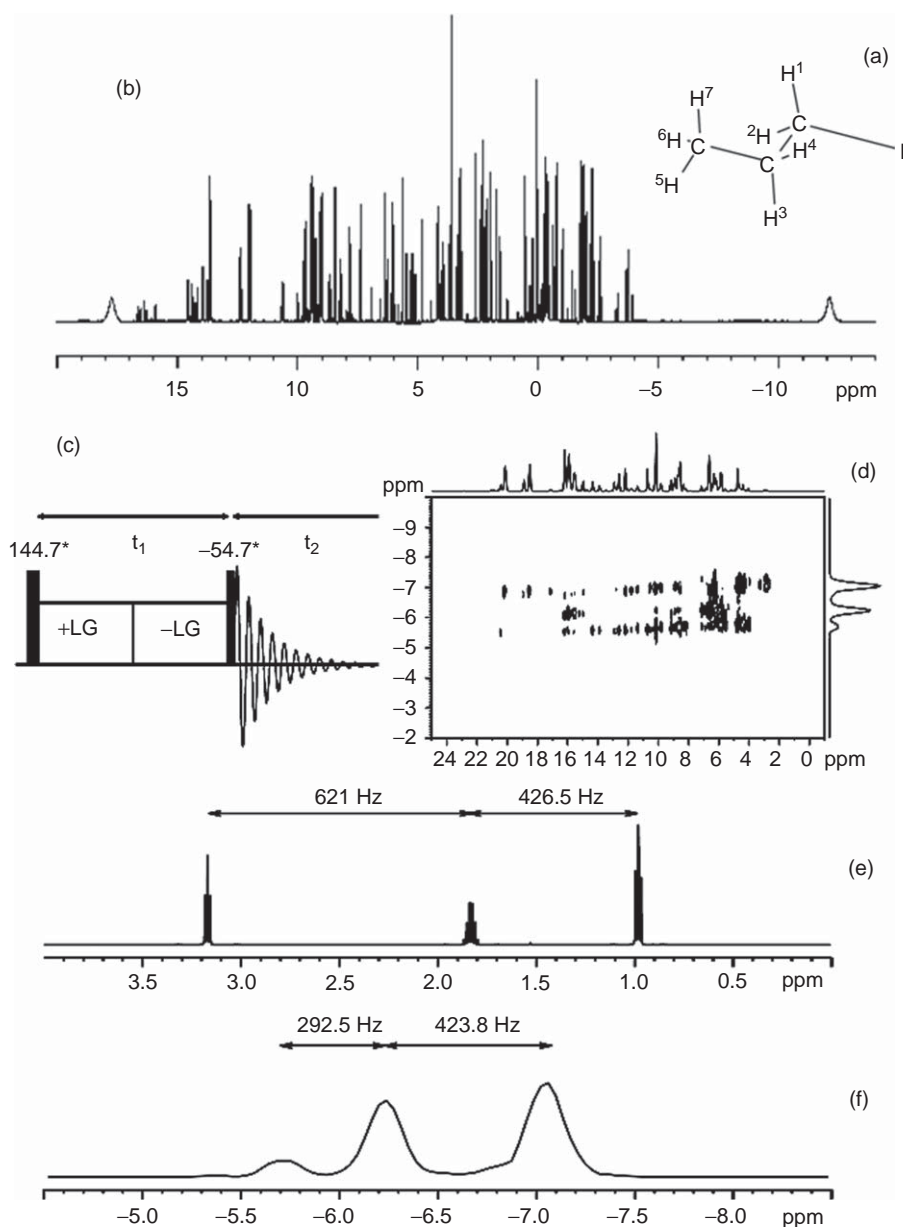


Figure 3 (a) The structure and numbering of the protons in 1-iodopropane. (b) The 500 MHz one-dimensional proton spectrum oriented in the liquid crystal solvent ZLI-1132. (c) The pulse sequence employed in the 2D experiment for the determination of individual chemical shifts of protons in the anisotropic phase. The LG decoupling is employed in the t_1 dimension. (d) The 500 MHz 2D spectrum of 1-iodopropane oriented in the liquid crystal ZLI-1132 with projections on F_1 and F_2 axes; proton is detected in both direct and indirect dimensions. The total length of the LG decoupling pulse increased two times for each t_1 increment. (e) The isotropic spectrum of 1-iodopropane in the solvent CDCl_3 . (f) The F_1 projection of the spectrum given in (d) plotted for comparison.

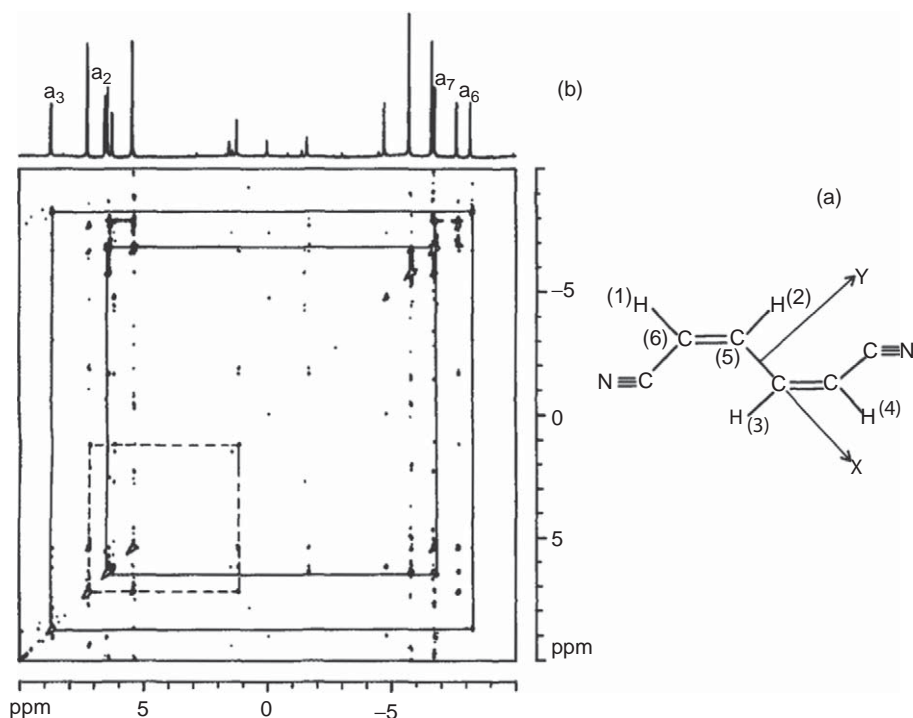


Figure 4 (a) The structure, the numbering of the spins, and the choice of the coordinate system in the molecule *cis,cis*-mucononitrile; and (b) two-dimensional modified Z-COSY spectrum of *cis,cis*-mucononitrile oriented in the liquid crystal solvent ZLI-1167. The corresponding one-dimensional spectrum is given at the top. The connected transitions a_2 and a_7 , and a_3 and a_6 are marked.

giving cross-peaks between the groups having two transitions each. There are 8 antisymmetric and 20 symmetric transitions for an AA'BB' spin system. Thus, the domain with larger connected transitions could be identified for symmetric domain. If the chemical shifts and indirect couplings are assumed to be very small, only four of the eight antisymmetric transitions have significant intensities and the spacing between them is given by

$$\left(\frac{3}{2}\right)(D_A + D_B) \pm 3R_3 \quad (30)$$

Similarly in the symmetric domain, both the extreme energy levels are pure states and show regressive connectivity to each other and yield unique values under the assumption that chemical shifts and indirect couplings are negligible. The spacing between them is given by

$$\left(\frac{3}{2}\right)(D_A + D_B) + 2(D + D') \pm R_1 \quad (31)$$

where the symbols D_A , D_B , D , D' , R_1 , and R_3 correspond to

$$\begin{aligned} D_A &= D_{14}, & D_B &= D_{23}, & D &= D_{12}, & D' &= D_{13} \\ R_1 &= \left[\frac{9}{4}(D_A - D_B)^2 + (D + D')^2 \right]^{1/2} \\ R_3 &= \left[\frac{1}{4}(D_A - D_B)^2 + (D - D')^2 \right]^{1/2} \end{aligned} \quad (32)$$

Using this information, a set of dipolar couplings was determined and utilized for iterative analysis. This information significantly simplified the analyses. The Z-COSY has been applied for the analyses of other molecules and has been discussed extensively in a book.⁶

4.4 Order parameter from natural abundance ^2H NMR

Information on the molecular ordering can be employed to derive the realistic starting parameters of the dipolar couplings that aid the analyses of the complicated proton spectra. The use of natural abundance ^2H NMR of the molecules dissolved in liquid crystal solvent has been suggested as a practical tool in deriving this information.⁴² The natural abundant ^2H NMR spectra of benzene and chloroform dissolved in a liquid crystalline solvent have been studied. In each case under identical conditions, proton spectra were also recorded. The quadrupole doublet was employed to determine the order parameter. In benzene, the quadrupole split doublet separation was 31.952 kHz. Using the reported value of 196.5 kHz for the deuteron quadrupole coupling constant, the quadrupole split doublet provided the order parameter in the plane of the benzene ring as 0.1084 in the liquid crystal solvent Merck ZLI-1114 (*trans*-pentyl-(4-cyanophenyl)-cyclohexane). Using this value of the order parameter, the dipolar coupling between the *ortho* protons of the benzene was estimated to be -852.1 Hz. Assuming an undistorted hexagonal geometry of the molecule, the remaining *meta* and *para* dipolar couplings were then calculated. The proton spectrum of benzene recorded under identical conditions of the concentration, temperature, and solvent was analyzed independently by conventional iterative procedure. The value of the dipolar couplings derived from the analysis of the proton spectrum and that derived by the knowledge of the order parameter from the natural abundance ^2H spectrum have been shown to be identical. Thus, this method paved another way to derive information that aids the analyses of complex spectra.

4.5 Multiple quantum (MQ) NMR

MQ coherence is a coherent superposition of states for which the change in total spin magnetic quantum number is $\neq 1$.^{93,94} Spins which undergo flipping are said to be active in the coherence and all the remaining spins are said to be passive. The information content of the MQ coherence depends on both its order and the

active spins and their interactions with the passive spins. The group of active spins can be construed as the super spin and the remaining passive spins are treated as spectator spins. As the size of the super spin increases, the number of spectator spins decreases and consequently the multiplet pattern of the coherence becomes simpler. The number of allowed transitions for the zeroth- and the m^{th} -order quantum coherence of N non-equivalent interacting half integer spins is given by

$$Z_0 = \frac{1}{2} [2^N C_N - 2^N] \quad (33)$$

$$Z_m = \frac{2N!}{(N-m)!(N+m)!} \quad (34)$$

where Z_0 refers to zero quantum (ZQ) and Z_m the m^{th} quantum for $m > 1$. Thus, the highest quantum is for $N = m$ and it pertains to a situation wherein all the spins are participating spins and there are no spectator spins. This corresponds to a situation where all the N spins flip simultaneously from the state $|\alpha\rangle$ to the state $|\beta\rangle$ or vice versa. It implies that the scalar and the dipolar fields do not influence the spectrum. The highest quantum spectrum, however, provides information on the sum of all the chemical shifts. The different MQ orders of N interacting spins can be selectively excited or detected.^{95,96}

The $N-1$ quantum is a situation in which $N-1$ spins flip in the presence of one left over spin. The super spin is then split by the scalar and/or the dipolar field of a spectator spin providing a doublet centered at the sum of the chemical shift positions of the active spins. The separation of the doublet provides the sum of the couplings of the active spins to the passive spin. For N non-equivalent spins, there are N doublets in the $N-1$ quantum spectrum. The $N-2$ quantum spectrum is a situation where $N-2$ spins flip at a time in the presence of the remaining two passive spins. This will have more number of transitions than $N-1$ quantum, but significantly less compared to SQ transitions. The number of transitions and thereby the complexity of the spectrum increases by going to lower quantum. The $N-1$ and $N-2$ quantum spectra have sufficient number of transitions to provide all the spectral parameters. Furthermore, the sensitivity of the precessional frequency of any higher quantum coherence is proportional to its order. Thus, the field inhomogeneity contributes to the m^{th} quantum order by m times. However, the ZQ coherence is insensitive to the field inhomogeneity.

4.5.1 Two-dimensional MQ–SQ correlation

The transfer of the MQ coherence to the observable SQ for different types of spin systems⁹⁷ and the flip angle dependence of the intensities for an AMX spin system have been discussed earlier.⁹⁸ In the schematic representation of the correlation of double quantum (DQ) coherence to its SQ coherence on a homonuclear J coupled AMX spin system,⁹⁷ the DQ dimension provides three doublets with the separation corresponding to the sum of the J -couplings between the passive spin and the active spins centered at the sum of the chemical

shift positions of the two active spins. Each of these doublets corresponds to the states $|\alpha\rangle$ and $|\beta\rangle$ of the passive spin. The cross-sections taken along the SQ dimension for any of the spin states of the passive spin provide all the 12 transitions expected for an AMX spin system, whose intensities depend on the flip angle. Thus, the application of a non-selective mixing pulse results in each $|\alpha\rangle$ and $|\beta\rangle$ states of A, M, and X spins correlating to all the allowed transitions in the SQ dimension. If, on the other hand, a selective pulse is applied only on the active spins and no pulse is applied on the passive spins during MQ–SQ conversion, then the states of the passive spins remain unperturbed in both MQ and SQ dimensions. Each state of the passive spins in the MQ dimension then encodes the spin states involved in the SQ transitions that arise only due to coupling between the active spins. This results in the selective detection of SQ transitions. The cross-section taken along SQ dimension for any one of the passive spin states has sufficient number of transitions essential to determine the couplings between active spins. This reduces the redundancy in the number of SQ transitions and simplifies the complexity of the spectrum. The application of spin state selective detection of transitions employing MQ for spectral simplification has been demonstrated on oriented doubly labeled acetonitrile and *ortho*-difluorobenzene⁹⁹ and is discussed in detail below.

4.5.2 Uniformly ^{13}C labeled acetonitrile ($^{13}\text{CH}_3^{13}\text{CN}$)

When aligned in the liquid crystal, the protons and carbons form a spin system of the type A_3MX . The ^1H SQ spectrum gives a 1:2:1 triplet due to D_{HH} , and each line of this triplet is further split into doublet of doublet of equal intensity giving rise to a total of 12 transitions. D_{HH} and D_{CH} can be determined by the first-order analysis of this spectrum, which is straightforward.

For the MQ studies, the two types of heteronuclei in this molecule can be treated as two isolated spins. Thus, it was possible to selectively detect homonuclear DQ and triple quantum (3Q) orders between protons and homonuclear DQ between carbons. The particular order was selected by using gradients and the selected MQ coherence was allowed to correlate to its SQ coherence. Depending on the order selectively detected, the MQ spectra have been analyzed treating as spin systems, such as, AMX, A_3X , and APMX.

4.5.2.1 Homonuclear proton 3Q–SQ coherence. The chemical structure with the numbering of interacting spins, the pulse sequence employed, and the 2D spectrum correlating the 3Q–SQ coherence of protons are given in Figure 5. The excitation of proton 3Q results in all the protons evolving at the sum of the resonance offset (chemical shifts can be treated as zero due to magnetic equivalence of all the three protons) under the sum of J_{CH} and D_{CH} couplings in the MQ dimension. This pertains to a situation where the selective mixing pulse is applied on A_3 spins and in the MQ dimension A_3MX spin system behaves like an AMX spin system, where proton is the active spin (A) and two carbons are passive spins (M and X). The 3Q spectrum corresponds to A part of AMX spectrum. In the spin product basis set, the spin states of two weakly coupled

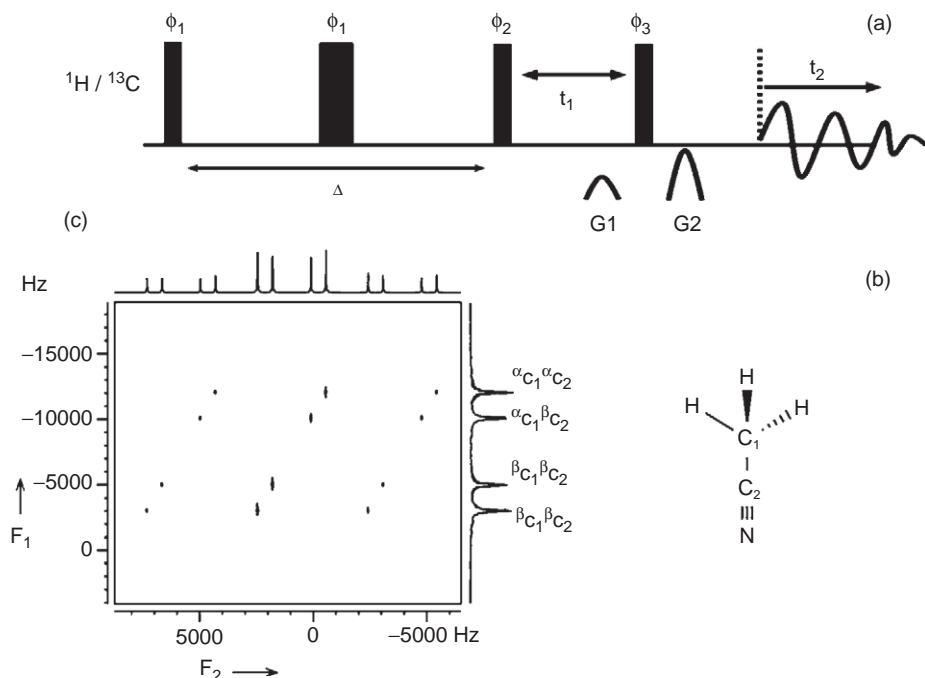


Figure 5 (a) The pulse sequence employed for multiple quantum–single quantum correlations experiments. The delay Δ was optimized for the selection of proton and carbon homonuclear multiple quanta. The phases of all the pulses and the receiver are set to zero. The gradient ratio is $G_2 = nG_1$ for homonuclear n th quantum of proton and carbon. (b) The structure and numbering of interacting spins in doubly labeled acetonitrile. (c) The 700 MHz 2D spectrum of acetonitrile in the liquid crystal ZLI-1132, correlating proton 3Q coherence to its SQ coherence. The $\alpha_{\text{C}_1}\alpha_{\text{C}_2}$, $\alpha_{\text{C}_1}\beta_{\text{C}_2}$, $\beta_{\text{C}_1}\alpha_{\text{C}_2}$, and $\beta_{\text{C}_1}\beta_{\text{C}_2}$ are different spin states of heteronuclei. For even quantum selection all phases are x , while for odd quantum $\Phi_1 = x$, $\Phi_2 = y$, $\Phi_3 = y$, and receiver phase = x .

M and X spins, coupled to triple quantum states of proton, $|\alpha_P\alpha_P\alpha_P\rangle$ and $|\beta_P\beta_P\beta_P\rangle$, are written as $|\alpha_{\text{C}_1}\alpha_{\text{C}_2}\rangle$, $|\alpha_{\text{C}_1}\beta_{\text{C}_2}\rangle$, $|\beta_{\text{C}_1}\alpha_{\text{C}_2}\rangle$, and $|\beta_{\text{C}_1}\beta_{\text{C}_2}\rangle$, where the subscript P represents protons and C1 and C2 are carbons of CH_3 and CN groups, respectively. The four transitions of the A spin in the 3Q dimension correspond to these four spin states. The doublet separation between the states $|\alpha_{\text{C}_1}\alpha_{\text{C}_2}\rangle$ and $|\alpha_{\text{C}_1}\beta_{\text{C}_2}\rangle$ provides $D_{\text{C}_2\text{H}}$ and that between the states $|\alpha_{\text{C}_1}\alpha_{\text{C}_2}\rangle$ and $|\beta_{\text{C}_1}\alpha_{\text{C}_2}\rangle$ provides $D_{\text{C}_1\text{H}}$.

The spectrum in the SQ dimension corresponds to normal one-dimensional spectrum of an A_3MX type spin system, and consists of four A_3 subspectra, one for each of the four mI (M and X) values $|\alpha_{\text{C}_1}\alpha_{\text{C}_2}\rangle$, $|\alpha_{\text{C}_1}\beta_{\text{C}_2}\rangle$, $|\beta_{\text{C}_1}\alpha_{\text{C}_2}\rangle$, and $|\beta_{\text{C}_1}\beta_{\text{C}_2}\rangle$, of the two carbons. For transitions within each subspectrum, the spin states of M and X do not change.

The one-dimensional spectrum along with the cross-sections taken on SQ dimension at different spin states of 3Q dimension are shown in Figure 6. Each of these cross-sections pertains to selectively detected SQ transitions originating

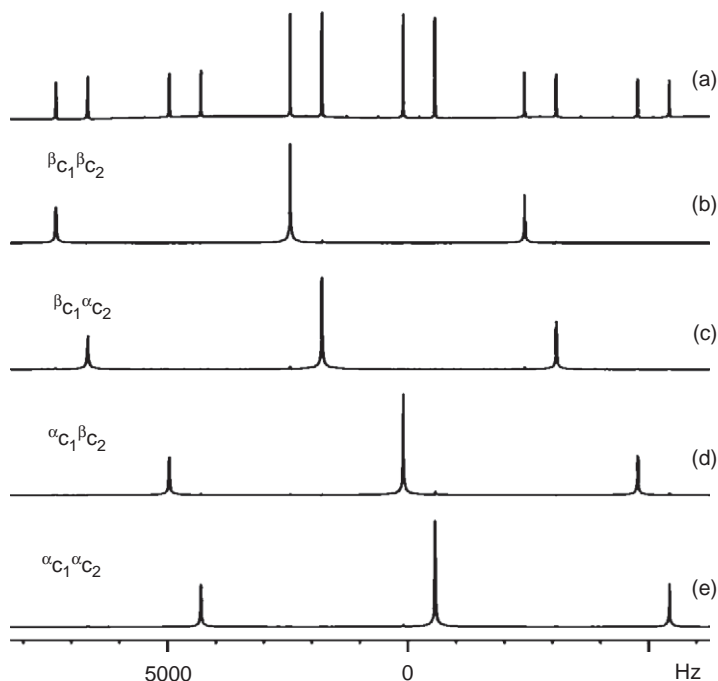


Figure 6 (a) 700 MHz proton 1D spectrum of acetonitrile in the liquid crystal ZLI-1132 and (b–e) cross-sections along SQ dimension taken, respectively, at the spin states $\beta_{C1}\beta_{C2}$, $\beta_{C1}\alpha_{C2}$, $\alpha_{C1}\beta_{C2}$, and $\alpha_{C1}\alpha_{C2}$ in 3Q dimension of Figure 5c. Reproduced with permission from American Chemical Society.

from the initial third quantum state which has two carbons, in either $|\alpha_{C1}\alpha_{C2}\rangle$ or $|\beta_{C1}\beta_{C2}\rangle$ state, and ends up in states where single proton spin flips but still has carbons in its initial $|\alpha_{C1}\alpha_{C2}\rangle$ or $|\beta_{C1}\beta_{C2}\rangle$ state. This is the result of the last 90° pulse on protons which do not perturb the spin states of heteronuclei. An example of such a transition is from the states $|\alpha_P\alpha_P\alpha_P\beta_{C1}\beta_{C2}\rangle$ and $|\beta_P\alpha_P\alpha_P\beta_{C1}\beta_{C2}\rangle$. This is a situation where all proton single quantum transitions pertaining to four A_3 subspectra get separated into different cross-sections depending on the four spin states of the heteronuclei. Each cross-section is a triplet, from which D_{HH} can be determined. Thus, as far as the determination of the D_{HH} is concerned, the redundancy in the number of SQ transitions required for the analysis in the normal one-dimensional spectrum is largely reduced.

The methodology when applied to bigger molecules will significantly simplify the analyses.

4.5.2.2 Homonuclear ^{13}C DQ–SQ coherence. In the ^{13}C spectrum, each carbon, M and X of the A_3MX spin system, is split into doublet of quartet by three protons (A_3) and the remaining carbon. The fully coupled ^{13}C spectrum, therefore, provides equal intensity doublets of 1:3:3:1 intensity quartets at the chemical shift positions of each carbon.

The DQ excitation of homonuclear carbon spins converts the five spin system of the type A_3MX into a four spin system of the type A_3X in the DQ dimension, where the three protons are passive spins (A_3) and two ^{13}C are active spins (X). The double quantum states of two carbons are $|\alpha_{C1}\alpha_{C2}\rangle$ or $|\beta_{C1}\beta_{C2}\rangle$ and they are coupled to eight different spin states (symmetrized spin states of A_3 spin system), $\alpha\alpha\alpha$, $(\alpha\alpha\beta + \alpha\beta\alpha + \beta\alpha\alpha)/\sqrt{3}$, $(\alpha\alpha\beta + \alpha\beta\alpha - 2\beta\alpha\alpha)/\sqrt{6}$, $(\alpha\alpha\beta - \alpha\beta\alpha)/\sqrt{2}$, $(\beta\beta\alpha + \beta\alpha\beta + \alpha\beta\beta)/\sqrt{3}$, $(\beta\beta\alpha + \beta\alpha\beta - 2\alpha\beta\beta)/\sqrt{6}$, $(\beta\beta\alpha - \beta\alpha\beta)/\sqrt{2}$, and $\beta\beta\beta$ of protons. The states $(\alpha\alpha\beta + \alpha\beta\alpha + \beta\alpha\alpha)/\sqrt{3}$, $(\alpha\alpha\beta + \alpha\beta\alpha - 2\beta\alpha\alpha)/\sqrt{6}$, and $(\alpha\alpha\beta - \alpha\beta\alpha)/\sqrt{2}$ are degenerate and form one group. The states $(\beta\beta\alpha + \beta\alpha\beta + \alpha\beta\beta)/\sqrt{3}$, $(\beta\beta\alpha + \beta\alpha\beta - 2\alpha\beta\beta)/\sqrt{6}$, and $(\beta\beta\alpha - \beta\alpha\beta)/\sqrt{2}$ are degenerate and form another group. This results in the splitting of the active spin transition into a quartet by passive spins in the DQ dimension. The ^{13}C -detected homonuclear DQ-SQ spectrum pertaining to methyl carbon is given in Figure 7. The carbon 1, directly bonded to protons, resonates at high field and also has large D_{C1H} . The transitions for carbon 2 remotely bonded to protons resonate at lower field and has small D_{C2H} . Furthermore, the resonance signal from the carbon 2 is significantly broadened due to quadrupolar nitrogen and is very weak in intensity. The cross-section taken along SQ dimension at each spin state of a passive spin in the MQ dimension is a doublet from which D_{CC} can be directly obtained. D_{C1H} can be

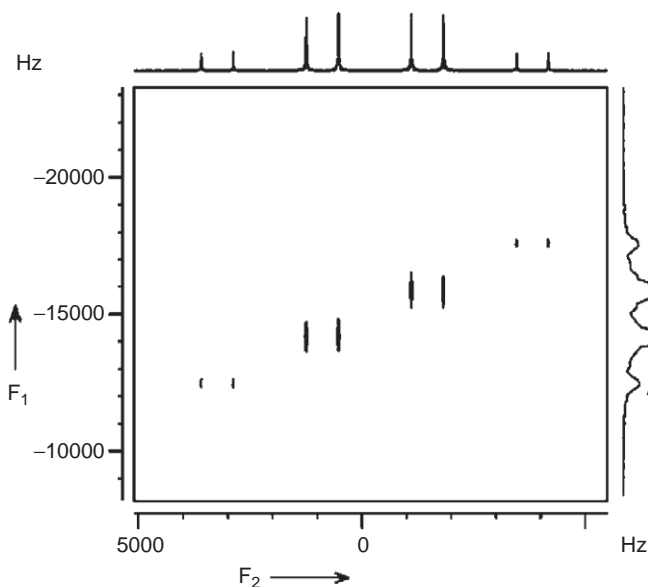


Figure 7 The 700 MHz 2D spectrum of homonuclear ^{13}C double quantum coherence correlating to its single quantum coherence of acetonitrile in the liquid crystal ZLI-1132. A and D correspond to spin states $\alpha_P\alpha_P\alpha_P$ and $\beta_P\beta_P\beta_P$, respectively, B and C correspond to degenerated spin states $(\alpha\alpha\beta + \alpha\beta\alpha + \beta\alpha\alpha)/\sqrt{3}$, $(\alpha\alpha\beta + \alpha\beta\alpha - 2\beta\alpha\alpha)/\sqrt{6}$, and $(\alpha\alpha\beta - \alpha\beta\alpha)/\sqrt{2}$; and $(\beta\beta\alpha + \beta\alpha\beta + \alpha\beta\beta)/\sqrt{3}$, $(\beta\beta\alpha + \beta\alpha\beta - 2\alpha\beta\beta)/\sqrt{6}$, and $(\beta\beta\alpha - \beta\alpha\beta)/\sqrt{2}$, respectively. Reproduced with permission from American Chemical Society.

determined from the combined analysis of any two consecutive cross-sections. Similarly the analysis of the low field region of the spectrum provides D_{C_2H} .

4.5.2.3 Homonuclear proton DQ–SQ coherence. The spin system of the type APMX is created in the DQ dimension when two protons are simultaneously flipped. Active spins for DQ could be any two protons of the CH_3 group. In the DQ dimension, this pertains to a weakly coupled four spin system of the type APMX, where A is the double quantum excited two protons of CH_3 (active spins) group, P the proton not participating in double quantum (passive spin), and M and X the two carbons (passive spins). The weakly coupled four spin system provides eight transitions for each spin. Thus, in the DQ dimension, A spin transition is split into eight transitions of equal intensity by the passive spins. The corresponding DQ coupled spin states of A are: $|\alpha_P\alpha_{C1}\alpha_{C2}\rangle$, $|\alpha_P\alpha_{C1}\beta_{C2}\rangle$, $|\alpha_P\beta_{C1}\alpha_{C2}\rangle$, $|\alpha_P\beta_{C1}\beta_{C2}\rangle$, $|\beta_P\alpha_{C1}\alpha_{C2}\rangle$, $|\beta_P\alpha_{C1}\beta_{C2}\rangle$, $|\beta_P\beta_{C1}\alpha_{C2}\rangle$, and $|\beta_P\beta_{C1}\beta_{C2}\rangle$. The cross-section taken along SQ dimension for each spin state in the DQ dimension is a triplet from which D_{HH} can be determined. As far as the determination of the D_{HH} is concerned, this information can also be obtained by the 3Q–SQ experiment.

4.5.3 Analyses of the complex 1H NMR spectrum: an AA'BB'XX' spin system

The application of the above-described spin state selective detection of MQ transitions has been demonstrated in the simplification of the iterative analysis of 1H spectrum of a six spin system, *ortho*-difluorobenzene aligned in a thermotropic liquid crystal. The structure and the numbering of the interacting spins in *ortho*-difluorobenzene and the 2D spectrum which correlates the homonuclear fourth quantum (4Q) coherence of protons to its SQ coherence are given in Figure 8. The coupled protons and fluorines of this molecule form a strongly coupled spin system of the type AA'BB'XX'. The one-dimensional spectrum along with the cross-sections taken along SQ dimension at different spin states of ^{19}F in 4Q dimension is given in Figure 9.

The gradient selected proton homonuclear 4Q excitation results in the flipping of all the protons and evolves under the sum of proton chemical shifts and heteronuclear couplings. This corresponds to AXX' type in the 4Q dimension, where A is the proton (active spin) and are XX' the two fluorines (passive spins). In the 4Q dimension, the active spin A is split due to couplings with two passive ^{19}F spins. The XX' part will have four possible spin states, viz.: (a) $|\alpha_1\alpha_2\rangle$, (b) $(|\alpha_1\beta_2\rangle + |\beta_1\alpha_2\rangle)/\sqrt{2}$, (c) $(|\alpha_1\beta_2\rangle - |\beta_1\alpha_2\rangle)/\sqrt{2}$, and (d) $|\beta_1\beta_2\rangle$. The degenerate central transition arises from the spin states $(|\alpha\beta\rangle + |\beta\alpha\rangle)/\sqrt{2}$ and $(|\alpha\beta\rangle - |\beta\alpha\rangle)/\sqrt{2}$. The other two outer transitions correspond to spin states $|\alpha\alpha\rangle$ and $|\beta\beta\rangle$.

The cross-sections taken along the SQ dimension, at three different spin states in the 4Q dimension, correspond to selectively detected single quantum transitions based on the spin state of the passive spins. The selectively detected transitions at each cross-section contain information on the proton chemical shifts and proton–proton dipolar couplings. The 12 SQ transitions are selectively detected for $|\alpha\alpha\rangle$ and $|\beta\beta\rangle$ states. The analysis of one of these suffices for the

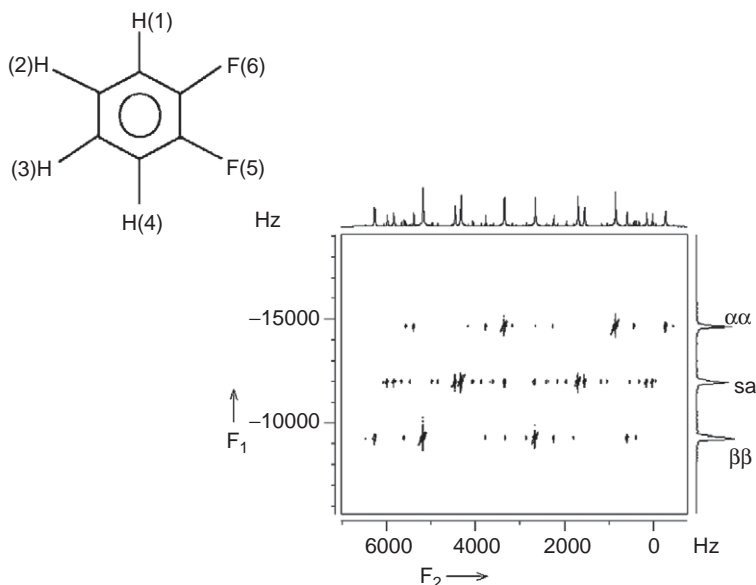


Figure 8 The structure and the numbering of the interacting spins in *ortho*-difluorobenzene along with the 500 MHz two-dimensional proton spectrum in the liquid crystal solvent ZLI-1132, correlating homonuclear 4Q coherence of protons to its SQ coherence. Two outer transitions in the 4Q dimension correspond to spin states $|\alpha\alpha\rangle$ and $|\beta\beta\rangle$ respectively. s and a refer to degenerate spin states $(|\alpha_1\beta_2\rangle + |\beta_1\alpha_2\rangle)/\sqrt{2}$ and $(|\alpha_1\beta_2\rangle - |\beta_1\alpha_2\rangle)/\sqrt{2}$, respectively. Reproduced with permission from American Chemical Society.

determination of proton chemical shifts and proton–proton dipolar couplings. Therefore, the complex spectrum is significantly simplified. Similar information can also be obtained using the SQ transitions that are selectively detected for the spin states $(|\alpha_1\beta_2\rangle + |\beta_1\alpha_2\rangle)/\sqrt{2}$ and $(|\alpha_1\beta_2\rangle - |\beta_1\alpha_2\rangle)/\sqrt{2}$ of fluorine, for which there are nearly 60 transitions.

The three selectively detected single quantum spectra have been independently analyzed numerically. Only proton–proton dipolar couplings and proton chemical shifts were varied during the iteration and all the 12 selectively excited transitions for $|\alpha\alpha\rangle$ and $|\beta\beta\rangle$ states were utilized for the analysis. Combined analyses of spectra from both $|\alpha\alpha\rangle$ and $|\beta\beta\rangle$ states also provide D_{HH} couplings. The analysis of the spectrum from the spin states $(|\alpha_1\beta_2\rangle + |\beta_1\alpha_2\rangle)/\sqrt{2}$ and $(-|\alpha_1\beta_2\rangle + |\beta_1\alpha_2\rangle)/\sqrt{2}$ of fluorines provides D_{HH} and D_{FH} couplings.

Therefore, the spin state selective detection of the SQ transitions using MQ coherence not only reduces the complexity of the spectrum drastically but also aids the analysis. The derived spectral parameters in all the above analyses are given in Figure 10 as a histogram. The standard deviations of the determined parameters, D_{HH} and D_{FH} , indicated that these parameters are very precise. Thus, MQ experiments have enormous potential in simplifying the analyses of complex spectra.

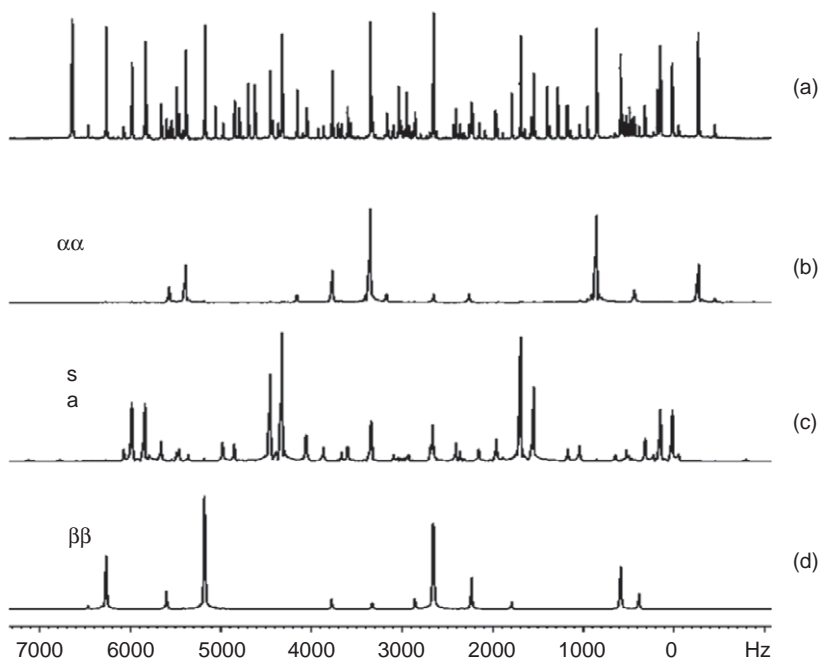


Figure 9 (a) The 500 MHz one-dimensional proton spectrum of *ortho*-difluorobenzene aligned in the liquid crystalline phase ZLI-1132; (b–d) the cross-sections extracted from the three spin states along 4Q dimension of Figure 8, plotted with identical scale for comparison. s and a refer to symmetric and antisymmetric states $(|\alpha_1\beta_2\rangle + |\beta_1\alpha_2\rangle)/\sqrt{2}$ and $(|\alpha_1\beta_2\rangle - |\beta_1\alpha_2\rangle)/\sqrt{2}$, respectively. Reproduced with permission from American Chemical Society.

4.6 Second-order spectra and estimation of an element of ordering matrix

In this work,¹⁰⁰ the MQ methodology has been extended for the direct estimation of one of the elements of the ordering matrix from the very intricate NMR spectra. The experimental methodology is applied for molecules containing two symmetrically disubstituted heteronuclei requiring two elements of the order matrix to define their orientations. The chemical structures of the molecules chosen for demonstration purposes and their complex one-dimensional spectra are given in Figure 11. The additional information derived can be employed to estimate the dipolar couplings more precisely to use as the starting parameters in the iterative analyses.

4.6.1 Analyses of ^1H NMR spectra of a five spin system: 2,6-difluoropyridine

The molecule 2,6-difluoropyridine has five interacting spins. In the liquid crystalline phase, the protons and fluorines form the spin system of the type ABB'XX' , where A and B refer to protons and X refers to fluorine. The molecule has C_{2v} symmetry and requires two elements of an ordering matrix to define its

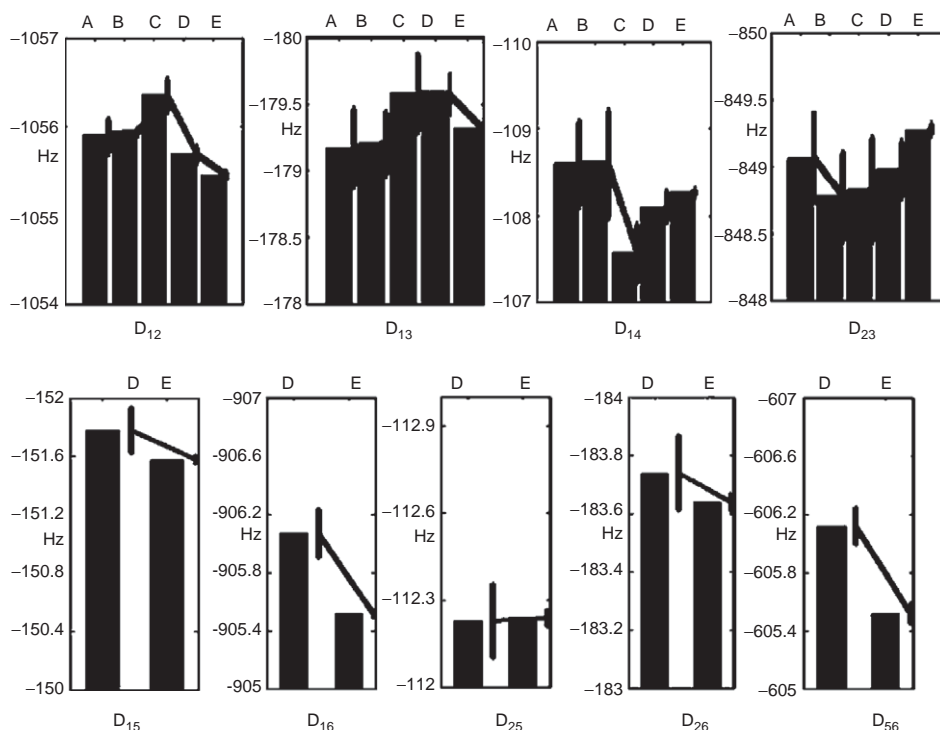


Figure 10 The histogram showing the values of dipolar couplings determined by the analyses of the different cross-sections of the spectrum shown in Figure 8 and from the one-dimensional proton spectrum. Top trace—homonuclear proton couplings obtained by: (A) the analysis of the cross-section taken along SQ dimension at the spin state $|\alpha\alpha\rangle$ in 4Q dimension, (B) the analysis of the cross-section taken along SQ dimension at the spin state $|\beta\beta\rangle$ in 4Q dimension, (C) the combined analysis of the two cross-sections from $|\alpha\alpha\rangle$ and $|\beta\beta\rangle$ states of 4Q dimension, (D) the combined analysis of the cross-sections of states $|\alpha\alpha\rangle$ and $(|\alpha_1\beta_2\rangle + |\beta_1\alpha_2\rangle)/\sqrt{2}$ and $(-|\alpha_1\beta_2\rangle + |\beta_1\alpha_2\rangle)/\sqrt{2}$, and (E) the analysis of one-dimensional proton spectrum. Bottom trace—dipolar couplings, D_{FH} (D_{15} , D_{16} , D_{25} , D_{26}) and D_{FF} (D_{56}) obtained by: (D) the combined analysis of the cross-sections of states $|\alpha\alpha\rangle$ and $(|\alpha_1\beta_2\rangle + |\beta_1\alpha_2\rangle)/\sqrt{2}$ and $(-|\alpha_1\beta_2\rangle + |\beta_1\alpha_2\rangle)/\sqrt{2}$ and (E) the analysis of one-dimensional proton spectrum. The vertical bars give standard deviations on the parameters determined. Reproduced with permission from American Chemical Society.

orientation. To combat the tedium of the analysis of one-dimensional spectrum, the blend of two-dimensional homonuclear 3Q–SQ correlation of protons and DQ–SQ correlation of fluorines has been employed.

The ^{19}F -detected DQ–SQ spectrum is reported in Figure 12a. In the DQ excitation, the simultaneous flipping of two ^{19}F spins transforms the spin system to the type $\text{ABB}'\text{X}$, where X corresponds to two fluorines (super spin). The X part of this spin system and its interaction with B and B' spins are detected in the direct and indirect dimensions, respectively. This retains the spin states of ^1H undisturbed in both SQ and DQ dimensions. This is analogous to mimicking the decoupling of ^{19}F spins with ^1H detection. In the indirect dimension, there are

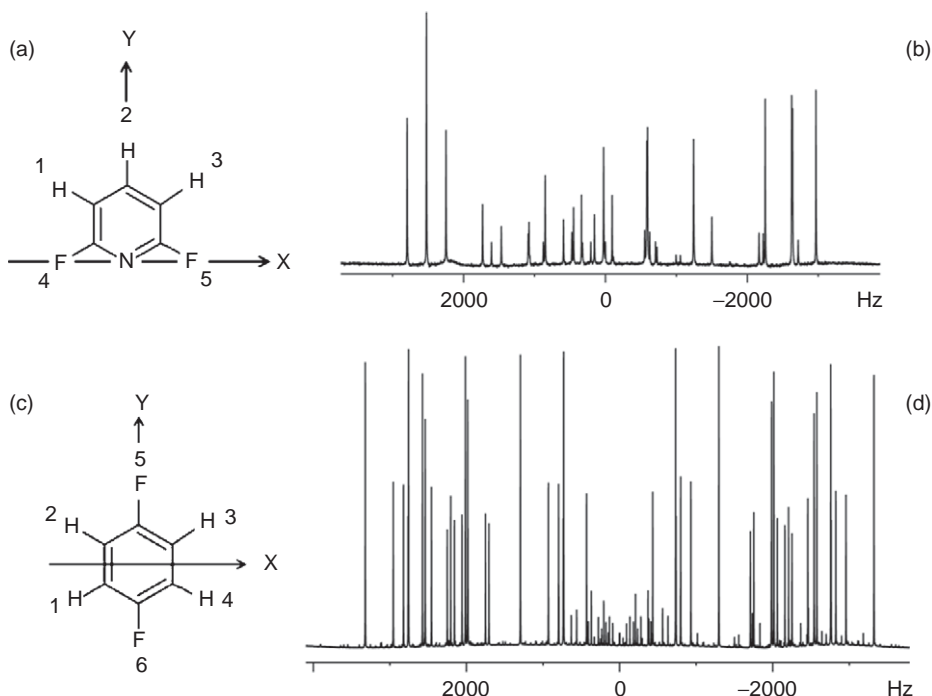


Figure 11 (a) The chemical structure and numbering of interacting spins in 2,6-difluoropyridine, (d) the one-dimensional proton spectrum of the molecule oriented in the liquid crystal solvent ZLI-1114, (c) the chemical structure and numbering of spins in 1,4-difluorobenzene, and (d) the one-dimensional proton spectrum of the molecule oriented in the liquid crystal solvent ZLI-1132.

eight basic symmetry functions of proton spins and nine allowed transitions.¹⁰¹ The spectral pattern depends on the ratio of the coupling to the chemical shift difference between the protons A and B. However, the experiment provided five distinct transitions of significant intensities. It is not possible to identify these transitions with any particular spin state of protons because of degeneracy of transitions. Nevertheless, for each transition in the DQ dimension, the cross-section taken along SQ dimension results in a doublet due to coupling between two active fluorine spins. This separation is a direct measure of $3D_{FF}$. In the coordinate frame chosen for the molecule and taking advantage of the knowledge of the reported geometry,¹⁰² the vital information on one of the elements of the order matrix, *viz.*, S_{XX} has been determined. This information has been employed for the analysis of the 3Q-SQ correlation spectrum given in Figure 12b.

In the proton 3Q-SQ correlation, the simultaneous flipping of all the protons transforms the spin system of the type $ABB'XX'$ to that of AXX' , where A corresponds to super spin with three protons. With the selective excitation of only protons, the spin states of ^{19}F are undisturbed in both F_1 and F_2 dimensions. The active spin A and its interactions with spins X and X' are detected in direct and indirect dimensions, respectively. The passive spins will have four spin states in

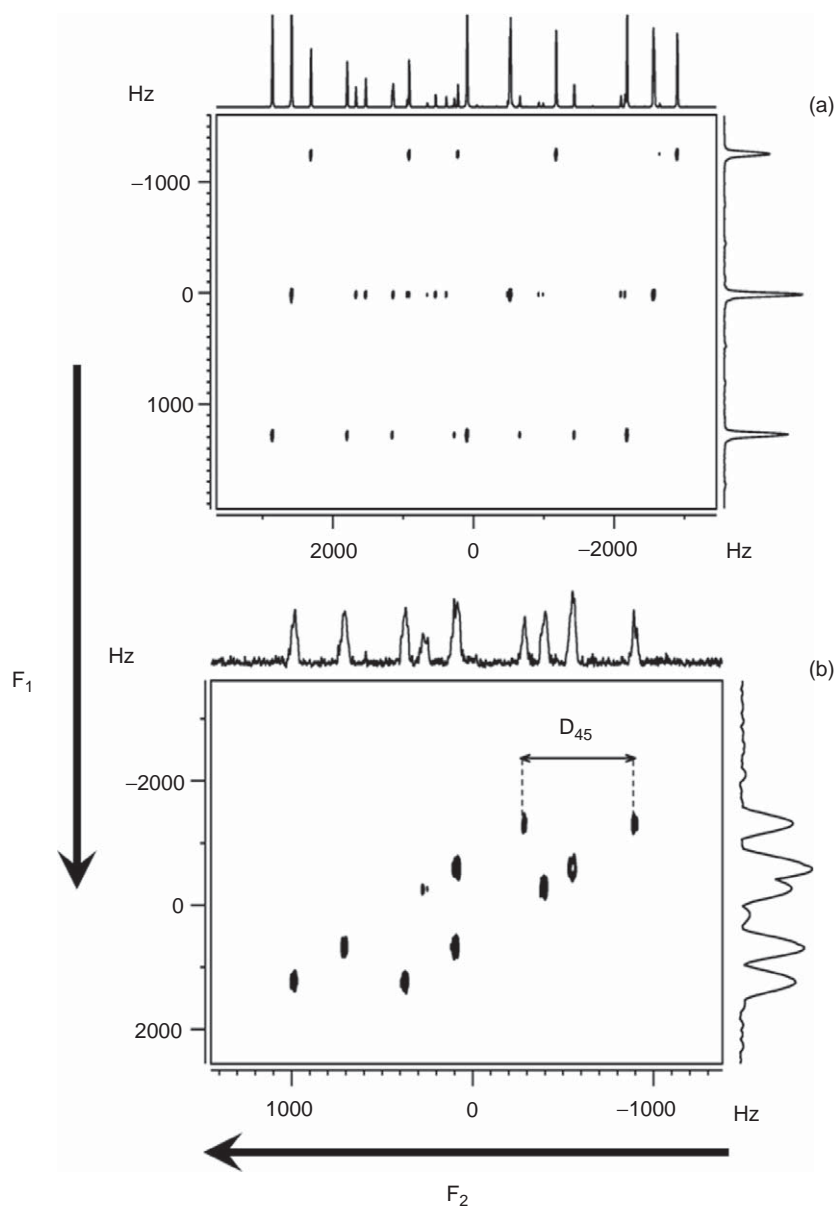


Figure 12 (a) The 500 MHz ^1H 3Q-SQ spectrum of 2,6-difluoropyridine oriented in the liquid crystal ZLI-1114 with corresponding F_1 and F_2 projections; proton is detected in both direct and indirect dimensions. (b) The 500 MHz ^{19}F DQ-SQ spectrum of 2,6-difluoropyridine oriented in the liquid crystal ZLI-1114 with corresponding F_1 and F_2 projections; ^{19}F is detected in both direct and indirect dimensions.

the indirect dimension corresponding to two fluorines numbered 4 and 5, *viz.*, $|\alpha_4\alpha_5\rangle$, $(|\alpha_4\beta_5\rangle + |\beta_4\alpha_5\rangle)/\sqrt{2}$, $(|\alpha_4\beta_5\rangle - |\beta_4\alpha_5\rangle)/\sqrt{2}$, and $|\beta_4\beta_5\rangle$ and with the degenerate central transition arising from the two spin states $(|\alpha_4\beta_5\rangle + |\beta_4\alpha_5\rangle)/\sqrt{2}$ and $(|\alpha_4\beta_5\rangle - |\beta_4\alpha_5\rangle)/\sqrt{2}$, there are three detectable transitions. The two outer transitions correspond to one of the spin states $|\alpha_4\alpha_5\rangle$ and $|\beta_4\beta_5\rangle$, respectively. For each spin state $|\alpha_4\alpha_5\rangle$ and $|\beta_4\beta_5\rangle$, eight different SQ transitions are selectively correlated. The analysis of any one of these cross-sections is sufficient for the determination of δ_H and D_{HH} . Nevertheless, the analysis of any of the cross-sections requires the realistic values of proton chemical shifts in addition to D_{HH} as the starting parameters. The knowledge of the elements of the ordering matrix is essential to estimate D_{HH} .

The analyses of correlated SQ transitions for each spin state $|\alpha_4\alpha_5\rangle$ and $|\beta_4\beta_5\rangle$ of ^{19}F provide two proton dipolar couplings and two proton chemical shifts. The knowledge of S_{XX} derived from the ^{19}F DQ-SQ experiment and the molecular symmetry aided the estimation of realistic value of D_{13} which was kept constant during initial iterations. The dipolar coupling D_{12} and the two proton chemical shifts are required to be determined from the detected eight transitions. Thus, iterative analysis not only speeded up but all the spectral parameters could also be determined precisely. Using these parameters together with the fixed geometry, approximate values of D_{HF} and both the elements of the order matrix could be estimated to a reasonable precision using the computer program SHAPE.¹⁰³ With the knowledge of the parameters derived from the analyses of both 3Q-SQ and DQ-SQ spectra, the complex one-dimensional spectrum could be analyzed in a conventional way keeping the D_{HH} and D_{FF} values as constant during the initial iteration. However, in the final step, all the parameters were iterated for better precision of the spectral parameters. It should be mentioned that the vital information derived on one of the order parameters was useful in the analysis of the spectrum and simplified the tedious procedure of varying this parameter while estimating the starting parameters. The final iterated dipolar couplings (D_{13} and D_{45}) agree with those estimated from the MQ-SQ spectra, thereby confirming the realistic estimate of an element of ordering matrix.

4.6.2 Analyses of the ^1H NMR spectra of a six spin system:

1,4-difluorobenzene

The above technique has also been applied for the analysis of the complex ^1H spectra of six coupled spins, *viz.*, 1,4-difluorobenzene. The coupled protons and fluorines of this molecule form the spin system of the type $\text{AA}'\text{A}''\text{A}'''\text{XX}'$. Possessing C_{2V} symmetry, in the coordinate system chosen, this molecule also requires two elements of the order matrix, *viz.*, S_{XX} and S_{YY} , to define its orientation. It is clearly evident from the one-dimensional spectrum of this molecule that it is impossible to estimate the value of any one of these parameters. The ^1H 4Q-SQ and ^{19}F DQ-SQ spectra of the molecule have been, therefore, employed and are given in Figure 13. The analysis of DQ-SQ spectrum provided the value of S_{YY} .

As in the previous molecule, the iterative analyses of the cross-sections along SQ dimension corresponding to the spin states $|\alpha_5\alpha_6\rangle$ and $|\beta_5\beta_6\rangle$ in the

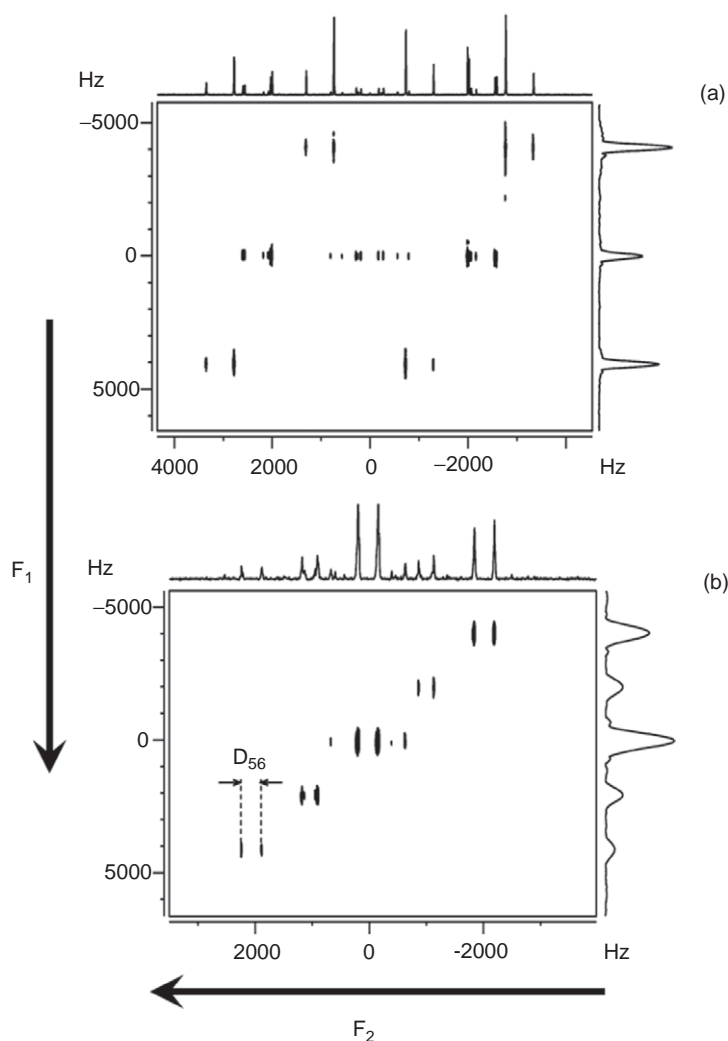


Figure 13 (a) The 500 MHz ^1H 4Q-SQ spectrum of 1,4-difluorobenzene oriented in the liquid crystal ZLI-1132 with corresponding F_1 and F_2 projections; (b) the 500 MHz ^{19}F DQ-SQ spectrum of 1,4-difluorobenzene oriented in the liquid crystal ZLI-1132 with corresponding F_1 and F_2 projections.

4Q-SQ spectra of Figure 13 have been carried out. Due to very few transitions in each of these cross-sections, the combined analysis of these cross-sections was essential. The iterative analysis of the cross-section requires three D_{HH} and the chemical shifts of all the protons were taken as zero. Yet again the realistic value of one of the three D_{HH} could be estimated. The conventional iterative analysis of the one-dimensional spectrum was carried out initially keeping all the D_{HH} fixed and varied in the final iterations. It is clearly evident from these studies that the

MQ spin state selective detection can be employed to estimate an element of the order matrix, which aids the analyses of the very intricate NMR spectra.

4.6.3 Domain filtering and additional spectral simplification

It may be appropriate to point out that in the molecules possessing symmetry elements, the homonuclear higher quantum correlation results in the filtering of the spectral domains. This concept of domain filtering based on the irreducible representations of the symmetry elements is well documented in the literature.¹⁰⁴

The symmetry preserving correlations are expected only between the transitions of the same domain.¹⁰⁵ Thus, for the molecules investigated, the total number of transitions detected in the SQ dimension from all the passive spin states is less than the single quantum transitions. This also depends on the molecular symmetry and the order of the quantum detected. It is appropriate to mention that the reduced number of transitions observed due to domain filtering also simplifies the complexity of the spectrum further.

Until this point, the discussion was restricted to simplifying the analyses of complex proton NMR spectra of strongly dipolar coupled systems. In the subsequent part of the chapter, the focus will be on the weakly dipolar coupled spin systems.

5. ANALYSES OF COMPLEX ^1H NMR SPECTRA OF WEAKLY DIPOLAR COUPLED SPINS

Despite several advances made in the field, the analyses of the proton NMR spectra of strongly dipolar coupled spins remain problematic, especially with larger dipolar coupled network of spins. In such situations, it may become impossible to identify the resonances because of numerous dipolar coupled pairs. Additional possible avenues to scale down these dipolar couplings have been explored. One such possibility is to exploit the larger diamagnetic susceptibility anisotropies of the molecules. Energy of interaction of such molecules is orientation dependent and results in additional splitting, whose direct measure provided the coupling information. The bigger macromolecules possess large diamagnetic susceptibility anisotropies and result in field-induced orientation. However, one must remember that in reality not many macromolecules possess large magnetic anisotropies and this is limited to metalloproteins and DNA helices which have regular structures. It also implies that the field-induced orientation of small molecules is a remote possibility.

To simplify the analyses and to extract the residual dipolar couplings, diverse weakly aligning media are reported in the literature, *viz.*, direct field-induced orientation, bicelles, chiral organic solvent such as PBLG, bacteriophage, anisotropically compressed polyacrylamide gel, detergent-compatible liquid crystals based on DNA nanotubes and nucleic acid G-tetrad structures, paramagnetic assisted alignment, collagen gel, etc. The residual dipolar couplings measured between the pairs of interacting spins provide long-range orientational restraints and have been extensively employed to obtain the high-quality

structures of proteins and the molecular dynamics. Most of aligning media are appropriate only to water-soluble proteins. The degree of molecular order and the high-resolution ^1H NMR spectra obtainable depend on the size of the molecules. One should also remember that as the molecular size increases, there is excessive line broadening of NMR signals due to larger strengths of long-distance dipolar couplings. Added advantage of weak molecular order is that the spectral complexity is tunable to certain extent. Thus, in majority of the studies, the choice of the aligning media is specific to molecules. Although voluminous amount of NMR literature is available in the application of these aligning media to determine the structure of bio-molecules such as proteins, there are limited studies on small organic molecules. For more discussion on the weak alignment and the measure of residual dipolar couplings, there are numerous studies documented in the literature.^{106–136} An excellent recent review¹³⁷ also provides information on the employment of RDCs for the structure determination. The present report is restricted to the use of weak aligning media for extracting the residual dipolar couplings in small molecules.

5.1 Thermotropic liquid crystals providing first-order spectra

Quaternary ammonium salts when dissolved in appropriate liquids are known to form several types of aggregates. They could be lyotropic liquid crystals, monolayers and bilayers,^{138,139} thermally reversible gels, and thermotropic mesophases.^{140,141} It is also reported that simple quaternary ammonium salts with one short and three long chains form enantiotropic thermotropic nematic phases.¹⁴² The properties and potential applications of one of the salts, *N*-methyl-*N,N,N*-triocadecylammoniumiodide (MTAI), has been studied by doping the small amounts of non-mesogenic solute *cis,cis*-mucononitrile.¹⁴² The important feature of this thermotropic liquid crystalline phase is that the order parameter is very small. Therefore, the dissolved molecules should provide spectra analogous to weakly coupled spins. This molecule has four protons and possesses C_{2h} symmetry. The weak alignment provided the simple first-order proton spectrum containing essentially two groups of lines centered nearly at the isotropic positions. The splitting within the two groups provided directly the dipolar coupling between the protons. It should be emphasized that the proton spectrum of *cis,cis*-mucononitrile in thermotropic liquid crystal ZLI-1167 pertains to strongly dipolar coupled spins and it is difficult to assign chemical shifts to specific protons or to extract the coupling information without numerical iterations. The low-order parameter of the liquid crystal MTAI thus aided the analysis of the complex spectrum.

5.2 Orientation in bicelles

Several compounds in aqueous solutions are shown to form liquid crystalline phases.^{109,143,144} Generally, they are mixture of phospholipids. In aqueous solutions, these lipids switch from a gel phase to a liquid crystal phase, where they form disc-shaped molecules. They are generally referred to as bicelles.¹⁴⁵

The percentage of water is the decisive factor in achieving such an ordered phase. At low concentrations, samples generally are very viscous and would not allow molecular reorientation in the NMR time scale. At very high concentrations, discoidal micelles are probably broken into smaller isotropically tumbling units that do not orient. At an intermediate concentration, the characteristic of the liquid crystalline orientation is seen. In such ordered systems, the surface of the disc is either parallel or perpendicular to the applied field. The lipids are generally diamagnetic and as a result orient with their normal orthogonal to the magnetic field. Structural information of small molecules aligned in such bicelles have been reported.^{146,147} The liquid crystallinity can be maintained even at very low concentrations of nearly 3% (w/v) of the bicelles. At low concentrations, the spacing between the bicelles is far greater than the size of the macromolecules such as proteins and nucleic acids. As a result, the macromolecules dissolved in such a medium undergo rotational diffusion. At low bicelle concentration, the degree of alignment obtained is large enough to measure only the dipolar couplings between nuclei in close proximity. This renders the NMR spectrum simple and is not complex as seen normally in thermotropic liquid crystals.

The use of bicelles for deriving the dipolar coupling information and thereby the geometry of the molecules has been demonstrated on pyridine.⁶⁴ The chemical structure, the numbering of interacting spins in pyridine, and the proton spectra in isotropic, bicelle, and EBBA phases are given in Figure 14.

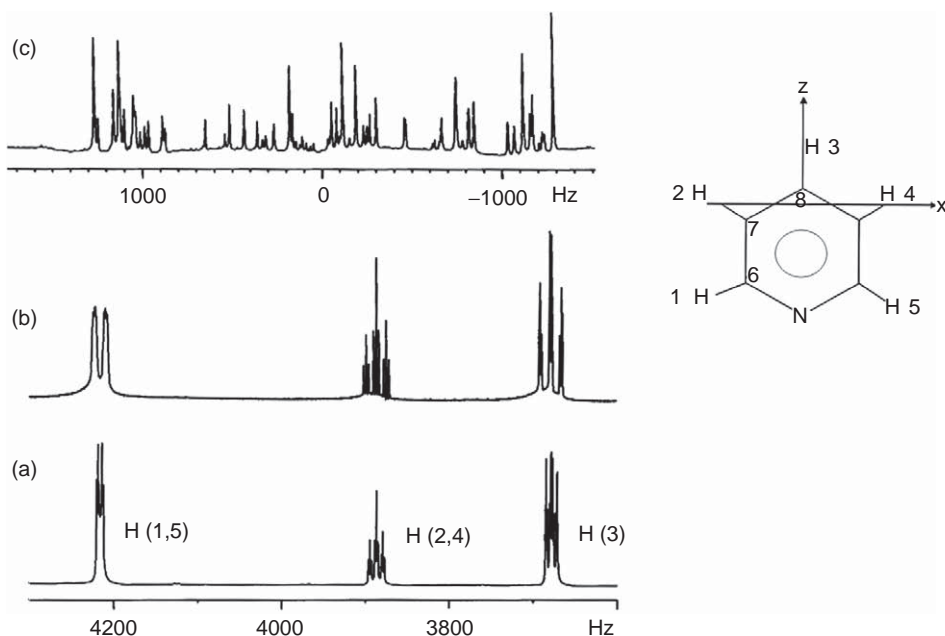


Figure 14 Structure and numbering of atoms in the molecule pyridine with the chosen Cartesian coordinate system. Proton spectrum of pyridine in (a) solvent D₂O, (b) bicelle phase, and (c) nematic phase of EBBA.

The weak coupling character of the spin system in the isotropic and bicelle phase and the strong coupling character in EBBA phase are evident from the figure. The proton spin system in the isotropic and bicelle phase is of the type AA'MM'X. On the other hand, in strongly orienting thermotropic liquid crystal EBBA, the coupled protons form spin system of the type AA'BB'C. The spectrum pertaining to H(2, 4) and H(3) in the bicelle phase has a close resemblance to the isotropic phase spectrum even with additional features arising from the presence of dipolar interactions. The analysis of the spectrum in the bicelle phase is straightforward and similar to the spectrum in the isotropic phase. The fully coupled ^{13}C spectra of this molecule in bicelle and isotropic phases are given in Figure 15. The separations of the transitions in bicelle phase provide $J_{ij}+2D_{ij}$. The knowledge of J_{ij} values provides the D_{ij} values in both ^1H and ^{13}C spectra.

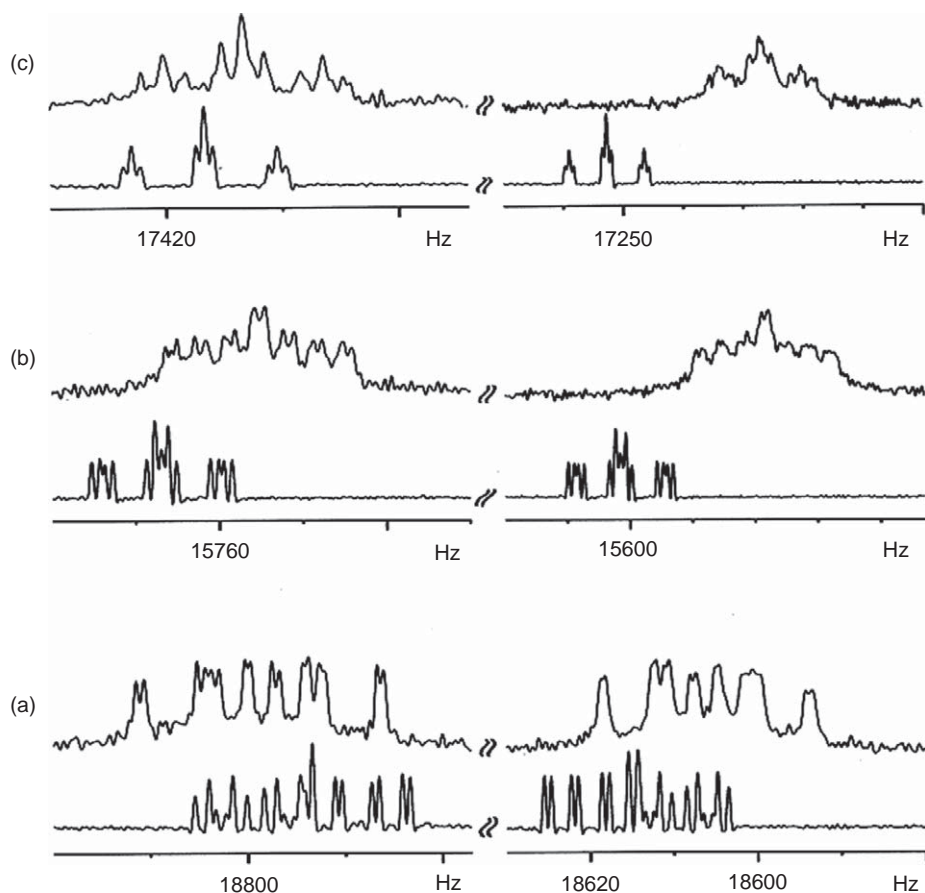


Figure 15 Expanded regions of fully coupled natural abundance ^{13}C spectrum of pyridine in the isotropic and bicelle phase corresponding to: (a) carbon 6, (b) carbon 7, and (c) carbon 8. In all a, b, and c, top traces correspond to the spectrum in bicellar phase and the bottom traces correspond to spectrum in isotropic phase.

However, though weakly coupled, the analysis of the ^1H spectrum is not first order and the iterative analyses of the spectrum are required to be carried out using the above estimated dipolar couplings and chemical shifts as the starting parameters. The dipolar couplings estimated directly and those derived precisely by iterative analyses in bicelle phase agree with each other. Furthermore, the structural and orientational parameters determined in bicelle phase have been reported to be in close agreement with those obtained from thermotropic liquid crystalline phase, implying that the simplified analyses of the spectra can be employed for structural studies of small molecules.

6. NMR STUDIES OF CHIRAL MOLECULES

Different compounds possessing identical molecular formula are called isomers.¹⁴⁸ The isomers having the same bond connectivity but differing in the arrangement of their atoms in space are called stereo isomers. Stereo isomers are classified as enantiomers and diastereomers. Enantiomers are stereo isomers that are mirror images of each other but at the same time are not super imposable and they rotate the plane polarized light in the opposite directions. On the other hand, stereo isomers which are not mirror images are called diastereomers. Molecules which are super imposable on their mirror images are called achiral. The rate of reaction of enantiomers with achiral molecules is same. In a chiral environment, the properties of enantiomers differ. They react at different rates with other chiral reagents. Thus, NMR frequencies of enantiotopic nuclei are isochronous in an achiral medium and do not permit discrimination of enantiomers. However, the resonances of diastereotopic nuclei are anisochronous and enantiodiscrimination is possible. Therefore, for the determination of enantiomeric purity using NMR, a chiral auxiliary is essential to convert the mixture of enantiomers into a diastereomeric mixture. The non-equivalent chemical shifts of diastereomers generally give a resolution of the appropriate signals and the diastereomeric composition can be measured directly from the area of the one-dimensional spectrum or from the volume of the two-dimensional contours, which give the enantiomeric ratio of the original mixture. Three types of chiral auxiliaries¹⁴⁹ are routinely employed for such a purpose. Chiral lanthanide shift reagents^{150,151} and chiral solvating agents (CSAs)^{152,153} form diastereomeric complexes in situ with substrate enantiomers and used directly. On the other hand, chiral derivatizing agents (CDAs)¹⁵⁴ form discrete diastereoisomers prior to NMR analysis. The chemical shift non-equivalence generated by CDA is five times larger than that for related complexes with CSA. However, the use of CDA has some intrinsic disadvantages. If the derivatizing agent is not enantiopure, a small quantity of enantiomeric compound leads to reduced values of enantiomeric purity. CDA can be used in the presence of a reactive function and great care is required to exclude the possibility of racemization or kinetic resolution due to differential reaction rates of the substrate enantiomers.

6.1 Chiral liquid crystal solvent and differential ordering effect (DOE)

It was recognized way back in 1968¹⁵⁵ that the NMR spectra of enantiomers dissolved in a chiral anisotropic media are not identical. Anisotropic interactions being order sensitive permit their discrimination. The PBLG solvent acts as a weakly orienting chiral medium for visualization of enantiomers by the multi-nuclear detection of NMR resonances. It has also been proved as an efficient and convenient tool for enantiomeric excess (ee) measurement. There is an enantioselective interaction between the polypeptide helices in the PBLG and the enantiomers. This leads to substantial orientational difference called DOE. The choice of the solvent is very critical^{156–158} for DOE. Geometric shape recognition as well as the enantioselective electrostatic interaction is the key mechanism behind the discrimination. This differential orientation of the principal axis system of the enantiomers is schematically depicted in a review.¹⁵⁶

It is observed from the extensive work¹⁵⁹ on measurement and analysis of the molecular ordering tensors of two enantiomers of a chiral molecule, (\pm)- β -(trichloromethyl)- β -propiolactone, oriented in a polypeptide liquid crystal system that the principal axis systems of the *R* and *S* enantiomers are not mirror images of each other. It is found that the two principal axis frames are tilted by an amount that can be expressed through Euler angles ($\theta = 16.02^\circ$, $\Phi = -0.41^\circ$, and $\chi = -2.50^\circ$). Through these three rotation angles of one of the principal axis system, this frame can be made to coincide with the mirror image of the other.

6.2 Desired properties of the PBLG solvent

The desired properties that a chiral liquid crystal (CLC) solvent should possess are: (a) good solubility of organic compounds to provide homogeneous anisotropic mesophase and flow viscosity, (b) there should not be any interference from CLC in the NMR spectrum of the solutes, and (c) anisotropic solvents should have low order to retain the first-order character of NMR spectra. The analysis of first-order spectrum does not require any numerical iterative calculations. Added advantage is that low-order parameter reduces the line width and provides higher signal to noise ratio (S/N) as well.

The liquid crystal PBLG with various organic helicogenic co-solvents^{160–162} is found to exhibit all the above desired characteristics. It is found that in such co-solvents, the main chain of the synthetic homo-polypeptide adopts a rigid α -helical conformation while the glutamate side chains branch out from the main helix forming a helix.^{163–165} PBLG solution displays liquid crystal property only over a certain range of concentrations. Over this concentration range, the chiral fibers orient so as to build themselves into a macroscopic supramolecular helical structure of directors in the mesophase. In a magnetic field, the supramolecular helix unwinds and the phase displays the property of a chiral nematic. The molecular diamagnetic susceptibility ($\Delta\chi_m > 0$) has positive anisotropy with the director homogeneously aligned parallel to the static magnetic field.^{166,167} Among the co-solvents, the most suitable are chloroform, dichloromethane, dioxane, and THF.^{164,168} The necessary requirement for co-solvents is that it

should homogeneously dissolve the polypeptide in addition to preserving the α -helical structure of the polymer solvent.

6.3 Order sensitive NMR parameters and chiral discrimination

The various anisotropic NMR interaction parameters employed for chiral discrimination are chemical shift anisotropy ($\Delta\sigma_k$), spin–spin coupling anisotropy (ΔT_{kl}), and the quadrupolar splitting for $I > 1/2$ nuclei ($\Delta\nu_{qk}$). ΔT_{kl} contains two contributions: dipolar coupling (D_{kl}) and anisotropic scalar coupling (Δj_{kl}). However, for protons, Δj_{kl} is not significant compared to the D_{kl} . The spectra in CLC have anisotropic contributions. Relative magnitudes of the anisotropic interactions toward the DOE of enantiomers follow the decreasing order $|\Delta\nu_{qk}| < |\Delta T_{kl}| < |\Delta\sigma_k|$. These anisotropic interactions are excellent tools and are employed as indicators for chiral discrimination.

The nuclei that are of interest in unlabeled organic chiral molecules are ^1H , ^{13}C , and ^2H in natural abundance. The observables that are employed for detecting DOE are: (a) chemical shift anisotropy of different nuclei, *viz.*, $\Delta\sigma_{\text{D}}$, $\Delta\sigma_{\text{H}}$, and $\Delta\sigma_{\text{C}}$; (b) spin–spin coupling anisotropy between different types of nuclei, ΔT_{HH} , ΔT_{HD} , ΔT_{DD} , ΔT_{CC} , ΔT_{CH} , and ΔT_{CD} ; and (c) quadrupolar coupling, $\Delta\nu_{\text{QD}}$. Because of dilute character of ^{13}C and ^2H , some of these parameters are insensitive toward DOE. Enantiomers containing active X nuclei such as ^{19}F , ^{31}P , and $I > 1/2$ nuclei such as ^{10}B and ^{11}B , etc., provide additional NMR observables such as $\Delta\sigma_{\text{X}}$, ΔT_{HX} , ΔT_{CX} , or $\Delta\nu_{\text{QX}}$ and thereby additional observables for the discrimination.

Unambiguous NMR results are obtained for samples with PBLG concentration between 12 and 25% (w/w).¹⁵⁶ Reasonable amount of the solute (1–20%, w/w) can be dissolved in PBLG/co-solvent mixtures without disturbing the liquid crystalline property of the solvent. The average molecular weight of PBLG plays a crucial role in determining the quality of discrimination. For the same co-solvent and PBLG concentration, significant reduction in viscosity of the phase is observed as the molecular weight of the solute is reduced. This is an important point because greater the fluidity, longer the T_2^* and hence better S/N ratio.

7. EXISTING NMR EXPERIMENTS FOR CHIRAL DISCRIMINATION

7.1 ^{13}C NMR in natural abundance

Carbon-13 detection in natural abundance is very useful for diverse reasons¹⁵⁶: (a) the absence of coupling between two dilute spins, (b) the ^{13}C spectra in PBLG can circumvent the problem of resolution and the severe overlap of transitions arising from too many residual dipolar couplings, (c) the high B_0 magnetic fields provide better sensitivity, even for a small amount of material in short experimental time, (d) the order parameter of PBLG being high compared to the solute molecules, its resonance signals are relatively broad, and (e) the large $\Delta\sigma_i$ for sp or sp² carbon atoms is also advantageous for discrimination.

Both one-dimensional proton coupled as well as proton decoupled ^{13}C experiments have been employed for discrimination. In the one-dimensional proton coupled ^{13}C experiments, chiral discrimination is achieved through the difference of $\Delta\sigma_i$ as well as D_{CH} . A methyl group displays a quartet where the separations between successive transitions are given by $T_{\text{CH}_3}^{R/S} = J_{\text{CH}_3} + 2D_{\text{CH}_3}^{R/S}$. A methylene group is a triplet with the separation between successive transitions being $T_{\text{CH}_2}^{R/S} = J_{\text{CH}_2} + 2D_{\text{CH}_2}^{R/S}$ and a methine group is a doublet $T_{\text{CH}}^{R/S} = J_{\text{CH}} + 2D_{\text{CH}}^{R/S}$. Additional splitting of methyl protons is observed due to coupling ($T_{\text{CH}_3\cdots\text{CH}}^{R/S}$) with methine proton in groups such as CH_3CH . However, the value of T_{CH} and $\Delta\sigma_i$ for individual carbons being different for the *R* and *S* enantiomers, chiral discrimination is feasible. The signs of $^1J_{\text{CH}}$ and $^3J_{\text{CH}}$ are known to be positive and considering that $^1D_{\text{CH}}$ and $^3D_{\text{CH}}$ are smaller than $^1J_{\text{CH}}$ and $^3J_{\text{CH}}$ in the PBLG phase the absolute signs of the dipolar couplings have been determined.¹⁵⁷ Since highly resolved spectrum is a prerequisite for the discrimination based on D_{CH} , the applicability of the proton coupled ^{13}C NMR is limited to small molecules.

One-dimensional proton decoupled ^{13}C experiments are advantageous in view of simplified analyses and sensitivity and greater precision in measuring enantiomeric excess (ee). Well-dispersed chemical shifts aid the assignment of resonances to chemically inequivalent ^{13}C spins. The chemical shift anisotropies of ^{13}C being small in PBLG, the ^{13}C chemical shift positions are nearly equal to the isotropic ones. Thus, the assignment to enantiomeric carbons is pretty straightforward. ee could be measured from the areas of the peaks discriminated. Accuracy of ee measurement using ^{13}C detection is between 5 and 10%.¹⁵⁶

7.2 ^2H NMR in natural abundance

The strength of the deuterium quadrupolar interaction being larger and most sensitive to order parameter, generally majority of the studies employs ^2H NMR for enantiomeric discrimination.^{169–172} There is voluminous amount of data reported in the literature on the use of ^2H detection. Many one- and two-dimensional experiments have been reported for such a purpose using deuterium in its natural abundance. The employment of ^2H NMR in natural abundance in the isotropic phase and in labeled molecules in both isotropic and anisotropic phases is well known from the early days of NMR spectroscopy.¹⁷³ The use of it in the natural abundance for chiral analyses is cited in the literature as NAD-NMR. As far as the sensitivity of NAD-NMR is concerned, the feasibility of routine employment of this technique has been pointed out.¹⁷⁴ It has also been pointed out that deuterium T_1 relaxation rates for solutes dissolved in PBLG are generally much lower than that of ^{13}C . Therefore, the faster acquisition of data is possible with similar S/N ratio. This also overcomes the tedium of isotopic enrichment for observing deuterium signals in PBLG.

At natural abundance, J_{DD} and D_{DD} are undetected. In ^1H decoupled NAD NMR spectra in PBLG, each non-equivalent ^2H site in a molecule gives rise to independent quadrupole split doublet. In a racemic mixture of enantiomers possessing '*n*' chemically inequivalent deuterium, '*2n*' doublets are observed.

When there is a severe overlap and the identification of the quadrupolar doublets becomes tedious, the well-known correlation of coupled energy states has been employed. Consequently, 2D autocorrelation deuterium NMR experiments such as QUOSY and QCOSY have been reported.^{175,176} The cross-peaks of the 2D matrix enabled the separation of all the sets of quadrupolar doublets. There are also reports of three-dimensional experiments and the phase sensitive versions of two-dimensional methods.^{177,178}

7.3 Advantages of proton NMR for chiral analyses

The routine employment of ^1H detection for chiral analyses is severely hindered due to enormous loss of resolution arising from numerous short- and long-distance couplings. The sensitivity of $\Delta\sigma_{\text{H}}$ toward DOE in PBLG is very weak and the chemical shift difference between the enantiomers is negligibly small. Thus, the indistinguishable superposition of two independent ^1H spectra from the two enantiomers for a racemic mixture is inevitable. This overlap combined with broad and featureless spectra renders the analyses of ^1H spectra difficult even for small molecules with five or six interacting spins. The discrimination and disentangling of this overlap is a formidable task. Thus, in the literature, the analyses of ^1H -detected spectra have been described as either difficult or impossible¹⁵⁶ and there are very few reported studies for chiral visualization. Nevertheless, the ^1H -detected NMR spectra, in spite of their severe complexity when employed for big molecules, are the preferred choice for chiral molecules because of their high sensitivity, high natural abundance, and enormous saving of experimental time.

As far as the spectra of enantiopure molecules in PBLG are concerned, the spins are generally weakly coupled and the first-order analyses are feasible in most of the situations. However, the spectral complexity arising from too many unresolved transitions hampers their analyses. The complexity and the first-order interpretation of different enantiopure chiral molecules with increasing order of their complexity will be initially discussed in the following sections. For this purpose, four different molecules, each possessing a chiral center, whose chemical structures and the labeling of the interacting spins are given in Figure 16, have been chosen. Subsequently the methodologies developed for combating the analyses of their complex ^1H spectra in the chiral liquid crystal PBLG, given in Figure 17, are discussed.

7.4 The first-order analyses of NMR spectra in PBLG solvent

7.4.1 ^1H NMR spectrum of (*R/S*)-2-chloropropanoic acid

The ^1H NMR spectra of (*R/S*)-2-chloropropanoic acid (Figure 17a) display well-isolated peaks for methyl and methine protons. The signal from the hydroxyl proton is broadened and does not display coupling to other protons. Thus, the coupled protons in (*R/S*)-2-chloropropanoic acid pertain to the spin system of the type A_3X , where A refers to methyl protons and X corresponds to methine proton. The spectrum is amenable for first-order analysis. The methyl protons

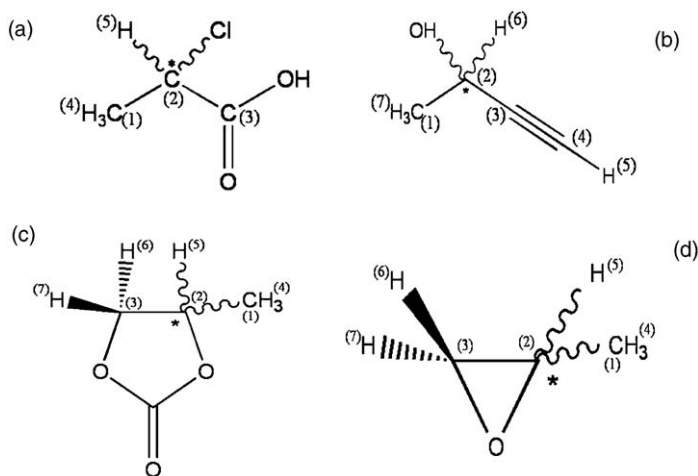


Figure 16 Racemic structures of the molecules: (a) (*R/S*)-2-chloropropanoic acid, (b) (*R/S*)-3-butyn-2-ol, (c) (*R/S*)-propylene carbonate, and (d) (*R/S*)-propylene oxide. The chiral centers are marked with ‘*.’

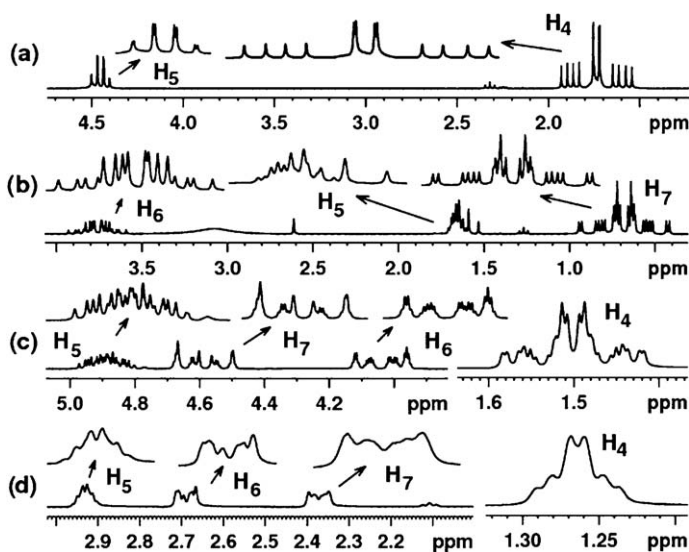


Figure 17 From top to bottom—500 MHz one-dimensional ^1H spectrum of: (a) (*R/S*)-2-chloropropanoic acid, (b) (*R/S*)-3-butyn-2-ol, (c) (*R/S*)-propylene carbonate, and (d) (*R/S*)-propylene oxide. The expansions of the particular regions of each spectrum and the assignment to different protons are shown.

are split into 1:2:1 triplet due to residual proton–proton dipolar couplings among the magnetically equivalent protons. The separation between two adjacent transitions provides $^2T_{\text{HH}}$ ($= 3 \times ^2D_{\text{HH}}$), where T refers to the sum of the three dipolar couplings ($^2D_{\text{HH}}$) among methyl protons and the superscript 2 refers to

the proton that is two bonds away. Due to magnetic equivalence, J_{HH} does not influence the spectrum and the separation of two consecutive transitions directly provides ($3 \times {}^2D_{HH}$). Each of these transitions is further split into doublets of equal intensity due to coupling (${}^3J_{HH} + 2 \times {}^3D_{HH}$) with methine proton. Thus, the six transitions observed can be visualized as two A_3 subspectra corresponding to two spin states of X spin. One of the A_3 subspectra correspond to methine proton in the $|\alpha\rangle$ state and the other for the methine proton in the $|\beta\rangle$ state. Similarly, the methine proton is a quartet due to its coupling with methyl protons. In a racemic mixture, there will be an overlap of spectra from both the enantiomers.

7.4.2 ${}^1\text{H}$ NMR spectrum of (*R/S*)-3-butyn-2-ol

The one-dimensional ${}^1\text{H}$ NMR spectrum of the molecule in the solvent PBLG is given in Figure 17b. The spectrum has well-resolved and isolated peaks for the CH_3 and two CH groups. The peak due to hydroxyl proton is broadened and does not display coupling pattern from any other protons. However, all the remaining protons are coupled among themselves. The protons of (*R/S*)-3-butyn-2-ol form a spin system of the type A_3MX . The methyl protons (A_3) experience three different types of couplings, *viz.*: (a) coupling among themselves (${}^2T_{HH}$) leading to a triplet, (b) coupling between methyl (A_3) and methine (M-spin) proton (${}^3T_{HH}$) giving a doublet for each transition of the triplet, and (c) coupling between methyl (A_3) and acetylenic (X-spin) proton (${}^5T_{HH}$) giving a doublet of doublet of a triplet. The 12 transitions observed can be construed as 4 A_3 subspectra corresponding to 4 possible passive spin states of M and X spins together. Similarly, each M and X spin is split into doublet of a quartet because of coupling to CH_3 protons and the remaining acetylenic/methine proton.

7.4.3 ${}^1\text{H}$ NMR spectra of (*R/S*)-propylene carbonate and (*R/S*)-propylene oxide

The one-dimensional spectra of (*R/S*)-propylene carbonate and (*R/S*)-propylene oxide are reported in Figures 17c and 17d, respectively. The protons of each molecule form a weakly coupled spin system of the type A_3MPX , where A_3 corresponds to methyl protons, M and P are the two methylene protons, and X is the methine proton. The methyl protons experience four different type of couplings, *viz.*: (a) couplings among themselves (${}^2T_{HH}$) leading to a triplet, (b) coupling between methyl (A_3) and methine (X-spin) proton (${}^3T_{HH}$) giving a doublet for each transition of the triplet, and (c) two different couplings from the two diastereomeric methylene protons (${}^4T_{HH}$) giving rise to further splitting of each transition to doublet of a doublet. Thus, 24 transitions are observed for methyl groups which can be visualized as 8 A_3 subspectra corresponding to 8 spin states of M, P, and X together. The multiplicity for each M, P, and X spin will be doublet of doublet of quartet.

Though the first-order interpretation of the multiplicity pattern of the ${}^1\text{H}$ spectra of all the molecules discussed above is generally feasible, in a racemic mixture the discrimination of the spectrum for each enantiomer and the discerning of the degenerate transitions is a prerequisite. Furthermore, when

the size of the molecule becomes bigger, the spectra become increasingly complex and the simplification of the complex multiplicity pattern is essential for their analyses. The novel experimental methods have been developed recently to combat many inherent problems and limitations in the proton detection. All the developed pulse sequences manipulate the spin dynamics to utilize the parameters, *viz.*, $\Delta\sigma_{\text{H}}$, D_{HH} , or D_{CH} (with ^{13}C in natural abundance) from the proton spectrum. Before discussing the recent developments, a short discussion on earlier reported works for the visualization of enantiomers will be highlighted.

7.5 Earlier ^1H experimental methods for chiral discrimination

7.5.1 Two-dimensional ^1H selective refocusing (SERF)

As discussed earlier, in PBLG the methyl resonance of a molecule is a triplet due to dipolar couplings (D_{HH}) among methyl protons. However, the presence of small RDCs to remote protons causes excessive broadening and precludes the observation of any fine structure, as in Figures 17c and 17d. If, on the other hand, all the remote couplings are refocused, then the dipolar split triplet patterns for the *R* and *S* enantiomers can be visualized. In SERF experiment, this is achieved in the t_1 dimension. This concept, originally demonstrated for isotropic systems,¹⁷⁹ has been applied for chiral molecules.¹⁸⁰ In the pulse sequence, a SERF pulse on the methyl protons in the middle of t_1 dimension refocuses the remote couplings and retains only the couplings among the methyl protons. In the t_1 dimension, the two distinct triplets for the *R* and *S* enantiomers are observed with the overlapped central transitions. Thus, the enantiomers are discriminated using methyl resonances. The integration of the outer components of the triplets for *R* and *S* enantiomers provided the ee. To detect the proton–proton couplings between methyl protons and the remote proton, two SERF pulses are used to selectively retain the coupling between them.¹⁸⁰

7.5.2 Heteronuclear selective refocusing (HETSERF)

The prerequisite for SERF experiment is that proton resonances should be well isolated for selective excitation. This may not always be possible. Also a specific proton–proton coupling may not lead to discrimination in all the cases. To overcome these difficulties, the HETSERF experiment was developed.¹⁸¹ This experiment takes advantage of the large chemical shift range of proton decoupled ^{13}C spectra and reduces the multiplicity of ^1H coupled ^{13}C transitions. This provides enhanced sensitivity. In HETSERF experiment, in the middle of the t_1 dimension, simultaneous application of a SERF pulse on the particular group of proton(s) and a non-SERF pulse on ^{13}C refocuses the ^{13}C chemical shifts and all the heteronuclear couplings except the coupling between the selectively excited proton(s) and all the ^{13}C in the molecule. Thus, the information content in the t_1 dimension is the couplings between the selected proton(s) and the carbons. This simplifies the spectral analysis. The differential values of heteronuclear couplings between selected proton(s) and carbons, at different ^{13}C sites, enabled chiral discrimination in the t_1 dimension.

7.5.3 BIRD module in X–H correlation experiments

The requirement of selective excitation limits the merits of SERF and HETSERF experiments. To overcome these limitations, a set of non-selective experiments has been reported where a BIRD module is incorporated in the t_1 dimension of X–H correlation experiments.¹⁸² These experiments involve either ^1H or ^{13}C coherences at the beginning of the t_1 evolution time and hence the spectrum in F_1 dimension retains one bond heteronuclear coupling and geminal proton–proton coupling. The experiments falling in this category are: ^{13}C -J-resolved-BIRD, J-HSQC-BIRD, J-HMQC-BIRD, and ^1H -J-HSQC-BIRD.

8. DOUBLE QUANTUM SELECTIVE REFOCUSING (DQSERF): A NOVEL CONCEPT

This is the novel pulse sequence developed recently.¹⁸³ The selective DQ excitation of methyl protons has a distinct advantage in the molecules where the ^1H signals from this group can be selectively excited. The DQ excitation corresponds to flipping of any two protons of the methyl group (active spins) in the presence of the third (passive spin) proton. The pulse sequence for DQSERF is shown in Figure 18. An application of a SERF 180° pulse on the methyl protons in the middle of the DQ dimension removes the effect of couplings from the long-distance protons and retains only short-distance passive coupling to a methyl proton, which is not involved in DQ coherence, resulting in a doublet. MQ coherence evolves at the sum of the passive couplings. The sum of the two passive couplings from the passive proton being different for two enantiomers, the doublets get separated from each other. The presence of DQ–SQ conversion pulse, unlike in SERF experiment, leads to coherence transfer from DQ to SQ in such a way that each cross-section along SQ dimension displays a normal enantiopure one-dimensional ^1H spectrum.

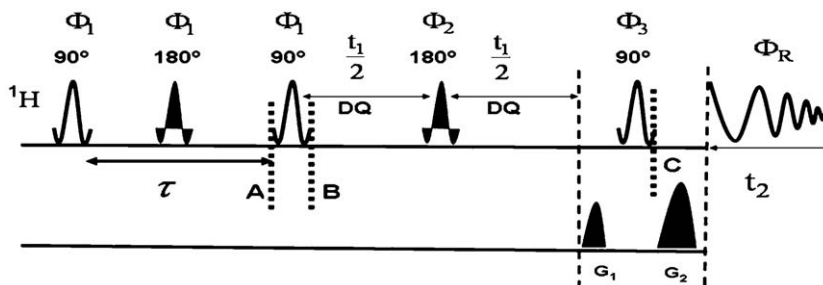


Figure 18 The pulse sequence for the selective excitation of DQ coherence of methyl protons in the molecules given in Figure 17. The pulse phase Φ_2 is x , y , $-x$, and $-y$ with the receiver phase being x all the time. Phases of all the remaining pulses were set to x . Double quantum to single quantum coherence transfer pathway has been selected by setting the gradient ratio $G_1:G_2$ as 1:2. Selective pulses are seduce-shaped pulses. Reproduced with permission from American Chemical Society.

8.1 Dynamics of nuclear spins in SERF and DQSERF sequences

In this section, we bring out the highlights of the SERF experiments and some salient features ignored in the initial report in the context of chiral discrimination.¹⁸⁰ The modified SERF experiment shows that in addition to measurement of couplings among particular group of protons in the t_1 dimension, the t_2 dimension can also be utilized to measure the couplings to remote protons.¹⁸³

The earlier reported work on SERF employs only the indirect dimension to determine a particular coupling, for example, among methyl protons of the molecule (*R/S*)-propylene oxide. To determine one of the remote couplings, say, coupling between methyl and methylene protons in a molecule, a second experiment is suggested¹⁸⁰ by applying a biselective pulse on these two groups. It has been demonstrated that in a single experiment, it is possible to determine the coupling among methyl protons and also some of the remote couplings in favorable cases. In the subsequent section, the DQSERF experiment is described. The polarization operator approach is employed in understanding the spin dynamics in both these sequences.¹⁸⁴

8.2 Behavior of magnetization in a SERF experiment

For theoretical understanding of the magnetization in the SERF sequence, a coupled A_3X spin system is considered where two different types of couplings T_{AA} ($= 3D_{HH}$) and T_{AX} ($= J+2D_{HH}$) ($T_{AA} > T_{AX}$) are present (T is the sum of dipolar and scalar couplings). Although for the theoretical understanding of the pulse sequence we have assumed a weakly coupled spin system of the type A_3X , in reality the A_3 spin system cannot be treated as a weakly coupled one. The real symmetric spin functions are to be taken into account in order to analyze the spectrum.

All the three possible couplings T_{AA} in A_3 are equal. Considering the selective excitation of A spin SQ coherences and the decoupling of X spin in the t_1 dimension, by SERF pulse on A spin, the SQ terms present in this dimension are

$$\frac{1}{2}[I_+^A]\frac{1}{2}[(I_\alpha^A + I_\beta^A)]\frac{1}{2}[I_\alpha^A + I_\beta^A] \quad (35)$$

Thus, t_1 dimension is a triplet pertaining to the four transitions $I_{+\alpha}^A I_{-\alpha}^A I_\alpha^A$, $I_{+\beta}^A I_{-\beta}^A I_\alpha^A$, $I_{+\alpha}^A I_{-\beta}^A I_\beta^A$, and $I_{+\beta}^A I_{-\alpha}^A I_\beta^A$ where the central two transitions are degenerate. As there is no mixing pulse between the t_1 and t_2 dimensions, the spin states involved in these transitions remain unperturbed in both the dimensions. The spin operators and the frequencies present in t_1 and t_2 dimensions are given in Table 1. The passive coupling T_{AX} being present in the direct dimension, the transitions can be rewritten as given in the third column of Table 1. The effective Hamiltonians, respectively, in t_1 and t_2 dimensions are

$$\bar{H} = \pi T_{IAIA} t_1 2I_A^Z I_A^Z \quad \text{and} \quad \bar{H} = \omega_A I_A^Z + \pi T_{IAIA} t_1 2I_A^Z I_A^Z + \pi T_{IAIX} t_1 2I_A^Z I_X^Z \quad (36)$$

Table 1 Correlation between the transitions in the t_1 and t_2 dimensions in a SERF experiment (frequencies are given inside bracket)

Spin operators in t_1 dimension	Frequencies in t_1 dimension	Spin operators in t_2 dimension	Frequencies in t_2 dimension
$I_+^A I_\alpha^A I_\alpha^A$	$(-T_{AA})$	$I_+^A I_\alpha^A I_\alpha^A \frac{1}{2}(I_\alpha^X + I_\beta^X)$	$\left(\omega_A \pm \frac{1}{2}T_{AX}\right) - T_{AA}$
$I_+^A I_\alpha^A I_\beta^A$	(0)	$I_+^A I_\alpha^A I_\beta^A \frac{1}{2}(I_\alpha^X + I_\beta^X)$	$\left(\omega_A \pm \frac{1}{2}T_{AX}\right) + 0$
$I_+^A I_\beta^A I_\alpha^A$	(0)	$I_+^A I_\beta^A I_\alpha^A \frac{1}{2}(I_\alpha^X + I_\beta^X)$	$\left(\omega_A \pm \frac{1}{2}T_{AX}\right) + 0$
$I_+^A I_\beta^A I_\beta^A$	$(+T_{AA})$	$I_+^A I_\beta^A I_\beta^A \frac{1}{2}(I_\alpha^X + I_\beta^X)$	$\left(\omega_A \pm \frac{1}{2}T_{AX}\right) + T_{AA}$

It is obvious from Table 1 that corresponding to each component of the triplet in the t_1 dimension, the direct dimension displays a doublet. The appearance of the SERF spectra (Figure 20) will be discussed in the later section. However, it is suffice to mention at this juncture that it is evident from Figure 20 that the separation T_{AA} in t_1 dimension being different for the *R* and *S* enantiomers, there is chiral discrimination visualized for the outer components of the triplets. But central transitions for the *R* and *S* enantiomers are, however, overlapped. The new feature in this SERF spectrum compared to that reported earlier¹⁸⁰ is that the remote couplings can be extracted from the direct dimension, *viz.*, transition at $-T_{AA}$ in the indirect dimension produces a doublet (Figure 20c) due to remote coupling at $(\omega_A \pm (1/2)T_{AX}) - T_{AA}$ in the direct dimension.

8.3 Dynamics of spin system in a DQSERF pulse sequence

The designed pulse sequence for DQSERF is reported in Figure 18. In this case also, the analysis of the pulse sequence is discussed for an A_3X spin system. However, the theory can be extended for different spin systems. The selective excitation of DQ coherence of A_3 spin is assumed. The magnetization immediately after the second 90° pulse at point B in Figure 18 is $-2I_X^A I_Y^A$. In terms of polarization operators, the terms I_X^A , I_Y^A , E^A , and E^X are written as:

$$I_X^A = \frac{1}{2}(I_+^A + I_-^A), \quad I_Y^A = \frac{1}{2i}(I_+^A - I_-^A), \quad E^X \equiv \frac{1}{2}(I_\alpha^X + I_\beta^X), \quad \text{and} \quad E^A \equiv \frac{1}{2}(I_\alpha^A + I_\beta^A) \quad (37)$$

Using the above operators, the MQ terms $(I_X^A I_Y^A + I_Y^A I_X^A) E^A E^X$ are written as:

$$\frac{1}{2i}(I_+^A I_+^A - I_+^A I_-^A + I_-^A I_+^A - I_-^A I_-^A) \frac{1}{2}(I_\alpha^A + I_\beta^A) \frac{1}{2}(I_\alpha^X + I_\beta^X) \quad (38)$$

However, the term $(1/2)(I_\alpha^X + I_\beta^X)$ must be neglected in the DQ dimension as the SERF pulse on A spin decouples X spin.

Thus, $(1/2i)(I_+^A I_+^A - I_+^A I_-^A + I_-^A I_+^A - I_-^A I_-^A)(1/2)(I_\alpha^A + I_\beta^A)$ is the only term required to be analyzed in the t_1 dimension. The first term $I_+^A I_+^A (1/2)(I_\alpha^A + I_\beta^A)$ of the above equation has a coherence order $p = 2$. This is a doublet in the DQ dimension with doublet separation $2T_{AA}$. This term is converted into SQ coherence by the last 90° pulse of the sequence at the point C. The DQ transition corresponding to $|\alpha\rangle$ state of passive spin A, the DQ-SQ transformation, is written as:

$$\begin{aligned} \frac{1}{2i}(I_+^A I_+^A) \frac{1}{2}(I_\alpha^A) &\rightarrow \frac{1}{2}[I_+^A + I_-^A + i(I_\alpha^A - I_\beta^A)] \frac{1}{2}[I_+^A + I_-^A + i(I_\alpha^A - I_\beta^A)] \\ &\times \frac{1}{2}[I_\alpha^A + I_\beta^A + i(I_+^A - I_-^A)] \end{aligned} \quad (39)$$

In the direct dimension, the A spin SQ coherences evolve under all the couplings T_{AA} as well as T_{AX} . Thus, right-hand side of Equation (39) can be rewritten as:

$$\frac{1}{2}[I_+^A + I_-^A + i(I_\alpha^A - I_\beta^A)] \frac{1}{2}[I_+^A + I_-^A + i(I_\alpha^A - I_\beta^A)] \frac{1}{2}[I_\alpha^A - I_\beta^A + i(I_+^A + I_-^A)] \frac{1}{2}(I_\alpha^X + I_\beta^X) \quad (40)$$

From the above equation, a SQ coherence of order $p = -1$ which is observable can be detected:

$$\frac{1}{2}[I_-^A] \frac{1}{2}[i(I_\alpha^A - I_\beta^A)] \frac{1}{2}[I_\alpha^A + I_\beta^A] \frac{1}{2}(I_\alpha^X + I_\beta^X) \quad (41)$$

Thus, the overall DQ-SQ transformation can be written in simple form as:

$$\frac{1}{2i}(I_+^A I_+^A) \frac{1}{2}(I_\alpha^A) \rightarrow \frac{1}{2}[I_-^A] \frac{1}{2}[i(I_\alpha^A - I_\beta^A)] \frac{1}{2}[I_\alpha^A + I_\beta^A] \frac{1}{2}(I_\alpha^X + I_\beta^X) \quad (42)$$

If $T_{AA} > T_{AX}$, the frequency modulation of this leads to a doublet of a triplet. Similarly for the DQ transition corresponding to $|\beta\rangle$ state of passive spin X, we get

$$\frac{1}{2i}(I_+^A I_+^A) \frac{1}{2}(I_\beta^A) \rightarrow \frac{1}{2}[I_-^A] \frac{1}{2}[i(I_\alpha^A - I_\beta^A)] \frac{1}{2}[I_\alpha^A + I_\beta^A] \frac{1}{2}(I_\alpha^X + I_\beta^X) \quad (43)$$

which also displays a doublet of a triplet. Thus, the same multiplicity, that is, doublet of a triplet in SQ dimension is repeated in both the cross-sections corresponding to the two DQ transitions in the t_1 dimension. The theoretical approach is valid for any molecule with an isolated CH_3 group, *viz.*, (*R/S*)-2-chloropropanoic acid, (*R/S*)-3-butyn-2-ol, (*R/S*)-propylene carbonate, and (*R/S*)-propylene oxide. The DQSERF spectra of the racemic mixtures of these molecules are discussed in the subsequent sections.

8.4 Total separation by DQSERF in a strongly coupled A_3 spin system

Although for the theoretical understanding of the pulse sequence we have assumed a weakly coupled spin system of the type A_3X , in reality the A_3 spin system cannot be treated as a weakly coupled one. The real symmetric spin functions are to be taken into account in order to analyze the spectrum. Thus, a more realistic situation is discussed below.

In a DQ-SERF experiment, the DQ dimension provides reduced multiplicity of transitions compared to the corresponding SERF experiment. Flipping of any two spins of the methyl protons (A_3 spin system) in the DQ dimension mimics the spin system of the type AX , where A is the super spin (with two protons) and X is the spectator spin. Exciting the DQ coherence and allowing it to evolve only under the sum of passive couplings to X spin (no chemical shift evolution due to refocusing pulse only on A) gives a doublet at frequencies $+T_{AA}$ and $-T_{AA}$ (where $T = 3 \times {}^2D_{HH}$) as discussed below. The basic symmetry functions for the three equivalent nuclei in A_3 spin system are available in the literature.¹⁰¹

The dipolar coupling Hamiltonian that influences the spectrum of an A_3 spin system can be written as ${}^23D_{HH}I_Z^1I_Z^2 + {}^23D_{HH}I_Z^1I_Z^3 + {}^23D_{HH}I_Z^2I_Z^3$, where the A_3 spin system is labeled as $A(1)$, $A(2)$, and $A(3)$. The DQ coherence evolves only under the sum of passive couplings and not the active coupling. The effective dipolar coupling Hamiltonian in the DQ dimension, for the DQ coherence of spins 1 and 2, can be written as ${}^23D_{HH}I_Z^1I_Z^3 + {}^23D_{HH}I_Z^2I_Z^3$. The frequency for the two DQ transitions $\alpha\alpha\alpha \rightarrow (\beta\beta\alpha + \beta\alpha\beta + \alpha\beta\beta)/\sqrt{3}$ and $(\alpha\alpha\beta + \alpha\beta\alpha + \beta\alpha\alpha)/\sqrt{3} \rightarrow \beta\beta\beta$, that is, $(A_1)_{3/2} \rightarrow (A_1)_{-1/2}$ and $(A_1)_{1/2} \rightarrow (A_1)_{-3/2}$ are at $+T_{AA}$ and $-T_{AA}$, where $T = 3({}^2D_{HH})$. Thus, the DQ dimension is a doublet with separation corresponding to $2T_{AA}$.

The value of T_{AA} being different for the R and S enantiomers, the DQ transitions of R and S have different frequencies for these doublets, one doublet at $-T_{AA}^R, +T_{AA}^R$ and the other doublet at $-T_{AA}^S, +T_{AA}^S$ enabling unambiguous chiral discrimination. As the last 90° pulse interacts with the spin state of the passive spin A which is not involved in the DQ transitions, there are three SQ transitions possible from each of the above DQ transitions. They are $(A_1)_{3/2} \rightarrow (A_1)_{1/2}$, $(A_1)_{1/2} \rightarrow (A_1)_{-1/2}$, and $(A_1)_{-1/2} \rightarrow (A_1)_{-3/2}$ with corresponding frequencies $-T_{AA}$, 0, and $+T_{AA}$. Thus, the two triplets in the SQ dimension arise at the already discriminated DQ transitions. Since the separation of the transitions of the R and S enantiomers has been achieved in the DQ dimension, the SQ transitions of the R and S forms appear in different cross-sections in the SQ dimension. Thus, complete separation is achieved for the methyl group. The DQSERF spectra of (R/S)-2-chloropropanoic acid, (R/S)-3-butyn-2-ol, and (R/S)-propylene oxide are reported in Figure 19.

8.5 Appearance of 2D SERF spectrum

In SERF experiment, the three transitions for the dipolar coupled A_3 spin system in the t_1 dimension can be calculated to be $-T_{AA}$, 0, and $+T_{AA}$. Since the central

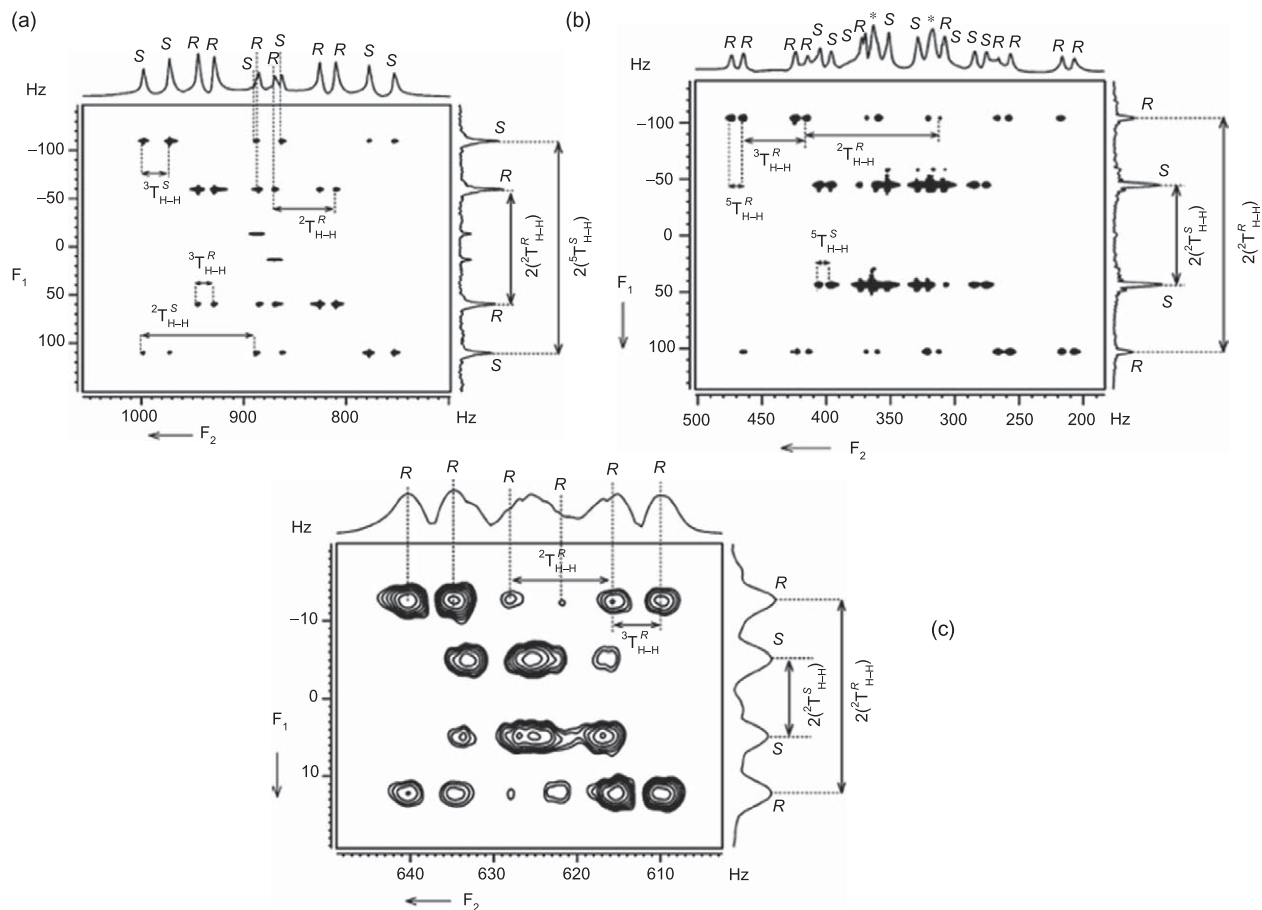


Figure 19 500 MHz ^1H 2D DQSERF spectrum of: (a) (*R/S*)-2-chloropropanoic acid, (b) (*R/S*)-3-butyn-2-ol, and (c) (*R/S*)-propylene oxide in the chiral liquid crystal PBLG correlating the DQ coherence of methyl protons to its SQ coherence. Peak separations providing the values of $(^nT_{\text{HH}})^{\text{R/S}}$ are marked. All the peaks of 2D projection in the direct dimension could be correlated to the peaks in R and S enantiomer cross-sections. The discrete vertical lines marked identify the closely resonating signals for each enantiomer in the SQ dimension. The DQ dimension provides $3 \times {}^2D_{\text{HH}}$ for both the enantiomers, thereby enhancing the resolution for better discrimination. Reproduced with permission from American Chemical Society.

transition from the methyl protons at the middle of the spectrum does not evolve, it is always at zero frequency. The frequencies in the t_2 dimension appear at $\omega_A - T_{AA}$, ω_A , and $\omega_A + T_{AA}$. The absence of the 90° pulse at the end of the t_1 dimension in SERF experiment, unlike in DQ-SERF experiment, indicates that the spin states involved in the SQ transitions remain same in both t_1 and t_2 dimensions. Thus, the transition at $-T_{AA}$ in t_1 dimension correlates to a transition at $\omega_A - T_{AA}$ in t_2 , the transition at 0 in t_1 correlates to a transition ω_A in t_2 , and the transition at $+T_{AA}$ correlates to a transition at $\omega_A + T_{AA}$. Hence, there is a diagonal tilt of the peaks (analogous to untilted 2D J-resolved spectrum) in such a 2D correlation matrix.

The different values of T_{AA} for the *R* and *S* enantiomers provide chiral discrimination in the t_1 dimension for the outer transitions at frequencies $+T_{AA}^R$, $-T_{AA}^R$ and $+T_{AA}^S$, $-T_{AA}^S$. However, the central transitions at zero frequency for both *R* and *S* forms are overlapped. In molecules possessing other interacting protons, the t_2 dimension is a multiplet due to the remote couplings for cross-sections taken at frequencies $+T^R$, $-T^R$ for the *R* enantiomer and $+T^S$, $-T^S$ for the *S* enantiomer and it is possible to pick up the transitions corresponding to each enantiomer at these cross-sections. However, the multiplets arising out of the remote couplings for both the enantiomers are overlapped for the cross-section taken along the t_2 dimension at central transition frequency of the t_1 dimension and the complete chiral discrimination is impossible in such a situation. As far as the extraction of the information is concerned, it is possible even without the central transition. The typical methyl proton excited SERF spectra of (*R/S*)-2-chloropropanoic acid, (*R/S*)-3-butyn-2-ol, and (*R/S*)-propylene oxide are given in Figure 20.

8.6 Optimization of τ delay in DQSERF sequence

In (*R/S*)-2-chloropropanoic acid, the methyl and the methine proton resonances are separated by more than 2 ppm. The methyl region exhibits a bandwidth of 140 Hz. Thus, the methyl protons of both the enantiomers could be simultaneously and selectively excited. However, the spectrum is a mixture of transitions from the *R* and *S* enantiomers. The excitation of the DQ coherence of the methyl protons in such a situation is non-uniform as the amplitude of excited coherence is dependent on the coupling constants (and hence τ delay) which is different for the *R* and *S* enantiomers. The τ delay is required to be optimized experimentally to create antiphase magnetization. A series of two-dimensional experiments have been carried out to optimize the τ delay for maximizing the signal intensity of the methyl protons for both the enantiomers. The intensity of the spectrum for the first t_1 incremental delay corresponding to each enantiomer was monitored as a function of τ delay as shown in Figure 21a. The average delay of 20 ms (25 Hz) provided maximum and comparable signal intensities for both the enantiomers and for all the lines and was taken as optimum value. Similar optimization for (*R/S*)-3-butyn-2-ol and (*R/S*)-propylene oxide is shown in Figure 21b and c, respectively.

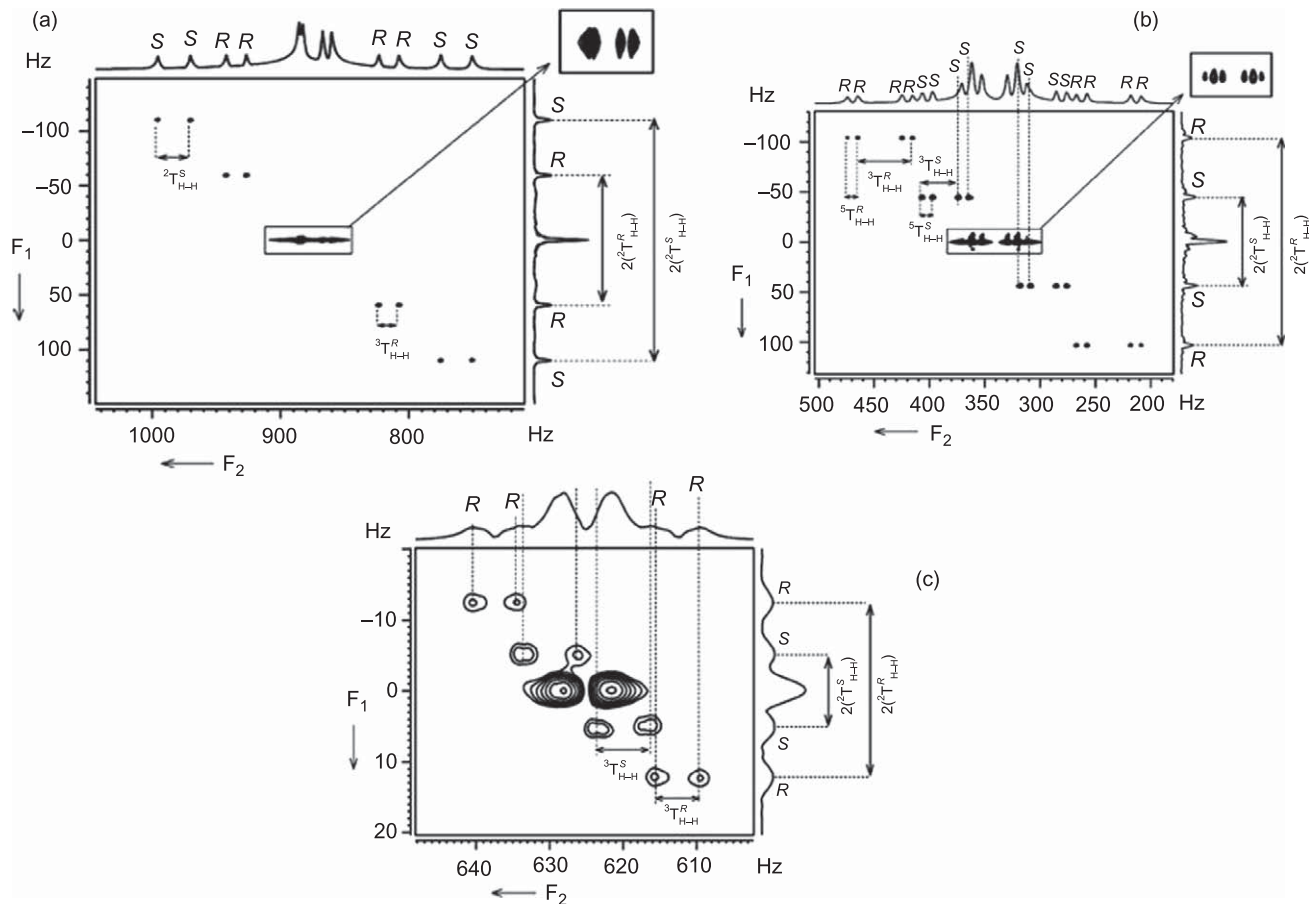


Figure 20 500 MHz ^1H 2D SERF spectrum of: (a) (R/S) -2-chloropropanoic acid, (b) (R/S) -3-butyn-2-ol, and (c) (R/S) -propylene oxide in the chiral liquid crystal PBLG. Peaks corresponding to the *R* and *S* enantiomers and the separations providing the values of $(T_{\text{HH}})^{\text{R/S}}$ are marked. The peaks in the central region of 2D projection in the direct dimension, shown in the enlarged plot in the box, cannot be correlated to the *R* and *S* for any of the molecules, as the central transitions overlap in the t_1 dimension. Reproduced with permission from American Chemical Society.

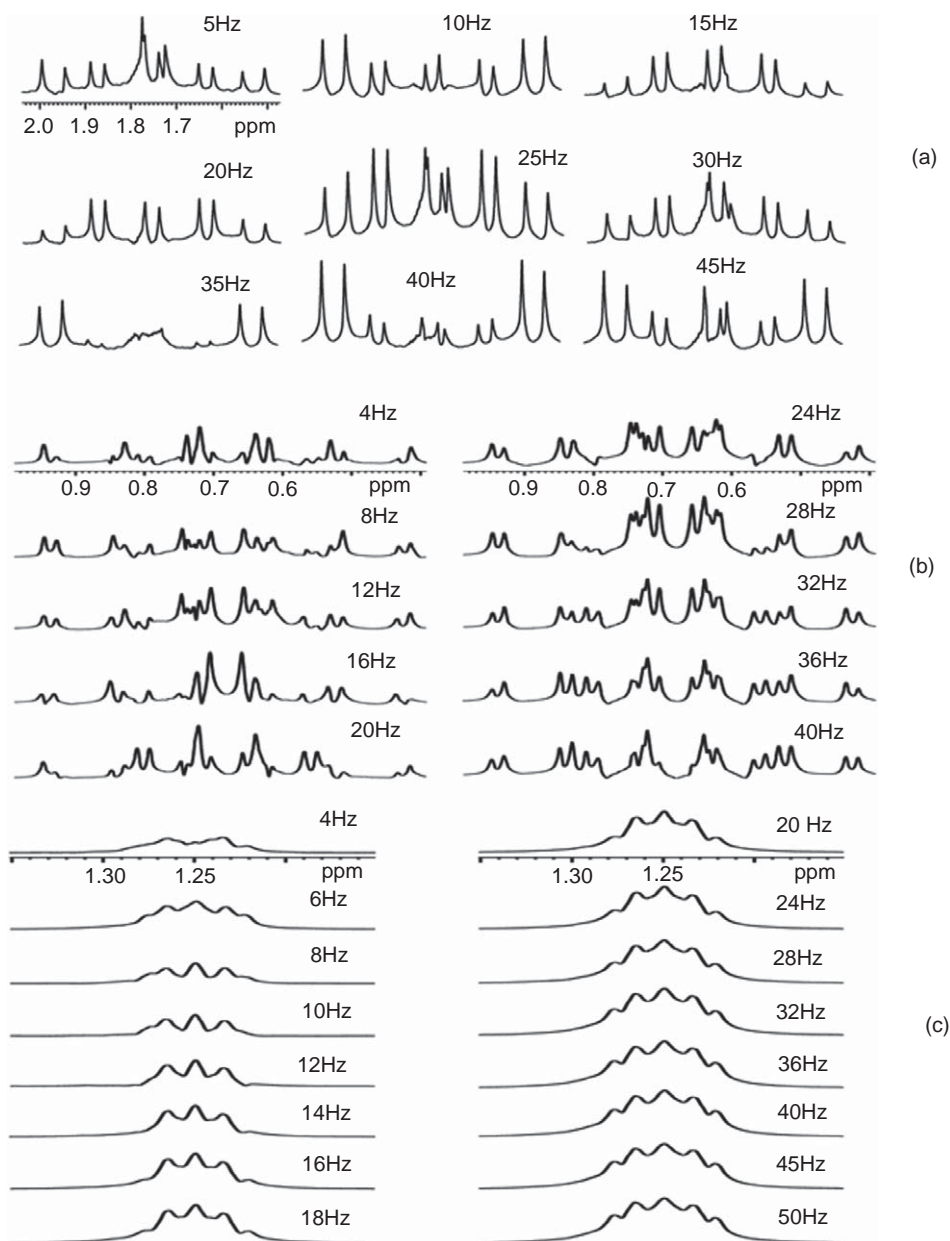


Figure 21 The intensity of the CH₃ resonances for different values of τ ($1/4(T_{HH})$) in: (a) 2-chloropropanoic acid (maximum intensity for all the peaks is appearing at 25 Hz), (b) 3-butyne-2-ol (maximum intensity for all the peaks is appearing at 32 Hz), and (c) propylene oxide (maximum intensity for all the peaks is appearing at 32 Hz). It can be observed that there is not much difference in the signal intensity from 32 to 50 Hz.

8.7 DQSERF and the measure of enantiomeric excess (ee)

It is well known that MQ excitation is non-uniform.⁹³ The amplitude of an excited coherence is dependent on the coupling constants. In the present case, though the nomenclature of the excited spin system is A_3 for both the enantiomers, each enantiomer has different coupling constants. To excite DQ coherence in an A_3 spin system, the delay, τ , between the first and the second 90° pulses should be less than $1/2(^2T_{HH})$, where $^2T_{HH}$ (which corresponds to $3(^2D_{HH})$) refers to the separation between the adjacent component of the triplets arising from proton that is two bonds away. However, the DQ excitation is maximum for $1/4(3 \times ^2D_{HH})$ or $1/4(^2T_{HH})$. This can be understood using the product operator formalism.¹⁸⁵ The terms present just before the second 90° pulse of the sequence shown in Figure 18, for an A_3 spin system, can be written as:

$$-I_Y \cos^2 \pi(^2T_{HH})\tau + 2I_X S_Z \sin 2\pi(^2T_{HH})\tau + 2I_Y S_Z R_Z \sin^2 \pi(^2T_{HH})\tau \quad (44)$$

However, the experimentally found optimum values generally do not agree with the theoretical one. One of the reasons for this is the long duration of 90° and 180° pulses and one has to consider the evolution of the magnetization during the pulses in the spin echo part of the spin selective DQ-SQ sequence. Furthermore, to derive optimum selectivity, only the central region of the spectrum was considered, implying there is also a definite offset dependence of the selective pulses employed. This is more so for (*R/S*)-3-butyn-2-ol where the methyl region spread is 280 Hz, the excitation width was restricted to central 40 Hz. Also the racemic mixture was made of unequal amount of *R* and *S* enantiomers and the delay, τ , had to be optimized to get the maximum signal intensity for both, which may be different from the maximum intensity of individual enantiomer. Therefore, the intensities of the DQSERF experiments are not comparable to that of normal one-dimensional spectrum. Thus, there are several constraints, such as: (a) the DQ excitation is maximum for $\tau = 1/4(3 \times ^2D_{HH})$ and there is a leakage of magnetization due to the first and third terms in Equation (44) for this τ value; (b) use of average τ delay; (c) the offset dependence of the shaped pulses used; and (d) loss of magnetization due to ZQ coherence. Therefore, the measurement of ee using the present method is tedious. However, there are other possible experiments to measure ee using uniform excitation of DQ coherence over a range of coupling constants, *viz.*, repeating the experiment with several values of τ and co-adding the data,^{186–190} incrementing the delay, τ , with the evolution time t_1 ⁹⁷ and thereby achieving τ averaging while 2D dataset is being acquired, and using composite excitation and mixing periods designed to have a uniform effect over a range of coupling constants.^{191,192}

8.8 Analyses of DQ-SERF spectra of A_3X , A_3MX , and A_3MPX spin systems

Initially the DQ-SERF experiments of all the three molecules are discussed in this section and the results are compared with SERF experiments in the subsequent section. As discussed previously, the selective DQ excitation of the methyl

protons in these molecules and the application of a selective 180° refocusing pulse in the middle of t_1 dimension result in an AX spin system in the DQ dimension. However, in the SQ dimension, they correspond to A_3X , A_3MX , and A_3MPX spin systems, respectively. The separation of the doublet, which is $2(3 \times {}^2D_{HH})$, for each enantiomer in the DQ dimension, therefore, corresponds to the separation of the outer lines of the triplet of the SERF experiment. The two distinct doublets for each enantiomer enable their unambiguous discrimination. The cross-section of the spectrum taken along the SQ dimension for each transition in the DQ dimension of an enantiomer corresponds to the normal one-dimensional spectrum of the methyl group. It is evident from Figure 19 that there is a complete separation of the overlapped spectra. Each cross-section provides 6, 12, and 24 transitions for, respectively, A_3X , A_3MX , and A_3MPX spin systems. The splitting patterns provide the dipolar couplings among the methyl protons (${}^2D_{HH}$) and between methyl and remaining coupled protons (${}^nT_{HH}$, where the superscript n refers to the proton that is n bonds away) for each enantiomer. Thus, analyses of the cross-sections of each enantiomer taken along the SQ dimension give all the couplings provided there is good resolution.

8.9 Advantages of DQSERF over SERF

The significant advantage of the DQ-SERF experiment is obvious when compared to the SERF experiment. In the SERF spectrum of (*R/S*)-2-chloropropanoic acid (Figure 20), the F_1 dimension is the X part of the AX_N type, where N is the number of equivalent spins centered at zero chemical shift. As observed from the spectrum, the central transitions from both the enantiomers are never distinguished. The diagonal tilt of the doublets is visible from the spectrum as discussed earlier. This situation appears in the weakly coupled spin systems. However, the advantage of this can be exploited as far as the determination of the couplings to long-distance protons is concerned. The cross-section taken along the SQ dimension for each outer transition is a doublet with the separation ${}^nT_{HH}$.

8.10 Simplification of the analyses of complex 1H NMR spectra

The DQ-SERF sequence developed for enantiomeric discrimination employed selective excitation of DQ coherence of coupled methyl protons for better enantiomeric discrimination and provided well-resolved and simplified spectrum in the DQ dimension. The coupling among methyl protons and to the methyl protons could be extracted from the DQ dimension. However, the enantiopure spectrum obtainable from the SQ dimension is very complex due to the presence of too many short- and long-distance couplings experienced by each proton. This is clearly evident from the cross-sections of (*R/S*)-propylene oxide and for the cross-sections of *S* enantiomers in (*R/S*)-3-butyne-2-ol shown in Figure 19. Thus, the determination of all the remote couplings is difficult. However, the determination of all the coupling parameters is crucial when one is interested in the determination of the molecular order. Therefore, there are several problems that remain to be combated, *viz.*, the simplification of spectra in

each cross-section, obtaining high resolution, and the determination of the relative signs and magnitudes of all the proton–proton couplings. There are several investigations in this direction. One of the ideas employed is the spin state selective detection to simplify the spectra in each cross-section by separating active and passive couplings into different subspectra containing fewer transitions. This could be achieved by editing the SQ transitions using the spin states of the passive spins. When the dipolar coupled methyl protons are concerned, 3Q–SQ correlation is feasible. This is of particular interest as this can be very informative in contrast to isotropic studies where the couplings among methyl protons are not reflected in spectra. In addition, the spin state selective detection is also possible for non-equivalent protons. Furthermore, the determination of coupling of protons to each inequivalent ^{13}C in their natural abundance can also be explored. The involvement of more number of coupling parameters is always advantageous for better discrimination.

9. SPIN STATE SELECTIVE COHERENCE TRANSFER: A NOVEL CONCEPTUAL DEVELOPMENT OF METHODOLOGY

In DQ-SERF sequence, there is a refocusing of the remote passive couplings in the DQ dimension and the DQ–SQ conversion pulse is non-selective for all the methyl protons. As a consequence, the spin state selective detection cannot be achieved in DQSERF experiment. In combating this difficulty, the spin state selective detection is developed by spin selective correlation of triple quantum (3Q)–SQ coherence¹⁹³ of the methyl protons and the retention of the entire passive homonuclear couplings in 3Q dimension by the application of a non-SERF pulse. The method also overcomes the problem of field inhomogeneity in addition to providing very high resolution. With 3Q excitation of the methyl protons, the 3Q dimension retains the long-distance small couplings (passive couplings) enhanced by a factor of three, whereas the SQ dimension retains only the short-distance couplings (active couplings). The differential scaling of dipolar couplings in the *R* and *S* enantiomers enables discrimination and also provides spectral simplification. As far as the methyl groups are concerned, due to magnetic equivalence, the resolution in 3Q spectrum is three times that of SQ spectrum and hence unambiguous chiral visualization is possible. The complex multiplet pattern gets simplified, by the separation of active and passive couplings in different dimensions, for each enantiomer. Another novelty of this method is that all the D_{HH} participate in enantio discrimination unlike only one D_{HH} among methyl protons in DQSERF and SERF experiments.

9.1 Spin state selective coherence transfer and enantiomeric discrimination

For spin state selective coherence transfer, two points are of vital importance: (a) couplings to a passive spin(s) should be retained in both the MQ and SQ dimensions and (b) the MQ–SQ conversion is carried out with spin selective

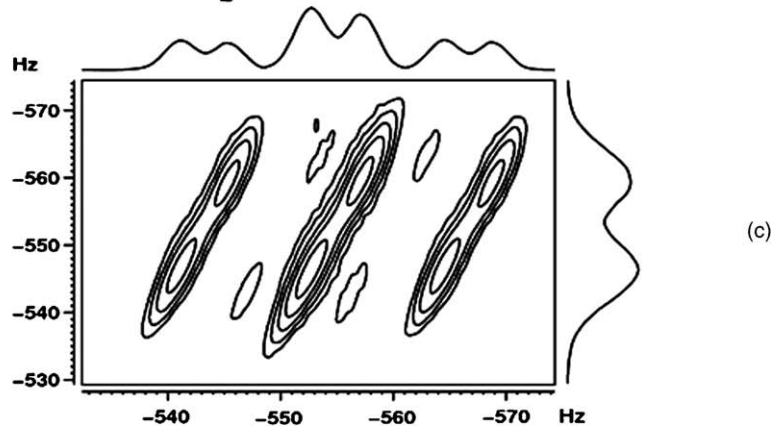
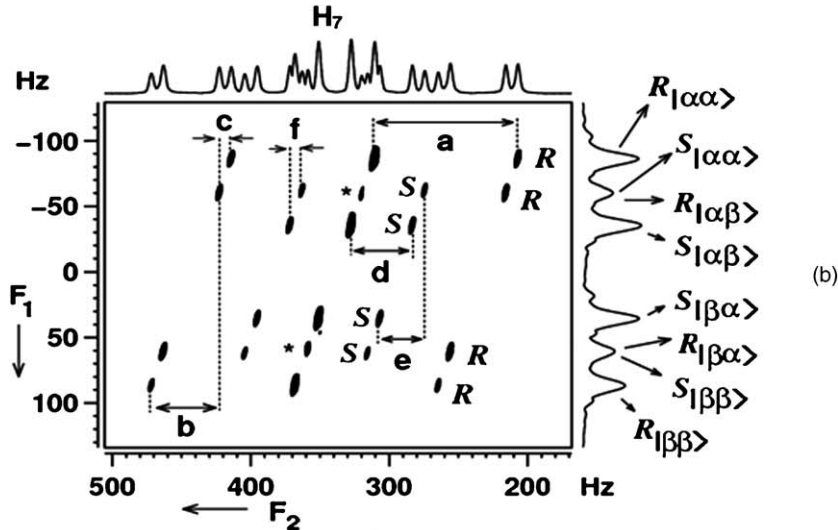
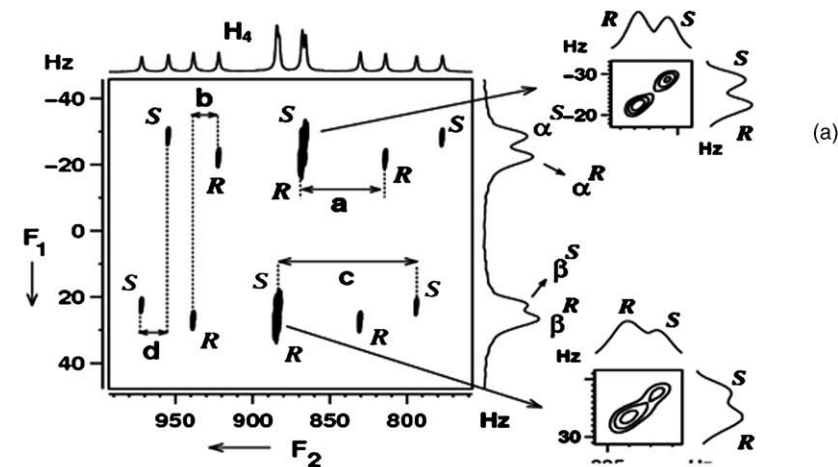
pulse without disturbing the states of the passive spin(s). In such an experiment, the $|\alpha\rangle$ domain of the MQ coherence is correlated to its corresponding SQ coherences of $|\alpha\rangle$ domain only and there is no coherence transfer to SQ coherences of $|\beta\rangle$ domain. The identical analogy holds good for $|\beta\rangle$ domain MQ coherence also. This is a vital difference compared to conventional non-selective MQ–SQ correlation experiments.

The important features of this methodology in the context of enantiomeric discrimination are: (i) A complex multiplet pattern which is difficult to analyze in the one-dimensional proton spectrum is simplified by separating into individual subspectra in different cross-sections depending on the passive spin states. Consequence of this is the separation of active and passive couplings leading to dramatically enhanced resolution in both SQ and MQ dimensions. (ii) Active couplings are present in each SQ cross-section corresponding to each passive spin state in MQ dimension. (iii) The separated subspectra in different cross-sections are displaced along SQ dimension. The magnitudes of these displacements provide the passive couplings. (iv) The tilts of the displacement vectors provide relative signs of the couplings unlike any of the earlier reported experiments including DQSERF.

9.2 Spin selective 3Q–SQ spectra of A_3X , A_3MX , and A_3MPX spin systems

The selective A_3 spin excited 3Q–SQ coherences in A_3X , A_3MX , and A_3MPX spin systems are given in Figure 22. The analyses of the spectra of all these molecules are discussed in greater detail below.

When all the methyl protons are flipped in (*R/S*)-2-chloropropanoic acid, the 3Q dimension pertains to A part of an AX spin system. The A part of AX spin system is detected in the 3Q dimension, which is a doublet. This doublet separation is $3(^3T_{HH}) = 3(2^3D_{HH} + ^3J_{HH})$ rather than $^3T_{HH}$ between adjacent SQ transitions in a SQ spectrum and plays a prominent role in enhanced separation of enantiomer peaks. The triple quantum states of the A_3 protons are $|\alpha\alpha\alpha\rangle$ and $|\beta\beta\beta\rangle$. There are two 3Q transitions for each enantiomer which are: $|\alpha_A\alpha_A\alpha_A(\alpha_X)\rangle \rightarrow |\beta_A\beta_A\beta_A(\alpha_X)\rangle$ and $|\alpha_A\alpha_A\alpha_A(\beta_X)\rangle \rightarrow |\beta_A\beta_A\beta_A(\beta_X)\rangle$, corresponding to $|\alpha\rangle$ and $|\beta\rangle$ spin states of the passive spin X. Thus, the two cross-sections correspond to passive proton spin states $|\alpha\rangle$ and $|\beta\rangle$. Thus, the spin state selective detection of A_3 SQ transitions is achieved. For the transition within each subspectrum, the spin state of X remains undisturbed in both t_1 and t_2 dimensions. Thus, the coupling to methine proton is removed in each cross-section resulting in half the number of transitions compared to one-dimensional spectrum and hence high resolution in the SQ dimension. This allows the precise measurement of $^2T_{HH}$. Therefore, in a single experiment, one can not only determine both $^2T_{HH}$ and $^3T_{HH}$, but also separate them which was not possible from any earlier reported experiments in the literature. This reduced the spectral complexity arising out of too many couplings leading to unresolved transitions in a single dimension and aids in the simplification of enantiomer spectra.



In addition to enhanced scaling of dipolar couplings, there is also an advantage due to the scaling of the chemical shift anisotropy for chiral discrimination. The difference in anisotropic chemical shifts between the *R* and *S* enantiomers in the SQ dimension is 4.6 Hz. Though it is possible to visualize in the one-dimensional spectrum, it is better visualized in 3Q dimension. Due to magnetic equivalence of methyl protons, this value is also enhanced three times in the 3Q dimension which can be viewed after discrimination by comparing the center of the two separated *R* and *S* spectra. The separations a and b provide ${}^2T_{\text{H4H4}}$ and ${}^3T_{\text{H4H5}}$, respectively, for the *R* enantiomer. The separations c and d provide similar information for the *S* enantiomer.

In (*R/S*)-3-butyn-2-ol, the spin system in the 3Q dimension is of the type AMX, where A is the super spin with three methyl protons, M the methine proton, and X the acetylenic proton, respectively. The A part of this AMX spin system is detected in the 3Q dimension. Corresponding to 4 spin states $|\alpha\alpha\rangle$, $|\alpha\beta\rangle$, $|\beta\alpha\rangle$, and $|\beta\beta\rangle$ of the passive spins M and X, there are 4 allowed 3Q transitions for spin A arising from each enantiomer, unlike 12 transitions in a SQ spectrum. Thus, there is enhanced resolution in the 3Q dimension. The cross-sections taken along the SQ dimension for each spin state of an enantiomer provide only the active coupling between the methyl protons, which is a triplet. There are four such triplets pertaining to four A_3 subspectra in different cross-sections. Thus, high resolution is achieved in SQ dimension also. Four such cross-sections with identical active coupling unambiguously differentiate the peaks arising from each enantiomer. From the 3Q dimension, the passive coupling information, ${}^3T_{\text{HH}}$ and ${}^5T_{\text{HH}}$, could be determined directly.

It is clear from the interpretation of the one-dimensional spectra of (*R/S*)-propylene carbonate and (*R/S*)-propylene oxide discussed earlier that the methyl region consists of 24 transitions for each enantiomer. The 24 transitions observed for methyl groups can be construed as 8 A_3 subspectra corresponding to 8 spin states of M, N, and X together. The complexity is obvious from their one-dimensional spectra, where one can see that the methyl protons are resonating in a narrow spectral width of 90 Hz in (*R/S*)-propylene carbonate and 40 Hz in (*R/S*)-propylene oxide. The broad and featureless spectrum due to too many

Figure 22 The 500 MHz ${}^1\text{H}$ 2D 3Q–SQ correlation spectrum of selectively excited methyl protons in: (a) (*R/S*)-2-chloropropanoic acid, $|\alpha_R\rangle$, $|\beta_R\rangle$ and $|\alpha_S\rangle$, $|\beta_S\rangle$ are the two spin states of the passive spin for the enantiomers *R* and *S*, respectively. The expansion of the two contours of the 2D matrix shown clearly identifies the two peaks of the enantiomers. The separations depicted in alphabets provide coupling information. For *R* enantiomer: a = ${}^2T_{\text{H4H4}}$ and b = ${}^3T_{\text{H4H5}}$. For *S* enantiomer: c = ${}^2T_{\text{H4H4}}$ and d = ${}^3T_{\text{H4H5}}$. (b) (*R/S*)-3-butyn-2-ol. The $R_{|\alpha\alpha\rangle}$, $R_{|\alpha\beta\rangle}$, $R_{|\beta\alpha\rangle}$, and $R_{|\beta\beta\rangle}$ and $S_{|\alpha\alpha\rangle}$, $S_{|\alpha\beta\rangle}$, $S_{|\beta\alpha\rangle}$, and $S_{|\beta\beta\rangle}$ are the spin states of the passive protons for the enantiomers *R* and *S*, respectively. For *R* enantiomer: a = ${}^2T_{\text{H7H7}}$, b = ${}^3T_{\text{H6H7}}$, and c = ${}^5T_{\text{H5H7}}$. For *S* enantiomer: d = ${}^2T_{\text{H7H7}}$, e = ${}^3T_{\text{H6H7}}$, and f = ${}^5T_{\text{H5H7}}$. The quality of discrimination achieved in the 3Q dimension is clearly evident. (c) 2D 3Q–SQ correlation spectrum of selectively excited methyl protons (*R/S*)-propylene oxide. Note that apart from $({}^2T_{\text{HH}})^{R/S}$, it is impossible to extract any other couplings from this spectrum.

long-distance couplings makes it impossible to recognize any fine structure. Achieving both high resolution in 3Q dimension and spin state selective detection, in spite of very small couplings from the two methylene protons which are unresolved, is a big challenge. It is evident from Figure 22c that the poor resolution hinders the determination of interaction parameters. This broad signal in the 3Q dimension is a result of the contributions from the field inhomogeneity at the higher quantum coherence.

9.3 Removal of B_0 field inhomogeneity at higher quantum

When the spatially dependent field inhomogeneity, $\Delta B_0(r)$, is taken into account, the precessional frequency of the higher quantum (ω_{HQ}) is given as

$$\omega_{\text{HQ}} = \sum \Delta m_I(\omega_I + \gamma_I \Delta B_0(r)) \quad (45)$$

Thus, the inhomogeneity contribution increases linearly with the detection of the higher quantum order. Therefore, the 3Q order has three times the enhanced signal broadening. One method to remove this field inhomogeneity contribution is to apply a non-selective 180° pulse in the middle of the t_1 dimension which refocuses the chemical shifts and retains all the passive couplings for the spin state selection.⁹³ The experiments on (R/S)-propylene carbonate and (R/S)-propylene oxide have therefore been performed using the pulse sequence given in Figure 23b and the corresponding spectra are given in Figure 24. The dramatic improvement in the resolution in 3Q dimension is clearly evident.

9.4 Totality of the coupling information from the overlapped and unresolved spectra of enantiomers

As far as the analyses of the 3Q–SQ spectrum, reported in Figure 24, are concerned, the spin systems are of the type AMPX in the 3Q dimension, where A is the super spin with three methyl protons and passive spins are protons M, P, and X. The ${}^2T_{\text{HH}}$ in A_3 are the active couplings while one ${}^3T_{\text{HH}}$ and two ${}^4T_{\text{HH}}$ constitute the passive couplings. The 3Q dimension must result in eight transitions for each enantiomer pertaining to eight spin states of M, P, and X together.

9.4.1 Complete analyses of ${}^1\text{H}$ spectrum of (R/S)-propylene carbonate

In (R/S)-propylene carbonate, for the S enantiomer, the two types of ${}^4T_{\text{HH}}$ are equal and hence results in a triplet of a doublet (due to ${}^3T_{\text{HH}}$) in the 3Q dimension. However, for the R enantiomer, the two types of ${}^4T_{\text{HH}}$ are unequal. Hence, 3Q dimension provide eight distinct transitions marked R in the figure. The cross-section taken along the SQ dimension for each passive spin state in 3Q dimension is a triplet due to active coupling ${}^2T_{\text{HH}}$. The eight A_3 subspectra (triplets) for eight passive spin states are observed for the S enantiomer. However, for R enantiomer, six triplets with smaller dipolar couplings are observed. The separations marked in the figure directly provide the spectral parameters, viz., $a = {}^2T_{\text{H4H4}}$, $b = {}^3T_{\text{H4H5}}$, and $c = d = {}^4T_{\text{H4H6}} = {}^4T_{\text{H4H7}}$ for the S enantiomer and $e = {}^2T_{\text{H4H4}}$, $f = {}^3T_{\text{H4H5}}$, $g = {}^4T_{\text{H4H6}}$, and $h = {}^4T_{\text{H4H7}}$ for the R enantiomer.

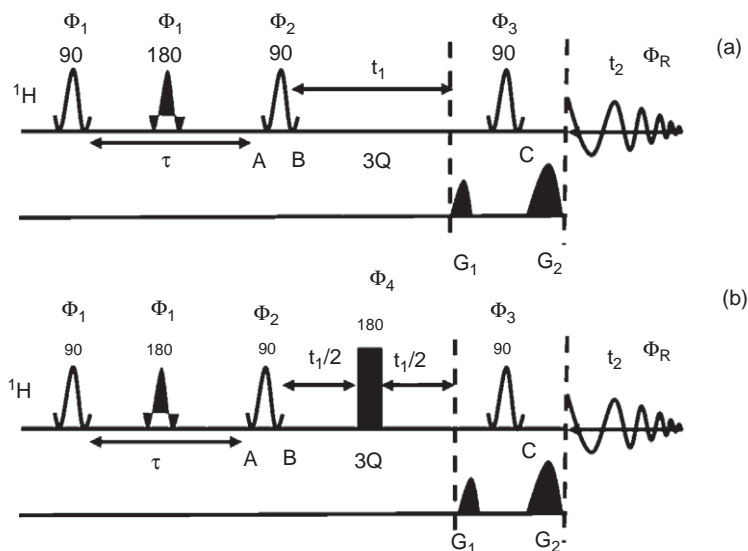


Figure 23 (a) The pulse sequence used for the selective excitation of 3Q coherence of methyl group in molecules (*R/S*)-2-chloropropanoic acid and (*R/S*)-3-butyne-2-ol. $\Phi_1 = X$, $\Phi_2 = Y$, $\Phi_3 = Y$, receiver phase is x and the selection of desired coherence pathway is achieved by the gradients. (b) The pulse sequence used for the selective excitation of 3Q coherence of methyl group for the molecules (*R/S*)-propylene carbonate and (*R/S*)-propylene oxide. Triple quantum EXORCYCLE phase cycling is used for the non-selective 180° pulse in the middle of 3Q dimension. This pulse sequence serves as a spin state selective 3Q resolved experiment.

Therefore, it should be borne in mind that the coupling information among protons numbered, 5, 6, and 7 is not reflected in either the 3Q or the SQ dimension. For the determination of the complete spectral information, another 3Q–SQ correlation experiment with 5, 6, and 7 protons as active spins is required to be carried out. This spectrum is given in Figure 25. In the 3Q dimension, the spin system is of the type AX_3 where super spin A pertains to M, N, and X spins and the methyl protons are the passive spins. The A part of this AX_3 detected in the 3Q dimension is, therefore, a quartet for each enantiomer, indicated by tilted broken lines for four *R* and *S* transitions each. The separations *i*, *j*, and *k* for *S* enantiomer and *l*, *m*, and *n* for *R* enantiomer providing all the coupling parameters are also marked in the figure. The passive couplings can also be determined from this experiment using the displacements of the subspectra. However, this information is redundant as it can be obtained from the 3Q–SQ spectrum of methyl protons.

9.4.2 Complete analyses of ${}^1\text{H}$ spectrum of (*R/S*)-propylene oxide

As far as the methyl proton excited 3Q–SQ spectrum of (*R/S*)-propylene oxide is concerned, the 3Q dimension provides eight well-resolved transitions for *R* enantiomer. However, for the *S* enantiomer, only four transitions are observed due to negligible strength of one of the remote couplings, which is clearly evident

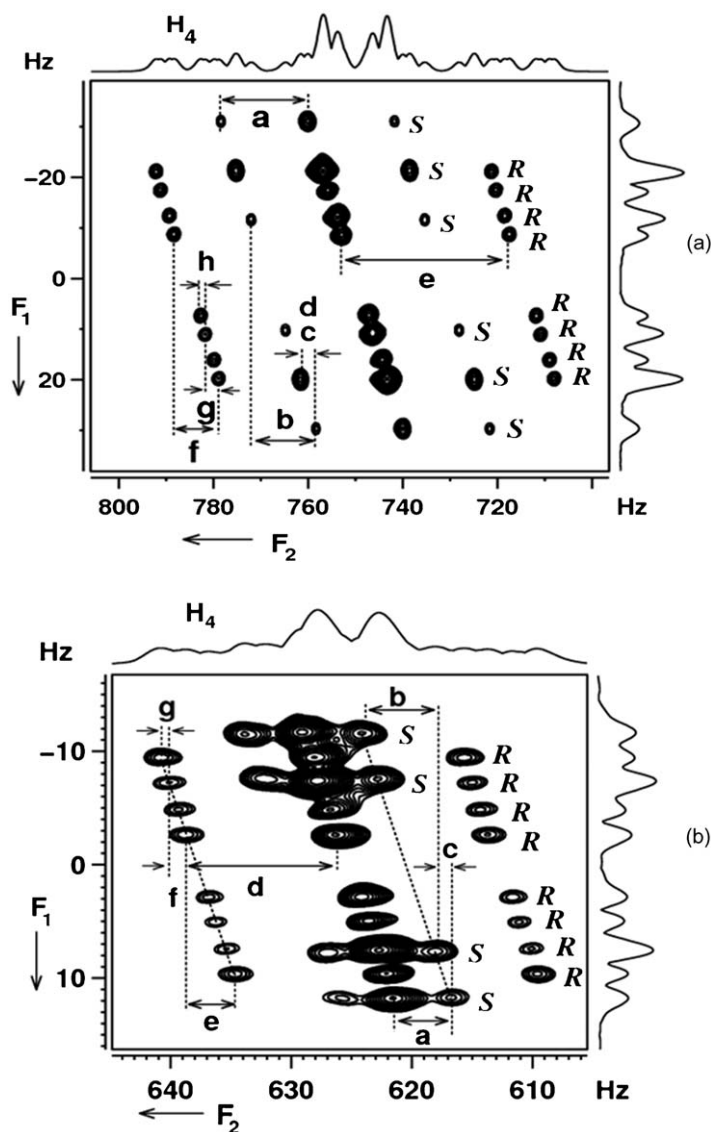


Figure 24 (a) 2D 3Q-SQ correlation spectrum of selectively excited methyl protons in (R/S)-propylene carbonate. The separations depicted in alphabets provide coupling information. They are for S enantiomer: $a = {}^2T_{H_4H_4}$, $b = {}^3T_{H_4H_5}$, $c = {}^4T_{H_4H_6}$, and $d = {}^4T_{H_4H_7}$. For R enantiomer: $e = {}^2T_{H_4H_4}$, $f = {}^3T_{H_4H_5}$, $g = {}^4T_{H_4H_6}$, and $h = {}^4T_{H_4H_7}$. Two types of ${}^4T_{HH}$ (between 4 and 6, and between 4 and 7) are equal for the S enantiomer. (b) 2D 3Q-SQ correlation spectrum of selectively excited methyl protons in (R/S)-propylene oxide. For S enantiomer: $a = {}^2T_{H_7H_7}$, $b = {}^3T_{H_4H_5}$, and $c = {}^4T_{H_4H_6}$. The separation ${}^4T_{H_4H_7}$ is not detectable due to its small strength. For R enantiomer: $d = {}^2T_{H_7H_7}$, $e = {}^3T_{H_4H_5}$, $f = {}^4T_{H_4H_6}$, and $g = {}^4T_{H_4H_7}$.

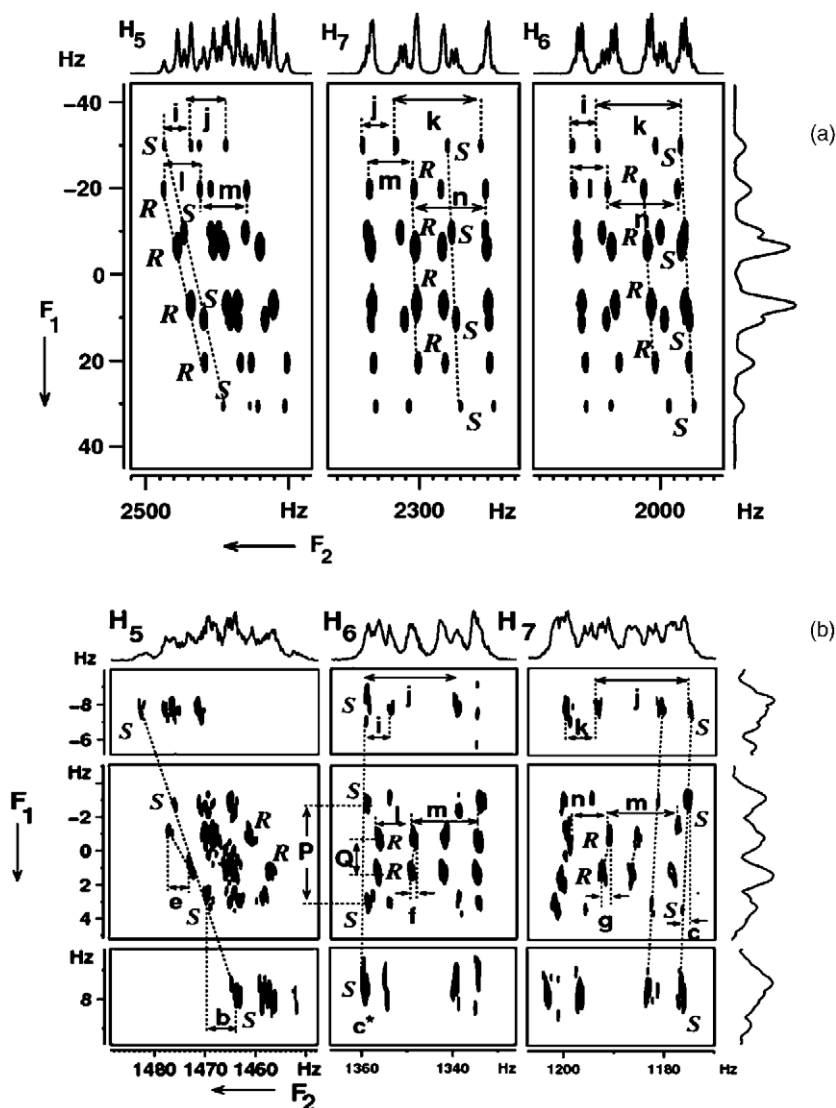


Figure 25 (a) 2D 3Q-SQ correlation spectrum of (*R/S*)-propylene carbonate with selective excitation of protons numbered 5, 6, and 7. The separations providing coupling information are marked. For *S* enantiomer: $i = {}^3T_{H5H6}$, $j = {}^3T_{H5H7}$, and $k = {}^3T_{H6H7}$. For *R* enantiomer: $l = {}^3T_{H5H6}$, $m = {}^3T_{H5H7}$, and $n = {}^3T_{H6H7}$. (b) 2D 3Q-SQ correlation spectrum of (*R/S*)-propylene oxide with selective excitation of protons numbered 5, 6, and 7. For *S* enantiomer: $b = {}^3T_{H4H5}$, $c = {}^4T_{H4H7}$, $c^* = {}^4T_{H4H6}$ (not detectable), $i = {}^3T_{H5H6}$, $k = {}^3T_{H5H7}$, and $j = {}^3T_{H6H7}$. For *R* enantiomer: $e = {}^3T_{H4H5}$, $f = {}^4T_{H4H6}$, $g = {}^4T_{H4H7}$, $l = {}^3T_{H5H6}$, $m = {}^3T_{H6H7}$, and $n = {}^3T_{H5H7}$.

from the spectrum. This is due to the fact that the residual dipolar coupling D_{H4H6} (c^* in Figure 25 which is 0.4 Hz, as will be discussed later) is opposite in sign to that of through bond coupling J_{H4H6} and hence $T_{\text{H4H6}} = 0$. The separations marked in the figure provide the spectral parameters.

The 3Q-SQ correlation experiment with 5, 6, and 7 protons as active spins is given in Figure 25. The H6 and H7 regions of the spectrum are relatively better resolved than H5 region. The quartet for *S* enantiomer is marked while only two lines of the *R* enantiomer quartet are marked in the figure. Each cross-section at H5, H6, and H7 is a doublet of doublet because of two active couplings. Displacements marked e, f, and g for *R* enantiomer and b, c, and c^* for *S* enantiomer contain individual passive couplings of H5, H6, and H7 to methyl protons.

9.5 Spin selective higher quantum and the relative signs of the couplings

From the direction of tilt of the displacement vector, it is possible to determine the relative signs between active and passive couplings. If the spin systems are strongly coupled, the question of determination of relative signs does not arise. Thus, the technique is applicable when the spectra are first order, that is, spins that are weakly scalar coupled, weakly dipolar coupled systems in strongly orienting media, and weakly dipolar coupled in chiral or bicellar media. There are situations when the relative signs of the couplings determined from the direction of the tilt of the displacement vector could be ambiguous.¹⁹⁴ However, it is important to remember that the selectively methyl proton excited correlation experiments do not provide the relative signs of the couplings. On the other hand, 3Q-SQ spectrum of H5, H6, and H7 as active spins provides the relative signs.

For (*R/S*)-propylene carbonate in the 3Q dimension, the quartet of each enantiomer is indicated by the tilted broken lines for four *R* and *S* transitions each. The left tilt of the quartet in each chemical shift position shown by broken line implies that all the passive couplings are of the same sign. On the other hand, in (*R/S*)-propylene oxide, the tilt direction at e is opposite to f and g (Figure 25) indicating coupling e is opposite in sign to f and g. Similarly b is opposite in sign to c.

9.6 Advantages of higher quantum–single quantum correlation method

The new pulse sequences discussed in the previous section have numerous advantages in the context of chiral discrimination and the analyses of broad and unresolved ^1H spectra. They can be listed as:

1. The dramatically enhanced resolution has been obtained in the otherwise broad and featureless spectra and the peaks that were separated by as low as separation 0.65 Hz could be measured.

2. In spin selective 3Q-SQ correlation experiments, the values of ${}^nT_{HH}$ ($n = 2-5$) being different for both the enantiomers, there was an unambiguous chiral discrimination in both the dimensions.
3. The active and passive couplings are separated from each other in a single experiment and both are utilized for discrimination. Active couplings are present in each cross-section while passive couplings are responsible for the displacement of the subspectra.
4. Using two selectively detected 3Q-SQ experiments, the complete analyses of the overlapped spectra of both the enantiomers in (*R/S*)-propylene carbonate and (*R/S*)-propylene oxide could be carried out.
5. In the methyl group excited experiments, the resolution in the 3Q dimension is $3({}^nT_{HH})$ and one in the SQ dimension results in a net total chiral dispersion of 3.3 times in the tilted direction as far as the measurement of the resonance frequencies between the chiral molecules is concerned. The difference between consecutive *R* and *S* peaks $\{T^R (= {}^nT_{HH}) - T^S (= {}^nT_{HH})\}$ becomes $3 \times \{T^R (= {}^nT_{HH}) - T^S (= {}^nT_{HH})\}$ in 3Q dimension which contributed to better chiral discrimination. In the earlier SERF experiments, the consecutive *R* and *S* peak separation was only $\{T^R (= {}^nT_{HH}) - T^S (= {}^nT_{HH})\}$.
6. The difference in $\Delta\sigma_i$ between the two enantiomers is also enhanced three times in 3Q dimension as is seen from the difference in the mean frequencies of the doublets of the two enantiomers in (*R/S*)-2-chloropropanoic acid.
7. The comparison of the tilt directions of the multiplets in different cross-sections for different chemical shift positions provides the relative signs of the couplings.
8. In favorable cases, the parameters derived from the 2D spectra can be used for the iterative analysis to derive all other spectral parameters. This simplifies the analyses to a large extent.

10. BINUCLEAR SPIN STATE SELECTION FOR CHIRAL DISCRIMINATION

With more number of passive couplings participating in the MQ dimension, there will be improved discrimination of the *R* and *S* enantiomers. In other words, discrimination should be benefited from the difference of as many parameters as possible. In such situations, one can derive the benefit from the comparatively larger heteronuclear coupling. However, as discussed earlier, with every addition of an interacting spin, the number of possible single quantum transitions increases by a factor of four. The inclusion of ${}^{13}\text{C}$ in its natural abundance as a participating spin poses several challenges, such as sensitivity enhancement, identification of ${}^{13}\text{C}$ satellite transitions for each enantiomer from the broad and featureless ${}^1\text{H}$ spectrum, and simplification of the spectra for determination of both homo- and heteronuclear couplings.

All these challenges have been combated by developing yet another methodology that exploits the natural abundant passive ${}^{13}\text{C}$ spin, for spin state selection in addition to protons.¹⁹⁵ The ${}^{13}\text{C}$ spin state selected proton spectra

provide well-resolved group of transitions in the SQ dimension at each spin state of ^{13}C in the 3Q dimension. Each group of these ^{13}C -spin state selected transitions is further spin state selected based on the spin states of the passive protons resulting in enhanced resolution.

10.1 Theoretical description of the pulse sequence

The pulse sequence developed for the inclusion of ^{13}C spin in its natural abundance for higher quantum correlation is depicted in Figure 26. The evolution of magnetization at different time points of the pulse sequence is easily understood by the product operator formalism.¹⁸⁵ The pulses with rectangular shapes are non-selective while the remaining pulses are spin selective. The pulse sequence starts with polarization transfer via INEPT block. At the end of delay τ^* , the antiphase ^1H magnetization is converted into longitudinal two spin-orders by the 90° ^1H pulse applied along the y -axis at time point A. At this stage, application of a homospoil gradient pulse eliminates undesired coherences and following this the two spin-orders are back converted into the antiphase proton magnetization of the methyl group by the selective 90° pulse on methyl protons at time point C via the antiphase coherence of ^{13}C spins. From the point C to D, the magnetization is allowed to evolve under D_{HH} among methyl protons by a SERF pulse which also decouples this group from the passive protons and the ^{13}C spin. At the time point D, there is doubly antiphase magnetization with respect to protons, that is, $I_{1Y}I_{2Z}I_{3Z}S_{2Z}$. The application of a selective 90° pulse of phase y on methyl resonance converts this into $I_{1Y}I_{2X}I_{3X}S_{2Z}$, homonuclear MQ, terms at time point E. The 3Q coherence is selected by a suitable gradient ratio and allowed to evolve under the sum of different homonuclear and heteronuclear passive couplings, by the non selective refocussing pulse on ^{13}C and ^1H in the middle of the 3Q evolution period. This also overcomes the problem of field inhomogeneity

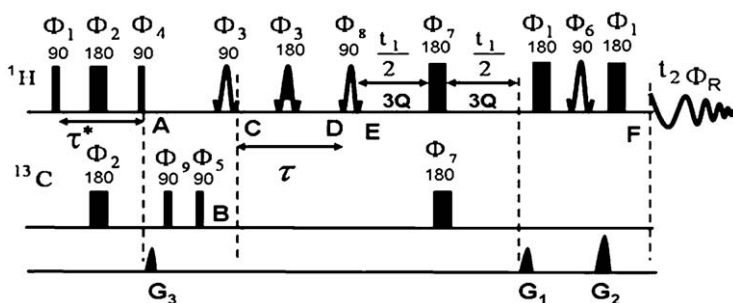


Figure 26 The pulse sequence for spin selective 3Q-SQ correlation of methyl protons edited by ^{13}C spin in addition to passive proton spins in (*R/S*)-3-butyne-2-ol and (*R/S*)-propylene carbonate. The behavior of the magnetization during different stages of pulse sequences, viz., A, B, C, D, and E is discussed in the text. Rectangular pulses are hard pulses. All the remaining pulses are spin selective. The phases of the pulses are: $\Phi_1 = x$, $\Phi_2 = xxxx-x-x-x-x$, $\Phi_3 = (12)x$, $\Phi_4 = y$, $\Phi_5 = x-xx-xx-xx-x$, $\Phi_6 = y$, $\Phi_7 = xxyy-x-x-y-y$, $\Phi_8 = (12)-y$, $\Phi_9 = xxxxxx-x-x-x-x-x-x-x-x$, $\Phi_R = x-x-xxx-x-xx-xxx-x-xxx-x$.

encountered in the 3Q coherence, thereby providing higher resolution. The last selective 90° y pulse on methyl protons results in the observable SQ magnetization in the direct dimension at time point F. The INEPT transfer edits the ^1H magnetization by ^{13}C spin states and also improves the overall sensitivity.

The 3Q exorcycle phase cycling is employed for non-selective 180° pulse in the middle of t_1 dimension. Double isotope filtration phase cycling is applied for the phases Φ_9 and Φ_5 . During the excitation of 3Q coherence and its evolution and conversion to SQ coherence, the spin states of the remaining protons (passive spins) in the molecule and ^{13}C spin of the methyl group are undisturbed in both the dimensions. This enables the detection of SQ transitions of the methyl protons (A_3 spin system) based on the spin states of the passive ^1H and ^{13}C spins and exploits all the advantages of the sequence discussed earlier.

10.2 The interpretation of ^{13}C edited 3Q–SQ spectrum of (*R/S*)-3-butyn-2-ol

Considering the 1% molecule where the protons of the methyl group are attached to ^{13}C , the spin system can be considered to be of the type $A_3\text{MPX}$ where A refers to methyl protons, M and P correspond to methine and acetylenic protons, and X is the ^{13}C spin. As discussed previously, when the magnetization is not routed through ^{13}C spin, there are 12 transitions for the methyl protons for each enantiomer. When ^{13}C is a participating spin, there are 24 transitions for each enantiomer, which can be visualized as 8 subspectra according to 8 possible spin states of M, P, and X spins. The designed pulse scheme separates all the eight subspectra from each other, and detects them independently in well-separated arrays of SQ dimension. The anisotropic proton chemical shift difference between the two enantiomers is negligibly small and hence the two sets of peaks arising from both *R* and *S* enantiomers are overlapped for the ^{12}C bound one-dimensional ^1H spectra as well as the ^{13}C bound satellite proton spectra.

The ^{13}C edited methyl proton excited 3Q–SQ spectrum is shown in Figure 27. The selective excitation of 3Q coherence of the methyl protons results in the simultaneous flipping of all the protons. However, the non selective refocussing pulse on ^{13}C and ^1H leads to refocusing of chemical shift evolution and retention of passive heteronuclear and homonuclear couplings. Thus, the spin system in the 3Q dimension will be of the type AMPX, where A is the super spin with three methyl protons. The 3Q dimension will be an A part of this AMPX type spin system. The spectrum in the SQ dimension is the ^{13}C satellite proton spectrum with suppression of peaks from ^{12}C attached protons. The connectivity of 3Q–SQ direct peaks forms a distinct pattern for each enantiomer in the 2D spectrum which unambiguously discriminates the enantiomers.

In the 3Q dimension, the largest coupling to spin A arises due to $J_{\text{CH}} + 2D_{\text{CH}}$, where J_{CH} and D_{CH} are the scalar and the dipolar couplings between proton and ^{13}C of the methyl group. In the spin product basis set, the 3Q states of proton are $|\alpha_A\alpha_A\alpha_A\rangle$ and $|\beta_A\beta_A\beta_A\rangle$. This is coupled to spin states $|\alpha\rangle$ and $|\beta\rangle$ of ^{13}C spin. Hence, the resonance of spin A is split into a doublet. Two such doublets are expected, one for each enantiomer. The value of D_{CH} being different for both the

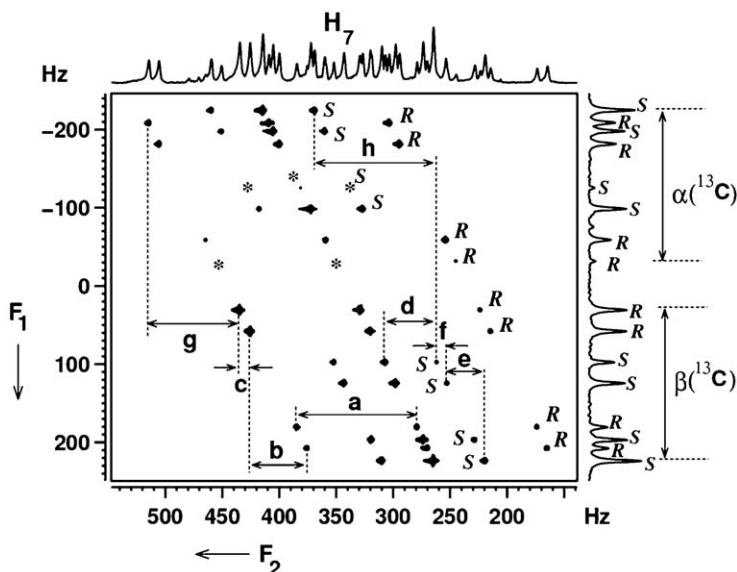


Figure 27 The ^{13}C edited methyl protons excited 2D 3Q-SQ correlated spectrum of (R/S)-3-butyne-2-ol. The spectrum is displayed in magnitude mode. F_1 dimension pertains to 3Q spectrum. $\alpha(^{13}\text{C})$ and $\beta(^{13}\text{C})$ regions in the F_1 dimension pertain to two spin states of ^{13}C . The assignments to R and S transitions are marked. The separations marked with alphabets a to h providing coupling parameters. $d = (3 \times {}^2D_{\text{H7H7}})^S$, $e = ({}^3T_{\text{H6H7}})^S$, $f = ({}^5T_{\text{H5H7}})^S$, $h = ({}^1T_{\text{C1H7}})^S$, $a = (3 \times {}^2D_{\text{H7H7}})^R$, $b = ({}^3T_{\text{H6H7}})^R$, $c = ({}^5T_{\text{H5H7}})^R$, and $g = ({}^1T_{\text{C1H7}})^R$. The “*” marks represent transitions of very low intensities.

enantiomers and scaling of the $(J_{\text{CH}} + 2D_{\text{CH}})$ by a factor of three due to magnetic equivalence resulted in enhanced spectral resolution and unambiguous enantiomer visualization. This also can be construed as the separation of ^{13}C satellites in the one-dimensional spectrum. The two 3Q transitions edited by the ^{13}C spin states are further split by the remaining two methine and acetylenic protons into four transitions according to their four spin states $|\alpha_{\text{M}}\alpha_{\text{P}}\rangle$, $|\alpha_{\text{M}}\beta_{\text{P}}\rangle$, $|\beta_{\text{M}}\alpha_{\text{P}}\rangle$, and $|\beta_{\text{M}}\beta_{\text{P}}\rangle$. Thus, a total of eight 3Q transitions are observed for each enantiomer. Four of them correspond to $|\alpha\rangle$ state of ^{13}C while another four correspond to $|\beta\rangle$ state.

The 3Q transitions corresponding to $|\alpha\rangle$ and $|\beta\rangle$ domains of ^{13}C are marked as $\alpha(^{13}\text{C})$ and $\beta(^{13}\text{C})$ as shown in Figure 27. Chiral discrimination is obvious from the highly resolved 3Q spectrum in the F_1 dimension. The subspectral analysis at any one of the ^{13}C spin states provides the coupling of methyl protons to all the passive protons. The different displacement vectors g and h, b and e, and c and f between subspectra drawn in Figure 27 provide passive coupling parameters $J_{\text{CH}} + 2D_{\text{CH}}$, ${}^3T_{\text{HH}}$, and ${}^5T_{\text{HH}}$ for the enantiomers.

The cross-sections taken along the SQ dimension at different passive proton spin states of 3Q dimension for the $\beta(^{13}\text{C})$ region are plotted in Figure 28. Each of these cross-sections pertains to selectively detected SQ transitions originating from the 3Q transition whose initial and final states have the same passive spin

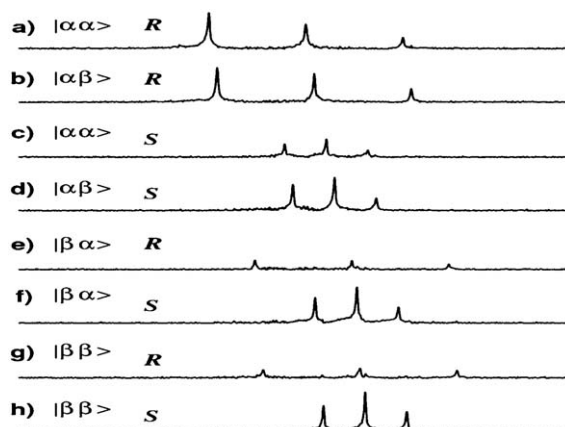


Figure 28 (a–h) The cross-sections taken along F_2 dimension for each subspectrum edited by passive spin states in Figure 27, plotted with identical horizontal scale for comparison. Only the cross-sections pertaining to $\beta(^{13}\text{C})$ regions are given. R and S assignments and the passive proton spin states in the 3Q dimension are also shown.

state. An example of such a SQ transition is from the state $|\alpha_A\alpha_A\alpha_A\beta_M\beta_P\beta_X\rangle$ to $|\beta_A\alpha_A\alpha_A\beta_M\beta_P\beta_X\rangle$ which arises from a 3Q transition such as $|\alpha_A\alpha_A\alpha_A\beta_M\beta_P\beta_X\rangle$ to $|\beta_A\beta_A\beta_A\beta_M\beta_P\beta_X\rangle$ where the initial and final passive spin state is $|\beta_M\beta_P\beta_X\rangle$. Thus, all the proton SQ transitions pertaining to eight A_3 subspectra get separated into different cross-sections depending on the spin states of the passive spins. Also each cross-section is a triplet, from which D_{HH} among methyl protons can be determined. The 'a' and 'd' marked in Figure 27 provide $^2T_{\text{HH}}$ for the R and S enantiomers, respectively.

A comparison of the 3Q–SQ correlation for ^{12}C attached protons and ^{13}C attached protons is shown in Figure 29. The isolated $\beta(^{13}\text{C})$ region is plotted separately in the expanded scale for comparison. The 3Q–SQ correlation of ^{12}C attached protons leads to spin state selection by only passive proton spins and discriminates 20 out of the 24 transitions. However, the transitions marked with '*' are the overlap of two transitions from the two enantiomers. The 3Q–SQ correlation of ^{13}C attached protons discriminates all the 24 transitions, a consequence of additional spin state selection by the ^{13}C spin.

10.3 The interpretation of ^{13}C edited 3Q–SQ spectrum of (R/S)-propylene carbonate

The protons and carbon of the methyl group of this molecule form a weakly coupled spin system of the type $A_3\text{MNPX}$, where A_3 corresponds to active methyl protons, M and N are the two methylene protons, P is the methine proton, and X is the ^{13}C spin. The methyl protons experience four different types of couplings, *viz.*: (a) the couplings among themselves ($^2T_{\text{HH}}$), (b) the coupling between methyl and methine (P) protons ($^3T_{\text{HH}}$), (c) the two different couplings from the two diastereomeric methylene (M and N) protons ($^4T_{\text{HH}}$), and (d) the

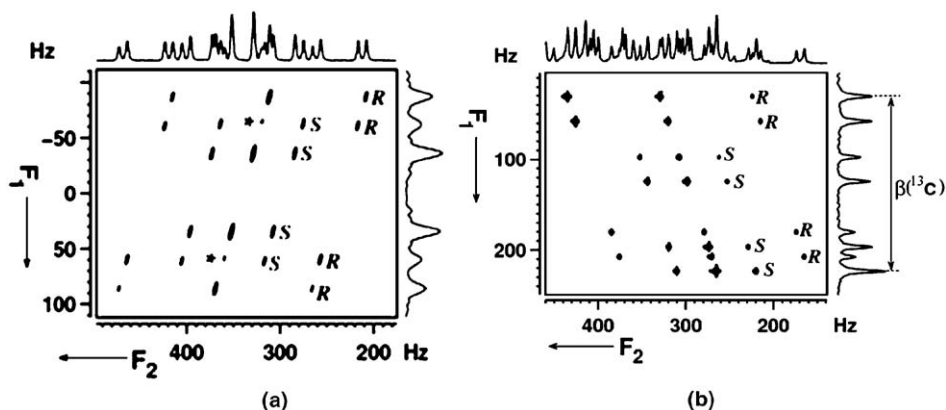


Figure 29 (a) ^{12}C attached methyl protons excited 2D 3Q-SQ correlated spectrum of (*R/S*)-3-butyne-2-ol obtained using pulse sequence given in Figure 23a. Assignments of spin state selected subspectrum to *R* and *S* enantiomers are shown. The “*” marks indicate overlap of two transitions from the *R* and *S* forms. (b) ^{13}C edited methyl protons excited 2D 3Q-SQ correlated spectrum of (*R/S*)-3-butyne-2-ol along with the corresponding projections using pulse sequence given in Figure 26. Only $\beta(^{13}\text{C})$ region is plotted in expanded scale for comparison. Assignments of spin state selected subspectrum to *R* and *S* enantiomers are shown. Note the advantage of binuclear spin state selection in the discrimination of even the peaks marked with “*” of a.

coupling from the ^{13}C spin (X). The first-order analysis indicates that there are 48 transitions for each enantiomer, which can be visualized as 16 A_3 subspectra corresponding to 16 passive spin states of M, N, P, and X together. Thus, there are total of 96 overlapped transitions from both the enantiomers. The separation and identification of these transitions is a challenging task.

The selective methyl protons excited, ^{13}C edited 2D 3Q-SQ correlation spectrum of (*R/S*)-propylene carbonate is given in Figure 30. In the 3Q dimension, the spin system is of the type AMNPX. The super spin A is the three methyl protons (the active spin), the methine and methylene protons (M, N, and P) and one ^{13}C spin (X) constitute the passive spins. $^2T_{\text{HH}}$ in A_3 is the active coupling while one $^3T_{\text{HH}}$ and two $^4T_{\text{HH}}$ along with heteronuclear $^1T_{\text{CH}}$ constitute the passive couplings. The 3Q dimension provides 16 transitions for each enantiomer pertaining to 16 spin states of M, N, P, and X. The displacements between the SQ transitions corresponding to $|\alpha\rangle$ and $|\beta\rangle$ domains of ^{13}C marked ‘a’ and ‘f’ are the passive heteronuclear coupling $^1T_{\text{CH}}$ for the *R* and *S* enantiomers, respectively.

The analysis of the spectra at any one of the spin states of ^{13}C is sufficient to derive all the homonuclear couplings with methyl protons. For the *S* enantiomer, the two types of $^4T_{\text{HH}}$ are equal and hence result in a triplet of a doublet (due to $^3T_{\text{HH}}$) in the 3Q dimension and are marked S. However, for the *R* enantiomer, the two types of $^4T_{\text{HH}}$ are unequal. Hence, 3Q dimension provides eight distinct transitions marked R in the figure.

For clarity, the expanded $\alpha(^{13}\text{C})$ region is also given Figure 30. The alphabets marked ‘b’ and ‘g’ denote the active coupling, $^2T_{\text{HH}}$ responsible for the triplet

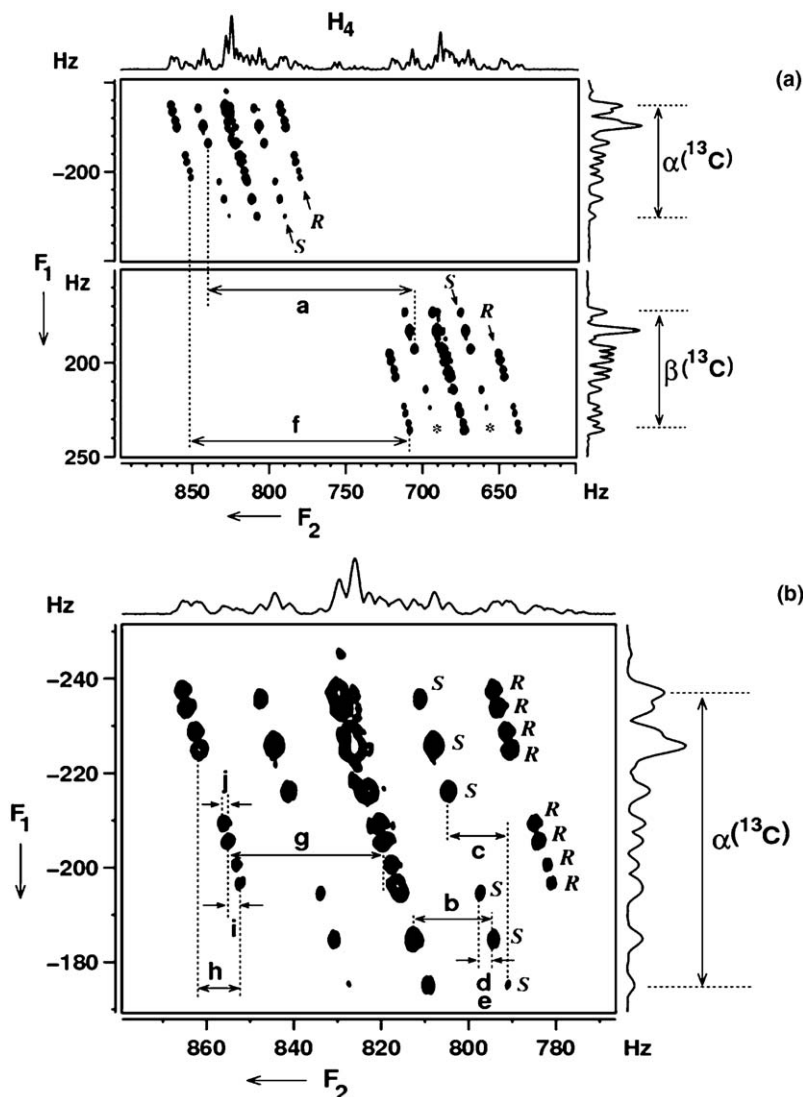


Figure 30 (a) Methyl protons excited 2D 3Q-SQ correlated spectrum of (*R/S*)-propylene carbonate. The optimized τ delay is 25 ms. The selective pulses are seduce-shaped pulses. The spectrum is displayed in magnitude mode. F_1 dimension pertains to 3Q spectrum. $\alpha(^{13}C)$ and $\beta(^{13}C)$ regions are marked in the F_1 dimension. The assignments of peaks to *R* and *S* form are marked and also shown with tilted arrows. The displacements of $\alpha(^{13}C)$ and $\beta(^{13}C)$ regions in the F_2 dimension providing heteronuclear passive couplings are marked as a and f for *S* and *R* enantiomers, respectively. (b) The expanded $\alpha(^{13}C)$ region of A. The separations marked with alphabets b-e and g-j provide proton-proton coupling information. Couplings are obtainable from the separations: $b = (3 \times {}^2D_{H4H4})^S$, $c = ({}^3T_{H4H5})^S$, $d = ({}^4T_{H4H6})^S$, $e = ({}^4T_{H4H7})^S$, $a = ({}^1T_{C1H4})^S$, $g = (3 \times {}^2D_{H4H4})^R$, $h = ({}^3T_{H4H5})^R$, $i = ({}^4T_{H4H6})^R$, $j = ({}^4T_{H4H7})^R$, and $f = ({}^1T_{C1H4})^R$. C1 is the carbon attached to methyl protons peaks with very low intensities are marked with '*.'

(subspectrum) in each SQ cross-section, for the *S* and *R* enantiomers, respectively. Thus, each cross-section taken along the SQ dimension for each passive spin state in 3Q dimension is a triplet. The eight A_3 subspectra (triplets) for eight passive spin states are observed for *S* enantiomer. However, for *R* enantiomer, six triplets with smaller dipolar couplings are observed. The passive homonuclear couplings are determined from the displacements marked c, d, e and h, i, j for the *S* and *R* enantiomers, respectively. It may be pointed out that the coupling information among protons numbered, 5, 6, and 7 is not reflected in either the 3Q or the SQ dimension. In addition to all the advantages of the method described in section 9, D_{CH} can also be derived.

11. SINGLE QUANTUM SPIN SELECTIVE CORRELATION: A METHOD FOR CHIRAL DISCRIMINATION AND ACHIEVING INCREDIBLE RESOLUTION

The conventional two-dimensional COSY experiment is carried out by the application of selective pulses. In spin selective excitation experiments on homonuclear spins (Soft-COSY), the passive spins mimic the heteronuclei. Consequently in the 2D selectively excited correlation experiment, there are several advantages: (a) separation of active and passive couplings in two dimensions, (b) reduced multiplicity compared to normal COSY spectrum, (c) a reduction in the experimental time by several orders of magnitude, and (d) higher resolution because of reduced spectral width chosen.¹⁹⁶ It implies that the experiment reveals several aspects of the spectrum which are otherwise not possible to derive from the normal broad and featureless one-dimensional spectrum. Furthermore, there is an enhanced resolution in each cross-section taken parallel to the F_2 dimension due to the fact that the states of the passive spins are not disturbed in both the F_1 and F_2 dimensions and the COSY peaks are labeled according to their spin states. As an example, in a simple three spin system of the type AMX, where X is the passive spin, the normal COSY spectrum gives 16 peaks. In contrast, the selectively excited COSY, with a phase sensitive detection, shows two antiphase peaks with splitting due to active coupling displaced by a vector representing the passive splitting in both the dimensions. The F_2 dimension reveals the coupling between the active spins and the displacement of arrays in the F_1 dimension reveals the passive couplings. This is also a significant advantage as the spectrum is drastically simplified in each cross-section aiding the analysis. Another interesting feature of this experiment is that the cross-peak multiplicity pattern is similar to that of an E-COSY spectrum^{197,198} and hence it is possible to determine the relative signs of the couplings whether the spins are scalar or dipolar coupled so long as the first-order analyses of the spectra are possible. This is an excellent technique for the molecules aligned in PBLG, both for unscrambling the overlapped spectra of enantiomers and also in simplifying the spectral complexity.¹⁹⁹ The examples of such application are discussed below initially for the simplification of the 1H NMR spectrum of an A_3MX spin system and then for a bigger spin system of the type A_3MPX .

11.1 Analysis of the spectrum of (*R/S*)-3-butyn-2-ol

The selective methyl group excited Soft-COSY spectrum of (*R/S*)-3-butyn-2-ol (racemic mixture) is reported in Figure 31. The active coupling is the dipolar coupling among methyl protons and the passive couplings are between methyl and the remaining two protons 5 and 6 (Figure 16b). The F_2 dimension results in 12 transitions for each enantiomer, construed as 4 A_3 subspectra, which are displaced in F_1 dimension due to passive couplings. Each cross-section pertains to an A_3 subspectra, which is a triplet and the separations of the adjacent transitions of which provides $(^2T_{H7H7})^{R/S}$. The separations marked with alphabets a, b, and c provide $^nT_{HH}$ ($n = 2, 3$, and 5) for *R* enantiomer and the separations d, e, and f provide similar information for *S* enantiomer. The first four cross-sections taken along the F_2 dimension for each transition of an enantiomer in the F_1 dimension (Figure 31b) depict the complete separation of four A_3 subspectra of both the enantiomers. As far as the determination of $^nT_{HH}$ ($n = 2, 3$, and 5) is concerned, the first three cross-sections are sufficient. The significant advantage of the spin selected correlation experiment is in spectral simplification, by separating the active and passive couplings in two dimensions. This is clearly evident from Figure 31.

The analysis is incomplete unless the coupling between the passive protons numbered 5 and 6 is determined, which is not reflected in either the F_1 or the F_2 dimension. Another experiment with the selective excitation of methine and acetylenic protons does provide this information along F_2 dimension and the passive couplings to these protons in the F_1 dimension. The difficulty in such simultaneous excitation is their frequency separation, which is more than 1 kHz. The problem has, however, been combated by utilizing bi-selective pulses. The bi-selective methine and acetylenic protons excited 2D spectrum is given in Figure 32. The coupling information can be derived by the analyses of the cross-peak multiplet pattern. The set of doublets due to coupling of active spins along F_2 dimension is displaced in the F_1 dimension due to passive couplings of protons 5 and 6 with methyl protons. From the expanded plot of the cross-peaks for the methine proton (6), it is evident that the passive coupling to proton 6, $^3T_{H6H7}$, results in a quartet. Each component of the quartet is further split into a doublet by another passive coupling to proton 6, that is, $^4T_{H5H6}$. Thus, F_1 dimension gives two sets of identical quartets for each enantiomer displaced according to their coupling strengths. The separations marked with alphabets a, b, and c provide $^4T_{H5H6}$, $^3T_{H7H6}$, and $^4T_{H5H7}$ for *R* enantiomer and the separations marked d, e, and f provide similar information for *S* enantiomer. Thus, the totality of the coupling information could be obtained by the first-order analyses of the spectra without resorting to iterative analysis.

11.2 Analyses of the spectra of (*R/S*)-propylene carbonate and (*R/S*)-propylene oxide

The 2D correlated spectrum of (*R/S*)-propylene carbonate (scalemic mixture) with selective excitation of methyl protons is given in Figure 33. The two

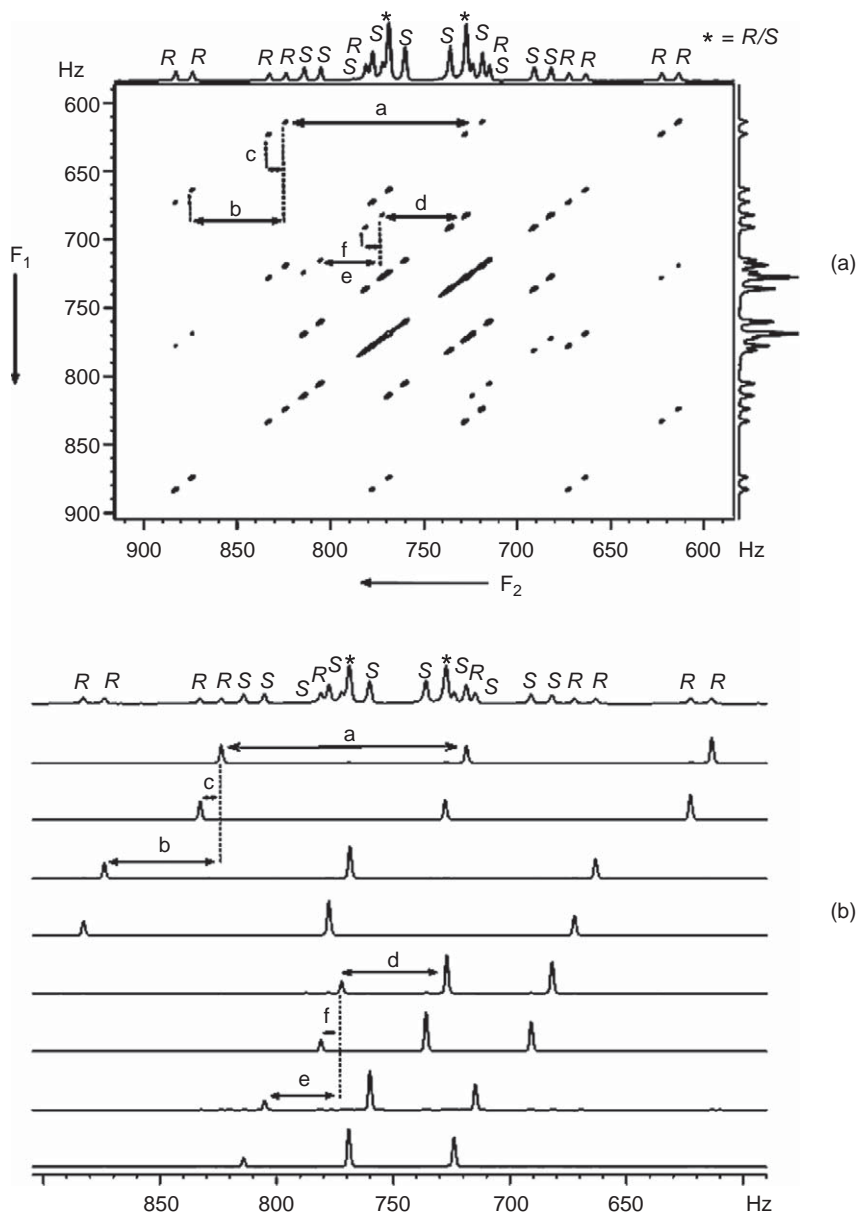


Figure 31 (a) The 500 MHz two-dimensional correlation spectra of selectively excited methyl resonance in racemic mixture of (*R/S*)-3-butyn-2-ol. The separations marked with alphabets a, b, and c provide ${}^2T_{H7H7}$, ${}^3T_{H6H7}$, and ${}^5T_{H5H7}$ for *R* enantiomer and the separations d, e and f provide ${}^2T_{H7H7}$, ${}^3T_{H6H7}$, and ${}^5T_{H5H7}$ for *S* enantiomer. Peak marked '*' indicate the overlapped transitions from *R* and *S*. Notice the unambiguous enantiomer separation and the spectral simplification. (b) The first four cross-sections of Figure 31a for each enantiomer taken along F_2 dimension. The separations marked with alphabets a, b, and c provide ${}^2T_{H7H7}$, ${}^3T_{H6H7}$, and ${}^5T_{H5H7}$ for *R* enantiomer and the separations d, e, and f provide ${}^2T_{H7H7}$, ${}^3T_{H6H7}$, and ${}^5T_{H5H7}$ for *S* enantiomer. Notice that first three cross-sections for each enantiomer is suffice for the determination of all the coupling information. Reproduced with permission from American Chemical Society.

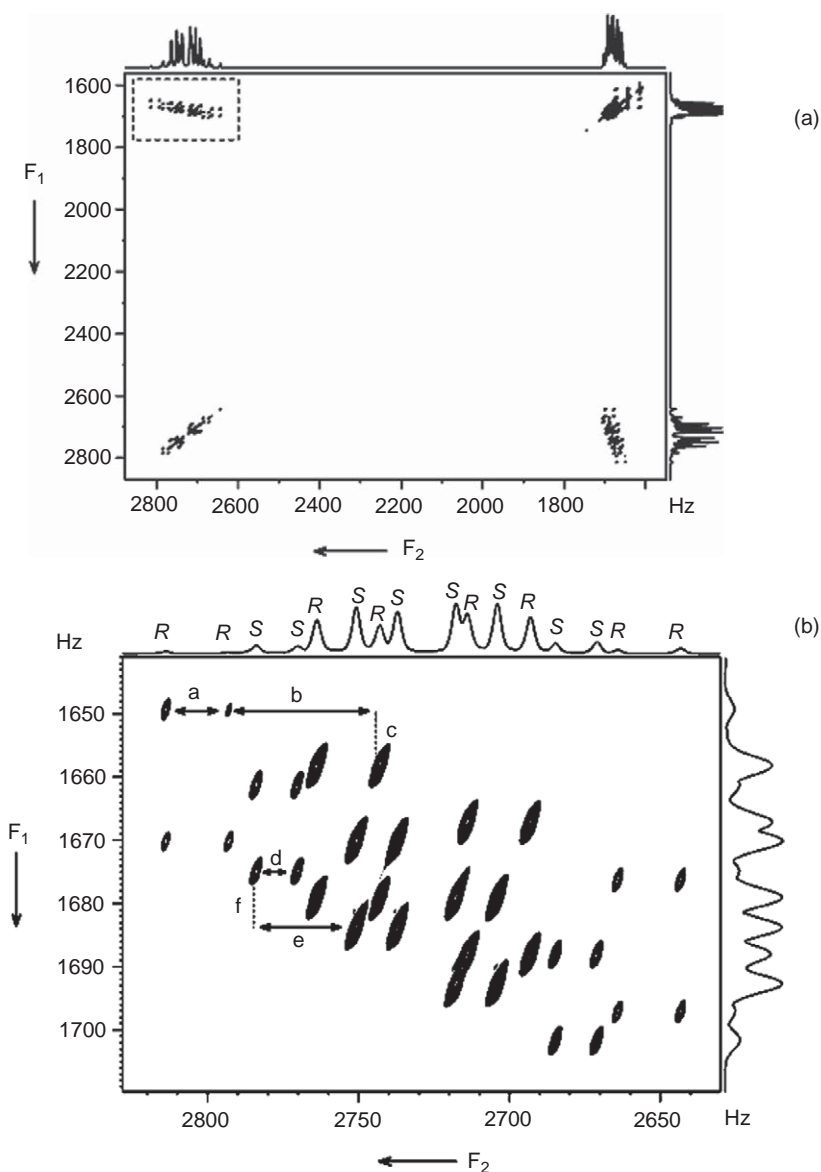


Figure 32 (a) The 500 MHz two-dimensional correlation spectra of simultaneous bi-selective excitation of methine (6) and acetylenic (5) resonances in racemic mixture of (*R/S*)-3-butyn-2-ol, along with F_1 and F_2 projections. (b) The expanded plot of cross-peaks pertaining to proton 6, marked with broken rectangle. The separations *a*, *b*, and *c* provide, respectively, $^4T_{H_5H_6}$, $^3T_{H_6H_7}$, and $^4T_{H_4H_7}$ for *R* enantiomer and those marked with *d*, *e*, and *f* provide, respectively, $^4T_{H_5H_6}$, $^3T_{H_6H_7}$, and $^4T_{H_4H_7}$ for *S* enantiomer. Notice the resolution achieved and the unambiguous discrimination of the enantiomers. Reproduced with permission from American Chemical Society.

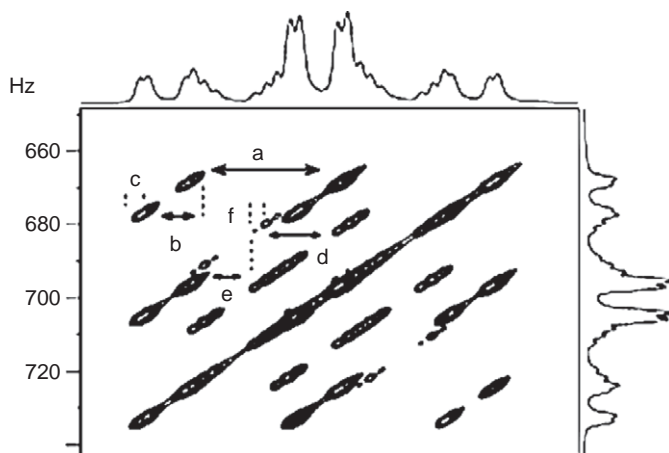


Figure 33 500 MHz two-dimensional Soft-COSY spectra of a salemic mixture of (*R/S*)-propylene carbonate. The separations marked with alphabets a, b, and c provide coupling information ${}^2T_{\text{H4H4}}$, ${}^3T_{\text{H4H5}}$, and ${}^4T_{\text{H4H6}}$ or ${}^4T_{\text{H4H7}}$ for *R* enantiomer and the separations d, e, and f and provide information ${}^2T_{\text{H4H4}}$, ${}^3T_{\text{H4H5}}$, and ${}^4T_{\text{H4H6}}$ or ${}^4T_{\text{H4H7}}$ for *S* enantiomer. Reproduced with permission from American Chemical Society.

non-equivalent methylene protons and the methine proton form the passive spins. The 2D spectrum then pertains to the A_3 part of $A_3\text{MPX}$ spin system containing 24 transitions, which can be construed as 8 A_3 subspectra corresponding to 8 spin states of M, P, and X together, displayed in both direct and indirect dimensions, for each enantiomer. In F_2 dimension, the active coupling is among the methyl protons and results in a triplet. Both F_1 and F_2 dimensions must display two sets of A_3 subspectra, one for each enantiomer with distinctly different coupling strengths enabling their discrimination. Experimentally four A_3 subspectra for *R* enantiomer and three A_3 subspectra for *S* enantiomer have been observed. This is due to the fact that long-distance couplings to methyl protons, *viz.*, ${}^4T_{\text{H4H6}}$ and ${}^4T_{\text{H4H7}}$, are nearly equal for *S* enantiomer and one of the long-distance couplings is negligibly small in *R* enantiomer. The cross-section taken parallel to F_2 dimension, at any one of the transitions of the subspectrum in F_1 dimension, gives the coupling among the methyl protons. Furthermore, the displacement of cross-sections along F_1 dimension permits the measure of $({}^nT_{\text{HH}})^{R/S}$ (where $n = 3$ and 4). Although the spectrum distinguishes the enantiomers and permits the determination of couplings, it does not identify the individual couplings, ${}^4T_{\text{H4H6}}$ and ${}^4T_{\text{H4H7}}$. Only four of the seven possible independent couplings could be obtained from this spectrum. However, the analysis is incomplete unless the couplings among the protons numbered 5, 6, and 7 (M, P, and X spins), which are not reflected in either dimension, and the individual values of ${}^4T_{\text{H4H6}}$ and ${}^4T_{\text{H4H7}}$ are determined. This problem was circumvented by the 2D correlated spectrum with selectively excited protons 5 and 7 given in Figure 34. The spectrum provides one active coupling, ${}^3T_{\text{H5H7}}$, and four passive couplings, ${}^2T_{\text{H6H7}}$, ${}^3T_{\text{H5H6}}$, ${}^3T_{\text{H4H5}}$, and ${}^4T_{\text{H4H7}}$.

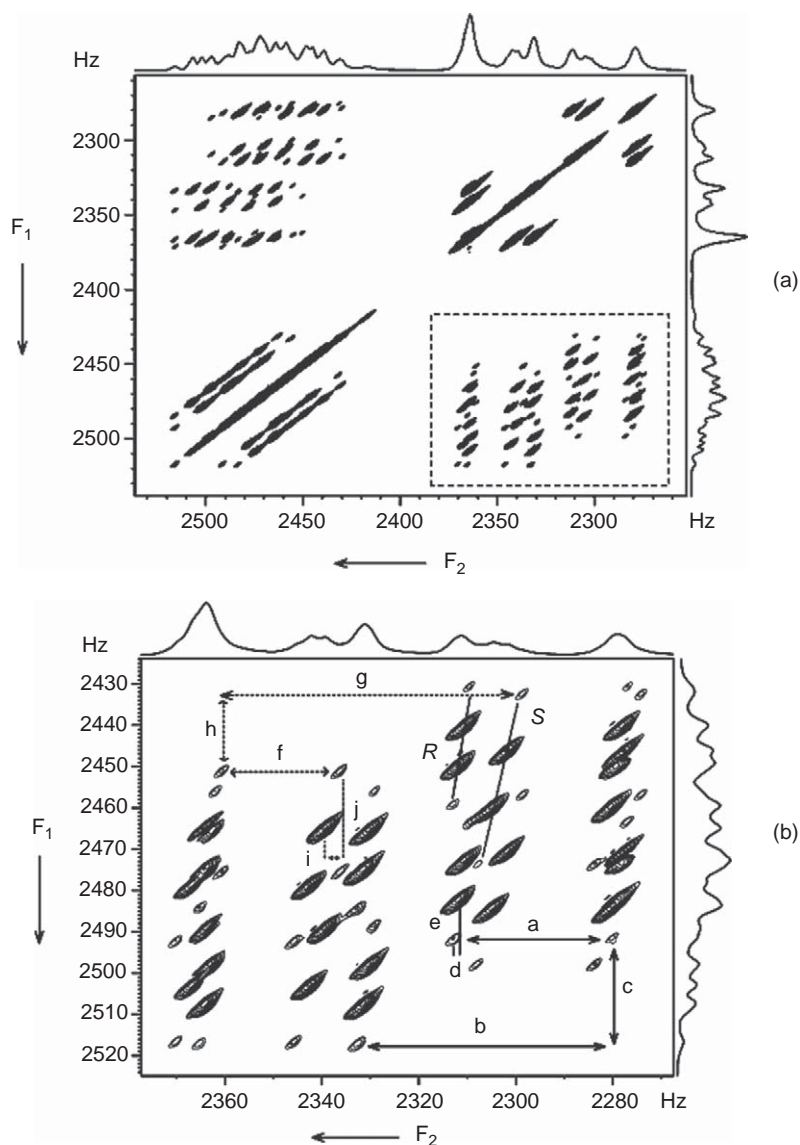


Figure 34 (a) The 500 MHz two-dimensional correlation spectra with bi-selective excitation of protons 5(methine) and 7(methylene) resonances in racemic mixture of (*R/S*)-propylene carbonate. (b) Expanded plot of A pertaining to cross-peaks of proton 7 marked with broken rectangle. The separations marked with solid arrows and represented by alphabets a, b, c, d, and e provide coupling information (${}^3T_{H5H7}$)^S, (${}^2T_{H6H7}$)^S, (${}^4T_{H4H7}$)^S, (${}^3T_{H5H6}$)^S, and (${}^3T_{H4H5}$)^S, whereas the separations marked with broken arrows and represented by alphabets f, g, h, i, and j provide (${}^3T_{H5H7}$)^R, (${}^2T_{H6H7}$)^R, (${}^4T_{H4H7}$)^R, (${}^3T_{H5H6}$)^R, and (${}^3T_{H4H5}$)^R. Note the resolution achieved and the quartet due to long-range coupling (${}^4T_{H4H7}$)^R and (${}^4T_{H4H7}$)^S, displaced according to passive coupling in the F_1 dimension. One such quartet for each *R* and *S* enantiomers is shown by a cross line joining them. Reproduced with permission from American Chemical Society.

The active coupling between methine protons is obtainable along the F_2 dimension at the chemical sites of both protons 6 and 7, which is a doublet of identical separation.

A region of the spectrum pertaining to the cross-peaks of proton 7 is also shown in Figure 34b. The active coupling of this proton with the geminal proton 6 splits its resonance into a doublet of larger separation (${}^2T_{\text{H6H7}}$), which is further split into a doublet from methine proton (${}^3T_{\text{H5H7}}$). Each component of the doublet of doublet is split into quartet from methyl protons (${}^4T_{\text{H4H7}}$). Thus, F_2 dimension provides four sets of quartets, which are displaced according to two passive couplings ${}^4T_{\text{H4H7}}$ and ${}^2T_{\text{H6H7}}$. The F_1 displacement provides two other passive couplings ${}^3T_{\text{H5H6}}$ and ${}^3T_{\text{H4H5}}$. The resolution of the quartet due to long-distance coupling ${}^4T_{\text{H4H7}}$ is exceptionally good. One such quartet for each enantiomer is shown by joining the peaks with a tilted line. This dramatically enhanced resolution permits the measure of the coupling strength of the order of 0.6 Hz for *R* enantiomer. The separations marked with solid lines and represented by alphabets a, b, c, d, and e, respectively, provide $({}^3T_{\text{H5H7}})^R$, $({}^2T_{\text{H6H7}})^R$, $({}^4T_{\text{H4H7}})^R$, $({}^3T_{\text{H5H6}})^R$, and $({}^3T_{\text{H4H5}})^R$. Similarly separations marked with broken lines and represented by alphabets g, h, i, j, and k, respectively, provide $({}^3T_{\text{H5H7}})^S$, $({}^2T_{\text{H6H7}})^S$, $({}^4T_{\text{H4H7}})^S$, $({}^3T_{\text{H5H6}})^S$, and $({}^3T_{\text{H4H5}})^S$. F_1 displacement also provides $({}^3T_{\text{H5H7}})^R$ and $({}^3T_{\text{H5H7}})^S$. From the cross-peak region of the spectrum corresponding to proton 5, similar information is obtainable. However, the values of $({}^4T_{\text{H4H6}})^{R/S}$ have not been determined precisely by this experiment. Another experiment with the selective excitation of protons 6 and 7 provided the above-mentioned couplings and $({}^4T_{\text{H4H6}})^{R/S}$ instead of $({}^4T_{\text{H4H7}})^{R/S}$. Thus, the values of $({}^4T_{\text{H4H6}})^{R/S}$ and $({}^4T_{\text{H4H7}})^{R/S}$ have been determined independently combining the two experiments. Thus, the combination of three spin selective correlation experiments provided the totality of the coupling information for this molecule. These parameters would have been otherwise impossible to obtain from the broad and featureless one-dimensional spectrum.

The advantage of this technique is evidently demonstrated in another spin system of the type $A_3\text{MPX}$ whose spectrum is more broad than the previously discussed molecule. The 2D correlated spectrum of (*R/S*)-propylene oxide with selective excitation of methyl protons and the biselective excitation of protons 6 and 7 is given in Figure 35. It is impossible to determine the small strengths of remote couplings due to significant loss of resolution from the methyl group excited spectrum. However, the resolution achieved is dramatic in the spectrum with biselective excitation of protons 6 and 7. The parameters $({}^3T_{\text{H4H5}})^{R/S}$ and $({}^4T_{\text{H4H6}})^S$ could be determined from the displacement vectors. The two different $({}^4T_{\text{H4H6}})^{R/S}$ and $({}^4T_{\text{H4H7}})^{R/S}$ could be unambiguously derived. The $({}^2T_{\text{H6H7}})^{R/S}$ between geminal protons of methine group is also extracted directly from the F_2 cross-section. Even though the one-dimensional proton spectrum of (*R/S*)-propylene oxide is more broad and featureless compared to (*R/S*)-propylene carbonate, the selectively correlated spectrum gave well-resolved cross-peaks for both *R* and *S* enantiomers. One additional feature of this spectrum is the relative signs of the couplings from the direction of tilt. The expanded portion of the spectrum given in Figure 36 clearly brings out this fact. The tilt of the

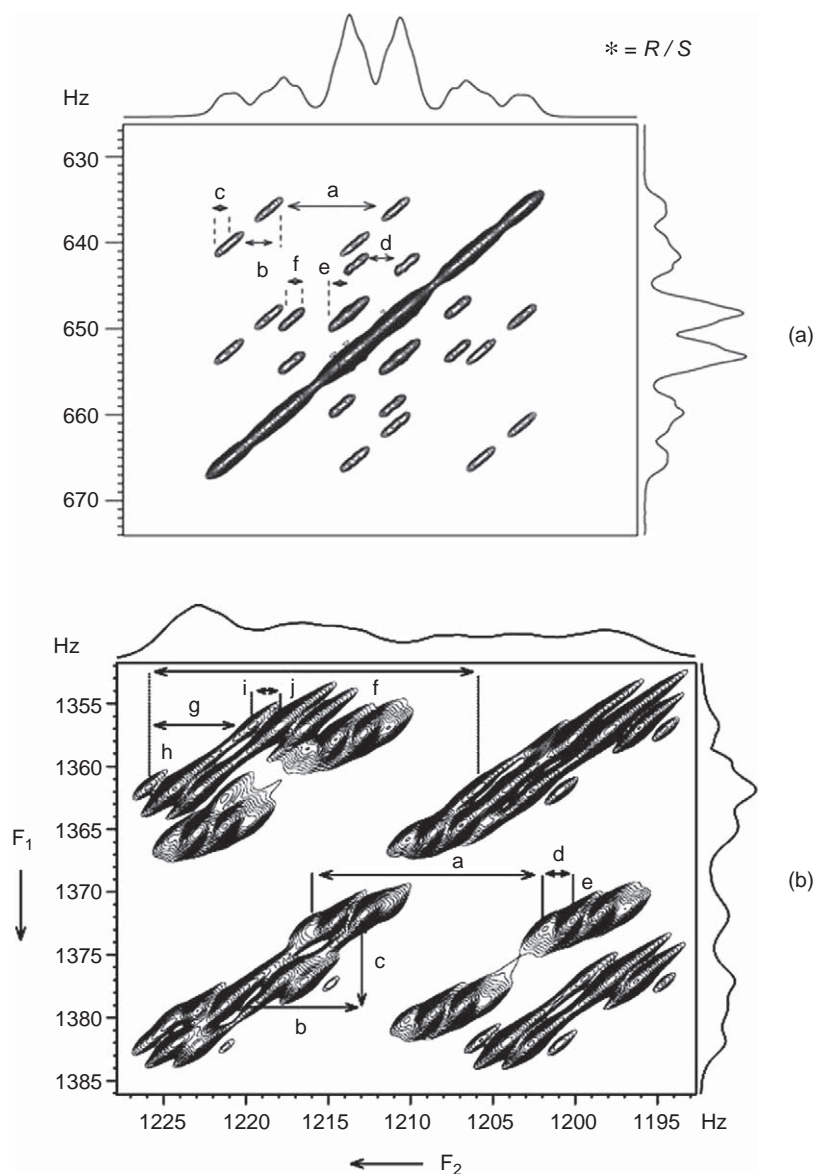


Figure 35 The two-dimensional Soft-COSY spectra of (*R/S*)-propylene oxide with selective excitation of methyl protons. The separations marked with alphabets a, b, and c provide coupling information ${}^2T_{\text{H4H4}}$, ${}^3T_{\text{H4H5}}$, and ${}^4T_{\text{H4H6}}$ or ${}^4T_{\text{H4H7}}$ for *R* enantiomer and the separations d, e, and f provide information ${}^2T_{\text{H4H4}}$, ${}^3T_{\text{H4H5}}$, and ${}^4T_{\text{H4H6}}$ or ${}^4T_{\text{H4H7}}$ for *S* enantiomer. (b) The 500 MHz two-dimensional correlated spectra of racemic mixture of (*R/S*)-propylene oxide with selective excitation of protons 6 and 7. The cross-peaks at the chemical shift position of proton 7 are given in an expanded scale along with *F*₁ and *F*₂ projections. The separations marked with alphabets a, b, c, d, and e provide ${}^2T_{\text{H6H7}}$, ${}^3T_{\text{H5H7}}$, ${}^4T_{\text{H5H6}}$, ${}^3T_{\text{H4H7}}$, and ${}^3T_{\text{H4H6}}$ for *S* enantiomer and the separations marked with alphabets f, g, h, i, and j provide ${}^2T_{\text{H6H7}}$, ${}^3T_{\text{H5H7}}$, ${}^4T_{\text{H5H6}}$, ${}^3T_{\text{H4H7}}$, and ${}^3T_{\text{H4H6}}$ for *R* enantiomer. Reproduced with permission from American Chemical Society.

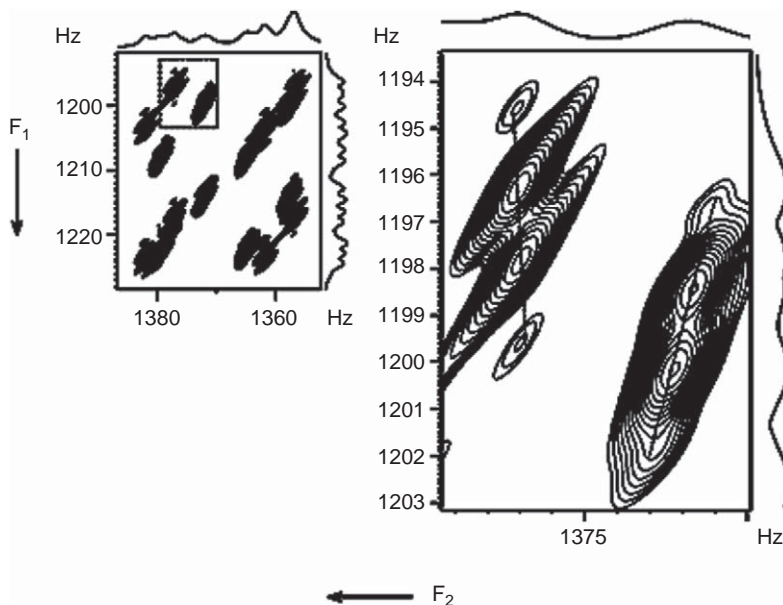


Figure 36 The cross-peaks at the chemical shift position of proton 6 from Figure 35b along with F_1 and F_2 projections. The expanded plot of the cross-peaks marked with broken rectangle shows the opposite direction of the tilt of the displacement vector indicating the long-range passive couplings ${}^4T_{\text{H4H7}}$ is opposite in sign with other couplings. Similarly the sign of the long-range coupling ${}^4T_{\text{H4H6}}$ is found to be opposite with others. Reproduced with permission from American Chemical Society.

displacement vector shown in the expanded part of the cross-peak in the figure is opposite to that of other couplings. This indicates that the long-range couplings $({}^4T_{\text{H4H6}})^R$ and $({}^4T_{\text{H4H7}})^R$ have opposite signs compared to all the other couplings of *R* enantiomer, whereas in *S* enantiomer $({}^4T_{\text{H4H6}})^S$ and $({}^4T_{\text{H4H7}})^S$ have similar signs relative to all the other couplings.

11.3 Advantages and limitations of the spin selected correlation experiments

The biggest advantage of the Soft-COSY experiment, which is not obvious from this selective methyl excited experiments, is in the selective excitation of two protons. When appropriately chosen, two or three such experiments provide magnitudes of all the proton–proton couplings in addition to their relative signs. Since the specific region of the spectrum is selectively excited, the resolution of the spectrum is dramatically enhanced due to smaller spectral width. With such incredible resolution achieved due to displacement of peaks in the F_1 dimension, it is possible to measure couplings smaller than line widths in Soft-COSY, whereas it is impossible to derive these couplings from the SERF or DQSERF

experiments. The coupling strength of 0.2 Hz has been determined using Soft-COSY from the broad and featureless spectra of (*R/S*)-propylene oxide. The only limitation of this experiment is in the natural line width.

Another additional advantage of this technique is the enormous saving in the instrument time compared to non-selective COSY experiment. Each two-dimensional selectively excited correlated spectrum requires typically less than half an hour (also depends on the T_1 relaxation delay) while the non-selective COSY spectrum, to achieve a similar resolution, requires several hours of the instrument time. In other words, all the spectral parameters could be derived by several spin selective correlation experiments in less than the total experimental time required for a single non-selective COSY experiment.

11.4 Spin selective correlation experiment and quantification of ee

The intensities of the NMR peaks are employed for the quantitative measurement of mixtures.²⁰⁰ When the excitation over a small band width is uniform, the ratio of the intensities of the contours can be utilized to quantify ee. On a scalemic mixture, the ee has been determined by measuring the contour volumes in A_3MX and A_3MPX spin systems.

12. BAND SELECTIVE SMALL FLIP ANGLE COSY (BASE- β -COSY)

In the spin selective correlation technique, several selective excitations were required to be carried out to derive complete spectral information. Each selective excitation demands large instrument time and the appropriate choice of several such experiments is essential to determine all the couplings. In combating this difficulty, the band selective homonuclear correlation experiment has been reported. This band selection combined with small flip angle detection pulse is an invaluable experimental tool in determining very small residual dipolar couplings from the broad and featureless 1H spectra of chiral molecules with minimum number of experiments and enormous saving of the instrument time.

The BASE-COSY experiment is a variant of the COSY experiment wherein a small band of frequencies is selectively excited in the t_1 dimension and correlated to the entire spectrum in the t_2 dimension.²⁰¹ The analysis of BASE-COSY spectrum is identical to normal COSY spectrum and provides couplings among all the coupled spins in a single experiment. Thus, the significant advantage of BASE-COSY experiment is the zooming of the small region of the spectra in the F_1 dimension providing high resolution. It is clearly obvious that there is enhanced spectral resolution in the F_1 dimension due to spectral zooming. The disadvantage of BASE-COSY is that the complexity in the F_2 dimension persists and the analyses of the spectra become very tedious with too many transitions in each cross-section. The problem is very severe when the number of interacting spins increases. This problem has been combated by manipulating the dynamics of the spins. One such possibility is the use of small angle for the second pulse²⁰²

in the BASE-COSY sequence which does not mix up all the energy states called BASE- β -COSY. The spin states of the passive spins then remain undisturbed in both the F_1 and F_2 dimensions, resulting in the separation of active and passive couplings in the direct and indirect dimensions at the respective chemical shift positions of the entire selected band. The problem of spectral overlap due to too many transitions is therefore overcome, thereby simplifying the spectrum in each cross-section. The displacement of the passive couplings in the F_1 and F_2 dimensions also enables the measurement of couplings that are less than line width. Therefore, as far as the analyses and the information content are concerned, this experiment is analogous to Soft-COSY experiment,^{203–205} where the small region of the spectrum is selectively excited with identical source and target frequencies, giving unambiguous chiral discrimination, enhanced resolution, and the separation of active and passive couplings in both the dimensions.²⁰⁶ The major advantage of BASE- β -COSY over Soft-COSY is that in BASE- β -COSY there is no need of several selective excitations to determine all the spectral parameters. Furthermore, it produces an E-COSY type spectrum and permits the determination of relative signs of the couplings. The experimental complications in employing biselective pulses for selective excitation can also be overcome.

12.1 BASE- β -COSY and the simplification of ^1H NMR spectrum of (*R/S*)-3-butyn-2-ol

The two-dimensional BASE-COSY and BASE- β -COSY spectra of (*R/S*)-3-butyn-2-ol are reported in Figure 37, where the source frequencies in the F_1 dimension correspond to methyl protons and the target frequency in the F_2 dimension is the entire single quantum spectrum. The manipulation of the spin dynamics in reducing the spectral complexity of BASE-COSY is obvious from the expanded region of the BASE- β -COSY spectrum corresponding to proton H6 (Figure 37c). The active coupling between the excited and detected spins is determined at the respective chemical shift positions in both the dimensions. The separation providing this information is a triplet for the methyl group and doublet for the other two protons. The passive couplings with respect to the excited spins are displaced along the F_1 dimension and those with respect to the detected spin are displaced along the F_2 dimension. The active coupling ($^3T_{\text{H6H7}}$)^{*R/S*} along F_1 dimension and the displacement provide passive couplings ($^2T_{\text{H7H7}}$)^{*R/S*}, ($^5T_{\text{H5H7}}$)^{*R/S*}. The passive coupling ($^4T_{\text{H5H6}}$)^{*R/S*} is extracted from the displacement along the F_2 dimension. Thus, all the couplings for both the enantiomers could be determined in a single experiment. Therefore, the problem of several spin selective excitations has been circumvented, in addition to simplifying the analyses of the broad, featureless, and complex spectra. The identical but redundant information could be obtained by the analyses of the resonances pertaining to proton H5, where the coupling along F_2 dimension is ($^3T_{\text{H5H7}}$)^{*R/S*} and the couplings obtainable from the displacements along F_1 and F_2 dimensions, respectively, are ($^2T_{\text{H7H7}}$)^{*R/S*}, ($^5T_{\text{H6H7}}$)^{*R/S*}, and ($^4T_{\text{H5H7}}$)^{*R/S*}.

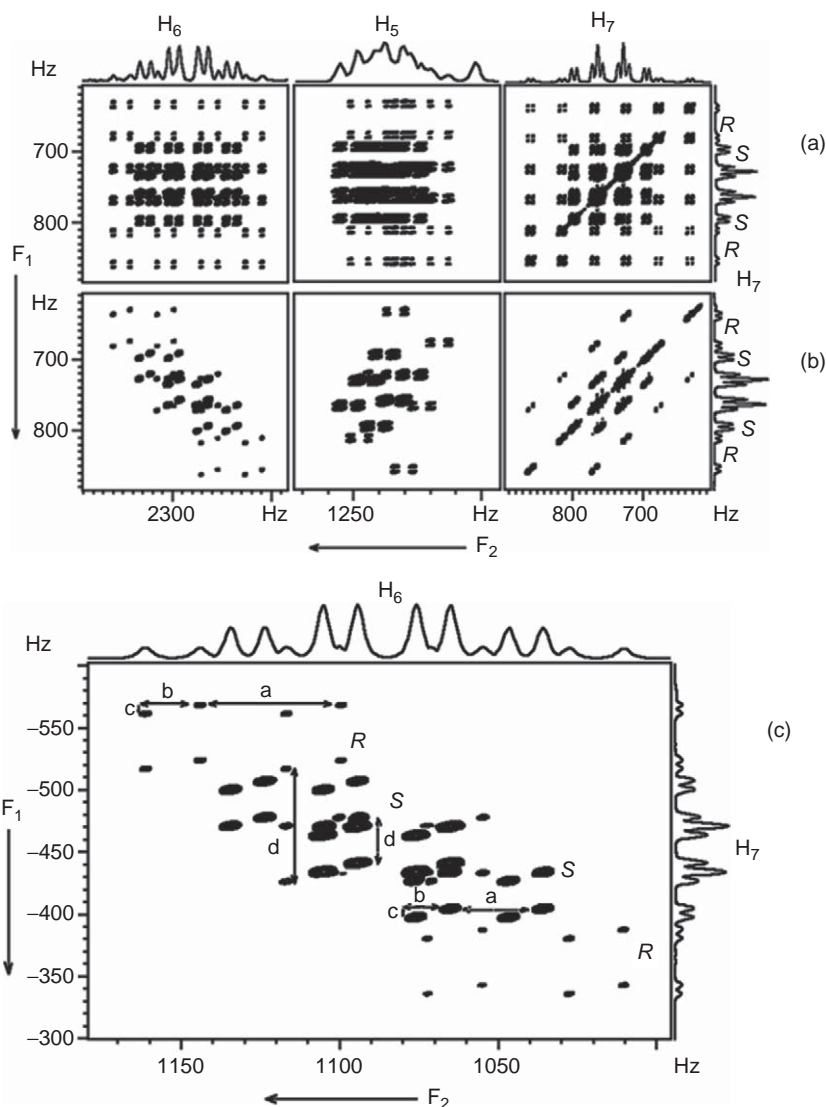


Figure 37 (a) 500 MHz proton two-dimensional BASE-COSY spectrum of (*R/S*)-3-butyn-2-ol with selective excitation of methyl protons (H_7) along with the corresponding F_1 and F_2 projections. (b) The 500 MHz proton 2D BASE- β -COSY spectrum with selective excitation of methyl protons (H_7). All the experimental and processing parameters are same as Figure 37a, except the flip angle of the second pulse is 15° . Assignments for different protons and to *R* and *S* forms are marked. Only few of the cross-sections for *R* and *S* forms have been marked. (c) The expanded portion of B pertaining to resonance of proton H_6 . The active and passive couplings derivable from both F_1 and F_2 dimensions are marked. The separations providing coupling information marked with solid lines are for *R* enantiomer and those with broken lines are for *S* enantiomer. The separations providing the coupling information are: for *R* enantiomer, $a = {}^3T_{H_6H_7}$, $b = {}^4T_{H_6H_5}$, $c = {}^5T_{H_5H_7}$, and $d = {}^2T_{H_7H_7}$; and for *S* enantiomer, $a = {}^3T_{H_6H_7}$, $b = {}^4T_{H_6H_5}$, $c = {}^5T_{H_5H_7}$, and $d = {}^2T_{H_7H_7}$. Only few of the cross-sections for *R* and *S* forms have been marked.

12.2 Analyses of 2D proton BASE- β -COSY spectrum of (R/S)- β -butyrolactone

The coupled protons of this molecule also form an A_3 MPX type spin system. The chemical structure, one-dimensional ^1H spectrum, and the selective methylene protons excited two-dimensional BASE-COSY and BASE- β -COSY spectra of (R/S)- β -butyrolactone are given in Figure 38. The two non-equivalent methylene protons and the methine proton are the passive spins. In the 2D spectrum, F_1 dimension pertains to the A_3 part of A_3 MPX spin system containing 24 transitions. The F_2 dimension has a band of all the four groups of protons. For this molecule, the analyses of the bunch of resonances pertaining to protons H6 and H5 are suffice to determine all the couplings. The expanded region of the spectrum pertaining to proton H6 and proton H5 is given in Figure 39 along with the separations providing the coupling information. At the chemical shift position of proton H6, the active coupling along F_2 dimension would be $(^3T_{\text{H4H6}})^{R/S}$ and the passive couplings of all the remaining spins with proton H4 and within the methyl proton themselves, that is, $(^2T_{\text{H4H4}})^{R/S}$, $(^3T_{\text{H4H5}})^{R/S}$, and $(^4T_{\text{H4H7}})^{R/S}$ are displaced along the F_1 dimension. On the other hand, in the F_1 dimension, the active coupling is $(^3T_{\text{H6H7}})^{R/S}$. However, the passive couplings with respect to proton H6, that is, $(^3T_{\text{H5H6}})^{R/S}$ and $(^2T_{\text{H6H7}})^{R/S}$ are displaced along F_2 dimension. Thus, seven couplings could be determined from this spectrum.

The coupling $(^3T_{\text{H5H7}})^{R/S}$ is derivable from the analysis of the resonances pertaining to proton H5. In this case, the coupling along F_2 dimension is $(^3T_{\text{H4H5}})^{R/S}$ and the couplings obtainable from the displacements along F_1 dimension are $(^4T_{\text{H4H6}})^{R/S}$, $(^4T_{\text{H4H7}})^{R/S}$, and $(^4T_{\text{H4H4}})^{R/S}$. From the F_1 dimension, the passive couplings to proton H5, that is, $(^3T_{\text{H5H6}})^{R/S}$ and $(^3T_{\text{H5H7}})^{R/S}$ can be determined. Except for $(^3T_{\text{H5H7}})^{R/S}$, all other information are redundant. The interesting point to be highlighted is that the parameters $(^4T_{\text{H4H6}})^{R/S}$ and $(^4T_{\text{H4H7}})^{R/S}$ could be obtained unambiguously from the present experiment unlike in Soft-COSY. This is clearly evident from the expanded regions of the spectrum corresponding to proton H7 shown in Figure 40, where it is obvious that the active coupling $(^4T_{\text{H4H7}})^S$ is not detectable indicating that it is negligibly small. As a consequence, there is no displacement of peaks with passive couplings in either the F_1 dimension or the F_2 dimension for *S* enantiomer. Therefore, these transitions are appearing exclusively from *R* enantiomer.

12.3 Advantages of the BASE- β -COSY technique over other methods

The significant advantages of the BASE- β -COSY method are the spectral discrimination of enantiomers, the spectral simplification by separating the active and passive couplings in the two dimensions. For example, unlike in the spin selected correlation experiments, where more than one selective excitation is required to determine all the couplings, a single BASE- β -COSY experiment

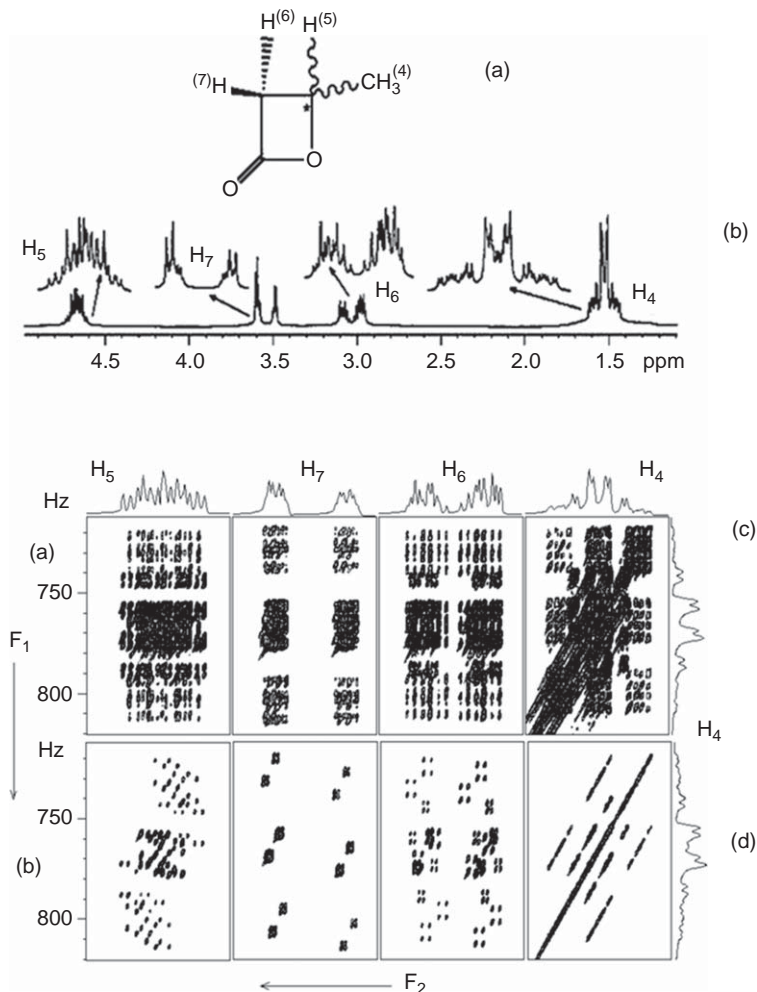


Figure 38 (a) Racemic structure and the numbering of interacting spin in (*R/S*)- β -butyrolactone. (b) The 500 MHz one-dimensional ^1H spectrum of (*R/S*)- β -butyrolactone in PBLG. The expanded regions of each spectrum and the assignment to different protons are shown. (c) The 500 MHz proton 2D BASE-COSY spectrum of (*R/S*)- β -butyrolactone aligned in the chiral liquid crystal PBLG, with selective excitation of methyl protons (H_4) along with the corresponding projections. (d) The 500 MHz proton 2D BASE- β -COSY spectrum with selective excitation of methyl protons (H_4) along with the corresponding projections. All the experimental and processing parameters are identical to that of (c), except the flip angle of the second pulse is 15° .

provides all the couplings resulting in the considerable saving of the instrument time. To quantify it more clearly, the time required for Soft-COSY experiment in (*R/S*)-3-butyne-2-ol is nearly 5 h compared to only 2 h for BASE- β -COSY experiment for deriving identical information.

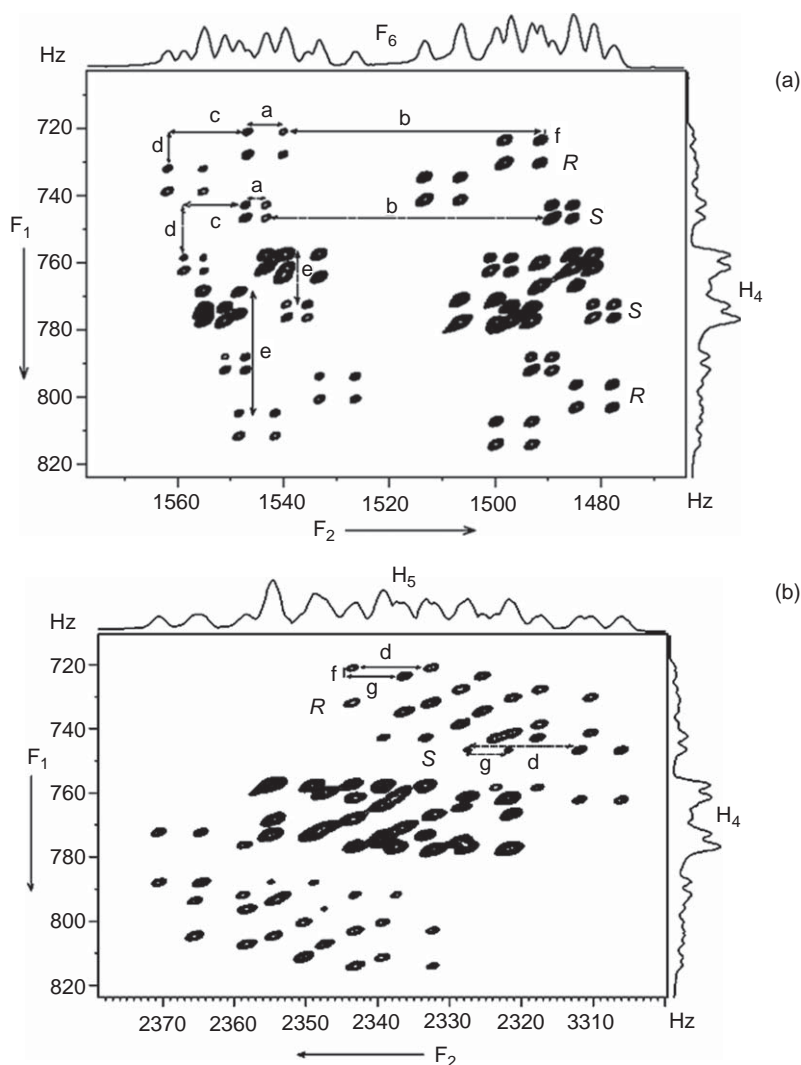


Figure 39 (a) The expanded portions of Figure 38d pertaining to the resonances of proton H6. Few of the cross-sections for *R* and *S* forms have been marked. Assignments to *R* and *S* enantiomers are arbitrary. The separations (only the magnitudes) providing coupling information reported in solid lines are for *R* enantiomer and those with broken lines are for *S* enantiomer. The parameters obtainable are: for *R* enantiomer, $a = {}^4T_{H4H6}$, $b = {}^2T_{H6H7}$, $c = {}^3T_{H5H6}$, $d = {}^3T_{H4H5}$, $e = {}^2T_{H4H4}$, and $f = {}^4T_{H4H7}$; and for *S* enantiomer, $a = {}^4T_{H4H6}$, $b = {}^2T_{H6H7}$, $c = {}^3T_{H5H6}$, $d = {}^3T_{H4H5}$, $e = {}^2T_{H4H4}$, and $f = {}^4T_{H4H7}$. (b) The expanded portions of Figure 38d; resonances corresponding to proton H5. The active coupling along F_2 dimension provides ${}^3T_{H4H5}$ and the displacement providing ${}^3T_{H5H7}$ is marked with alphabet. These separations are $d = {}^3T_{H4H5}$ and $g = {}^3T_{H5H7}$.

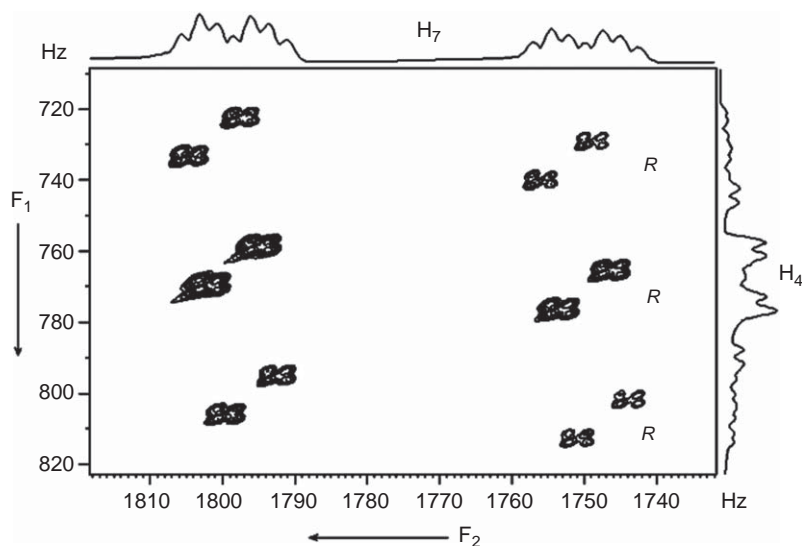


Figure 40 Resonances corresponding to proton H7 of Figure 38d. Notice the active coupling (T_{H4H7})^S is not detectable. Thus, there is no displacement of peaks due to passive couplings. Consequently, this spectrum pertains to that of proton H7 from pure *R* enantiomer. The analysis of this spectrum provides redundant information (i.e., active coupling ${}^nT_{H4H7}$ along F_2 dimension and passive couplings of H4 to other protons along F_1 dimension) and hence the separations are not marked.

12.4 BASE- β -COSY and the relative signs of the couplings

Like in many of the methodologies discussed before, even in BASE- β -COSY experiment the direction of tilt of the displacement vector provides the relative signs between active and passive couplings. The BASE- β -COSY spectra of (*R/S*)- β -butyrolactone and (*R/S*)-propylene oxide where, respectively, the spins H6 and H7 are selectively excited are given in Figure 41. It is clearly evident from the direction of the displacement, marked with tilted lines, that the long-range couplings (${}^4T_{H4H6}$)^R and (${}^4T_{H4H7}$)^R are opposite in (*R/S*)-propylene oxide for *R* enantiomer, whereas for *S* enantiomer (${}^4T_{H4H6}$)^S and (${}^4T_{H4H7}$)^S have similar signs relative to all the other couplings. In (*R/S*)- β -butyrolactone, as one of the long-range couplings (${}^4T_{H4H7}$)^S is negligibly small (tilted line is nearly horizontal), it is difficult to talk about the relative signs in this case.

13. CONCLUSIONS

In the present chapter, we have discussed the origin of the complexity of proton NMR spectra in both strongly and weakly dipolar coupled spin systems. The in-depth discussion is provided about the NMR interaction parameters in the oriented media and their influence on the spectra, the nomenclature of

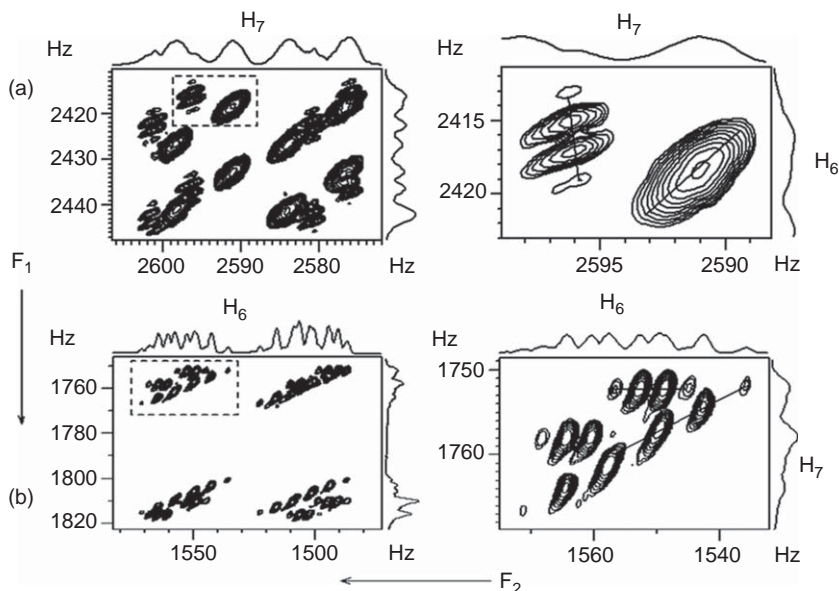


Figure 41 (a) The 500 MHz proton 2D BASE- β -COSY spectrum of (*R/S*)-propylene oxide with selective excitation of proton 6. The region marked with broken rectangle is plotted with an expanded scale on the right. Notice the incredible resolution achieved in separating the quartet for the long-distance coupling of H7 with H4 in *R* enantiomer. The directions of their tilt are opposite indicating that their relative signs of the couplings are opposite. (b) 500 MHz proton 2D BASE- β -COSY spectrum of (*R/S*)- β -butyrolactone with the selective excitation of proton numbered 7. Only portion of the spectrum corresponding to proton 7 (H7) is plotted. The region marked with broken rectangle is plotted with an expanded scale on the right. The quartet for the long-distance coupling of H7 with H4 could be resolved for both *R* and *S* enantiomers. This parameter is undetectable for *S* enantiomer and hence there is no displacement in F_1 dimension.

the spin system, the spectral complexity, and the difficulties in analyzing them. The biggest challenge is in analyzing the complex spectra, be it first and second order, for determining the spectral parameters, especially the dipolar couplings that are essential for the determination of molecular structure. The several recently developed methodologies for either simplifying the spectral complexity or deriving information that aids their analyses have been discussed. As far as the molecules in the weakly aligning media are concerned, the special emphasis on the proton NMR detection for chiral discrimination, the separation of the overlapped spectra of enantiomers, and several methodologies in discerning the degenerate transitions from the broad and featureless one-dimensional spectra of chiral molecules have been discussed. Each developed technique, utilizing spin selective MQ and single quantum correlation techniques, has been discussed taking specific examples of different types of spin systems. The relative signs of the couplings and the feasibility of measuring the ee have been discussed.

REFERENCES

1. A. Saupe and G. Englert, *Phys. Rev. Lett.*, 1963, **11**, 462.
2. J. W. Emsley and J. C. Lindon, *NMR Spectroscopy using Liquid Crystal Solvents*, Pergamon, New York, NY, 1975.
3. C. L. Khetrapal, A. C. Kunwar, A. S. Tracey and P. Diehl, in: *NMR Basic Principles and Progress*, P. Diehl, E. Fluck and R. Kosfeld, eds., Vol. 9, Springer-Verlag, Berlin, New York, 1975.
4. B. J. Forest and L. W. Reeves, *Chem. Rev.*, 1981, **81**, 1.
5. O. Söderman, G. Lindblom, L. B. A. Johansson and K. Fontell, *Mol. Cryst. Liq. Cryst.*, 1980, **59**, 121.
6. R. Christy Rani Grace and N. Suryaprakash, in: *New Advances in Analytical Techniques*, Atta-ur-Rahman, ed., Vol. 1, Harwood Academic Press, The Netherlands, 1998.
7. N. Suryaprakash, *Concepts Magn. Reson.*, 1998, **10(3)**, 167.
8. N. Suryaprakash, *Curr. Org. Chem.*, 2000, **4**, 85.
9. P. Diehl and C. L. Khetrapal, in: *NMR Basic Principles and Progress*, P. Diehl, E. Fluck and R. Kosfeld, eds., Vol. 1, Springer-Verlag, Berlin, New York, 1969.
10. C. L. Khetrapal and A. C. Kunwar, in: *Advances in Magnetic Resonance*, J. S. Waugh, ed., Vol. 9, Academic Press, New York, NY, 1977, p. 301.
11. C. L. Khetrapal and A. C. Kunwar, in: *Advances in Liquid Crystals*, G. H. Brown, ed., Vol. 6, Academic Press, New York, NY, 1983, p. 173.
12. C. L. Khetrapal, R. G. Weiss and A. C. Kunwar, in: *Liquid Crystals—Applications and Uses*, B. Bahadur, ed., Vol. 2, World Scientific, London, 1990.
13. C. L. Khetrapal and E. D. Becker, *Magnetic Resonance Review* Vol. 16 Gordon and Breach, UK, 1991, p. 35.
14. C. L. Khetrapal, *Int. J. Mod. Phys. B*, 1995, **9(18–19)**, 2573.
15. A. D. Buckingham and K. A. McLauchan, *Prog. Nucl. Magn. Reson.*, 1967, **2**, 63.
16. J. Lounila and J. Jokisaari, *Prog. Nucl. Magn. Reson.*, 1982, **15**, 249.
17. G. R. Luckhurst, *Mol. Cryst. Liq. Cryst.*, 1973, **21**, 125.
18. M. H. Levitt, *Spin Dynamics Basics of Nuclear Magnetic Resonance*, 2nd edn., Wiley, New York, NY, 2008.
19. E. E. Burnell and C. A. de Lange, *J. Chem. Phys.*, 1982, **76**, 3474.
20. J. G. Snijders, C. A. de Lange and E. E. Burnell, *J. Chem. Phys.*, 1982, **77**, 5386.
21. A. Saupe, G. Englert and A. Povh, *Advances in Chemistry Series*, No. 63, *Ordered Fluids and Liquid Crystals*, American Chemical Society, Washington D.C., 1967, p. 51.
22. N. Suryaprakash, R. Ugolini and P. Diehl, *Magn. Reson. Chem.*, 1991, **29**, 1024.
23. R. Christy Rani Grace and N. Suryaprakash, *Proc. Natl. Acad. Sci. India Section A*, 1996, **66**, 237.
24. G. A. Nagana Gowda, S. Vivekanandan, N. Suryaprakash and C. L. Khetrapal, *J. Magn. Reson.*, 1996, **A118**, 33.
25. E. K. Foord, J. Cole, M. J. Crawford, J. W. Emsley, G. Celebre, M. Longeri and J. C. Lindon, *Liq. Cryst.*, 1995, **18**, 615.
26. M. E. Rosen, S. P. Rucker, C. Schmidt and A. Pines, *J. Phys. Chem.*, 1993, **97**, 3858.
27. G. Celebre, G. De Luca, M. Longeri, D. Catalano, M. Lumetti and J. W. Emsley, *Mol. Phys.*, 1995, **85**, 221.
28. J. W. Emsley, M. I. C. Furby and G. De Luca, *Liq. Cryst.*, 1996, **21**, 877.
29. G. Celebre, G. De Luca, J. W. Emsley, E. K. Foord, M. Longeri, F. Lucchesini and G. Pileio, *J. Chem. Phys.*, 2003, **118**, 6417.
30. G. Celebre, M. Concistré, G. De Luca, M. Longeri, G. Pileio and J. W. Emsley, *Chem. Eur. J.*, 2005, **11**, 3599.
31. M. Concistré, G. De Luca, M. Longeri, G. Pileio and J. W. Emsley, *ChemPhysChem*, 2005, **6**, 1483.
32. J. W. Emsley, *Phys. Chem. Chem. Phys.*, 2006, **8**, 3726.
33. D. Merlet, J. W. Emsley, J. Jokisaari and J. Kaski, *Phys. Chem. Chem. Phys.*, 2001, **3**, 4918.
34. P. Diehl, C. L. Khetrapal and H. P. Kellerhals, *Mol. Phys.*, 1968, **15**, 333.
35. D. S. Stephenson and G. Binsch, *Org. Magn. Reson.*, 1980, **14**, 226.
36. D. S. Stephenson and G. Binsch, *Mol. Phys.*, 1980, **43**, 697.
37. D. S. Stephenson and G. Binsch, *J. Magn. Reson.*, 1980, **37**, 395.

38. G. Hägele, R. Fuhler, H. W. Höffken, Th. Lenzen, R. Spiske and U. Weber, *Comput. Chem.*, 1995, **19**, 283.
39. V. Zinn, A. Ilyasov, H. Thiele, G. Hagele and U. Weber, *Appl. Magn. Reson.*, 1995, **8**, 311.
40. R. Laatikainen, M. Niemitz, U. Weber, J. Sundelin, T. Hassinen and J. Vespäläinen, *J. Magn. Reson. A*, 1996, **120**, 1.
41. R. Christy Rani Grace, N. Suryaprakash, A. Kumar and C. L. Khetrapal, *J. Magn. Reson. A*, 1994, **107**, 79.
42. C. L. Khetrapal, K. V. Ramanathan, N. Suryaprakash and S. Vivekanandan, *J. Magn. Reson.*, 1998, **135**, 265.
43. L. Lu, G. A. N. Gowda, N. Suryaprakash, C. L. Khetrapal and R. G. Weiss, *Liq. Cryst.*, 1998, **25**, 295.
44. G. K. Pierens, T. A. Carpenter, L. D. Colebrook, L. D. Field and L. D. Hall, *J. Magn. Reson.*, 1992, **99**, 398.
45. J. C. T. Rendell and E. E. Burnell, *Mol. Phys.*, 1997, **90**, 541.
46. S. W. Sinton, D. B. Zax, J. B. Murdoch and A. Pines, *Mol. Phys.*, 1984, **53**, 333.
47. R. T. Syvitski, N. Burlinson, E. E. Burnell and J. Jeener, *J. Magn. Reson.*, 2002, **155**, 251.
48. R. T. Syvitski and E. E. Burnell, *J. Magn. Reson.*, 2000, **144**, 58.
49. L. D. Field, S. A. Ramadan and G. K. Pierens, *J. Magn. Reson.*, 2002, **156**, 64.
50. J. M. Polson and E. E. Burnell, *J. Magn. Reson. A*, 1994, **106**, 223.
51. J. C. T. Rendell and E. E. Burnell, *J. Magn. Reson. A*, 1995, **112**, 1.
52. T. Chandrakumar, J. M. Polson and E. E. Burnell, *J. Magn. Reson. A*, 1996, **118**, 264.
53. G. Celebre, F. Castiglione, M. Longeri and J. W. Emsley, *J. Magn. Reson. A*, 1996, **121**, 139.
54. J. M. Polson and E. E. Burnell, *J. Chem. Phys.*, 1995, **103**, 6891.
55. W. S. Warren, S. Sinton, D. P. Weitekamp and A. Pines, *Phys. Rev. Lett.*, 1979, **43**, 1791.
56. L. Frydman, P. C. Rossomando and B. Frydman, *J. Magn. Reson.*, 1991, **95**, 484.
57. P. Lesot, J. M. Ouvreard, B. N. Ouvreard and J. Courtieu, *J. Magn. Reson. A*, 1994, **107**, 141.
58. D. Nanz, M. Ernst, M. Hong, M. A. Ziegeweid, K. R. Schmidt and A. Pines, *J. Magn. Reson. A*, 1995, **113**, 169.
59. T. O. Levante, T. Bremi and R. R. Ernst, *J. Magn. Reson. A*, 1996, **121**, 167.
60. L. C. Snyder and S. Meiboom, *J. Chem. Phys.*, 1973, **58**, 5096.
61. S. Vivekanandan and N. Suryaprakash, *Chem. Phys. Lett.*, 2001, **338**, 247.
62. J. W. Emsley, D. Merlet, K. J. Smith and N. Suryaprakash, *J. Magn. Reson.*, 2002, **154**, 303.
63. H. S. Vinay Deepak, J. Anu and N. Suryaprakash, *Magn. Reson. Chem.*, 2006, **44**, 553.
64. S. Vivekanandan, J. Anu and N. Suryaprakash, *J. Mol. Struct.*, 2004, **694**, 241.
65. S. Caldarelli, M. Hong, L. Emsley and A. Pines, *J. Phys. Chem.*, 1996, **100**, 18696.
66. M. Hong, A. Pines and S. Caldarelli, *J. Phys. Chem.*, 1996, **100**, 14815.
67. M. Marjanska, F. Castiglione, J. D. Walls and A. Pines, *J. Magn. Reson.*, 2002, **158**, 52.
68. R. C. Hewitt, S. Meiboom and L. C. Snyder, *J. Chem. Phys.*, 1973, **58**, 5089.
69. J. W. Emsley, J. C. Lindon and J. M. Tabony, *J. Chem. Soc. Faraday Trans. II*, 1973, **69**, 10.
70. J. W. Emsley and D. L. Turner, *J. Chem. Soc. Faraday Trans. II*, 1981, **77**, 1493.
71. Anil Kumar and C. L. Khetrapal, *J. Magn. Reson.*, 1978, **30**, 137.
72. J. Courtieu, D. W. Alderman, D. M. Grant and J. P. Bayle, *J. Chem. Phys.*, 1982, **77**, 723.
73. A. Kimura, N. Kuni and H. Fujiwara, *J. Phys. Chem.*, 1996, **100**, 14056.
74. P. Pfandler and G. Bodenhausen, *J. Magn. Reson.*, 1991, **91**, 65.
75. F. Castiglione, M. Carravetta, G. Celebre and M. Longeri, *J. Magn. Reson.*, 1998, **132**, 1.
76. P. Diehl and J. Vogt, *Org. Magn. Reson.*, 1976, **8**, 638.
77. P. Diehl, S. Sykora and J. Vogt, *J. Magn. Reson.*, 1975, **19**, 67.
78. K. Inoue, H. Takeuchi and S. Konaka, *J. Phys. Chem. A*, 2001, **105**, 6711.
79. W. Leo Meerts, C. A. de Lange, A. C. J. Weber and E. E. Burnell, *Chem. Phys. Lett.*, 2007, **441**, 342.
80. J. S. Waugh, L. M. Huber and U. Haeberlen, *Phys. Rev. Lett.*, 1968, **20**, 180.
81. M. Lee and W. I. Goldburg, *Phys. Rev.*, 1965, **140**, A1261.
82. M. Mehring and J. S. Waugh, *Phys. Rev. B*, 1972, **5**, 3459.
83. B.-J. van Rossum, H. Förster and H. J. M. de Groot, *J. Magn. Reson.*, 1997, **124**, 516.
84. M. H. Levitt, A. C. Kolbert, A. Bielecki and D. J. Ruben, *Solid State NMR*, 1993, **2**, 151.

85. E. Vinogradov, P. K. Madhu and S. Vega, *Chem. Phys. Lett.*, 1999, **314**, 443.
86. A. Ramamoorthy, L. M. Gierasch and S. J. Opella, *J. Magn. Reson. B*, 1996, **110**, 102.
87. C. H. Wu, A. Ramamoorthy and S. J. Opella, *J. Magn. Reson. A*, 1994, **109**, 270.
88. K. Nishimura and A. Naito, *Chem. Phys. Lett.*, 2005, **402**, 245.
89. D. K. Lee, T. Narasimhaswamy and A. Ramamoorthy, *Chem. Phys. Lett.*, 2004, **399**, 359.
90. K. Yamamoto, L. Ermakov, D. K. Lee and A. Ramamoorthy, *Chem. Phys. Lett.*, 2005, **408**, 118.
91. A. Ramamoorthy, Y. Wei and D. K. Lee, *Ann. Rep. NMR Spectrosc.*, 2004, **52**, 1.
92. R. G. Mavinkurve, H. S. Vinay Deepak, K. V. Ramanathan and N. Suryaprakash, *J. Magn. Reson.*, 2007, **185**, 240.
93. T. J. Norwood, *Prog. NMR Spectrosc.*, 1992, **24**, 295.
94. G. Bodenhausen, *Prog. NMR Spectrosc.*, 1981, **14**, 137.
95. S. Sinton and A. Pines, *Chem. Phys. Lett.*, 1980, **76**, 263.
96. W. S. Warren and A. Pines, *J. Am. Chem. Soc.*, 1981, **103**, 1613.
97. L. Braunschweiler, G. Bodenhausen and R. R. Ernst, *Mol. Phys.*, 1983, **48**, 535.
98. N. Murali, Y. V. S. Ramakrishna, K. Chandrasekhar, M. Albert Thomas and Anil Kumar, *Pramana*, 1984, **23**, 547.
99. B. Bikash and N. Suryaprakash, *J. Phys. Chem. A*, 2007, **111**, 5211.
100. G. N. M. Reddy and N. Suryaprakash, *Magn. Reson. Chem.*, 2009, DOI 10.1002/mrc.2428.
101. J. A. Pople, W. G. Schneider and H. J. Bernstein, *High Resolution Nuclear Magnetic Resonance*, McGraw Hill, New York, NY, 1959.
102. M. Duchêne, J. W. Emsley, J. C. Lindon, D. S. Stephenson and S. R. Salman, *J. Magn. Reson.*, 1976, **22**, 207.
103. P. Diehl, P. M. Henrichs and W. Niederberger, *Mol. Phys.*, 1971, **20**, 139.
104. A. G. Avent, *J. Magn. Reson.*, 1983, **53**, 513.
105. K. Rukmani and Anil Kumar, *Chem. Phys. Lett.*, 1987, **133**, 485.
106. J. A. B. Lohman and C. MacLean, *Chem. Phys.*, 1978, **35**, 269.
107. E. W. Bastiaan, C. Mac Lean, P. C. M. van Zijl and A. A. Bothner-By, *Annu. Rep. NMR Spectrosc.*, 1987, **19**, 35.
108. E. W. Bastiaan and C. Mac Lean, *NMR Basic Princ. Prog.*, 1990, **25**, 17.
109. P. Ram and J. H. Prestegard, *Biochim. Biophys. Acta*, 1988, **940**, 289.
110. A. A. Bothner-By, P. J. Dommelle and C. Gayathri, *J. Am. Chem. Soc.*, 1981, **103**, 5602.
111. A. A. Bothner-By, J. Dadok, P. K. Mishra and P. C. M. van Zijl, *J. Am. Chem. Soc.*, 1987, **109**, 4180.
112. A. A. Bothner-By, C. Stluka and P. K. Mishra, *J. Magn. Reson.*, 1990, **86**, 441.
113. E. W. Bastiaan, L. Huis and C. MacLean, *Mol. Phys.*, 1989, **67**, 615.
114. K. L. Facchine, S. W. Staley, P. C. M. van Zijl, P. K. Mishra and A. A. Bothner-By, *J. Am. Chem. Soc.*, 1988, **110**, 4900.
115. C. Gayathri, A. A. Bothner-By, P. C. M. van Zijl and C. MacLean, *Chem. Phys. Lett.*, 1982, **87**, 192.
116. J. R. Tolman, J. M. Flanagan, M. A. Kennedy and J. H. Prestegard, *Proc. Natl. Acad. Sci. U.S.A.*, 1995, **92**, 9279.
117. H. C. Kung, K. Y. Wang, I. Gojler and P. H. Bolton, *J. Magn. Reson. B*, 1995, **109**, 323.
118. N. Tjandra, S. Grzesiek and A. Bax, *J. Am. Chem. Soc.*, 1996, **118**, 6264.
119. J. R. Tolman and J. H. Prestegard, *J. Magn. Reson. B*, 1996, **112**, 245.
120. N. Tjandra and A. Bax, *J. Magn. Reson.*, 1997, **124**, 512.
121. J. R. Tolman, J. M. Flanagan, M. A. Kennedy and J. H. Prestegard, *Nat. Struct. Biol.*, 1997, **4**, 292.
122. J. H. Prestegard, C. M. Bougault and A. I. Kishore, *Chem. Rev.*, 2004, **104**, 3519.
123. A. Bax, G. Kontaxis and N. Tjandra, *Methods Enzymol.*, 2001, **339**, 127.
124. E. De Alba and N. Tjandra, *Methods Mol. Biol.*, 2004, **278**, 89.
125. J. H. Prestegard, H. M. al-Hashimi and J. R. Tolman, *Q. Rev. Biophys.*, 2000, **33**, 371.
126. N. Tjandra and A. Bax, *Science*, 1997, **278**, 1111.
127. G. M. Clore, M. R. Starich and A. M. Gronenborn, *J. Am. Chem. Soc.*, 1998, **120**, 10571.
128. M. Ottiger and A. Bax, *J. Biomol. NMR*, 1998, **12**, 361.
129. M. R. Hansen, L. Mueller and A. Pardi, *Nat. Struct. Biol.*, 1998, **5**, 1065.
130. Y. Ishii, M. A. Markus and R. Tycko, *J. Biomol. NMR*, 2001, **21**, 141.

131. J. Sass, F. Cordier, A. Hoffman, M. Rogowski, A. Cousin, J. G. Omichinski, H. Lwen and S. Grzesiek, *J. Am. Chem. Soc.*, 1999, **121**, 2047.
132. J. Sass, G. Musco, S. J. Stahl, P. T. Wingfield and S. Grzesiek, *J. Biomol. NMR*, 2000, **18**, 303.
133. M. Ruckert and G. Otting, *J. Am. Chem. Soc.*, 2000, **122**, 7793.
134. J. J. Chou, S. Gaemers, B. Howder, J. M. Louis and A. Bax, *J. Biomol. NMR*, 2001, **21**, 377.
135. R. S. Lipsitz and N. Tjandra, *Annu. Rev. Biophys. Biomol. Struct.*, 2004, **33**, 387.
136. J. Ma, G. I. Goldberg and N. Tjandra, *J. Am. Chem. Soc.*, 2008, **130**, 16148.
137. C. M. Thiele, *Eur. J. Org. Chem.*, 2008, **34**, 5673.
138. M. C. Everaars, A. T. M. Marcelis and E. J. R. Sudholter, *Colloids Surfaces A: Physiochem. Eng. Aspects*, 1995, **102**, 117.
139. D. Danino, Y. Talman, H. Levy, G. Beinert and R. Zana, *Science*, 1995, **269**, 1420.
140. L. Lu and R. G. Weiss, *Langmuir*, 1995, **11**, 3630.
141. N. Sharma, G. A. Nagana Gowda, C. L. Khetrapal and R. G. Weiss, *Liq. Cryst.*, 1997, **22**, 23.
142. L. Lu, N. Sharma, G. A. Nagana Gowda, N. Suryaprakash, C. L. Khetrapal and R. G. Weiss, *Liq. Cryst.*, 1998, **25(3)**, 295.
143. C. R. Sanders II and J. P. Schwonek, *Biochemistry*, 1992, **31**, 8898.
144. C. R. Sanders II and G. C. Landis, *Biochemistry*, 1995, **34**, 4030.
145. C. R. Sanders II, B. J. Hare, K. P. Howard and J. H. Prestegard, *Prog. Nucl. Magn. Reson. Spectrosc.*, 1994, **26**, 421.
146. L. Zidek, H. Wu, J. Feigon and V. Sklenar, *J. Biomol. NMR*, 2001, **21**, 153.
147. P. Krajewski and M. Bardet, *Magn. Reson. Chem.*, 2002, **40**, 225.
148. P. S. Kalsi, *Stereochemistry, Conformation and Mechanism*, New Age International Pvt. Ltd., New Delhi, 2005.
149. P. L. Rinaldi, *Prog. Nucl. Magn. Reson. Spectrosc.*, 1982, **15**, 291.
150. R. R. Fraser, in: *Asymmetric Synthesis*, J. D. Morrison, ed., Vol. 1, Academic Press, New York, NY, 1983. Chapter 9.
151. T. C. Morrill, ed., *Methods in Stereochemical Analysis* Vol. 5, VCH Publishers Inc., New York, NY, 1986.
152. G. R. Weisman, in: *Asymmetric Synthesis*, J. D. Morrison, ed., Vol. 1, Academic Press, New York, NY, 1983. Chapter 8.
153. W. H. Pirkle and D. J. Hoover, *Top. Stereochem.*, 1982, **13**, 263.
154. S. Yamaguchi, in: *Asymmetric Synthesis*, J. D. Morrison, ed., Vol. 1, Academic Press, New York, NY, 1983. Chapter 7.
155. E. E. Sackmann, S. Meiboom and L. C. Snyder, *J. Am. Chem. Soc.*, 1968, **90**, 2183.
156. M. Sarfati, P. Lesot, D. Merlet and J. Courtieu, *Chem. Commun.*, 2000, 2069.
157. P. Lesot, Y. Gounelle, D. Merlet, A. Loewenstein and J. Courtieu, *J. Phys. Chem.*, 1995, **99**, 14871.
158. E. Lafontaine, J. P. Bayle and J. Courtieu, *J. Am. Chem. Soc.*, 1989, **111**, 8294.
159. P. Lesot, Y. Gounelle, D. Merlet, A. Loewenstein and J. Courtieu, *J. Phys. Chem.*, 1996, **100**, 14569.
160. A. Elliot and E. J. Ambrose, *Discuss. Faraday Soc.*, 1950, **9**, 246.
161. C. Robinson, *Trans. Faraday Soc.*, 1956, **52**, 571.
162. C. Robinson, *Mol. Cryst. Liq. Cryst.*, 1966, **1**, 467.
163. K. Czarniecka and E. T. Samulki, *Mol. Cryst. Liq. Cryst.*, 1981, **63**, 205.
164. P. Doty, J. H. Bradbury and A. M. Holtzer, *J. Am. Chem. Soc.*, 1956, **78**, 947.
165. L. Pauling, R. B. Corey and H. R. R. Brandson, *Proc. Natl. Acad. Sci.*, 1951, **37**, 205.
166. M. Panar and W. D. Phillips, *J. Am. Chem. Soc.*, 1968, **90**, 3880.
167. E. T. Samulski and A. V. Tobolsky, *Macromolecules*, 1968, **1**, 555.
168. J. C. Mitchell, A. E. Woodward and P. Doty, *J. Am. Chem. Soc.*, 1957, **79**, 3955.
169. D. Merlet, B. Ancian, J. Courtieu and P. Lesot, *J. Am. Chem. Soc.*, 1999, **121**, 5249.
170. I. Canet, J. Courtieu, A. Loewenstein, A. Meddour and J. M. Péchiné, *J. Am. Chem. Soc.*, 1995, **117**, 6520.
171. I. Canet, A. Meddour, J. Courtieu, J. L. Canet and J. Salaün, *J. Am. Chem. Soc.*, 1994, **116**, 2155.
172. W. Smadja, S. Auffret, P. Berdagué, D. Merlet, C. Canlet, J. Courtieu, J. Y. Legros, A. Boutros and J. C. Fiaud, *Chem. Commun.*, 1997, 2031.
173. H. H. Mantsch, H. Saito and I. C. P. Smith, *Prog. NMR Spectrosc.*, 1977, **11**, 211.

174. P. Lesot, D. Merlet, A. Loewenstein and J. Courtieu, *Tetrahedron Asym.*, 1998, **9**, 1871.
175. D. Merlet, M. Sarfati, B. Ancian, J. Courtieu and P. Lesot, *Phys. Chem. Chem. Phys.*, 2000, **2**, 2283.
176. D. Merlet, B. Ancian, W. Smadja, J. Courtieu and P. Lesot, *Chem. Commun.*, 1998, 2301.
177. O. Lafon and P. Lesot, *Chem. Phys. Lett.*, 2005, **404**, 90–94.
178. P. Lesot and O. Lafon, *Chem. Phys. Lett.*, 2008, **458**, 219.
179. T. Fäcke and S. Berger, *J. Magn. Reson. A*, 1995, **113**, 114.
180. J. Farjon, D. Merlet, P. Lesot and J. Courtieu, *J. Magn. Reson.*, 2002, **158**, 169.
181. J. Farjon, J. P. Baltaze, P. Lesot, D. Merlet and J. Courtieu, *Magn. Reson. Chem.*, 2004, **42**, 594.
182. L. Ziani, J. Courtieu and D. Merlet, *J. Magn. Reson.*, 2006, **183**, 60.
183. B. Bikash, U. R. Prabhu and N. Suryaprakash, *J. Phys. Chem. B*, 2007, **111**, 12403.
184. J. Keeler, *Understanding NMR Spectroscopy*, Wiley, England, 2005.
185. O. W. Sørensen, G. W. Eich, M. H. Levitt, G. Bodenhausen and R. R. Ernst, *Prog. NMR Spectrosc.*, 1983, **16**, 163.
186. D. P. Weitekamp, *Adv. Magn. Reson.*, 1983, **11**, 111.
187. D. P. Weitekamp, J. R. Garbow and A. Pines, *J. Magn. Reson.*, 1982, **46**, 529.
188. O. W. Sørensen, M. H. Levitt and R. R. Ernst, *J. Magn. Reson.*, 1983, **55**, 104.
189. M. Rance, O. W. Sørensen, W. Leupin, H. Kogler, K. Wüthrich and R. R. Ernst, *J. Magn. Reson.*, 1985, **61**, 67.
190. J. B. Murdoch, W. S. Warren, D. P. Weitekamp and A. Pines, *J. Magn. Reson.*, 1984, **60**, 205.
191. M. Munowitz and A. Pines, *Adv. Chem. Phys.*, 1987, **66**, 1.
192. T. M. Barbara, R. Tycko and D. P. Weitekamp, *J. Magn. Reson.*, 1985, **62**, 54.
193. B. Bikash, U. R. Prabhu and N. Suryaprakash, *J. Magn. Reson.*, 2008, **192**, 101.
194. H. Sankeerth and N. Suryaprakash, *J. Magn. Reson.*, 2008, **194**, 192.
195. B. Bikash, U. R. Prabhu and N. Suryaprakash, *J. Magn. Reson.*, 2008, **192**, 92.
196. L. Emsley, *Methods Enzymol.*, 1994, **239**, 207.
197. C. Griesinger, O. W. Sørensen and R. R. Ernst, *J. Am. Chem. Soc.*, 1985, **107**, 6394.
198. C. Griesinger, O. W. Sørensen and R. R. Ernst, *J. Chem. Phys.*, 1986, **85**, 6837.
199. R. P. Uday, B. Bikash and N. Suryaprakash, *J. Phys. Chem. A*, 2008, **112**, 5658.
200. P. Giraudeau, N. Guignard, E. Hillion, E. Baguet and S. Akoka, *J. Pharm. Biomed. Anal.*, 2007, **43**, 1243.
201. R. Brüschweiler, C. Griesinger, O. W. Sørensen and R. R. Ernst, *J. Magn. Reson.*, 1988, **78**, 178.
202. A. Bax and R. Freeman, *J. Magn. Reson.*, 1981, **44**, 542.
203. R. Brüschweiler, J. C. Madsen, C. Griesinger, O. W. Sørensen and R. R. Ernst, *J. Magn. Reson.*, 1987, **73**, 380.
204. L. Emsley and G. Bodenhausen, *J. Magn. Reson.*, 1989, **82**, 211.
205. J. Cavanagh, J. P. Waltho and J. Keeler, *J. Magn. Reson.*, 1987, **74**, 386.
206. R. P. Uday and N. Suryaprakash, *J. Magn. Reson.*, 2008, **195**, 145.

SUBJECT INDEX

- Acetonitrile, MQ coherence, 351–355
 - ^{13}C DQ-SQ coherence, 353–355
 - DQ-SQ coherence, 355
 - 3Q-SQ coherence, 351–353
- Alanines, 311
- AlPO_4 -berlinite, 316
- Aluminophosphate molecular sieve, 316
- γ -Aminobutyric acid (GABA), 317–319
- Aminosilanes, 117–119
- Ammonium formate, 309–310
- β -amyloid peptides, 308
- Anisotropic liquids
 - chemical shift in, 336, 345–346
 - dipolar coupling in, 338
 - quadrupolar interaction in, 339
- Anisotropies
 - coupling, spin-orbit effects and, 80–83
 - shielding tensor, 66–68
- Anti-phase (AP) doublets, 270
- AP magnetization, 273, 290, 317
- Apparent diffusion coefficient (ADC), 320–324
- Au–Au spin–spin couplings in WAu_{12} , ^{183}W chemical shifts and, 63
- Automatic analysis, of oriented molecules, 343–344
- BABA, 306–307
- BASE- β -COSY, 411–417
 - advantage of, 414–415
 - and couplings, 417
 - overview, 411–412
 - of (*R/S*)- β -butyrolactone, 414
 - of (*R/S*)-3-butyn-2-ol, 412
 - vs.* Soft-COSY, 412
- Bathorhodopsin, 312
- BEBOP pulses, 298
- Benchmarks, for NMR computations
 - acronyms used, 32–33
 - FC term in PbH_4 and spin–orbit shielding in HI, 33–38
- Bent's rule, 115
- BIBOP pulses, 298
- Bicelles, dipolar couplings, 364–367
- Bilinear operators, $22n$
- Binuclear spin state selection, for chiral discrimination, 395–402
 - ^{13}C edited 3Q-SQ spectrum, 397–402
 - (*R/S*)-3-butyn-2-ol, 397–399
 - (*R/S*)-propylene carbonate, 399–402
 - pulse sequence, 396–397
- Ψ -BIRD-HMQC experiment, 108–109, 110
- ^1H – ^{29}Si , applied to $\text{Si}(\text{OMe})_4$, 109
- Ψ -BIRD-HSQC experiment, 108–109, 110
- BIRD module, in X-H correlation experiments, 375
- Bisphenol A polycarbonate, 310
- Bohr model, 5
- Bond-order parameters, 117
- Born–Oppenheimer approximation, 4
- Born–Oppenheimer molecular dynamics simulations (BOMD), 58
- Boys-localized MOs, 31
- Breit–Pauli operator, 24, 33, 43
- Breit–Pauli perturbation approach, 47
- Broadband rotary resonance recoupling sequence (B^2R^3), 282
- Brushite, 313
- ^{13}C
 - coupling with ^{29}Si . *See* ^{29}Si - ^{13}C couplings, 100
 - INADEQUATE experiment, 101
 - in natural abundance, 370–371
 - one-pulse experiments, 98, 99
 - properties, 98–100
 - satellites in ^{29}Si , 100
 - spectrum formation, 101
- $[\text{C}_3]$ -alanine, 311
- Carbon chemical shifts, of transition metal carbonyls $[\text{M}(\text{CO})_6]^{n+}$, 45
- Carbon, $\text{Si}(\text{sp}^3)$ -C(sp^2) bonds
 - and chlor(s), possibly to hydrogen(s), silicon(s) bonded to, 187–190
 - and hydrogen(s), silicon(s) bonded to, 182–184
 - nitrogen(s) and, silicon(s) bonded to, 184–185
 - oxygen(s) and, silicon bonded to, 185–186
 - silicon bonded only to, 175–180
- ^{13}C -*cys*-labeled proteorhodopsin, 312
- ^{13}C -detected IPAP INADEQUATE, 298
- Chang–Pélissier–Durand Hamiltonian, 13

- Chemical shift (δ)
 in anisotropic liquid, 336, 345–346
 defined, 6
 in heavy-element systems
 benchmark data, spin-orbit effects,
 halogen dependence, 40–46
 gold cages and poly-oxo-metallates,
 63–66
 heavy-atom shielding, 46–52
 heavy metal, 52–62
 shielding tensor anisotropies, 66–68
 in isotropic liquid, 335
- Chiral discrimination, 369–375
 binuclear spin state selection for, 395–402
 ^{13}C edited 3Q-SQ spectrum, 397–402
 pulse sequence, 396–397
- BIRD module, in X–H correlation, 375
- ^{13}C experiment for, 369–370
- HETSERF for, 374
- ^1H NMR for
 advantage, 371
 (R/S)-3-butyn-2-ol, 373
 (R/S)-2-chloropropanoic acid, 371–373
 (R/S)-propylene carbonate, 373
 (R/S)-propylene oxide, 373
- ^2H NMR for, 370–371
- SERF for, 374
- single quantum spin selective correlation
 for, 402–411
 advantage and limitation, 410–411
 enantiomeric excess (ee), quantification,
 411
 (R/S)-3-butyn-2-ol, spectral analysis, 403
 (R/S)-propylene carbonate, spectral
 analysis, 403–408
 (R/S)-propylene oxide, spectral analysis,
 408–410
- Chiral liquid crystal (CLC), properties of,
 368–369
- Chiral molecules, 367–369
 and DOE, 368
 PBLG solvents, properties, 368–369
- ^{13}C -labeled $(\text{CH}_3)_2\text{COHSO}_3\text{Na}$, 308
- ^{13}C -labeled polycrystalline L-alanine, 311
- ^{13}C -labeled rhodopsins, 312
- CLC. *See* Chiral liquid crystal (CLC), 368–369
- Coherence order and spin state-selective
 (COS^3) transformations, 288
- Composite refocusing (CR), 285
 one-dimensional version of
 INADEQUATE with, 287
- Conductor-like screening model (COSMO),
 57, 65, 74–75, 79
- Continuous set of gauge transformations
 (CSGT), 28
- Core orbitals, relativistic effects and, 32
- Corundum ($\alpha\text{-Al}_2\text{O}_3$), 315
- COSMO. *See* Conductor-like screening model
 (COSMO), 57, 65, 74–75, 79
- COSY, 272, 311
- Coulomb's law, 4
- Coupled cluster (CC) ansatz, 9
- Couplings
 anisotropies, spin-orbit effects and, 80–83
 effects, 274
 homonuclear proton-proton, 106
 results
 general theory, 112–113
 $^1\text{J}(^{29}\text{Si}, ^{13}\text{C})$. *See* $^1\text{J}(^{29}\text{Si}, ^{13}\text{C})$ couplings,
 113–116
 ^{29}Si - ^{13}C . *See* ^{29}Si - ^{13}C couplings, 100
 spin-spin, 112
- CSGT. *See* Continuous set of gauge
 transformations (CSGT), 28
- [2,3- $^{13}\text{C}_2$]sodium propionate, 310
- ^{13}C spin state selected spectra, 395–396
 pulse sequence, 396–397
 3Q-SQ spectrum
 of (R/S)-3-butyn-2-ol, 397–399
 of (R/S)-propylene carbonate, 399–402
 1- ^{13}C -Val-A $\beta_{(10-35)}$, 308
- Cyclic carbosilanes
 dependence of $^1\text{J}(\text{Si}, \text{C})$, 118
- CYCLOPS, 270
- Cyclosilazoxanes, 117
- DANSOM, 343–344
- Darwin operator, 15–16, 25
- 3,3'-d $_2$ -camphor, 315
- DCB. *See* Dirac-Coulomb-Breit Hamiltonian
 (DCB), 9
- 2D correlated spectrum
 of (R/S)-propylene carbonate, 403–408
 of (R/S)-propylene oxide, 408–410
- Decoupling, 101
- Density functional theory (DFT), 8, 9, 16,
 18–19, 28, 33. *See also* ZORA DFT
 computations, 66, 67, 71
 computations, of transition metal chemical
 shifts, 3
 proton shift in HI and, 42
 Pt chemical shifts and, 55–57
 ^{125}Te shielding constants and, 48–49
- Deuterium (^2H)
 decoupling, 345
 natural abundance, 370–371
 order parameter from, 349
- DFT. *See* Density functional theory (DFT), 8,
 9, 16, 18–19, 28, 33

- DFT-ZORA method. *See* ZORA DFT computations, 66, 67, 71
- Diamagnetic (bilinear) perturbation operators, 18
- Diamagnetic shielding, 26, 44
- Diamagnetic spin-orbital (DSO), 22
- Diels–Alder poly(phenylene) polymer membranes, 306
- Differential ordering effect (DOE), and chiral molecules, 368
- Diffusion-controlled echo attenuation, 321
- 1,4-difluorobenzene, ^1H NMR spectra of, 361–363
- 2,6-difluoropyridine, ^1H NMR spectra of, 357–361
- Dipolar-assisted rotational resonance (DARR), 312
- Dipolar couplings
- in aligned molecules, 336–338
 - in anisotropic liquids, 338
 - in isotropic liquids, 337–338
 - pseudo-dipolar coupling, 338
 - and spin system, 337
- of lecithin molecules, 306
- of weakly aligned molecules, 363–364
- bicelles, orientation in, 364–367
 - thermotropic liquid crystals, 364
- Dipolar dephasing, 311
- Dipolar recovery with a windowless sequence, 308
- Dipolar shift correlation spectroscopy, 310
- Dirac–Coulomb–Breit Hamiltonian (DCB), 9
- Dirac delta function, 112
- Dirac equation, 10–11, 22, 24, 35–36
- DKH method. *See* Douglas–Kroll–Hess (DKH) method, 14, 20, 48, 86
- DNA oligomers, 308
- 3,3'-d₂-norcamphor, 315
- DOE. *See* Differential ordering effect (DOE), 368
- Double J-modulated (DJM), 298
- Double quantum coherences (DQCs), 267, 270
- Double quantum crosspolarization (DQCP), 314
- Double quantum filters (DQF)
- localized single shot, 317
 - in the solid state and in ordered phases, 271
 - in spatially resolved NMR, 271
- Double quantum pulses, 277
- Double quantum selective refocusing (DQSERF), 375, 385–386
- in A₃ spin system, 379
 - in AX spin system, 385
 - τ delay in, 381
 - and enantiomeric excess (ee), 384
 - in A₃MX spin system, 385
 - spin dynamics in, 377–378
 - vs. SERF, 385
 - in A₃X spin system, 385
- Double quantum transitions for finding unresolved lines' (DOUBTFUL), 297
- Double resonance, 106
- Double single quantum, 311–312
- Douglas–Kroll–Hess (DKH) method, 14, 20, 48, 86
- DKH1 scheme, perturbation operator in, 24
- DQ coherence transfer spectroscopy, 320–321
- DQ-DRAWS, 308, 309
- DQ filtering prior to evolution (DOPE), 312
- DQ filtering prior to evolution (DOPE) and after mixing (DOAM), 312
- DQ filtration, 282
- DRAMA, 278–279
- two-pulse sequence, 279
- DSO. *See* Diamagnetic spin-orbital (DSO), 22
- Dysprosium bis(tripolyphosphate), 304
- Dysprosium triethylenetetramine-*N,N,N',N'',N''',N''''*-hexaacetic acid (TTHA), 304
- E-COSYpattern, 108, 109
- ECPs. *See* Effective core potentials (ECPs), 15, 39
- Effective core potentials (ECPs), relativistic, 15, 39
- ^{235}U chemical shifts and, 54
- EFG. *See* Electric field gradients (EFG), 3, 83–87
- Einstein's special relativity, 2, 4
- Electric field gradients (EFG), NMR
- computations and, 3, 83–87
 - operator, 83–84
- Electron correlation effects, on heavy-nucleus shielding, 46, 48
- Electronegativity
- Pauling, 119
 - spin–spin couplings and, 115
- Electron–electron Coulomb repulsion, 15
- Electron–electron SO operator, 16
- Electronic *g*-factor, 22
- Elimination of small component (ESC) scheme, 11–12, 14
- Enantiomeric excess (ee)
- DQSERF and, 384
 - spin selective correlation experiment and, 411

- endoneurium, 303
Energy (E)
 computing second derivatives of, 16–20
 defined, 7–8
 and wavefunctions, 8–16
epineurium, 303
Erythrocytes, 305
ESC scheme. *See* Elimination of small component (ESC) scheme, 11–12, 14
- FC+SD-OP mechanism, 38
FC term, in PbH_4 , 33–38
Fermi contact term, 113–114
 spin–spin couplings and, 115
First-order response, $7n$
First-principles theory, 7
 NMR parameters from, analyzing, 30–32
Five spin system, ^1H NMR spectra of, 357–361
Foldy–Wouthuysen transformation, 12
- Galilei’s principle of relativity, 2, 4
gauge including atomic orbital (GIAO), 28–29
gHSQC-RELAY (D) pulse sequence, 109–110, 111
gHSQC-RELAY (P) pulse sequence, 109–110
GIAO. *See* Gauge including atomic orbital (GIAO), 28–29
Glassy thiophosphates, 313
Glycine, 308
Gravitational forces, $2n$
- HAHA. *See* Heavy-atom (relativistic) effects on heavy-atom (HAHA), 33, 38, 40, 48, 51, 63
HALA. *See* Heavy-atom effect on light-atom (HALA), 33, 38
Halogen dependence, proton chemical shifts and, 40–46
Hamiltonian, of aligned molecules, 335
HAOHA. *See* Heavy atom-other heavy atom (HAOHA), 51, 63
Hartmann–Hahn matching, 314
Hartree atomic units (a.u.), 4
Hartree–Fock (HF) method, 8, 28, 69
 ^{125}Te shielding constants and, 48–49
 ^1H – ^{13}C HMQC experiment, 109
Heavy-atom effect on light-atom (HALA), 33, 38
Heavy-atom-heavy-atom coupling constants, 73–79
Heavy-atom-light-atom couplings, 69–73
Heavy atom-other heavy atom (HAOHA), 51, 63
Heavy-atom (relativistic) effects on heavy-atom (HAHA), 33, 38, 40, 48, 51, 63
Heavy-atom shielding, 46–52
Heavy-element systems
 chemical shifts in
 benchmark data, spin–orbit effects, halogen dependence, 40–46
 gold cages and poly-oxo-metallates, 63–66
 heavy-atom shielding, 46–52
 heavy metal, 52–62
 shielding tensor anisotropies, 66–68
 spin–spin coupling in
 heavy-atom-heavy-atom coupling constants, 73–79
 heavy-atom-light-atom couplings, 69–73
 small-molecule benchmark data, 68–69
 spin–orbit effects and coupling anisotropies, 80–83
 two/multi-bond couplings, 79–80
 valence orbitals in, 5
Heavy metal chemical shifts, 52–62
Heavy-nucleus shielding, electron correlation effects on, 46
Hellmann–Feynman theorem, 17, 19
Hermitian operator, $17n$
Heteronuclear INADEQUATE, 100
 pulse sequence, 101
Heteronuclear recoupling sequences, 281
Heteronuclear selective refocusing (HETSERF), 374
HET-s(218–289), 310
HETSERF. *See* Heteronuclear selective refocusing (HETSERF), 374
Hexadecanoic acid, 298
Hexahypothiophosphate, 313
Hexamethylbenzene (HMB), 310
Hexanoic acid, 298
HF method. *See* Hartree–Fock (HF) method, 8, 28, 69
Hg chemical shifts, NMR computations and, 61–62, 66
Hg–Hg coupling constants, 76, 78
HI, spin–orbit shielding in, 37–38
 ^1H NMR spectra
 anisotropic chemical shift, 345–346
 deuterium decoupling, 345
 of 1,4-difluorobenzene, 361–363
 of 2,6-difluoropyridine, 357–361
 energy level connectivity, 346–349
 MQ NMR. *See* Multiple quantum (MQ) coherence, 266, 349–350
 natural abundant deuterium for, 349
 of (*R/S*)-3-butyn-2-ol, 373
 of (*R/S*)-2-chloropropanoic acid, 371–373

- of (*R/S*)-propylene carbonate, 373
- of (*R/S*)-propylene oxide, 373
- of weakly dipolar coupled spins. *See*
Dipolar couplings, of weakly aligned
molecules, 306, 336–338, 363–367
- Z-COSY experiment, 346–349
- [3,3'-²H₂]norcamphor, 300
- Homogeneity, of aligned molecules, 341
- Homonuclear proton–proton couplings, 106
- Homonuclear scalar couplings, 311
- HORROR, 281
- Hückel theory, 68, 78
- HXeCCH molecule, as model for
organo-xenon compounds, 50–51
- HX series
 - computed halide shielding constants
in, 47
 - computed proton chemical shifts
in, 41–42
- Hydroxyapatite, 313
- Hyperconjugation
 - effect of, ²⁹Si-¹³C couplings, 123–126
- IGLO. *See* Individual gauge of localized
orbitals (IGLO), 28
- IHD. *See* Inverse halogen dependence (IHD),
44, 46
- INADEQUATE experiment, 101
- Incredible Natural Abundance Double
QUAntum Transfer Experiment
(INADEQUATE), 268–271
 - offset-compensated, 275
 - phase cycling, 269–270
 - pulse sequence, 269
 - basic J-compensated, 275, 276
 - INEPT, 277
 - symmetric, 271*n*
- Individual gauge of localized orbitals (IGLO),
28
- INEPT-(Si, C, Si)gHMQC, 104–105
 - pulse sequence, 103
- INEPT-(Si, C)gCOSY, 103–104
- Infinite-order regular approximation (IORA),
14
- Internuclear repulsion potential (*V*_{NN}), 8–9,
8*n*
- Intra-axonal compartments, 303
- Inverse halogen dependence (IHD), 44, 46.
See also Halogen dependence, 40–46
- IORA. *See* Infinite-order regular
approximation (IORA), 14
- ISIS mode, 316
- Isotope effects, NMR computations and,
29–30
- Isotope-induced chemical shifts
¹J(Si, C) and, 129–130
- Isotropic liquids
 - chemical shift in, 335
 - dipolar coupling in, 337–338
 - quadrupolar interaction in, 339
- Jeener–Broekaert sequence, 304
- ¹J(Si, C) couplings
 - correlation between ¹J(²⁹Si, ¹⁵N) and, 119
 - dependence of, in cyclic carbosilanes, 118
 - and isotope-induced chemical shifts,
129–130
 - values of, 120, 122
- ¹J(²⁹Si, ¹³C) couplings, 113–116
 - aminosilanes, 117–119
 - assignments, 130–131
 - complexes, 128–129
 - ¹J(Si, C) and isotope-induced chemical
shifts, 129–130
 - Si = C, Si = Si bonds, 123
 - Si–C≡C fragments, 126–128
 - Si–C=C fragments, 119–123
 - silacyclobutanes and silacyclopentanes,
117
- ¹J(²⁹Si, ¹⁵N)
 - correlation between ¹J(Si, C) and, 119
- ²⁹J(Si-¹³C) couplings, over two and more
bonds
 - ⁿJ(Si, C)
 - signs, 131–133
 - values of, 133–135
 - structural studies, 135–136
- K*_{AB}. *See* Spin–spin coupling, 6–8, 39, 112
- Kohn–Sham (KS) equations, 18, 28
- KS equations. *See* Kohn–Sham (KS)
equations, 18, 28
- ¹³⁹La chemical shifts, ZORA DFT
computations and, 54–55
- Lactic acid, 320–321
- LAOCOONOR, 343
- Larmor frequency, 277
- LBR sequence, 288
 - 1D INADEQUATE, 288
- LCNMR. *See* Liquid-crystal NMR (LCNMR),
66
- Lee Goldberg (LG) sequences, 346
- LG sequences. *See* Lee Goldberg (LG)
sequences, 346
- Linear response equation, 17
- Liquid crystalline phases, 302–303
- Liquid-crystal NMR (LCNMR), 66

- Liquid crystals, molecules alignment in
 chemical shift
 in anisotropic liquid, 336
 in isotropic liquid, 335
 dipole–dipole coupling, 336–338
 Hamiltonian, 335
 homogeneity, 341
 order parameter, in nematic phase,
 339–341
 and experimental conditions, 341
 and molecular symmetry, 340–341
 quadrupolar interaction, 338–339
 spectral analysis. *See* Spectral analysis, of
 oriented molecules, 342–344
 spin system, 341–342
- Localized orbital/local origin (LORG), 28
- Lone-pair effect, 120
- Lorentzian component, 305
- LORG. *See* Localized orbital/local origin
 (LORG), 28
- MAD. *See* Mean absolute deviation (MAD),
 48
- Magic angle spinning (MAS), 271
- Magnetic moment, 6, 7, 22
- [M(CO)₆]ⁿ (transition metal carbonyls),
 carbon chemical shifts of, 45
- MCSCF. *See* Multiconfigurational SCF
 (MCSCF), 28, 33, 37
- Mean absolute deviation (MAD), 48
- Methionine, 308
- Methylethoxysilanes, 116
- MOBILE Universal Surface Explorer
 (MOUSE), 319–320
- Molecules alignment, in liquid crystals
 chemical shift
 in anisotropic liquid, 336
 in isotropic liquid, 335
 dipole–dipole coupling, 336–338
 Hamiltonian, 335
 homogeneity, 341
 order parameter, in nematic phase,
 339–341
 and experimental conditions, 341
 and molecular symmetry, 340–341
 quadrupolar interaction, 338–339
 spectral analysis. *See* Spectral analysis, of
 oriented molecules, 342–344
 spin system, 341–342
- Monte-Carlo-type (MC) simulations, 30
- MQ coherence. *See* Multiple quantum (MQ)
 coherence, 266, 349–350
- MTAI. *See* *N*-methyl-*N,N,N*-
 trioctadecylammoniumiodide (MTAI),
 364
- Multiconfigurational SCF (MCSCF), 28, 33, 37
- Multi-exponential relaxation, 305
- Multiple quantum coherences (MQCs), 266,
 349–350
 for acetonitrile, 351–355
 ¹³C DQ-SQ coherence, 353–355
 DQ-SQ coherence, 355
 3Q-SQ coherence, 351–353
 defined, 267
 2D experiments, 272
 2D MQ-SQ correlation, 350–351
 for *ortho*-difluorobenzene, 355–356
 preparation, 271–277
 under conditions of multi-exponential
 relaxation, 282–283
- N. madagascariensis*, 310
- N*-acetylalanine, 322
- N*-acetyl-L-valine, 308
- NADH *c*-2'-phosphate (NADPH), 297
- Nafion, 306
- Natural bond orbitals (NBOs), 30
- Natural localized MOs (NLMOs), 31
 Pb–H spin–spin coupling in PbH₄
 and, 37
 in [PtCl₄]²⁻ and [PtCl₆]²⁻, 60–61
- Na₂ZrO₃, 316
- NBOs. *See* Natural bond orbitals (NBOs), 30
- NHD. *See* Normal halogen dependence
 (NHD), 37–38, 42, 46
- β-nicotinamide adenine dinucleotide
 (NADH), 297
- ¹⁵N-labeled 2-ureido-4[¹H]-pyrimidinone,
 306
- NLMOs. *See* Natural localized MOs
 (NLMOs), 31
- N*-methyl-*N,N,N*-trioctadecylammonium-
 iodide (MTAI), 364
- NMR computations, relativistic methods for,
 4
 benchmarks for, and case studies
 acronyms used, 32
 electric field gradients, 83–87
 FC term in PbH₄ and spin–orbit
 shielding in HI, 33–38
 heavy-element systems. *See* Heavy-
 element systems, 40–80
 energy, computing second derivatives of,
 16–20
 first-principles, analyzing parameters
 from, 30–32

- nuclear magnetic shielding, 26–27
 gauge-origin problem for, 28–29
nuclear shielding, 6–8
 requirement of, time for, 38–40
special relativity in chemistry, importance of, 5–6
spin–spin coupling, 6–8
 indirect nuclear, 27–28
vibrational and thermal averaging
 isotope effects, 29–30
vs. nonrelativistic
 energy and wavefunctions, 8–16
 perturbation operators, 20–26
NMR *K*-coupling, 7
4-*n*-octyloxybenzoic acid, 341
NOE. *See* Nuclear Overhauser Effect (NOE), 98
Nonrelativistic many-electron theory, 9
Non-selective elements, 286
Normal halogen dependence (NHD), 37–38, 42, 46. *See also* Halogen dependence, 40–46
Nuclear Magnetic Resonance, Specialist Periodical Reports series, 3
Nuclear magnetic shielding, 26–27
 gauge-origin problem for, 28–29
Nuclear magneto-gyric ratio, 6
Nuclear Overhauser Effect (NOE), 98
Nuclear quadrupole coupling tensor, 3
Nuclear shielding, 6–8
Nutation frequencies, 277, 316
Nylon-6 fibers, 306

Off-magic angle spinning (OMAS), 313
One bond, silicon–carbon couplings, 116
 measurement of, 114
One-dimensional experiments, 106–108
One-electron magnetic perturbation operators, 21
One-pulse experiments
 of ^{13}C , 98, 99
 of ^{29}Si , 98, 99
OP–OZ term, defined, 26*n*
Optimal control theory, 281
Order parameter, of aligned molecule, 339–341
 and experimental conditions, 341
 and molecular symmetry, 340–341
ortho-difluorobenzene, MQ coherence, 355–356
orthothiophosphate, 313

Paramagnetic (bilinear) perturbation operators, 18
Paramagnetic spin–orbital (PSO), 22
Passive nucleus, 108

Pauli DFT approach, 52
 for tetraoxo-metallates, 53
 tungsten chemical shifts and, 52
 ^{235}U chemical shifts and, 54
Pauli Hamiltonian, 12, 15, 43
Pauling electronegativities, 119
Pauli SO operator, 62, 69
Pauli spin-matrices, 9, 11
Pb chemical shifts, ZORA DFT computations and, 51–52
PbH₄, FC term in, 33–38
Pb–H spin–spin coupling constant, in plumbanes, 33–35
 ^{31}P – ^{13}C HMQC experiment, 109
Perturbation, 106
 operators, for NMR, 20–26
Perturbation theory, relativistic, 15, 43, 47
 nonsingular four-component, 43*n*
Phase cycling, 101, 288
Phase of the preparation sandwich, 275*n*
Phase shift, 267
 of the reconversion sequence, 268*n*
[(Ph₃PAu)₆C]²⁺, structure of, 63–64
Picture-change effects, 11*n*
Planck's constant, 4
Plumbanes, Pb–H spin–spin coupling constant in, 33–35
Point resolved spectroscopy (PRESS), 319
Polarization transfer experiments
 ^{29}Si , 99
Poly- γ -benzyl-L-glutamate (PBLG), 334
 first order analysis of, 371–374
 properties of, 368–369
1,4-*cis*-poly(isoprene), 319–320
Poly-oxo-metallates (POM), 64–66
Polyvinazene (PV), 307
POM. *See* Poly-oxo-metallates (POM), 64–66
Proton–proton couplings, 106
Pseudo-dipolar coupling, 338
Pt chemical shifts, NMR computations and, 55–61
[PtCl₄]²⁻ and [PtCl⁶]²⁻, NLMOs in, 60–61
Pt–Pt spin–spin coupling, 73–74
Pt[S₂C₂(CF₃)₂]₂ (Pt bis-dithiolene), 57–58
Pt–Ti bonded complexes, metal chemical shifts of, 56–57
Pt–Ti coupling constants, 75–77
Pulse sequence, 396–397
 gHSQC-RELAY (D), 109–110, 111
 gHSQC-RELAY (P), 109–110
 heteronuclear INADEQUATE, 101
 INEPT-(Si, C, Si)gHMQC, 103, 104
 INEPT-(Si, C)gCOSY, 103
[PW₁₁TiO₄₀]⁵⁻, structure of, 65
Pyrothiophosphate, 313

- QED. *See* Quantum electrodynamics (QED), 9
- Quadrupolar interaction, liquid crystals,
338–339
in anisotropic liquid, 339
in isotropic liquid, 339
secular, 338
- Quadrupole–EFG interaction, 83
- QUADSHIFT experiment, 315
- Quantum electrodynamics (QED), 9
- Quasi-axial (endo), silicon-bonded methyls
one-bond silicon–carbon couplings for, 128
- Quasi-equatorial (exo), silicon-bonded
methyls
one-bond silicon–carbon couplings for,
128–129
- “Quasi-relativistic”, 12
- Quaternary ammonium, 364
- Ramsey equations, 22
- Ramsey’s formulas, 112
- Rat sciatic nerve, 303
- RbNO₃, 316
- Reconversion strategy for a DQF experiment,
285
CR reconversion, 285–288
detuned LBR sequence, 293–294
LBR reconversion, 288–293
reconversion in the solid state, 294–296
signal resulting on reconversion of MQC
mediated by multi-exponential
relaxation, 296–297
- Recoupled polarization transfer (REPT), 306
- REDOR, 312
- Relativistic effects
in chemistry, importance of, 5–6
on coupling, 39
defined, 2
on heavy-atom shieldings, 46
on NMR parameters, 27–28
scalar, 46
- Relativistic quantum chemical methods, 8–16
- Relativistic scaling factors (RSFs), 68
- Relativistic *vs.* nonrelativistic approaches,
20–26
- Relaxation effects, 289, 290
- Residual quadrupolar coupling, 305
- RFDR, 278
zero quantum dipolar recoupling
sequence, 311
- ¹⁰³Rh NMR, 6
- Rotational resonance, 281–282
- (*R/S*)-3-butyn-2-ol
BASE-β-COSY of, 412
¹H NMR spectra of, 373
- 3Q-SQ spectrum of
¹³C spin state selected spectra, 397–399
spin state selective coherence transfer,
389
soft-COSY spectrum of, 403
- (*R/S*)-2-chloropropanoic acid
¹H NMR spectra of, 371–373
- 3Q-SQ spectra
spin state selective coherence transfer,
387–389
- RSFs. *See* Relativistic scaling factors (RSFs), 68
- (*R/S*)-propylene carbonate
2D correlated spectrum of, 403–408
¹H NMR spectra of, 373, 390–391
- 3Q-SQ spectra
¹³C spin state selected spectra, 399–402
spin state selective coherence transfer,
389
- (*R/S*)-propylene oxide
2D correlated spectrum, 408–410
¹H NMR spectra, 373
spin state selective coherence transfer
¹H NMR spectra, 391, 394
3Q-SQ spectra, 389
- ⁹⁹Ru chemical shifts, 53–54
- SAPA. *See* Sum-of-atomic-potentials
approximation (SAPA), 14
- Satellites
¹³C, in ²⁹Si, 100
²⁹Si, in ¹³C, 100
- Satellite transition (ST₁), 315–316
- Scalar-relativistic approach, 13
- Schrödinger equation, 4, 8
- Second order energy derivatives, computing,
16–20
- Second-order regular approximation (SORA),
44
- SEDRA, 278
- Selective polarization transfer (SPT), 106
- Selective refocusing (SERF), 375
magnetization in, 376–377
spin dynamics in, 376
vs. DQSERF, 385
- Self-consistent field (SCF) procedure, 19
- SEMINA-2 pulse sequence, 284
- SEMINA sequence, 283–284
- SEMINA-1 sequence for SEMUT edited
INADEQUATE, 284
- SEMUT type editing, 283–284
- ²⁹Si
coupling with ¹³C. *See* ²⁹Si-¹³C couplings,
100
INADEQUATE experiment, 101

- one-pulse experiments, 98, 99
- polarization transfer experiments, 99
- properties of, 98–100
- satellites in ^{13}C , 100
- Si–Br–Si bridging
 - in trisilylamine, 119
- Si=C bond, 123
- Si–C \equiv C fragments, 126–128
- Si–C=C fragments, 119–123
- ^{29}Si – ^{13}C couplings, 100
 - absolute values, 100
 - effect of hyperconjugation, 123–126
 - INEPT–HMQC correlation, 102–105
 - INEPT–(Si, C, Si)gHMQC and, 104–105
 - INEPT–(Si, C)gCOSY and, 103–104
 - magnitudes of, measurement of, 100–105
 - over two and more bonds
 - $^1\text{J}(\text{Si}, \text{C})$ signs, 131–133
 - results
 - general theory, 112–113
 - $^1\text{J}(^{29}\text{Si}, ^{13}\text{C})$ couplings. *See* $^1\text{J}(^{29}\text{Si}, ^{13}\text{C})$ couplings, 113–116
 - with signs, 105
 - one-dimensional experiments, 106–108
 - two-dimensional experiments, 108–111
- ^{19}Si chemical shifts, 43
- Si–C \equiv C fragment in molecule, Si(sp³)–C(sp) bond and
 - more than two, 240–244
 - one, 230–234
 - two, 234–240
- Silacyclobutanes, 117
- Silacyclopentanes, 117
- Si–carbon coupling constants
 - in complexes, 248–264
- Si(sp³)–C(sp) bond and
 - ring/within ring, silicon(s) bonded to, 244–248
 - Si–CR \equiv C fragment in molecule, more than two, 240–244
 - Si–CR \equiv C fragment in molecule, one, 230–234
 - Si–CR \equiv C fragment in molecule, two, 234–240
 - X₃Si–C \equiv N structures, 248
- Si(sp³)–C(sp²) bonds and
 - carbons, silicon bonded only to, 175–180
 - carbons and hydrogen(s), silicon(s) bonded to, 182–184
 - chlor(s) and carbon(s) and possibly to hydrogen(s), silicon(s) bonded to, 187–190
 - nitrogen(s) and carbon(s), silicon(s) bonded to, 184–185
 - oxygen(s) and carbon(s), silicon bonded to, 185–186
 - to ring(s), Si bonded to. *See* Si(sp³)–C(sp²) bond, Si bonded by, to ring(s), 192–202
 - within ring(s), Si bonded by. *See* Si(sp³)–C(sp²) bond, Si bonded by, within ring(s), 203–228
 - ring(s)/within ring(s) by Si(sp³)–C(sp³) bond(s), silicon bonded to, 190–191
 - X = Y = Z fragment(s), silicon bonded to, 228–229
- Si(sp³)–C(sp³) bonds and
 - bi-cycles and multi-cycles, silicon(s) within, 171–175
 - five-membered ring, silicon(s) within, 163–167
 - four-membered ring, silicon(s) bonded to, 162–163
 - Si–chalcogen and possible Si–N/Si–Si bond(s), 150–157
 - Si–C/Si–H bonds, 142–144
 - silicon-halogens bonds and possible silicon bonds to chalcogens, N, Si or H, 157–158
 - silicon(s) bonded to cycle(s), 159–161
 - Si–N/Si–P and possible Si–Si/Si–H bonds, 145–150
 - Si–Si/Si–Sn and possible Si–H bonds, 145
 - six-membered and larger rings, silicon(s) within, 167–169
 - two rings, silicon(s) within, 169–170
- β -silyl hyperconjugation, 125–126
- α -silylstyrenes, 119
- Single quantum spin selective correlation, for chiral discrimination, 402–411
 - advantage and limitation, 410–411
 - enantiomeric excess (ee), quantification, 411
- spectral analysis
 - (*R/S*)-3-butyn-2-ol, 403
 - (*R/S*)-propylene carbonate, 403–408
 - (*R/S*)-propylene oxide, 408–410
- Si(OMe)₄
 - ^1H – ^{29}Si Ψ -BIRD-HMQC experiment, applied to, 109
- Si=Si bonds, 123
- Si(sp³)–C(sp) bond, silicon-carbon coupling constants in molecules containing
 - ring/within ring, silicon(s) bonded to, 244–248
- Si–CR \equiv C fragment in molecule, more than two, 240–244

- Si-CR \equiv C fragment in molecule, one, 230–234
- Si-CR \equiv C fragment in molecule, two, 234–240
- X₃Si-C \equiv N structures, 248
- Si(sp³)-C(sp²) bond, Si bonded by to ring(s)
- heteroaromatic, 201
 - more five-membered, 195–196
 - one five-membered, 192–194
 - six-membered, 196–198
 - six-membered, and by Si(sp³)-X(sp³) bond(s) to/within other cycles, 199–200
 - six-membered, and to substituted vinyl(s)/C \equiv O, 200–201
 - spiro structures/to other bi-cycles, 201–202
- within ring(s)
- 1-azonia-2-sila-5-boratoles, 203–209
 - bi-cycles, 223–226
 - four-membered, 203
 - 1-oxonia-2-sila-5-boratoles, 209–211
 - 1-sila-2, 4-cyclopentadienes, 213–218
 - silacyclohepta-2-enes and disilacycloheptadienes, 221–223
 - silacyclohexa-2-enes, 219–221
 - silacyclopenta-2-enes, 219
 - 1-thionia-2-sila-5-boratoles and 1-selenia-2-sila-5-boratoles, 211–213
 - tri-cycles and tetra-cycle, 227–228
- Si(sp³)-C(sp²) bonds, silicon-carbon coupling constants in molecules containing
- carbons, silicon bonded only to, 175–180
 - carbons and hydrogen(s), silicon(s) bonded to, 182–184
 - chlor(s) and carbon(s) and possibly to hydrogen(s), silicon(s) bonded to, 187–190
 - nitrogen(s) and carbon(s), silicon(s) bonded to, 184–185
 - oxygen(s) and carbon(s), silicon bonded to, 185–186
 - to ring(s), Si bonded to. *See* Si(sp³)-C(sp²) bond, to ring(s), Si bonded by, 192–202
 - within ring(s), Si bonded by. *See* Si(sp³)-C(sp²) bond, within ring(s), Si bonded by, 203–228
 - ring(s)/within ring(s) by Si(sp³)-C(sp³) bond(s), silicon bonded to, 190–191
 - X = Y = Z fragment(s), silicon bonded to, 228–229
- Si(sp³)-C(sp³) bonds, silicon-carbon coupling constants in molecules containing
- bi-cycles and multi-cycles, silicon(s) within, 171–175
 - five-membered ring, silicon(s) within, 163–167
 - four-membered ring, silicon(s) bonded to, 162–163
 - Si-chalcogen and possible Si-N/Si-Si bond(s), 150–157
 - Si-C/Si-H bonds, 142–144
 - silicon-halogens bonds and possible silicon bonds to chalcogens, N, Si or H, 157–158
 - silicon(s) bonded to cycle(s), 159–161
 - Si-N/Si-P and possible Si-Si/Si-H bonds, 145–150
 - Si-Si/Si-Sn and possible Si-H bonds, 145
 - six-membered and larger rings, silicon(s) within, 167–169
 - two rings, silicon(s) within, 169–170
- Six spin system, ¹H NMR spectra of, 361–363
- SO coupling. *See* Spin-orbit (SO) coupling, 10, 15, 27–28, 37–38, 40, 45
- Sodium ammonium tartarate tetrahydrate, 314
- Sodium pyrophosphate decahydrate, 313
- Soft-COSY spectrum, 402
- advantage of, 410–411
 - of (*R/S*)-3-butyn-2-ol, 403
- Solid-state NMR (SSNMR), 3
- SOO interaction. *See* Spin-other orbit (SOO) interaction, 16, 25
- SORA. *See* Second-order regular approximation (SORA), 44
- SOS equation. *See* Sum-over-states (SOS) equation, 17–18, 28
- Spectral analysis, of oriented molecules, 342–344
- automatic analysis, 343–344
 - DANSOM for, 343–344
 - LAOCOONOR for, 343
 - simulation for, 343
- Spectral editing, 283–284
- S-PEEK, 306
- SPI. *See* Selective polarization transfer (SPT), 106
- Spin
- decoupling, 106, 107
 - filtering, 283
 - tickling, 106, 107
- Spin-dipolar term, 117
- Spin-free relativistic approach, 13
- Spin-orbital term, 117

- Spin-orbit effects and coupling anisotropies, 80–83
- Spin-orbit shielding, in HI, 37–38
- Spin-orbit (SO) coupling, 10, 15, 27–28, 37–38, 40, 45
- effects, 3
 - for EFGs of heavy-element molecules, 85
- Spin-other orbit (SOO) interaction, 16, 25
- Spin-spin couplings, 6–8, 39, 112
- electronegativity and, 115
 - Fermi contact term and, 115
 - in heavy-element systems
 - heavy-atom–heavy-atom coupling constants, 73–79
 - heavy-atom–light-atom couplings, 69–73
 - small-molecule benchmark data, 68–69
 - spin-orbit effects and coupling anisotropies, 80–83
 - two/multi-bond couplings, 79–80
 - indirect nuclear, 27–28
- Spin state selective coherence transfer
- enantiomeric discrimination, 386–387
 - field inhomogeneity removal, 390
- ^1H NMR spectra
- of (*R/S*)-propylene carbonate, 390–391
 - of (*R/S*)-propylene oxide, 391, 394
- 3Q–SQ spectra
- (*R/S*)-3-butyne-2-ol, 389
 - (*R/S*)-2-chloropropanoic acid, 387–389
 - (*R/S*)-propylene carbonate, 389
 - (*R/S*)-propylene oxide, 389
- and relative signs of couplings, 394
- Spin system
- and dipolar couplings, 337
 - nomenclature of, 341–342
- SPT. *See* Selective polarization transfer (SPT), 106
- SR26₄, 313
- Sum-of-atomic-potentials approximation (SAPA), 14
- Sum-over-states (SOS) equation, 17–18, 28
- Surface-immobilized peptides, 309
- SYNCHRON4, 309
- ^{181}Ta NMR chemical shifts, ZORA DFT computations and, 53
- Tc–O spin–spin coupling, 29
- TEDOR, 278
- ^{125}Te shielding constants, HF and DFT and, 48–49
- Tetraphenyldiphosphine-1-oxide, 313
- Transition metal chemical shifts
- DFT computations of, 3
- Trisilylamine
- Si–Br–Si bridging in, 119
- Two-dimensional experiments, 108–111
- Two-electron (2e[−]) SO operators, 44
- Two/multi-bond couplings, 79–80
- Ubiquitin, 310
- ^{235}U chemical shifts, ZORA DFT computations and, 54
- Ultrahigh resolution NMR, 100
- Valence orbitals
- in heavy atoms, 5
 - relativistic effects and, 32
- Vector potential, 20
- V_{NN} . *See* Internuclear repulsion potential (V_{NN}), 8–9, 8*n*
- W_{Au12}, Au–Au spin–spin couplings in, ^{183}W chemical shifts and, 63
- Wavefunctions, energy (*E*) and, 8–16
- ^{183}W chemical shifts, 52
- and Au–Au spin–spin couplings in W_{Au12}, 63
- ^{129}Xe chemical shifts, scalar ZORA DFT computations for, 50
- Xenon, NMR computations and, 49–51
- ^{129}Xe chemical shifts, 50
- X–H correlation experiments, BIRD module in, 375
- $\text{X}_3\text{Si}-\text{C}\equiv\text{N}$ structures, Si(sp³)–C(sp) bond and, 248
- X = Y = Z fragment(s), silicon bonded to Si(sp³)–C(sp²) bonds and, 228–229
- Zero quantum coherence (ZQC), 267
- Zeroth-order regular approximation (ZORA) operator, 13–15, 20, 22–24, 31, 35–36, 48–49
- z filter, 284, 298, 311, 321
- Zinc acetate, 308
- ZLI-1167, 341
- ZORA DFT computations, 66, 67, 71
- Hg chemical shifts and, 61–62
 - ^{139}La chemical shifts and, 54–55
 - Pb chemical shifts and, 51–52
 - Pt chemical shifts and, 57–59
 - ^{181}Ta NMR chemical shifts, 53
 - tungsten chemical shifts and, 52
 - ^{235}U chemical shifts and, 54
 - for Xe shieldings, 49–50
- ZORA operator. *See* Zeroth-order regular approximation (ZORA) operator, 13–15, 20, 22–24, 31, 35–36, 48–49
- ZORA SO DFT approach, 51